UNIVERSITY OF LATVIA
FACULTY OF PHYSICS, MATHEMATICS AND OPTOMETRY
PHYSICS DEPARTMENT

ON-CHIP NANOELECTROMECHANICAL SWITCHES FOR OPERATION AT ROOM AND CRYOGENIC TEMPERATURES

DOCTORAL THESIS

Author **Liga Jasulaneca**
Supervisor Prof. *Dr. Chem.* **Donats Erts**

RIGA 2024

Abstract

The demand for low-power portable devices has led to a search for alternatives to the fundamental component of computing and logic – the electronic transistor. The nanoelectromechanical (NEM) switch is one such alternative device whose leakage current in the off state is negligible, because the current-carrying components are physically separated. The exploration of these switches at low temperatures is motivated by their potential applications in space and quantum technologies.

Researchers are considering bottom-up synthesized 1D nanostructures as future electronic components due to their high quality and material diversity. However, these nanostructures exhibit significant variation in morphology and electromechanical properties, making their application in integrated NEM switches challenging. Another challenge is their integration with the existing planar technology.

To overcome these challenges, this Thesis investigates bottom-up grown copper oxide (CuO), bismuth selenide (Bi_2Se_3), and germanium (Ge) semiconductor 1D nanostructures as active elements in NEM switches. This study aims to develop switch technology and expand its applications using the unique properties of semiconductor nanostructures grown by the bottom-up method. The work involves synthesizing nanostructures, characterizing their morphology, electrical and mechanical properties, transferring and aligning them onto substrates, and creating and characterizing NEM switches at room and cryogenic temperatures.

NEM switch operation is studied *in situ* in a scanning electron microscope and in integrated devices. The fabricated integrated NEM switches demonstrate repeatable switching, implementing both logic and memory functions. The switch operation is achieved at room temperature and down to 2 K, with a minimum switch-ON voltage of 4.5 V and a maximum ON/OFF state current ratio of 10^3. A novel type of control in a NEM switch is demonstrated, based on measuring the current that flows through the nanostructure during deformation.

The results presented in this Thesis open possibilities for developing faster and more robust memory and mechanical computing devices, as well as more sensitive sensors for a wide range of operational temperatures.

The results are published in 11 scientific papers.

Keywords: nanoelectromechanical switches; nanowires; nanoribbons; cryogenic temperatures; Bi_2Se_3; CuO; Ge.

CONTENTS

1 Introduction **9**

1.1 Motivation . . . 9

1.2 Research aim . . . 10

1.3 Research objectives . . . 10

1.4 Theses to be defended . . . 10

1.5 Scientific novelty . . . 11

1.6 Practical significance . . . 12

1.7 Author's contribution . . . 12

1.8 List of publications . . . 13

2 Literature review and theoretical background **15**

2.1 Nanoelectromechanical switches . . . 15

2.1.1 State-of-the-art NEM switches and their characteristics . . . 15

2.1.2 The simplest model of a NEM switch . . . 17

2.2 Quasi-one-dimensional semiconductor nanostructures . . . 22

2.2.1 CuO nanowires . . . 23

2.2.2 Bi_2Se_3 nanowires and nanoribbons . . . 23

2.2.3 Ge nanowires . . . 26

2.3 One-dimensional nanostructure electrical transport . . . 26

2.4 Mechanical properties of one-dimensional nanostructures . . . 30

2.4.1 Dynamic deformation . . . 32

2.4.2 Quasi-static deformation . . . 33

2.5 Topological insulators . . . 35

2.5.1 Quantum Hall effect . . . 35

2.5.2 2D and 3D topological insulators . . . 39

2.5.3 Quantum oscillations and interference phenomena in Bi_2Se_3 . . . 40

2.5.4 Modulating Fermi level of Bi_2Se_3 nanostructures . . . 42

2.6 On-chip integration of suspended one-dimensional nanostructures . . . 43

2.6.1 On-chip nanostructure integration methods . . . 43

2.6.2 Fabrication of suspended nanostructures . . . 46

3 Experimental **48**
3.1 Synthesis, morphology and yield of one-dimensional nanostructures 48
3.1.1 Synthesis of one-dimensional nanostructures 48
3.1.2 Characterization of morphology of one-dimensional nanostructures 48
3.1.3 Characterization of mechanical and electrical properties of one-dimensional nanostructures 49
3.2 *In situ* characterization of NEM switches 50
3.3 On-chip integration of a NEM switch 51
3.3.1 Fabrication of source, drain and gate electrodes in bottom-contact configuration 51
3.3.2 One-dimensional nanostructure transfer 54
3.3.3 Top contact fabrication 55
3.3.4 Supercritical drying 55
3.4 Characterization of operation of an on-chip integrated NEM switch 56

4 Results and discussion **58**
4.1 Bottom-up growth of one-dimensional nanostructures 58
4.1.1 Growth and morphology of CuO nanowires 58
4.1.2 Growth and morphology of Bi_2Se_3 nanobelts 58
4.1.3 Morphology of Ge nanowires 59
4.2 Mechanical and charge carrier transport properties of CuO and Bi_2Se_3 one-dimensional nanostructures 60
4.2.1 Mechanical properties of CuO and Bi_2Se_3 one-dimensional nanostructures 60
4.2.2 Charge transport properties of CuO and Bi_2Se_3 one-dimensional nanostructures 68
4.3 NEM switches *in situ* 75
4.4 Fabrication of on-chip NEM switches 78
4.4.1 Calculation of the NEM switch geometry 78
4.4.2 Positioning of nanostructures on-chip 81
4.4.3 Nanostructure/metal contact fabrication 83
4.4.4 Minimizing stiction of suspended nanostructures 84
4.4.5 Characterization of the geometry of the integrated NEM switches . . 86
4.5 Operation of integrated NEM switches 88
4.5.1 Operation of CuO switch for room temperature applications 89

4.5.2 Operation of Bi_2Se_3 switch for cryogenic temperature applications . 91

Conclusions **97**

Bibliography **99**

Appendices **109**

A.1 Processing methods 110

A.1.1 Mask fabrication for photolithography 110

A.1.2 Fabrication of NEM switches by photolithography 111

A.1.3 Fabrication of NEM switches by e-beam lithography 112

B.2 Circuit for electrical detection of resonant frequency 113

Acknowledgements **115**

NOMENCLATURE

Abbreviations

1D NS one-dimensional nanostructure

2D NS two-dimensional nanostructure

2T two-terminal

3T three-terminal

4T four-terminal

AC alternating current

AFM atomic force microscope

CMOS complementary metal oxide semiconductor

CNT carbon nanotube

D drain electrode

DC direct current

FET field-effect transistor

G gate electrode

IPA isopropyl alcohol

MEM microelectromechanical

MEMS microelectromechanical systems

NC nanocontact

NEM nanoelectromechanical

NEMS nanoelectromechanical systems

NP nanoparticle

NR nanoribbon

NS nanostructure

NW nanowire

PMMA poly(methyl methacrylate)

QHE Quantum Hall Effect

QSHE Quantum Spin Hall Effect

RF radio-frequency

S source electrode

SdH Shubnikov-de Haas (oscillatons/frequencies)

SEM scanning electron microscope

SOC spin-orbit coupling

SS sub-threshold slope

TI topological insulator

TSS topological surface states

WAL weak anti-localization

Selected symbols and units

A area [m^2]

B magnetic field [T]

d diameter [m]

E Young's modulus [E]

f frequency [Hz]

L length [m]

R resistance [Ω]

t thickness [m]

w width [m]

z height/gap height [m]

1.INTRODUCTION

1.1 Motivation

The nanoelectromechanical (NEM) switch is a type of energy-efficient mechanical device that overcomes the limitations of nanoscale electronic switches [1–3]. The electronic switches are bound by a thermionic limit, meaning that energy consumption and driving current cannot be optimized separately. The efficiency of the NEM switch results from the physical gap between a moving component and a stationary component of the device, which reduces leakage currents to negligible levels.

NEM switches have already displayed their potential for low-voltage [4–6], low standby-power [7] and for high-temperature operation [8, 9]. They are currently being explored for use in conjunction with complementary-metal-oxide-semiconductors (CMOS) [10]. Compared to their larger microelectromechanical (MEM) counterparts, NEM switches boast higher operation speeds and integration density. Despite the promising results of high-temperature operation, a lack of data exists on low-temperature operation. This demonstration would be particularly interesting for developing quantum computing devices [11].

NEM switches employ one-dimensional (1D) and two-dimensional (2D) materials to create and break physical contact. The moving element in these switches is very small, measuring in the nanoscale. Lateral dimensions for a 1D element range from several tens to several hundreds of nanometers, while its length is in the micrometre range. The small size, large surface-to-volume ratio, and quantum confinement effects of quasi-1D materials manifest as unique physical properties, including size-dependent energy levels and bandgap. Due to immense efforts in lithography techniques, it is now possible to create moving elements with top-down fabrication using conventional semiconductor thin-film technologies.

By contrast, using bottom-up grown elements in NEM switches opens a new perspective on NEM switch research and applications. Semiconductor nanowires grown from the bottom-up are considered the future's electronic building blocks due to their atomically smooth surface, tunability, possibility to build high-quality heterostructures and material versatility [12]. Bottom-up technology is, however, not yet as mature as top-down and integrating bottom-up nanostructures into devices remains a significant challenge. In addition, there is a lack of fundamental investigation into the properties of these elements and they exhibit high variability, which makes it difficult to predict their electromechanical behaviour. Another significant challenge is associated with the reliability of these NEM switches. During the physical contact formation, high current impacts the active element, which can result in its deterioration or even permanent failure.

By suspending a nanostructure over a substrate, researchers can endow the device with mechanical degrees of freedom. This approach also provides access to the entire surface of the nanostructure, which maximizes its surface area for interaction with the environment. Additionally, it eliminates any undesired interactions between the substrate and the nanostructure, which could interfere with the exploration of their intrinsic properties [13, 14].

The focus of this Thesis is to explore the interplay between the mechanical and electrical properties of various bottom-up grown 1D nanostructures, such as nanowires and nanoribbons, in the NEM switch architecture. The nanostructures studied include CuO, Bi_2Se_3 and Ge. NEM Switches that can operate repeatedly at room and cryogenic temperatures are fabricated based on the characterization results. To minimize the risk of nanostructure degradation during contact formation in NEM switches, a method for current control during deformation in the non-contact phase is implemented.

1.2 Research aim

Investigation of operating principles of bottom-up synthesized one-dimensional semiconductor nanostructure-based NEM switches on-chip for their use at room and cryogenic temperatures.

1.3 Research objectives

1. To find synthesis parameters that can produce the necessary yield and morphology suitable for one-dimensional nanostructure application in NEM switches.

2. To determine mechanical and electrical properties of the synthesized one-dimensional nanostructures for understanding their applicability in NEM switches and for NEM switch fabrication guidance.

3. To find optimal parameters for the operation of a NEM switch by using the determined morphology and electromechanical properties of nanostructures, *in situ* investigation and theoretical model.

4. To fabricate electrode systems for alignment of one-dimensional nanostructures, and to explore the methods of nanostructure transfer and alignment.

5. To fabricate NEM switches and to demonstrate their operation at room temperature and cryogenic temperatures.

1.4 Theses to be defended

1. The developed bottom-up growth methods enable obtaining optimal nanostructure yield and morphology for creating integrated nanoelectromechanical switches (pub-

lications V and VII).

2. Bottom-up semiconductor nanostructures (CuO and Bi_2Se_3) grown using the controlled synthesis can be integrated into planar nanoelectromechanical switches using transfer and alignment of nanostructures on electrodes, supercritical drying and contact fabrication (publications I, III, IV and VI).

3. Repeatable operation of integrated bottom-up grown one-dimensional nanostructure-based nanoelectromechanical switches is demonstrated at room (with CuO nanowires) and cryogenic (with Bi_2Se_3 nanobelts) temperatures. Current that flows through the Bi_2Se_3 nanobelt during switching, is connected to the deformation of the nanostructure and could be used to control NEM switching (publications I, III and VI).

1.5 Scientific novelty

This Thesis focuses on the application of bottom-up grown nanostructures in nanoelectromechanical (NEM) switches. The following important findings could advance the field of NEM switch research:

- It is shown for the first time how the diameter of a gold catalyst influences the morphology of Bi_2Se_3 nanobelts.
- A fabrication flow of bottom-up one-dimensional semiconductor nanostructure integration into planar NEM switches is developed.
- Operation of a NEM switch with CuO nanowire as the active element is demonstrated for the first time.
- Operation of a NEM switch with topological insulator Bi_2Se_3 nanobelt as the active element is demonstrated for the first time, paving way for use of topological surface states in NEM switches.
- NEM switch operation at temperatures lower than 77 K is demonstrated for the first time.
- It is demonstrated for the first how monitoring current through the nanostructure could be used to control the deformation of the active element during NEM switching.
- Repeatable and stable CuO nanowire-based volatile NEM switch operation is demonstrated for the first time.
- Bi_2Se_3 nanobelt-based NEM switch operation at cryogenic temperatures and a novel method of current control during the non-contact deformation phase are demonstrated for the first time.

1.6 Practical significance

The bottom-up growth of semiconductor nanostructures holds significant promise for the development of next-generation NEM (nanoelectromechanical) switches, which could offer a wide range of functionalities in electronics, sensing, material characterization, and quantum computing.

Advancing our understanding of the controlled synthesis and electromechanical behavior of one-dimensional nanostructures, such as CuO and Bi_2Se_3, has the potential to propel both research and industrial applications beyond nanoelectromechanical switches. This knowledge could be particularly valuable in fields like flexible electronics, thermoelectrics, electrochemical CO_2 reduction, and advanced sensors.

The integration method developed in this thesis can be broadly applied to various nanostructures grown using bottom-up techniques. Moreover, it can be extended to include other low-dimensional materials, such as graphene and van der Waals two-dimensional materials.

Demonstrating NEM switching with Bi_2Se_3 at cryogenic temperatures could lead to the development of NEM switches that leverage the unique properties of topological surface states. Such switches could be crucial for implementing logic and memory functions in quantum computing and space technologies. Additionally, the development of a novel switching control mode, where the current is controlled through the nanostructure, could enhance the reliability and performance of NEM switches.

1.7 Author's contribution

The author contributed to the characterization of synthesis yield of one-dimensional nanostructures, characterization of their mechanical and electrical properties, fabrication of nanoelectromechanical switches, their characterization and operation testing and optimization. The author contributed to planning and conducting experiments, data analysis and summary, and publication writing and editing.

J. Kosmaca (J.K.), R. Meija (R.M.), R. Sondors (R.S.) and M. Antsov contributed to characterization of mechanical properties of nanostructures and J. K., R. M. and R. S. to the creation of NEM switches. G. Kunakova contributed to the electrical characterization of nanostructures. R. S. carried out synthesis experiments, J. K. and M. M. Ramma contributed to investigation of CuO dielectrophoresis. A. I. Livshits developed the theoretical model for calculation of NEM switch-ON voltage, K. Niherysh contributed to NEM switch measurements at low tempertures. J. Prikulis and R. Poplausks contributed to development of the electrical resonant frequency detection system. E. Dzene and E. Kauranens contributed to NEM switch fabrication and characterization. D. Erts contributed to experiment planning and revising publications.

1.8 List of publications

Publications included in this Thesis

I. Niherysh, K.; Jasulaneca, L.; Dzene, E.; Lombardi, F.; Erts D. Effect of Bending Deformation on Suspended Topological Insulator Nanowires: Towards a Topological Insulator Based NEM Switch. *Sensors and Actuators, A: Physical*, **2024**, *371*, 115292.

II. Jasulaneca, L.; Poplausks, R.; Prikulis, J.; Dzene, E.; Yager, T.; Erts, D. Characterization of Mechanical Oscillations in Bismuth Selenide Nanowires at Low Temperatures. *Micromachines* **2023**, *14* (10), 1910.

III. Jasulaneca, L.; Meija, R.; Kauranens, E.; Sondors, R.; Andzane, J.; Rimsa, R.; Mozolevskis, G.; Erts, D. Cryogenic Nanoelectromechanical Switch Enabled by Bi_2Se_3 Nanoribbons. *Materials Science and Engineering: B* **2022**, *275*, 115510.

IV. Ramma, M. M.; Katkevics, J.; Jasulaneca, L.; Kunakova, G.; Sondors, R.; Meija, R.; Erts, D.; Kosmaca, J. Dielectrophoretic Alignment and Electrical Characterization of CuO Nanowire-Based Systems. *Surfaces and Interfaces* **2021**, *27*, 101531.

V. Sondors, R.; Kunakova, G.; Jasulaneca, L.; Andzane, J.; Kauranens, E.; Bechelany, M.; Erts, D. High-Yield Growth and Tunable Morphology of Bi_2Se_3 Nanoribbons Synthesized on Thermally Dewetted Au. *Nanomaterials* **2021**, *11* (8), 2020.

VI. Jasulaneca, L.; Livshits, A. I.; Meija, R.; Kosmaca, J.; Sondors, R.; Ramma, M. M.; Jevdokimovs, D.; Prikulis, J.; Erts, D. Fabrication and Characterization of Double- and Single-Clamped CuO Nanowire Based Nanoelectromechanical Switches. *Nanomaterials* **2021**, *11* (1), 117.

VII. Sondors, R.; Kosmaca, J.; Kunakova, G.; Jasulaneca, L.; Ramma, M. M.; Meija, R.; Kauranens, E.; Antsov, M.; Erts, D. Size Distribution, Mechanical and Electrical Properties of CuO Nanowires Grown by Modified Thermal Oxidation Methods. *Nanomaterials* **2020**, *10* (6), 1051.

VIII. Meija, R.; Livshits, A. I.; Kosmaca, J.; Jasulaneca, L.; Andzane, J.; Biswas, S.; Holmes, J. D.; Erts, D. Resonance Assisted Jump-in Voltage Reduction for Electrostatically Actuated Nanobeam-Based Gateless NEM Switches. *Nanotechnology* **2019**, *30* (38), 385203.

IX. Jasulaneca, L.; Kosmaca, J.; Meija, R.; Andzane, J.; Erts, D. Review: Electrostatically Actuated Nanobeam-Based Nanoelectromechanical Switches – Materials Solutions and Operational Conditions. *Beilstein Journal of Nanotechnology* **2018**, *9* (1), 271–300.

X. Livshits, A. I.; Jasulaneca, L.; Kosmaca, J.; Meija, R.; Holmes, J. D.; Erts, D. Extra Tension at Electrode-Nanowire Adhesive Contacts in Nano-Electromechanical Devices. *European Journal of Mechanics*, A/Solids **2017**, *66*, 412–422.

XI. Kosmaca, J.; Jasulaneca, L.; Meija, R.; Andzane, J.; Romanova, M.; Kunakova, G.; Erts,

D. Young's Modulus and Indirect Morphological Analysis of Bi_2Se_3 nanoribbons by Resonance Measurements. *Nanotechnology* **2017**, *28* (32), 325701.

Publications not included in this Thesis

XII. Kosmaca, J.; Katkevics, J.; Andzane, J.; Sondors, R.; Jasulaneca, L.; Meija, R.; Niherysh, K.; Rublova, Y.; Erts, D. Humidity-Dependent Electrical Performance of CuO Nanowire Networks Studied by Electrochemical Impedance Spectroscopy. *Beilstein Journal of Nanotechnology* **2023**, *14* (1), 683–691.

XIII. Kosmaca, J.; Jasulaneca, L.; Meija, R.; Sondors, R.; Erts, D. Nanowires for NEMS Switches. *NATO Science for Peace and Security Series B: Physics and Biophysics* **2020**, 201–207.

List of selected international conference presentations

1. Jasulaneca, L.; Dzene, E.; Sondors, R.; Prikulis, J.; Erts, D. Bottom-Up Semiconductor 1D Nanostructures for Mechanical Switching. The 23rd IEEE International Conference on Nanotechnology (IEEE-NANO 2023), July 2 – 5, 2023, Jeju Island, Korea.

2. Dzene, E.; Jasulaneca, L.; Sondors, R.; Prikulis, J.; Niherysh, K.; Erts, D. Suspended nanostructures for substrate-free magnetoelectric characterization and device applications. The 23rd IEEE International Conference on Nanotechnology (IEEE-NANO 2023), July 2 – 5, 2023, Jeju Island, Korea.

3. Sondors, R.; Kunakova, G.; Andzane, J.; Jasulaneca, L.; Salnajs, D.; Lombardi, F.; Erts, D. Physical Vapor Deposition Synthesis Methods for Bi_2Se_3 NR with Tunable Geometry. International Conference on Materials Science, October 26 – 28, 2022, Verona, Italy.

4. Jasulaneca, L.; Meija, R.; Kauranens, E.; Sondors, R.; Dzene, E.; Prirodins, M.; Erts, D. Cryogenic temperature nanoelectromechanical switch. Joint International Scientific Conference "Functional Materials and Nanotechnologies" and "Nanotechnologies and Innovations in the Baltic Sea Region" conference (FM&NT - NIBS 2022), July 3 – 6, 2022, Riga, Latvia.

5. Jasulaneca, L.; Meija, R.; Kauranens, E.; Sondors, R.; Andzane, J.; Prikulis, J.; Dzene, E.; Erts, D. On-chip Bi_2Se_3 nanowire nanoelectromechanical switches for cryogenic switching. International Symposium on Novel Materials and Quantum Technologies (ISNTT2021), December 14-17, 2021, Atsugi, Japan.

2.LITERATURE REVIEW AND THEORETICAL BACKGROUND

2.1 Nanoelectromechanical switches

2.1.1 State-of-the-art NEM switches and their characteristics

As building blocks of future electronic components, NEM switches could offer unique advantages in terms of low-power operation, high-temperature resilience, non-volatility, and scalability.

Low-power advantage stems from the negligible OFF-state leakage and from the possibility to achieve steep subthreshold slope (SS). OFF-state leakage is minimized for these devices due to the physical interruption of the contact between the active element and the electrode. Steep SS means that they need only a small voltage to switch the current by a large amount. For example, a SS of less than 2 mV per decade has been achieved with a top-down Si-based NEM switch [15]. In contrast, CMOS switching has the fundamental limit of 60 mV per decade at room temperature, set by the thermal voltage of $\frac{k_B T}{q}$. This is the main reason why trying to reduce threshold voltage in a MOSFET to save power brings along substantial increase in OFF-state leakage current, thus adding to the static power consumption. Several reports have compared the power consumption between NEM switches and electronic components. For example, logic gate inverters based on NEM switches consume less power than CMOS inverters [16, 17].

The impact of **high temperature** on the operation of NEM switches is very different in comparison to electronic switches. For electronic switches, raising the temperature increases the collisions between the charge carriers, thus decreasing mobility and increasing OFF-state leakage current. That is why most CMOS circuits will undergo a decrease in performance and an increase in power dissipation as temperature rises. For NEM switches, decrease in mobility is not an issue and literature reports no increase in OFF-state leakage current at higher temperatures [8, 9, 18]. On the contrary, higher temperature operation has resulted in performance improvements by cleaning of contacts by removing the adsorbed contaminants [9] and increasing the number of switching cycles and stability of contact resistance. Due to their large melting point, CuO (1326 °C) and Ge (938 °C) 1D NS based switches could be prospective candidates for high temperature switching.

Recently, **low-temperature** applications of nanostructure-based electronics have gained increased interest due to the advancement of space and quantum technologies [11, 19].

However, at lower temperatures than liquid nitrogen (demonstrated for a graphene switch

[20]), which could be particularly interesting for quantum computing, the operation of NEM switches is left unexplored. The challenges that need to be solved for successful semiconductor NEM switch operation at cryogenic (lower than 120 K) temperatures are both from the mechanical and electrical realms. For example, increasing material brittleness and different thermal expansion coefficients of the structures during cooling may lead to changing stiffness, breakage of the active element or damage to contacts. The freeze-out of the charge carriers can reduce the conductivity of the device and the difficulty of dissipating charge can lead to irreversible stiction or changes in operating parameters over time, or electrical breakdown of the active element [21].

Some of these low-temperature effects have been explored in the behaviour of larger MEM instead of NEM switches. Most of the efforts have been devoted to radiofrequency (RF) MEMS [21–24] due to their prospective applications in, e.g., cryogenic microwave setups [25]. Also, MEM relays for logic applications operating at 4 K have been demonstrated [26].

By considering the difference in the thermal expansion coefficients of the active element and the substrate and the residual stress in the active element, a simple first-order model to calculate the switch-ON voltage was derived in [23]. To experimentally verify the model, an Al-based switch was fabricated and measured in the temperature range from -45 to 70 °C. The calculated deviation of the model from the data was less than 8 %. The same model was used to describe switch-ON voltage temperature dependence in Au-based capacitive shunt switch [22]. The model showed a reasonable fit with the experimental data in the temperature range of 293 K to 4 K and the registered V_{ON} increase was approximately 10-fold for temperature change between 293 K to 13 K.

Reliability testing of Au switches at temperatures lower than 6 K showed that substrate charging is responsible for early failure of these switches [21]. At low temperatures, the charges that are trapped in the dielectric substrate experience long discharge times because the charge carriers lack the thermal energy necessary to dissipate. As a result, the built-up charge creates and additional electrostatic field, that exerts a force on the beam even when the bias voltage is off, and the switch remains closed. Due to their good conductivity at temperatures as low as 2 K, Bi_2Se_3 1D NS could be potential candidates for cryogenic switching devices.

NEM switches can be designed to operate in **volatile and non-volatile** [6, 27, 28] mode, implementing logic and memory functions, respectively. In volatile switching, the active element detaches from the electrode after the voltage is removed, while it stays connected in non-volatile regime. Non-volatile operation is particularly attractive for applications requiring instant-on functionality or data retention in the absence of power. Here the NEM switch offers a distinct advantage in comparison with a CMOS, which needs power to sustain the

ON-state. The regime can be controlled by design, actuation scheme and adhesion between the contacting materials [29].

The **integration** of NEM switches into existing semiconductor platforms is easier for top-down NEM switches [30, 31]. For example, copper NEM memory switches were fabricated using metal interconnection line layer in standard CMOS process with additional HF-vapor etching [30]. Hybrid CMOS-mechanical switch technologies have been demonstrated for such applications as CMOS power gating [32], field programmable gate arrays (FPGAs) [33], reconfigurable logic circuits [30] and energy-efficient look-up tables (LUTs) [34], proving increase of speed and/or energy efficiency.

While most of the reliability-related milestones [18, 35] have been achieved using top-down approach, bottom-up fabricated low-dimensional materials offer ultimate miniaturization and speed while maintaining very high material quality. Prototypical materials used for demonstration of NEM switch operation are carbon-derivatives such as carbon nanotubes [1, 36–38] and graphene [4, 39] due to their exceptional mechanical properties. Graphene-based NEM switches have shown very good characteristics, such as ultra-low pull-in voltage of 0.5 V [4] and smaller [39] with more than 50,000 hot-switching cycles of operation [39]. Moreover, these NEM switches exhibited excellent switching characteristics, such as ≈20mV/dec switching slope, nearly-zero hysteresis, and $> 10^5$ ON/OFF current ratio [39].

While some advantages are inherent to the technology itself, others can only be achieved with the right material combination. For example, an increase in switching cycles can be obtained by changing the contact materials [36]. High temperature operation obviously can only be achieved using materials with high enough melting point [8, 9]. In contrast to silicon technology, there is still a wide selection of materials, both established and emerging, that is being explored for NEM switching.

Table 4.4 presents a summary of selected state-of-the-art NEM switches. The representative examples are chosen to highlight the most significant achievements regarding operation parameters, including various material classes and fabrication methods. Focus is kept on NEM switches, although some of the listed examples are on the border between nano and micro size scales.

Next chapter will look at how to control these operating parameters by adjusting the NEM switch design.

2.1.2 The simplest model of a NEM switch

In OFF state, no force is applied between the active element and the electrode, and as a consequence, no current flows through the NEM switch. When voltage is applied between the active element and the electrode, electrostatic force bends the active element towards

Table 2.1: Summary of state-of-the-art low-dimensional NEM switches

Highlights	**Material**	**Active element**	**V_{ON}, V**	**ON/OFF Current ratio**	**Subthreshold slope, mV/dec**	**OFF-state current, pA**	**Size, μm^2**	**Cycles**	**Ref.**
Low power	Graphene	Bottom-up	<0.5	10^5	20	≈ 1	8	$5 \cdot 10^4$	[39]
	Cr/Au	Top-down	0.05	10^9	2	≈ 1	≈ 336	at least 50	[15]
High T	SiC	Top-down	6	—	—	<0.01	8	$\geq 2 \cdot 10^9$	[8]
	Mo	Top-down	8.1-25.6	$1 \cdot 10^3$	<2.5	<10	~ 840	$2 \cdot 10^4$	[9]
Low T	poly-SiGe (4 K)	Top-down	<0.025	10^8	<1	0.1	~ 3800	$>10^8$	[26]
	Graphene (78 K)	Bottom-up	<5	—	—	—	~ 20	10–30	[20]
Volatile	SiC	Top-down	~ 15	10^5	—	0.1	~ 3	$2 \cdot 10^{10}$	[18]
	CNT	Bottom-up	20-40	10^2	—	~ 100	—	10^5	[36]
Non-volatile	W	Top-down	>8.6	10^6	—	~ 0.1	2	23	[28]
	CNT	Bottom-up	1.7	10^5	—	~ 10	<1	10	[40]

the electrode. ON state is registered as a sharp current increase at the moment when the active element makes physical contact with the electrode. By lowering the voltage, the switch returns again to the OFF state.

By careful design optimisation and choice of material combination it is possible to achieve the desired V_{ON}, hysteresis width, speed, ON/OFF current ratio among other parameters.

NEM switches are used most often in two configurations: two-terminal (2T) [36, 41] and three-terminal (3T) [42] (Figure 2.1). In 2T configuration, one of the terminals is the active element that undergoes mechanical deformation, the other terminal serves as a static electrode. One of the electrodes is designated as the source and the other one as the drain or sometimes gate. In the case of the 3T NEM switch configuration, the resemblance to MOSFET terminals is more visible, as the grounded electrode connected to the active element in OFF-state is called the source, the contact electrode is called drain and the third electrode supplying the necessary force to actuate the switch is called the gate. The G electrode can be placed at a slightly larger distance from the active element than the D. While this increases actuation voltage, it allows decreasing the operating voltage and thus poses less risk of damaging the active element.

The moving element can undergo different mechanical movements, starting from simple bending [43] to torsional movement [44] and rotation [6] and may have one or two fixed points, referred to as single-clamped and double-clamped configuration.

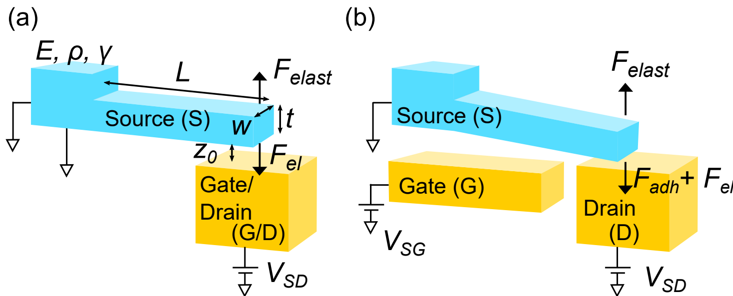

Figure 2.1: Schematics of single-clamped NEM switch configurations. (a) Two-terminal switch in OFF state, where one electrode (Gate/Drain) is used both for actuation and carrying current signal. (b) Three-terminal switch in ON state, employing one electrode for actuation (Gate), placed at a slightly greater distance than current path forming electrode (Drain). Larger voltage is needed for actuation, while the operation can be kept at lower voltages. Young's modulus E, density ρ and surface energy γ are the main material parameters, that govern the operation of the switch.

Regardless of the configuration employed, pull-in instability is central to the operation of most NEM switches [45, 46]. This phenomenon in nonlinear dynamics arises because the

electrical force increases more rapidly than the elastic force during electrostatic actuation. As a result, when the critical deflection is reached, the deforming electrode moves rapidly towards the static electrode. However, relying on pull-in instability for operation has its drawbacks. The active element undergoes significant impact, leading to potential degradation and reduced reliability of the device. Non-volatile repeatable switching without pull-in has been demonstrated using a NEM switch in a semicircular beam configuration rotating around a hinge [6].

The electrostatic force that acts between the active element and the electrode depends on the geometry of the system. It can be calculated either as between two plates (for, e.g., nanomembranes) or between a cylinder/beam and a plate (for nanowires, nanotubes [47] and cantilever-shaped thin films). Let's consider a parallel plate capacitor with plates separated by distance z_0 (Figure 2.2 (a)). One of the plates can move, modelling the active element in the NEM switch, and its displacement is denoted as y. The electrostatic force $F_{electric}$ between the two conducting plates can be described by formula

$$F_{electric} = \frac{1}{2}\frac{\epsilon_0 A V^2}{(z_0 - y)^2}, \tag{2.1}$$

where ϵ_0 - vacuum dielectric permittivity, A - area of the plate, V - voltage applied between the plates. More realistic force description would include fringing fields at the edges of the plates and van der Waals forces for nanoscale devices [47].

Modelling the movable plate with mass m suspended in a spring with effective spring constant k, then the elastic force $F_{elastic}$ can be expressed as a function of displacement y as

$$F_{elastic} = ky \tag{2.2}$$

Equation of motion for this linear system is

$$m\ddot{y}(t) + b\dot{y}(t) + ky(t) = F_{el} \tag{2.3}$$

Using formulas 2.1 and 2.2 it can immediately be seen that the electrostatic force is a quadratic function of distance to the electrode, while the elastic force exhibits a linear dependence. Figure 2.3 illustrates these forces as functions of relative displacement $\frac{y}{z_0}$. For voltage values lower than the switch-ON voltage ($V < V_{ON}$), both functions have crossings at two points (blue $F_{electric}$ curve and black $F_{elastic}$ line), but only the solution for small relative displacements is stable. Increasing voltage, distance between the plates gets smaller and the capacitance increases. As the electrical force curve touches the elastic force line (orange $F_{electric}$ curve for $V = V_{ON}$), pull-in instability is reached and the movable plate rapidly traverses the remaining distance until contact with the static plate is established.

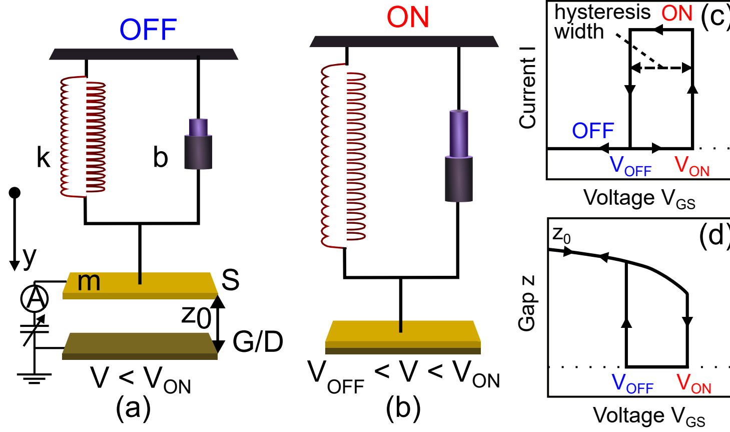

Figure 2.2: Schematics of a 2T NEM switch modelled as a plate with mass m attached to a spring and a damper in (a) OFF state and (b) ON state. Movable plate (source electrode S) is separated from the static plate (gate/drain electrode G/D) by an initial distance z_0 and constitutes a variable capacitor. (c) Schematics of a typical OFF-ON switching cycle, where current rises abruptly reaching voltage $V_{GS} = V_{ON}$. Hysteresis arises from the adhesion force between the active element and the contact electrode. (d) Gap height z between the plates as a function of voltage between the plates.

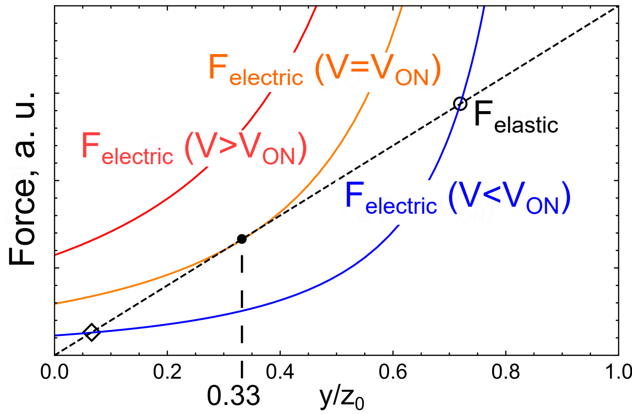

Figure 2.3: Elastic and electric forces as a function of the relative displacement $\frac{y}{z_0}$ in a 2T NEM switch. Electric force is illustrated at 3 different voltage levels ($V < V_{ON}$, $V = V_{ON}$ and $V > V_{ON}$). Applied voltage V is equal to the switch-ON voltage V_{ON} when $F_{electric}$ curve is a tangent to $F_{elastic}$ line. This pull-in instability occurs at relative displacement of 0.33.

By using critical relative displacement value of 0.3, switch-ON voltage V_{ON} can be expressed as

$$V_{ON} = \sqrt{\frac{8kz_0^3}{27\varepsilon_0 A}}, \tag{2.4}$$

where A - area upon which the electrostatic force acts (equal to electrode length times width of the active element). By increasing voltage further ($V > V_{ON}$), the elastic force will always be smaller than the electric force (red $F_{electric}$ curve) and thus both plates will stay in contact.

Now decreasing the voltage, the switch returns to its OFF position when $V = V_{OFF}$. Here the adhesion force between the contacting surfaces determines whether switching-OFF will occur spontaneously without supplying extra energy or if it needs additional energy to return to the initial position. Switching-OFF can be realized with or without supplying extra energy, resulting in either non-volatile or volatile behaviour, respectively [29]. The voltage difference between V_{ON} and V_{OFF} is also called the width of hysteresis and characterizes the adhesion strength between the active element and the electrode. In general, small hysteresis width is desired, as implemented in, e.g., a graphene-hexagonal boron nitride switch [4]. Here the material combination is the key to achieve hysteresis width of 0.1 V.

The preceding derivation of V_{ON} is based on couple of assumptions. One is that the system is treated as linear, which means that it operates in linear elastic force and small deformation regime and exhibits linear losses. Another assumption is that it only treats viscous damping, where the force is proportional to the velocity [47].

Next sections will look at candidate bottom-up grown 1D NS as active elements for NEM switches proposed in this thesis and will look at the electrical and mechanical domains separately to understand their behaviour in NEM switches.

2.2 Quasi-one-dimensional semiconductor nanostructures

Quasi-1D semiconductor nanostructures draw a lot of attention because of their atomically smooth surface, possibility to combine highly distinctive materials and create structures with selective doping and tightly controlled chemical composition [12]. The material requirements for the NEM switch active element depend on the intended application (e.g., memory, logic, sensing) [1].

Materials with high Young's modulus allow to achieve high-speed switching and necessary stiffness to overcome stiction at the contact for repeatable ON/OFF cycling [48]. Low Young's modulus, however, allows expending very little energy for non-volatile applications [49]. Surface energy of the active element and electrodes determines the adhesion force when in contact and therefore the observed hysteresis width [50]. High melting temperature allows to withstand Joule heating due to the current flow in the active element [8, 9].

The required electrical conductivity of the NEM switch active element also depends on the application – e.g., radio-frequency switches require very high metallic conductivity while lower conductivity is desired for current-limiting applications. Achieving electrically and mechanically stable interface between active element and immobile electrode is also important for predictable long-term operation. To increase the operating temperature range of the NEM switch, it is crucial to have predictable electromechanical properties as a function of temperature.

2.2.1 CuO nanowires

CuO is a p-type semiconductor with a band gap of 1.2 eV [51] and monoclinic crystal structure. It has been considered as a perspective material for chemical/gas sensing [52], particularly in the form of nanowires, as they possess well-defined crystal orientations, fast response and high sensitivity. Field-effect transistor based on CuO nanowires has also been demonstrated [53], showing p-type behaviour but relatively poor conductivity.

Due to the relatively high melting temperature of 1326°C [54], CuO NS can be considered for high temperature NEM switch applications.

Inclusion of CuO nanowires in integrated circuits is particularly attractive due to high-yield and relatively simple growth methods, for example, thermal oxidation [55]. External electric field [56, 57] and humidity [58] are two important parameters that can be used to tune the resulting distributions. The electric field promotes ion diffusion, while adding water vapour increases oxidation rate. The influence of these factors were explored both separately and in combination.

2.2.2 Bi_2Se_3 nanowires and nanoribbons

Bi_2Se_3 is a semiconductor with bandgap of 0.3 eV and rhombohedral crystal structure [59]. It has a layered structure that originates from covalently bonded quintuple atomic Se-Bi-Se-Bi-Se layers. These charge neutral layers are mutually held together by van der Waals forces, allowing facile exfoliation of Bi_2Se_3 crystals to produce few-layer sheets [60]. Unit cell of Bi_2Se_3 consists of 3 quintuple layers with lattice constants a $\sim$ 4.14 Å and c $\sim$ 28.64 Å. Thickness of one quintuple layer is approximately 1 nanometer. Along the c-axis, Bi_2Se_3 is an insulator in the bulk, while its surface is conducting. This is one of the hallmarks of the so-called topological insulator (TI) material class.

TI properties of Bi_2Se_3 arise from its band structure and the effect of spin-orbital coupling. Bi_2Se_3 is called the prototype three-dimensional (3D) TI due to its simple band structure containing a single ring-like surface Fermi surface [59]. Experimentally band structure of Bi_2Se_3

has been elucidated using surface sensitive photoemission techniques - the most notable example being angle resolved photoemission spectroscopy (ARPES) [59, 61]. ARPES is based on a photoelectric effect and can directly visualize electron energy as a function of wave vector components.

2D surface states are induced by the topology of the bulk band structure in TIs. Electrons responsible for surface conduction in TIs exhibit linear energy/momentum dispersion (Figure 2.4 (a) red and blue curves in the band gap) and are so-called massless Dirac electrons. Generally Dirac electrons have high mobility and controllable density, beneficial for electronic device applications. In TIs particularly, they are also locked at right angles to momentum through strong spin-momentum coupling (Figure 2.4 (b)), thus they do not get scattered by impurities, except if the impurities are magnetic.

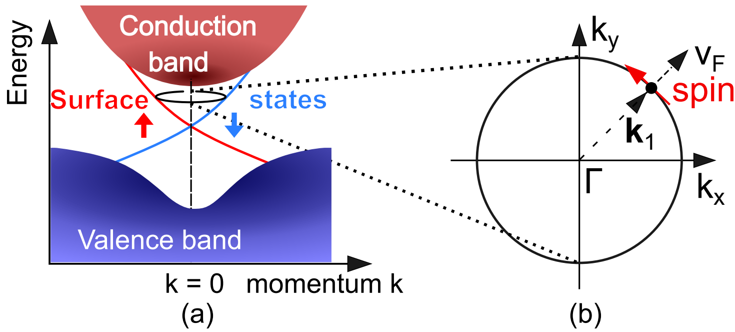

Figure 2.4: Band structure schematics of bulk Bi_2Se_3. (a) Surface states (red and blue curves) exist in the bulk band gap and are spin nondegenerate and helically spin polarized. (b) Representation of Dirac cone contour of constant-energy. Spin vector (red) is orthogonal to the wave vector k_1 (dashed black) and Fermi velocity vector v_F (solid black). Figure adapted from [62]

Electronic probing of surface and bulk states in Bi_2Se_3 has also been carried out, and will be discussed in more detail in section 2.5. Specifically, to confirm the topological nature of the material it has to be shown that the measured signal comes from the surface charge carriers and that these carriers are Dirac fermions. Most notable techniques for characterizing the topological nature in Bi_2Se_3 are [62]:

- Spin-resolved photoemission spectroscopy [59];
- Scanning tunneling spectroscopy in magnetic fields [63].
- Magnetotransport (especially conductivity oscillations such as angle-dependent Shubnikov-de Haas and Aharonov-Bohm [64]);

For a material to exhibit TI properties, its Fermi level has to lie in the band gap. Native Bi_2Se_3 crystals contain defects such as Se vacancies and Se interstitials [65] that move the Fermi level up in the bulk conduction band. They are difficult to obtain insulating in the bulk, thus properties of the surface states get obscured. There exists a criterion for critical doping concentration that defines metal to insulator transition (i.e., Mott criterion). In conventional TIs such as Bi_2Se_3 and Bi_2Te_3, this criterion predicts practically difficult to achieve doping concentrations ($\approx 10^{14}$ defects/cm^3 [66]) due to weak bonding in these materials.

The main goal is to adjust the placement of the Fermi level, while keeping sufficiently high mobility. Several strategies have been explored, including making materials thinner [67, 68], compensation doping and fabrication of capping layers [69].

Nanomaterials are particularly convenient structures that allow to access surface states due to the large surface area/volume ratio. By decreasing the thickness of nanoribbons below 30 nm it has been shown that the contribution from the insulating bulk is removed [67]. For thin films with thickness of approximately 10 nm ambipolar transport has been demonstrated [68]. This means that the Fermi level could be tuned through the whole band gap.

Another approach besides using nanomaterials, is using compensation doping and encapsulation in protective layers [69]. It has been shown that doping with Sb is an efficient method to reduce bulk carriers, while encapsulation in ZnO shell shields Bi_2Se_3 from various contamination during handling and processing.

These techniques are part of the growth and fabrication process of the device and cannot be reversibly and actively changed during device operation. In turn, strain engineering can be a promising route for modifying the electronic structure in TI materials reversibly. It has been shown that the bulk band topology in Bi_2Se_3 is sensitive to uniaxial in-plane strain [70].

From the previous discussion, it is clear that compared to Ge and CuO nanowire growth, growth of 1D Bi_2Se_3 NS is more challenging, as it is crucial to ensure the correct stoichiometry and doping level to achieve its topological properties. Topological Bi_2Se_3 NS have been grown using such methods as molecular beam epitaxy [71, 72], physical vapor deposition [73] and chemical vapor deposition [74].

The impetus for using Bi_2Se_3 in NEM switches that operate at cryogenic temperatures is the material's good conductivity in this temperature range. Also, the possibility to tune ON-state current with mechanical deformation/electrostatic gating would enhance functionality of the switch. The understanding of TSS response to strain would allow to build NEM devices that exploit the exotic TI properties.

2.2.3 Ge nanowires

Ge is a notorious semiconductor material for solid state electronics, sharing the same diamond cubic crystal structure as Si. Ge was used in the very first transistor [75]. Shortly after the transistor action was demonstrated in Ge, the semiconductor technology was completely overtaken by Si. Although Ge exhibits higher electron and hole mobilities than Si, one of the main reasons behind this shift was that Si surpass Ge in terms of the chemical stability of interface with its oxide SiO_2. Nowadays, Ge has regained its place in the silicon industry in the form of strained SiGe [76] layers. Ge nanowires are considered for gate-all-around transistors [77] and more recently for quantum computing applications [78], as well as in Li ion batteries [79, 80]. They have a relatively high Young's modulus of 112 $\pm$ 43 GPa [81], prospective for volatile NEM switching.

Ge nanowires have demonstrated repeatable nanoelectromechanical switching *in situ* inside scanning electron microscope [82, 83]. Similar to other semiconductor nanowires, in air ambient Ge develops a native oxide. The oxide layer functions as a tunnel barrier that impedes electron injection from the metallic contacts into the nanowire. Consequently, at low voltages (2–4 V) [41, 82] NEM switches exhibit high resistance, thus significantly lowering ON/OFF current ratio in this voltage range. Current barrier issue can be resolved by etching the native oxide layer and encapsulating the devices in an inert atmosphere. On the other hand, native oxide protects the switching element, enabling operation at voltages up to 40 V without burnout [82].

Both solution phase and vapor phase bottom-up methods have been used to grow Ge nanowires [84–86]. Highest yields of up to 80% have been achieved using supercritical fluid-liquid-solid synthesis (SCF) [85], corresponding to milligram quantities over a reaction time period of up to 10 minutes. The advantage of the synthesis of crystalline nanomaterials in SCFs is the facile control of viscosity, diffusivity and surface tension [87] by adjusting pressure and temperature. As a result, this method allows controlling mass-transfer and increasing solubilities of the reactants and the products.

2.3 One-dimensional nanostructure electrical transport

Quasi-1D nanostructures are attractive for electronic applications as they have prospects for realizing ballistic, non-dissipative transport and offer possibility to modulate current using electrostatic fields and mechanical strain. Depending on the cross-sectional dimensions and the length of the nanostructure, different electronic transport regimes can be accessed (Figure 2.5). For large lengths and cross-sectional dimensions in comparison with the mean-free-path l_e of the charge carrier, drift-diffusion mechanism takes place [88]. In Figure 2.5 (a), the movement of electrons in an electric field in shown. According to this model developed

by Drude, electrons change direction after colliding with crystal defects. l_e is the distance between two successive collisions, occurring after a time τ. The electric conductivity σ_0 is given by

$$\sigma_0 = \frac{e^2 n_0 \tau}{m}, \tag{2.5}$$

where e and m is the electron charge and mass and n_0 is the density of electrons. In drift-diffusion regime, mobility μ, which is inversely proportional to τ, is an important parameter that determines speed and on-current levels in nanowire-based electronic devices. It also determines, how pronounced will quantum interference effects be in TI materials.

For small cross-sectional dimensions and lengths L (i.e., $L << l_e$), the scattering effects can be neglected, i.e., ballistic transport can be achieved (Figure 2.5 (b)). For ballistic conductors, conductance will be quantized in units of $G = \frac{e^2}{\pi\hbar}$, and it can easily be destroyed due to impurities. However, quantization can also occur due to edge states in Quantum Hall effect. This quantization is immune to impurities and will be discussed in subsection 2.5.1.

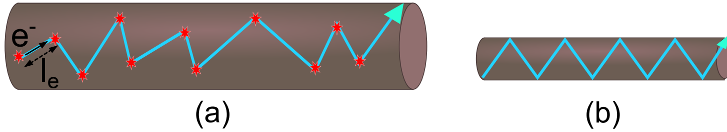

Figure 2.5: Electrical transport in a 1D-nanostructure. (a) Diffusive transport occurs when the length L is larger than the mean-free-path of the charge carrier l_e. (b) Ballistic transport is realized when L is shorter than l_e.

To use 1D NS as current conduction pathways in electromechanical devices efficiently, the properties of 1D NS and their contacts with metal electrodes need to be taken into account. In a NEM switch, at least 2 different type contacts are employed: one is a permanent and mechanically static and the other one is dynamic that makes intermittent contact during the switching-ON. Electrical properties of the NC will determine both the ON-state current levels in the NEM switch, their stability and operational voltage region.

When a contact between a metal and a semiconductor material is made, a potential barrier develops that impedes the flow of charge carriers from one material to another. Applying a voltage bias to the metal/semiconductor junction, either effectively decreases or increases the barrier height seen from the semiconductor side. In general, metal/semiconductor contact type is determined by metal's Fermi level E_F placement in relation to semiconductor's valence and conduction band edges E_V and E_C, respectively (Figure 2.6). If E_F is located between E_V and E_C, then Schottky barrier ϕ_B develops at the junction (Figure 2.6 (a) and (b)). When E_F is either higher than E_C or lower than E_V, ohmic contact is formed (Figure 2.6 (c) and

(d)).

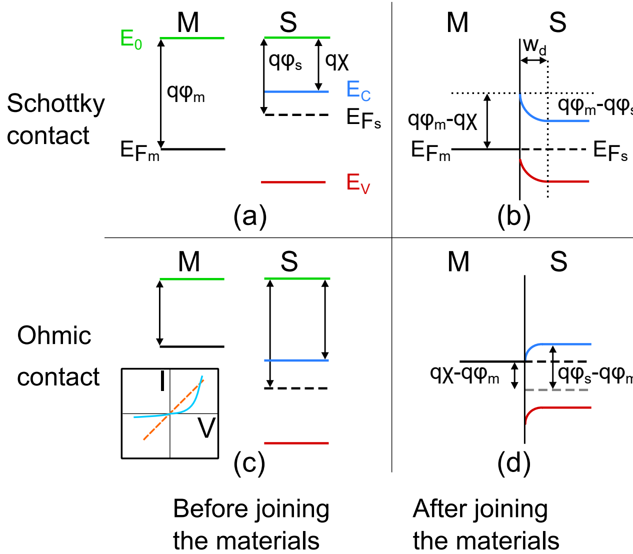

Figure 2.6: Contact formation between a metal M and an n-type semiconductor S. Schottky contact (a) before and (b) after joining of the two materials. Ohmic contact before (c) and (d) after joining of the two materials. Inset in (c) shows the current-voltage characteristics for Schottky (blue, continuous) and ohmic (orange, dashed) contacts.

Ohmic contacts are generally desired for signal transfer across metal/semiconductor junction. The carriers are free to flow in both directions across the junction. Ohmic characteristics can be achieved by lowering the barrier height (using proper material combinations or by thermal annealing) or by making the barrier very narrow (e.g., by doping) to allow tunneling through it. For sensor devices, modulation of Schottky barrier height modulation can serve as a means of detection.

Many semiconductor, including Ge [89] and Bi_2Se_3 [90], and metal nanostructures develop a thin native oxide layer in air ambient. If not removed before metal deposition, a metal /oxide /semiconductor contact is created at the interface. Oxide layer forms a tunnel barrier that can be overcome by direct, Fowler-Nordheim or thermionic emission. This has several implications for NEM switch operation. A thin insulating layer can decrease the current density in NEM switch dynamic contact, thus reducing ON-OFF current ratio, while also mitigating burnout risks of the active element. Intentional deposition of insulating layer (encapsulation) has been included in the fabrication of some NEM switches [refs].

For fabrication of NC, metals are usually evaporated or sputtered in vacuum on the ends of the active element or active elements are placed on top of prefabricated metal electrodes,

creating an adhesive contact (usually with a high contact resistance R_C). Electrical contact characteristics depend severely on the fabrication method used [91].

Two most popular electrical property measurement configurations are used for characterizing properties of 1D NS. Two-terminal contact configuration is important from the practical standpoint, as they require less space and are usually employed in device applications. However, in such systems electronic properties of the 1D NS are difficult to decouple from the electrical properties of the contact itself. Therefore four-terminal (or more as in transfer line method [92]) measurement schemes are used. The former can be used to determine electrical resistivity ρ of the NS, while the latter allows to determine value of R_C.

In four-terminal (4T) measurement, outer contacts serve the current injection function, while the inner are the so-called voltage probes (Figure 2.7). As the voltmeter has an infinite input resistance, no current is drawn through the voltage probes. Thus the voltage drop measured arises due to resistance of the NS itself. Scaling this resistance according to the total length of the NS, total NS resistance is determined.

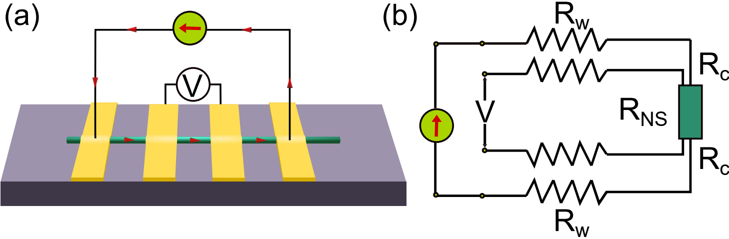

Figure 2.7: Four-terminal measurement setup schematics (a) and equivalent electrical schematics (b) for characterizing nanowire resistivity without the impact of contact resistance.

Resistivity temperature dependence can be exploited to get information about dominant scattering mechanisms in the material. In metals, resistivity usually decreases with lowering the temperature. At room temperature, electron-phonon scattering dominates, while at low temperatures electron-electron interaction is responsible for non-zero resistivity. At the limit of zero temperature, there is still some residual resistivity ρ_0 that arises from scattering of electrons with Fermi energy by lattice defects. Resistivity temperature dependence is classically described by equation [93]

$$\rho(T) = \rho_0 + AT^n, \tag{2.6}$$

where constant $A > 0$ and n is 2 for electron-electron scattering and from 3 to 5 for electron-phonon scattering. However, at low temperatures, interaction between electrons in

disordered systems leads to strong anomalies. For example, at low temperatures exponent n in 2.6 is 1/2 instead and coefficient A can be both positive and negative. For 2D systems (e.g., thin films), a logarithmic increase of residual resistivity has been observed.

Bi_2Se_3 synthesized without intentional doping usually shows a metallic decrease of ρ from room temperature to some intermediate temperature, dominated by phonon scattering [94, 95] (Figure). From intermediate to lower temperatures, different trends have been observed.

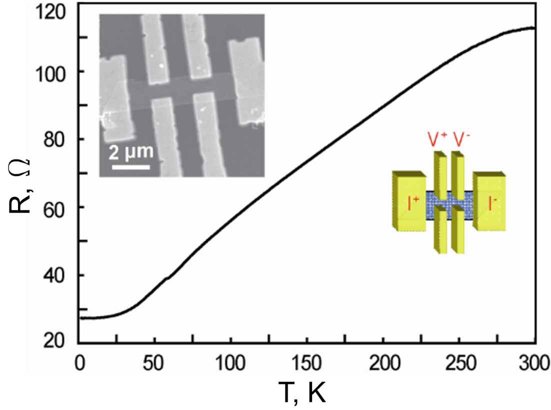

Figure 2.8: Four-terminal longitudinal resistance of Bi_2Se_3 nanostructure from room temperature to 2 K. Insets are an SEM image of the Hall bar device and the measurement contact configuration. Figure adapted from Ref. [95].

Exponential Arrhenius-type increase of ρ can be either attributed to bulk band gap or to impurity band conduction. Activation energy E_a can be extracted from the slope of $\ln \rho$ vs T^{-1}. Saturation of ρ approaching a constant value at low temperatures has been associated with bulk carrier freeze-out accompanied by a combination of surface state and impurity band conduction. Low temperature (2 K to 30 K) $\rho \propto T^{-1/4}$ dependence has been attributed to Mott variable range hopping mechanism [96, 97] in the impurity band. Resistivity behaviour depends also on NS thickness, e.g., for Bi_2Se_3 thin films a critical thickness of 6.4 QLs has been identified [94] where most of the conduction comes from the surface channel.

2.4 Mechanical properties of one-dimensional nanostructures

1D NS exhibit mechanical properties that are different from their bulk counterparts, moreover, a pronounced size-dependence has been reported in the literature for, e.g., Young's modulus and yield strength [98]. Size-dependence has been attributed to the increased contribution from the surface effects – i.e., the fact that surface atoms experience less influence from the neighbouring atoms than the atoms in the bulk. Surface effects manifest themselves

in different ways – as surface tension, surface reconstruction and different electron density among others.

To characterize mechanical properties of a single 1D NS, tools that can apply controlled force in the range of nanonewtons and register deformation in the range of nanometers or even subnanometers are needed. Deformation can be caused mechanically, using calibrated mechanical structures (e.g., atomic force microscope cantilevers or MEMS devices) and detecting the deflection visually using high resolution microscopes or a laser. The elastic and plastic regions of single 1D NS deformation have been characterized both in tension and in bending. Surface effects manifest themselves differently in each of these deformation modes (more in bending, less in tension) [99], which has to be taken into account when interpreting the obtained results.

For electrostatically actuated NEM switches and resonators, 1D are deformed using electromechanical coupling, during which an electrostatic DC field or time varying AC field is applied. In case of DC field, 1D NS bends towards the electrode, while AC field induces mechanical resonance of the NS at certain frequencies.

NEM switches have been reported with the active element operating in bending mode (both in-plane and out-of-plane), and in shear mode. This thesis will mainly cover bending deformation of 1D NS (Figure 2.9) – both to determine the Young's modulus of the nanostructures and to implement NEM switching. During bending, moment M causes the beam axis to bend with radius R. One side of the beam experiences tension and the other one – compression, while the mechanical stress σ changes linearly along the y direction. On the neutral axis, σ is equal to zero.

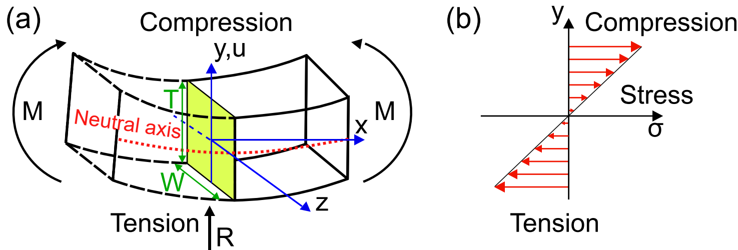

Figure 2.9: Schematics of a rectangular beam under bending deformation (a) and stress distribution along y axis (b). M – bending moment, R – bending radius, σ – mechanical stress σ.

Depending on the ratio between 1D NS deflection u and characteristic size, different continuum models can be applied to describe the resulting dynamics. Generally, the dynamics of a 1D NS, when an external time-varying force F_{ext} is applied can be described using formula 2.7

$$\rho A \frac{\partial^2 u}{\partial t^2} + \eta \frac{\partial u}{\partial t} + EI \frac{\partial^4 u}{\partial x^4} - T \frac{\partial^2 u}{\partial x^2} = F_{ext}(x, t), \tag{2.7}$$

where the first term is the acceleration of displacement $u(x)$ with ρA denoting the linear mass density. The second term describes damping proportional to the velocity of the 1D NS with proportionality coefficient η. EI is the bending rigidity with E being Young's modulus and I – the area moment of inertia.

2.4.1 Dynamic deformation

Neglecting damping and tension terms in 2.7, Euler-Bernoulli equation for a resonating beam can be obtained as

$$EI_x \frac{d^4 u}{dx^4} + \rho A \frac{d^2 u}{dt^2} = 0. \tag{2.8}$$

After solving eq. (2.8) with the appropriate boundary conditions, resonance eigenfrequencies can be obtained as

$$f = \frac{\beta^2}{2\pi L^2} \sqrt{\frac{EI}{\rho A}}. \tag{2.9}$$

β is approximately 4.730 for fixed-fixed boundary conditions and 1.875 for fixed-free case.The resonant frequency is the frequency where the vibration amplitude is maximum. In the linear regime, the vibration amplitude has a Lorentzian-shaped dependence on frequency at resonance. Figure 2.10 shows single-clamped (i.e., fixed-free) 1D NS in resonance and its corresponding amplitude-frequency curve.

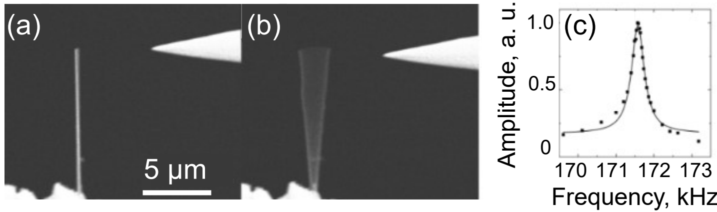

Figure 2.10: *In situ* resonance excitation of Sb_2S_3 nanowire. SEM images of nanowire with dimensions: length L = 10 μm and radius r=67 nm taken when the applied electric field frequency is (a) far from the natural resonance frequency of the nanowire and (b) at the resonance frequency. Increased vibration amplitude can be seen and described by a Lorentzian fit (f_0=171.57 kHz) (c). Figure adapted from [100].

It should be noted that, depending on the tension force, the 1D NS can be described either

as a beam or as a string. Crossover from one regime to another by varying the tension force has been demonstrated for CNTs in [101].

In situ SEM experiments in real time involving the excitation and detection of resonant behaviour lay a solid ground for understanding the electromechanical behaviour of 1D nanostructures. However, typical SEM studies are limited to the room temperature. To explore the temperature-dependent and low-temperature dynamical characteristics, other detection schemes that are compatible with cryostat should be implemented.

In the case of NEM switches, resonance can determine the temperature-dependent elastic properties of 1D NS and exploit resonance energy for switching ON and OFF.

There are two popular schemes for detecting resonance in low-dimensional nanostructures: optical [102] and electrical [101]. Optical detection has some limitations, such as lower coupling strength with 1D NS compared to electrical detection, potential heating of the sensitive nanostructures, and difficulties in integrating it with the electrical connections and wiring already present in some cryostat systems. On the other hand, electrical detection has its own challenges, such as low signal-to-noise ratio due to the very small capacitance of the 1D NS-electrode system in comparison to parasitic capacitances of cables.

This issue can be addressed by (a) converting and detecting resonance at lower frequencies, (b) using a local gate electrode close to the vibrating nanostructure. To exploit both benefits of fast detection and minimized parasitic capacitance, the local gate electrode could be combined with a preamplifier circuit that is placed near the measured NEM switch.

2.4.2 Quasi-static deformation

In the **quasi-static** case, displacement u of the rectangular beam in the y direction under bending moment $M(x)$ is described using equation

$$EI_x \frac{d^2u}{dx^2} = -M(x) \tag{2.10}$$

For rectangular cross-section

$$I_x = \frac{WT^3}{12}, \tag{2.11}$$

where W is the width and T represents the thickness of the NS.

If a point load is applied at the end $x = L$ of the NS, then the bending moment $M(x)$ can be expressed as

$$M(x) = -F(L - x) \tag{2.12}$$

For a beam that is clamped at one end, boundary conditions require that displacement

and deflection at the clamped end is zero:

$$u_{x=0} = 0$$
$$(\frac{du}{dx})_{x=0} = 0 \tag{2.13}$$

By integrating 2.10 twice with respect to x and using boundary conditions 2.13 to find the integration constants, the displacement u of the beam as a function of distance x is obtained:

$$u(x) = \frac{F}{6EI}(3Lx^2 - x^3) \tag{2.14}$$

Maximum displacement is at $x = L$ and by employing Hooke's law, spring constant of the single-clamped beam in the linear regime can be expressed as

$$k_{single-clamped} = \frac{3EI}{L^3}. \tag{2.15}$$

Spring constant for a double-clamped 1D NS is derived in a similar manner and can be used to extract Young's modulus in AFM three-point bending experiments. However, to interpret actual experimental force-displacement curves, which are usually non-linear, intrinsic stress and surface effects are invoked [81, 103, 104]. Typical experimental force-displacement curve is shown in Figure 2.11. The top and bottom surfaces of a double-clamped 1D NS under bending experience different deformations – one surface is under compression (top surface in Figure 2.9), while another surface – under tension (bottom surface in Figure 2.9), with neutral axis experiencing no stress in the elastic regime. After removing the bending moment M, the 1D NS will be restored to its initial position.

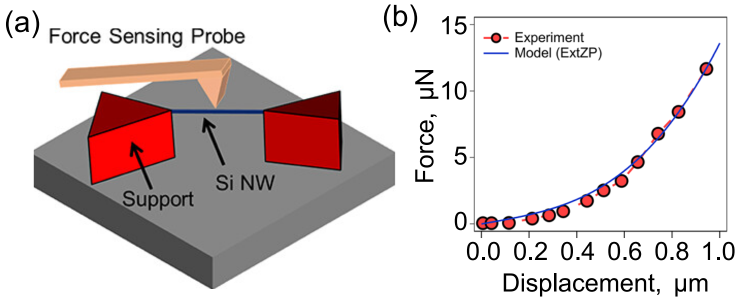

Figure 2.11: Quasi-stationary mechanical deformation of a 1D NS in three-point bending experiment. (a) Experimental schematics using atomic force microscope cantilever for force application and displacement measurement. (b) Typical force-displacement curve (discrete points) and theoretical approximation (solid curve). Figure adapted from Ref. [104].

The bending strain of an elastically deformed 1D NS in the thickness direction can be calculated using thickness T and radius of curvature R as

$$\epsilon = \frac{T}{2R}. \tag{2.16}$$

The previous formula can be applied for cases when $R >> T$.

Both quasi-static and dynamic loading may lead to buckling deformation – a sudden change in shape of the nanostructure. Buckling deformation is regarded as a highly controllable nanomechanical deformation mode with the potential for achieving large displacements [105]. In addition, a buckled nanostructure could lead to a record electrical frequency tunability as it has been shown for CNT resonators [106].

2.5 Topological insulators

Band theory [107] has been successfully used to explain a plethora of electronic and optical phenomena in different materials, dividing materials into three general classes – insulators, semiconductors and metals. According to band theory, an insulator possesses an energy gap between the highest occupied energy level and the lowest unoccupied energy level, and the gap is roughly some orders of magnitude larger than the thermal energy at room temperature. The allowed energy levels in the system can be found by solving time-independent Schrodinger equation

$$H\psi = E\psi, \tag{2.17}$$

where H is the Hamiltonian operator, ψ is the wavefunction and E is the energy eigenvalue.

Topology is a branch of mathematics that studies properties of geometric objects under continuous deformation. In physics, topology studies smooth transformations of Hamiltonians of the physical system and offers an additional paradigm for classification of materials according to *topological invariant*. If two insulators can be turned into one another by slowly changing the Hamiltonian such that the energy gap is never closed (i.e., there are no energy eigenvalues that fall in the gap), then they are topologically equivalent. Consequently, if two topologically inequivalent insulators are joined, a gap closing must take place. When this gap closing occurs, gapless conducting states with peculiar properties emerge at the interface between the two insulators.

2.5.1 Quantum Hall effect

One of the simplest examples to illustrate the emergence of gapless states, is the *integer quantum Hall effect* (IQHE). When a conductor or a semiconductor is placed in a perpendicular magnetic field, the charge carriers get deflected due to Lorentz force and transversal

voltage develops across the sample. Hall effect measurement schematics shown in Figure 2.12. Classically, a linear dependence of transversal resistance $R_{xy} = \frac{B}{ne}$ on B field is observed, while longitudinal resistance $R_{xx} = \frac{L/W}{ne\mu}$ does not depend on the B field (Figure 2.12 (b)). However, it turns out that the situation is very different when a 2D electron gas (2DEG, free electrons confined in two dimensions) is placed in a very strong perpendicular magnetic field. Electrons start to orbit around circular trajectories and Hall resistivity changes in steps with increasing B field, forming plateaus of values that are multiples of the inverse of conductance quantum e^2/h as

$$\rho_{xy} = \frac{h}{e^2\nu}, \tag{2.18}$$

where h – Planck's constant, e – electron charge and ν – integer (Figure 2.12 (c)). It has to be emphasized that values of ρ_{xy} change proportionally to two fundamental constants and that at these plateaus the resistivity value changes as little as one part in a billion. Longitudinal resistivity ρ_{xx} stays zero during each step, appearing only during transitions from one step to another.

From the microscopic view, electrons in a magnetic field undergo circular motion because of the Lorentz force. The size of the resulting cyclotron orbit depends on the magnetic field strength B and electron velocity v as

$$r_c = \frac{mv}{eB}. \tag{2.19}$$

The orbiting electron thus acquires angular momentum $L = mvr_c = eBr_c^2$. Because angular momentum in quantum theory is quantized as $L = n\hbar$, only a set of discrete values are allowed for r_c, i.e., $r_n = \sqrt{n}l_B$, where $l_B = \sqrt{\hbar/eB}$ is the magnetic length. The energy of an electron in a quantized orbit is $L\omega_c = n\hbar\omega_c$, where $\omega_c = eB/m$ is the same for all sizes of cyclotron orbits. As the energy levels are shifted up from zero energy by $\hbar\omega_c/2$, the resulting allowed energy levels are

$$E_n = \hbar\omega_c(n + \frac{1}{2}), \tag{2.20}$$

known as Landau levels (Figure 2.13 (a)). Each Landau level can hold many electrons – one electron per magnetic flux quantum $\Psi_0 = h/e$, and the number of electrons in a level will be proportional to the area of the sample. Landau levels can be compared to a band structure. If n Landau levels are filled and the rest are empty, then an energy gap separates those states similar to an ordinary insulator. With Fermi level in the gap, QH system represents the first topological insulator.

Semiclassically, the movement of electrons around the edge can be imagined as skipping

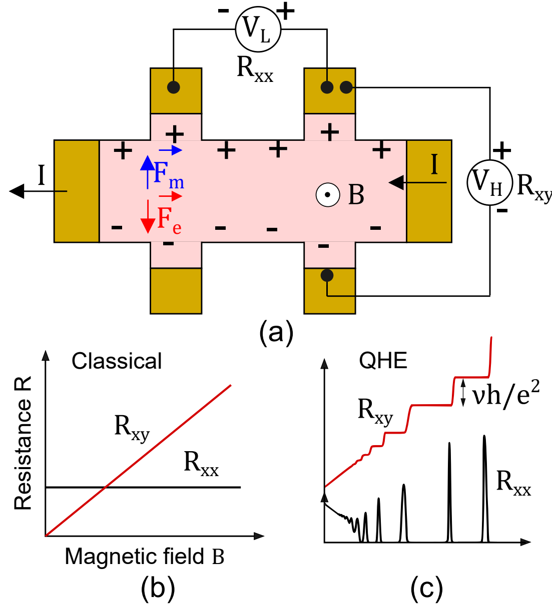

Figure 2.12: Hall effect. (a) Hall effect measurement schematics with depiction of charge carriers and forces. F_m – magnetic force acting on positive charge carriers, F_e – electric force arising from the charge build-up. (b) In the classical Hall effect, transversal resistance depends linearly on the magnetic field, while longitudinal resistance is independent of it. (c) Quantum Hall effect shows steps in transversal resistance that lead to plateaus of nearly straight lines, accompanied by peak of longitudinal resistance at each step. Figure adapted from [108].

orbits, since the circular electron trajectories cannot be completed at the edges (Figure 2.13 (b)). This results in propagation in different directions along each edge, and restricts backscattering, as electron would need to traverse the whole sample to access available states that travel in reverse direction. These states propagating in different directions are called *chiral edge states*. In addition, conduction in these edge states is ballistic. The semiclassical picture also supports the notion that edge conductivity is impossible without the existence of an insulating bulk.

The quantization of transversal conductance does not depend on the system geometry or materials used and therefore can be used as a resistance standard. The robustness and generality of this effect is most completely described using topological arguments.

To explain how topology is connected to QHE, the ideas of Berry phase and Berry curvature need to be introduced. In a sense, Berry phase classifies loops in momentum space, in analogy to magnetic field in the real space.

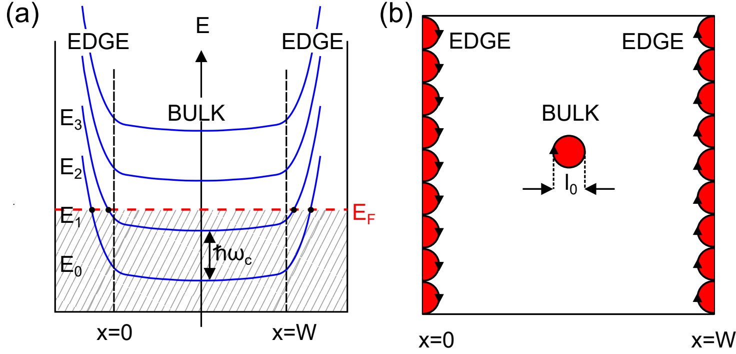

Figure 2.13: Microscopic and semiclassical picture of QHE, showing difference between bulk and edge states. (a) Landau levels as a function of position x along the sample. States close to the edge disperse and can carry current. Even if the Fermi level is in the gap in the bulk of the sample, there are states at both edges that cross the Fermi level, resulting in quantized transversal resistance. (b) In the bulk, electrons undergo circular motion and cannot carry current. At the edges, the full circular trajectory cannot be completed, resulting in a current-carrying motion. Figure adapted from [109].

Bloch states under cyclic evolution in the momentum space gain a phase shift

$$\gamma = i \oint_C d\mathbf{k} \cdot \langle \phi_n | \nabla_k | \phi_n \rangle, \tag{2.21}$$

where γ is the Berry phase. Similarly to vector potential in electromagnetism, the integrand in 2.21 can be defined as Berry potential as

$$\mathbf{A} = i \langle \phi_n | \nabla_k | \phi_n \rangle \tag{2.22}$$

Taking the curl of **A** and employing Stoke's theorem, Berry phase shift can be expressed over a surface as

$$\gamma = \int_S d\mathbf{S} \cdot (\nabla \times \mathbf{A}) \tag{2.23}$$

For QHE systems, Berry phase shift stays constant under smooth adiabatic transformation of the Brillouin zone. TKNN model [110] used Berry shift to express the Hall conductance as

$$\begin{aligned} \sigma_{xy} &= n\frac{e^2}{h} = \frac{e^2}{h}\frac{-i}{(2\pi)^2}\int_S d\mathbf{S} \cdot (\nabla \times \mathbf{A}) \\ n &= \frac{-i}{(2\pi)^2}\int_S d\mathbf{S} \cdot (\nabla \times \mathbf{A}), \end{aligned} \tag{2.24}$$

where n is the topological invariant for QHE, known as the Chern number. Chern number is a positive integer, that corresponds to the number of filled Landau levels. For a trivial band insulator, n is always zero. The topological invariant of a trivial insulator can not change to that of a QH insulator under smooth Brillouin zone transform.

It turns out, that there exist physical systems, in which QH effects arise without application of strong external magnetic fields and low temperatures, known as 2D and 3D TIs.

2.5.2 2D and 3D topological insulators

It turns out that the topological structure can exist even without the application of a strong magnetic field. Instead, spin-orbit coupling (SOC) can function as a source of local magnetic flux. SOC is a relativistic effect that describes interaction between electron's spin and orbital angular momentum (Figure 2.14 (a)), and is explored for technological applications in spintronics. Using SOC, Quantum Spin Hall effect (QSHE) in 2D was theoretically formulated [111]. It was later demonstrated using transport experiments in a CdTe/HgTe/CdTe semiconductor heterostructure quantum well [112], confirming the existence of 1D edge channels with quantized conduction.

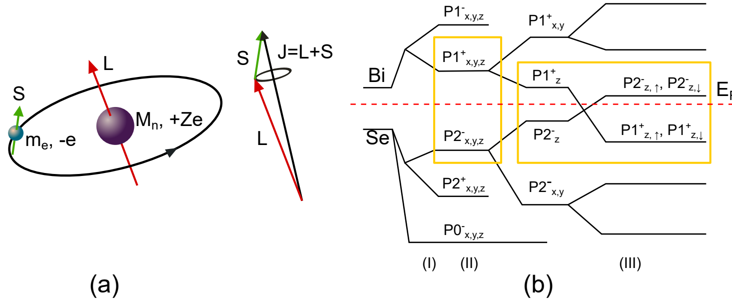

Figure 2.14: (a) Origin of band inversion in 3D TIs. Spin-orbit coupling (SOC) describes the interaction between electron's orbital angular momentum L and spin's intrinsic momentum S, leading to a total momentum J. Strong SOC leads to band inversion in topological insulators as shown for two Bi_2Se_3 p_z orbitals in (b). (b) Schematics of combination of Bi and Se atomic orbitals to form molecular orbitals and then conduction and valence bands in Bi_2Se_3. Three interactions that change the placement of the energy levels are shown: (I) chemical bonding, (II) crystal-field splitting and (III) SOC. Figure adapted from [113]

The strong SOC can easily invert valence and conduction bands in narrow gap semiconductors in 3D TIs. More specifically, in Bi_2Se_3 inversion occurs between Bi p_z orbital and Se p_z orbital with opposite parity at the Γ point (Figure 2.14 (b)) [113]. This means that in the final band structure the conduction band has contributions from the original valence band and

vice versa. Band inversion causes change in topological invariant and leads to development of topological surface states (TSS).

To exploit the properties of the TSS, Fermi level has to lie in the insulating band gap, which can be achieved using both electrical field and mechanical deformation.

2.5.3 Quantum oscillations and interference phenomena in Bi_2Se_3

The effects of magnetic flux on quantum transport in Bi_2Se_3 and other TI materials unveil various oscillatory and interference phenomena. These phenomena provide insights into the material's electronic characteristics, encompassing its band structure, carrier density and mobility. Particularly important for TIs, distinct signatures in these phenomena allow also distinguishing Dirac fermions of surface states from those of an ordinary metal, 2DEG or surface layer [62].

One important consequence of this interplay between electrons and magnetic field is Landau quantization of energy levels, already discussed in the context of QHE. Raising the magnetic field increases both the spacing between these levels and the available states per each level (Figure 2.15). As a result, electrons tend to occupy lower and lower levels with increasing field until all electrons occupy the lowest Landau level. The depopulation of Landau levels is expressed as oscillating longitudinal conductivity, revealing Shubnikov-De Haas oscillations:

$$\Delta\sigma_{xx} \propto [2\pi(\frac{F}{B} - \frac{1}{2} + \beta)], \tag{2.25}$$

where F is the frequency and β is the phase shift $(0 \leq \beta < 1)$.

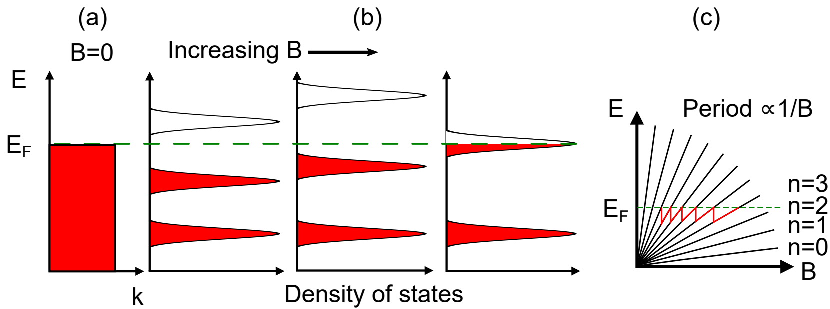

Figure 2.15: Formation and population of Landau levels as a function of B field. (a) For $B = 0$ there are no Landau levels. (b) Increasing B field leads to increased spacing between Landau levels. As the Landau level passes through the Fermi level, it gets depopulated, creating an oscillatory pattern with period proportional to $1/B$ (c). Figure adapted from [62].

Phase factor β in SdH oscillations allows to determine the Berry phase of the system [62]. For parabolic dispersion, Berry phase is zero (for the corresponding $\beta = 0$) and for Dirac fermions (and also TIs for large number of LLs) it is π (for $\beta = \frac{1}{2}$). Moreover, it is possible to determine the carrier density by analyzing the frequency F of the SdH oscillations employing Onsager's equation.

$$f = \frac{\hbar c}{2\pi e} \pi k_F^2, \tag{2.26}$$

where k_F is the Fermi wave vector. For a circular cross section of Fermi surface F_s, an averaged value of k_F can be calculated and thus the carrier density n.

Quantum interference phenomena such as universal conductance fluctuations (UCFs) [114], weak anti-localization [115, 116] and Aharonov-Bohm oscillations [117, 118] are useful tools for probing carrier transport properties in TIs. These phenomena emerge from the wave-like nature of charge carriers, a characteristic that the semi-classical drift-diffusion charge transport model does not account for.

In the case of open electron trajectories, random phase variations preclude interference effects. However, in self-intersecting trajectories that form closed loops, a different scenario takes place. Constructive interference of the trajectories increases probability of charge carrier backscattering and manifests as increased resistivity – an effect known as weak localization (Figure 2.16 (a)). In materials like Bi_2Se_3, where the electron's spin couples with its orbital motion, destructive interference of amplitudes results in a reduction of classical resistivity. This effect, referred to as weak antilocalization (WAL) (Figure 2.16 (b)), becomes observable when the spin-orbit scattering length l_{SO} is smaller than phase coherence length l_ϕ. Here the electron gains an additional phase π after completing a closed trajectory.

The introduction of a magnetic field into this system further influences closed electron trajectories by modulating the phase difference. This modulation leads to the suppression of both weak localization and weak antilocalization effects. Consequently, magnetoresistance measurements become valuable tools for determining the phase coherence length l_ϕ and spin-orbit scattering length l_{SO}.

These parameters can be extracted using Hikami-Larkin-Nagaoka (HLN) model [119].

$$\delta G_{WAL}(B) \equiv G(B) - G(0) = \alpha \frac{e^2}{2\pi^2 \hbar} [\psi(\frac{1}{2} + \frac{B_\phi}{B}) - \ln \frac{B_\phi}{B}], \tag{2.27}$$

where $B_\phi = \hbar / 4 e l_\phi^2$, ψ – digamma function and α – a prefactor, that characterizes SOC and the coupling between surface and bulk states.

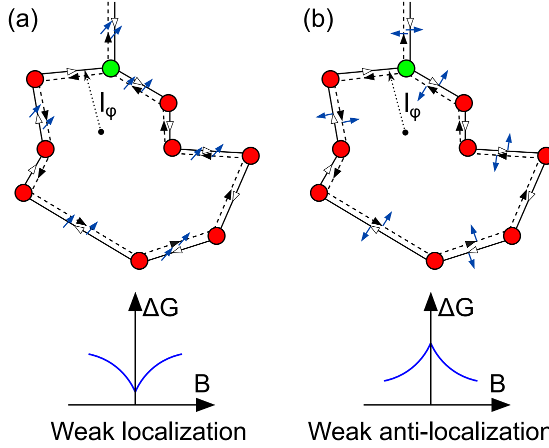

Figure 2.16: Origin of weak localization and anti-localization in disordered systems with diffusive transport. (a) The interference between to closed time reversed paths is constructive without spin-orbit coupling and leads to increased backscattering (WL). (b) With spin-orbit coupling included, interference is destructive and leads to reduced backscattering (WAL). Figure adapted from [66].

2.5.4 Modulating Fermi level of Bi_2Se_3 nanostructures

In a NEM switch configuration, both electrostatic field and mechanical strain impacts the charge carrier properties in the Bi_2Se_3 NS. As stated previously, to exploit the phenomena of TSS, E_F has to lie in the insulating bulk band gap. Due to difference in E_F for bulk and TSS on both top and bottom surfaces, charge transfer occurs to equilibriate the E_F. This leads to a development of a potential difference and corresponding band bending (Figure 2.17a).

Electrostatic gating has been employed as an effective means of tuning the Fermi level of Bi_2Se_3 NS (Figure 2.17). Both bottom gate and top gate configurations (Figure 2.17b) have been employed to observe field effect and demonstrate ambipolar transport [120]. Resistance dependence on gate voltage can be used to confirm, if samples are bulk-insulating – then a clear resistance maximum is observed, when the Dirac point is crossed.

Adding mechanical strain to the TI, it is possible to switch the topological character on and off [70]. Straining materials to change their electronic properties is not a new concept – for example, one of the major achievements in CMOS technology was the introduction of strained Si to increase channel mobility. The straining can be achieved either by chemical substitution or by epitaxial mismatch. Both of these approaches allow to either expand or contract the crystal lattice, however, they do not offer reversibility. By using pure mechanical deformation, it is possible to switch between topologically trivial and non-trivial material and

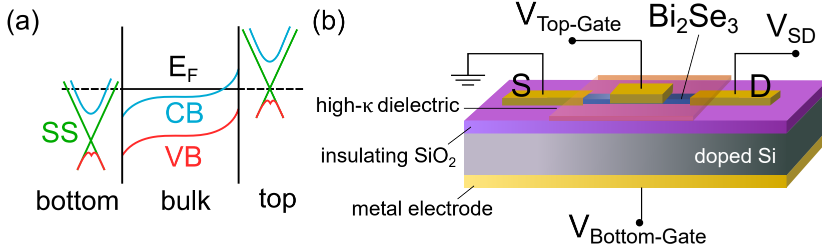

Figure 2.17: (b) Band structure schematics of Bi_2Se_3, showing topological surface state (TSS) Dirac dispersion on bottom and top surfaces, Fermi level E_F and bulk conduction (CB) and valence (VB) band bending. (a) Schematics showing typical gating setup with top (TG) and bottom (BG) gates insulated from Bi_2Se_3 NS using high-κ dielectric and SiO_2 respectively. Figure adapted from [120]

back. This means we either switch on or off the spin current or low-dissipation properties of the surface.

The shift of Dirac point has been demonstrated using ARPES for Bi_2Se_3 films with tensile elastic strains up to 2.1% [121] and using transport experiments [122].

2.6 On-chip integration of suspended one-dimensional nanostructures

2.6.1 On-chip nanostructure integration methods

In situ investigation of NEM switches in SEM and transmission electron microscope (TEM) [41, 83, 123] has greatly expanded the understanding about NEM switch operational principles. *In situ* measurements allow following the dynamic processes that occur in NEM switches in real time. Also, they are an invaluable tool for exploring vast space of geometrical configurations – by using a manipulator, distances between the active elements and the electrodes can be adjusted for the same active element and electrodes. Considering the variability of nanoscale elements, this allows for more certainty of interpretation of the results. Thus *in situ* measurements are a crucial step before fabricating integrated NEM switches with comparably low reconfigurability but high robustness and repeatability.

In planar top-down integrated NEM switch technology, fabrication process is carried out on the same substrate. Fabrication of a SiC NEM inverters can serve as a typical example [8]. NEM inverter consists of two in-plane NEM switches with beam length of 8 μm, width 200 nm and gap of 150 nm, with total area of approximately 8 μm^2. Si with 500 nm thick thermal SiO_2 layer was used as a substrate. Chemical vapor deposition was used to deposit 400 nm thick heavily nitrogen-doped polycrystalline 3C-SiC layer. To pattern the SiC layer, hard mask was fabricated by first thermally evaporating 40 nm thick Ni layer and then patterning it by electron-beam lithography and lift-off. The pattern was then transferred into SiC by

deep reactive ion etching with SF_6 gas. Wet etching was used to remove SiO_2 layer to release the devices, and supercritical CO_2 drying to avoid stiction of the SiC beams to the substrate.

Integration of bottom-up 1D NS NEM switches on-chip usually involves at least two substrates. 1D NS are grown on a separate growth substrate (e.g., glass, Si, quartz, foil, anodized alumina) and are subsequently integrated on a device substrate with electrodes. The need for different substrates can be understood considering the classical vapor-liquid-solid (VLS) bottom-up growth mechanism of 1D nanostructures. VLS growth results in vertical or angled with respect to the substrate NS that subsequently need to be integrated with planar thin film electrodes. Integration involves transfer of 1D NS, alignment in desired positions, contact fabrication and in case of NEM switches, also suspension of the NS to enable mechanical movement.

Despite the exciting application prospects of 1D NS, their on-chip integration still needs to address the following main challenges:

- How to position 1D NS with nanometer accuracy?
- How to select 1D NS with defined size, stoichiometry, morphology and properties?
- How to ensure parallel scalable integration with high yield?
- How to fabricate stable and reliable electrical contacts to 1D NS?
- How to ensure mechanical movement and avoid stiction due to capillary forces?
- How to preserve physical and chemical properties during integration?

Mechanical transfer is a simple method, where the growth substrate is pressed against the device substrate either with or without pre-fabricated electrodes. Mechanical transfer is often employed for characterization of individual 1D NS. This represents a relatively low level of alignment, which can be greatly increased by applying a directed force [124].

The most accurate positioning can be achieved using nanomanipulation methods, where the individual 1D NS can be manually placed in a target position using piezomotors [125]. While this method allows to implement exciting configurations, it is inherently serial and thus results in low yield.

High placement accuracy and at the same time parallel process is offered by dielectrophoresis (DEP) method [126]. In DEP, 1D NS are suspended in a dielectric media, and respond to distribution of electric field gradient. DEP can control both the position and number of aligned 1D NS. However, DEP requires a dedicated electrode structure that can differ from the electrical connections in the final device. Similar to DEP, magnetic alignment can be employed, and variations with assistance of microfluidic flow have been reported.

Selective growth explores the patterning options of the device substrate that enhances preferential 1D NS growth, thus avoiding the need for NS transfer completely [127–130]. Besides being a parallel process, it also allows to minimize chemical interaction with other processing chemicals, as the NS growth can be one of the last fabrication steps. Vertical selective 1D NS growth is very similar to the conventional VLS mechanism and can be employed for 3D integration, while lateral growth requires novel techniques. Some promising approaches have been demonstrated by confining NS growth in narrow pre-patterned channels or utilizing the epitaxial interactions with the underlying crystalline substrate [128]. Some approaches focus on planarization of vertically grown 1D NS. First, an array of growth sites is patterned to initiate vertical or angled growth of 1D NS, then a technique is employed to bend 1D NS so that they lie horizontally on the substrate. For example, contact printing involves detachment of 1D NS from the growth substrate with the help of van der Waals forces, while defining the alignment direction using hard-contact sliding [129]. Use of elastocapillary forces for planarization of 1D NS has also been reported [130].

Morphology, stoichiometry, size and physical properties of the 1D NS can be controlled already in the synthesis phase before transfer. However, in some cases a variety of NS are grown during one synthesis run and transfer and alignment methods should exhibit some form of selectivity towards the necessary NS characteristics. This has been demonstrated in case of DEP alignment, where 1D NS were sorted according to their conductivity. Figure 2.18 and Table 2.2 summarize and give a qualitative comparison of approaches for 1D NS integration.

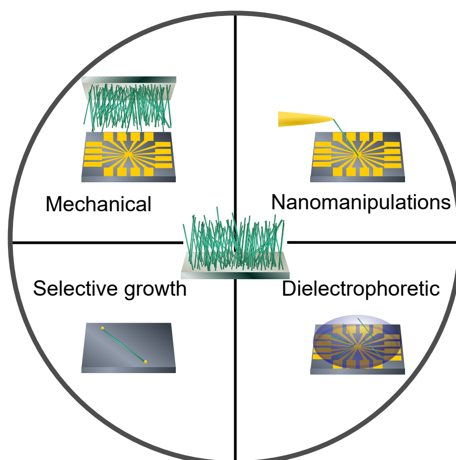

Figure 2.18: Schematic depiction of methods for on-chip integration of 1D NS.

Table 2.2: Comparison of methods for on-chip integration of 1D NS in terms of positioning accuracy, yield and implementation specifics.

Method	Positioning accuracy	Yield	Comments	References
Mechanical transfer	Low	Medium	Easy to implement, no contamination	[124, 131]
Nanomanipulations	High	Low	Serial process	[83, 125]
Dielectrophoresis	High	Medium	Dedicated electrode structures needed	[132–134]
Selective growth	High	High	Growth and device on the same substrate	[37, 127]

2.6.2 Fabrication of suspended nanostructures

Enabling of mechanical movements adds the next challenge to the integration process. In top-down thin film fabrication processes, release of the active element by creating a suspended structure is conventionally done as the last step, using wet or dry etching of the substrate beneath the structure. A similar approach has been employed also in devices using bottom-up fabricated active elements (e.g., CNTs [101]). Here it is very important to ensure that the etchant exhibits high selectivity and attacks only the substrate material, leaving active element intact. Alternatively, 1D NS can be transferred to substrates already containing pre-patterned gaps, but this increases the risk of sticking to the substrate during next processing steps. NEM switches can also be fabricated without top contacts, relying on adhesive force between the suspended 1D NS and bottom contacts. This reduces number of steps and device loss during fabrication, however, may increase contact resistance.

Dealing with nano-sized air gaps in processes involving liquids involves a high risk for stiction due to capillary forces. When a liquid and vapor phase exists simultaneously (e.g., drying after lift-off and wet etch), it causes capillary forces and thus shrinkage. According to Laplace's equation, the pressure depends inversely on the distance d between the two plates as (Figure 2.19(a))

$$\Delta P \approx -\frac{2\sigma cos\theta}{d}, \tag{2.28}$$

where σ is the surface tension and θ is the angle between solid and liquid meniscus.

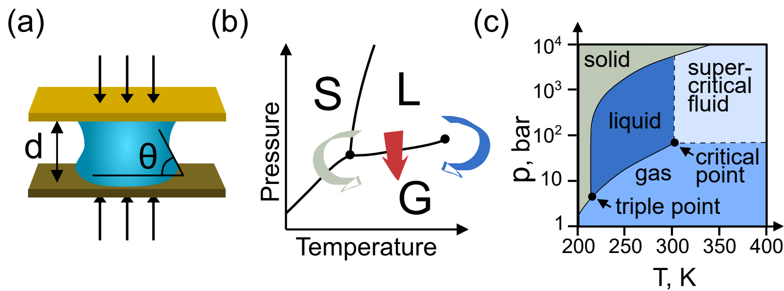

Figure 2.19: Supercritical drying. (a) Capillary forces between two plates depend on the separation d and angle between liquid and gas θ. (b) Liquid-gas phase transition (red arrow) can be avoided by operating beyond the critical point as in supercritical drying (blue arrow) or going through liquid-solid-gas transition as in freeze drying (grey arrow). (c) CO_2 phase diagram, showing the region of supercritical fluid phase above 304.25 K and 73.9 bar.

Therefore in microscale and nanoscale separations the capillary forces become very strong and need to be eliminated when handling fragile suspended structures. The idea behind supercritical drying is to avoid the phase boundary between the liquid and the gas by operating at a critical point. Phase diagram of CO_2 used in this work for supercritical drying in shown in Figure 2.19 (b-c).

3.EXPERIMENTAL

3.1 Synthesis, morphology and yield of one-dimensional nanostructures

3.1.1 Synthesis of one-dimensional nanostructures

CuO nanowires and Bi_2Se_3 nanobelts were grown at the Institute of Chemical Physics, University of Latvia, in a quartz tube furnace, using thermal oxidation and physical vapour deposition, respectively.

For CuO nanowire growth, Cu foil was used as the growth substrate. Oxidation cycle consisted of heating with rate 16 °C/min up to 500 °C with 210 min oxidation at constant 500 °C. Then the furnace was allowed to cool down to room temperature. To raise the humidity in the air while synthesizing, a small container carrying 7 μL of distilled water was placed inside the furnace tube near the substrate. This was done after the temperature reached 374 °C to prevent droplets from forming on the substrate. To create an electric field, a piece of Cu foil was put between two steel electrodes 1 cm apart, and a voltage of 200 V was applied using a Keithley 6487 Picoammeter/Voltage source (Tektronix).

Bi_2Se_3 nanobelts were grown on glass from a Bi_2Se_3 powder in an N_2 ambient via physical vapor deposition, modified from [135]. Temperature cycle consisted of increasing temperature from room temperature to 585 °C in 45 min, then keeping constant 585 °C for 15 min and allowing to cool down to 545 °C. During this stage, Bi_2Se_3 evaporation took place. Afterwards, the tube was pumped until its temperature reached 535 °C. At the next stage, N_2 flow at 20–25 Torr was used to initiate 1D NS growth. During growth, the temperature of the glass substrate was in the range of 375–490 °CC. N_2 flow was stopped as the temperature reached 500 °C, pumping was stopped at 475 °C. To finish the process, the tube was filled with N_2 and the glass substrate was removed when the temperature was in the range of 110–170 °C.

Both catalyst-free and synthesis with Au catalyst was used for growth of Bi_2Se_3 nanobelts. Au catalyst particles were obtained by thermally evaporating Au thin film layers of thickness 1.5 to 16 nm and heating them.

Ge nanowires were synthesized in University College Cork (Cork, Ireland) using synthesis in supercritical fluid (SCF) from alkanethiol-coated gold nanocrystals [87, 136, 137].

3.1.2 Characterization of morphology of one-dimensional nanostructures

The cross-sectional shape and its uniformity along the length determines mechanical response of the 1D NS, allows to estimate the switch-ON voltage in a NEM switch and resonant

frequencies.

Morphology of the as-synthesized 1D NS was characterized using scanning electron microscope (SEM) Hitachi FE-SEM S 4800 and atomic force microscope (AFM) Asylum Research MFP-3D. The best resolution for SEM imaging was as as high as 1 nm (at 15 kV voltage and 4 mm working distance) and was used for determination of length, width and thickness.

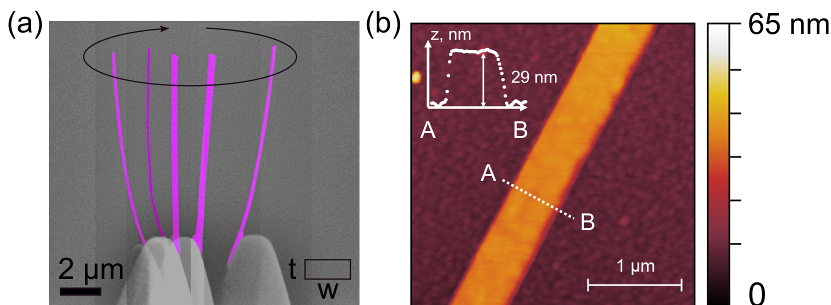

Figure 3.1: (a) Overlayed colored SEM images, showing different projections of Bi_2Se_3 nanobelt fixed on an etched Au tip. The smallest and largest projection of the cross-section reveals the rectangular ribbon-like shape. SEM was used to determine the length, width and thickness of free-standing 1D NS. (b) AFM image of a Bi_2Se_3 nanobelt lying on a substrate and its corresponding line profile (AB in inset), from which the thickness of 29 nm was obtained.

For *in situ* measurements, 1D NS were fixed to sharply etched gold electrodes. The sample was rotated inside SEM using a micromotor Faulhaber ADM0620. This allowed taking images of projections at different angles (Figure 3.1 (a)) and thus determining maximum and minimum cross-section corresponding to width and thickness, respectively, as well as the maximum length values.

AFM with resolution up to 0.04 nm in z direction and 10 nm in xy directions was used for thickness measurements for 1D NS lying on a flat substrate (Figure 3.1 (b)). AFM with cantilevers AC160TS (resonant frequency 300 ± 100 kHz and spring constant in the range of 8.4–57 N/m) was used in AC dynamic oscillation regime to minimize shear force that could damage or displace the 1D NS. Due to the angle of the AFM tip, AFM scans were used only for rough determination of width values.

3.1.3 Characterization of mechanical and electrical properties of one-dimensional nanostructures

Mechanical properties were determined in the elastic regime using quasi-static and dynamic methods of deformation. The quasi-static approach involved deforming a 1D NS by applying a gradually increasing force to its middle point with an AFM tip while measuring

the force and the deformation. The dynamic method involved inducing vibrations in the 1D NS by application of alternating voltage combined with direct voltage. Sourcemeters Keithley 6430 and Keithley 6487 were used to apply DC voltage and measure current between S, D and G electrodes. To induce resonance in the suspended NS, an Agilent N9310A RF Signal Generator was used for applying AC voltage. The resulting oscillatory AC+DC signal was monitored using a Textronix TDS-1012 oscilloscope. The fundamental resonant frequency was determined by registering the frequency at which the amplitude of vibration is maximum. In addition, the amplitude-frequency dependence shows a Lorentzian-shaped profile at resonance. The vibrations were detected visually in SEM and electrically using a vector network analyzer (VNA) Rohde & Schwarz ZNB 8. For electrical detection of mechanical resonance, a circuit was designed and implemented on a printed circuit board (PCB) that is compatible with the PPMS puck holder. The readout principle of the circuit was based on registering changes in AC transfer parameter S_{21} as it gets modulated by a capacitively coupled resonating Bi_2Se_3 nanobelt. The electrical circuit diagram along with the element values is shown in Appendix B.2.

The fundamental resonant frequency and dimensions of the 1D NS were employed to calculate Young's modulus.

Charge carrier transport was measured in two-terminal and four-terminal configurations, fabricating metal electrodes on top of the 1D NS. Temperature-dependent resistance was characterized for Bi_2Se_3 nanobelts in physical property measurement system (PPMS) DynaCool 9T, Quantum Design) in the temperature range from 300 to 2 K. Bi_2Se_3 magnetoresistance was characterized at low temperatures in a perpendicular magnetic field up to 9 T, and field effect was characterized by measuring longitudinal resistance R_{S-D} as a function of gate voltage through SiO_2 dielectric.

3.2 *In situ* characterization of NEM switches

In situ measurements were carried out inside SEM, using nanopositioning system SmarAct 13D. SmarAct 13D consisted of 12 SLC-1720 linear positioners with step widths 50 to 1500 nm and scan range of 1.5 μm. Four 3D nanomanipulators could each be connected to an electrode to investigate different configurations between the active elements and electrodes. Electrochemically etched sharp gold tips with bending radii as low as 10 nm and gold-coated flat AFM cantilevers with dimensions of 160 x 40 x 3.7 μm) were used as electrodes.

During the process of gating and measuring current in the nanostructure, special care was taken to apply voltage in small steps to ensure a steady charge redistribution in the NS and minimize the risk of generating large current peaks. Moreover, electrical measurements were carried out with the electron beam off to avoid any increase in current through the nanostructure caused by the electron beam. In cases where the beam was turned on, the

additional current was registered and subtracted from the measured data.

3.3 On-chip integration of a NEM switch

Two main configurations of NEM switches were employed in this thesis (Figure 3.2). The simplest version had 1D NS placed on top of previously structured electrodes, forming an adhesive bottom contact. An optimized version included additional fabrication of ohmic contacts on top of the 1D NS. Both architectures employed a bottom gate electrode, placed directly under the suspended active element.

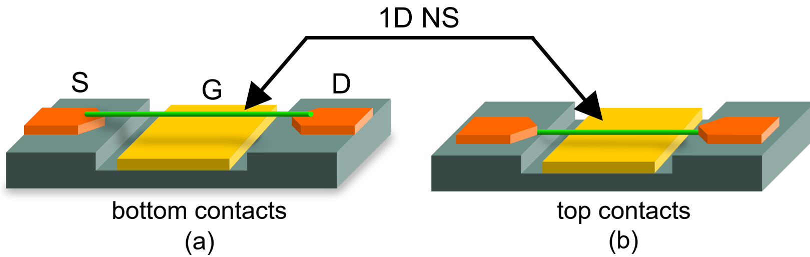

Figure 3.2: Two main S and D contact configurations employed in this thesis: (a) with adhesive bottom metal contact and (b) with top metal contact.

3.3.1 Fabrication of source, drain and gate electrodes in bottom-contact configuration

1D NS were integrated on Si/SiO_2 substrates diced in 10 x 10 mm chips with Si resistivity levels from 1 $\Omega \cdot$ cm (p-type) to 50000 $\Omega \cdot$ cm (undoped) and thermal oxide thickness from 200 to 1000 nm. High resistivity substrates were used for resonance characterization. Different oxide thickness allowed to vary trench depths.

NEM switch electrodes were fabricated with photolithography and electron beam lithography (EBL), etching, thermal evaporation and lift-off. Optical lithography was used for patterning relatively large electrodes (with lower width limit of about 1 μm), and electron beam for patterning submicrometer features and to increase overlay alignment accuracy of different layers. The best achievable alignment accuracy depends on the patterning parameters and the size of the overlay markers fabricated in the previous step and for optical lithography is on the order of several hundreds of nanometers, while for EBL better than 40 nanometers.

Photolithography uses light to transfer a design pattern into light-sensitive thin film polymer – resist – on a substrate. Two types of exposure tools were used: direct writer and mask aligner. Direct laser writer with 375 nm wavelength laser diode source (Heidelberg μPG 101 Tabletop Micro Pattern Generator, minimum feature size 0.6 μm) exposed the design

pattern from a CAD file without any contact with the substrate. The exposed areas were defined using acousto-optic modulator and mechanical stage movement. This tool was used for low volume fabrication during the design testing process, as the maskless process offers high design flexibility. After confirming the final version of the design, the direct writer was used for patterning of photomasks. To fabricate a photomask, the final design was exposed on a glass substrate covered with opaque 100 nm thick chromium or semi-transparent iron oxide thin film. Mask aligner (Mask aligner Suss MA/BA6 Gen4) aligned this pre-patterned photomask with the substrate and pressed against it. 350 W Hg lamp source was used, and the wavelength was controlled with a set of filters and dose with exposure time, transferring the pattern in a 1:1 ratio. The main difference between the direct write and fixed design mask aligner tools was the speed – exposure of 10 x 10 mm area took about 1 hour in a direct writer, whereas mask aligner completed the exposure in several seconds.

Positive Novolak-based **photoresists** AZ1505 and AZ1518 with thickness from 0.6 to 1.8 μm were used for designs with minimum feature size of approximately 1 μm and 2 μm respectively. Exposure with light of a certain wavelength increases the solubility of the photoresist in the developer. Exposure dose and development time was optimized such that the photoresist was cleared completely after development. For efficient lift-off (removal of the unnecessary metal on top of the resist), an additional approximately 200 nm thick lift-off resist LOR-3 was used before spin coating of AZ resist to ensure undercut of the resist stack. Undercut ensured that the subsequently deposited metal forms a discontinuous film, making it easier for the solvent to reach the photoresist underneath it during lift-off.

Finer size electrodes for four-probe contact geometry were patterned using **EBL**, either using mix and match technique (EBL combined with photolithography) or fully-EBL. EBL is a direct-write technique, similarly to laser writer. In terms of resolution, EBL can achieve much higher resolution ($\approx$ 10 nm), as it uses electron beam with shorter wavelength and beam spot size. In EBL, polymer chains are either broken in case of positive resist or cross-linked in case of negative resist to increase or decrease its solubility during development, respectively. Positive polymethyl methacrylate (PMMA) resists with thickness from 200 nm to 1.7 μm with bottom copolymer layer (El6 and El9) were used for sample fabrication in this thesis.

Gate electrodes were fabricated by first patterning trenches into SiO_2, using **wet or dry etching**, followed by metal electrode definition and thermal evaporation into the trench. For wet etching, HF-based etchant was used with AZ1505 and AZ1518 photoresists as masking layers. Crucial step prior to wet etching, was hardbake of the photoresist (optimized to 120 $^{\circ}C$ for 5 minutes on a hotplate) to increase its etch-resistance and minimize underetch. Without hardbake, trenches would become too wide and lead to stiction of the 1D NS to the electrode.

A benefit for wet etching procedure was that the same masking layer could be used for trench fabrication and metal deposition, securing a self-aligned procedure. Self-alignment was not possible using dry etch. During dry etch, the photoresist got too thin both for successful liftoff and for fabrication of trenches with larger depth, therefore during dry etching a process using metal hard mask was optimized.

Dry etching of gate electrode trenches was done to get more anisotropic trench edge profiles and larger trench depths, without compromising the width. SiO_2 was etched with CHF_3-Ar gas at 10 °C table temperature with reactive ion etch system RIE Cobra. Different thickness PMMA resists (approximately 200 nm thick PMMA A4 and 1700 nm thick PMMA A9) were tested as masking layers for relatively shallow trenches and 100 nm thick Cr hard mask was used for deep trenches up to 0.7 μm depth. Dry etch process required removal of the masking layer using O_2 plasma prior to metal deposition into trenches.

For **thermal evaporation** of 60 nm thick Au electrodes with Ti adhesion layer, vacuum system Sidrabe was used. With this physical vapor deposition technique, the source material is converted from solid to gas phase by heating it in a boat or crucible, made of a material with high melting temperature (e.g., tungsten, molybdenum). Compared to other metal deposition techniques such as magnetron sputtering, the deposition is relatively directional, thus avoiding the coverage of resist sides and facilitating its removal during lift-off.

Figure 3.3 schematically depicts typical fabrication process steps from blank mask to metal electrodes, patterned on a Si chip. The main stages of the fabrication process for one design layer are:

- Substrate cleaning (wet cleaning in an ultrasonic bath using acetone and isopropyl alcohol, followed by N_2 drying and dry cleaning with O_2 plasma);
- Spin-coating of the photoresist to achieve the desired thickness of the film;
- Soft-bake of the photoresist on hot plate to evaporate the excess solvent from the film;
- Exposure of the design pattern;
- Development of the design pattern;
- Optional hard-bake to make photoresist more resistant to etching step;
- Optional wet or dry etching of the opened areas on substrate for patterning electrodes in trenches;
- Ashing with oxygen plasma to remove organic residues;
- Metal deposition using either thermal evaporation;

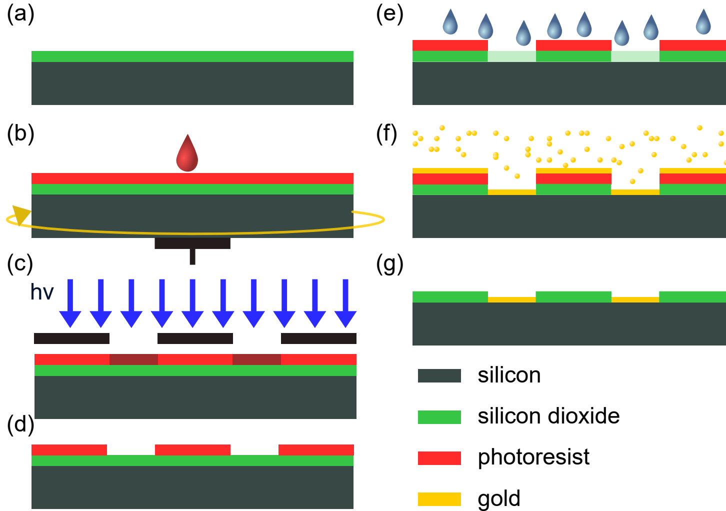

Figure 3.3: Electrode fabrication process steps. (a) Silicon coated with SiO_2 substrate. (b) Spin-coating of photoresist/e-beam resist. (c) Exposure. (d) Developed resist. (e) Etching. (f) Metal deposition. (g) The final sample with electrodes in the trenches after lift-off.

- Lift-off process, where the excess metal is removed by dissolving the underlying photoresist.

Detailed recipes of the processes are given in the Appendix A.1 of this thesis.

3.3.2 One-dimensional nanostructure transfer

Three different methods were used to transfer 1D NS to the device substrate: nanomanipulations, dielectrophoretic alignment (DEP) and mechanical dry transfer.

By using nanomanipulator with an electrochemically etched sharp Au tip, an individual 1D NS was broken off from the growth substrate, picked up and either fixed to the tip or placed at a desired location on thin film electrodes. Fixing on the Au tip was done with electron beam-induced platinum deposition (EBID) in SEM (Tescan Lyra). As-fabricated samples were employed in electromechanical experiments *in situ*.

For DEP alignment, 1D NS were first transferred from the growth substrate to a liquid media (isopropyl alcohol).CuO nanowires were removed from Cu foil and dispersed in IPA using 37 kHz ultrasonic agitation for 3 seconds. Bi_2Se_3 nanobelts were rinsed from the growth substrate to obtain the suspension to avoid their breaking during ultrasonication.

The 1D NS concentration was measured by placing 20 μl of the suspension on a clean Si substrate and letting it air-dry, then taking images in SEM and counting the number of 1D

NS in ImageJ software.

For the DEP assembly of nanowires at the desired electrode sites, the Si chip was submerged in the NW/IPA suspension and an AC voltage with 5 V–13 V amplitude was applied between the countering electrodes for 10–20 minutes.

1D NS were also transferred to the chip by mechanically pressing it on the growth substrate, resulting in randomly placed NS.

3.3.3 Top contact fabrication

CuO and Ge 1D NS were used in bottom adhesive contact configuration. To increase the contact conductivity, control over the metal/1D N interface and mechanical stability, contacts need to be placed on top of the suspended 1D NS, as was optimized in this thesis for Bi_2Se_3 nanobelt-based NEM switches.

Firstly, after resist exposure for top contacts, development time needs to be optimized. Overdevelopment is more favorable than underdevelopment, as it is crucial to remove as much resist residues as possible fro the surface of the nanostructure. Remaining nanometer-thick residuals were removed using O_2 plasma ashing (400 W power, 600 sccm at 1.3 mbar pressure for 1 minute with Faraday cage). It must be ensured that there are no residues or adsorbates left from the lithography process. However, O_2 plasma promotes oxidation of the surface of the NS. For semiconductor NS, native oxide layer forms in minutes or hours under ambient conditions. For obtaining ohmic contact characteristics, the oxide layer needs to be removed without damaging the NS and the metal deposition needs to be carried out shortly after. TI NS need even more care during processing and interface preparation to avoid increasing bulk electron concentration. Dilute HCl/acetic acid treatment for 60 seconds and bombarment with Ar ions was used to remove native oxide of Bi_2Se_3. Typically, 3–5 nm thick Cr, Ti and Pt adhesion layers were used as adhesion layers for fabricating Au contacts on 1D NS at a pressure not larger than $4 \cdot 10^{-7}$ mbar. For TIs, only two latter are used to avoid unintentional doping with Cr. For low resistance contacts, the deposited metal thin film should cover the NS conformally, which imposed limits on allowable resist and metal thickness. Reliable top-contact fabrication was achieved using metal with thickness not greater than 200 nm. Electrical performance of the as-fabricated top contacts was characterized using both two-terminal and four-terminal measurements.

3.3.4 Supercritical drying

Many fabrication process steps involved having the suspended 1D NS in a liquid that needs to be subsequently removed. For example, CuO 1D NS were suspended in IPA after

DEP process, Bi_2Se_3 1D NS with top contacts were suspended in acetone after lift-off.

Setup for supercritical drying of suspended 1D NS consisted of a chamber with inlet for introducing CO_2 and for removing IPA and CO_2, with valves controlling the flow (Figure 3.4). A thermocouple was used for temperature control during the process and a manometer for pressure control. Chamber was cooled for approximately 90 minutes in an ice bath to a temperature of 10 °C. A small glass vessel with approximately 1 ml IPA containing the submerged sample was then placed in the chamber. Then liquid CO_2 was introduced, reaching a pressure of 100 bar in the chamber. After the temperature stabilized, process of IPA rinsing was started. The rinsing was done, gradually releasing IPA and CO_2, while maintaining the temperature within the range of 0–15 °C and pressure between 65–100 bar. After all IPA was released, the temperature in the chamber was raised to 35 °C. CO_2 was gradually released while ensuring temperature in the range of 35–40 °C.

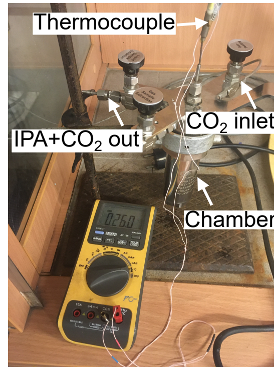

Figure 3.4: Setup for supercritical drying of NEM switches.

3.4 Characterization of operation of an on-chip integrated NEM switch

Characterization of integrated NEM switches was carried out both *in situ* inside SEM at room temperature to enable visual inspection and with PPMS at temperatures from 2 K to 300 K at 0.6 Torr pressure. For connecting to electrical contacts of external devices, Au tips were contacted to thin films electrodes using nanomanipulator (Figure 3.5 (a)). For PPMS measurements, thin film electrodes were connected to the measurement puck via ultrasonic bonding with Au or Al wire (Figure3.5 (b)). Two electrical measurement setups were used: one used solely in-built PPMS measurement options, while another used external sourcemeters connected via BNC cables.

PPMS resistivity option operates via resistance bridge, where one sourcemeter multiplexes to 3 channels. A DC current source provides 5 nA to 5 mA excitation, and voltmeter

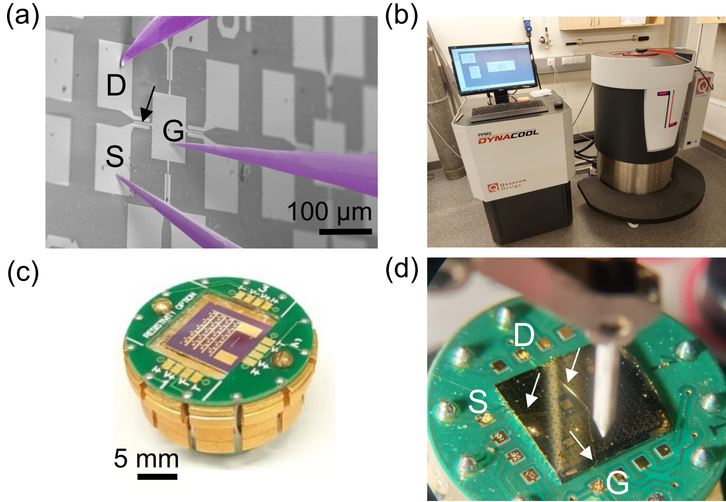

Figure 3.5: Setups for room temperature and cryogenic temperature characterization of on-chip NEM switches. (a) Colored SEM image of Au tips (purple) contacting source (S), drain (D) and gate (G) electrodes on a single NEM switch on chip (black arrow marks location of the active element). (b) Physical property measurement system for characterization in the temperature range from 2 K to 300 K by integrating chip with NEM switches on a puck with 12 electrical contacts (c) using ultrasonic bonding (d). In (d), S, D and G connections are marked and white arrows indicate Al wire.

has up to 4 reads/second. The option is well-suited for resistance values of 1 Ω to 1 MΩ. PPMS ETO option uses an an AC signal and digital lock-in detection that is based on phase-sensitive read-out of a signal at a specific frequency and phase. Low impedance mode (current source 10 nA to 100 mA, voltmeter 1 nV to 5 V) was used for I-V and resistance measurements. For gate voltage application, an external source meter was used. Magnetic field B was applied perpendicular to the sample surface.

4.RESULTS AND DISCUSSION

4.1 Bottom-up growth of one-dimensional nanostructures

*The findings of this section are published in papers **V** and **VII**.*

Several requirements guided the development of synthesis methods of 1D NS for application in integrated on-chip NEM switches. The length of the NS needed to be as large as possible and not smaller than 5 μm due to the constraints of the lithographic processing. In addition, larger lengths allowed the creation of more stable contacts by increasing the nanostructure contact area with the bottom or top electrode. The diameters and thicknesses governed the elastic force stored in the active element. Too small diameter/thickness would lead to either stiction-induced failure during the fabrication process or to too small elastic force for volatile operation. Too large diameter/thickness would lead to contact reliability issues and too high operating voltages which could lead to degradation of the active element during contact formation.

4.1.1 Growth and morphology of CuO nanowires

An investigation was conducted to examine the effect of an external electric field and increased humidity on the growth of CuO nanowires by thermal oxidation. The results showed that nanowires have cylindrical shape and the diameters of the nanowires range from 20 nm to 320 nm under all growth conditions.

The most suitable geometric parameters and yield for use in NEM switches were achieved through electric field-enhanced oxidation on the cathode side under wet air conditions. These conditions resulted in the production of nanowires with an average diameter of approximately 70 nm and an average length of 5 µm. Assuming a trench depth of 120 nm, these dimensions would lead to an approximate V_{ON} of 10 V. Increasing air humidity during the initial stage of electric field-assisted growth produced high yields of nanowires with large aspect ratios and diameters smaller than 100 nm.

4.1.2 Growth and morphology of Bi_2Se_3 nanobelts

Au catalyst-assisted synthesis was explored as a means of controlling yield and morphology of stoichiometric Bi_2Se_3 nanobelts. Au catalyst nanoparticles with mean diameters from 8 to 150 nm were obtained by dewetting Au layers of thicknesses of 1.5 to 16 nm.

The synthesis resulted in nanobelts with rectangular cross-section. During the synthesis process, it was found that the highest yield of Bi_2Se_3 nanobelts occurred when it was carried out on a dewetted 3 nm thick Au layer. This layer contained Au nanoparticles with a mean diameter of 10 nm, and by the corresponding synthesis approximately 100 nanobelts per 1000 μm^2 were produced. The achieved yield was almost 50 times greater than the yield obtained in catalyst-free synthesis according to [135].

The method involving the use of a catalyst has made it possible to adjust the mean length of Bi_2Se_3 nanobelts within the range of approximately 3 to 6 μm, and the mean thickness within the range of 30 nm to 110 nm. Assuming a typical trench depth of 200 nm, these dimensions would lead to an estimated V_{ON} range of 13 V to 32 V, and resonant frequencies ranging from 7.5 MHz to 8.2 MHz.

4.1.3 Morphology of Ge nanowires

The supercritical fluid synthesis produced Ge nanowires with cylindrical cross-section and high aspect ratios (length to diameter ratio of approximately 700).

Figure 4.1 shows examples of the as-synthesized one-dimensional nanostructures both on the growth substrate ((a) is copper foil, (c) is glass, inset in (c) is silicon) and transferred to a separate substrate for *in situ* characterization (a copper grid shown in (b)).

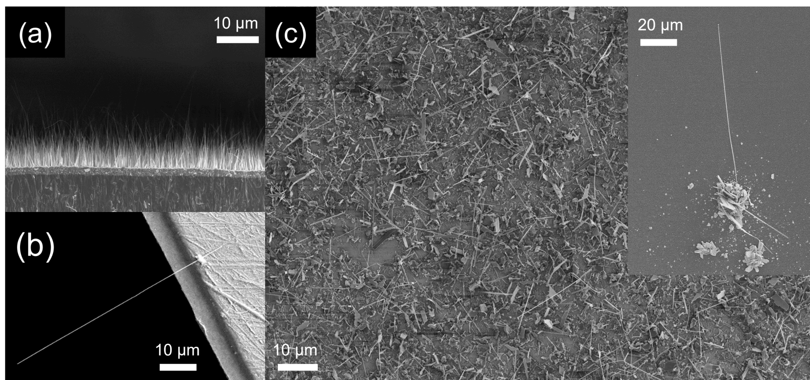

Figure 4.1: SEM images of as-grown one-dimensional nanostructures. (a) CuO nanowires on the growth Cu foil substrate (side-view). (b) A single free-standing Ge nanowire fixed to a substrate for characterization. (c) Top-view of the growth substrate of Bi_2Se_3 nanobelts. Different-shaped products are formed during the synthesis, including platelets, nanowires and nanobelts. The inset shows a single Bi_2Se_3 nanobelt growing from Bi_2Se_3 platelets.

4.2 Mechanical and charge carrier transport properties of CuO and Bi_2Se_3 one-dimensional nanostructures

*The results of this section are published in papers **I, II, V, VII** and **XI**.*

4.2.1 Mechanical properties of CuO and Bi_2Se_3 one-dimensional nanostructures

CuO nanowires

The Young's modulus of CuO nanowires was determined using AFM three-point bending tests and in situ SEM resonance tests. The results, which are shown in Figure 4.2, indicate that the two methods are in good agreement within a diameter range of 20 nm to 160 nm. An exponential trendline (dashed line in Figure 4.2) can describe the data. As the diameter of the nanowires increases, the trendline tends to 95 GPa, which is similar to the value for bulk CuO [138]. However, for nanowires with diameters smaller than 50 nm, the size-dependence becomes more noticeable, reaching Young's modulus values of 550 GPa. This value is comparable to high-speed NEM switches that use materials like SiC [8]. The size-dependence effect is more pronounced for bending deformation than for resonance.

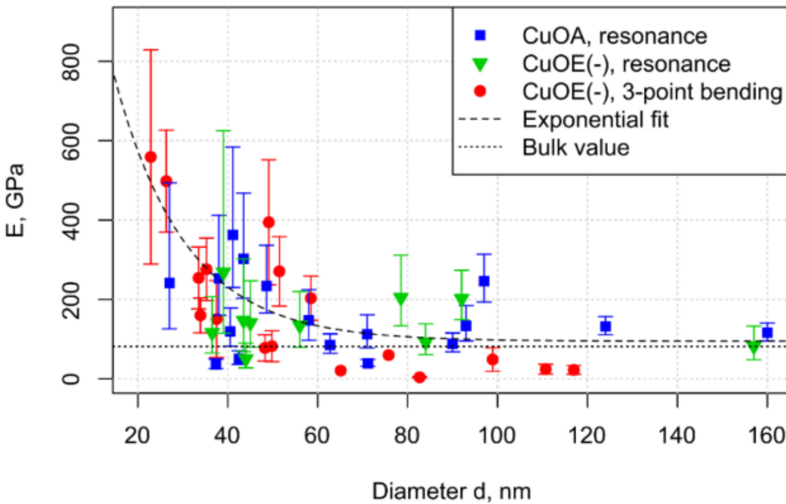

Figure 4.2: Size dependence of the effective Young's modulus E of CuO nanowires, determined by resonance and three-point bending methods. Markers denote experimentally obtained values for different growth methods and mechanical test methods. Dashed line is an exponential fit to the data, while dotted line corresponds to the Young's modulus value of 82 GPa for the bulk CuO. CuOA denotes nanowires synthesized by thermal oxidation in dry air, CuOE(-) denotes nanowires synthesized in an electric field on the cathode side in wet air.

Several important factors may contribute to size-dependent effective Young's modulus and its apparent dominance in bending. For example, tensile surface stresses have been invoked to account for size-dependent effective Young's modulus [139]. Tensile surface stress depends on, whether the loading mode is static bending, dynamic resonance or pure tension. Also, single-clamped nanowires in resonance do not have fabrication-related intrinsic stress [140], which can easily develop for double-clamped nanowires used in three-point bending.

A similar increase of Young's modulus with decreasing diameter has been reported previously for CuO nanowires with a diameter smaller than 190 nm [138]. The study also used three-point bending, however, the explored diameter range was limited to 80 nm and resulted in an approximately three-fold increase in Young's modulus [138] in contrast to the five-fold increase reported in this work.

Bi_2Se_3 nanobelts

Young's modulus of single-clamped Bi_2Se_3 nanobelts was determined using *in situ* SEM resonance tests. The previously described physical vapour deposition growth of Bi_2Se_3 results in predominantly rectangular-shaped ribbon-like 1D NS. For a nanobelt with rectangular cross-section, two mutually orthogonal fundamental resonance frequencies exist – one along its width, the other along its thickness (f_w and f_t, respectively). For an ideal rectangle, the ratio of f_w over f_t would be equal to w over t.

However, as a consequence of its layered growth, Bi_2Se_3 nanobelts often possess characteristic steps or terraces, that can be most accurately observed by AFM. The presence of terraces affects the cross-section and therefore also the area moment of inertia I of the nanobelt and need to be taken into account when calculating Young's modulus E. A method was developed that allows to differentiate nanobelts with rectangular cross-section from those with terraced cross-section. This method involves using a parameter k, which quantifies the ratio of resonant frequencies to the ratio of thickness and width according to

$$k = \frac{f_t/f_w}{t/w}. \tag{4.1}$$

k measures how much the cross-section deviates from the rectangular. This indirect method of morphology determination was validated by measuring the resonance and dimensions of a single Bi_2Se_3 nanobelt with SEM and confirming detailed morphology (i.e., the presence of terraces) using AFM.

After the rectangular nanobelts were distinguished from those with terraces, only data for rectangular nanobelts was used for determination of Young's modulus of Bi_2Se_3. Resonant frequency parameters F_w and F_t were plotted as a function of width and thickness respectively (Figure 4.3). The linear trend indicates the Young's modulus does not depend

on the cross-sectional dimensions of the Bi_2Se_3 nanobelts. The slope of the line corresponds to $\sqrt{E/\rho}$ which is proportional to propagation of the speed of sound in the corresponding crystallographic direction, and allows to extract E. Using the mass density of a macroscopic Bi_2Se_3 crystal ρ of 7680 kg m^{-3}, E was calculated according to

$$\begin{aligned} F_t &= t \times \sqrt{E/\rho} \\ F_w &= w \times \sqrt{E/\rho} \end{aligned} \tag{4.2}$$

where

$$\begin{aligned} F_t &= \frac{4\sqrt{3}\pi f_t L^2}{\beta^2} \\ F_w &= \frac{4\sqrt{3}\pi f_w L^2}{\beta^2} \end{aligned} \tag{4.3}$$

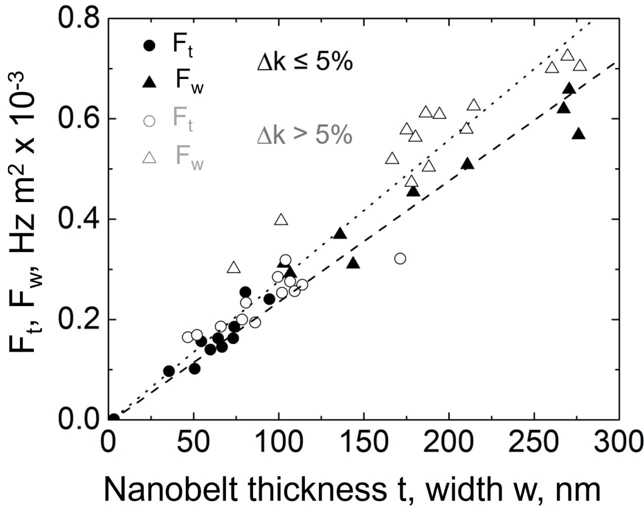

Figure 4.3: Determination of average Young's modulus of Bi_2Se_3 nanobelts via resonance measurements. The dependence of measured resonant frequency parameters F_t and F_w on thickness t (filled circles) and width w (filled triangles) of the nanoribbon, approximated by a straight line (dashed). Empty circles and triangles represent how the calculated Young's modulus values would increase if all nanobelts (both with and without terraces) would be included in the calculation.

From the slope of the linear fit of the experimental data ($2.4 \pm 0.1 \cdot 10^3$ m s^{-1}, Figure 4.3), the average E value of 44 $\pm$ 4 GPa was determined. This value is close to that of macroscopic Bi_2Se_3 crystal (47 $\pm$ 9 GPa) [141], which can be explained by the low defect density in the as-

grown nanobelts, as well as their relatively large thickness and width. In contrast, reported E values for thin films of Bi_2Se_3 range from 18 to 25 GPa [142].

Figure 4.3 also shows that incorporating all measured data, including that from the nanobelts with terraces, increases the E value by approximately 30% (from a slope of $2.8 \pm\ 0.1 \cdot 10^3$ m s^{-1}). The increased value of E for terraced nanobelts could be explained by enhanced surface effects due to the larger surface/volume ratio.

System for on-chip resonant frequency read-out at cryogenic temperatures

The measurement of the mechanical properties of double-clamped nanostructures using the three-point bending tests with AFM is a well-established method. However, it has limitations such as low throughput and incompatibility with low-temperature measurements which are necessary for the development of the cryogenic NEM switch. To overcome these limitations, an electrical system for resonance detection was developed and integrated onto a printed circuit board (PCB). The developed system is compatible with a cryostat, which expands the measurement temperature range for TI-based NEM switches to temperatures as low as 5 K.

The circuit operates by detecting changes in the AC transfer parameter S_{21} caused by the modulation of a capacitively coupled resonating Bi_2Se_3 nanobelt. An on-PCB source follower (SF) circuit is an essential part of the circuit. SF circuits, also known as common-drain amplifiers, have the advantage of being relatively insensitive to variations in transistor parameters and other component values at extreme temperatures. A detailed circuit schematic with element values can be found in the Appendix B.2.

An operating frequency range of up to 10 MHz was selected because at higher frequencies, oscillations were observed, attributed to the cables. To ensure that the electronic components function correctly at temperatures well below their specified operating temperatures – which are typically above −55 °C – test measurements were conducted before inserting the sample.

A 5 MHz quartz resonator was used to examine gain and frequency variations of the circuit as a function of temperature (Figure 4.4 (a)). In the temperature range from 300 K to 4.2 K a small ∼0.005 MHz frequency shift of the resonance was observed. This was expected as the lower operating temperature limit of the quartz resonator is −20 °C. However, lowering the temperature did not have an impact on the amplification of the circuit. The gain of the system remained nearly constant with only ∼2 dB variation in this temperature range.

A standard resistor of 20 kΩ whose resistance matched a typical two-terminal resistance of a Bi_2Se_3 nanobelt was used for ensuring that there do not appear any unwanted resonances in the circuit (Figure4.4 (b) grey curve) in the frequency range from 0.1 MHz to 10 MHz.

Two Bi_2Se_3 nanobelts with small and large thickness-to-length ratios of 1:34 (No. 1 in Table 4.1) and 1:237 (No. 2 in Table 4.1), respectively, were selected to test the circuit and

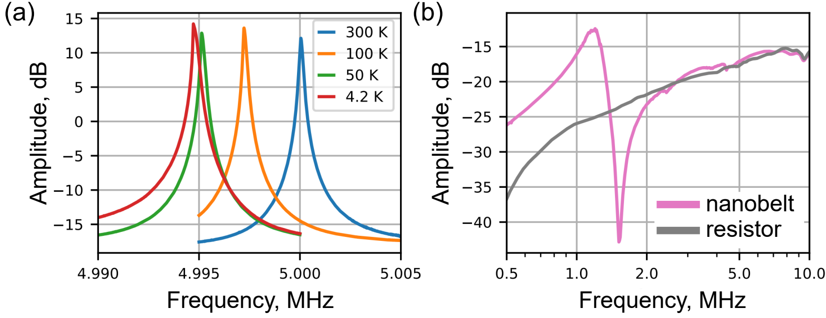

Figure 4.4: (a) A 5 MHz quartz resonator connected between G and D functions as a test element instead of a Bi_2Se_3 nanobelt. Amplitude spectra at different temperatures show nearly constant gain and small frequency variation. (b) Amplitude spectra of a Bi_2Se_3 nanobelt device (No. 1 in Table 4.1) in comparison with 20 kΩ resistor connected between S and D at 8 K.

examine their resonant response (Figure 4.5). Calculated resonant frequencies using the dynamic Euler-Bernoulli beam equation were 1.2 MHz for the 35 nm thin nanobelt (No. 1) and 9.8 MHz for the 224 nm thick nanobelt (No.2), respectively. Both exhibited similar lengths of 7.6–8.3 μm.

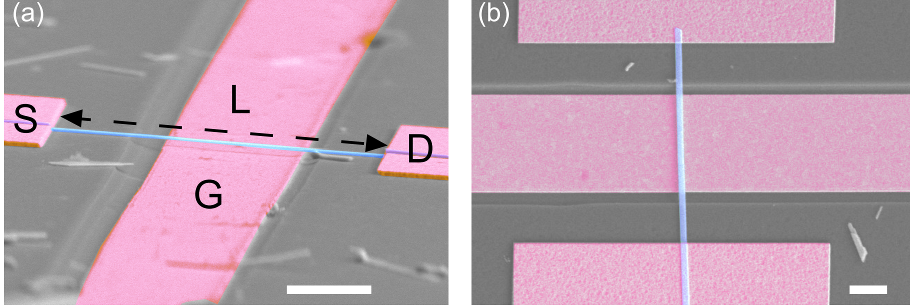

Figure 4.5: (a) Scanning electron microscopy images of the measured Bi_2Se_3 nanobelts with source (S), drain (D) and gate (G) electrodes in an angled view (No. 1 in Table 4.1) and (b) top view (No. 2). Scale bar: 2 μm. A false colour was added for clarity, where magenta highlights the deposited source, drain and gate electrodes, whilst the suspended nanobelt is highlighted in blue.

The discrepancies in the expected frequency for nanobelt No.1 could be explained by changes in clamping of the nanobelt ends due to differential expansion or compression of the nanobelt and its contacting materials during cooling and heating cycles.

The current $\tilde{I}$ through the nanobelt is modulated by the driving frequency ω. The relation between the current and the amplitude of oscillation $\tilde{z}$ can be expressed as [99, 143]

Table 4.1: Geometrical parameters (length L, thickness t, width w), source-drain resistance R, measured f_{meas} and calculated f_{calc} resonant frequencies of the Bi_2Se_3 nanobelts.

Device	L, μm	t, nm	w, nm	R, $k\Omega$	f_{meas}, MHz	f_{calc}, MHz
No. 1	7.6	224	124	50	1.5	9.8
No. 2	8.3	35	266	36	1.2	1.2

$$\tilde{I} = j\omega C_{tot}\tilde{V_g} + V_d\frac{dG}{dV_g}\tilde{V_g} - j\omega C_g V_g\frac{\tilde{z}}{z_0} - V_d V_g\frac{dG}{dV_g}\frac{\tilde{z}}{z_0}, \tag{4.4}$$

where $\tilde{V_g}$ is the RF voltage and V_g is the DC gate bias voltage, V_d is the S-D voltage applied across the nanobelt, C_g and C_{tot} are the capacitance between the nanobelt and the gate and the total capacitance, respectively, and z_0 is the distance between the nanobelt and the gate. At resonance, $\tilde{z}$ is maximum and can be measured via the transmission coefficient S_{21} of the device with network analyzer, where $S_{21} = 50\ \Omega\tilde{I}/\tilde{V_g}$.

The first two terms in Eq. 4.4 are independent of $\tilde{z}$ and thus account for the background signal. The last two terms depend on $\tilde{z}$, and give maximum contribution to $\tilde{I}$ at resonance. The last term depends on transconductance $\frac{dG}{dV_g}$ which makes the dominant contribution to $\tilde{I}$. Thus devices with high transconductance will have large signal-to-noise ratio in amplitude-frequency spectra.

Figure 4.4 (b) compares the amplitude spectra obtained for a Bi_2Se_3 nanobelt No. 1 with a thickness of 224 nm and a length of 7.6 μm with a test circuit, where the nanobelt was substituted with a similar resistance (20 kΩ) resistor.

Clear differences between the nanobelt and the resistor spectra were observed for frequencies up to approximately 2 MHz. Here, the spectrum with the nanobelt shows a positive peak at approximately 1.20 MHz, followed by a negative peak at 1.52 MHz. These antisymmetric peaks were attributed to the mechanical resonance of the nanobelt. Near the resonance, the phase of the mechanical oscillations changes relative to the phase of the driving electric field from the gate electrode. The observed net signal is a sum of several factors, including capacitive coupling and cross-talk between the wires. The asymmetric shape of the gated nanobelt spectra may be explained by constructive and destructive interference between the signal modulated by the nanobelt and all other contributing factors. Similar pairs of positive-negative peaks associated with a phase change have been reported in the literature [101, 143]. Another explanation of the asymmetric spectral peaks could be the positive and negative mechanical feedback due to in-phase and out-of-phase oscillations [144].

An alternative way to confirm if the observed spectral characteristics arise from the nanobelt and not the from the electrical circuit itself is to measure gate voltage dependence.

For Bi_2Se_3 nanobelt No. 1, a series of spectra $A(f) = |V_{AC-out}(f)|/|V_{AC-in}(f)|$ were recorded at 8 K at different bias voltages V_g (Figure 4.6 (a)) to investigate the frequency and amplitude dependence on the gate voltage.

Small systematic changes were detected by comparing spectra obtained at different gate voltages. Figure 4.6 (b) shows the deviation ΔA from the mean spectrum recorded at V_g intervals from -8 V to $+8$ V.

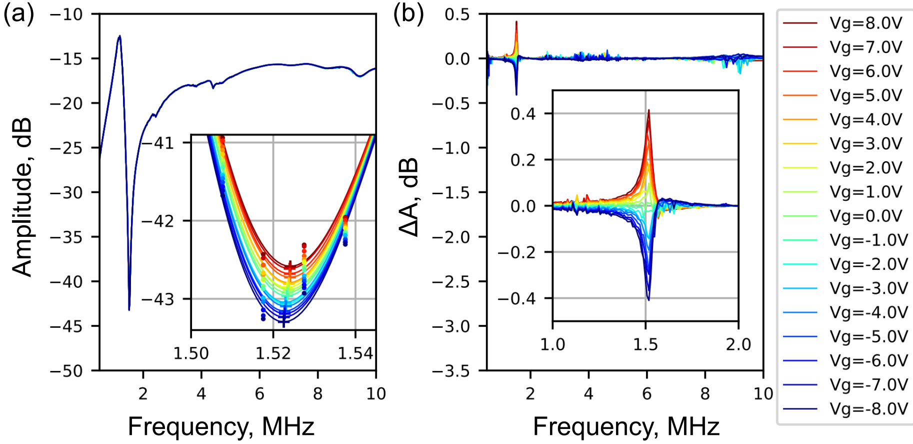

Figure 4.6: (a) Amplitude spectra of system with a Bi_2Se_3 nanobelt (No. 1) and a preamplifier at different gate voltages at 8 K temperature. (b) Difference in the amplitude spectra from the mean spectrum. Insets show a narrow region of spectra near 1.5 MHz. The extreme points of the fitted polynomial are marked by "+".

The maximum difference occurs at approximately 1.52 MHz, which corresponds to the minimum of the original spectra (Figure 4.6(a)).

Figure 4.7 shows the linear amplitude and frequency response to the applied gate voltage, which decreases for negative voltage values and increases for positive values. Although a parabolic dependence on V_g is expected, the relation observed in this study may appear linear due to the low transconductance of the Bi_2Se_3 nanobelt.

Nevertheless, there is a strong correlation between amplitude and frequency and the applied DC voltage, confirming the tunability of the system. Other features in the spectra did not exhibit as high a correlation, supporting the conclusion that the chosen frequency represents the mechanical resonant frequency of the nanobelt.

After confirming the mechanical origin of the observed spectral features, the circuit was

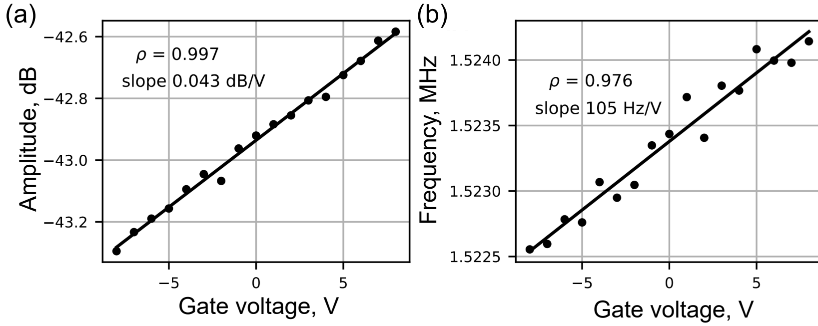

Figure 4.7: Extreme amplitude (a) and frequency (b) dependence on gate voltage for Bi_2Se_3 nanobelt No. 1.

used to investigate temperature dependence of resonant frequency of Bi_2Se_3 nanobelts.

For the thin nanobelt No. 2, a series of spectra were recorded while heating the device from 5 K to 300 K (Figure 4.8). At 5 K, the detected resonant frequency matched the value estimated using a dynamic Euler-Bernoulli beam equation and previously determined Young's modulus value of 44 GPa (see section 4.2). Upon heating, the resonant frequency decreased almost twice, reaching a minimum value at about 200 K. Then it increased back to its low-temperature value at 300 K. The unexpected upwards shift in the resonant frequency from 200 K to 300 K was observed in repeated measurements for this sample.

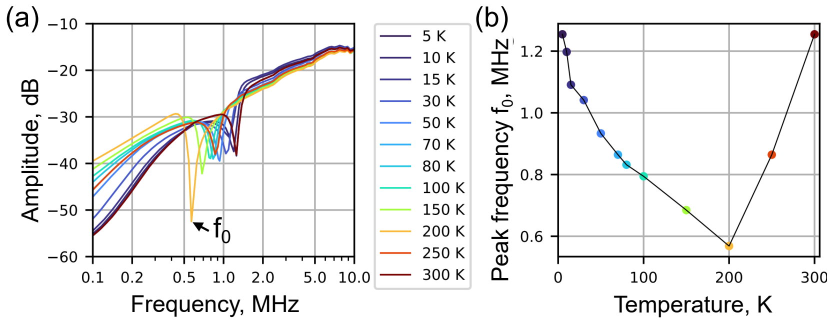

Figure 4.8: (a) Amplitude spectra of a Bi_2Se_3 nanobelt (No. 2) at different temperatures from 300 K to 5 K. (b) Negative peak frequency f_0 dependence on temperature.

In general, resonant frequency change with temperature is proportional to Young's modulus temperature coefficient and linear thermal expansion temperature coefficient, as well as on the thermal stresses induced in the nanobelt due to differential thermal expansion between the nanobelt and the substrate [145]. If thermal expansion of the nanobelt would be the main contributing factor to the observed resonant frequency temperature dependence, a

systematic decrease in the resonant frequency would be expected with raising the temperature.

Studies using differential reflectivity have reported an anomaly in the thermal expansion coefficient and Young's modulus of Bi_2Se_3 at $\sim$180 K [146, 147]. These findings report increased Young's modulus values around $\sim$180 K. Therefore, it was concluded that changes in Young's modulus cannot be the main reason for observed frequency change in our experiments. More likely, tension in the nanobelt that arises from fabrication-induced stress and differential thermal expansion of the materials, is the origin of the frequency temperature dependence. Further studies would be needed to elucidate the impact of differential thermal expansion of Bi_2Se_3, SiO_2 substrate and Au thin film contacts on the observed resonance temperature dependence.

The developed method for inducing and detecting mechanical vibrations in nanostructures on-chip can be further used in NEM switches for assessing the change of mechanical state of the active element as a function of temperature. In addition, dynamic excitation can be applied along with direct voltage to reduce voltage required for the switch to turn on.

4.2.2 Charge transport properties of CuO and Bi_2Se_3 one-dimensional nanostructures

CuO nanowires

The electrical resistivity of CuO nanowires with top Pd/Au contacts obtained using thermal evaporation was measured using transfer line method (TLM). The TLM involves creating a series of contacts at different distances along a 1D NS. By measuring the total resistance between pairs of contacts, the resistance as a function of the contact spacing can be plotted. The resulting data can then be analyzed to extract the contact resistance R_C. A significant scatter in the measured resistivity values was observed, ranging from 0.05 to 160 Ω·m. The contacts exhibited high R_C values, reaching up to 540 MΩ. These results suggest that specialized contact treatment and a different combination of metals are necessary to achieve a high ON/OFF current ratio in NEM switches with top contacts. For simplicity, untreated CuO nanowires were integrated into NEM switches with adhesive bottom Au contacts.

Bi_2Se_3 nanobelts

The resistivity of Bi_2Se_3 nanobelts in this work was determined using both two-terminal and four-terminal configurations, with top and bottom contact geometries, for DEP-aligned and mechanically transferred nanobelts in both suspended and supported configurations. It was anticipated that R_C in bottom adhesive contacts would greatly contribute to the total resistance, and this was confirmed by the measurements. However, top contacts using

thermally evaporated Cr/Au and Ti/Au metal thin film combinations also exhibited high R_C, comparable to that of bottom contacts, similar to CuO nanowires.

R_C was reduced by wet etching of Bi_2Se_3 surface oxide in an acetic acid/HCl mixture, which decreased the total resistance by several orders of magnitude and changed the I-V characteristics from non-linear to linear. Table 4.2 and Figure 4.9 summarize the measured total two-terminal resistance R, resistivity ρ, and I-V dependence for different contact geometries and interface fabrication methods for Bi_2Se_3 nanobelts.

Table 4.2: Electrical properties of Bi_2Se_3 nanobelts with different contact preparation schemes. Note that top contacts without oxide etching result in the highest total two-terminal resistance. In contrast, suspended and supported nanobelts exhibit significantly lower and comparable resistance values. For non-linear I-V curves, the voltage value at which the resistance was determined is given in parentheses.

Contact type and fabrication	$\boldsymbol{R_{two-probe}, k\Omega}$	$\boldsymbol{\rho, \Omega \cdot m\ (RT)}$	**I-V characteristics**	**Comments**
(a) bottom/ not etched	$8.7 \cdot 10^3$ (at 0.9 V)	–	Non-linear	supported on Au and SiO_2
(b) top/ not etched	$9.0 \cdot 10^5$ (at 4.4 V)	–	Non-linear	supported on SiO_2
(c) top/ etched	13	$2.4 \cdot 10^{-5}$	Linear	supported on SiO_2
(d) top/ etched	8	$3.8 \cdot 10^{-5}$	Linear	suspended

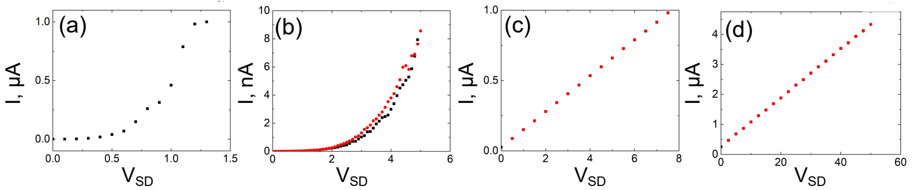

Figure 4.9: Typical I-V characteristics of Bi_2Se_3 nanobelts using different contact fabrication methods. (a) Bottom contacts and (b) top contacts without oxide etch both show nonlinear Shottky-type conduction with relatively high resistance. (c) Top contacts with oxide etch with nanobelt lying on surface and in (d) suspended configuration show linear I-V dependence with small resistance.

To characterize the **temperature dependence of resistance**, as well as the low-temperature gate voltage dependence of resistance and magnetoresistance, all Bi_2Se_3 nanobelt samples were fabricated with etched top contacts.

The resistance of both suspended and non-suspended Bi_2Se_3 nanobelts was measured over a temperature range from 300 K to 2 K. Figure 4.10 (a) shows the sheet resistance, calculated

as $R_{sheet} = \frac{Rw}{L}$ as a function of temperature for three different suspended nanobelts with thicknesses of 60, 61, and 93 nm. Here, w is the width of the nanobelt, and L is the distance between the electrical contacts.

Most of the measured nanobelts exhibited metallic behavior, with resistance decreasing linearly as the temperature was lowered (nanobelts with thicknesses 93 and 60 nm), demonstrating the typical characteristics of Bi_2Se_3 with Se vacancies. The increase in conductivity at lower temperatures is beneficial for NEM switches as it enhances the ON/OFF current ratio. At temperatures below 20 K, the resistance either reached a saturation plateau (nanobelts with thicknesses 60 and 61 nm) or showed a slight upturn (nanobelt with thickness 93 nm). The resistance saturation effect is typical for semiconductors at low temperatures and has been observed previously for Bi_2Se_3. For low temperatures, most of the carriers lack the thermal energy necessary to get excited into the conduction band and further temperature reduction does not significantly change the carrier concentration, leaving them 'frozen' in their donor sites [148]. The upturn has also been observed previously and is explained by electron-electron interaction influencing their coherence times [149, 150].

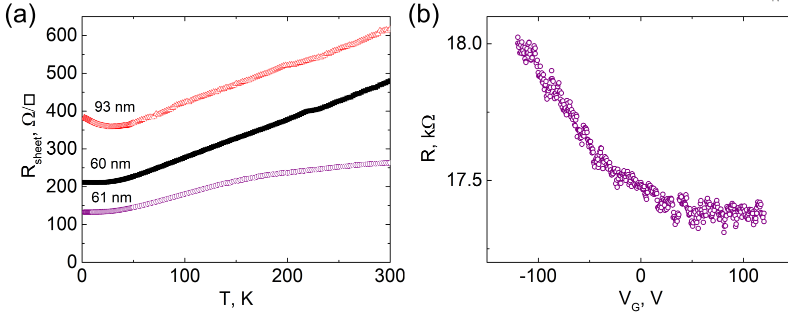

Figure 4.10: Resistance dependence on temperature for suspended nanobelts and gate voltage for a supported Bi_2Se_3 nanobelt. (a) Sheet resistance as a function of temperature for three nanobelts of different thicknesses, showing upturn (red data points) and saturation (black and purple data points). (b) Resistance versus back-gate voltage at room temperature for a nanobelt with thickness of 61 nm shows n-type semiconductor behaviour far from the charge neutrality point.

Field-effect measurements were conducted on nanobelts supported on the substrate to characterize the type of majority charge carriers. Gating of Bi_2Se_3 nanobelts in a two-probe configuration was performed using a global Au back-gate through a 300 nm thermal SiO_2 dielectric layer at temperatures below 2 K. The source-gate voltage was slowly swept from zero to negative voltages and then to positive while monitoring the source-drain current. The observed trend of increasing resistance with increasingly negative voltage corresponds to n-

type semiconductor behavior, as shown in Figure 4.10 (b) for a 61 nm thick nanobelt. This is consistent with the observations from temperature-dependent transport measurements. As the increasingly negative voltage repelled electrons from the surface, the resistance increased from approximately 17.5 kΩ at 0 V to 18.0 kΩ at -120 V, resulting in a small relative change of approximately $\sim$2.86%. The bulk charge carriers from the relatively thick nanobelt, along with carriers from the accumulation layer on the surface of the SiO_2, all participate in conduction. However, the contribution from the accumulation layer is reduced due to suspension. These factors make it difficult to achieve the charge neutrality point and demonstrate ambipolar transport [67, 120] in our samples. Reducing the thickness of the nanobelts could be used to access surface states more effectively.

Magnetoresistance (MR) measurements offer a way to probe the transport properties of TIs and distinguish between surface and bulk states. Figure 4.11 (a) shows the MR, defined as $((R(B)-R(0))/R(0)$, in a perpendicular magnetic field for both suspended and supported samples. In the high-field regime, MR exhibits a parabolic B^2 dependence due to the deflection of carriers under the influence of the Lorentz force. This cyclotron motion shortens the mean free path of the carriers, thereby increasing the resistance. The maximum observed magnetoresistance for all suspended and supported samples was 35% (Figure 4.11 (b)), which is consistent with other studies on Bi_2Se_3 nanomaterials [151]. No systematic difference between MR values of supported and suspended samples was observed, when the experiments were carried out on different nanobelts.

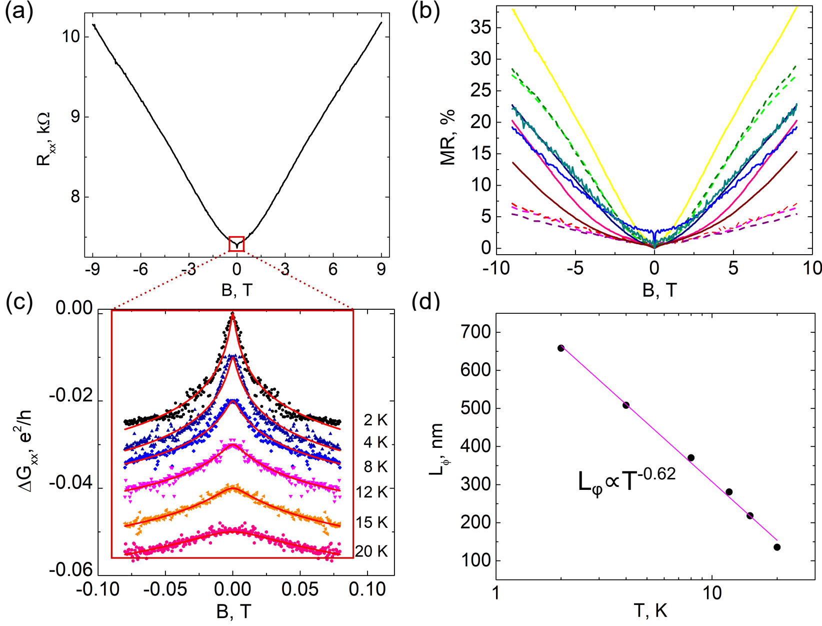

Figure 4.11: Magnetoresistance (MR) measurements of supported and suspended Bi_2Se_3 nanobelts. (a) Longitudinal MR of a single suspended Bi_2Se_3 nanobelt at 2 K from −9 to 9 T. (b) MR curves for suspended (dashed lines) and supported (solid lines) Bi_2Se_3 nanobelts at 2 K. (c) MR of the suspended nanobelt shown in (a), measured at different temperatures from 2 K to 20 K and expressed as longitudinal conductance difference for analysis of weak anti-localization. (d) Phase coherence length extracted from (c) using Hikami-Larkin-Nagaoka equation, as a function of temperature.

Most of the measured nanobelts exhibited a sharp negative peak in MR near zero magnetic field, characteristic of the weak anti-localization (WAL) effect Figure 4.11 (a). By comparing WAL at different temperatures, from 2 K to 20 K, it could be seen that the line shape gets less sharp at higher temperatures. This can be attributed to an increase in phonon scattering, which suppresses quantum interference, as thermal vibrations disrupt the coherent paths of electrons. To analyze these observations, we converted the magnetoresistance curves to conductance, symmetrized the data, and fitted it using the 2D Hikami-Larkin-Nagaoka (HLN) equation for WAL effect (Figure 4.11 (c)). At 2 K, we determined a phase coherence length of approximately 0.7 μm, which decreased to 0.1 μm at 20 K (Figure 4.11 (d)). The high phase coherence length at 2 K is comparable to the literature value of approximately 0.7 μm observed in ∼20 nm thin Bi_2Se_3 film fabricated by molecular beam epitaxy on sapphire substrate at 2 K [115], indicating the high quality of the nanobelts synthesized in our work.

By fitting the data to a power function, an exponent of −0.62 was obtained, which is close to the theoretical value of -0.5 for a 2D system where electron-electron interaction is the dominant decoherence mechanism [115]. This suggests that electron-electron interactions significantly influence the decoherence in our nanobelts.

To minimize sample-to-sample variation in transport properties, we fabricated samples containing both suspended and supported segments of the same Bi_2Se_3 nanobelt (Figure 4.12). This design ensures that any differences in transport properties are due to the suspension rather than variations between different samples. Measurements were conducted by sourcing current through the source (S) and drain (D) electrodes and measuring the voltage using probes V_1, V_2 and V_3. This setup allows for precise comparison of electrical properties in different regions of the same nanobelt.

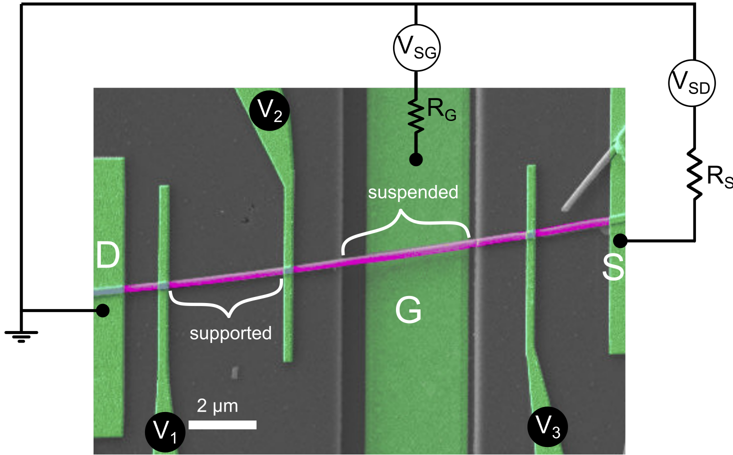

Figure 4.12: False-colored SEM image of a Bi_2Se_3 nanobelt with one part suspended over a gate electrode, one part supported on SiO_2. The current was sourced through S and D electrodes, and the resistance was measured with voltage probes V_1, V_2 and V_3 Series resistances R_S and R_G were added to decrease the current flowing through the nanobelt.

In Figure 4.13 (a), MR is plotted for the two segments of the same nanobelt with a thickness of 71 nm, a width of 200 nm and a suspended length of 9.2 μm, showing slightly higher MR values for the suspended part. To investigate possible Shubnikov-de Haas (SdH) oscillations in the longitudinal resistance at high magnetic fields, the following procedure was implemented: first, a polynomial background was subtracted from the raw $R(B)$ data and the results were plotted for medium and high fields (4 T to 13 T). Then, ΔR_{xx} versus inverse magnetic field B^{-1} was plotted, and its derivative $\partial^2\Delta R_{xx}/\partial B^2$ was analyzed using Fast Fourier Transform (FFT) (Figure 4.13 (b) and (c)). The FFT of the supported part revealed two

frequencies at $F_{supp,1}$ = 52.9 T and $F_{supp,2}$ = 96.9 T.

Each frequency in SdH oscillations corresponds to a different conductance channel, either at the bottom surface, top surface, or in the bulk [67]. For states at the bottom surface, lower charge carrier mobility is expected due to charge accumulation layer on the substrate. Lower mobility may impede the observation of SdH oscillations due to increased scattering, making it less likely that oscillations stem from the bottom surface. Thus, the observed $F_{supp,1}$ and $F_{supp,2}$ were attributed to the top surface states at the interface with vacuum, and to the bulk, respectively.

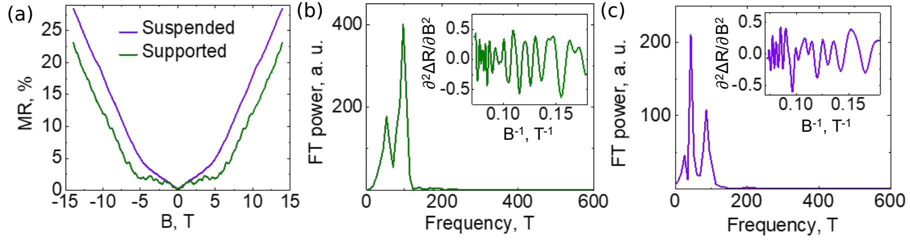

Figure 4.13: Magnetotransport measurements of a Bi_2Se_3 nanobelt with one part suspended, one part supported. (a) Magnetoresistance of suspended and supported parts. Data from (a) was processed and analyzed to reveal Shubnikov-de Haas oscillations at high fields (b-c). Fourier transform power spectra of $\partial^2 \Delta R_{xx}/\partial B^2$ (inset) are shown for supported (b) and suspended (c) parts, revealing two (b) and three (c) dominant frequencies.

For the suspended part, the FFT of the $\partial^2 \Delta R_{xx}/\partial B^2$ oscillations showed three frequencies: $F_{susp,1}$ =25.9 T, $F_{susp,2}$ = 43.4 T and $F_{susp,3}$ = 93.6 T (Figure4.13 (c)). The appearance of the lowest frequency could be explained by the states from the bottom surface, which were no longer masked by the accumulation layer at the nanobelt-substrate interface. A similar triple-frequency pattern was observed in [122] using suspended pre-bent Bi_2Se_3 nanowires.

Table 4.3 summarizes the electrical and mechanical characterization results described in this section, including room-temperature effective Young's modulus E and electrical resistivity ρ values for CuO nanowires and Bi_2Se_3 nanobelts. The determined high Young's modulus values make CuO and Bi_2Se_3 promising candidates for implementing volatile switching in a 2T configuration. Particularly, CuO nanowires with diameters smaller than 50 nm could be used to create NEM switches with high elastic restoring force for volatile operation. The high electrical resistivity of CuO nanowires makes them less susceptible to variations in electrical characteristics due to high contact resistance. The low resistivity of Bi_2Se_3 nanobelts motivates their use for the development of NEM switches with a high ON/OFF current ratio at cryogenic temperatures.

Table 4.3: Room temperature Young's modulus E and electrical resistivity ρ of 1D NS examined as active switch elements.

1D NS	E**, GPa**	**Method and remarks**	$\rho, \Omega \cdot m$	**Method and remarks**
Bi_2Se_3	44 ± 4	Resonance method, size-independent E	2.4–3.8·10^{-5}	Optimized contact resistance
CuO	95–550	Resonance method, 3-point bending, size-dependent E	0.05–160	Transfer length method, large ρ scatter

4.3 NEM switches *in situ*

*Findings described in this section are published in papers **VIII** and **X**.*

Finding forces in a NEM switch contact

In contrast to the simplified 2T NEM switch modelled as a parallel plate capacitor (see section 2.1), the deformation of the active element in a real NEM switch is non-uniform. The force distribution at the 1D NS-electrode contact in the ON state, and consequently the deformation profile of the 1D NS, is influenced by both the dynamics of contact formation and surface reaction forces. Conversely, analyzing the experimentally determined deformation and comparing it to the theoretical model can provide valuable insights into the contact forces.

Measurements of the deformation profile of the active element were conducted on a single-clamped Ge nanowire with a length of 139 μm and a radius of 99 nm. A gold-coated Si AFM chip was used as a plane counter electrode, positioned at a distance of $L_0 h$ from the nanowire, where h is a non-dimensional parameter, defined as the ratio between deflection and length of the nanowire. The voltage between the nanowire and the electrode was gradually increased from 0 V in 0.1 V increments until the nanowire made contact with the surface, which was recorded. Figure 4.14 (a) illustrates the distances and forces acting on the nanowire during the experiment.

The deformation profile of the nanowire was determined by comparing SEM images before and immediately after the contact was established. Deformation profiles were analyzed for various values of h. The experimentally obtained profiles, shown in Figure 4.14 (b), cexplained by considering the effects of static friction f and bending moment M at the contact point.

Force component parallel to the electrode surface $f_x$representing static friction exhibited large scatter in the determined values (Figure 4.14 (c)). The absolute value of the parallel force component was comparable or even exceeded normal force component value f_y (Figure 4.14 (d)). These differences could be explained by acceleration of the free end of the active element and its sliding on the surface of the electrode during jump-in. Right after establishment of the contact, surface adhesion forces prevent the active element to return to its equilibrium position. These results indicate that in the ON state the single-clamped active element experiences both bending and axial tension. The theoretical approach described in this section can also be used to derive the reaction forces in a double-clamped NEM switch from its deformed shape, e.g., for a lateral NEM switch configuration with gate electrodes in the sides of the active element.

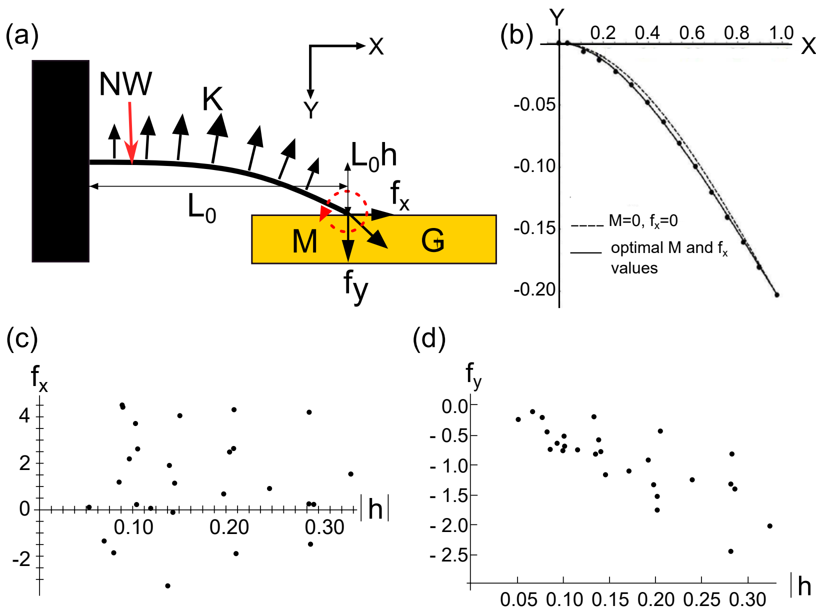

Figure 4.14: Determination of forces acting in a single-clamped 2T NEM switch contact. (a) Schematic of the experiment, showing the bent nanowire with length L_0 at a distance L_0h from plane electrode (e1). (b) Typical example of the shape of the nanowire in contact, where X is the coordinate along the axis of the nanowire and Y is the coordinate perpendicular to the axis of the nanowire. Circles represent experimental measurements, the dashed line represents the analytical solution for $f_x = 0$ and $M = 0$ and the solid line represents the fitted solution with optimal values of f_x and M for the deflection describing parameter $h = 0.21$. Reaction force component (c) f_x parallel and (d) f_y normal to the surface as a function of h.

Reduction of V$_{ON}$ using dynamic AC-DC actuation

For a 2T switch, V_{ON} can either be decreased by reducing distance between the active element and the electrode or by reducing stiffness of the active element. Both methods decrease the elastic force stored in the deformed nanowire. When the elastic force becomes insufficient to overcome the adhesion force at the contact, the switch cannot return to its OFF position after the voltage is removed. To address this issue, an approach was developed that allows for the reduction of V_{ON} while keeping the elastic energy at a sufficient level for volatile operation by combining DC actuation with AC at the nanowire's resonant frequency.

This principle of dynamic V_{ON} reduction was tested in single-clamped $Ge_{1-x}Sn_x$ nanowire and Bi_2Se_3 nanobelt switches. The geometric and vibrational parameters of the $Ge_{1-x}Sn_x$ active element were $L_0 = 14.8$ μm, radius $R = 115$ nm, resonant frequency $f_0 = 623$ kHz, Young's modulus $E = 106$ GPa un quality factor $Q = 550$. Figure 4.15 (a) shows the NEM switching I-V curve with the voltage applied between the source and gate electrodes.

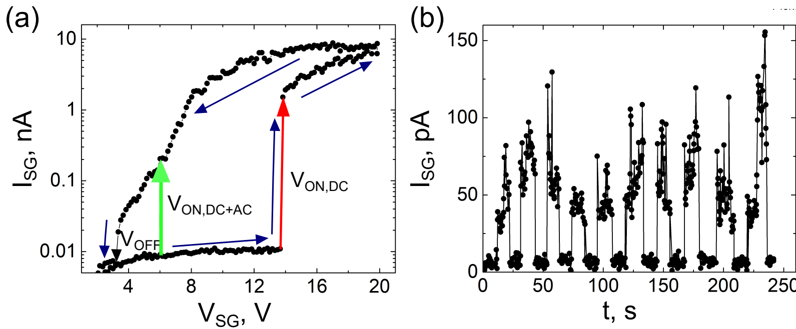

Figure 4.15: The effect of combining AC and DC actuation. (a) I-V curve for a $Ge_{1-x}Sn_x$ NEM switch. Using DC only actuation, the switch turns on at 13.8 V (red arrow). By adding AC actuation, the switch-ON voltage is lowered to 5.0 V (green arrow). (b) A plot of current versus time showing repeatable switching of a Bi_2Se_3 NEM switch *in situ* from low to high current levels using AC-DC actuation.

By ramping the DC voltage from 0 V, a current jump was registered at 13.8 V, indicating the establishment of contact. Detachment occurred at 3.3 V, denoted as V_{OFF}. When a continuous AC voltage with a frequency of 610.8 kHz and amplitude $V_{ON,AC}$ = 0.45 V was applied, a current jump was registered at a reduced DC voltage of 5.0 V. This approach not only reduces energy consumption but also minimizes the risk of degradation of sensitive nanostructures, as demonstrated with Bi_2Se_3 nanobelts. Continuous volatile switching was only achievable with AC-DC actuation (4.15 (b)), whereas DC-only actuation resulted in the electrical burn-out of the nanobelt.

A similar switching principle can be applied also to on-chip NEM switches. Figure 4.16

shows a Ge nanowire-based integrated NEM switch in resonance.

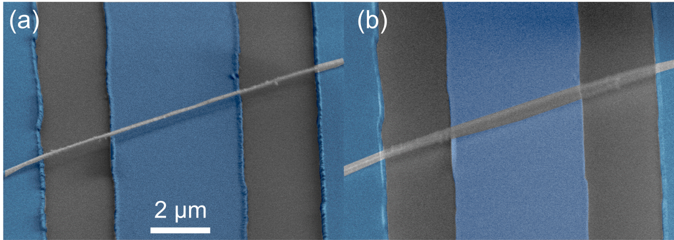

Figure 4.16: SEM image of a double-clamped Ge nanowire NEM switch (a) with no voltage applied and (b) with AC-DC voltage applied between the nanowire and the G electrode at the resonant frequency of the nanowire.

In situ experiments identified the optimal distances between the active elements and the electrodes to enable repeatable volatile switching. By using real-time imaging and monitoring the ON-state current, it was confirmed that current-induced heating and repeatable mechanical deformation do not degrade the active element.

These experiments also established the operating voltage range, up to 50 V for CuO and up to 20 V for Bi_2Se_3, which was critical for detecting a significant current signal in the ON state while avoiding current-induced damage and burnout. It was especially important to optimize the voltage range for Bi_2Se_3 nanobelts, as they were found to be more susceptible to current-induced breakdown compared to CuO.

4.4 Fabrication of on-chip NEM switches

*The findings of this section are published in papers **III, IV** and **VI**.*

4.4.1 Calculation of the NEM switch geometry

Having established the current and corresponding operating voltage range for repeatable volatile NEM switch operation (as described in section 4.3), it became possible to determine the geometry of the integrated NEM switch.

From a technological standpoint, the simplest parameters to adjust are the effective length L_0 (i.e., the distance between the two mechanical clamping points of the active element) and the distance between the bottom surface of the active element and the gate electrode, denoted as z_0. Both L_0 and z_0 are determined by the fabrication process. The minimum value of L_0 was constrained from bottom by resolution and alignment precision of the lithography process, which was approximately 5 μm in the case of photo lithography. The diameter or

thickness range corresponded to the characteristic size distribution determined for each specific synthesis. For instance, for CuO nanowires obtained by thermal oxidation, the diameter ranged from 50 to 200 nm. Consequently, the V_{ON} range was explored for various (L_0; z_0) combinations across a broader diameter d and thickness t range.

Using a combined numerical-analytical model, we derived the geometrical parameters of a double-clamped NEM switch at room temperature, as detailed below.

To find the switch-ON voltage, the system was modeled using the Euler-Bernoulli equation for a double-clamped nanowire subjected to electrostatic forces:

$$Y^{(4)}(\xi) - F_x(\xi)Y^{(2)}(\xi) - F_E(\xi) = 0, \xi = \frac{L}{L_0} \tag{4.5}$$

In Eq. 4.5, Y represents the perpendicular displacement of the nanowire, ξ is the normalized coordinate along its length, F_x is the tension force, F_E is the linear density of the electrostatic force, and L_0 is the suspended length. The superscripts in parentheses denote derivatives with respect to the normalized coordinate.

The linear density of the electrostatic force is expressed as an integral of the electrostatic potential over the circular cross-section perimeter of the cylindrical nanowire:

$$F_E = \frac{4\varepsilon_0}{\pi E L_0 R^3} \int_0^{2\pi} (\frac{d\phi}{dr})^2 cos\alpha d\alpha. \tag{4.6}$$

In Eq. 4.6 E is the Young's modulus, ε_0 is the permittivity of vacuum, R is the radius of the nanowire, ϕ is the electrical potential of the surface, and α represents the angular coordinate.

If axial displacement is restricted, the nanowire experiences tension force F_x. From this it is possible to obtain analytic formula for electrostatic potential and, using Eq. 4.6, the required electrostatic force as

$$F_E = \frac{16}{E L_0 R^4} \frac{V^2 \varepsilon_0}{\sqrt{z^2 - R^2} Lnc^2}, c = \frac{2z^2}{R^2} \left(1 - \sqrt{1 - \frac{R^2}{z^2}} \right) - 1 \tag{4.7}$$

Here, z is the distance from the axis of the nanowire to the gate electrode, and V is the applied voltage. To use Eq. 4.7 in Eq. 4.5, the distance to the gate electrode must be adjusted for each cross-section based on the nanowire's deflection:

$$z = z_0 + Y(\xi), \tag{4.8}$$

where z_0 denotes the initial distance from the nanowire axis to the gate electrode. Since the fixed ends of a double-clamped nanowire prevent axial movement, the nanowire experiences tension when it bends towards the gate. This tension force can be expressed as:

$$F_x = \frac{4}{R^2}\left[1 - \int_0^1 \sqrt{1 - (Y^{(1)}(\xi))^2 d\varepsilon}\right] \tag{4.9}$$

The corresponding boundary conditions for this fixed-fixed case are:

$$Y(0) = Y(1) = Y^{(1)}(0) = Y^{(1)}(1) = 0 \tag{4.10}$$

To estimate the switch-ON voltage V_{ON}, the set of equations 4.5 and 4.7 – 4.10 were numerically solved for a set of increasing values of applied voltage. The threshold voltage, V_{ON}, was identified as the voltage at which no solution could be found, indicating that the deformed nanowire intersected the counter electrode surface.

As an example, the calculated V_{ON} values for a CuO NEM switch as a function of nanowire diameter are shown in Figure 4.17. The values of L_0 (6.0, 8.0, and 8.6 μm) and z_0 (120, 180, and 200 nm) were set by the fabrication process. Assuming a Young's modulus of 155 GPa (the average value determined for this diameter range in section 4.2) and rigid clamping of both ends, the calculated V_{ON} values ranged from 2 V to 48 V.

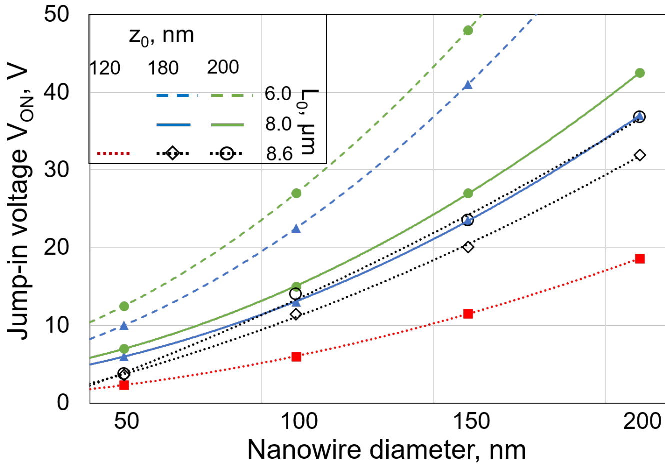

Figure 4.17: Calculation of V_{ON} as a function of nanowire diameter d for a CuO nanowire-based NEM switch. Experimentally relevant gap height z_0 and suspended length L_0 combinations are considered. Lines are guides to the eye, with line types corresponding to L_0 values (dashed line 6.0 μm, solid line 8.0 μm, dotted line 8.6 μm), and colours corresponding to z_0 values (red square to 120 nm, blue triangle to 180 nm and green circle to 200 nm).

4.4.2 Positioning of nanostructures on-chip

Two main configurations of double-clamped NEM switches were fabricated: one with bottom contacts and the other with top contacts (Figure 4.18). For the positioning of one-dimensional nanostructures on-chip, different electrode designs were fabricated for mechanical transfer and dielectrophoresis (DEP) methods.

For mechanical transfer, dense electrode arrays were used, whereas DEP utilized electrodes with fewer electrode pairs per chip. Various suspended length L_0 and gap height z_0 combinations detailed in subsection 4.4.1 were used to set the distances between source and drain electrodes and trench depths of the gate electrode.

Three main challenges were identified in integrating 1D NS into planar NEM switches using the methods described in the Experimental section: 1) accurate positioning of 1D NS on the device substrate; 2) ensuring reliable electrical contacts to the 1D NS; and 3) avoiding stiction. The following discussion outlines the solutions implemented to overcome these challenges, thereby increasing the yield of successfully fabricated devices per chip.

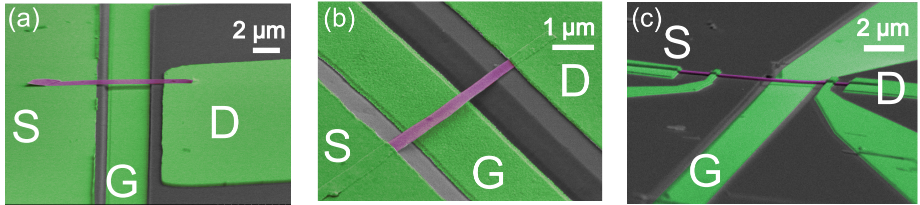

Figure 4.18: NEM switch configurations. SEM images of fabricated NEM switches with (a) bottom (where the 1D NS lies on top of a metal thin film) and (b), (c) top (where the 1D NS is fixed under a metal thin film) contacts in two-terminal (b) and four-terminal (c) configuration.

The ideal alignment scenario involves positioning a single 1D NS across a single gate electrode, with both ends supported on the substrate. This setup avoids any additional structures that could potentially create an electrical short between the source and gate connections. Tuning the DEP parameters was found to be the most effective method for achieving this.

The concentration of nanostructures in the isopropanol suspension was adjusted to $\sim 10^4$ nanowires/ nanobelts per μL. The amplitude and duration of the applied AC voltage were selected based on previous studies with similar DEP electrode configurations and spacings [152, 153]. It was observed that larger amplitudes led to 1D NS degradation, while smaller voltages weakened the DEP force, resulting in an insufficient number of aligned 1D NS. Extending the DEP duration allowed more 1D NS to reach the electrode sites, where they were attracted by the DEP force; however, excessively long duration increased the likelihood of multiple connections forming at the same site.

Optimal DEP parameters were determined by conducting experiments on chips without gate electrodes and with symmetrically aligned electrode pairs (Figure 4.19). The maximum number of aligned single nanowires per chip was obtained using 100 kHz frequency and 5 V amplitude applied to the S-D electrodes for 20 minutes. This configuration resulted in 20% of all S-D electrode pairs being connected with a single nanowire. Although the introduction of a gate electrode slightly reduced this yield, CuO nanowire-based NEM switches were successfully fabricated using these parameters.

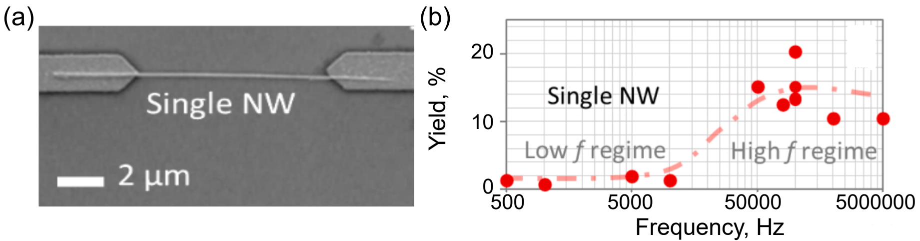

Figure 4.19: (a) SEM image showing a single CuO nanowire aligned between the source (S) and drain (D) electrodes using dielectrophoresis, with an adhesive bottom contact. (b) Experimentally determined yield of single-nanowire interconnects as a function of the applied AC frequency f. The dashed line serves as a visual guide.

Bi_2Se_3 also showed promising preliminary DEP alignment results at a frequency of 2 MHz, with an 8 V amplitude and a duration of up to 10 minutes (Figure 4.20 (a)).

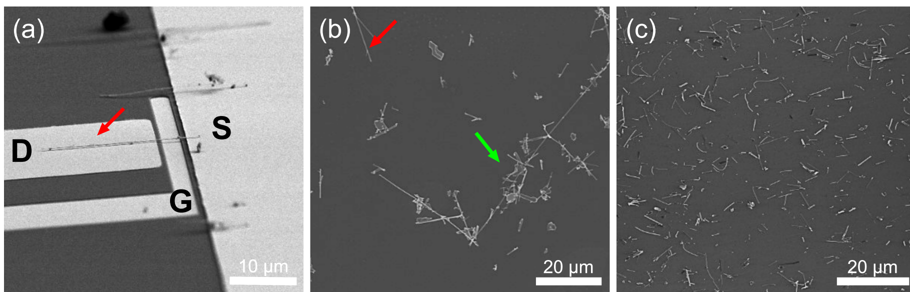

Figure 4.20: Positioning of Bi_2Se_3 nanobelts on the device substrate. SEM images showing: (a) DEP aligned nanobelts perpendicular to the metallic S and D electrodes and spanning across the G electrode. The red arrow marks a single suspended nanobelt; (b) Bi_2Se_3 nanobelts on a silicon surface obtained by drop-casting and drying a suspension, showing agglomerates of various morphologies. The red arrow points to a single nanobelt, while the green arrow indicates an agglomerate of a nanobelt surrounded by platelets of various sizes; (c) High-yield transfer of non-agglomerated nanobelts achieved by mechanically pressing the growth substrate against the silicon substrate.

However, difficulties arose in preparing a suspension with a sufficiently high concentration of Bi_2Se_3 nanobelts without contaminants of other morphologies. During synthesis, in addition to the desired nanobelts and nanowires, variously-sized platelets also formed on the glass substrate. These different products tended to agglomerate in the suspension (Figure 4.20 (b)) and were deposited on the NEM switch electrodes during DEP. To successfully align Bi_2Se_3 nanobelts via DEP, it was concluded that some form of filtering or morphology selectivity should be introduced either during suspension preparation or the DEP process.

On the other hand, dry mechanical transfer proved highly effective for transferring long, non-agglomerated Bi_2Se_3 nanobelts (Figure 4.20 (c)). Although this method resulted in random placement and alignment, it achieved the highest yield of switches per chip (>20 single-nanobelt connections) for Bi_2Se_3 nanobelts.

4.4.3 Nanostructure/metal contact fabrication

A common challenge in fabricating thin film electrodes using the lift-off process is the formation of metal side edges (Figure 4.21).

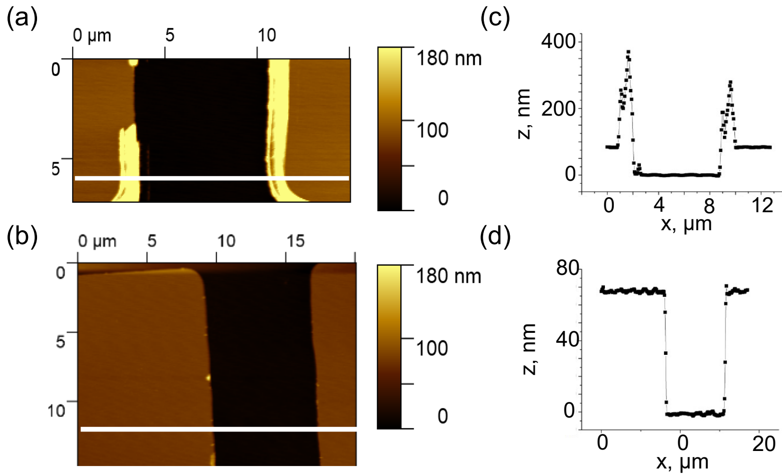

Figure 4.21: Optimization of NEM switch contacts in bottom adhesive source-drain contact configuration and for gate fabrication. AFM scans of S and D electrodes show pronounced metal side-edges rising approximately 300 nm above the metal surface (a) and smooth surface with no side-edges by using an optimized photoresist processing recipe (b). (c) and (d) are the corresponding line profiles for (a) and (b), respectively.

This issue is particularly problematic for bottom-contact configurations in NEM switch fabrication. These edges can reach heights of up to 500 nm, reducing the contact area between

the electrode and the 1D NS and complicating the transfer process of 1D NS. Consequently, it becomes difficult to predict the exact gap height in the NEM switch.

The side-edge issue was pronounced in NEM switch fabrication using photolithograpy. These edges are a result of thin film covering the sidewalls of the resist and can be avoided by adjusting the resist profile from positive to negative. It was solved by using a two-resist process with fine-tuned soft-bake temperature, soft-bake time and development time, given in detail in Appendix A.1.

For Bi_2Se_3 NEM switches, a top-contact approach was introduced to decrease contact resistance, achieve ohmic I-V characteristics, and enhance the mechanical stability of the switch during continuous operation. However, despite the metal layer appearing continuous over the nanostructure, closer inspection sometimes revealed breaks, leading to open circuits (Figure 4.22 (a)). This problem was alleviated by using a metal layer thicker than the 1D NS (Figure 4.22 (b)). It is important to note that increasing the metal layer thickness requires a corresponding increase in resist layer thickness, which reduces resolution and complicates the lift-off process, potentially breaking suspended wires. The maximum top-layer thickness found to be successful for NEM switch fabrication was 200 nm.

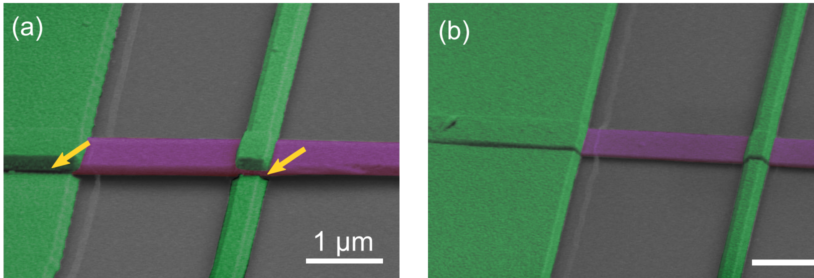

Figure 4.22: Fabrication of top contacts on Bi_2Se_3 nanobelts. SEM images of metal (green) covering the nanobelt (purple) (a) with breaks and (b) continuously. Yellow arrows in (a) mark the areas with discontinuities in the metal film. Scale bar: 1 μm.

4.4.4 Minimizing stiction of suspended nanostructures

Suspended nanostructures are highly susceptible to deformation and, in severe cases, stiction failure due to capillary forces that arise during various fabrication processes, such as resist deposition, development, wet etching, and lift-off. It was observed that thinner 1D NS are particularly prone to stiction due to their lower elastic forces, with the maximum stiction-free suspended length being 5-6 μm, allowing for minimal deformation.

Besides using supercritical drying, another fabrication approach was introduced to further reduce the risks of stiction. In the "etch-last" method, a conducting layer (Au) is first

deposited on the substrate, followed by the deposition of an insulating layer (Al_2O_3, SiO_x). The 1D NS are then released from the substrate after top-contact fabrication by selectively etching part of the underlying insulator layer beneath the 1D NS. This approach allows for wet processing after the 1D NS are securely clamped at their ends, significantly minimizing the risk of deformation and stiction. Figure 4.23 shows the fabrication flow with Al_2O_3 as the insulator.

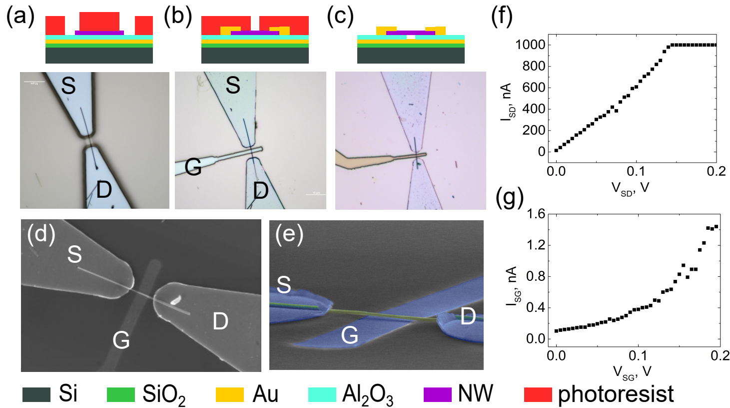

Figure 4.23: NEM switch fabricated using the etch-last method to minimize stiction risks. A series of optical images with corresponding cross-sectional schematics showing: (a) 1D NS on substrate with patterned top electrodes; (b)the patterned bottom gate; (c) the etched bottom gate. SEM images of the fabricated device with 100 nm gap in both (d) top-view and (e) angled-view. I-V characteristics between the source and drain (f) show ohmic behavior, while the source-gate (g) current of 1.5 nA at 0.2 V is only three orders of magnitude smaller than source-drain, indicating leakage through Al_2O_3 layer.

However, the etch-last method presents challenges, such as the potential for chemical or physical modification of the 1D NS due to aggressive etchants. Additionally, leakage through the insulator layer can limit the operating voltage range of these switches. As shown in Figure 4.23 (f) and (g), the source-gate (S-G) current leakage at 0.2 V is only three orders of magnitude lower than the source-drain (S-D) current through the 1D NS, indicating a limitation of this approach.

Also, the profile of the trench was identified as a critical factor in controlling stiction during NEM switch fabrication. Key trench features include the aspect ratio (width to depth) and the sidewall profile. The fabrication method significantly influences these characteristics: for instance, isotropic wet etching of SiO_2 results in sidewalls with a small angle, while dry etching can produce nearly vertical sidewalls (close to 90 degrees). Small sidewall angles were found to be undesirable, as they complicate the suspension of 1D NS, potentially leading to

slack or unintentional contact with the bottom gate electrode. Moreover, with small angles, the bottom dimension of the trench is smaller than its top, which reduces the span of the gate electrode along the length of the 1D NS, thereby diminishing electromechanical coupling. To optimize the process, dry etching of SiO_2 and Si was adopted for trench fabrication, ensuring better control over sidewall angles and minimizing stiction risks.

4.4.5 Characterization of the geometry of the integrated NEM switches

The fabricated switches were systematically characterized at various stages of the fabrication process, using optical microscopy, SEM, and AFM, both before and after electrical testing (Figure 4.24). This thorough characterization is crucial for determining the precise height, profile, suspended length, and thickness of the active elements. In some instances, slack in nanostructures can develop over trenches, particularly when trenches are fabricated prior to the transfer of 1D NS, resulting in a non-uniform gap (Figure 4.24 (b)) that can significantly affect the measured V_{ON} values.

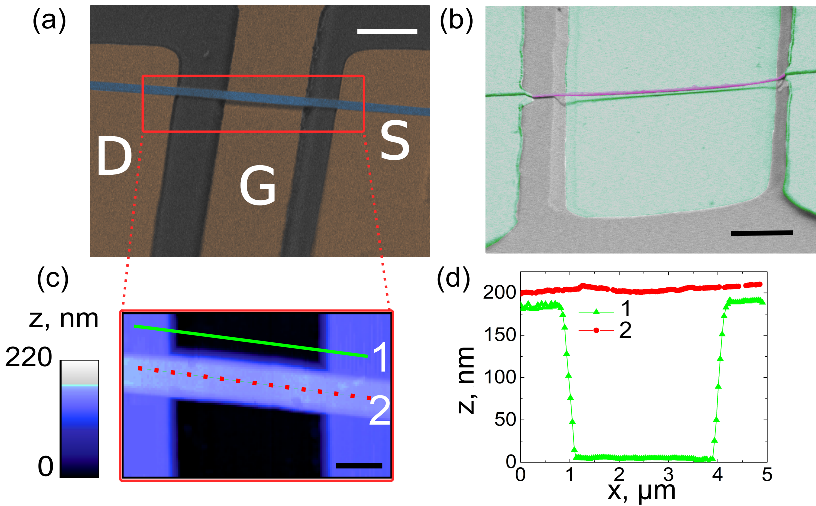

Figure 4.24: Characterization of the fabricated 1D NS-based switches. (a) Coloured SEM image of a bottom-contact Bi_2Se_3 nanobelt-based NEM switch, showing source (S), gate (G) and drain (D) electrodes. (b) NEM switch with a non-uniform gap between the active element (magenta) and gate electrode (green). (c) AFM image and corresponding line profiles (d) of a suspended portion of the nanobelt shown in (a). Scale bars are 2 μm in (a, b) and 1 μm in (c).

It is important to minimize electron beam exposure during SEM characterization to prevent charge injection into the electrodes, local changes in the conductivity of 1D NS [154], and carbon deposition. Similarly, AFM characterization should be conducted with caution

— using slow scanning speeds and minimal force — to avoid unwanted mechanical deformation of the active element. Excessive shear force during AFM can potentially damage or even break the 1D NS. Among the materials tested, Ge and CuO were found to be more robust, exhibiting superior mechanical and electrical performance compared to Bi_2Se_3.

4.5 Operation of integrated NEM switches

*The findings of this section are published in papers **III**, **VI** and **VIII**.*

Integrated NEM switches based on CuO and Bi_2Se_3 1D NS were fabricated with bottom adhesive contacts and with top contacts. These switches were designed using experimentally determined mechanical and electrical properties, the appropriate operating voltage ranges (sections 4.2 and 4.3), and geometries derived from the numerical calculations described in 4.4. Two different switching modes were investigated as shown in Figure 4.25 (a): one with current control through the nanostructure before contact formation with the gate electrode (employing V_{SG} and V_{SD} voltages), and one without (employing V_{SG} only). CuO nanowires were tested at room temperature, while Bi_2Se_3 nanobelts were tested at cryogenic temperatures.

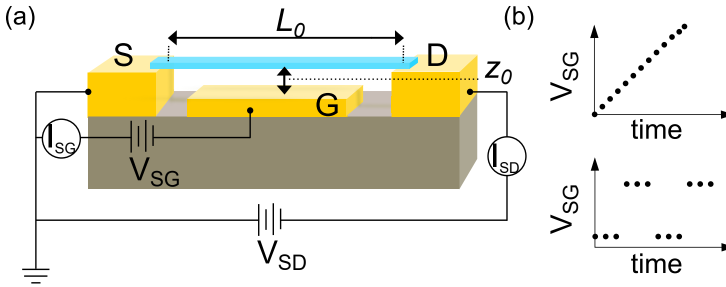

Figure 4.25: Operation of integrated 1D NS-based switches. (a) Schematics of electrical connections and terminal designations for NEM switch operation testing. NEM switches were tested using either V_{SG} only, or V_{SG} combined with V_{SD}. (b) Top: Sweeping of V_{SG} to precisely determine V_{ON} and its evolution; Bottom: Square V_{SG} signal to observe time evolution of I_{ON} and I_{OFF}.

The operational characterization of these NEM switches involved ramping the voltage V_{SG} in small increments while registering the current I_{SG} response (Figure 4.25 (b) top panel). Gradually increasing the voltage allowed for the observation of the evolution of the operating voltages, V_{ON} and V_{OFF}, over time, making it particularly useful for the initial examination of switch dynamics. For devices that exhibited non-volatile, one-time switching, only V_{ON} and subthreshold slope data were obtainable from the experiments.

In contrast, for switches demonstrating volatile and repeatable operation, a periodically changing square voltage signal V_{SG} was applied at the appropriate levels (Figure 4.25 (b) bottom panel) to induce and study the ON and OFF sates, along with the time evolution of the ON-state and OFF-state currents.

Table 4.4 summarizes the geometrical and elastic parameters, along with the experimentally obtained and calculated V_{ON} values, for the double-clamped CuO and Bi_2Se_3 NEM

switches. A total of 6 CuO and 4 Bi_2Se_3 NEM switches were fabricated and measured. The diameters of the active CuO nanowire elements ranged from 50 nm to 210 nm, while the Bi_2Se_3 nanobelts had thicknesses from 51 nm to 145 nm. Suspension gap heights were from 120 nm to 200 nm, with measured V_{ON} values ranging from 4.5 V to 49 V.

Table 4.4: Summary of CuO and Bi_2Se_3 1D NS NEM switch data, showing geometrical parameters (diameter d or thickness t, suspended length L_0, gap height z_0 and area moment of inertia I), elastic parameters (elastic force F_{elas} and spring constant k) and experimentally obtained and calculated V_{ON} values.

No.	d/t, nm	L_0, μm	z_0, nm	$I \cdot 10^{-29}$, m^4	k, nN/nm	F_{elas}, nN	$V_{ON,exp}$, V	$V_{ON,calc}$, V
CuO-1	50	6.2	120	0.03	0.08	11.1	4.5	4.3
CuO-2	125	8.6	120	1.20	1.12	16.8	12	8.5
CuO-3	210	6.4	120	9.60	21.7	325	49	39
CuO-4	100	7.4	190	0.49	0.72	17.1	26	17
CuO-5	118	9.2	190	0.95	0.73	17.3	16	12
CuO-6	150	6.7	190	2.50	4.92	117	28	37
Bi_2Se_3-1	51	3.3	190	0.57	2.80	64.0	20	23
Bi_2Se_3-2	122	3.3	190	3.30	15.7	368	25	27
Bi_2Se_3-3	86	3.6	200	1.00	3.60	91.0	17	15
Bi_2Se_3-4	145	6.7	200	2.70	1.50	28.0	27	27

Discrepancies between the experimentally obtained and theoretically calculated V_{ON} values can be attributed to several factors. For both CuO and Bi_2Se_3, lower experimental V_{ON} values for some of the switches may result from movement-induced sliding of the active element during the switching-ON process, as the element is only fixed to the S and D electrodes by adhesion forces. Higher experimental V_{ON} values for CuO nanowire switches might arise from the size-dependent effective Young's modulus of the nanowires. For Bi_2Se_3 switches, the higher V_{ON} values could be due to cooling-induced contraction and tension in the nanobelt at low temperatures.

4.5.1 Operation of CuO switch for room temperature applications

To fabricate an integrated CuO NEM switch designed for volatile switching, we utilized the nanowire morphology results from section 4.1, the Young's modulus and electrical resistivity characterized in section 4.2 and the V_{ON} calculation detailed in section 4.4. A switch with typical dimensions of d = 150 nm, L_0 = 6.7 μm and z_0 = 190 nm was fabricated for im-

plementing volatile switching. Figure 4.26 (a) illustrates the switch's performance over five consecutive voltage ramping cycles, ranging from 0 V to 30 V in 0.5 V increments.

Across all cycles, the current exhibits two distinct levels, corresponding to high and low voltage regions. It remains at a noise level of approximately 0.01 nA during the voltage ramp-up phase and increases to a maximum of approximately 12 nA. However, each cycle shows a progressively decreasing V_{ON} value.

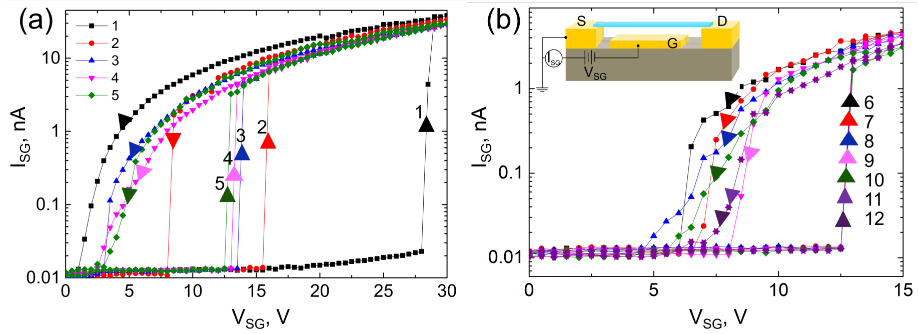

Figure 4.26: Initial stages of CuO NEM switch operation. (a) Voltage ramping during the first five cycles shows a decrease in V_{ON} from 28.0 V (black curve) to 12.5 V (green curve). The switching-ON process is abrupt (except for cycle #2), while the switching-OFF process is gradual, suggesting that the active element the active element detaches from the electrode gradually, piece by piece. (b) A regime, where V_{ON} retains a constant value of 12.5 V over multiple cycles, suggesting that the active element no longer undergoes any mechanical changes. Inset shows electrical terminal connections.

In the first cycle, a sharp increase in current is observed at 28 V, which then returns to the noise level at 1 V. In contrast, the second cycle reaches a high current state at a much lower voltage of 15.5 V. This initial reduction in V_{ON} is consistent with observations in other studies [36, 155]. One possible explanation for this behaviour is that a mechanical relaxation occurs at the adhesive interface of CuO nanowire and bottom electrode, which results in changes of nanowire position. Another reason could be related to material degradation due to power dissipation at the moment of contact. Sufficiently high energy release could result in changes of Young's modulus of CuO nanowire. Despite these potential causes, our data suggests that material degradation is unlikely. Firstly, the bending radii in our setup are minimal. Secondly, the electrical properties remain consistent, with the ON-state current stable across the cycles.

In the following three cycles, the reduction in V_{ON} is less pronounced, stabilizing at 12.5 V by the fifth cycle. After this point, V_{ON} remains constant across many cycles, and V_{OFF} stabilizes in the range of 2.5 to 3.5 V, as shown in (Figure 4.26 (b)).

With a stable V_{ON}, we extended the examination to analyze the ON and OFF state cur-

rent levels. Figure 4.27 shows an excerpt containing 5 cycles, each applying three voltage levels in square pulses:: 0 V (OFF state), 8 V (control) and 15 V (ON state). The intermediate voltage level of 8 V serves to verify that the CuO nanowire remains in the volatile operation regime. If contact with the gate electrode occurs, significant current would be observed at this level, whereas the current remains at the noise level at 0 V. Throughout the 100 cycles, no decrease in the ON-state current was detected, indicating that CuO nanowires are resilient and promising candidates for high-voltage NEM switch applications.

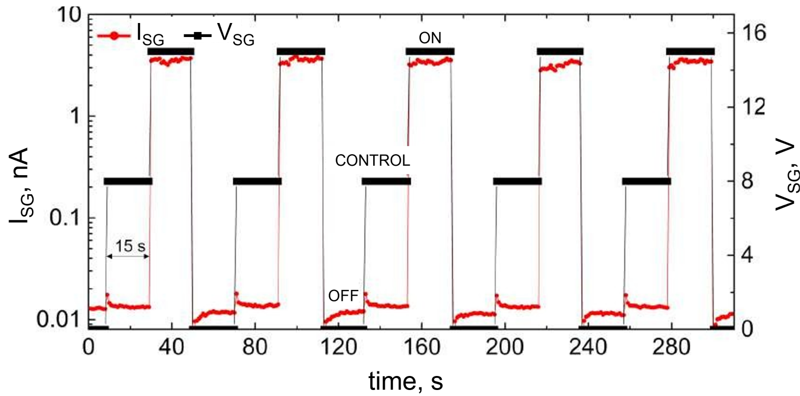

Figure 4.27: An excerpt of extended cycling of a CuO NEM switch by applying square voltage pulses. Red circles indicate current level at different applied voltages (black squares) of 0 V (OFF), 8 V (OFF, control), 15 V (ON). For 0 V and 8 V, the current stays at the noise level, whereas ON-current reaches nanoampere level, when the applied voltage is 15 V.

4.5.2 Operation of Bi_2Se_3 switch for cryogenic temperature applications

2T NEM switch with a S-G current control

Based on the morphological, mechanical, and electrical characterizations described in sections 4.1 through 4.2, the *in situ* switching experiments in section 4.3 and the calculations in section 4.4, double-clamped Bi_2Se_3 nanobelt NEM switches were fabricated in both bottom contact 2T and top contact 3T configurations. The bottom contact configuration, fabricated similarly to CuO nanowire-based switches, to demonstrate proof-of-principle operation at cryogenic temperatures. The top-contact configuration was employed to investigate deformation-induced electrical changes and processes in the nanostructure prior to contact formation with the gate electrode.

The fabricated Bi_2Se_3 NEM switches featured active element thicknesses ranging from 51 to 145 nm, with gaps between 190 and 200 nm and exhibited V_{ON} values between 17 V and

27 V.

For a typical switch with the following Bi_2Se_3 nanobelt parameters – L_0 = 3.3 μm, t = 51 nm, z_0= 190 nm, and w = 512 nm (device Bi_2Se_3-1 in Table 4.4) –, the calculated V_{ON} value was approximately 23 V, while the experimentally determined V_{ON} was 20 V. This discrepancy can be attributed to two competing mechanisms that could influence the observed value. If the active element was fully clamped, lowering the temperature would increase V_{ON} compared to the room temperature value due to the induced tension in the structure, as reported in previous NEM switch studies [20]. However, in a bottom-contact structure, where the nanobelt is held by adhesion forces, some sliding of the active element on top of the electrode may occur during the jump-in process [20]. This sliding would result in a decrease in V_{ON}, as observed for devices Bi_2Se_3-1 and Bi_2Se_3-2.

The behavior of the full ON-OFF cycle varied depending on the balance between the adhesion forces at the contact points and the elastic restoring force of the active element.

hen the adhesion force exceeded the elastic force, the active element remained in contact after the voltage was removed. This behavior was inferred from a cycle that exhibited a pronounced current jump (Figure 4.28 cycle #1), followed by a cycle displaying non-linear Schottky-type I-V characteristics (Figure 4.28 cycle #2).

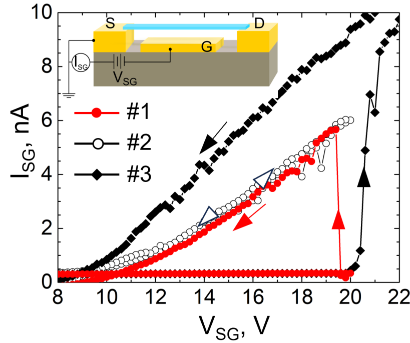

Figure 4.28: Repeatable non-volatile Bi_2Se_3 NEM switch operation with I_{SG} current control at 5 K. The first switching cycle (red filled circles) is followed by a cycle with no sharp current jump (empty circles), followed again by a cycle with a sharp current jump (black filled diamonds) after a heating-cooling cycle. The sharp pull-in behaviour is recovered after a heating cooling cycle, as seen in cycle #3. Inset shows electrical terminal connections.

When the difference between the opposing forces was small, additional energy in the form of heat was sufficient to detach the active element from the electrode. By increasing temperature to 300 K and then lowering it back to 5 K, NEM switch Bi_2Se_3-1 operated in a typical reversible nonvolatile regime, exhibiting a repeated current jump (Figure 4.28 cycle

#3), similar to memory devices made from Si and Ge nanowires in [41].

Volatile NEM switching was achieved when the elastic force was larger than the adhesion force at the contact point. In Figure 4.29 (a), the current initially remained at the noise level of 0.1 nA until a sharp rise reaching the set level of current compliance of 100 nA was recorded at 9.2 V. From cycle #1 to cycle #2, V_{ON} decreased to approximately 8.2 V. The detachment of the nanobelt from the contact was marked by a sharp current decrease to the noise level at V_{OFF} of approximately 2.3 V. With each subsequent cycle, V_{ON} gradually decreased, albeit by a smaller amount than between cycles #1 and #2 – similar to the behavior previously observed in CuO switches during the initial cycles of operation.

The volatile switch exhibited ON-OFF current ratio of approximately 10^3, corresponding to leakage current levels of 0.1 nA and ON-state current levels, set by compliance, of 100 nA. The average subthreshold slopes (SS) for transition to the ON-state, calculated as $\mathrm{mV}/\log_{10} I$, were 135 mV/decade at 10 K and to as low as 80 mV/decade at 5 K (Figure 4.29 (b)). Although these values are higher than the thermal limit for MOSFET transistors of 60 mV/decade at room temperature, they represent the upper limit of the SS value for this Bi_2Se_3 NEM switch. The SS value could be further reduced by increasing the current compliance and decreasing the voltage step size.

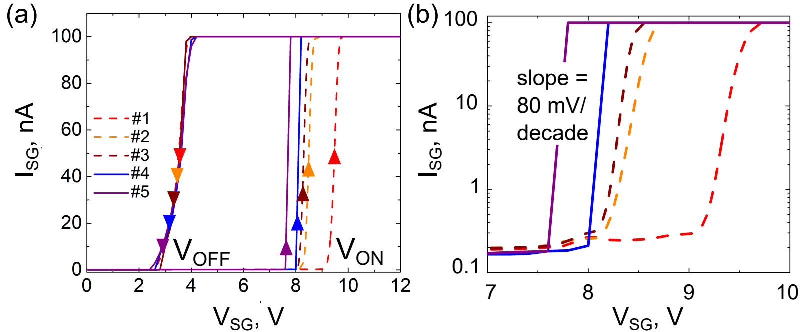

Figure 4.29: (a) Cryogenic temperature operation of a volatile reversible Bi_2Se_3-based NEM switch. (a) Three cycles at 10 K (#1 − #3, dashed lines) are followed by two cycles at 5 K (#4 − #5, solid lines). Upwards arrows indicate transition to ON-state, downwards–transition to OFF-state. (b) Log scale representation of the I-V characteristics in (a) to estimate the subthreshold slope.

3T NEM switch with a S-D and S-G current control

In previous sections, the operation of NEM switches that utilize source-gate (S-G) current for switching between states was demonstrated. While this is a simple and effective technique,

it also possesses some drawbacks. The most apparent is the physical contact formation and release, which may lead either to degradation or stiction. This issue is exacerbated by the size distribution of the synthesized nanobelts. Although the synthesis process was optimized to produce nanobelts with a well-defined size distribution, variability still exists. This variability impacts the elastic restoring force of NEM switches, resulting in differences in the balance between ON-state adhesion and the nanobelt's elastic force across different switches on the same chip, potentially leading to stiction in some of the fabricated switches.

To address these challenges, an alternative method of deformation control during switching was explored, which involves monitoring changes in source-drain (S-D) current as the nanobelt approaches the gate electrode.

When a relaxed nanobelt is electrostatically bent, the deformation and mechanical strain in the structure change gradually and smoothly. However, if the nanobelt is initially buckled, a sharper transition in its mechanical state can be observed during deformation. Anticipating also sharp changes in the electrical characteristics, a NEM switch was fabricated using an upwards buckled Bi_2Se_3 nanobelt to measure gate voltage-induced changes in its resistance (Figure 4.30).

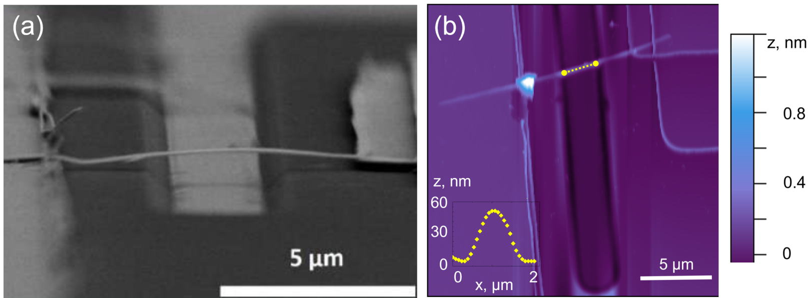

Figure 4.30: (a) Angled SEM and AFM (b) images of the upwards-buckled Bi_2Se_3 nanobelt NEM switch. The inset in (b) shows the line profile of the nanobelt measured just above the gate electrode (yellow dotted line in (b)).

The gating of this NEM switch in a three-terminal (3T) configuration was carried out at 2 K and 4 K. Both negative and positive DC gate voltage sweeps were performed from 0 V to maximum amplitude of $\pm$ 80 V (Figure 4.31). In both cases, a change in resistance slope was observed at a gate voltage of $\pm$ 35 V, which was attributed to a transition in the nanobelt's deformation state from upwards to downwards bending.

For a typical highly doped n-type Bi_2Se_3 field effect, a resistance increase would be expected at negative voltages, with little to no significant change in resistance under positive polarity voltage, as discussed in section 4.2. However, in this case, the observed decrease

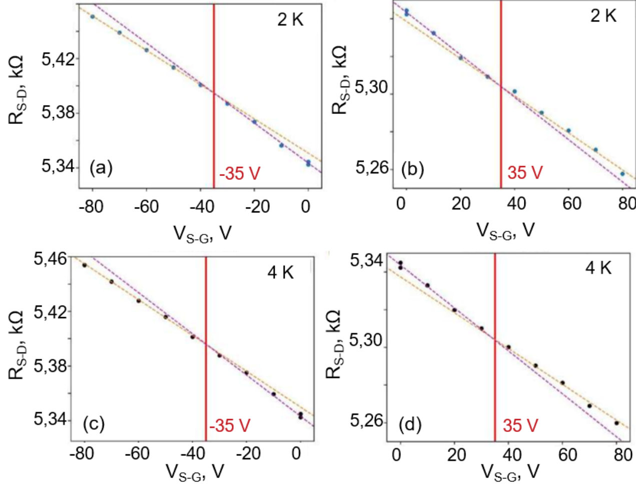

Figure 4.31: Source-drain resistance as a function of V_{SG} voltage at 2 K (a-b) and 4 K (c-d) temperatures. The orange dashed line is a linear fit in the high electric field range, while the purple dashed line represents a linear fit in the low electric field range. The solid red lines indicate the voltage value of $\pm$ 35 V.

in S-D resistance during a positive voltage sweep was attributed to the relaxation of the nanobelt from its upwards-buckled shape. When the voltage polarity was reversed, an increase in resistance was observed, which likely corresponded to the nanobelt returning to its initial shape, as well as charge redistribution due to the electrostatic field effect. The magnitude of the resistance change during the positive gate sweep from 0 and 80 V was modest at -1.62%, comparable to the resistance changes observed during electrostatic gating on a SiO_2 substrate, as presented in section 4.2.

To validate the assumption of a mechanical deformation change, the same buckled sample was tested *in situ* inside an SEM. A series of S-D I-V measurements were taken as a function of V_{SG}, while simultaneously monitoring the nanobelt's deformation from an angle. Figure 4.32 (b) shows SEM images of the nanobelt in its initial state (green) and after applying a voltage of $\pm$ 40 V (red). The images clearly demonstrate that the nanobelt undergoes a buckling deformation, transitioning from an upwards to a downwards bend. This observation was consistent with the low-temperature gate measurements (Figure 4.31), where the change in resistance slopes occurred at $\pm$ 35 V.

The implementation of I_{SD} monitoring in NEM switches provides a precise determination of the V_{ON} value. Additionally, at small nanobelt-to-gate distances, it would be possible to access a regime with two parallel currents, as the tunneling current I_{SD} would contribute

to the overall current. The geometry of this NEM switch suggests that a top gate electrode could be added for additional control, potentially enabling its use as a non-volatile memory device due to its upwards-bent shape.

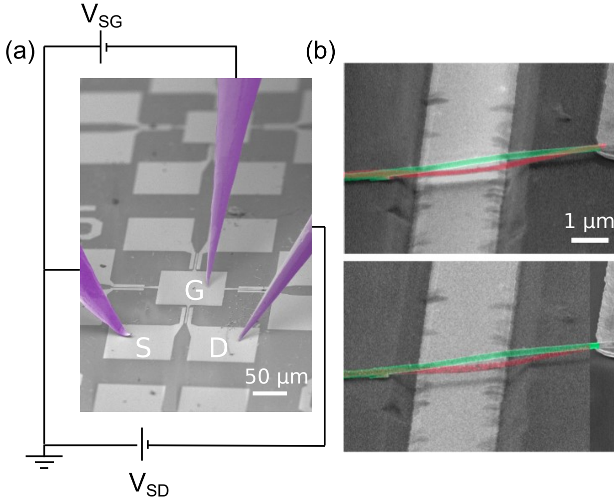

Figure 4.32: *In situ* measurement of R_{SD} versus V_{SG}. (a) False-color SEM image of Au electrodes connected to a single NEM switch. (b) Overlayed false-color SEM images, showing pronounced deformation of the Bi_2Se_3 nanobelt as the applied gate voltage changes from initial voltage of 0 V (green) to final voltage (red). Top image corresponds to negative voltage, bottom – to positive.

CONCLUSIONS

1. For CuO nanowires, the required yield and geometric parameters with a mean diameter of approximately 70 nm and a mean length of 5 μm for application in NEM switches are achieved via electric field-enhanced oxidation on the cathode side in a wet air atmosphere. Synthesis on a 3 nm thick Au layer produces the optimal yield for NEM switch fabrication of approximately 100 Bi_2Se_3 nanobelts per 1000 μm^2 with mean lengths of 3 to 6 μm, and mean thicknesses within the range of 30 to 110 nm.

   These nanostructure dimensions enable reliable fabrication of NEM switches with repeatable operation. Further scaling would enable reduction of switch-ON voltage below 4 V.

2. The effective Young's modulus of CuO nanowires with diameters smaller than 50 nm is found to exhibit size dependence, increasing up to 550 GPa. For Bi_2Se_3 nanobelts Young's modulus is found to remain at a constant average value of 44 GPa in the examined thickness range from 35 nm to 171 nm.

   A method for electrical characterization of mechanical vibrations of double-clamped nanostructures as a function of temperature in the temperature range from 5 K to 300 K and frequencies up to 10 MHz is developed. Using this method, Bi_2Se_3 nanobelts exhibit strong temperature-dependent vibrations, that could possibly be explained by differential thermal expansion of the nanobelt-electrode-substrate system.

3. A process flow for bottom-up integrated NEM switch fabrication is developed using photo- and electron beam lithography. Using this process flow, single CuO nanowire and topological insulator Bi_2Se_3 nanobelt switches with gap heights from 120 nm to 200 nm are fabricated.

4. Repeatable operation of a two-terminal CuO nanowire-based NEM switches at room temperature is demonstrated. Switching for 100 cycles is demonstrated with stable switching-ON voltage of 12.5 V and stable ON-state current of approximately 4 nA. CuO nanowire NEM switches are thus suitable for robust high-voltage applications.

5. Volatile and non-volatile repeatable operation is demonstrated with Bi_2Se_3 nanobelt-based two-terminal NEM switches at temperatures as low as 5 K. It exhibits switching-ON voltage of 8.0 V, ON/OFF current ratio of 10^3 and a subthreshold slope of 80 mV/decade, which is close to the 60 mV/decade thermionic limit of electronic transistors at room temperature.

6. Bi_2Se_3 nanobelt-based three-terminal NEM switch with continuous current monitoring through the nanobelt during OFF state was demonstrated at 2 K temperature. This novel switching mode could enable precise determination of switch-ON voltage and increase switch reliability.

BIBLIOGRAPHY

[1] O. Y. Loh and H. D. Espinosa, *Nature Nanotechnology*, 05/2012, **7**, 283–295.

[2] V. Pott, H. Kam, R. Nathanael, J. Jeon, E. Alon and T.-J. King Liu, *Proceedings of the IEEE*, 12/2010, **98**, Conference Name: Proceedings of the IEEE, 2076–2094.

[3] L. Wang, P. Zhang, Z. Liu, Z. Wang and R. Yang, *Chip*, 02/2023, 100038.

[4] J. Kulothungan and K. Kandhasamy, *Advanced Physics Research*, 2200050.

[5] J. O. Lee, Y.-H. Song, M.-W. Kim, M.-H. Kang, J.-S. Oh, H.-H. Yang and J.-B. Yoon, *Nature Nanotech*, 01/2013, **8**, 36–40.

[6] S. Rana, J. Mouro, S. J. Bleiker, J. D. Reynolds, H. M. H. Chong, F. Niklaus and D. Pamunuwa, *Nature Communications*, 03/2020, **11**, 1181.

[7] A. Peschot, C. Qian and T.-J. K. Liu, *Micromachines*, 08/2015, **6**, 1046–1065.

[8] T.-H. Lee, S. Bhunia and M. Mehregany, *Science*, 09/2010, **329**, 1316–1318.

[9] Y. Qian, B. W. Soon, P. Singh, H. Campanella and C. Lee, *Nanoscale*, 05/2014, **6**, 5606–5611.

[10] J. L. Muñoz-Gamarra, A. Uranga and N. Barniol, *Micromachines*, 02/2016, **7**, 30.

[11] X. Deng, N. Kang and Z. Zhang, *Chip*, 12/2023, **2**, 100064.

[12] C. Jia, Z. Lin, Y. Huang and X. Duan, *Chem. Rev.*, 08/2019, **119**, 9074–9135.

[13] A. Iorio, M. Rocci, L. Bours, M. Carrega, V. Zannier, L. Sorba, S. Roddaro, F. Giazotto and E. Strambini, *Nano Lett.*, 02/2019, **19**, 652–657.

[14] J. Cao, Q. Wang and H. Dai, *Nature Mater*, 10/2005, **4**, 745–749.

[15] S. Saha, M. S. Baghini, M. Goel and V. R. Rao, *IEEE Transactions on Electron Devices*, 09/2020, **67**, 3894–3897.

[16] H. Samaali, F. Najar and A. Chaalane, *Analog Integr Circ Sig Process*, 07/2020, **104**, 17–26.

[17] H. Kam, T.-J. K. Liu, V. Stojanović, D. Marković and E. Alon, *IEEE Transactions on Electron Devices*, 01/2011, **58**, 236–250.

[18] T. He, R. Yang, V. Ranganathan, S. Rajgopal, M. A. Tupta, S. Bhunia, M. Mehregany and P. X.-L. Feng, 2013 IEEE International Electron Devices Meeting, 12/2013, pp. 4.6.1–4.6.4.

[19] Y. Xie, D. Zhong, C. Fan, X. Deng, L.-M. Peng and Z. Zhang, *Advanced Electronic Materials*, 2021, **7**, 2100202.

[20] X. Liu, J. W. Suk, N. G. Boddeti, L. Cantley, L. Wang, J. M. Gray, H. J. Hall, V. M. Bright, C. T. Rogers, M. L. Dunn, R. S. Ruoff and J. S. Bunch, *Advanced Materials*, 2014, **26**, 1571–1576.

[21] R. R. Benoit and N. S. Barker, *Microelectronics Reliability*, 08/2020, **111**, 113706.

[22] J. G. Noel, A. Bogozi, Y. A. Vlasov and G. L. Larkins, *Journal of Microelectromechanical Systems*, 04/2008, **17**, 351–355.

[23] C. Goldsmith and D. Forehand, *IEEE Microwave and Wireless Components Letters*, 10/2005, **15**, Conference Name: IEEE Microwave and Wireless Components Letters, 718–720.

[24] S. Gong, H. Shen and N. S. Barker, *IEEE Transactions on Microwave Theory and Techniques*, 12/2009, **57**, 3442–3449.

[25] M. Pechal, J.-C. Besse, M. Mondal, M. Oppliger, S. Gasparinetti and A. Wallraff, *Phys. Rev. Appl.*, 08/2016, **6**, 024009.

[26] X. Hu, S. F. Almeida, Z. Alice Ye and T.-J. K. Liu, 2019 IEEE International Electron Devices Meeting (IEDM), ISSN: 2156-017X, 12/2019, pp. 34.2.1–34.2.4.

[27] Y. J. Kim and W. Y. Choi, *IEEE Transactions on Electron Devices*, 02/2015, **62**, 673–679.

[28] Y.-B. Lee, M.-H. Kang, P.-K. Choi, S.-H. Kim, T.-S. Kim, S.-Y. Lee and J.-B. Yoon, *Nat Commun*, 01/2023, **14**, 460.

[29] S. Kumar, D. S. Arya and P. Singh, *Applied Physics Letters*, 01/2021, **118**, 013505.

[30] H. S. Kwon, J. W. Ko and W. Y. Choi, *IEEE Electron Device Letters*, 08/2020, **41**, 1257–1260.

[31] Y. Li, E. Worsey, S. J. Bleiker, P. Edinger, M. Kumar Kulsreshath, Q. Tang, A. Yuji Takabayashi, N. Quack, P. Verheyen, W. Bogaerts, K. B. Gylfason, D. Pamunuwa and F. Niklaus, *Nanoscale*, 2023, **15**, 17335–17341.

[32] H. Fariborzi, M. Spencer, V. Karkare, J. Jeon, R. Nathanael, C. Wang, F. Chen, H. Kam, V. Pott, T.-J. K. Liu, E. Alon, V. Stojanović and D. Marković, IEEE Custom Integrated Circuits Conference 2010, 09/2010, pp. 1–4.

[33] C. Chen, R. Parsa, N. Patil, S. Chong, K. Akarvardar, J. Provine, D. Lewis, J. Watt, R. T. Howe, H.-S. P. Wong and S. Mitra, Proceedings of the 18th annual ACM/SIGDA international symposium on Field programmable gate arrays, Association for Computing Machinery, New York, NY, USA, 02/2010, pp. 273–282.

[34] K. Kato, V. Stojanović and T.-J. K. Liu, *IEEE Electron Device Letters*, 12/2016, **37**, 1563–1565.

[35] T. He, V. Ranganathan, R. Yang, S. Rajgopal, S. Bhunia, M. Mehregany and P. X.-L. Feng, 2013 Transducers & Eurosensors XXVII: The 17th International Conference on Solid-State Sensors, Actuators and Microsystems (TRANSDUCERS & EUROSENSORS XXVII), 06/2013, pp. 669–672.

[36] O. Loh, X. Wei, J. Sullivan, L. E. Ocola, R. Divan and H. D. Espinosa, *Advanced Materials*, 2012, **24**, 2463–2468.

[37] A. B. Kaul, E. W. Wong, L. Epp and B. D. Hunt, *Nano Lett.*, 05/2006, **6**, 942–947.

[38] S. N. Cha, J. E. Jang, Y. Choi, G. a. J. Amaratunga, D.-J. Kang, D. G. Hasko, J. E. Jung and J. M. Kim, *Appl. Phys. Lett.*, 02/2005, **86**, 083105.

[39] M. Muruganathan, N. H. Van, M. E. Schmidt and H. Mizuta, *Advanced Functional Materials*, 2022, **32**, 2209151.

[40] J. Zhang, Y. Deng, X. Hu, J. P. Nshimiyimana, S. Liu, X. Chi, P. Wu, F. Dong, P. Chen, W. Chu, H. Zhou and L. Sun, *Advanced Science*, 2018, **5**, 1700588.

[41] K. J. Ziegler, D. M. Lyons, J. D. Holmes, D. Erts, B. Polyakov, H. Olin, K. Svensson and E. Olsson, *Applied Physics Letters*, 2004, **84**, 4074–4076.

[42] X. L. Feng, M. H. Matheny, C. A. Zorman, M. Mehregany and M. L. Roukes, *Nano Lett.*, 08/2010, **10**, 2891–2896.

[43] C. Ke and H. D. Espinosa, *Small*, 2006, **2**, 1484–1489.

[44] W. Xiang and C. Lee, *Applied Physics Letters*, 05/2010, **96**, 193113.

[45] W.-M. Zhang, H. Yan, Z.-K. Peng and G. Meng, *Sensors and Actuators A: Physical*, 08/2014, **214**, 187–218.

[46] T. Cai, Y. Fang, Y. Fang, R. Li, Y. Yu and M. Huang, *Beilstein J. Nanotechnol.*, 04/2022, **13**, 390–403.

[47] M. Dequesnes, S. V. Rotkin and N. R. Aluru, *Nanotechnology*, 01/2002, **13**, 120.

[48] A. M. Mayet, M. A. Muqeet, H. H. Alhashim, F. Kurdahi and E. Eftekhari-Zadeh, *Frontiers in Materials*, 2024, **10**.

[49] T. Szkopek and E. Martel, *Progress in Quantum Electronics*, 03/2021, **76**, 100315.

[50] J. L. Mead, S. Wang, S. Zimmermann, S. Fatikow and H. Huang, *Engineering*, 05/2023, **24**, 39–72.

[51] F. Marabelli, G. B. Parravicini and F. Salghetti-Drioli, *Phys. Rev. B*, 07/1995, **52**, 1433–1436.

[52] N. Kaur, M. Singh and E. Comini, *Langmuir*, 06/2020, **36**, 6326–6344.

[53] A. M. B. Gonçalves, L. C. Campos, A. S. Ferlauto and R. G. Lacerda, *Journal of Applied Physics*, 2009, **106**, 034303.

[54] G. Filipič and U. Cvelbar, *Nanotechnology*, 04/2012, **23**, 194001.

[55] X. Jiang, T. Herricks and Y. Xia, *Nano Lett.*, 12/2002, **2**, 1333–1338.

[56] C. Tang, X. Liao, W. Zhong, H. Yu and Z. Liu, *RSC Adv.*, 01/2017, **7**, 6439–6446.

[57] X. Li, J. Zhang, Y. Yuan, L. Liao and C. Pan, *Journal of Applied Physics*, 07/2010, **108**, 024308.

[58] C. H. Xu, C. H. Woo and S. Q. Shi, *Superlattices and Microstructures*, 07/2004, **36**, 31–38.

[59] Y. Xia, D. Qian, D. Hsieh, L. Wray, A. Pal, H. Lin, A. Bansil, D. Grauer, Y. S. Hor, R. J. Cava and M. Z. Hasan, *Nature Phys*, 06/2009, **5**, 398–402.

[60] A. Ambrosi, Z. Sofer, J. Luxa and M. Pumera, *ACS Nano*, 12/2016, **10**, 11442–11448.

[61] B. Lv, T. Qian and H. Ding, *Nat Rev Phys*, 10/2019, **1**, 609–626.

[62] Y. Ando, *J. Phys. Soc. Jpn.*, 10/2013, **82**, 102001.

[63] P. Roushan, J. Seo, C. V. Parker, Y. S. Hor, D. Hsieh, D. Qian, A. Richardella, M. Z. Hasan, R. J. Cava and A. Yazdani, *Nature*, 08/2009, **460**, 1106–1109.

[64] A. A. Taskin, S. Sasaki, K. Segawa and Y. Ando, *Advanced Materials*, 2012, **24**, 5581–5585.

[65] J. Dai, D. West, X. Wang, Y. Wang, D. Kwok, S.-W. Cheong, S. B. Zhang and W. Wu, *Phys. Rev. Lett.*, 08/2016, **117**, 106401.

[66] M. Brahlek, N. Koirala, N. Bansal and S. Oh, *Solid State Communications*, 07/2015, **215-216**, 54–62.

[67] G. Kunakova, L. Galletti, S. Charpentier, J. Andzane, D. Erts, F. Léonard, C. Spataru, T. Bauch and F. Lombardi, *Nanoscale*, 2018, **10**, 19595–19602.

[68] D. Kim, S. Cho, N. P. Butch, P. Syers, K. Kirshenbaum, S. Adam, J. Paglione and M. S. Fuhrer, *Nature Phys*, 06/2012, **8**, 459–463.

[69] S. S. Hong, J. J. Cha, D. Kong and Y. Cui, *Nat Commun*, 03/2012, **3**, 757.

[70] S. M. Young, S. Chowdhury, E. J. Walter, E. J. Mele, C. L. Kane and A. M. Rappe, *Phys. Rev. B*, 08/2011, **84**, 085106.

[71] Y. Zhang, K. He, C.-Z. Chang, C.-L. Song, L.-L. Wang, X. Chen, J.-F. Jia, Z. Fang, X. Dai, W.-Y. Shan, S.-Q. Shen, Q. Niu, X.-L. Qi, S.-C. Zhang, X.-C. Ma and Q.-K. Xue, *Nature Phys*, 08/2010, **6**, 584–588.

[72] G. M. Knebl, J. R. Gessler, M. Kamp and S. Höfling, *Applied Physics Letters*, 10/2014, **105**, 133109.

[73] G. Kunakova, R. Meija, J. Andzane, U. Malinovskis, G. Petersons, M. Baitimirova, M. Bechelany, T. Bauch, F. Lombardi and D. Erts, *Scientific Reports*, 2019, **9**.

[74] F. Liu, M. Liu, A. Liu, C. Yang, C. Chen, C. Zhang, D. Bi and B. Man, *J Mater Sci: Mater Electron*, 06/2015, **26**, 3881–3886.

[75] W. H. Brattain, *The Physics Teacher*, 09/2006, **6**, 109.

[76] S. Thompson, M. Armstrong, C. Auth, M. Alavi, M. Buehler, R. Chau, S. Cea, T. Ghani, G. Glass, T. Hoffman, C.-H. Jan, C. Kenyon, J. Klaus, K. Kuhn, Z. Ma, B. Mcintyre, K. Mistry, A. Murthy, B. Obradovic, R. Nagisetty, P. Nguyen, S. Sivakumar, R. Shaheed, L. Shifren, B. Tufts, S. Tyagi, M. Bohr and Y. El-Mansy, *IEEE Transactions on Electron Devices*, 2004, **51**, 1790–1797.

[77] S. Thomas, *Nature Electronics*, 07/2021, **4**, 452–452.

[78] S. P. Ramanandan, P. Tomić, N. P. Morgan, A. Giunto, A. Rudra, K. Ensslin, T. Ihn and A. Fontcuberta i Morral, *Nano Letters*, 05/2022, **22**, 4269–4275.

[79] D. McNulty, S. Biswas, S. Garvey, C. O'Dwyer and J. D. Holmes, *ACS Appl. Energy Mater.*, 12/2020, **3**, 11811–11819.

[80] A. Garcia, S. Biswas, D. McNulty, A. Roy, S. Raha, S. Trabesinger, V. Nicolosi, A. Singha and J. D. Holmes, *ACS Appl. Energy Mater.*, 02/2022, **5**, 1922–1932.

[81] L. T. Ngo, D. Almécija, J. E. Sader, B. Daly, N. Petkov, J. D. Holmes, D. Erts and J. J. Boland, *Nano letters*, 2006, **6**, 2964–2968.

[82] J. Andzane, N. Petkov, A. I. Livshits, J. J. Boland, J. D. Holmes and D. Erts, *Nano letters*, 2009, **9**, 1824–1829.

[83] J. Andzane, R. Meija, A. I. Livshits, J. Prikulis, S. Biswas, J. D. Holmes and D. Erts, *Journal of Materials Chemistry C*, 2013, **1**, 7134–7138.

[84] C. O'Regan, S. Biswas, N. Petkov and J. D. Holmes, *J. Mater. Chem. C*, 11/2013, **2**, 14–33.

[85] M. Aghazadeh Meshgi, S. Biswas, D. McNulty, C. O'Dwyer, G. Alessio Verni, J. O'Connell, F. Davitt, I. Letofsky-Papst, P. Poelt, J. D. Holmes and C. Marschner, *Chem. Mater.*, 05/2017, **29**, 4351–4360.

[86] H.-J. Yang and H.-Y. Tuan, *J. Mater. Chem.*, 01/2012, **22**, 2215–2225.

[87] J. D. Holmes, D. M. Lyons and K. J. Ziegler, *Chemistry – A European Journal*, 2003, **9**, 2144–2150.

[88] N. W. Ashcroft and N. D. Mermin, *Solid state physics*, OCLC: 934604, Holt, Rinehart and Winston, New York, 1976.

[89] K. Park, Y. Lee, J. Lee and S. Lim, *Applied Surface Science*, 05/2008, **254**, 4828–4832.

[90] A. J. Green, S. Dey, Y. Q. An, B. O'Brien, S. O'Mullane, B. Thiel and A. C. Diebold, *Journal of Vacuum Science & Technology A*, 10/2016, **34**, 061403.

[91] T. Hanrath and B. Korgel, *Proceedings of the Institution of Mechanical Engineers, Part N: Journal of Nanoengineering and Nanosystems*, 2004, **218**, 25–34.

[92] S. E. Mohney, Y. Wang, M. A. Cabassi, K. K. Lew, S. Dey, J. M. Redwing and T. S. Mayer, *Solid-State Electronics*, 02/2005, **49**, 227–232.

[93] B. L. Al'tshuler and P. A. Lee, *Physics Today*, 12/1988, **41**, 36–44.

[94] L. He, F. Xiu, X. Yu, M. Teague, W. Jiang, Y. Fan, X. Kou, M. Lang, Y. Wang, G. Huang, N.-C. Yeh and K. L. Wang, *Nano Lett.*, 03/2012, **12**, 1486–1490.

[95] D. Kong, J. C. Randel, H. Peng, J. J. Cha, S. Meister, K. Lai, Y. Chen, Z.-X. Shen, H. C. Manoharan and Y. Cui, *Nano Lett.*, 01/2010, **10**, 329–333.

[96] R. Jones and W. Schaich, *J. Phys. C: Solid State Phys.*, 01/1972, **5**, 43–54.

[97] B. I. Shklovskii and A. L. Efros, in *Electronic Properties of Doped Semiconductors*, ed. B. I. Shklovskii and A. L. Efros, Springer, Berlin, Heidelberg, 1984, pp. 202–227.

[98] M. Nasr Esfahani and B. E. Alaca, *Advanced Engineering Materials*, 2019, **21**, 1900192.

[99] F. Xu, Q. Qin, A. Mishra, Y. Gu and Y. Zhu, *Nano Res.*, 04/2010, **3**, 271–280.

[100] L. Jasulaneca, R. Meija, A. I. Livshits, J. Prikulis, S. Biswas, J. D. Holmes and D. Erts, *Beilstein J. Nanotechnol.*, 02/2016, **7**, 278–283.

[101] B. Witkamp, M. Poot and H. Van Der Zant, *Nano Letters*, 2006, **6**, 2904–2908.

[102] M. Belov, N. J. Quitoriano, S. Sharma, W. K. Hiebert, T. I. Kamins and S. Evoy, *Journal of Applied Physics*, 04/2008, **103**, 074304.

[103] A. Heidelberg, L. T. Ngo, B. Wu, M. A. Phillips, S. Sharma, T. I. Kamins, J. E. Sader and J. J. Boland, *Nano Lett.*, 06/2006, **6**, 1101–1106.

[104] S. Zare Pakzad, M. Nasr Esfahani, Z. Tasdemir, N. Wollschläger, T. Li, X. Li, M. Yilmaz, Y. Leblebici and B. E. Alaca, *ACS Appl. Nano Mater.*, 09/2023, **6**, 15465–15478.

[105] S. O. Erbil, U. Hatipoglu, C. Yanik, M. Ghavami, A. B. Ari, M. Yuksel and M. S. Hanay, *Phys. Rev. Lett.*, 01/2020, **124**, 046101.

[106] S. Rechnitz, T. Tabachnik, M. Shlafman, S. Shlafman and Y. E. Yaish, *Nat Commun*, 10/2022, **13**, 5900.

[107] L. Hoddeson, G. Baym and M. Eckert, *Rev. Mod. Phys.*, 01/1987, **59**, 287–327.

[108] S. Basu, in *Topological Phases in Condensed Matter Physics*, ed. S. Basu, Springer Nature, Singapore, 2023, pp. 55–79.

[109] H. A. Fertig, *Physics*, 02/2009, **2**, 15.

[110] Q. Niu, D. J. Thouless and Y.-S. Wu, *Phys. Rev. B*, 03/1985, **31**, 3372–3377.

[111] B. A. Bernevig, T. L. Hughes and S.-C. Zhang, *Science*, 12/2006, **314**, 1757–1761.

[112] M. König, S. Wiedmann, C. Brüne, A. Roth, H. Buhmann, L. W. Molenkamp, X.-L. Qi and S.-C. Zhang, *Science*, 11/2007, **318**, 766–770.

[113] H. Zhang, C.-X. Liu, X.-L. Qi, X. Dai, Z. Fang and S.-C. Zhang, *Nature Phys*, 06/2009, **5**, 438–442.

[114] S. Zhang, Z. Li and F. Song, *Acta Phys. Sin.*, 2015, **64**, 097202.

[115] S. Matsuo, K. Chida, D. Chiba, T. Ono, K. Slevin, K. Kobayashi, T. Ohtsuki, C.-Z. Chang, K. He, X.-C. Ma and Q.-K. Xue, *Phys. Rev. B*, 10/2013, **88**, 155438.

[116] J. Kölzer, D. Rosenbach, C. Weyrich, T. W. Schmitt, M. Schleenvoigt, A. R. Jalil, P. Schüffelgen, G. Mussler, V. E. Sacksteder IV, D. Grützmacher, H. Lüth and T. Schäpers, *Nanotechnology*, 08/2020, **31**, 325001.

[117] S. S. Hong, Y. Zhang, J. J. Cha, X.-L. Qi and Y. Cui, *Nano Lett.*, 05/2014, **14**, 2815–2821.

[118] J. H. Bardarson and J. E. Moore, *Rep. Prog. Phys.*, 05/2013, **76**, 056501.

[119] S. Hikami, A. I. Larkin and Y. Nagaoka, *Progress of Theoretical Physics*, 02/1980, **63**, 707–710.

[120] H. Steinberg, D. R. Gardner, Y. S. Lee and P. Jarillo-Herrero, *Nano Lett.*, 12/2010, **10**, 5032–5036.

[121] D. Flötotto, Y. Bai, Y.-H. Chan, P. Chen, X. Wang, P. Rossi, C.-Z. Xu, C. Zhang, J. A. Hlevyack, J. D. Denlinger, H. Hong, M.-Y. Chou, E. J. Mittemeijer, J. N. Eckstein and T.-C. Chiang, *Nano Lett.*, 09/2018, **18**, 5628–5632.

[122] C. Schindler, C. Wiegand, J. Sichau, L. Tiemann, K. Nielsch, R. Zierold and R. H. Blick, *Appl. Phys. Lett.*, 10/2017, **111**, 171601.

[123] T. Rueckes, K. Kim, E. Joselevich, G. Y. Tseng, C.-L. Cheung and C. M. Lieber, *Science*, 07/2000, **289**, 94–97.

[124] J. Yao, H. Yan and C. M. Lieber, *Nature Nanotech*, 05/2013, **8**, 329–335.

[125] Q. Li, S.-M. Koo, M. D. Edelstein, J. S. Suehle and C. A. Richter, *Nanotechnology*, 07/2007, **18**, 315202.

[126] E. M. Freer, O. Grachev, X. Duan, S. Martin and D. P. Stumbo, *Nature Nanotech*, 07/2010, **5**, 525–530.

[127] H. Zhu, C. A. Richter, E. Zhao, J. E. Bonevich, W. A. Kimes, H.-J. Jang, H. Yuan, H. Li, A. Arab, O. Kirillov, J. E. Maslar, D. E. Ioannou and Q. Li, *Sci Rep*, 04/2013, **3**, 1757.

[128] D. Tsivion, M. Schvartzman, R. Popovitz-Biro, P. von Huth and E. Joselevich, *Science*, 08/2011, **333**, 1003–1007.

[129] A. Pevzner, Y. Engel, R. Elnathan, T. Ducobni, M. Ben-Ishai, K. Reddy, N. Shpaisman, A. Tsukernik, M. Oksman and F. Patolsky, *Nano Lett.*, 04/2010, **10**, 1202–1208.

[130] K. Jung, W. Choi, H.-C. Huang, J. D. Kim, K. Chabak and X. Li, *ACS Appl. Mater. Interfaces*, 03/2021, **13**, 11177–11184.

[131] A. Colli, A. Tahraoui, A. Fasoli, J. M. Kivioja, W. I. Milne and A. C. Ferrari, *ACS Nano*, 06/2009, **3**, 1587–1593.

[132] A. Subramanian, A. R. Alt, L. Dong, B. E. Kratochvil, C. R. Bolognesi and B. J. Nelson, *ACS Nano*, 10/2009, **3**, 2953–2964.

[133] S. A. Abbasi, T.-h. Kim, S. Somu, H. Wang, Z. Chai, M. Upmanyu and A. Busnaina, *J. Phys. D: Appl. Phys.*, 04/2020, **53**, 23LT02.

[134] S. W. Lee, D. S. Lee, R. E. Morjan, S. H. Jhang, M. Sveningsson, O. A. Nerushev, Y. W. Park and E. E. B. Campbell, *Nano Lett.*, 10/2004, **4**, 2027–2030.

[135] J. Andzane, G. Kunakova, S. Charpentier, V. Hrkac, L. Kienle, M. Baitimirova, T. Bauch, F. Lombardi and D. Erts, *Nanoscale*, 2015, **7**, 15935–15944.

[136] T. Hanrath and B. A. Korgel, *J. Am. Chem. Soc.*, 02/2002, **124**, 1424–1429.

[137] J. D. Holmes, K. P. Johnston, R. C. Doty and B. A. Korgel, *Science*, 02/2000, **287**, 1471–1473.

[138] E. P. S. Tan, Y. Zhu, T. Yu, L. Dai, C. H. Sow, V. B. C. Tan and C. T. Lim, *Applied Physics Letters*, 04/2007, **90**, 163112.

[139] G. Wang and X. Li, *Journal of Applied Physics*, 12/2008, **104**, 113517.

[140] A. M. Abazari, S. M. Safavi, G. Rezazadeh and L. G. Villanueva, *Sensors*, 11/2015, **15**, 28543–28562.

[141] A. Cavallin, V. Sevriuk, K. N. Fischer, S. Manna, S. Ouazi, M. Ellguth, C. Tusche, H. L. Meyerheim, D. Sander and J. Kirschner, *Surface Science*, 04/2016, **646**, 72–82.

[142] H. Yan, C. Vajner, M. Kuhlman, L. Guo, L. Li, P. T. Araujo and H.-T. Wang, *Applied Physics Letters*, 07/2016, **109**, 032103.

[143] C. B. Maliakkal, J. P. Mathew, N. Hatui, A. A. Rahman, M. M. Deshmukh and A. Bhattacharya, *Journal of Applied Physics*, 09/2015, **118**, 114301.

[144] S. T. Bartsch, A. Rusu and A. M. Ionescu, *Applied Physics Letters*, 10/2012, **101**, 153116.

[145] R. G. DeAnna, S. Roy, C. A. Zorman and M. Mehregany, San Juan, 01/1999.

[146] X. Chen, H. D. Zhou, A. Kiswandhi, I. Miotkowski, Y. P. Chen, P. A. Sharma, A. L. Lima Sharma, M. A. Hekmaty, D. Smirnov and Z. Jiang, *Applied Physics Letters*, 12/2011, **99**, 261912.

[147] G. Prakash, K. Pal, U. V. Waghmare and A. K. Sood, *Phys. Scr.*, 08/2019, **94**, 115706.

[148] L. He, F. Xiu, Y. Wang, A. V. Fedorov, G. Huang, X. Kou, M. Lang, W. P. Beyermann, J. Zou and K. L. Wang, *Journal of Applied Physics*, 05/2011, **109**, 103702.

[149] H. Wang, H. Liu, C.-Z. Chang, H. Zuo, Y. Zhao, Y. Sun, Z. Xia, K. He, X. Ma, X. C. Xie, Q.-K. Xue and J. Wang, *Sci Rep*, 07/2014, **4**, 5817.

[150] J. Wang, A. M. DaSilva, C.-Z. Chang, K. He, J. K. Jain, N. Samarth, X.-C. Ma, Q.-K. Xue and M. H. W. Chan, *Phys. Rev. B*, 06/2011, **83**, 245438.

[151] Y. S. Kim, M. Brahlek, N. Bansal, E. Edrey, G. A. Kapilevich, K. Iida, M. Tanimura, Y. Horibe, S.-W. Cheong and S. Oh, *Phys. Rev. B*, 08/2011, **84**, 073109.

[152] S. Raychaudhuri, S. A. Dayeh, D. Wang and E. T. Yu, *Nano Lett.*, 06/2009, **9**, Publisher: American Chemical Society, 2260–2266.

[153] N. K. R. Palapati, E. Pomerantseva and A. Subramanian, *Nanoscale*, 02/2015, **7**, Publisher: The Royal Society of Chemistry, 3109–3116.

[154] H. Ji, J. Choi, Y. Cho, I.-S. Hwang, S.-J. Kim, J.-H. Lee, S. Roth and G.-T. Kim, *Journal of Applied Physics*, 07/2011, **110**, 013705.

[155] P. Ryan, Y.-C. Wu, S. Somu, G. Adams and N. McGruer, *Journal of Micromechanics and Microengineering*, 2011, **21**.

Appendices

A.1 Processing methods

A.1.1 Mask fabrication for photolithography

- **Fabrication of Cr masks**

  1. Rinse Cr blank in acetone and isopropyl alcohol
  2. Blow dry with N_2
  3. Dehydration bake at 100 °C for 2 minutes on a hotplate, let cool down for 5 minutes
  4. Spin coat AZ1518 at 4000 rpm with 4000 rpm/s acceleration for 40 seconds (for 1.7 μm thickness)
  5. Soft-bake at 100 °C for 2 minutes on hotplate, let cool down for 5 minutes
  6. Expose design with Heidelberg Instruments Micro Pattern generator μPG101 (approximate dose 30 mJ/cm^2)
  7. Develop 70 seconds in AZ 726 metal ion free developer (TMAH-based)
  8. Rinse in DIW
  9. Blow dry with N_2
  10. Hard bake at 100 °C for 5 minutes on hotplate, let cool down for 5 minutes
  11. Etch for 35 seconds in Cr etchant containing perchloric acid and ceric ammonium nitrate
  12. Rinse in deionised water (DIW)
  13. Strip AZ1518 in warm Technistrip solvent ($\approx$ 80 °C) for 30 minutes
  14. Rinse in isopropyl alcohol
  15. Blow dry with N_2

- **Fabrication of Fe_2O_3 masks**

  1. Repeat same steps as for Cr blank up to etch step
  2. Etch for 90–100 seconds in concentrated HCl etch
  3. Repeat same steps as for Cr blank

A.1.2 Fabrication of NEM switches by photolithography

- **Gate electrodes in trenches**

  1. Clean Si die 10 minutes using ultrasonic agitation in acetone followed by 10 minutes in isopropyl alcohol
  2. Blow dry with N_2
  3. Prime with hexamethyldisilazane (HMDS) at 150 °C
  4. Cool down for 5 minutes
  5. Spin coat positive AZ1505 resist at 4000 rpm with 4000 rpm/s acceleration for 40 seconds (for 600 nm thickness)
  6. Soft-bake at 100 °C for 50 seconds on hotplate, let cool down for 5 minutes
  7. Expose design with dose 30–40 mJ/cm^2
  8. Develop for 35–50 seconds
  9. Rinse in DIW
  10. Blow dry with N_2
  11. Hardbake at 120 °C for 5 minutes, let cool down
  12. Etch in buffered hydrofluoric acid (BOE), with approximate rate of 1.4 nm/s at room-temperature
  13. Stop etch and rinse thoroughly in DIW
  14. O_2 plasma ash for 60 seconds
  15. Evaporate 5 nm Ti and 55 nm Au
  16. Lift-off in warm Technistrip ($\approx$ 80 °C)
  17. Rinse in acetone and isopropyl alcohol
  18. Blow dry with N_2

- **Electrodes on top of Bi_2Se_3 nanobelts**

  1. Short and mild O_2 plasma ash for 2 seconds
  2. Prime with hexamethyldisilazane (HMDS) at 150 °C
  3. Cool down for 5 minutes
  4. Spin coat lift-off resist LOR-3 at 3000 rpm with 3000 rpm/s acceleration
  5. Soft-bake at 150 °C for 3 minutes on hotplate, let cool down for 5 minutes

6. Spin coat AZ1505 at 4000 rpm with 4000 rpm/s acceleration for 40 seconds (for 600 nm thickness)
7. Soft bake at 100 °C for 50 seconds on hotplate, let cool down for 5 minutes
8. Expose design with dose 30–40 mJ/cm^2
9. Develop for 50 seconds
10. Rinse in DIW
11. Blow dry with N_2
12. Etch Bi_2Se_3 oxide in acetic acid/HCl mixture for 60 seconds
13. Rinse in DIW
14. Load into thermal evaporator immediately after etch
15. Evaporate 5 nm Ti and 120–200 nm (depending on the thickness of 1D NS) Au at pressure of <7e^{-7} mbar
16. Lift-off in warm Technistrip ($\approx$ 80 °C)
17. Rinse in acetone and isopropyl alcohol
18. Blow dry with N_2 for 1D NS on substrate. Follow a supercritical drying procedure for 1D NS on trenches to avoid capillary action.

A.1.3 Fabrication of NEM switches by e-beam lithography

- **Gate electrodes in trenches**

1. Clean Si die for 10 minutes using ultrasonic agitation in acetone followed by 10 minutes in isopropyl alcohol
2. Blow dry with N_2
3. O_2 plasma clean for 60 seconds
4. Spin coat PMMA A9 at 4000 rpm with 4000 rpm/s acceleration for 1 minute (for a thickness of 1700 nm)
5. Soft-bake at 160 °C for 5 minutes on hotplate, let cool down for 5 minutes
6. Expose design with dose of 210 μC/cm^2
7. Develop in isopropyl alcohol/DIW mixture (93:7 v/v) for 15 seconds
8. Blow dry with N_2
9. O_2 plasma ash for 20 seconds

10. Reactive ion etch using CHF_3-Ar at 10 °C for 5 minutes for trench depth of 260 nm
11. Ash with O_2 plasma for 20 seconds
12. Evaporate 5 nm Ti and 55 nm Au
13. Lift-off in acetone
14. Rinse in isopropyl alcohol
15. Blow dry with N_2

- **Electrodes on top of Bi_2Se_3 nanobelts**

1. Spin coat EL6 copolymer at 4000 rpm with 4000 rpm/s acceleration for 1 minute
2. Soft-bake at 150 °C for 5 minutes on hotplate, let cool down for 5 minutes
3. Spin coat PMMA A4 at 4000 rpm with 4000 rpm/s acceleration for 1 minute (for a thickness of 200 nm)
4. Soft-bake at 150 °C for 5 minutes on hotplate, let cool down for 5 minutes
5. Expose design with a dose of 210 mJ/cm^2
6. Develop in IPA/DIW mixture (93/7 v/v) for 15 seconds
7. Blow dry with N_2
8. Ash with O_2 plasma for 20 seconds
9. Etch Bi_2Se_3 oxide in acetic acid/HCl mixture for 60 seconds
10. Evaporate 5 nm Ti and 120–200 nm (depending on the thickness of 1D NS)
11. Lift-off in acetone
12. Rinse in isopropyl alcohol
13. Blow dry with N_2

B.2 Circuit for electrical detection of resonant frequency

Figure B.2.1 shows the electrical circuit schematic of the integrated preamplifier used to characterize temperature-dependent resonant vibrations in Bi_2Se_3 nanobelts.

The conductivity of the Bi_2Se_3 nanobelt was modulated by the gate (G) electrode, which applied a DC voltage V_g through a resistor R_2, provided by a programmable external source Keithley-6430. Gate electrode was connected to the input terminal V_{AC-in} through the capacitor C_2. A V_{AC-in} signal was generated using a vector network analyzer VNA, Rohde & Schwarz ZNB 8 port 1. The output signal V_{AC-out} was connected to VNA port 2 and the S_{21}

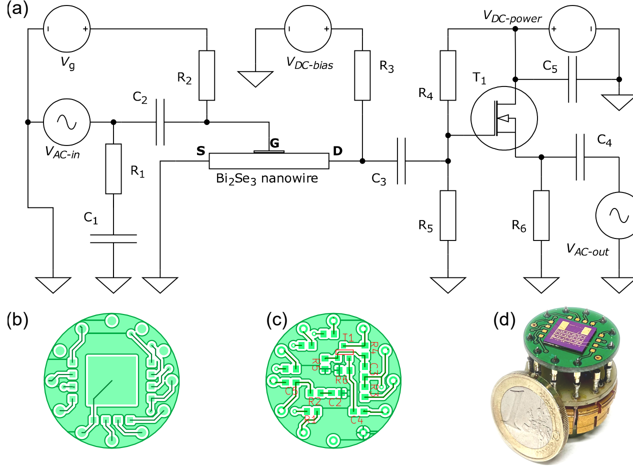

Figure B.2.1: (a) Electrical circuit schematic of the integrated preamplifier. Element values were R_1—50 Ω; R_2, R_4, R_5—2 MΩ; R_3 approximately equal to DC resistance of Bi_2Se_3 nanowire; R_6—1.2 kΩ; C_1, C_2, C_3, C_4—0.1 µF; C_5—0.5 µF; T_1—2N7002. PCB layout with corresponding element designations shown from (b) top and (c) bottom sides. (d) PCB mounted on a PPMS holder with sample bonded on the top.

parameter was used to characterize the system amplitude transfer function $A(f)$. The typical operating parameters were $V_{AC-in,rms}$ 0.22 V, $V_{DC-power}$ 15 V and $V_{DC-bias}$ 0.04 V with a corresponding I_{SD} in the range of 0.5–1.0 μA.

The AC component of the voltage drop across the Bi_2Se_3 nanobelt was connected through the capacitor C_3 to the gate of the transistor T_1 (2N7002), which operated as a source follower. The resistors R_4 and R_5 ensured that the transistor gate was biased above the gate-source threshold voltage V_T of T_1.

Bi_2Se_3 nanobelt and the resistor R_3 formed a voltage divider, which was connected to a $V_{DC-bias}$ source Keithley-2400. Source-drain current monitoring allowed to determine, whether the nanobelt was damaged, while R_3 was used for limiting current flow through it.

The resistance of R_6 was chosen relatively high to avoid heating inside the cryostat. C_5 is a bypass capacitor for the supply voltage $V_{DC-power}$.

Monitoring the direct current at V_g indicated whether a jump-to-contact event had occurred. To avoid the risk of the nanobelt contacting the gate electrode, the gate voltage was kept in the range of $\pm$ 8 V.

The R_1C_1 matching network additionally provided a load of V_{AC-in} voltage for diagnostic of electric connections.

ACKNOWLEDGEMENTS

I would like to thank my supervisor, Donats Erts, a pioneer of significant developments in the field, for introducing me to and guiding me through the exciting world of nanoelectromechanics. I enjoyed your relentlesness, creative and sometimes nearly-impossible-to-implement ideas, as well as your ability to question the results and focus on the big and small picture of the scientific research.

My colleagues at the Institute of Chemical Physics sustained my motivation throughout many years by being passionate, funny, patient and by simply being who they are. Special thanks to the nanoelectromechanics group: Lena, Raimonds, Raitis, Juris, Alexander Livshits, Jana, Edijs, Matiss. Thanks to Elza, for being with me through the loneliest phase of the research. I learnt quite a lot from all of you, and it was a pleasure working together.

Thanks to my colleagues at the Institue of Solid State Physics for their cooperation, support, and for introducing me to the exciting world of micro- and nanofabrication.

And finally, thanks to Elina, Vyacheslavs, Kiryl and Gunta for trying to explain things that are hard to understand.

Most importantly, thanks to my family and friends, especially my daughter Emma, for saying that if grown-ups have such boring occupations as mine, she would rather not grow up. (I am looking forward to your thesis).

Paper I

Sensors & Actuators: A. Physical 371 (2024) 115292

Contents lists available at ScienceDirect

Sensors and Actuators: A. Physical

journal homepage: www.journals.elsevier.com/sensors-and-actuators-a-physical

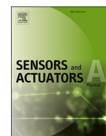

Effect of bending deformation on suspended topological insulator nanowires: Towards a topological insulator based NEM switch

Kiryl Niherysh [a], Liga Jasulaneca [a], Elza Dzene [a], Floriana Lombardi [b], Donats Erts [a,c,*]

[a] Institute of Chemical Physics, University of Latvia, Raina blvd. 19, Riga LV-1586, Latvia
[b] Quantum Device Physics Laboratory, Department of Microtechnology and Nanoscience, Chalmers University of Technology, Kemivägen 9, Gothenburg 41258, Sweden
[c] Faculty of Chemistry, University of Latvia, Raina blvd. 19, Riga LV-1586, Latvia

ARTICLE INFO

Keywords:
Topological insulator
Deformation
Nanoscale electromechanical (NEM) switch

ABSTRACT

Nanodevices consisting of the suspended and supported parts of topological insulator Bi_2Se_3 nanowires were fabricated and measured at low and room temperatures. Probing of topological surface states, accompanied by the electrostatic field effect used to dynamically manipulate bending deformation, was carried out to monitor the external strain introduced into the suspended and supported parts within the same Bi_2Se_3 nanowire. Depending on the device geometry, pure elastic and elastoplastic types of concave deformation, as well as convex buckling deformation, were realized in the suspended parts of the nanowires. For various types of observed deformations, different magnitudes of increase in the Source-Drain resistance of the deformed part compared to the relaxed part of the same devices were determined. All suspended devices exhibit external strain-sensitive Shubnikov-de Haas oscillation frequencies representing the carriers of top and bottom surface states and bulk, whereas, in the case of supported devices, the bottom surface states are masked by a trivial 2DEG. The obtained results may be useful for strain engineering of TI materials, as well as for applications in NEMS and other areas related to suspended nanostructures.

1. Introduction

Suspended devices based on nanosized structures in the form of nanowires (NWs), nanobelts, nanoribbons, and thin films (TF) are successfully implemented in a wide field of various applications in electronics [1-4], biosensing [5-7], gas sensing [10,8,9], photonics [11], thermoelectric performance devices [12,13], nanomechanical resonators [14-16], devices for fundamental phenomena investigations [17, 18], and nanoelectromechanical switches [19-22] due to their small size, low mass, high crystalline quality, significant anelasticity, plasticity, and ultra-high strength [23,24]. Indeed, the coupling of mechanical and other degrees of freedom, such as electrical, spin or optical, allows the creation of novel devices with improved characteristics.

One class of these devices is nanoelectromechanical (NEM) switches, which exploit mechanical and electrical interaction between movable and static elements [22,25,26]. Most of the NEM switches based on suspended TF (graphene) [27,28] or NWs [21,29,30] have previously been demonstrated at room temperature. However, the use of a material with a high melting point, such as molybdenum or silicon carbide, in NEM switches makes it possible to implement devices at high temperatures (up to 800 K) [31,32]. Thus, NEM switches have already proven their superiority as low-voltage [33-35], low standby-power devices [36], and suitability for harsh environment applications [31, 32]. These energy-efficient devices can be used as memory, logical and sensing elements, endowed with high sensitivity and speed. Moreover, the use of a material with suitable physical properties at low temperatures (e.g. graphene, or topological insulators (TIs)) as the active element of NEM switches will lead to new applications in space installations [37] or quantum computing applications [38]. Recently, a NEM switch operating at temperatures as low as 5 K has been demonstrated by our group using a layered topological insulator material – bismuth selenide (Bi_2Se_3) [39].

Three-dimensional topological insulators (3D TIs) are a novel class of quantum materials that are insulating in the bulk, but host conducting topological surface states (TSSs) protected by time-reversal symmetry. Due to spin-momentum locking of Dirac fermions originating from TSSs, the material provides an opportunity to realize a broad range of applications inaccessible in ordinary materials [40,41]. Experimentally accessing TSSs has been a challenge due to a significant contribution from the bulk carriers that place the Fermi level in the bulk conduction

* Corresponding author at: Institute of Chemical Physics, University of Latvia, Raina blvd. 19, Riga LV-1586, Latvia.
E-mail address: donats.erts@lu.lv (D. Erts).

https://doi.org/10.1016/j.sna.2024.115292
Received 23 November 2023; Received in revised form 26 February 2024; Accepted 18 March 2024
Available online 26 March 2024
0924-4247/© 2024 Elsevier B.V. All rights reserved.

band [42-44]. To overcome this problem (reduce the concentration of bulk carriers), efforts have been aimed at: a) synthesis of 3D TIs with an increased surface-to-volume ratio [45,46], b) introduction of chemical compensating dopants into TI materials [43,47,48], and c) control of Dirac states in TIs by introducing various strain (strain engineering) [49-53]. While the synthesis of reduced-size nanostructures and the compensating doping approaches allow optimization of TI material properties before device fabrication and are irreversible, strain engineering provides a reversible route for modifying the electronic structure in TI-based devices [54]. Since 3D TI materials as Bi_2Se_3, Bi_2Te_3 and Sb_2Te_3 have a tetradymite structure formed by five covalently bonded atomic sheets (e.g., Se–Bi–Se–Bi–Se) defined as a quintuple layer (QL), which are weakly bonded between each other (van der Waals) [40], the bulk band topology of TIs would be expected to be sensitive to uniaxial in-plane stain [54]. Thus, strain is a particularly exciting way to manipulate and control the Fermi level in TIs, since different types of deformations can lead to different properties [55]. For example, strain may lead to phase transitions from topological to trivial states and vice-versa [56,57]. It has been theoretically calculated that the electronic band gap of Bi_2Se_3 decreases with tensile in-plane strain and increases with compressive in-plane strain [58].

TI-based NEM switches could take advantage of both the strain tunability of electronic properties of Bi_2Se_3 and the suitable electromechanical properties for undergoing electromechanical «ON/OFF» switching. Typically, the moment of «ON/OFF» switching is determined by a significant and sharp change in current after closing or opening the contact: in the case of a Source-Drain current a nanorelay configuration is implemented, and in the case of a Gate-Drain current a two-terminal switch is realized. The disadvantage of currently implemented 2-terminal switches based on Bi_2Se_3 nanowires is the large distribution of the geometric dimensions of the synthesized nanostructures, which causes differences in the elastic properties of nanowires. As a result, the balance between «ON» state adhesion and nanowire elastic force is different for individual nanowires, so often when the gate voltage is released, the elastic force of the nanowire does not exceed the adhesion force, and the nanowire can remain in the «ON» state. However, the strain-induced rearrangement of the electronic properties of Bi_2Se_3 makes it possible to continuously control the Source-Drain current not only at the moment of switching but also at all stages of nanowire bending, as well as to monitor the state of the nanowire under different bending modes.

The active element in the form of nanowires used in NEM devices can be repeatedly exposed to external mechanical stress (compression, tension, bending and buckling), which requires excellent resistance to bending fatigue. However, as was recently shown by *Kong at al.* [23], previous studies (theoretical and experimental) have mainly focused on the loading behavior of nanowires (tensile/compressive) in NEMS, while the bending deformation behavior of nanowires remains less studied [59-65].

In this study, based on the sensitivity of TSSs to external strain, we exploited the magnetotransport properties of the suspended and supported parts within the same Bi_2Se_3 nanowire to investigate the effects of nanowire bending/buckling deformation for further use in NEM applications. Temperature dependence of resistance, magnetoresistance as a function of a magnetic field, and Hall effect measurements are used to describe the properties of TI nanowires in relaxed and strained states. The electrostatic field effect was used to deform the nanowire at room and low temperatures. Our results may pave the way towards a single device in which «ON/OFF» switching would be complemented by the possibility of dynamical manipulation of the Fermi level and topological states via electrostatically induced strain.

2. Materials and methods

The free-standing Bi_2Se_3 nanowires were synthesized by vapor-liquid-solid (VLS) growth in a quartz tube furnace on a glass substrate using the Au catalyst nanoparticles, formed by a dewetted ultrathin Au film as described in [66]. For better comparability, nanowires from the same batch were used to fabricate samples for bending experiments. The 7 × 7 mm sized Si/SiO_2 (300 nm) chips were patterned via electron-beam lithography (EBL) to define the shape of the trenches. After that, the pre-patterned chips were etched either by reactive ion etching (RIE) in a mixture of CHF_3 (20 sccm) and O_2 (5 sccm) at 10°C and 200 W power for 8 min (using Cr metal mask) (***Device 1***) or in buffered hydrofluoric acid 7 : 1 (BOE) (HF : NH_4F = 12.5 : 87.5%) for approx. 3 min to fully etch a silicon oxide layer (***Device 2*** and ***3***). Next, Ti/Au (5/95 nm) back-gate contacts were formed by the e-beam evaporator. Then the NWs were transferred to the substrate with the trenches, slightly pressing this chip (a flip-chip method) to the glass with nanowires (***Device 1*** and ***2***). For ***Device 3*** the NWs were suspended in isopropyl alcohol for alignment across the trenches with the gates using floating-electrode dielectrophoresis [39,67]. Supercritical CO_2 drying was used to remove the isopropyl residuals and avoid capillary forces between the nanowire and the gate electrode.

Then, the nanowires transferred across the trenches were patterned using EBL to create electrical contacts. To remove the native oxide layer and provide a robust ohmic contact, the surface of the nanowires was etched off (approximately 3–4 nm) with Ar-ion milling prior to the deposition of the metal electrodes.

The width, thickness and suspended/supported length of the devices were determined using an atomic force microscope (AFM, Bruker Dimension ICON). In-situ transport measurements (2-probe configuration) of ***Device 3*** at room temperature were carried out using a scanning electron microscope (SEM, Hitachi FE-SEM S-4800) equipped with a nanomanipulator.

Tilted SEM images of the devices were obtained using SEM-Zeiss Supra 60 VP. Electron-beam lithography (JEOL JBX 9300FS), Reactive Ion Etcher (Oxford Instruments PlasmaPro Cobra), Ar-ion beam etching (Oxford Ionfab 300 Plus), and vacuum evaporator (Lesker PVD 225) were used to fabricate the trenches and create electrical contacts to the individual nanowires in a cleanroom environment. Magnetotransport measurements were performed in the physical property measurement system PPMS (Quantum Design DynaCool (14 T)) equipped with external electronics at the temperature of 2 K. All devices were measured in DC bias mode. The biasing circuit consists of a voltage source V_b (Keithley 2400), a bias resistor R_b (for current biasing), and a sampling resistor R_s that is used for probing the current supplied to the device (Figs. 1a and 6b). Both the voltage drops across the supported V_{supp} and suspended V_{susp} parts of the device as well as I_bR_s are measured using a setup consisting of two low-noise differential amplifiers (Stanford Instruments) connected to the digital multimeters (Keithley 2000), to get voltages and current across the device, respectively. The gate electrode was connected to another source meter V_b^G (Keithley 2400) through a bias resistor R_b^G with a nominal 1 MΩ to reduce the noise. The Gate-Drain current was simultaneously monitored during applying the back-gate voltage.

3. Results and discussion

3.1. Magnetotransport properties of synthesized Bi_2Se_3 nanowires

After synthesis, several nanowires of different thicknesses (30–120 nm) were characterized in terms of electron transport properties. All nanowires demonstrate nearly linear behavior of the longitudinal magnetoresistance as a function of temperature, which indicates metallic conduction frequently observed in Bi_2Se_3 due to conductive bulk states [68]. Magnetoresistance as a function of a magnetic field measured at 2 K exhibits oscillations at the magnetic field above ~5 T attributed to the Shubnikov–de Haas (SdH) oscillations (quantum transport phenomena representing magneto-oscillations of the resistance in systems with high-mobility electrons at sufficiently low temperatures). They arise as a result of the cyclotron motion of electrons and

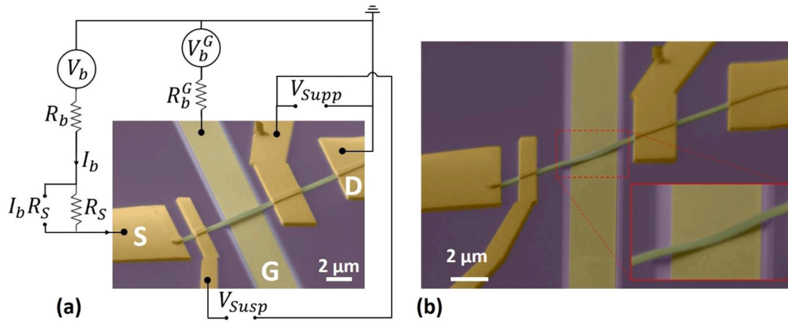

Fig. 1. Tilted false-color SEM images of fabricated ***Device 1*** based on a Bi_2Se_3 nanoribbon (green) transferred onto a Si/SiO_2 substrate (violet), containing an etched trench with a gold back-gate electrode (light-yellow) inside. The metal electrodes are shown in yellow. The device consists of the suspended and supported parts. (a) The device (with the measurements scheme) in the «OFF» configuration (an unstrained suspended wire above the back-gate electrode). (b) The device in the «ON» configuration (a wire is touching the gate). The inset is a zoom-in region showing that the suspended nanowire is deformed by the electrostatic force and attached to the gate.

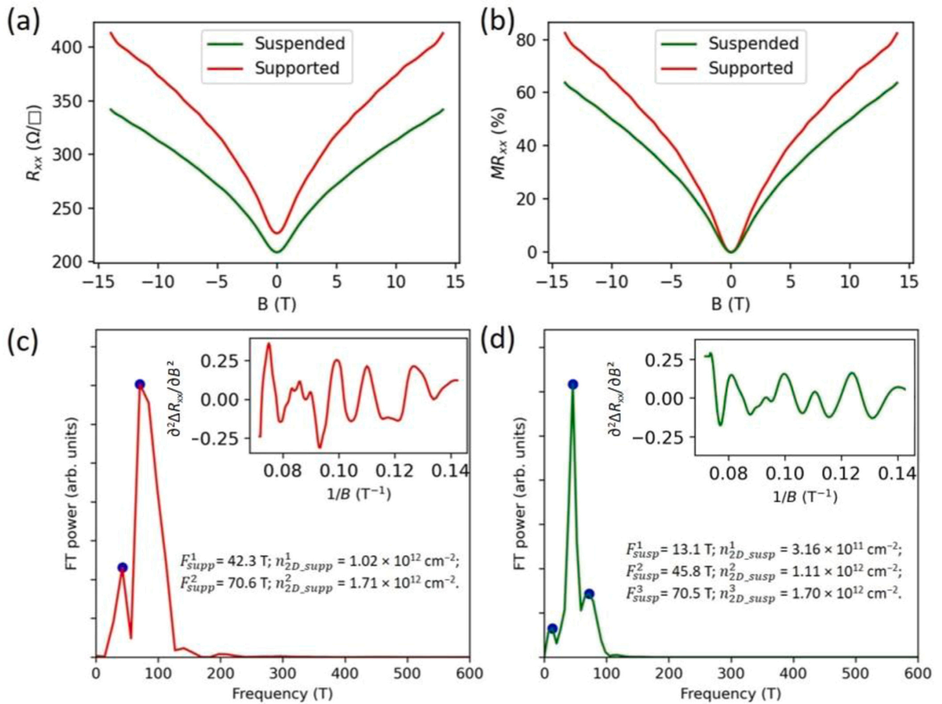

Fig. 2. Magnetotransport measurements of ***Device 1*** presented in Fig. 1a. (a) The longitudinal sheet resistance $R_{xx}(\Omega/\square)$ as a function of a magnetic field for the suspended and supported parts. (b) Magnetoresistance $MR = (R_{xx}(B) - R_{xx}(0))/R_{xx}(0)$ as a function of a magnetic field. Shubnikov-de Haas oscillations analysis: the Fourier transform power spectra of $\partial^2\Delta R_{xx}/\partial B^2$ (presented in the insets) for the supported part shown in (c), and for the suspended part shown in (d), respectively.

the sequential crossings of the discrete Landau Levels through the Fermi energy [69]. These observed oscillations are not strictly periodic in $1/B$, and the Fourier transform (FT) of them reveals a few frequencies, which leads to a beating pattern of the SdH oscillations. Such multiple frequencies for Bi_2Se_3 nanowires with thicknesses above ~30 nm have previously been reported by our group in [46,66,70] and also by other groups [71,72]. The complex pattern of the SdH oscillations originates from the coexistence of the 3D bulk carriers and the 2D topological surface states. Thus, the nanowires synthesized in this study exhibit features of both surface states and bulk carriers, which is consistent with previously observed phenomena in Bi_2Se_3 synthesized by various methods. In general, the transport behavior of measured nanowires is qualitatively the same with transport of the supported parts of the devices presented below.

3.2. Magnetotransport properties of an elastically deformed suspended nanowire

To implement a micron-sized long NEM switch based on a Bi_2Se_3 nanowire, ***Device 1*** containing the supported and the suspended over the trench with the gate electrode parts was fabricated (Fig. 1).

To study the electronic properties and distinguish the difference in Source-Drain transport between the suspended and supported parts of ***Device 1***, the magnetotransport measurements with a magnetic field applied perpendicularly to the nanowire were performed at 2 K. Fig. 2a represents the longitudinal sheet resistance, calculated as R_{xx} (Ω/□)= R_{xx}(Ω)×w/L, where w is the actual nanowire width and L is the distance between the longitudinal contacts, as a function of a magnetic field. The value R_{xx}(Ω/□) is slightly different for the suspended and supported parts. We attribute this difference to the influence of contact resistance in the case of supported part measurements (three-probe configuration). Since the values of R_{xx} are different, we plot magnetoresistance MR= $(R_{xx}(B)-R_{xx}(0))/R_{xx}(0))$ as a function of a magnetic field to show the difference between two parts within one nanowire (Fig. 2b).

For both suspended and supported parts of the wire, the ΔR_{xx} oscillations were found by subtracting a polynomial background. This effect is associated with the Shubnikov-de Haas oscillations. The Fourier transform of the $\partial^2\Delta R_{xx}/\partial B^2$ for the supported part reveals only two frequencies F^1_{supp}=42.3 T and F^2_{supp}=70.6 T. Following the Onsager relation [73], these frequencies correspond to $n^1_{2D_supp}=1.02\times10^{12}$ cm^{-2} and $n^2_{2D_supp}=1.71\times10^{12}$ cm^{-2}, respectively (Fig. 2c). A similar multi-frequency pattern (with two dominating frequencies) for Bi_2Se_3 nanoribbons with thicknesses above 30 nm was previously observed by our group [46]. Since the surface states (at the substrate-nanowire interface) are overlapped with the charge accumulation layer having lower charge carrier mobility, the bottom surface SdH oscillations do not usually appear in magnetoresistance. Moreover, these frequencies (previously observed in [46]) were unaffected by the applied gate voltage (up to −75 V), indicating that they correspond to either bulk or surface state carriers at the top surface (at the nanoribbon-vacuum interface) [45,46, 74]. Thus, we attribute observed F^1_{supp} and F^2_{supp} to the top surface states at the interface with vacuum and to the bulk, respectively.

For the suspended part, the FT of the $\partial^2\Delta R_{xx}/\partial B^2$ oscillations demonstrates three frequencies: F^1_{susp}=13.1 T, F^2_{susp}=45.8 T and F^3_{susp}=70.5 T, which correspond to $n^1_{2D_susp}=3.16\times10^{11}$ cm^{-2}, $n^2_{2D_susp}=1.11\times10^{12}$ cm^{-2} and $n^3_{2D_susp}=1.70\times10^{12}$ cm^{-2}, respectively (Fig. 2d). We attribute the appearance of the third (lowest) frequency to the states from the bottom surface, which are no longer masked by the accumulation layer. Since the SdH frequencies of TI are sensitive to external strain [53], the fact that the frequencies corresponding to the top surface states for the suspended and supported parts remain almost the same is in good agreement with the absence of deformation at the suspended part, as shown in Fig. 1a.

After examination of the suspended and supported parts in a relaxed state, the R_{xx} as a function of the gate voltage has been studied for ***Device 1***.

According to existing analytical models of bending [75,76], the strain of a bent nanowire in the thickness direction can be divided into three types: pure elastic, elastoplastic, and pure plastic deformation (Fig. 3). In the case of pure elastic deformation, the top surface (inner side) of the nanowire experiences compressive stress, while the bottom surface (outer side) is under tensile stress, and there is no stress in the middle (neutral layer (NL)). After removing the bending moment M, the elastic deformation will be restored. As shown in [77], if the radius of bending curvature R is much larger than the substrate thickness t and the dominant deformation occurs in the longitudinal direction, the bending strain can be calculated using the formula of the continuum mechanics model for elastic beams: $\varepsilon = t/2R$. In the case of elastoplastic deformation, the NL is displaced from the centroid of the cross-section due to the mass conservation effect, which induces a transition of tensile/-compressive stresses across the thickness of the nanowire. The direction of NL displacement is related to the material properties and the bending curvature. In most cases (for materials with similar behavior under compressive/tensile stresses), the neutral layer is shifting towards the center of curvature. After releasing the bending moment M, the elastic deformation is restored, but the plastic deformation remains, which leads to deviations in the dimensions of the nanowire. If the stretching applied during the bending process is large enough, NL can extend beyond the cross-section, thus the stress gradient across the thickness of the nanowire will reduce and elasticity will decrease sharply (plastic deformation) compared to the pure bending effect [76].

Applying a negative voltage to the gate electrode first of all leads to the formation of oppositely charged carriers (depletion layer) at the bottom surface of the naturally n-doped nanowire. As far as a depletion layer is formed, an electrostatic attractive force acts on the wire uniaxially bending it towards the gate (Fig. 1b). A similar procedure occurs if a positive voltage is applied to the gate electrode. First, an accumulation layer (negatively charged carriers) is formed at the bottom surface of the nanowire, and then, as a consequence, the nanowire bends towards the gate under the influence of the electrostatic attractive force. During such bending, the top surface of the nanowire experiences compressive stress, while the bottom surface is under tensile stress (Fig. 3b). When a negative voltage is applied to the device, there is a clear increase in the resistance of the suspended part (Fig. 4a bottom panel), while the resistance of the supported part remains unchanged (Fig. 4a top panel (inset)). As the dielectric constant of SiO_2 (ε_{SiO2}=3–4) [78] is higher than that of vacuum (ε_{vac}=1) [79], the effect of changing Fermi energy via the gating effect (at the initial moment when the distance to the wire is the same) should be more effective in the case of the supported wire, even in the presence of the accumulation layer, since the trivial 2DEG at the bottom extends well inside the bulk, and is therefore screened by topological surface states [72]. Thus, we attribute the change in resistance when the wire is suspended to the mechanical deformation (bending towards the gate).

During the gate voltage sweep, the current between the gate electrode and the nanowire I_{GD} (similar to 2-terminal switches[20,25,29,39, 67]) also was monitored (Fig. 4a top panel). At a certain point (−1.45 V) the I_{GD} starts increasing because the distance (separation) between the nanowire and the gate becomes small and a tunneling effect appears. A further increase in the potential at the back gate leads to the emersion of pronounced peaks in the Gate-Drain current and resistance curves. This may be due to the logarithmically increasing tunneling current with decreasing distance [80], as well as the action of additional attractive van der Waals forces that come into play when the distance between the nanosized objects is several nanometers [81]. The change in the resistance slopes (purple dashed lines in Fig. 4a bottom panel) indicates the point of initial action of additional van der Waals forces. At −1.84 V (left orange line in Fig. 4a), I_{GD} starts to increase sharply, which is a sign of the device switching to the «ON» mode. To prove the fact that the increase in Source-Drain resistance (with gate range from 0 to −1.84 V) is

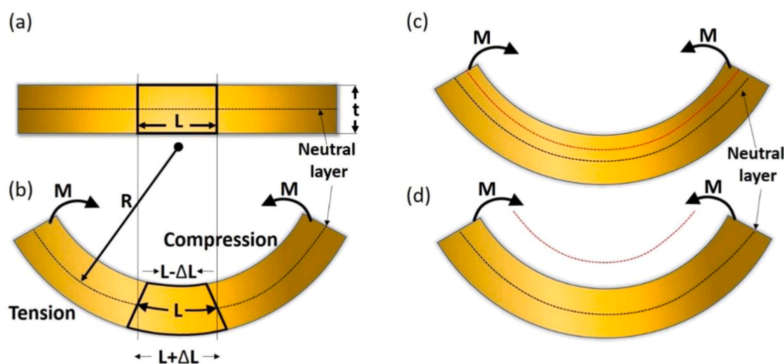

Fig. 3. The scheme of the distribution of various types of deformation along the thickness of the nanowire. (a) A nanowire before bending (relaxed state). (b) A nanowire under elastic deformation. The predominant deformation occurs in the longitudinal direction. (c) A nanowire in elastoplastic deformation regime. (d) Shift of NL beyond the nanowire cross-section (the entire cross-section is under tensile strain) (plastic deformation).

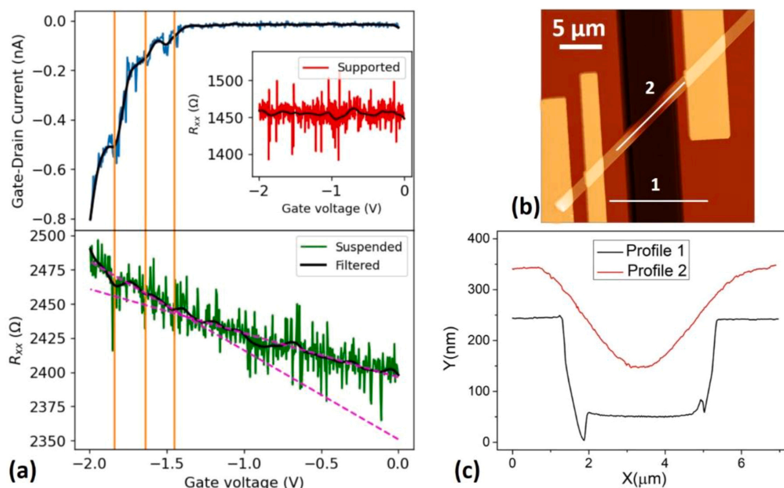

Fig. 4. (a) Gate-Drain current and R_{xx} of the suspended and supported (in the inset) parts as a function of the back-gate voltage (***Device 1***). The blue, red and green lines represent experimental data. The black lines depict filtered data. The vertical orange lines indicate pronounced peaks due to mechanical deformation. The change in the slopes of the two purple dashed lines indicates the point of the initial action of the additional van der Waals forces to the electrostatic attractive force, resulting in faster deformation of the nanowire. (b) AFM image of the device in «ON» mode. (c) Height profile of the bent nanowire, presented in (b).

a result of mechanical deformation and not of the tuning of the Fermi energy due to the field effect, we increased the back-gate voltage to -2 V. After this the Gate-Drain current value increased linearly from ≈ -0.6 nA to -1.7 μA, which means the device is in stable «ON» mode. Even after that, the increased resistance of the suspended part remains at the same value (does not decrease to the initial value before gating/-bending). It is a sign of the deformation effect since the influence of the electric field does not affect the wire anymore. SEM image as well as AFM image and height profile of the bent wire in «ON» mode are presented in Fig. 2b and Figs. 4b and 4c, respectively.

To investigate the strain-induced rearrangement of the electronic properties after bending the wire to the gate contact, magnetotransport of ***Device 1*** was remeasured in «ON» mode at a fixed voltage on the back gate of -2 V. The longitudinal sheet resistance and MR as a function of a magnetic field are presented in Fig. 5a and b, respectively. It is clearly seen, that $R_{xx}(\Omega/\square)$ value of the supported part remains unaffected by the gate voltage, while the suspended part reveals an increase in resistance (3,84%) in comparison with the data presented in Fig. 3. Following the analysis of the SdH oscillations described above, we did not find any difference for the supported part before and after applying

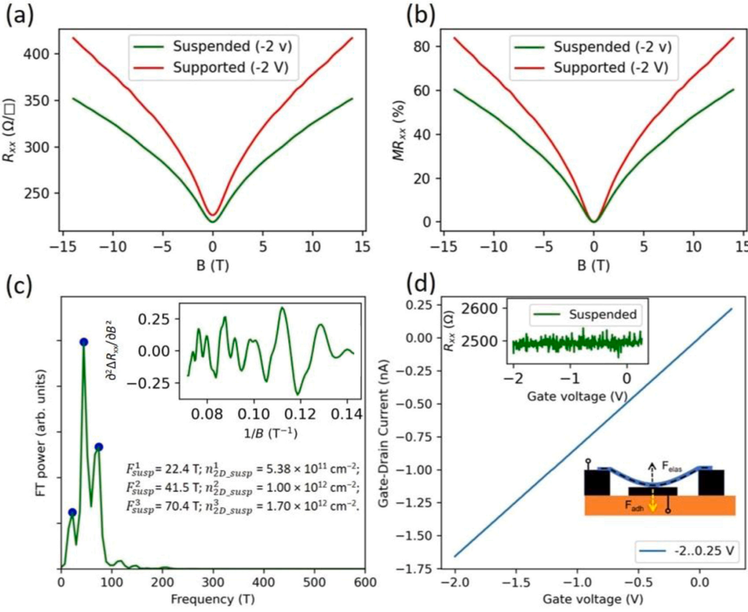

Fig. 5. Magnetotransport measurements of ***Device 1*** presented in Fig. 2b in «ON» regime (with a fixed gate voltage of −2 V). (a) The longitudinal sheet resistance $R_{xx}(\Omega/\square)$ as a function of a magnetic field for the suspended and supported parts. (b) The magnetoresistance $MR = (R_{xx}(B) - R_{xx}(0))/R_{xx}(0))$ as a function of a magnetic field. (c) The Fourier transform power spectra of $\partial^2\Delta R_{xx}/\partial B^2$ (presented in the insets) for the suspended part. (d) Gate-Drain current of the suspended parts as a function of the back-gate voltage after magnetotransport measurements. The top inset is R_{xx} as a function of the gate voltage. The bottom inset is the schematic of «ON» regime of the switch, when $F_{vdW} + F_{elec} > F_{elas}$.

the gate voltage, as expected. However, the suspended part exhibits a slight shift of $F_{susp}^{2_-2V}$=41.5 T ($n_{2D_susp}^{2_-2V}$=1.00×10^{12} cm^{-2}) towards lower frequency in comparison with F_{susp}^{2} =45.8 T ($n_{2D_susp}^{2}$=1.11×10^{12} cm^{-2}), as well as $F_{susp}^{1_-2V}$=22.4 T ($n_{2D_susp}^{1_-2V}$=5.38×10^{11} cm^{-2}) towards higher value comparing to F_{susp}^{1}=13.1 T ($n_{2D_susp}^{1}$=3.16×10^{11} cm^{-2}), while the third frequency remains the same $F_{susp}^{3_-2V} \approx F_{susp}^{3}$. All values of the SdH frequencies, as well as 2D carrier concentrations in relaxed and deformed states are summarized in Table 1.

Table 1
Deformation type of the nanowire.

	Design	Channel	SdH frequency, T	n_{2D}, cm^{-2}	Deformation	Deformation type	ΔR, %
Device 1	Suspended	Top surface	45.8	1.11×10^{12}	relaxed	Relaxed	-
		Bottom surface	13.1	3.16×10^{11}	relaxed		
		Bulk	70.5	1.70×10^{12}	relaxed		
	Supported	Top surface	42.3	1.02×10^{12}	relaxed	Relaxed	-
		Bottom surface	-	-	relaxed		
		Bulk	70.6	1.70×10^{12}	relaxed		
Device 1 (−2 V)	Suspended	Top surface	41.5	1.00×10^{12}	compression	Elastic	3.84
		Bottom surface	22.4	5.38×10^{11}	tension		
		Bulk	70.4	1.70×10^{12}	relaxed		
	Supported	Top surface	42.3	1.02×10^{12}	relaxed	Relaxed	-
		Bottom surface	-	-	relaxed		
		Bulk	70.6	1.70×10^{12}	relaxed		
Device 2	Suspended (Deformed)	Top surface	43.4	6.29×10^{11}	compression	Elastoplastic	21.85
		Bottom surface	25.9	1.05×10^{12}	tension		
		Bulk	93.6	2.26×10^{12}	compression		
	Supported	Top surface	52.9	1.28×10^{12}	relaxed	Relaxed	-
		Bottom surface	-	-	relaxed		
		Bulk	96.9	2.34×10^{12}	relaxed		
Device 3	Suspended (Buckled)	Top surface	41.4	1.00×10^{12}	tension	Buckled	-1.62
		Bottom surface	20.7	5.01×10^{11}	compression		
		Bulk	69.1	1.67×10^{12}	-		

The observed results are consistent with [53,82], where the tensile strain shifts the Dirac point towards lower energies, while compressive strain causes a shift to higher energies. So, the SdH frequencies experience upshift/downshift with tension/compression of the nanowire on the bottom/top surface. We attribute the downshift of $F_{susp}^{2-{-2V}}$ frequency (top surface states) to the induced compressive deformation on the top surface of the nanowire and the upshift of $F_{susp}^{1-{-2V}}$ (bottom surface states) to the induced tensile deformation on the bottom surface of the nanowire, respectively. The fact that the SdH frequency representing bulk charge carriers remains unchanged after the performed measurements and is identical to the value of the relaxed (supported) part, indicates that the NL is not displaced from the centroid of the nanowire cross-section, and there is a balance of stresses on the top and bottom surfaces, which is a clear sign of elastic deformation regime.

Taking into consideration an elastic deformation regime, the formula $\varepsilon = t/2R$ can be used to estimate the amount of nanowire deformation. For given ***Device 1***, the radius of curvature is equal to R=21.5 μm (calculated based on AFM measurements (Fig. 4c)), and therefore the strain is $\varepsilon = 0.22\%$.

After completing the magnetoresistance measurements, the gate swept from −2 to 0.25 V. The Gate-Drain current as well as the gate dependence of resistance for the suspended part are shown in Fig. 5d. The linear behavior of the current-voltage characteristic and the absence of a change in resistance during the sweep indicate that the balance between attractive van der Waals F_{vdW} + electrostatic F_{elec} and repulsive elastic F_{elas} forces is violated ($F_{vdW} + F_{elec} > F_{elas}$), which results in strong attachment of the wire to the gate electrode (Fig. 2b, Fig. 5d bottom inset) [25]. In our case, this procedure was performed intentionally to demonstrate the strain distribution in the nanowire under different «ON» and «OFF» regimes. For the repeatable operation of the device in «ON – OFF» regimes (as in the electromechanical switch), the gate bias voltage must be less than the value of −1.84 V (the left vertical orange line in Fig. 4a).

In summary, uniaxial electrostatic bending of the nanowire towards the gate results in compressive strain on the top surface and tensile strain on the bottom surface, as evidenced by a shift in the SdH oscillation frequencies corresponding to these surfaces. The bulk frequency remains the same for the supported part, suspended and suspended deformed parts, which is a sign of the elastic deformation regime. During the bending process, an increase in the Source-Drain resistance by 3.84% was observed. We associate it with the effect of deformation, since after the switching to «ON» regime the resistance value remained unchanged. To regulate the distance between the nanowire and the gate electrode, an electrostatic potential should be precisely applied. It will allow to monitor the Source-Drain current continuously and to access (at certain gate voltages) the regime in which two parallel currents (Source-Drain current as well as Gate-Drain tunneling current) are present. Simultaneous control of these two currents makes it possible to accurately define the moment when it is necessary to stop bending and consider the nanowire to be in the «ON» regime. As a result, a stable balance is determined between the adhesion force and the elastic force of the nanowire, so when the gate voltage is released, the latter one exceeds the adhesion force and the device should turn into the «OFF» state, and hence the switch can operate in a repeatable manner.

3.3. Magnetotransport properties of an elastoplastically deformed suspended nanowire

To study the electrical and mechanical properties of suspended nanowires in the elastoplastic deformation mode, ***Device 2*** was fabricated. To introduce a plastic component of deformation, a certain amount of strain (greater than in the elastic mode) must be applied to the nanowire, which will cause an irreversible change in geometry. In order to introduce additional strain to the device (for example, due to the load on the sample) without significant change in the fabrication process, it was decided to increase the length of the suspended part. According to the classical beam deformation theory, in the case of the beam fixed at both ends with a uniform continuously distributed load on top, the maximum deflection of the beam at center is $\delta_{max} = \frac{qL^4}{384EI}$, where q is the uniform load [N/m], L is the distance between fixed ends, E is the modulus of elasticity [Pa·N/m^2], I is the area moment of inertia [m^4] [83]. Indeed, due to $\delta_{max} \sim L^4$, an increase in L at the same load on the top of the suspended nanowire (for example, a resist) will bend the nanowire more efficiently. Using the property of isotropic etching of SiO_2 with wet chemicals (BOE), we increased the trench width from 3 up to 8 μm. Since ***Device 2*** was fabricated identically to ***Device 1***, the suspended part of the nanowire experienced significant loading (resist and metal), resulting in elastoplastic bending of the nanowire towards the gate electrode. After removal of the loading from the suspended part (Lift-off), the deformation of the nanowire remains even without applying voltage to the back-gate electrode. Representative optical and AFM images of ***Device 2*** with the suspended and supported parts of the nanowire, as well as AFM profile of the deformed nanowire (in «ON» regime) are presented in Fig. 6. The provided geometry of contacts allows independent measurements of the supported and suspended parts of the nanowire in a four-probe configuration, thus eliminating the contact resistance effects. Moreover, the additional pair of Hall bars allows to measure the type and concentration of charge carriers.

Since the stress during elastoplastic deformation is distributed over the nanowire cross-section, the formula $\varepsilon = t/2R$ can no longer be used for strain value estimation. We carried out transport measurements to compare the relaxed (supported) part of the nanowire with the suspended part that experienced elastoplastic deformation. This comparison will help to evaluate the effect of strain on the properties of the nanowire.

First, we checked whether the nanowire was touching the gate contact by measuring the current between the gate and the nanowire (I_{GD}), which indicated an open circuit. Then, to measure transport properties in elastoplastic deformation mode, ***Device 2*** was cooled down from room temperature (RT) to 2 K. A metallic temperature dependence of the longitudinal sheet resistances $R_{xx}(\Omega/\square)$ for the supported and suspended parts was observed (Fig. 7a). As shown in Fig. 7a, the $R_{xx}(\Omega/\square)$ of the suspended part is higher than that of the supported part (21,85% at 2 K), and we attribute this fact to the bending effect and elastoplastic deformation of the nanowire introduced during fabrication.

To estimate the type and charge carrier's concentration of the examined nanowire (***Device 2***), the Hall resistance R_{xy} was measured as a function of a magnetic field at the temperature of 2 K at the supported part. The negative $R_{xy}(B)$ slope indicates n-type carriers (Fig. 7a inset). The values of the 2D carrier concentration were calculated from the Hall resistance as [46]: $n_{2D_Hall} = (w_H/w)/(e \cdot \partial R_{xy}/\partial B)$, where w is the actual nanowire width, w_H is the distance between the Hall contacts, and e is the elementary charge. The linear fit of the Hall resistance (blue dashed line in the inset of Fig. 7a) in the low magnetic field range depicts the deviation from the linearity at higher magnetic fields (orange dashed line in the inset of Fig. 7a). This non-linearity indicates the contribution of another band (for example an accumulation layer at the interface between the nanoribbon and substrate with different mobility and concentrations of carriers) to the entire transport through the nanowire [45,46,74]. The fitting results of the experimental Hall data yield n_{2D_Hall}=2.81×10^{13} cm^{-2} and μ_{Hall}=2.02×10^3 cm^2 (Vs)$^{-1}$ which are typical values for Bi_2Se_3 nanowires synthesized by our group using physical vapor deposition method [46,66,70,74,84].

Likewise to ***Device 1***, magnetotransport measurements with a magnetic field applied perpendicularly to the nanowire at 2 K were performed for ***Device 2***. The Fourier transform of the $\partial^2 \Delta R_{xx}/\partial B^2$ oscillations for the supported part reveals two frequencies F_{supp}^1=52.9 T and F_{supp}^2=96.9 T, corresponding to $n_{2D_supp}^1$=1.28×10^{12} cm^{-2} and $n_{2D_supp}^2$=2.34×10^{12} cm^{-2}, respectively (Fig. 7c). Similar to ***Device 1***, we

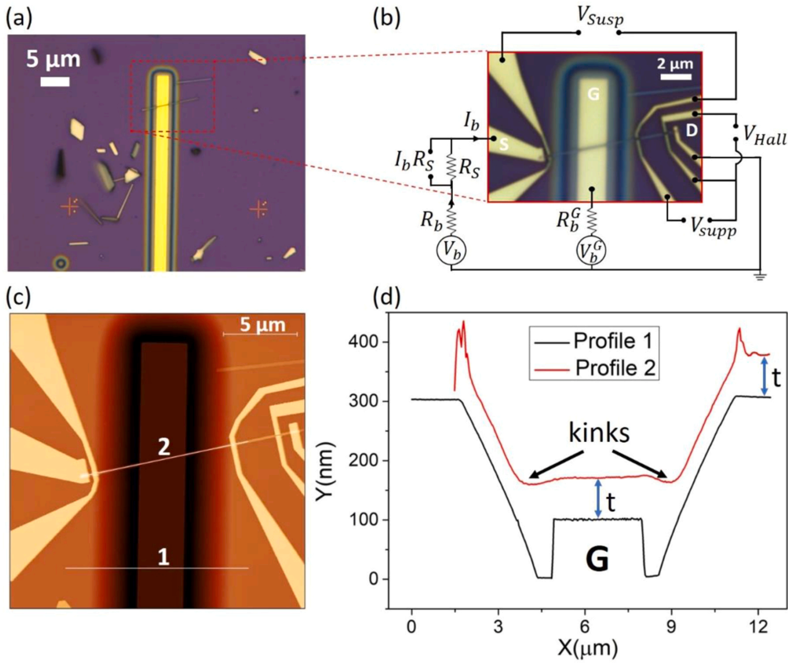

Fig. 6. (a) Optical image of a transferred Bi_2Se_3 nanowire across the pre-patterned trench with a gold electrode inside. (b) Optical image (with measurements scheme) of ***Device 2*** containing the suspended and supported nanowire parts, shown in panel (a). (c) AFM image and (d) corresponding height profiles of ***Device 2***, indicating full mechanical contact («ON» regime) of the nanowire with the gate electrode after applying gate voltage.

attribute observed F^1_{supp} and F^2_{supp} to the top surface states at the interface with vacuum and to the bulk, respectively. It should be noted here, that the deviation from the linearity at high magnetic fields for the Hall effect measurements (Fig. 7a inset) and the discrepancy in 2D carrier concentrations extracted from the SdH oscillations analysis and the Hall effect measurements confirm that the charge accumulation layer formed at the substrate-nanowire interface dominates in the Hall conductance and mask bottom topological surface states.

In the case of the suspended part, the FT of the $\partial^2\Delta R_{xx}/\partial B^2$ oscillations depicts three frequencies: F^1_{susp}=25.9 T, F^2_{susp}=43.3 T, and F^3_{susp}=93.6 T, which according to the Onsager relation correspond to $n^1_{2D_susp}$=6.29×10^{11} cm^{-2}, $n^2_{2D_susp}$=1.05×10^{12} cm^{-2}, and $n^3_{2D_susp}$=2.26×10^{12} cm^{-2}, respectively (Fig. 7d). All observed frequencies are summarized in Table 1. As for ***Device 1***, the lowest frequency F^1_{susp} represents the states from the bottom surface. The frequency F^1_{supp}=52.9 T representing the top surface states carriers under relaxed condition (supported part) exhibits shift to lower frequency F^2_{susp}=43.3 T, indicating compression of the Bi_2Se_3 nanowire on the top surface. Moreover, the frequency representing bulk in the suspended case also experiences a downshift in comparison with the bulk states in a relaxed mode. This means that, due to the elastoplastic deformation regime, the NL is displaced from the centroid of the cross-section towards the center of curvature, and the balance of stresses on the top and bottom surfaces of the nanowire changes (Fig. 3c). This may result in a change in the overall conductance of the wire. Moreover, in [53] it is shown that relaxed or compressed surfaces demonstrate lower mobility of carriers than under tension, therefore $\sigma = en\mu$ for a surface deformed under compression is much lower than under tensile deformation or in a relaxed state, due to lower mobility and charge carrier concentration. Assuming that the top and bottom surface states act as parallel conductive transport channels, decrease of conductance at the top surface results in an increase in the overall resistance of the nanowire. Thus, in the particular case of ***Device 2***, we attribute the higher resistance of the suspended part (in comparison with the supported part (Fig. 7a)) to the effect of elastoplastic deformation of the nanowire.

Since the formula $\varepsilon = t/2R$ is no longer applicable, we tried to evaluate the strain by comparing the resistance for the relaxed and strained modes. As it is shown in [85] for materials based on bismuth chalcogenides, the relative changes in the resistance of the samples $\Delta R/R$ are proportional to ε. Using the coefficient of strain sensitivity $\Delta R/\varepsilon R$, which ranged from 100 to 200 for different samples measured at room temperature [85], the strain $\varepsilon \approx$ 0.27–0.53% (the ratio $\Delta R/R$=0.53 is extracted from Fig. 7a at 300 K) for ***Device 2*** at RT can be roughly evaluated.

Fig. 8a represents the Gate-Drain current of the suspended part as a function of the back-gate voltage. Due to a very short distance between the suspended nanowire and the gate electrode (approximately ten nanometers), upon applying negative gate voltage, the suspended nanowire is immediately attached to the gate electrode (Fig. 8b). This behavior was expected, since basing upon numerical calculation

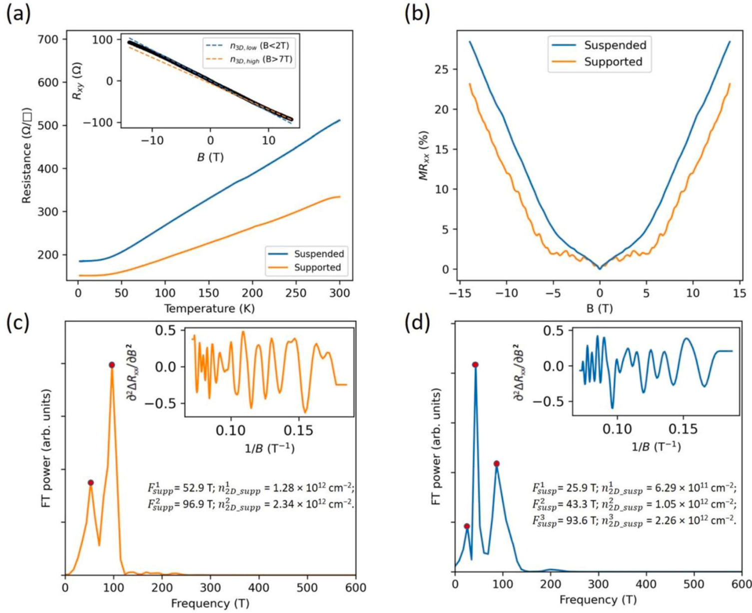

Fig. 7. Magnetotransport measurements of ***Device 2*** presented in Fig. 6. (a) Temperature dependence of $R_{xx}(\Omega/\square)$ for the suspended and supported parts. The inset is anti-symmetrized Hall effect measurements $R_{xy}(B)$. The blue dashed line is the linear fit in the range from 0 to 2 T, while the orange dashed line is the linear fit in the range from 7 to 14 T. (b) Magnetoresistance $MR = (R_{xx}(B) - R_{xx}(0))/R_{xx}(0)$ as a function of a magnetic field. Shubnikov-de Haas oscillations analysis: the Fourier transform power spectra of $\partial^2\Delta R_{xx}/\partial B^2$ (presented in the insets) for the supported part shown in (c) and for the suspended part shown in (d), respectively.

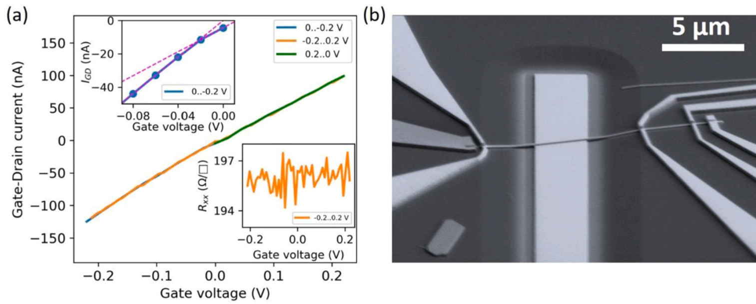

Fig. 8. (a) The gate-drain current measured as a function of the gate voltage for the suspended part of ***Device 2***. The blue, orange, and green curves represent scan sweeps with different directions. The top inset is a zoom-in view of the 0..−0.2 V sweep. The purple dashed lines show the deviation from linearity at −0.02 V, indicating the «ON» state switching. The bottom inset is R_{xx} as a function of the gate voltage, indicating a stable «ON» state even after the gate voltage is removed or swept positively. (b) SEM image of switched «ON» device after performed measurements.

described in [67], we found that for a certain device geometry (nanowire thickness t=71 nm, width w=200 nm, distance between electrodes (suspended part) L_{susp}=9.2 µm, and distance between the gate and nanowire d≈6–8 nm) at back-gate voltage of ≈−25 mV, the nanowire should collapse to the gate electrode. Indeed, the current between the gate electrode and nanowire (I_{GD}), monitored during the gate sweep, shows a linear dependence (with a small deviation around 0 V gate voltage (top inset in Fig. 8a), indicating an ohmic contact between the nanowire and the back-gate electrode (Fig. 8a). After switching to the «ON» state, the Source-Drain resistance of the suspended part R_{xx} (Ω/□) increased by 6.52% compared to the wire resistance in the «OFF» state. Moreover, according to the numerical calculation of the distribution of

electrostatic forces near the corner of the gate electrode, the electric field causes an infinite force on an infinitesimal part of the conductor [86], which results in the wire deformation near both sides of the gate (Fig. 6d). The radii of these bends (kinks) are much smaller than the radius of curvature of the suspended device, which causes large localized deformations. Turning off the back-gate voltage does not lead to the detaching of the nanowire from the gate. The increased Source-Drain resistance persists after the gate voltage is removed (bottom inset in Fig. 8a). We attribute this fact to the presence of van der Waals interaction between the wire and the gate electrode. Due to the very large contact area, as well as to the plastic deformation (kinks) of the nanowire, it leads to the changes in the geometry of the device. Figs. 6b and 8b show AFM and SEM images of ***Device 2*** after the measurements were performed. It is clearly visible, that the nanowire is lying on the surface of the gate electrode. According to AFM data, the bending radius of the suspended part of ***Device 2*** is equal to ≈ 53 μm, and the radii of small kinks are ≈ 23,4 μm. The overall nature of strain in the switched-«ON» ***Device 2*** becomes more complicated due to the presence of localized (at the kinks) deformations. The magnitudes of the change in Source-Drain resistance in the «OFF» and «ON» states are 21.85% and 29.80%, respectively, which is significantly higher in comparison with elastically deformed ***Device 1*** (where the difference was 3.84%).

The use of elastoplastically deformed nanowires in NEM switches will provide more effective bending in contrast to a pure elastically deformed nanowire. However, the presence of a plastic deformation term will play a negative role in the resistance to bending fatigue, which may adversely affect the repeatability of the device in «ON»–«OFF» regimes, and most probably the life-time of the device will be significantly shorter than in the case of pure elastic deformation.

3.4. Magnetotransport properties of a convex-buckled suspended nanowire

Since the distribution of stresses over the cross-section of a suspended nanowire during deformation with upward and downward bending can be different (the NL can move in different directions), ***Device 3***, which experiences a convex shape deformation, in contrast to ***Device 1*** and ***2*** (concave shape), was fabricated.

During the cooling process from RT to 2 K, the Source-Drain resistance measured in the two-probe configuration experiences a metallic behavior (Fig. 9a inset). Magnetotransport analysis of ***Device 3*** at 2 K shows similar behavior with the suspended part of ***Device 1***, demonstrating three SdH oscillation frequencies: F^1_{susp}=20.7 T, F^2_{susp}=41.4 T, and F^3_{susp}=69.1 T after the Fourier transform of the $\partial^2\Delta R_{xx}/\partial B^2$ (Fig. 9b). Observed frequencies with corresponding charge carrier densities $n^1_{2D_susp}$=5.01×10^{11} cm^{-2}, $n^2_{2D_susp}$=1.00×10^{12} cm^{-2}, and $n^3_{2D_susp}$=1.67×10^{12} cm^{-2} refer to the bottom, top surface, and bulk states, respectively. All data related to the SdH oscillations are summarized in Table 1.

Then, the gate dependence of Source-Drain resistance was measured at 2 and 4 K (Fig. 10). Both negative and positive gate voltage sweeps show deviation in resistance change with gate voltage at ±35 V (denoted as the intersection of linear fits (the dashed lines in Fig. 10) of experimental data in high and low electric fields). For the buckled beam fixed at both sides, the transition from the first stable position (convex shape) (Fig. 11) to the opposite stable position (concave shape) under the influence of an electrostatic field leads to the appearance of a third (curved) intermediate state [87]. We associate the observed change in slopes with the transition of the nanowire from the initial state to the second stable (concave shape) position (via an intermediate curved mode), while a further increase in voltage leads to the deformation of the nanowire towards the gate.

Since the selenium vacancies exist in Bi_2Se_3 and are the main origin of *n*-doping, it is reasonable that charges in the Bi_2Se_3 nanowires can be redistributed under the influence of a strong external electric field. Thus, we associate the decrease in the Source-Drain resistance of the buckled nanowire (during a positive voltage sweep at the gate) with the relaxation of the nanowire from its convex shape. Changing the voltage polarity on the gate sweep leads to an increase in resistance, which is presumably related to returning the nanowire to its original (convex) shape, as well as with charge redistribution due to the electrostatic field effect. With a negative voltage sweep, we assume an additional Fermi energy tuning process, because a much higher voltage is applied to ***Device 3*** compared to ***Devices 1*** and ***2***.

The observed magnitude of the change in Source-Drain resistance with a positive gate sweep between 0 and 80 V is −1.62%, which is twice less in comparison to the elastically deformed ***Device 1*** (which has a similar lateral geometry). Here, the change in resistance is calculated as the difference from 0 V, however, the nanowire is not relaxed at this point due to its buckled nature. Thus, this value indicates the change in resistance that occurred during bending from the first stable point to the maximum deformed position for ***Device 3***. However, it is worth noting here that the bending distance in the case of ***Device 3*** is much higher compared to ***Device 1***, but the resistance changes during bending are still lower. Negative strain values indicate a relaxation process after the initial convex state. Due to the smaller resistance change during the operation of buckled ***Device 3*** (with a significantly larger initial distance

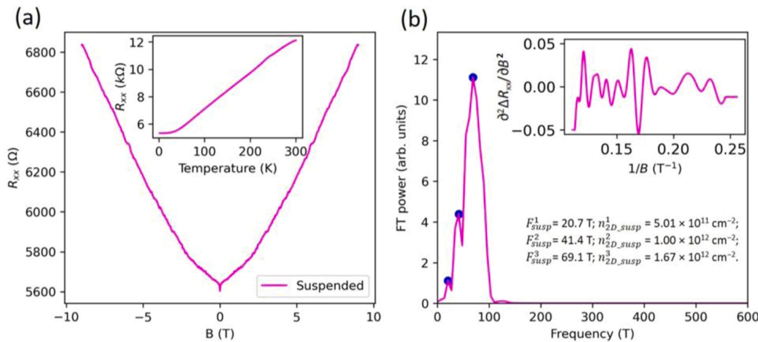

Fig. 9. Magnetotransport measurements of ***Device 3***. (a) R_{xx} as a function of a magnetic field. The inset is the temperature dependence of R_{xx}. (b) Shubnikov-de Haas oscillations analysis: the Fourier transform power spectra of $\partial^2\Delta R_{xx}/\partial B^2$ (presented in the inset).

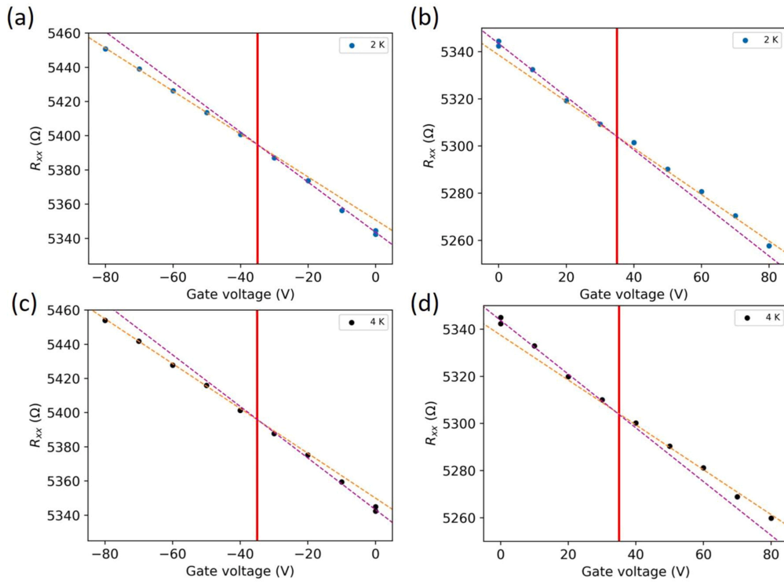

Fig. 10. Source-Drain R_{xx} as a function of back-gate voltage measured at 2 K (a-b) and 4 K (b-c) for ***Device 3***. Each data point represents the averaged R_{xx} value extracted from twenty *I-V* curves measured at a certain voltage value. The orange dashed line is the linear fit in the high electric field range, while the purple dashed line is the linear fit in the low electric field range. The solid red lines indicate the voltage value of ±35 V.

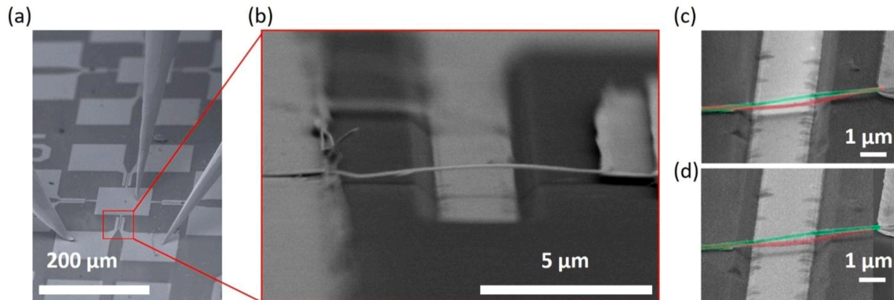

Fig. 11. (a) SEM image of suspended ***Device 3***, connected via an on-SEM manipulator (two-probe configuration) and (b) zoom-in tilted SEM image of the nanowire suspended across the back-gate electrode after transfer and contacts fabrication. (c, d) Overlayed SEM images, showing sharp deformation of the nanowire as the applied gate voltage changes from 0 V (green) to −40 V (c, red) and 40 V (d, red). Images are colored for improved comprehension.

between the nanowire and the gate) compared to the conventional ***Device 1***, buckled devices are promising candidates for NEM switches. This fact is a good advantage of buckled devices in terms of the resistance to bending fatigue. In addition, the convex shape allows the use of an additional (top gate) electrode to implement a three-terminal switch, and also such devices can be used for non-volatile memory applications.

To confirm that the wire deforms from the initial state (convex) to a second stable state (concave) after the gate voltage reaches ±35 V, we used an on-SEM nanomanipulator equipped with sharp gold tips to electrically connect the nanowire and the back-gate electrode to perform an in-situ measurement at room temperature, as shown in Fig. 11 and S1 (Supplementary material). Figs. 11c and 11d show in-situ measured SEM images of the buckled nanowire in the initial state (green) and after applying a voltage of ±40 V (red in panel c and d). It is clearly seen that the shape of the nanowire changes to concave. This fact is in good agreement with the low temperature gate measurements (Fig. 10), in which the change in resistance slopes occurred at ±35 V.

4. Conclusions

Suspended devices based on VLS-grown topological insulator Bi_2Se_3 nanowires were fabricated using different methods. The effect of mechanical deformation on the suspended part of the devices was studied using magnetotransport measurements (at low temperature), as well as in-situ SEM measurements at room temperature. The electrostatic field effect was used to dynamically manipulate bending deformation, while the magnetotransport measurements were performed to monitor the external strain introduced into the suspended and supported parts within the same Bi_2Se_3 nanowire. The pure elastic and elastoplastic types as well as a buckled deformation were realized in the suspended parts of the nanowires. All devices exhibit the Shubnikov-de Haas oscillation frequencies representing the carriers of the top and bottom surface states and the bulk (see Table 1). In the case of supported devices, the bottom surface states are masked by the trivial 2DEG, and only two frequencies were observed, whereas for the suspended parts, a third frequency appears because the carriers of the bottom surface states are not masked by trivial 2DEG, formed at the interface between the substrate and the nanowire. It can be seen that, regardless of the type of deformation (elastic, elastoplastic), the SdH frequencies experienced downshift and upshift with compressive and tensile strain, respectively. Changes in the Source-Drain resistance as well as the Gate-Drain current were continuously monitored as the nanowire was bent towards the gate electrode to determine the moment of contact with the gate, as well as to monitor the type of deformation induced and changes in the electrical transport properties of the device. During the bending of the suspended nanowires, an increase in the Source-Drain resistance was observed by 3.84% for elastic deformation, 21.85% for elastoplastic deformation, and only 1.62% for deformation of the buckled nanowire. Thus, elastoplastic deformation provides more effective bending compared to the pure elastically deformed and buckled nanowire. However, the presence of a plastic term will play a negative role in the resistance to bending fatigue compared to pure elastic deformation. The buckled devices are also promising candidates for NEM switches because the convex shape allows the use of an additional electrode to implement a three-terminal switch, and such devices can also be used for non-volatile memory applications. It should be noted here, that the results presented in this work are in good agreement and extend previous study [53], where Bi_2Se_3 nanowires were initially (statically) deformed (without the gate effect). We implemented more precise control during strain injection and demonstrated three different deformation regimes. The obtained results can be useful for strain engineering of TI materials, as well as for applications in NEMS and other fields related to suspended nanostructures (thermoelectric, sensing, etc.).

CRediT authorship contribution statement

Kiryl Niherysh: Writing – original draft, Investigation, Formal analysis. **Elza Dzene:** Writing – review & editing, Investigation. **Liga Jasulaneca:** Writing – review & editing, Visualization, Investigation. **Donats Erts:** Writing – review & editing, Validation, Supervision, Project administration, Methodology. **Floriana Lombardi:** Writing – review & editing, Supervision, Resources, Conceptualization.

Declaration of Competing Interest

The authors declare that they have no known competing financial interests or personal relationships that could have appeared to influence the work reported in this paper.

Data Availability

Data will be made available on request.

Acknowledgements

This research was funded by the Latvian Council of Science (project No. lzp-2019/1-0349). Authors would also like to acknowledge support from the Swedish infrastructure for micro- and nanofabrication - MyFab.

Appendix A. Supporting information

Supplementary data associated with this article can be found in the online version at doi:10.1016/j.sna.2024.115292.

References

[1] K. Akarvardar, C. Eggimann, D. Tsamados, Y.S. Chauhan, G.C. Wan, A. Mihai Ionescu, R.T. Howe, H.-S.P. Wong, Analytical modeling of the suspended-gate FET and design insights for low-power logic, IEEE Trans. Electron Devices (2008) *55*.

[2] N. Abelé, R. Fritschi, K. Boucart, F. Casset, P. Ancey, A.M. Ionescu, Suspended-Gate MOSFET: Bringing New MEMS Functionality into Solid-State MOS Transistor. IEEE International Electron Devices Meeting, 2005, IEDM Tech. Dig. (2005) 479–481.

[3] S. Sasaki, K. Tateno, G. Zhang, H. Suominen, Y. Harada, S. Saito, A. Fujiwara, T. Sogawa, K. Muraki, Encapsulated Gate-All-around InAs Nanowire Field-Effect Transistors, Appl. Phys. Lett. *103* (2013) 213502.

[4] H.-C. Lin, C.-H. Kuo, G.-J. Li, C.-J. Su, T.-Y. Huang, Operation of a Novel Device with Suspended Nanowire Channels, IEEE Electron Device Lett. (2010) *31*.

[5] A. Thiha, F. Ibrahim, S. Muniandy, I.J. Dinshaw, S.J. Teh, K.L. Thong, B.F. Leo, M. Madou, All-carbon suspended nanowire sensors as a rapid highly-sensitive label-free chemiresistive biosensing platform, Biosens. Bioelectron. *107* (2018) 145–152.

[6] A. Boisen, T. Thundat, Design & fabrication of cantilever array biosensors, Mater. Today *12* (2009) 32–38.

[7] F. Bendriaa, F. Le Bihan, A.C. Salaün, T. Mohammed-Brahim, O. Bonnaud, Study of mechanical stability of suspended bridge devices used as PH sensors, J. Non Cryst. Solids *352* (2006) 1246–1249.

[8] K.-W. Choi, M.-S. Jo, J.-S. Lee, J.-Y. Yoo, J.-B. Yoon, K. Choi, M. Jo, J. Lee, J. Yoo, J. Yoon, Perfectly aligned, air-suspended nanowire array heater and its application in an always-on gas sensor, Adv. Funct. Mater. *30* (2020) 2004448.

[9] Y. Lim, Y. Lee, J.Il Heo, H. Shin, Highly sensitive hydrogen gas sensor based on a suspended palladium/carbon nanowire fabricated via batch microfabrication processes, Sens Actuators B Chem. *210* (2015) 218–224.

[10] J. Choi, J. Kim, Highly sensitive hydrogen sensor based on suspended, functionalized single tungsten nanowire bridge, Sens Actuators B Chem. *136* (2009) 92–98.

[11] D. Hatanaka, A. Bachtold, H. Yamaguchi, Electrostatically induced phononic crystal, Phys. Rev. Appl. *11* (2019) 024024.

[12] G. Li, D. Liang, R.L.J. Qiu, X.P.A. Gao, Thermal conductivity measurement of individual Bi_2Se_3 nano-ribbon by self-heating Three-ω method, Appl. Phys. Lett. *102* (2013) 43104.

[13] Dedi, P.C. Lee, P.C. Wei, Y.Y. Chen, Thermoelectric characteristics of a single-crystalline topological insulator Bi_2Se_3 nanowire, Nanomaterials *11* (2021) 819.

[14] M. Kim, J. Kim, Y. Hou, D. Yu, Y.J. Doh, B. Kim, K.W. Kim, J. Suh, Nanomechanical characterization of quantum interference in a topological insulator nanowire, Nat. Commun. *10* (2019) 1–7.

[15] C.B. Maliakkal, J.P. Mathew, N. Hatui, A.A. Rahman, M.M. Deshmukh, A. Bhattacharya, Fabrication and characterization of GaN nanowire doubly clamped resonators, J. Appl. Phys. *118* (2015) 114301.

[16] A. Husain, J. Hone, H.W.C. Postma, X.M.H. Huang, T. Drake, M. Barbic, A. Scherer, M.L. Roukes, Nanowire-based very-high-frequency electromechanical resonator, Appl. Phys. Lett. *83* (2003) 1240–1242.

[17] A. Iorio, M. Rocci, L. Bours, M. Carrega, V. Zannier, L. Sorba, S. Roddaro, F. Giazotto, E. Strambini, Vectorial control of the spin-orbit interaction in suspended InAs nanowires, Nano Lett. *19* (2019) 652–657.

[18] R.I. Shekhter, F. Santandrea, G. Sonne, L.Y. Gorelik, M. Jonson, Nonequilibrium and quantum coherent phenomena in the electromechanics of suspended nanowires (Review Article), Low. Temp. Phys. *35* (2009) 662–678.

[19] M. Liao, S. Hishita, E. Watanabe, S. Koizumi, Y. Koide, Suspended single-crystal diamond nanowires for high-performance nanoelectromechanical switches, Adv. Mater. *22* (2010) 5393–5397.

[20] K.J. Ziegler, D.M. Lyons, J.D. Holmes, D. Erts, B. Polyakov, H. Olin, K. Svensson, E. Olsson, Bistable nanoelectromechanical devices, Appl. Phys. Lett. *84* (2004) 4074–4076.

[21] L. Boodhoo, L. Crudgington, H.M.H. Chong, Y. Tsuchiya, Z. Moktadir, T. Hasegawa, H. Mizuta, Fabrication and characterisation of suspended narrow silicon nanowire channels for low-power nano-electro-mechanical (NEM) switch applications, Micro Eng. *145* (2015) 66–70.

[23] L. Kong, G. Cao, H. Zhou, J. Wang, In Situ observation of high bending strain recoverability in Au nanowires, Crystals *13* (2023) 1159.

[22] O.Y. Loh, H.D. Espinosa, Nanoelectromechanical contact switches, Nat. Nanotechnol. *7* (2012) 283–295.

[24] W. Tomita, S. Sasaki, K. Tateno, H. Okamoto, H. Yamaguchi, Novel fabrication technique of suspended nanowire devices for nanomechanical applications, Phys. Status Solidi (b) *257* (2020) 1900401.

[25] L. Jasulaneca, J. Kosmaca, R. Meija, J. Andzane, D. Erts, Review: electrostatically actuated nanobeam-based nanoelectromechanical switches – materials solutions and operational conditions, Beilstein J. Nanotechnol. *9* (2018) 271–300.
[26] L. Wang, P. Zhang, Z. Liu, Z. Wang, R. Yang, On-chip mechanical computing: status, challenges, and opportunities, Chip *2* (2023) 100038.
[27] N. Huynh Van, M. Muruganathan, J. Kulothungan, H. Mizuta, Fabrication of a three-terminal graphene nanoelectromechanical switch using two-dimensional materials, Nanoscale *10* (2018) 12349.
[28] P. Li, G. Jing, B. Zhang, S. Sando, T. Cui, Single-crystalline monolayer and multilayer graphene nano switches, Appl. Phys. Lett. *104* (2014) 39.
[29] J. Andzane, R. Meija, A.I. Livshits, J. Prikulis, S. Biswas, J.D. Holmes, D. Erts, An AC-assisted single-nanowire electromechanical switch, J. Mater. Chem. C. Mater. *1* (2013) 7134–7138.
[30] R. He, X.L. Feng, M.L. Roukes, P. Yang, Self-transducing silicon nanowire electromechanical systems at room temperature, Nano Lett. *8* (2008) 1756–1761.
[31] Y. Qian, B.W. Soon, P. Singh, H. Campanella, C. Lee, All metal nanoelectromechanical switch working at 300 °C for rugged electronics applications, Nanoscale *6* (2014) 5606–5611.
[32] T.H. Lee, S. Bhunia, M. Mehregany, Electromechanical computing at 500°C with silicon carbide, Science *1979* (2010) 1316–1318. *329*.
[33] J. Kulothungan, K. Kandhasamy, Large scale fabrication of graphene based nano-electromechanical (NEM) contact switches with Sub-0.5 volt actuation, Adv. Phys. Res. *2* (2023) 2200050.
[34] J.O. Lee, Y.H. Song, M.W. Kim, M.H. Kang, J.S. Oh, H.H. Yang, J.B. Yoon, A Sub-1-Volt Nanoelectromechanical Switching Device, Nat. Nanotechnol. *8* (2012) 36–40.
[35] S. Rana, J. Mouro, S.J. Bleiker, J.D. Reynolds, H.M.H. Chong, F. Niklaus, D. Pamunuwa, Nanoelectromechanical Relay without Pull-in Instability for High-Temperature Non-Volatile Memory, Nat. Commun. *11* (2020) 1–10.
[36] A. Peschot, C. Qian, T.-J.K. Liu, Nanoelectromechanical Switches for Low-Power Digital Computing, Micromachines *6* (2015) 1046–1065.
[37] R.R. Benoit, N.S. Barker, Reliability of RF MEMS Switches at Cryogenic (Liquid He) Temperatures, Microelectron. Reliab. *111* (2020) 113706.
[38] E. Lee, J.W. Kang, Molecular Dynamics Analysis of Graphene-Based Nanoelectromechanical Switch, ECS Trans. *72* (2016) 1–6.
[39] L. Jasulaneca, R. Meija, E. Kauranens, R. Sondors, J. Andzane, R. Rimsa, G. Mozolevskis, D. Erts, Cryogenic Nanoelectromechanical Switch Enabled by Bi_2Se_3 Nanoribbons, Mater. Sci. Eng.: B *275* (2022) 115510.
[40] Y. Ando, T, opological Insul. Mater. *82* (2013).
[41] C. Felser, S. Zhang, B. Yan, J.J. Cha, K.J. Koski, Y. Cui, Topological Insulator Nanostructures. Physica status solidi (RRL), Rapid Res. Lett. *7* (2013) 15–25.
[42] S.S. Hong, J.J. Cha, D. Kong, Y. Cui, Ultra-Low Carrier Concentration and Surface-Dominant Transport in Antimony-Doped Bi_2Se_3 Topological Insulator Nanoribbons, Nat. Commun. *3* (2012) 1–7.
[43] D. Kong, Y. Chen, J.J. Cha, Q. Zhang, J.G. Analytis, K. Lai, Z. Liu, S.S. Hong, K. J. Koski, S.K. Mo, et al., Ambipolar Field Effect in the Ternary Topological Insulator $(Bi_xSb_{1-x})_2Te_3$ by Composition Tuning, Nat. Nanotechnol. *6* (2011) 705–709.
[44] H. Steinberg, D.R. Gardner, Y.S. Lee, P. Jarillo-Herrero, Surface State Transport and Ambipolar Electric Field Effect in Bi_2Se_3 Nanodevices, Nano Lett. *10* (2010) 5032–5036.
[45] R. Sondors, K. Niherysh, J. Andzane, X. Palermo, T. Bauch, F. Lombardi, D. Erts, Low-Vacuum Catalyst-Free Physical Vapor Deposition and Magnetotransport Properties of Ultrathin Bi_2Se_3 Nanoribbons, Nanomaterials *13* (2023) 2484.
[46] G. Kunakova, L. Galletti, S. Charpentier, J. Andzane, D. Erts, F. Léonard, C. D. Spataru, T. Bauch, F. Lombardi, Bulk-Free Topological Insulator Bi_2Se_3 Nanoribbons with Magnetotransport Signatures of Dirac Surface States, Nanoscale *10* (2018) 19595–19602.
[47] Z. Ju, Y. Hou, A. Bernard, V. Taufour, D. Yu, S.M. Kauzlarich, Ambipolar Topological Insulator and High Carrier Mobility in Solution Grown Ultrathin Nanoplates of Sb-Doped Bi_2Se_3, ACS Appl. Electron Mater. *1* (2019) 1917–1923.
[48] J. Lee, J. Park, J.H. Lee, J.S. Kim, H.J. Lee, Gate-Tuned Differentiation of Surface-Conducting States in $Bi_{1.5}Sb_{0.5}Te_{1.7}Se_{1.3}$ Topological-Insulator Thin Crystals, Phys. Rev. B Condens Matter Mater. Phys. *86* (2012) 245321.
[49] Y. Yan, X. Zhou, H. Jin, C.Z. Li, X. Ke, G. Van Tendeloo, K. Liu, D. Yu, M. Dressel, Z. M. Liao, Surface-Facet-Dependent Phonon Deformation Potential in Individual Strained Topological Insulator Bi_2Se_3 Nanoribbons, ACS Nano *9* (2015) 10244–10251.
[50] K.A. Niherysh, J. Andzane, M.M. Mikhalik, S.M. Zavadsky, P.L. Dobrokhotov, F. Lombardi, S.L. Prischepa, I.V. Komissarov, D. Erts, Correlation Analysis of Vibration Modes in Physical Vapour Deposited Bi_2Se_3 Thin Films Probed by the Raman Mapping Technique, Nanoscale Adv. *3* (2021) 6395–6402.
[51] H. Aramberri, M.C. Muñoz, Strain effects in topological insulators: topological order and the emergence of switchable topological interface states in Sb_2Te_3/Bi_2Te_3 heterojunctions, Phys. Rev. B *95* (2017) 205422.
[52] J. Liu, Y. Xu, J. Wu, B.L. Gu, S.B. Zhang, W. Duan, Manipulating Topological Phase Transition by Strain, Acta Cryst. *70* (2014) 118–122.
[53] C. Schindler, C. Wiegand, J. Sichau, L. Tiemann, K. Nielsch, R. Zierold, R.H. Blick, Strain-induced dirac state shift in topological insulator Bi_2Se_3 nanowires, Appl. Phys. Lett. *111* (2017).
[54] S.H. Park, J. Chae, K.S. Jeong, T.H. Kim, H. Choi, M.H. Cho, I. Hwang, M.H. Bae, C. Kang, Reversible fermi level tuning of a Sb_2Te_3 topological insulator by structural deformation, Nano Lett. *15* (2015) 3820–3826.
[55] E. Tang, L. Fu, Strain-Induced Partially Flat Band, Helical Snake States and Interface Superconductivity in Topological Crystalline Insulators, Nat. Phys. *10* (2014) 964–969.
[56] C. Lin, M. Ochi, R. Noguchi, K. Kuroda, M. Sakoda, A. Nomura, M. Tsubota, P. Zhang, C. Bareille, K. Kurokawa, et al., Visualization of the strain-induced topological phase transition in a quasi-one-dimensional superconductor $TaSe_3$, Nat. Mater. *20* (2021) 1093–1099.
[57] M. Shafiei, F. Fazileh, F.M. Peeters, M.V. Milošević, High Chern Number in Strained Thin Films of Dilute Magnetic Topological Insulators, Phys. Rev. B *107* (2023) 195119.
[58] X. Luo, M.B. Sullivan, S.Y. Quek, First-Principles Investigations of the Atomic, Electronic, and Thermoelectric Properties of Equilibrium and Strained Bi_2Se_3 and Bi_2Te_3 Including van Der Waals Interactions, Phys. Rev. B Condens Matter Mater. Phys. *86* (2012) 184111.
[59] S. He, B. Jiang, C. Wang, C. Chen, H. Duan, S. Jin, H. Ye, L. Lu, K. Du, High Reversible Strain in Nanotwinned Metals, ACS Appl. Mater. Interfaces *13* (2021) 46088–46096.
[60] H. Liu, J. Zhou, Plasticity in Nanotwinned Polycrystalline Ni Nanowires under Uniaxial Compression, Mater. Lett. *163* (2016) 179–182.
[61] X. Zhang, X. Li, H. Gao, Size and Strain Rate Effects in Tensile Strength of Penta-Twinned Ag Nanowires, Acta Mech. *33* (2017) 792–800.
[62] Y. Yue, Q. Zhang, X. Zhang, Z. Yang, P. Yin, L. Guo, In Situ Observation of Twin Boundary Sliding in Single Crystalline Cu Nanowires, Small *13* (2017) 1604296.
[63] W. Xu, W.K. Kim, Molecular Dynamics Simulation of the Uniaxial Tensile Test of Silicon Nanowires Using the MEAM Potential, Mech. Mater. *137* (2019) 103140.
[64] L. Liu, Q. Deng, M. Su, M. An, R. Wang, Strain rate and temperature effects on tensile behavior of Ti/Al multilayered nanowire: a molecular dynamics study, Superlattices Micro *135* (2019) 106272.
[65] G. Cheng, S. Yin, T.H. Chang, G. Richter, H. Gao, Y. Zhu, Anomalous tensile detwinning in twinned nanowires, Phys. Rev. Lett. *119* (2017) 256101.
[66] R. Sondors, G. Kunakova, L. Jasulaneca, J. Andzane, E. Kauranens, M. Bechelany, D. Erts, High-Yield Growth and Tunable Morphology of Bi_2Se_3 Nanoribbons Synthesized on Thermally Dewetted Au, Nanomaterials *11* (2021) 2020.
[67] L. Jasulaneca, A.I. Livshits, R. Meija, J. Kosmaca, R. Sondors, M.M. Ramma, D. Jevdokimovs, J. Prikulis, D. Erts, Fabrication and characterization of double- and single-clamped CuO nanowire based nanoelectromechanical switches, Nanomaterials *11* (2021) 117.
[68] M. Brahlek, N. Koirala, N. Bansal, S. Oh, Transport properties of topological insulators: band bending, bulk metal-to-insulator transition, and weak anti-localization, Solid State Commun. *215–216* (2015) 54–62.
[69] J. Hajdu, Shubnikov–De. Haas Eff.: Introd. Theory *27* (1991) 997–1030.
[70] G. Kunakova, R. Meija, J. Andzane, U. Malinovskis, G. Petersons, M. Baitimirova, M. Bechelany, T. Bauch, F. Lombardi, D. Erts, Surface structure promoted high-yield growth and magnetotransport properties of Bi_2Se_3 nanoribbons, Sci. Rep. *9* (2019) 1–10.
[71] L. Fang, Y. Jia, D.J. Miller, M.L. Latimer, Z.L. Xiao, U. Welp, G.W. Crabtree, W. K. Kwok, Catalyst-free growth of millimeter-long topological insulator Bi_2Se_3 nanoribbons and the observation of the π-Berry phase, Nano Lett. *12* (2012) 6164–6169.
[72] L. Veyrat, F. Iacovella, J. Dufouleur, C. Nowka, H. Funke, M. Yang, W. Escoffier, M. Goiran, B. Eichler, O.G. Schmidt, et al., Band bending inversion in Bi_2Se_3 nanostructures, Nano Lett. *15* (2015) 7503–7507.
[73] Z. Ren, A.A. Taskin, S. Sasaki, K. Segawa, Y. Ando, Large bulk resistivity and surface quantum oscillations in the topological insulator Bi_2Te_2Se, Phys. Rev. B Condens Matter Phys. *82* (2010) 241306.
[74] G. Kunakova, T. Bauch, X. Palermo, M. Salvato, J. Andzane, D. Erts, F. Lombardi, High-mobility ambipolar magnetotransport in topological insulator Bi_2Se_3 nanoribbons, Phys. Rev. Appl. *16* (2021) 024038.
[75] J. Zhou, X. Yang, B. Wang, W. Xiao, Springback prediction of 7075 aluminum alloy V-shaped parts in cold and hot stamping, Int. J. Adv. Manuf. Technol. *119* (2022) 203–216.
[76] J. Ma, T. Welo, Analytical springback assessment in flexible stretch bending of complex shapes, Int J. Mach. Tools Manuf. *160* (2021) 103653.
[77] R. Roldán, A. Castellanos-Gomez, E. Cappelluti, F. Guinea, Strain engineering in semiconducting two-dimensional crystals, J. Phys.: Condens. Matter *27* (2015) 313201.
[78] S.M. Sze, VLSI Technol. (1983) 654.
[79] J.J. Licari, D.W. Swanson, Test and inspection methods, Adhes. Technol. Electron. Appl. (2011) 345–377.
[80] G. Binnig, N. Garcia, H. Rohrer, J.M. Soler, F. Flores, Electron-metal-surface interaction potential with vacuum tunneling: observation of the image force, Phys. Rev. B *30* (1984) 4816.
[81] D. Erts, A. Lõhmus, R. Lõhmus, H. Olin, A.V. Pokropivny, L. Ryen, K. Svensson, Force interactions and adhesion of gold contacts using a combined atomic force microscope and transmission electron microscope, Appl. Surf. Sci. *188* (2002) 460–466.
[82] W. Liu, X. Peng, C. Tang, L. Sun, K. Zhang, J. Zhong, Anisotropic interactions and strain-induced topological phase transition in Sb_2Se_3 and Bi_2Se_3, Phys. Rev. B Condens Matter Phys. *84* (2011) 245105.
[83] The Engineering ToolBox (2004). Beams - Fixed at Both Ends - Continuous and Point Loads. [Online] Available online: ⟨https://www.engineeringtoolbox.com/beams-fixed-both-ends-support-loads-deflection-d_809.html⟩ (accessed on 21 October 2023).
[84] J. Andzane, G. Kunakova, S. Charpentier, V. Hrkac, L. Kienle, M. Baitimirova, T. Bauch, F. Lombardi, D. Erts, Catalyst-free vapour–solid technique for deposition of Bi_2Te_3 and Bi_2Se_3 nanowires/nanobelts with topological insulator properties. Nanoscale *7* (2015) 15935–15944.

[85] E.K. Iordanishvili, M.B. Nabiev, K.O. Olimov, Y.I. Ravich, Study of the Strain-Resistance Properties of Massive Samples of Bi_2Te_3-Sb_2Te_3 and Bi_2Te_3-Bi_2Se_3, J. Eng. Phys. 56 (1989) 77–79.
[86] S.D.A. Hannot, D.J. Rixen, V. Rochus, Rounding the corners in an electromechanical FEM model, Proc. Second Int. Conf. Comput. Methods Couple Probl. Sci. Eng. (2007) 507–510.
[87] H. Hussein, P. Le Moal, G. Bourbon, Y. Haddab, P. Lutz, Modeling and stress analysis of a pre-shaped curved beam: influence of high modes of buckling, Int. J. Appl. Mech. (2015) 1550055.

Kiryl Niherysh: received the B.S. and M.S. Engineering degrees in Micro-and Nano-electronics from the Belarusian State University of Informatics and Radioelectronics, Minsk, Belarus, in 2017 and 2018, respectively. He is currently pursuing the Ph.D. degree in Physics from the University of Latvia, Riga, Latvia. Currently he is a researcher at the Institute of Chemical Physics of the University of Latvia. His research interests include nanofabrication of electronic devices, low temperature transport measurements, and synthesis and characterization of nanostructures.

Liga Jasulaneca: received the B.S. and M.S. degrees in Natural Sciences in Physics from the University of Latvia in Riga, Latvia in 2012 and 2015, respectively. Currently, she is actively pursuing the Ph.D. degree in Physics at the same institution. Since 2016, she has been a researcher in the nanotechnology group at the Institute of Chemical Physics, University of Latvia. Her current research focus spans nanoelectromechanical systems, low-dimensional materials and low temperature transport measurements.

Elza Dzene: received the B.S. degree in Chemistry from the University of Latvia, Riga, Latvia in 2022. She is currently pursuing the M.S. degree in Chemistry at the same institution. She is a research assistant in the Institute of Chemical Physics of the University of Latvia. Her current research interests include the low-dimensional materials growth and their structural characterization.

Floriana Lombardi: received the Ph.D. in Physics in 1996 from the University of Napoli, Italy. Her Ph.D. thesis was dedicated to high critical temperature superconductor Josephson devices. From 1996–1998 she was a Postdoctoral Associate at Chalmers University of Technology, Sweden. From 1998–2001 she was a Postdoctoral Associate at the University of Napoli, Italy. From 2002–2006 she was an Assistant Professor, at Chalmers University of Technology. From 2007–2009 she worked as an Associate Professor at Chalmers University of Technology. From 2009 she has been a professor in Condensed Matter physics at Chalmers University of Technology, Department of Microtechnology and Nanoscience MC2. Since 2023, she has been a Full Professor at Quantum Device Physics. Her main research activities focus on superconducting nanostructures, Coulomb blockade devices, and electron transport in topological insulators.

Donats Erts: received the Ph.D. in Chemistry in 1985 (Candidate of Sciences in Chemistry, 1992 equated to Dr. chem.) from the Institute of Inorganic Chemistry, Academy of Latvian SSR. His thesis was dedicated to lyoluminescence of irradiated alkali crystals. From 1985 to the present, he has been a Senior, Leading Researcher at the Faculty of Chemistry, Department of Chemical Physics of Condensed Matter (now the Institute of Chemical Physics) at the University of Latvia. From 1992–2009, he was a part-time visiting researcher at Chalmers University of Technology, Sweden, Cork University College and CRANN, Ireland. Since 2002, he has been Acting Director, Director of the Institute of Chemical Physics at the University of Latvia. From 2013 he has an Associate Professor and since 2021 – Professor at the Department of Chemistry of the University of Latvia. From 2016 he has been a Full Member of Latvian Academy of Sciences. His main research interests are related to the synthesis of nanostructured materials, the investigation of their properties and potential applications.

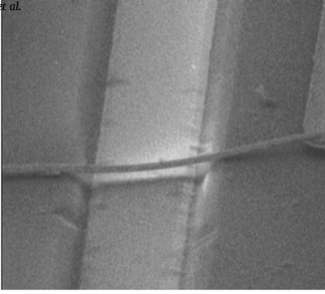

Video S1. A video clip is available online.A video clip is available online. Supplementary material related to this article can be found online at doi:10.1016/j.sna.2024.115292.

Paper II

micromachines MDPI

Article

Characterization of Mechanical Oscillations in Bismuth Selenide Nanowires at Low Temperatures

Liga Jasulaneca [1,*,†], Raimonds Poplausks [1,†], Juris Prikulis [1,†], Elza Dzene [1], Tom Yager [2] and Donats Erts [1,3]

[1] Institute of Chemical Physics, University of Latvia, 19 Raina Blvd., LV-1586 Riga, Latvia; raimonds.poplausks@lu.lv (R.P.); juris.prikulis@lu.lv (J.P.); elza.dzene@lu.lv (E.D.); donats.erts@lu.lv (D.E.)
[2] Institute of Solid State Physics, University of Latvia, 8 Kengaraga Str., LV-1063 Riga, Latvia; tom.yager@cfi.lu.lv
[3] Faculty of Chemistry, University of Latvia, 1 Jelgavas Str., LV-1004 Riga, Latvia
* Correspondence: liga.jasulaneca@lu.lv
† These authors contributed equally to this work.

Abstract: A single transistor preamplifier circuit was designed to facilitate electrical detection of mechanical oscillations in nanoelectromechanical systems (NEMSs) at low temperatures. The amplifier was integrated in the close vicinity of the nanowire inside the cryostat to minimize cabling load and interference. The function of the circuit was impedance conversion for current flow measurements in NEMSs with a high internal resistance. The circuit was tested to operate at temperatures as low as 5 K and demonstrated the ability to detect oscillations in double-clamped bismuth selenide nanowires upon excitation by a 0.1 MHz–10 MHz AC signal applied to a mechanically separated gate electrode. A strong resonance frequency dependency on temperature was observed. A relatively weak shift in the oscillation amplitude and resonance frequency was measured when a DC bias voltage was applied to the gate electrode at a constant temperature.

Keywords: resonance detection; radio-frequency; 1D nanomaterials; bismuth selenide

check for updates

Citation: Jasulaneca, L.; Poplausks, R.; Prikulis, J.; Dzene, E.; Yager, T.; Erts, D. Characterization of Mechanical Oscillations in Bismuth Selenide Nanowires at Low Temperatures. *Micromachines* **2023**, *14*, 1910. https://doi.org/10.3390/mi14101910

Academic Editors: Xiaotian Zhang and Tianyi Zhang

Received: 31 July 2023
Revised: 29 September 2023
Accepted: 5 October 2023
Published: 7 October 2023

Copyright: © 2023 by the authors. Licensee MDPI, Basel, Switzerland. This article is an open access article distributed under the terms and conditions of the Creative Commons Attribution (CC BY) license (https://creativecommons.org/licenses/by/4.0/).

1. Introduction

Nanoelectromechanical systems (NEMSs) are a continuously developing technology that exploit the quasi-static and dynamic mechanical motion of nanostructures to convey signals with high energy efficiency [1–3]. In the quasi-static mode, structural deformations of the nanostructure are used to switch from one stability point to another, also usually employing formation of electrical and mechanical contact. This is used in logic and memory elements (switches and relays) to create fast switching suitable for harsh environment applications [2–4]. Dynamic NEMSs exploit their vibrations in non-contact mode. They are characterized by high resonance frequencies and a broad tuning range [5,6], enabling precise and versatile devices such as high-performance resonators, filters, oscillators and sensors [7,8]. Besides device applications, mechanical phenomena can also be exploited as a means for material property characterization of nanoscale components (e.g., effective Young's modulus [9,10]) for studying energy losses, current-induced processes [6,11] and even sensitive mesoscopic interference phenomena [12].

There are various transduction methods that can be used to excite and detect mechanical resonances in nanomaterials, including electric [13,14], electrothermal [6], piezoelectric [15] and optical [6,15] methods. Due to the extremely small displacement amplitudes of the resonant structures in the range of nanometers or less, detection of the vibrations is the most complicated part of the experiment. Detection schemes widely applied in microelectromechanical systems (MEMSs) need to be adapted for nanoscale use. The detection often needs to be performed in customized setups, e.g., to conduct experiments at very low or high temperatures, in a vacuum or in high magnetic fields, requiring increasing

amounts of wiring. Low temperature applications have been actively explored for quantum computers [16] and space technologies.

Among the readout schemes, direct observation with electron and light microscopes [17,18] and electrical [13,14] and optical [6,15] schemes are commonly employed. Electrical detection schemes are widely used for resonance registration, as they are easy to integrate with other components and, in the case of one-dimensional (1D) materials, have larger coupling than, e.g., optical detection schemes. Although optical detection has been adapted to detect resonance at low temperatures [19], its implementation is more complicated [20]. Optical probing may induce local heating that may change the properties of sensitive nanomaterials [15]. By using the same electrical setup in a cryostat both for magnetotransport measurements and resonance detection, it would be possible to obtain information about charge carriers and mechanical properties simultaneously without added complexity. A common electrical detection technique employs electrical mixing [21,22] that allows for efficient detection of the resonance by converting it to another frequency that does not suffer from parasitic elements of the circuit, such as electrodes and wires contacting the nanostructure. Another approach is to employ a local gate electrode close to the vibrating nanostructure [13,23] to minimize parasitic circuit contribution and facilitate readout at the same frequency as the excitation, thus increasing the detection speed.

Bismuth selenide (Bi_2Se_3) nanostructures are attractive for various applications, for example, spintronic and energy-efficient electronic devices [24,25], owing to their topological insulator properties and the possibility to access and manipulate unique surface states [26]. Another application is their potential use as NEM switch-active elements at low temperatures [27]. Resonant frequency detection allows rapid characterization of NEM switching elements and presents the possibility for on-chip voltage reduction [28] of a NEM switch operating at low temperatures. In addition, as a semiconductor, Bi_2Se_3 exhibits gate tunability that would allow modulation of ON-state current in the NEM switch and to employ direct readouts of the resonance frequency, similarly to graphene [13,29].

In this study, we develop a setup for the electrical detection of the mechanical resonance of nanostructures at low temperatures by integrating a preamplifier next to the measured device. We show that this setup allows efficient detection of the resonant frequency of 1D nanostructures by measuring individual double-clamped Bi_2Se_3 nanowires. The detection setup is generic and may potentially be used for studies of other NEMSs.

2. Materials and Methods

2.1. Device Fabrication

Devices with suspended Bi_2Se_3 nanoribbons on Si substrates were fabricated using electron beam lithography (EBL, eLINE Plus, Raith, Dortmund, Germany) on commercially available high-resistivity Si substrates (10 kΩ cm) with a 200 nm-thick dry thermal SiO_2 layer. Trenches for gate electrodes were patterned using reactive ion etching (PlasmaPro 100 Cobra ICP RIE, Oxford Instruments, Abingdon, UK) with SiO_2 using a PMMA A9 electron beam resist as a mask and CHF_3-O_2 (20 sccm CHF_3 and 5 sccm O_2 at 10 °C and 200 W HF power) gas as the etchant. Trenches with depths down to 270 nm were fabricated, followed by another lithography step for thermal evaporation (Sidrabe Vacuum, Riga, Latvia) of a 5 nm/60 nm Ti/Au metal layer in the trenches to form local gate electrodes.

Bi_2Se_3 nanoribbons were grown using a high-yield vapor–solid synthesis method with a Au catalyst reported previously [30]. They were transferred mechanically to the as-fabricated substrate with gate electrodes. Suitable nanoribbons were identified using an optical microscope for patterning source and drain electrodes via electron beam lithography. To create ohmic contacts between Bi_2Se_3 and Au, native oxide covering Bi_2Se_3 was etched in a hydrochloric acid/acetic-acid-based solution prior to metallization with 200 nm Ti/Au layers.

The final devices were inspected via scanning electron microscopy (SEM, Hitachi FE-SEM S-4800, Hitachi, Chiyoda City, Tokyo, Japan) to check that they had not adhered to the gate electrode and there was a continuous metal layer over the nanostructure. The

thickness of the nanoribbons and depth of the trenches were measured using atomic force microscopy (AFM, Asylum Research MFP-3D, Santa Barbara, CA, USA).

Nanowires with thicknesses from 35 to 224 nm, widths from 124 to 266 nm and lengths from 7.6 to 8.3 µm, with a distance to the gate electrode of 157 nm and two-terminal resistances up to 50 kΩ, were analyzed using an electrical detection method described below.

2.2. Electronic Measurements

Figure 1 shows the diagram of the preamplifier circuit inside the physical property measurement system (PPMS, Dynacool 9T, Quantum Design, San Diego, CA, USA). Bi_2Se_3 nanowires and the resistor R_3 formed a voltage divider, which was connected to a $V_{DC-bias}$ source (Keithley-2400, Tektronix, Bracknell, UK). Current flow measurements at the $V_{DC-bias}$ source indicated whether the Bi_2Se_3 nanowire was damaged, while R_3 also served as a current limiter. The capacitor C_3 connected the AC component of the voltage drop across the Bi_2Se_3 nanowire to the gate of the transistor T_1 (2N7002, Diodes Incorporated, Plano, TX, USA), which operated as a source follower (SF). The advantage of SF circuits (common drain amplifier) is that they are relatively immune to transistor parameters and other component value variations at extreme temperatures. The resistors R_4 and R_5 ensured that the transistor gate was biased above the gate-source threshold voltage V_T of T_1. For an ideal SF scheme, the AC component of the voltage drop across the resistor R_6 is equal to that of the Bi_2Se_3 nanowire, but with a much lower impedance for driving the load at terminal V_{AC-out} via capacitor C_4. The resistance of R_6 was chosen relatively high to avoid heating inside the cryostat. C_5 is a bypass capacitor for the supply voltage $V_{DC-power}$. The conductivity of the Bi_2Se_3 nanowire was modulated by the middle (G) electrode, which through the capacitor C_2 was connected to the input terminal V_{AC-in} and through the resistor R_2 was biased by a DC voltage V_g that was provided by a programmable external source (Keithley-6430, Tektronix, Bracknell, UK). Monitoring the DC current at V_g indicated whether a jump-to-contact event had occurred. To avoid the risk of nanowires contacting the gate electrode, the gate voltage was kept in the range of ±8 V. The R_1C_1 matching network additionally provided a load of V_{AC-in} voltage for diagnostic of electric connections.

All components including the Si substrate with the Bi_2Se_3 nanowire were assembled on a miniature printed circuit board (PCB) (Figure 1b–d), that was mounted on a sample holder of the PPMS. The connections between the PCB and sample substrate were made with a 25 µm diameter Au bonding wire using a UniTemp WB-100 (UniTemp, Pfaffenhofen, Germany) ultrasonic wire bonder (Figure 1d). The holder with the bonded sample was loaded into the PPMS and measurements were taken at a pressure of approximately 0.6 Torr.

A V_{AC-in} signal was generated using a vector network analyzer (VNA, Rohde & Schwarz ZNB 8, Rohde & Schwarz, Columbia, MD, USA) port 1. The output signal V_{AC-out} was connected to VNA port 2 and the S_{21} parameter was used to characterize the system amplitude transfer function $A(f)$. The typical operating parameters were $V_{AC-in,rms}$ 0.22 V, $V_{DC-power}$ 15 V and $V_{DC-bias}$ 0.04 V with a corresponding I_{SD} in the range of 0.5–1.0 µA.

According to the manufacturer's datasheets, the operating temperature of the electronic components is specified to a limited range, typically above −55 °C. However, they often can function even at cryogenic temperatures [31,32], although with deviations from guaranteed parameter tolerances. Indeed, at low temperatures, the resistor values were several times higher than nominal, as measured by the PPMS (not shown). The cabling in the PPMS is designed for DC or low frequency measurements and at higher frequencies suffers from parasitic reactive elements, interference and poor impedance matching. Moreover, no proper VNA calibration was possible for samples inside the cryostat. To account for these issues, the response of the electrical circuit was characterized prior to the nanowire measurements by using:

1. A standard MOSFET as a test three-terminal device to determine if the amplification of the circuit remains consistent at low temperatures;

2. A 5 MHz quartz resonator to examine gain and frequency variations in response to lowering the temperature;
3. A standard 20 kΩ resistor to check for unwanted resonances in the circuit.

These tests allowed determination of the operation bandwidth. Here, we observed that amplification of the signal remains consistent until 5 K, which is the lowest temperature achievable in our setup, and unwanted resonances do not appear in the frequency range from 0.1 MHz to 10 MHz.

The 5 MHz quartz resonator (Abracon ABLS-5.000MHZ-B2-T, Abracon, Spicewood, TX, USA) was connected to G and D terminals (Figure 1) with $V_{DC-bias}$ disconnected. A standard 20 kΩ resistor was connected to S and D terminals.

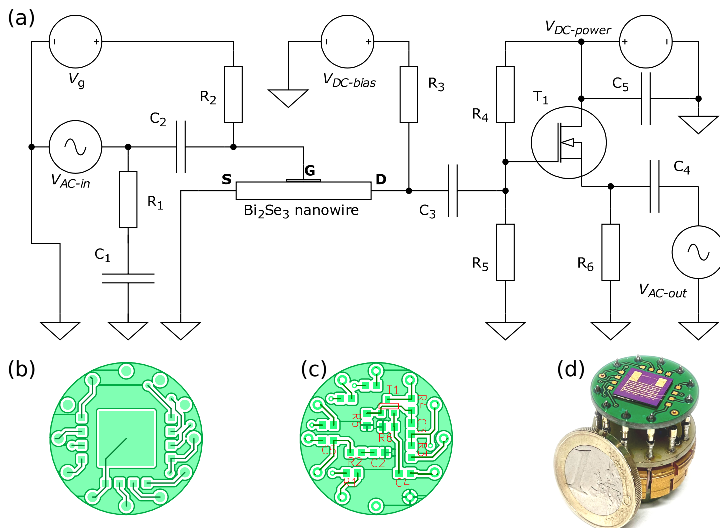

Figure 1. (**a**) Schematic of the preamplifier circuit. Element values: R_1—50 Ω; R_2, R_4, R_5—2 MΩ; R_3 equal to DC resistance of Bi_2Se_3 nanowire; R_6—1.2 kΩ; C_1, C_2, C_3, C_4—0.1 µF; C_5—0.5 µF; T_1—2N7002. Layout of the PCB shown from (**b**) top and (**c**) bottom sides. (**d**) PCB mounted on a PPMS holder with the sample bonded to the top.

3. Results and Discussion

Figure 2a shows the amplitude spectra for a 5 MHz quartz resonator in temperature range of 300 K to 4.2 K. There is a small ∼0.005 MHz frequency shift in the resonance, as the lower operating temperature limit of quartz resonator is −20 °C. However, lowering the temperature does not impact amplification, as the gain of the system remained nearly constant with only a ∼2 dB variation until approximately 4 K. The general characteristics of MOSFET operation at these temperatures are expected to change insignificantly [32]. Although changes in DC output due to variation in the gate threshold voltage with temperature could be expected, by operating the circuit as a source follower, the AC component is insensitive to parameter changes.

Although an increase in the quality factor of the quartz resonator alone would be expected by lowering the temperature, in our setup, we measured the response of the whole system. Here, the quartz resonator is effectively connected in series with a biasing circuit (∼ 1M R_4 and R_5 in parallel with a small ∼50 pF input capacitance of T_1). This configuration may limit the apparent quality factor of the test circuit.

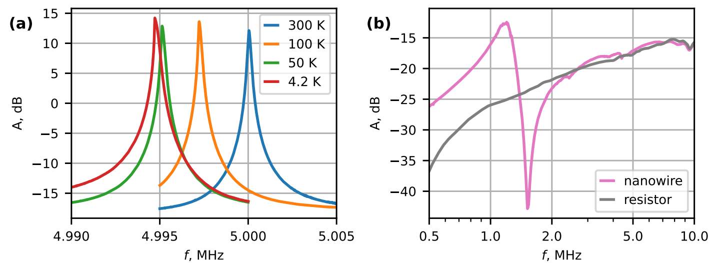

Figure 2. (**a**) Amplitude spectra of a 5 MHz quartz resonator at different temperatures. (**b**) Amplitude spectra of a Bi_2Se_3 nanowire device (No. 1) and a 20 kΩ resistor at 8 K.

Two Bi_2Se_3 nanowire devices with small and large thickness to length ratios (1:34 for device No. 1 and 1:237 for device No. 2) were selected to test the circuit and examine their resonant response (Figure 3). The relevant geometrical parameters of the nanowires, S-D resistance and measured and calculated resonant frequencies are shown in Table 1.

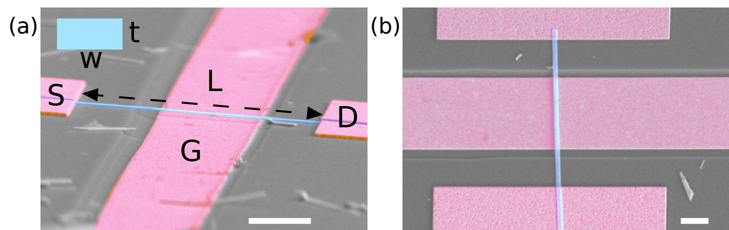

Figure 3. (**a**) Scanning electron microscopy images of the tested devices with source (S), drain (D) and gate (G) electrodes in an angled view (device No. 1) (**b**) and top view (device No. 2). Scale bar: 2 µm. A false colour was added for clarity, where magenta highlights the deposited source, drain and gate electrodes, whilst the suspended nanowire is highlighted in blue. The rectangular cross section of the Bi_2Se_3 nanowire is shown in the schematic inset with width w and thickness t.

Table 1. Geometrical parameters (length L, thickness t, width w), resistance R, measured f_{meas} and calculated f_{calc} resonant frequencies of the Bi_2Se_3 resonators.

Device	L, µm	t, nm	w, nm	R, kΩ	f_{meas}, MHz	f_{calc}, MHz
No. 1	7.6	224	124	50	1.5	9.8
No. 2	8.3	35	266	36	1.2	1.2

Figure 2b compares the amplitude spectra obtained for a Bi_2Se_3 nanowire device (No. 1) with a thickness of 224 nm and a length of 7.6 µm with a test circuit, where the nanowire was substituted with a similar resistance (20 kΩ) resistor. In contrast with the quartz resonator, the amplitude for both systems is negative. These differences can be understood by considering that the quartz resonator is connected between G and D terminals (Figure 1) and at resonance, its impedance becomes very low, raising the overall system gain to a positive ∼13 dB. However, for nanowires, the system detects a small modulation in the DC conductivity between S and D terminals of the nanowire induced by the gate electrode. As the transconductance of the gated nanowire is very low in comparison with, e.g., a regular field-effect transistor, the net gain of the system remains negative. At the same time, this does not hinder the detection of clear differences between the nanowire and the resistor spectra for frequencies up to approximately 2 MHz. Here, the spectrum with

the nanowire shows a positive peak at approximately 1.20 MHz, followed by a negative peak at 1.52 MHz. We associate these antisymmetric peaks with the mechanical resonance of the nanowire. Near the resonance, the phase of the mechanical oscillations changes relative to the phase of the driving electric field from the gate electrode. The observed net signal is a sum of several factors, including capacitive coupling and cross-talk between the wires. The asymmetric shape of the gated nanowire spectra may be explained by constructive and destructive interference between the modulated nanowire signal and all other contributing factors. Similar pairs of positive–negative peaks associated with a phase change, as well as negative amplitudes of the resonance signal, have been reported in the literature [14,33–35]. Since the gate-induced electric field depends on the distance to the nanowire, the response may become nonlinear at large oscillation amplitudes. Another explanation of the asymmetric spectral peaks could be the positive and negative mechanical feedback due to in-phase and out-of-phase oscillations [36].

To calculate the expected resonant frequencies, we use the dynamic Euler–Bernoulli equation for the fundamental resonant frequency f_0 of a double-clamped beam [37]:

$$f_0 = \frac{22.4}{2\pi L^2}\sqrt{\frac{EI}{\rho A}},$$

where L—suspended length, E—Young's modulus, I—area moment of inertia, ρ—density and A—actuation area. For E, the room temperature value of 44 GPa, determined for Bi_2Se_3 nanoribbons via the electromechanical resonance method [9], was used. Whilst the most interesting quantum phenomena of Bi_2Se_3 occur at low temperatures, there is currently very little experimental data about the elastic and thermoelastic properties of nanoscale Bi_2Se_3 at low temperatures to the best of our knowledge. A recent study has reported the resonance of two double-clamped Bi_2Se_3 nanowire devices [12] at millikelvin temperatures. In this report, for a device with nanowire dimensions of a width of 105 nm, a thickness of 116 nm and a length of 1.5 µm, a resonant frequency of 115 MHz was determined, which is 10% lower than estimated using a room temperature Young's modulus value of 44 GPa [9]. It must be taken into account that nanomaterials may exhibit size dependence in the Young's modulus and its temperature dependence may differ from its bulk counterpart [38,39]. However, for Bi_2Se_3 nanoribbons in particular, in a thickness range of 30 to 100 nm, no size dependence has been reported [9].

By comparing the results for device No. 1 and device No. 2, it is apparent that the device with the thickest nanowire (No. 1) exhibits an almost 7 times lower frequency than expected, while the thinner nanowire (No. 2) matches closely with the expected value. The discrepancies in the expected frequency could be explained by changes in clamping of the nanowire ends due to differential expansion or compression of the nanowire and its contact with material during cooling and heating cycles.

For the thin nanowire device (No. 2), a series of spectra were recorded while heating the device from 5 K to 300 K (Figure 4). The resonant frequency decreased almost two-fold with increasing temperature. Then, it reached a minimum value at about 200 K and increased back to its low-temperature value. The observed temperature response is significant and can be compared to a graphene monolayer resonator [40,41], which exhibits an up to two-fold increase in frequency while cooling from 300 K to 125 K. However, for graphene, the upwards shift in frequency came from the isotropic contraction of metal contacts that were also suspended. In contrast, for double- and single-clamped Si [15] and GaN [42] nanowires, a frequency increase of only up to 1% has been observed down to 12 K, attributed to a temperature-dependent Young's modulus and thermal contraction of the resonating materials.

The unexpected upwards shift in the resonant frequency from 200 K to 300 K was observed in repeated measurements for this sample and requires further investigation to determine if its origin is connected to differential thermal compression/expansion of the structure leading to changes in the boundary conditions of the resonator.

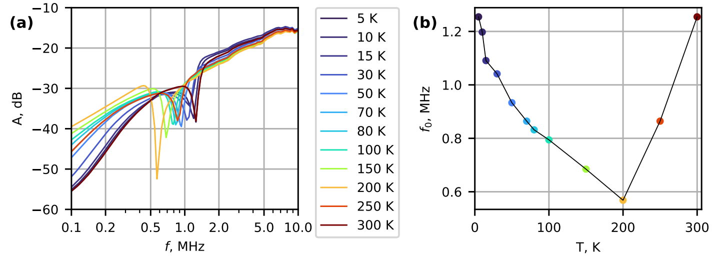

Figure 4. (**a**) Amplitude spectra of a Bi_2Se_3 nanowire (device No. 2) at different temperatures from 300 K to 5 K. (**b**) Negative peak frequency f_0 dependence on temperature.

The differences in observed line shapes for both samples could be accounted for by different geometries and Q factors that all contribute to phase shifts in resonant systems. To understand the occurrence of asymmetric line shapes and their different appearance for both examined devices, the expected response was simulated using an equivalent circuit (Figure 5a), which is typical for modeling NEM resonators [43]. Without any other components, the network of C_s, L_s and R_s would produce a series resonance that can be observed as a positive peak in the amplitude transfer function. With C_p added parallel to the series network, a negative peak is introduced in the spectrum. Such pairs of positive and negative peaks in experimentally measured NEMS transfer functions have been reported previously [14,43]. In our equivalent circuit, we included an additional resistor R_b and capacitor C_g, which represent the biasing resistors in a real circuit and the effective input capacitance of the MOSFET amplifier. In the presence of R_b and C_g, the positive peak broadens and reduces in magnitude in comparison to the negative peak (Figure 5b). The input attenuator Γ characterizes the coupling strength of the gate electrode and the nanowire. The simulated spectrum of $A = 20\log_{10}|\frac{V_{ac-out}}{V_{ac-in}}| - \Gamma$ (Figure 5b) with element values detailed in the figure caption corresponds well with measured spectrum of device No. 1 (Figure 2b). The choice of element value combinations in the equivalent circuit changes the relative magnitude of the positive and negative peaks and can make the positive peak less prominent as in the case of device No. 2.

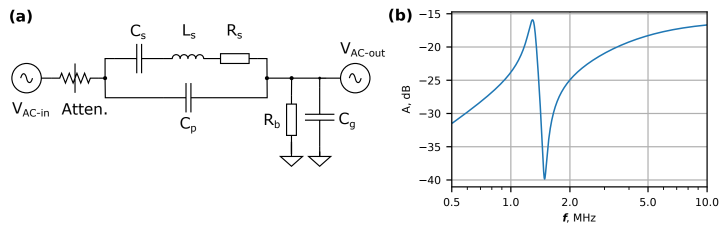

Figure 5. (**a**) Equivalent circuit diagram of the Bi_2Se_3 nanowire resonator. Element values: C_s—0.3 pF; L_s—50 mH; R_s—20 kΩ; C_p—1 pF; R_b—20 kΩ; C_g—1 pF; 10 dB attenuator (Atten.) models the coupling strength of the gate electrode. (**b**) Simulated response of (**a**) with aforementioned parameters shows asymmetric shape of the resonance spectrum, qualitatively similar to that of device No. 1.

For Bi_2Se_3 nanowire device No. 1, a series of spectra $A(f) = |V_{AC-out}(f)|/|V_{AC-in}(f)|$ were recorded at 8 K at different bias voltages V_g (Figure 6a) to investigate the frequency and amplitude dependence on the gate voltage.

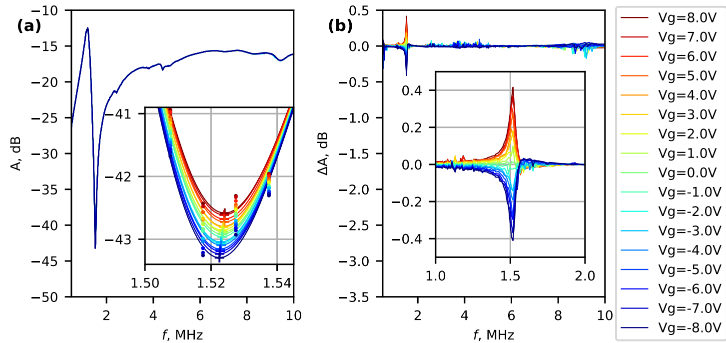

Figure 6. (**a**) Amplitude spectra of system with a Bi_2Se_3 nanowire (device No. 1) and a preamplifier at different gate voltages at 8 K temperature. (**b**) Difference in the amplitude spectra from the mean spectrum. Insets show a narrow region of spectra near 1.5 MHz.

Small systematic changes were detected by comparing spectra at different gate voltages. Figure 6b shows the deviation ΔA from the mean spectrum recorded at V_g intervals from −8 V to +8 V. The maximum difference occurs at approximately 1.52 MHz, which corresponds to the minimum of the original spectra (Figure 6a). In order to find the amplitude and frequency changes, the spectra near 1.52 MHz were fitted with a polynomial function. The extreme points of the fitted polynomial are marked by "+" in the inset of Figure 6a.

Figure 7 shows the linear amplitude and frequency response to the applied gate voltage, which decreases for negative voltage values and increases for positive values. For the nanowire dimensions characterized in our study, we can use the continuum model to describe the force that is exerted by AC and DC voltages by

$$F_{ext}(x,t) = \frac{1}{2}\frac{dc_g}{du}(x)\left(V_g^2 + \frac{1}{2}V_g^{ac^2} + 2V_g V_g^{ac} cos(2\pi f t) + \frac{1}{2}V_g^{ac^2} cos(4\pi f t)\right),$$

where c_g—capacitance per unit length and $u(x)$—displacement. Assuming the AC voltage is much smaller than the DC voltage, the quadratic terms in the equation can be neglected. A parabolic dependence on V_g is expected; however, the relation observed in this study may appear linear due to the low-tunability of the device.

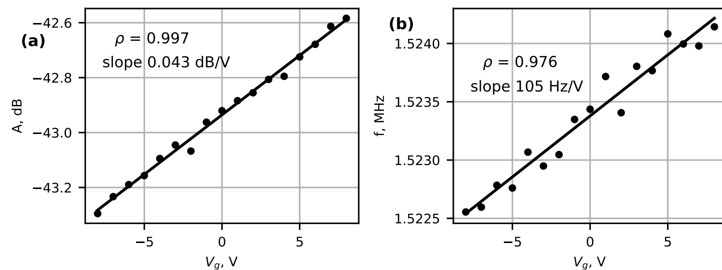

Figure 7. Extreme amplitude (**a**) and frequency (**b**) dependence on gate voltage for device No. 1.

The anti-symmetric amplitude and frequency dependence around zero V_g can be explained by work function differences between the Bi_2Se_3 and Au electrode materials, similar to [17]. The changes in amplitude (Figure 7a) and frequency (Figure 7b) were

relatively small, at 0.043 dB/V and 105 Hz/V, in comparison to, e.g., graphene modulation in [29], which was in the MHz/V range. One possible reason for the low tunabilty could be the thickness of the nanowire. For example, in a 2D layered ReS_2 nanoresonator device [44], a device with a thickness of 106 nm exhibited no tunability, while a 7 nm-thick device exhibited pronounced gate-induced frequency changes. The mechanical strain induced in the nanowire during cooling can also reduce the gate effect.

Nevertheless, there is a strong correlation between amplitude and frequency and the applied DC voltage, confirming the tunability of the system. Other features in the spectra did not exhibit as high a correlation, supporting the conclusion that the chosen frequency represents the mechanical resonant frequency of the nanowire.

4. Conclusions

We have presented an electrical preamplifier circuit for the detection of 1D nanomaterial resonance inside a cryostat. Placing the preamplifier in close vicinity of the resonator allows minimization of the contribution from the parasitic wire capacitance and enables facile readouts at the same frequency as the excitation. The temperature and gate voltage dependence of the resonant frequency was investigated for Bi_2Se_3 nanowire samples at temperatures as low as 5 K, showing large changes in resonant frequency with temperature and the possibility to tune the oscillations with gating. Samples with higher transconductances possibly using thinner Bi_2Se_3 nanowires would allow obtaining a higher response from the system to understand in detail how the elastic properties change with temperature. This would allow a precise NEM switch design for operation at low temperatures for future quantum and space technologies. Although the system was demonstrated using Bi_2Se_3 nanowires, the circuit is a generic common drain amplifier and may be used for studies of other NEMSs at low temperatures.

Author Contributions: L.J.: Investigation, Formal analysis, Methodology, Writing—original draft, review and editing. R.P.: Conceptualization, Investigation. J.P.: Conceptualization, Investigation, Writing—original draft. E.D.: Investigation. T.Y.: Investigation, Writing—review and editing. D.E.: Conceptualization, Methodology, Supervision, Writing—review and editing. All authors have read and agreed to the published version of the manuscript.

Funding: This research was funded by the Latvian Council of Science, project no. lzp-2019/1-0349. L. J. acknowledges the support of the University of Latvia patron "MikroTik". The patron's donations are administered by University of Latvia Foundation. L. J. acknowledges funding from the project "Strengthening of the capacity of doctoral studies at the University of Latvia within the framework of the new doctoral model", identification No. 8.2.2.0/20/I/006.

Data Availability Statement: The data presented in this study are available on request from the corresponding authors.

Conflicts of Interest: The authors declare no conflict of interest.

References

1. Xu, B.; Zhang, P.; Zhu, J.; Liu, Z.; Eichler, A.; Zheng, X.Q.; Lee, J.; Dash, A.; More, S.; Wu, S.; et al. Nanomechanical Resonators: Toward Atomic Scale. *ACS Nano* **2022**, *16*, 15545–15585. [CrossRef] [PubMed]
2. Loh, O.Y.; Espinosa, H.D. Nanoelectromechanical contact switches. *Nat. Nanotechnol.* **2012**, *7*, 283–295. [CrossRef]
3. Jasulaneca, L.; Kosmaca, J.; Meija, R.; Andzane, J.; Erts, D. Review: Electrostatically actuated nanobeam-based nanoelectromechanical switches—Materials solutions and operational conditions. *Beilstein J. Nanotechnol.* **2018**, *9*, 271–300. [CrossRef]
4. Wang, L.; Zhang, P.; Liu, Z.; Wang, Z.; Yang, R. On-chip mechanical computing: Status, challenges, and opportunities. *Chip* **2023**, *2*, 100038. [CrossRef]
5. Kozinsky, I.; Postma, H.W.C.; Bargatin, I.; Roukes, M.L. Tuning nonlinearity, dynamic range, and frequency of nanomechanical resonators. *Appl. Phys. Lett.* **2006**, *88*, 253101. [CrossRef]
6. Ye, F.; Lee, J.; Feng, P.X.L. Electrothermally Tunable Graphene Resonators Operating at Very High Temperature up to 1200 K. *Nano Lett.* **2018**, *18*, 1678–1685. [CrossRef] [PubMed]
7. Sahafi, P.; Rose, W.; Jordan, A.; Yager, B.; Piscitelli, M.; Budakian, R. Ultralow Dissipation Patterned Silicon Nanowire Arrays for Scanning Probe Microscopy. *Nano Lett.* **2020**, *20*, 218–223. [CrossRef]

8. Dominguez-Medina, S.; Fostner, S.; Defoort, M.; Sansa, M.; Stark, A.K.; Halim, M.A.; Vernhes, E.; Gely, M.; Jourdan, G.; Alava, T.; et al. Neutral mass spectrometry of virus capsids above 100 megadaltons with nanomechanical resonators. *Science* **2018**, *362*, 918–922. [CrossRef] [PubMed]
9. Kosmaca, J.; Jasulaneca, L.; Meija, R.; Andzane, J.; Romanova, M.; Kunakova, G.; Erts, D. Young's modulus and indirect morphological analysis of Bi_2Se_3 nanoribbons by resonance measurements. *Nanotechnology* **2017**, *28*, 325701. [CrossRef]
10. Jasulaneca, L.; Meija, R.; Livshits, A.I.; Prikulis, J.; Biswas, S.; Holmes, J.D.; Erts, D. Determination of Young's modulus of Sb_2S_3 nanowires by in situ resonance and bending methods. *Beilstein J. Nanotechnol.* **2016**, *7*, 278–283. [CrossRef] [PubMed]
11. Chiout, A.; Brochard-Richard, C.; Marty, L.; Bendiab, N.; Zhao, M.Q.; Johnson, A.T.C.; Oehler, F.; Ouerghi, A.; Chaste, J. Extreme mechanical tunability in suspended MoS2 resonator controlled by Joule heating. *npj 2D Mater. Appl.* **2023**, *7*, 20. [CrossRef]
12. Kim, M.; Kim, J.; Hou, Y.; Yu, D.; Doh, Y.J.; Kim, B.; Kim, K.W.; Suh, J. Nanomechanical characterization of quantum interference in a topological insulator nanowire. *Nat. Commun.* **2019**, *10*, 4522. [CrossRef]
13. Xu, Y.; Chen, C.; Deshpande, V.V.; DiRenno, F.A.; Gondarenko, A.; Heinz, D.B.; Liu, S.; Kim, P.; Hone, J. Radio frequency electrical transduction of graphene mechanical resonators. *Appl. Phys. Lett.* **2010**, *97*, 243111. [CrossRef]
14. Witkamp, B.; Poot, M.; van der Zant, H.S.J. Bending-Mode Vibration of a Suspended Nanotube Resonator. *Nano Lett.* **2006**, *6*, 2904–2908. [CrossRef]
15. Belov, M.; Quitoriano, N.J.; Sharma, S.; Hiebert, W.K.; Kamins, T.I.; Evoy, S. Mechanical resonance of clamped silicon nanowires measured by optical interferometry. *J. Appl. Phys.* **2008**, *103*, 074304. [CrossRef]
16. Södergren, L.; Olausson, P.; Lind, E. Low-Temperature Characteristics of Nanowire Network Demultiplexer for Qubit Biasing. *Nano Lett.* **2022**, *22*, 3884–3888. [CrossRef] [PubMed]
17. Poncharal, P.; Wang, Z.L.; Ugarte, D.; de Heer, W.A. Electrostatic deflections and electromechanical resonances of carbon nanotubes. *Science* **1999**, *283*, 1513–1516. [CrossRef]
18. Vogl, L.M.; Schweizer, P.; Denninger, P.; Richter, G.; Spiecker, E. Sensing Capabilities of Single Nanowires Studied with Correlative In Situ Light and Electron Microscopy. *ACS Nano* **2022**, *16*, 18110–18118. [CrossRef] [PubMed]
19. Nichol, J.M.; Hemesath, E.R.; Lauhon, L.J.; Budakian, R. Nanomechanical detection of nuclear magnetic resonance using a silicon nanowire oscillator. *Phys. Rev. B* **2012**, *85*, 054414. [CrossRef]
20. Castellanos-Gomez, A.; Singh, V.; van der Zant, H.S.J.; Steele, G.A. Mechanics of freely-suspended ultrathin layered materials. *Ann. Phys.* **2015**, *527*, 27–44. [CrossRef]
21. Sazonova, V.; Yaish, Y.; Üstünel, H.; Roundy, D.; Arias, T.A.; McEuen, P.L. A tunable carbon nanotube electromechanical oscillator. *Nature* **2004**, *431*, 284–287. [CrossRef]
22. Lassagne, B.; Tarakanov, Y.; Kinaret, J.; Garcia-Sanchez, D.; Bachtold, A. Coupling Mechanics to Charge Transport in Carbon Nanotube Mechanical Resonators. *Science* **2009**, *325*, 1107–1110. [CrossRef] [PubMed]
23. Manzeli, S.; Dumcenco, D.; Migliato Marega, G.; Kis, A. Self-sensing, tunable monolayer MoS2 nanoelectromechanical resonators. *Nat. Commun.* **2019**, *10*, 4831. [CrossRef]
24. Li, C.H.; van 't Erve, O.M.J.; Robinson, J.T.; Liu, Y.; Li, L.; Jonker, B.T. Electrical detection of charge-current-induced spin polarization due to spin-momentum locking in Bi_2Se_3. *Nat. Nanotechnol.* **2014**, *9*, 218–224. [CrossRef]
25. Lu, Q.; Li, P.; Guo, Z.; Dong, G.; Peng, B.; Zha, X.; Min, T.; Zhou, Z.; Liu, M. Giant tunable spin Hall angle in sputtered Bi2Se3 controlled by an electric field. *Nat. Commun.* **2022**, *13*, 1650. [CrossRef] [PubMed]
26. Kunakova, G.; Galletti, L.; Charpentier, S.; Andzane, J.; Erts, D.; Léonard, F.; Spataru, C.; Bauch, T.; Lombardi, F. Bulk-free topological insulator Bi2Se3 nanoribbons with magnetotransport signatures of Dirac surface states. *Nanoscale* **2018**, *10*, 19595–19602. [CrossRef]
27. Jasulaneca, L.; Meija, R.; Kauranens, E.; Sondors, R.; Andzane, J.; Rimsa, R.; Mozolevskis, G.; Erts, D. Cryogenic nanoelectromechanical switch enabled by Bi2Se3 nanoribbons. *Mater. Sci. Eng. B* **2022**, *275*, 115510. [CrossRef]
28. Meija, R.; Livshits, A.I.; Kosmaca, J.; Jasulaneca, L.; Andzane, J.; Biswas, S.; Holmes, J.D.; Erts, D. Resonance assisted jump-in voltage reduction for electrostatically actuated nanobeam-based gateless NEM switches. *Nanotechnology* **2019**, *30*, 385203. [CrossRef]
29. Chen, C.; Deshpande, V.V.; Koshino, M.; Lee, S.; Gondarenko, A.; MacDonald, A.H.; Kim, P.; Hone, J. Modulation of mechanical resonance by chemical potential oscillation in graphene. *Nat. Phys.* **2016**, *12*, 240–244. [CrossRef]
30. Sondors, R.; Kunakova, G.; Jasulaneca, L.; Andzane, J.; Kauranens, E.; Bechelany, M.; Erts, D. High-Yield Growth and Tunable Morphology of Bi2Se3 Nanoribbons Synthesized on Thermally Dewetted Au. *Nanomaterials* **2021**, *11*, 2020. [CrossRef] [PubMed]
31. Gui, H.; Chen, R.; Niu, J.; Zhang, Z.; Tolbert, L.M.; Wang, F.F.; Blalock, B.J.; Costinett, D.; Choi, B.B. Review of Power Electronics Components at Cryogenic Temperatures. *IEEE Trans. Power Electron.* **2020**, *35*, 5144–5156. [CrossRef] [PubMed]
32. Luo, C.; Li, Z.; Lu, T.T.; Xu, J.; Guo, G.P. MOSFET characterization and modeling at cryogenic temperatures. *Cryogenics* **2019**, *98*, 12–17. [CrossRef]
33. Mathew, J.P.; Bhushan, A.; Deshmukh, M.M. Tension mediated nonlinear coupling between orthogonal mechanical modes of nanowire resonators. *Solid State Commun.* **2018**, *282*, 17–20. [CrossRef]
34. Solanki, H.S.; Sengupta, S.; Dhara, S.; Singh, V.; Patil, S.; Dhall, R.; Parpia, J.; Bhattacharya, A.; Deshmukh, M.M. Tuning mechanical modes and influence of charge screening in nanowire resonators. *Phys. Rev. B* **2010**, *81*, 115459. [CrossRef]
35. Yu, L.; Pajouhi, H.; Nelis, M.R.; Rhoads, J.F.; Mohammadi, S. Tunable, Dual-Gate, Silicon-on-Insulator (SOI) Nanoelectromechanical Resonators. *IEEE Trans. Nanotechnol.* **2012**, *11*, 1093–1099. [CrossRef]

36. Bartsch, S.T.; Rusu, A.; Ionescu, A.M. Phase-locked loop based on nanoelectromechanical resonant-body field effect transistor. *Appl. Phys. Lett.* **2012**, *101*, 153116. [CrossRef]
37. Cleland, A.N. *Foundations of Nanomechanics*; Advanced Texts in Physics; Springer: Berlin/Heidelberg, Germany, 2003. [CrossRef]
38. Yibibulla, T.; Jiang, Y.; Wang, S.; Huang, H. Size- and temperature-dependent Young's modulus of SiC nanowires determined by a laser-Doppler vibration measurement. *Appl. Phys. Lett.* **2021**, *118*, 043103. [CrossRef]
39. Ma, L.; Yibibulla, T.; Jiang, Y.; Mead, J.L.; Lu, M.; Wang, S.; Huang, H. Temperature and size dependent mechanical properties of vapor synthesized zinc tungstate nanowires. *Phys. E Low-Dimens. Syst. Nanostructures* **2022**, *136*, 114990. [CrossRef]
40. Chen, C.; Rosenblatt, S.; Bolotin, K.I.; Kalb, W.; Kim, P.; Kymissis, I.; Stormer, H.L.; Heinz, T.F.; Hone, J. Performance of monolayer graphene nanomechanical resonators with electrical readout. *Nat. Nanotech.* **2009**, *4*, 861–867. [CrossRef]
41. Arjmandi-Tash, H.; Allain, A.; Han, Z.V.; Bouchiat, V. Large scale integration of CVD-graphene based NEMS with narrow distribution of resonance parameters. *2D Mater.* **2017**, *4*, 025023. [CrossRef]
42. Montague, J.R.; Bertness, K.A.; Sanford, N.A.; Bright, V.M.; Rogers, C.T. Temperature-dependent mechanical-resonance frequencies and damping in ensembles of gallium nitride nanowires. *Appl. Phys. Lett.* **2012**, *101*, 173101. [CrossRef]
43. Arcamone, J.; Misischi, B.; Serra-Graells, F.; van den Boogaart, M.A.F.; Brugger, J.; Torres, F.; Abadal, G.; Barniol, N.; Perez-Murano, F. A Compact and Low-Power CMOS Circuit for Fully Integrated NEMS Resonators. *IEEE Trans. Circuits Syst. II Express Briefs* **2007**, *54*, 377–381. [CrossRef]
44. Xu, B.; Zhu, J.; Xiao, F.; Jiao, C.; Liang, Y.; Wen, T.; Wu, S.; Zhang, Z.; Lin, L.; Pei, S.; et al. Identifying, Resolving, and Quantifying Anisotropy in ReS2 Nanomechanical Resonators. *Small* **2023**, *19*, 2300631. [CrossRef] [PubMed]

Disclaimer/Publisher's Note: The statements, opinions and data contained in all publications are solely those of the individual author(s) and contributor(s) and not of MDPI and/or the editor(s). MDPI and/or the editor(s) disclaim responsibility for any injury to people or property resulting from any ideas, methods, instructions or products referred to in the content.

Paper III

Materials Science and Engineering B 275 (2022) 115510

Contents lists available at ScienceDirect

Materials Science & Engineering B

journal homepage: www.elsevier.com/locate/mseb

Cryogenic nanoelectromechanical switch enabled by Bi_2Se_3 nanoribbons

Liga Jasulaneca [a], Raimonds Meija [a], Edijs Kauranens [a], Raitis Sondors [a], Jana Andzane [a], Roberts Rimsa [b], Gatis Mozolevskis [b], Donats Erts [a,c,*]

[a] Institute of Chemical Physics, University of Latvia, Raina Blvd. 19, LV-1586 Riga, Latvia
[b] Institute of Solid State Physics, University of Latvia, 8 Kengaraga St., LV-1063 Riga, Latvia
[c] Faculty of Chemistry, University of Latvia, Raina Blvd. 19, LV-1586 Riga, Latvia

ARTICLE INFO

Keywords:
Bi_2Se_3
Nanoribbon
Nanoelectromechanical system
Nanoelectromechanical switch
Cryogenic

ABSTRACT

Nanoelectromechanical (NEM) switches are potential candidates for memory and logic devices for low standby-current and harsh environment applications. Cryogenic operation of these devices would allow to use them, e.g., in space probes and in conjunction with quantum computers. Herein, it is demonstrated that cryogenic application requirements such as good flexibility and conductivity are satisfied by using Bi_2Se_3 nanoribbons as active elements in NEM switches. Experimental proof of principle NEM switching at temperatures as low as 5 K is achieved in volatile and non-volatile reversible regimes, exhibiting distinct ON and OFF states, backed by theoretical modelling. The results open new avenues for research and development of NEM systems at cryogenic temperatures.

1. Introduction

Nanoelectromechanical (NEM) switches belong to a class of steep subthreshold slope devices, such as tunneling field-effect transistors, suspended gate field-effect transistors and metal–insulator-transition devices [1–3]. This distinctive switching behavior is enabled by the operation principle of the NEM switch. A conducting active element is separated from an electrode by a physical gap, creating an open circuit (OFF state) with a negligible leakage current. By applying energy, e.g., in the form of an electrostatic field, the active element is deflected until a certain critical deflection is reached. At this deflection, when the gradient of the attractive force exceeds the spring constant of the active element, the active element jumps into contact with the electrode and current can flow through the circuit (ON state). Upon removal of the field, the active element detaches from the electrode and volatile operation is achieved. If the active element remains in contact after removal of the field, the switch exhibits non-volatile behavior. Additional energy needs to be supplied to return the switch to its original position. Thus, the same principle of operation can be used to perform logic and memory functions [4].

NEM switches have been realized using various structures such as single nanowires [4–5] and nanotubes [6], bundles of nanowires [7] and thin films [8–9]. The exact choice of active element (metals [10–11], semiconductors [12–14] or carbon allotropes [8,9,15,16]) and electrode materials for NEM switches is governed by the application-specific combination of mechanical, thermal and electrical properties. Most of the state-of-the-art NEM switches have been demonstrated at room temperature [12,5–9]. High temperature application (e.g., aerospace, automotive) requirements can be satisfied by choosing materials with high melting point such as Mo [10] and SiC [14]. On the other end of the temperature scale, cryogenic NEM switches would be useful for space installations [17] and cryogenic industrial applications and research areas such as quantum computers, superfluids and in conjunction with superconductors [18]. A few reports have demonstrated cryogenic operation at temperatures lower than 6 K of larger micro-electromechanical (MEM) switches using Au thin films as the active elements [17,19]. However, to the best of our knowledge, the lowest operating temperature reported in the nanoscale domain is 78 K for a graphene NEM switch [16]. This could be explained by a lack of materials with suitable physical properties.

Bi_2Se_3 is a semiconductor material with room-temperature mechanical and electrical properties suitable for applications in NEM switches [20–21]. Bi_2Se_3 1D nanostructures exhibit room-temperature Young's modulus of 44 GPa [20], high enough value for implementing efficient reversible switching in a two-terminal NEM switch configuration and low enough for energy-efficient operation in downscaled devices. Room-temperature volatile switching has already been demonstrated both for a collective switching of Bi_2Se_3 nanoribbons in

* Corresponding author.
E-mail address: donats.erts@lu.lv (D. Erts).

https://doi.org/10.1016/j.mseb.2021.115510
Received 27 January 2021; Received in revised form 29 September 2021; Accepted 21 October 2021
Available online 11 November 2021
0921-5107/© 2021 Published by Elsevier B.V.

sandwich-like structures [22] and for a single nanoribbon [23] *in situ* inside a scanning electron microscope. The good conductivity of Bi_2Se_3 nanoribbons even at cryogenic temperatures [21] would enable fabrication of cryogenic devices with high ON/OFF current ratio.

In this work, we present fabrication and the first experimental demonstration of cryogenic operation of single-nanoribbon NEM switch at temperatures as low as 5 K. The active elements, Bi_2Se_3 nanoribbons, are dielectrophoretically aligned and suspended on micropatterned electrodes. We employ a cost-effective and scalable fabrication approach without using top electrical contacts for fixing of the nanoribbon-electrode contact. Repeatable non-volatile and volatile switching is achieved with switch-ON voltage as low as 7.8 V, subthreshold slope as low as 80 mV/dec and ON/OFF current ratio of 10^3.

2. Methods

Bi_2Se_3 nanoribbons were synthesized on glass using both catalyst-free [24] and Au catalyst-assisted [25] physical vapor deposition. Fig. 1 depicts the as-synthesized nanoribbons along with the schematics of a NEM switch array and of a single device. Commercially available Si wafer with thermally grown 1 μm thick SiO_2 was used as a substrate. On this substrate, first photolithography step defined an array of gate (G) electrodes, patterned by wet etching of SiO_2 and subsequent thermal evaporation of 10 nm Cr adhesion layer and 80 nm Au layer. Wet etching of SiO_2 allowed to obtain different distances between the suspended nanoribbon and the G electrode (i.e., gaps). Second lithography step defined source (S) and drain (D) electrodes via thermal evaporation. The nanoribbons were suspended in isopropyl alcohol for alignment at the desired sites on S and D electrodes using floating-electrode dielectrophoresis [26] with 2 MHz AC frequency and 13 V peak-to-peak amplitude. Supercritical CO_2 drying was used to remove the solvent avoiding capillary forces that could induce stiction of the active element to the G electrode. The final device consisted of a single nanoribbon lying on S and D electrodes and suspended over a bottom G electrode. More in-depth details of the fabrication method can be found in [27].

The width and suspended length of the as-fabricated NEM switch active elements were determined using scanning electron microscope (SEM, Hitachi FE-SEM S-4800), thickness and initial distance between nanoribbon and bottom electrode were determined using atomic force microscope (AFM, Asylum Research MFP-3D) before electrical testing.

NEM switch electrodes on SiO_2/Si chip were wire-bonded (Wire Bonder UniTemp WB-100) to a physical property measurement system (PPMS DynaCool 9 T) holder pads. Electrical measurements at cryogenic temperatures were carried out in PPMS, using an external current–voltage source Keithley 6430 (Keithley Model 6430 Sub-Femtoamp Remote SourceMeter).

For theoretical modelling, numerical calculations were carried out with R studio software using bvpSolve package [28].

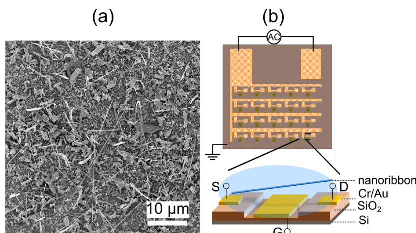

Fig. 1. (a) SEM image of the as-synthesized Bi_2Se_3 nanoribbons on glass substrate; (b) top-view schematics of a microchip with patterned arrays of electrodes which was immersed in nanoribbon suspension for dielectrophoretic (DEP) alignment and dried supercritically using CO_2 to avoid nanoribbon sticking to bottom G electrode; zoom-in view shows side-view schematics of the final structure with single nanoribbon approaching Cr/Au S and D electrodes during DEP alignment.

3. Results and discussion

NEM switches were fabricated for operation at 5 K temperature in different regimes: reversible non-volatile and volatile, depending on the force balance between adhesion force in contact and the elastic restoring force of the active element.

A typical device with suspended length $L_0 = 3.3$ μm, thickness $t = 51$ nm, and initial distance between nanoribbon and bottom electrode $z_0 = 190$ nm and width $w = 512$ nm is shown in Fig. 2.

Prior to cryogenic operation testing, the resistance of the nanoribbon-electrode system was measured at room temperature using a 2-point configuration with the voltage applied between S and D electrodes (Fig. 2a-c). As the nanoribbon was held to the supporting electrode by mechanical (adhesive) contact only, its mechanical strength and electrical conductivity had to be stabilized to ensure stable NEM switch operation [27]. For this purpose, voltage was cycled several times (Fig. 3a) causing current induced modification of the contact. With every next cycle, the resistance of the nanoribbon-electrode system gradually decreased (Fig. 3b) until reaching a stable value. The final resistance of the system was estimated to be approximately 0.9 MΩ, measured at 0.8 V. As expected in case of a mechanical contact, the main contribution to the measured resistance was from contact resistance. The nanoribbons themselves would exhibit room temperature electrical resistivity of the order of 10^{-5} Ω · m as determined in 4-point measurements [21]. This would translate to resistance in the range of several to several tens of kiloohms for the geometry considered above.

Numerical modelling was used to estimate the V_{ON} for Bi_2Se_3 nanoribbon NEM switches [27]. Bi_2Se_3 nanoribbon was modelled as a conducting rectangular beam with suspended length L_0 at an initial distance z_0 from an infinite conducting plane electrode. Voltage applied between the S and G electrodes induced an incremental deflection of the

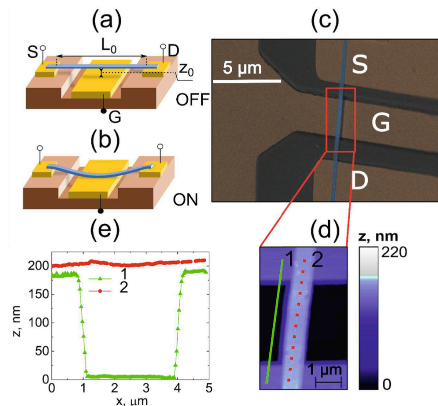

Fig. 2. Schematics of the suspended nanoribbon NEM switch, showing relevant geometrical parameters and electrical connections in OFF (a) and ON (b) states. (c) SEM image (false-colored) of a nanoribbon lying on source (S) and drain (D) electrodes suspended over a bottom gate (G) electrode. A selected area marked with a red rectangle was imaged with AFM in AC topography mode, shown in (d); (e) corresponding line scans, showing electrode (1) and nanoribbon (2) height profiles. (For interpretation of the references to colour in this figure legend, the reader is referred to the web version of this article.)

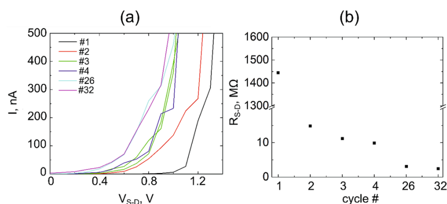

Fig. 3. (a) NEM switch I-V cycling in a 2-point configuration at 300 K, with voltage applied between S and D electrodes; (b) Evolution of NEM switch S-D resistance $R_{S\text{-}D}$. $R_{S\text{-}D}$, measured at 0.8 V, decreases with every next I-V cycle until reaching a stable value.

nanoribbon, now at a new distance z between the nanoribbon and electrode. Relative deflection of the nanoribbon in the presence of applied electrostatic force was approximated numerically by solving the Euler-Bernoulli equation:

$$Y^{(4)}(\xi) - F_x(\xi)Y^{(2)}(\xi) - F_E(\xi) = 0, \xi = \frac{L}{L_0} \tag{1}$$

where Y denotes the displacement perpendicular to the beam, ξ is the normalized coordinate along the nanoribbon, F_x is the force created by tension, and F_E is the linear density of the electrostatic force.

Boundary conditions for a double-clamped nanoribbon were:

$$Y(0) = Y(1) = Y^{(1)}(0) = Y^{(1)}(1) = 0 \tag{2}$$

The experimentally determined $V_{ON,exp}$ and calculated $V_{ON,model}$ values at 5 K, along with the geometrical parameters of devices are listed in Table 1. The NEM switches had active element thickness in the range of 51–145 nm, gaps of 190–200 nm and exhibited $V_{ON,\text{exp}}$ in the range from 17 V to 27 V.

4 of 5 NEM switches showed lower experimentally determined switching voltage than the modelled value (Fig. 4), the reasons for which will be discussed in the following.

For a typical device with Bi_2Se_3 nanoribbon parameters $L_0 = 3.3$ µm, $t = 51$ nm, $z_0 = 190$ nm and $w = 512$ nm (device no 1 in Table 1; Fig. 2), the calculated V_{ON} value was approximately 22.6 V, while the experimentally determined was 20 V (Fig. 4b). Lowering the temperature would increase V_{ON} in comparison with the room temperature value for a clamped active element due to induced tension in the structure, as reported previously for NEM switch devices [16]. As the nanoribbon is fixed by contact area-dependent adhesion force only, some sliding of the active element on top of the electrode may occur during jump-in, as also reported for other NEM switches without top contacts [16,27]. This, on the contrary, would result in decreased V_{ON}, as observed for devices no 1, 2 and 4.

Different operating regimes were achieved for the full ON-OFF cycle, depending on the balance between adhesion forces in contact and elastic restoring force of the active element. When the adhesion force was larger than the elastic force, the active element remained in contact after removal of the voltage. When the difference between the opposing forces was small, additional energy supplied in form of heat detached the active element from the electrode. By increasing temperature to 300 K and back to 5 K, device no 1 was operated in a typical reversible non-volatile regime (Fig. 4b cycle #2), similar to memory device in [4].

Table 1
Fabricated Bi_2Se_3-based non-volatile NEM switches, along with geometrical parameters and experimentally and theoretically calculated V_{ON} voltages at 5 K.

Device no.	t, nm	w, nm	L_0,µm	z_0, nm	$V_{ON,\ exp}$,V	$V_{ON,model}$, V
1	51	512	3.3	190	20	22.6
2	75	90	4.0	200	23	28.4
3	86	190	6.1	200	17	14.9
4	122	220	5.6	190	24	27.4
5	145	107	6.7	200	27	26.7

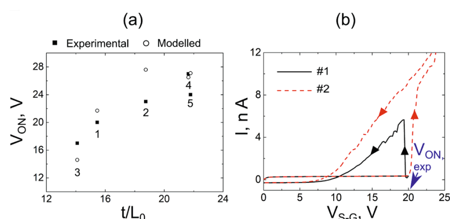

Fig. 4. (a) Comparison of experimentally determined (filled rectangles) and theoretically calculated (empty circles) V_{ON} values as a function of Bi_2Se_3 nanoribbon t/L_0 ratio for devices 1 to 5; (b) Reversible non-volatile operation of a NEM switch (device no 1) at 5 K. I-V cycling characteristics with voltage applied between S and G electrodes show 2 subsequent switching cycles (#1 and #2). In between the cycles, temperature was raised to 300 K and cooled down to 5 K again.

Volatile NEM switching was achieved when the elastic force was larger than the adhesion force in contact (Fig. 5). During the voltage sweep between S and G electrodes, the current initially was at the noise level of 0.1 nA until a sharp rise in current reaching the set level of current compliance of 100 nA was recorded at 9.2 V (Fig. 5 cycle #1).

After the initial switch-ON, V_{ON} decreased from 9.2 V to approximately 8.2 V from cycle #1 to cycle #2. Nanoribbon detachment from the contact manifested as sharp current decrease from current compliance level to the noise level at V_{OFF} of approximately 2.3 V. With every next cycle, V_{ON} gradually decreased by an amount smaller than between cycles #1 and #2 (Fig. 5b). V_{OFF} remained at a stable value of 2.3 V through all cycles. Similar decrease of V_{ON} has been reported for other NEM switches, using both clamped [9] and non-clamped active element configurations [27,29], which was explained either by sliding or mechanical stress release in the nanowire-electrode contact. Even with sliding of the nanoribbon during the first switching cycles, repeatable switching with stable V_{ON} can be achieved without using top-contacts for clamping. A similar behavior was shown for NEM switches at room temperature, making this simple fabrication method attractive for high-yield outcome [27].

The volatile switch exhibited ON-OFF current ratio of approximately 10^3 (leakage current levels at 10^{-10} A, ON-state current levels set by compliance at 10^{-7} A). The average subthreshold slopes (SS) for

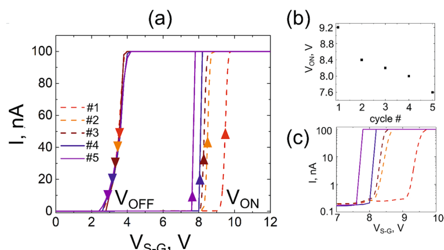

Fig. 5. (a) NEM switch volatile reversible operation at low temperatures: three cycles at 10 K (#1-#3, dashed lines) followed by two cycles at 5 K (#4-#5, solid lines). Upwards arrows mark transition to ON-state, downwards – transition to OFF-state. (b) V_{ON} versus switching cycle number. (c) Log scale representation of the I-V switching from (a) to estimate the subthreshold slope.

transition to the ON-state, calculated as mV/$\log_{10}$I were 135 mV/dec at 10 K and to 80 mV/dec at 5 K (Fig. 5c). These values are higher than the thermal limit for MOSFET transistors of 60 mV/dec at room temperature, however, they represent the upper limit of SS value for this device. By increasing the current compliance and decreasing the voltage step, SS value could be further decreased.

4. Conclusions

In summary, cryogenic operation of a NEM switch employing Bi_2Se_3 nanoribbons as active elements is demonstrated, extending the materials choice suitable for NEM systems at cryogenic temperatures. Proof-of-principle reversible operation at temperatures down to 5 K is demonstrated in non-volatile and volatile regimes. The characterized devices exhibit switch-ON voltages as low as to 7.8 V and OFF-voltages of 2.3 V, with an upper limit of the subthreshold slope value of 135 mV/dec and ON/OFF current ratio of 10^3 for the volatile NEM switch. Differences between experimental and modelled values of V_{ON} are observed (up to 14%) and can be explained by competing effects – increase of V_{ON} with increased tension at lower temperatures and decrease of V_{ON} due to mechanical sliding of the active element along the supporting electrode. Although a decrease in the value of V_{ON} is observed due to active element sliding on contact electrodes in the first cycles, continued operation of the device ensures switching at nearly constant ON and OFF voltages. The proposed fabrication method offers a simple way to achieve high-yield outcome with potential for repeatable and stable operation. An easily implemented solution to reduce or eliminate sliding during the first cycles would be to increase the length of the supported ends of the active element. Additional fixing of the active element by using top-metal electrodes would increase the operational stability of the NEM switch, however this would also increase the fabrication complexity.

Declaration of Competing Interest

The authors declare that they have no known competing financial interests or personal relationships that could have appeared to influence the work reported in this paper.

Acknowledgements

This research was funded by the Latvian Council of Science (project no. lzp-2019/1-0349). L. J. acknowledges the support of the University of Latvia patron "Mikrotīkls". The patron's donations are administered by University of Latvia Foundation. R. R. and G. M. acknowledge funding from the European Union's Horizon 2020 Framework Programme WIDESPREAD-01-2016-2017-TeamingPhase2 under grant agreement No. 739508, project CAMART[2].

Data availability statement

The raw/processed data required to reproduce these findings cannot be shared at this time as the data also forms part of an ongoing study.

References

[1] L. Jasulaneca, J. Kosmaca, R. Meija, J. Andzane, D. Erts, Beilstein J. Nanotechnol. 9 (2018) 271.
[2] O.Y. Loh, H.D. Espinosa, Nat. Nanotechnol. 7 (2012) 283.
[3] S. Cristoloveanu, J. Wan, A. Zaslavsky, IEEE J. Electron Devices Soc. 4 (2016) 215.
[4] K.J. Ziegler, D.M. Lyons, J.D. Holmes, D. Erts, B. Polyakov, H. Olin, K. Svensson, E. Olsson, Appl. Phys. Lett. 84 (2004) 4074.
[5] J. Andzane, R. Meija, A.I. Livshits, J. Prikulis, S. Biswas, J.D. Holmes, D. Erts, J. Mater. Chem. C 1 (2013) 7134.
[6] C. Ke, H.D. Espinosa, Small 2 (2006) 1484.
[7] J. Andzane, J. Prikulis, D. Dvorsek, D. Mihailovic, D. Erts, Nanotechnology 21 (2010), 125706.
[8] P. Li, G. Jing, B. Zhang, S. Sando, T. Cui, Appl. Phys. Lett. 104 (2014), 113110.
[9] N. Huynh Van, M. Muruganathan, J. Kulothungan, H. Mizuta, Nanoscale 10 (2018) 12349.
[10] Y. Qian, B.W. Soon, P. Singh, H. Campanella, C. Lee, Nanoscale 6 (2014) 5606.
[11] J.L. Muñoz-Gamarra, A. Uranga, N. Barniol, Micromachines 7 (2016) 30.
[12] J. Andzane, N. Petkov, A.I. Livshits, J.J. Boland, J.D. Holmes, D. Erts, Nano Lett. 9 (2009) 1824.
[13] Q. Li, S.-M. Koo, M.D. Edelstein, J.S. Suehle, C.A. Richter, MRS Online Proceedings Library 1018 (2007) 907.
[14] T.-H. Lee, S. Bhunia, M. Mehregany, Science 329 (2010) 1316.
[15] O. Loh, X. Wei, J. Sullivan, L.E. Ocola, R. Divan, H.D. Espinosa, Adv. Mater. 24 (2012) 2463.
[16] X. Liu, J.W. Suk, N.G. Boddeti, L. Cantley, L. Wang, J.M. Gray, H.J. Hall, V. M. Bright, C.T. Rogers, M.L. Dunn, R.S. Ruoff, J.S. Bunch, Adv. Mater. 26 (2014) 1571.
[17] R.R. Benoit, N.S. Barker, Microelectron. Reliab. 111 (2020), 113706.
[18] Y. Bar-Cohen (Ed.), Low Temperature Materials and Mechanisms, CRC Press, Boca Raton, 2016.
[19] S.S. Attar, S. Setoodeh, R.R. Mansour, D. Gupta, IEEE Trans. Microw. Theory Tech. 62 (2014) 1437.
[20] J. Kosmaca, L. Jasulaneca, R. Meija, J. Andzane, M. Romanova, G. Kunakova, D. Erts, Nanotechnology 28 (2017), 325701.
[21] G. Kunakova, L. Galletti, S. Charpentier, J. Andzane, D. Erts, F. Léonard, C. D. Spataru, T. Bauch, F. Lombardi, Nanoscale 10 (2018) 19595.
[22] J. Kosmaca, J. Andzane, M. Baitimirova, F. Lombardi, D. Erts, ACS Appl. Mater. Interfaces 8 (2016) 12257.
[23] R. Meija, A.I. Livshits, J. Kosmaca, L. Jasulaneca, J. Andzane, S. Biswas, J. D. Holmes, D. Erts, Nanotechnology 30 (2019).
[24] J. Andzane, G. Kunakova, S. Charpentier, V. Hrkac, L. Kienle, M. Baitimirova, T. Bauch, F. Lombardi, D. Erts, Nanoscale 7 (2015) 15935.
[25] R. Sondors, G. Kunakova, L. Jasulaneca, J. Andzane, E. Kauranens, M. Bechelany, D. Erts, Nanomaterials 11 (2021) 2020.
[26] L. Dong, V. Chirayos, J. Bush, J. Jiao, V.M. Dubin, R.V. Chebian, Y. Ono, J. F. Conley, B.D. Ulrich, J. Phys. Chem. B 109 (2005) 13148.
[27] L. Jasulaneca, A.I. Livshits, R. Meija, J. Kosmaca, R. Sondors, M.M. Ramma, D. Jevdokimovs, J. Prikulis, D. Erts, Nanomaterials 11 (2021) 1.
[28] F. Mazzia, J.R. Cash, K. Soetaert, Opuscula Mathematica 34 (2014).
[29] P. Ryan, Y.-C. Wu, S. Somu, G. Adams, N. McGruer, J. Micromech. Microeng. 21 (2011).

Paper IV

Surfaces and Interfaces 27 (2021) 101531

Contents lists available at ScienceDirect

Surfaces and Interfaces

journal homepage: www.sciencedirect.com/journal/surfaces-and-interfaces

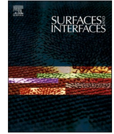

Dielectrophoretic alignment and electrical characterization of CuO nanowire-based systems

Matiss Martins Ramma [a], Juris Katkevics [a], Liga Jasulaneca [a], Gunta Kunakova [a], Raitis Sondors [a], Raimonds Meija [a], Donats Erts [a,b,*], Jelena Kosmaca [a,*]

[a] Institute of Chemical Physics, University of Latvia, 1 Jelgavas str., Riga LV-1004, Latvia
[b] Faculty of Chemistry, University of Latvia, 1 Jelgavas str., Riga LV-1004, Latvia

ARTICLE INFO

Keywords:
Dielectrophoresis
Nanowire
CuO, Space charge limited current

ABSTRACT

Dielectrophoresis is used to assemble nanowires between metallic electrodes to form scalable functional interconnects. The dielectrophoresis parameters are investigated for semiconductor copper oxide (CuO) nanowires that are desirable for energy conversion and storage, gas sensors and nanoelectromechanical systems. Experimental yields of multiple- and single-nanowire interconnects are explored at dielectrophoresis frequencies from 500 Hz to 500 kHz. The electrical properties of nanowire-electrode physical contact interfaces formed by dielectrophoresis, metal deposition, and dry mechanical transfer are investigated. The electrical transport mechanism in these interconnects is determined to be ohmic conductivity at small electric field, which is overtaken by an order of magnitude higher space charge limited conductivity for electric fields above 10^5 V/m. The developed method is demonstrated as a promising route to produce nanowire interconnects towards scalable on-chip nanoelectromechanical systems.

1. Introduction

Copper oxide (CuO) nanowires are desirable components for building functional nanosystems, such as sensors and nanoelectromechanical systems (NEMS), owing to scalable low-cost synthesis [1] and versatile properties [2]. The high specific surface area and semiconductor electronic structure can be used for highly-sensitive [3] and fast response [4] gas sensors. One-dimensional shape and high mechanical stiffness [5,6] in combination with robust electrical performance [6–8] suggest these nanowires as promising candidates for NEMS switches, where electrical connections are provided by mechanical actuation of the nanowires [9,10].

Nanowire interconnects are typically established by top-down approaches, for example, using lithography and metal deposition to form electrical contacts [1,11]. To assemble nanowires at predetermined positions, bottom-up approaches, such as direct mechanical transfer, nanomanipulations or liquid assembly can be used. Conventional mechanical transfer methods result in randomly distributed nanowires, that typically require examination of the nanowire sites and additional adjustments by nanomanipulations. Nanomanipulations have proven efficiency for accurate alignment of individual nanowires [12], however, it is a time-consuming approach unsuitable at an industrial level.

Scalable controlled alignment of nanowires on electrode sites can be achieved using dielectrophoresis (DEP) in liquid media [13,14]. The yield of the nanowire interconnects established during DEP process has been found to be influenced by various factors, such as density of the nanowires and solution flow rate near electrodes [13], electrode configuration [15], amplitude and frequency of the applied AC signal [16–18]. The AC frequency region for nanowire alignment is usually selected based on the properties of nanowires and liquid [14,15]. At some frequencies, DEP can be disrupted by electro-osmosis and electrode polarization [16,17], therefore experimental investigation is needed for the determination of optimal frequencies for selected combinations of nanowire and liquid materials.

To date, DEP alignment has been demonstrated for only few frequencies to produce CuO nanowire interconnects [7,19]. It would be useful to further develop the DEP parameters for the fabrication of scalable yield CuO nanowire systems to optimize the process. Single- and multiple-nanowire interconnects are both desirable depending on the nature of their application. For example, single nanowires are typically preferred for NEMS [10,12], whilst gas sensors can utilize CuO nanowire networks [20]. The factors influencing the number of

* Corresponding authors at: Institute of Chemical Physics, University of Latvia, 1 Jelgavas str., Riga LV-1004, Latvia.
E-mail addresses: donats.erts@lu.lv (D. Erts), jelena.kosmaca@gmail.com (J. Kosmaca).

https://doi.org/10.1016/j.surfin.2021.101531
Received 27 July 2020; Received in revised form 22 September 2021; Accepted 9 October 2021
Available online 17 October 2021
2468-0230/© 2021 Elsevier B.V. All rights reserved.

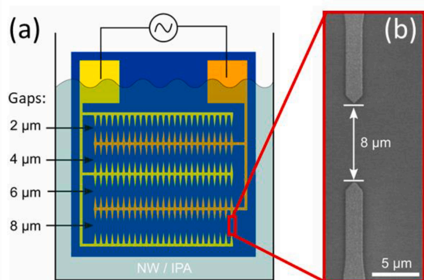

Fig. 1. (a) Schematic diagram of the dielectrophoresis experimental setup with a microelectrode chip submerged in nanowire-isopropanol (NW/IPA) suspension. The microelectrode and gap sizes in the design schematics are not to scale; (b) Scanning electron microscope image showing a microelectrode pair with a gap of 8 µm.

interconnects and electrical properties of these nanowire systems need further determination for their technological implementation.

Dielectrophoresis has the potential to produce aligned nanowire interconnects whilst preserving the pristine structure of the as-grown nanowires. However, the physical interface of the nanowire-electrode contacts after dielectrophoresis can differ from the nanocontacts after metal deposition or dry transfer. Variability of the resulting mechanical contact area can lead to high electrical contact resistances. For nanowires with intrinsically high resistivities, such as CuO [1], system performance is expected to be more resilient to high resistance contacts, than low resistivity nanowires, which often require post-DEP contact modification by etching, metallization or annealing [21,22]. Moreover, strong space charge limited currents (SCLC) manifested for semiconducting nanowires [23–25], have been recently reported for CuO nanowire interconnects [7,8]. Ability to conduct high currents in the SCLC regime suggests CuO nanowires are suitable for transducing electrical signal in NEMS switches. Electrical characterization of the produced nanowire interconnects is required to reveal the conduction mechanisms in the system and analyze how decisive the nanowire-electrode contact interface is for the electrical behavior of CuO nanowires.

In this work, CuO nanowire interconnects are optimized by DEP and electrically characterized. The nanowires are synthesized by a thermal oxidation method [6] and aligned between lithographically defined Au electrodes. Optimized yields for achieving aligned multiple- or single-nanowire interconnects are experimentally determined depending on the DEP field frequency. Current-voltage measurements are performed on individual CuO nanowires to assess their electrical transport properties. The nanowires suspended on electrodes by DEP are compared to nanowires aligned by dry mechanical transfer, and the impact of contact metallization is investigated. Electrical characterization of individual nanowires can improve understanding of the electrical behavior of single and multiple nanowire-based systems, whilst optimization of dielectrophoresis frequencies will foster their further technological development.

2. Materials and methods

Copper oxide nanowires were synthesized by thermal oxidation of Cu foil substrates (GoodFellow, 99.9% purity) in air at 500 °C for 210 min inside a GSL-1100X tube furnace [6]. To transfer the synthesized nanowires from the foil substrate to liquid, the samples were placed in isopropanol and processed in ultrasonication bath for 3 s. The nanowire concentration in the suspension was adjusted to $\sim 10^4$ nanowires per µL, which is similar to concentrations used in previously reported DEP with CuO [19], as well as other composition nanowires [14,26]. The

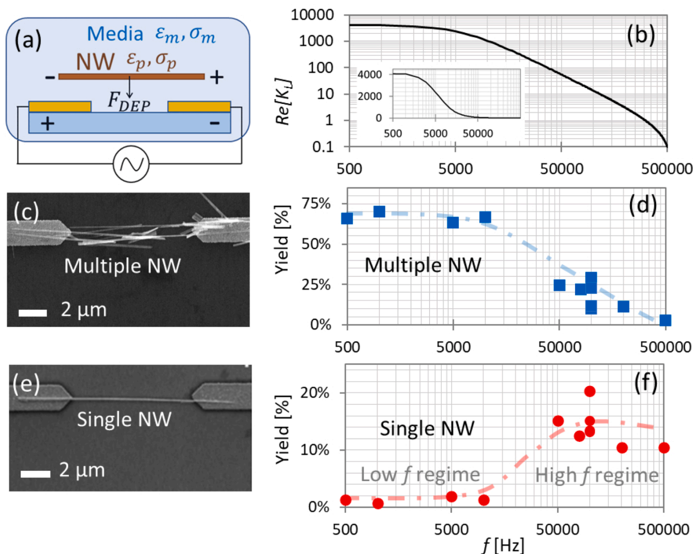

Fig. 2. (a) Schematics of nanowire in liquid media near electrodes in DEP setup (side view); (b) Log-Log plot of the real part of Clausius-Mossotti factor about the long axis $Re[K_L]$ vs. AC frequency f (calculation parameters $\varepsilon_m = 18.6$, $\varepsilon_p = 10$, $\sigma_m = 6 \cdot 10^{-6}$ S/m and $\sigma_p = 0.025$ S/m); inset – Log-Linear plot; (c) Representative SEM image of a multiple-nanowire interconnect (top view); (d) Experimentally determined yield of the multiple-nanowire interconnects vs. applied AC frequency f, dashed line is a guide for eyes; (e) Representative SEM image of a single-nanowire interconnect (top view); (f) Experimentally determined yield of the single-nanowire interconnects vs. applied AC frequency f, dashed line is a guide for eyes.

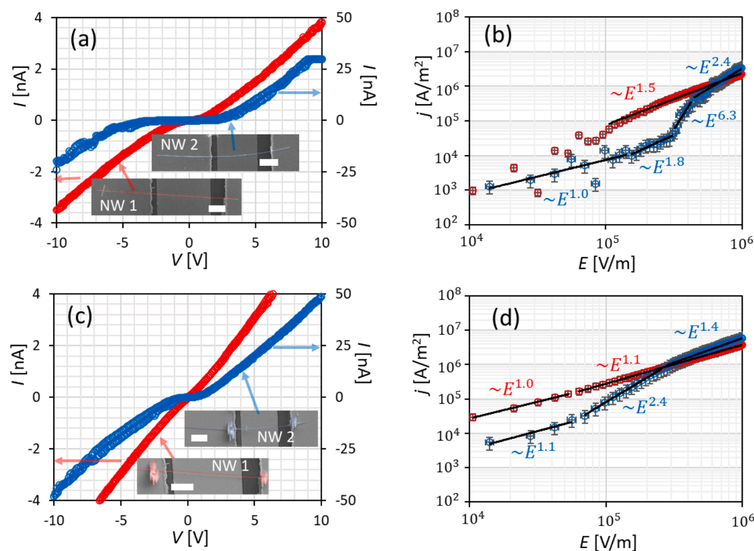

Fig. 3. (a) Representative 2-point *I-V* characteristics for DEP aligned CuO nanowires on Au electrodes in voltage interval from 0 up to +10 V, down to −10 V and back to 0 V with a voltage step 0.1 V. Insets – SEM images of nanowire 1 with effective length 9 μm, mean radius 23 nm, and nanowire 2 with effective length 7 μm, mean radius 41 nm (scale bar 2 μm); (b) Log-Log plot of the calculated current densities *j* in nanowire 1 and nanowire 2 vs. electric field *E* between the electrodes, obtained at increasing voltage from 0.1 to 10 V; (c),(d) – *I-V* characteristics and Log-Log plot of *j* vs. *E* for nanowire 1 and 2 after contact metallization.

nanowire-isopropanol (NW/IPA) suspension was stored in 2 mL vessels. A fresh vessel was used each time to perform DEP at a selected frequency.

Arrays of microelectrodes were lithographically pre-patterned on 1 cm^2 chips for DEP (Fig. 1a). The chips were diced from a commercially available Si/SiO_2 wafer substrates (MTI Corporation) with thermally grown 1000 nm thick SiO_2 layer. The metallic Cr/Au microelectrodes with heights of 3/60 nm, widths of 1 μm and triangle shaped tips were interspaced by 2, 4, 6, 8 μm gaps to form 152 microelectrode pairs on each chip (Fig. 1a,b).

For the DEP assembly of nanowires on microelectrodes, the chip was submerged in the NW/IPA suspension (Fig. 1a) and an AC voltage with 5 V amplitude was applied to microelectrodes for 20 min. These parameter values were chosen considering previously reported intervals of voltage and time for nanowire DEP at similar electrode configurations (e.g., 0.5–2 V and 2–8 min in [26], 5 V in [15], 10 V in [27]). Our preliminary experiments showed that 10 V and higher voltages could lead to dielectric breakdown at the electrode sites, whilst 3 V or smaller voltages would result in too few nanowires being aligned in the used setup. The voltage and time parameter values were preset to show how the proportion of aligned multiple- and single-nanowires can vary for the range of explored frequencies. Previous reports [26] have suggested that increasing voltage and time increases the yield of multiple-nanowire rather than single-nanowire interconnections. The time is coupled with the nanowire concentration, defining the number of nanowires able to reach the region near the electrodes, where they can be captured by the DEP force.

To avoid contact of suspended nanowires with the bottom surface due to capillary forces during the drying process, DEP was complemented by a supercritical drying step in liquid CO_2. Metallization of the nanowire-electrode contacts was performed by e-beam induced deposition of Pt stripes in SEM (Tescan Lyra).

Number and morphology of the individual nanowires and nanowire interconnects on microelectrodes were determined by scanning electron microscopy (Hitachi SEM S4800) analysis. The DEP yield percentages for single- or multiple-nanowire interconnects were determined by SEM analysis of all electrode sites over the chip. Electrical measurements on individual nanowires were carried out in a high vacuum chamber (10^{-6} Torr) inside SEM at room temperature, using Keithley 6430 SourceMeter.

3. Results and discussion

3.1. Dielectrophoresis of CuO nanowires in kilohertz-frequency range

The nanowires synthesized by thermal oxidation and extracted from the isopropanol suspension had straight shapes with radii of 18–73 nm and lengths of 2–12 μm. Electrodes with gaps from 2 to 8 μm were fabricated to achieve optimal ratios of gap size to nanowire length in the range of 0.4–1.0, where DEP force acting on a nanowire is expected to be maximal [16,27].

During the DEP process, CuO nanowires in isopropanol become oriented parallel to the electric field gradient near the electrodes (Fig. 2a). In such configuration, the DEP force acting on the nanowire is proportional to the real part of Clausius-Mossotti factor about the long axis of the nanowire $Re[K_L]$ [15,27]:

$$K_L = \frac{\sigma_p - \sigma_m - i\varepsilon_0(\varepsilon_m - \varepsilon_p)\omega}{\sigma_m + i\varepsilon_0\varepsilon_m\omega}, \quad (1)$$

where $\omega = 2\pi \cdot f$ is the angular frequency, ε_m and ε_p denote the dielectric constants, and σ_m and σ_p are electrical conductivities for the media and nanowire. The nanowires become attracted to the regions of highest

electric field gradient near the electrodes, when the DEP force is positive, i.e. when $Re[K_L] > 0$, which is frequency-dependent [14,26].

Fig. 2b shows a plot of $Re[K_L]$ calculated for CuO nanowires in isopropanol. It is high at low frequencies, more significantly decreases in the frequency interval of 1–50 kHz (Fig. 2b, inset) and tends to zero near a cross-over frequency of ~500 kHz (Fig. 2b).

The CuO nanowire DEP was performed at nine frequencies between 500 Hz and 500 kHz with aim to localize the working frequency intervals suitable for multiple- and single-nanowire alignment on electrodes to form interconnects (Fig. 2c,e). The yield of the nanowire interconnects detected at various frequencies is shown in Fig. 2d,f. The overall yield is dominated by multiple-nanowire interconnects, reaching 60–70% below 10 kHz frequencies. However, at higher frequencies it gradually decreases (Fig. 2d, dashed line) similarly to the theoretical trend of $Re[K_L]$ plotted in Log-Log scale (Fig. 2b). In contrast, the yield of single-nanowire interconnects shows an opposing trend. By comparing the average experimental yields for the low and high frequency regions, it is possible to distinguish two regimes (Fig. 2f). In the low f regime (from 500 Hz to 10 kHz), the yield of the single-nanowire interconnects is around only 1–2%. In the high f regime (from 50 kHz to 500 kHz) the yield of the single-nanowire interconnects is in the range of 11–20%, which was confirmed by multiple experiments near 100 kHz (Fig. 2f). Therefore, DEP in high f regime is yielding in single-nanowire interconnects, whilst the low f regime is sufficient for multiple-nanowire interconnects.

The highest yield of single-nanowire connections is observed near cross-over frequencies, which is similar to previously reported for Si, InAs, Rh, ZnO and MnO_2 nanowires [14–16,26]. Here, the lower magnitude DEP force balances with the direction that could provide a better control over nanowire positioning in the proximity of a microelectrode site [14,26]. For the studied CuO nanowires in isopropanol, the frequencies near 100 kHz, yielding on maximal 20% in the used setup, can be assumed optimal for precise single-nanowire placement. Previously reported frequencies of 20 kHz–0.5 MHz used for CuO nanowire DEP [7,19] are close to our determined values.

After these optimal DEP frequencies for the nanowire suspension have been determined, the yield of the aligned single nanowires can be further improved by adjusting other DEP parameters, such as the voltage, time and concentration, for example, by following the director–disruptor framework proposed in [16]. Finally, optimization of the DEP yield can be achieved by modifying the setup, for example, involving the fluid flow [13] or capillary action [14] in the process, as well as by post-process nanomanipulations [10].

3.2. I-V characterization of single CuO nanowire interconnects

To assess electrical transport properties of such interconnects, current-voltage (*I-V*) curves were obtained for several DEP aligned CuO nanowires in two-point configuration. The nanowires were suspended on high Au electrodes above substrate with a gate electrode, in a configurationthat was used for fabrication of nanoelectromechanical switches described in [10].

Fig. 3a shows two typical examples of the measured *I-V* curves, for DEP aligned CuO nanowires: near linear (ohmic) *I-V* for a nanowire 1 with effective length 9 μm, mean radius 23 nm, and non-linear *I-V* for nanowire 2 with effective length 7 μm, mean radius 41 nm. For the applied voltages of 0 ± 10 V, registered electrical current values do not exceed few tens of nA (Fig. 3a), meaning the resistances of such single-nanowire interconnects are in GΩ range, which is in agreement with literature data on their 10–40 Ω m resistivities [1,11]. Log-Log plots of the forward (positive) branches of current density j vs. electric field E values extracted from these *I-V* curves are shown in Fig. 3b. Both curves (near linear and non-linear) can be approximated by power functions in form $j \sim E^{\alpha}$, where the power factor α shows different values (from 1 to 6.3) for selected E intervals (black lines, Fig. 3b). This behavior can be attributed to a combination of ohmic and space charge limited current (SCLC) conduction mechanisms in CuO nanowires on Au electrodes [7, 8]. In such case, at small electric field the current is driven by intrinsic charge carriers in the nanowire and increases linearly to follow Ohm's law. At higher electric field, it transits to SCLC regime as the number of charge carriers injected from electrode material grows. There the current increase deviates from linear to a power law $j \sim E^{\alpha}$, $\alpha > 1$ for increasing electric field, until a saturation regime, where α is again expected to decrease down to 1. For trap-free SCLC regime, $\alpha = 2$, and increase of α above 2 can be attributed to presence of traps in the CuO nanowire material [7,8].

From Fig. 3b, the power law approximation takes over ohmic linear law at electric field above 10^5 V/m, which agrees well with previously reported $0.9 \cdot 10^5$ V/m [6]. For example, for near linear *I-V* (nanowire 1), the current density dependence on electric field above 10^5 V/m can be approximated with a power function $j \sim E^{1.5}$ (Fig. 3b). For non-linear *I-V* (nanowire 2), the current density curve follows linear law at low electric fields up to $\sim 1.5 \cdot 10^5$V/m ($j \sim E^{1.0}$) which then changes to higher order power law with $\alpha = 1.8$, $\alpha = 6.3$, $\alpha = 2.4$ approximated for certain E intervals above 10^5 V/m. Increase of α from 1.8 to 6.3 refers to switching to trap-filling regime, which will transform to trap-free SCLC at electric fields above $0.5 \cdot 10^6$ V/m.

The range of conductivities about 0.01–1 S/m can be estimated from the current densities of 10^3–10^4 A/m^2 at low electric fields of 10^4–10^5 V/m, where the ohmic conductivity mechanism is prevalent (Fig. 3b). This range includes the conductivity used for $Re[K_L]$ calculation, and previously reported values of 0.02–0.1 S/m for CuO nanowires [1,11]. At higher electric field above 10^5 V/m, the conductivities of the measured nanowires significantly increase, within 1–10 S/m at 10^6 V/m (Fig. 3b).

Nanowire-electrode contact after DEP can be further improved by metallization, which increases the effective contact area and eliminates possible tunneling barriers that may develop for mechanical contact. The *I-V* curves taken for the nanowires after contact metallization with Pt strips (Fig. 3c) show approximately 1.5 times higher currents, compared to their initial near linear and non-linear *I-V* curves (Fig. 3a). Corresponding Log-Log plots of the current density vs. electric field values and their approximation by power functions after metallization are shown in Fig. 3d. The *j-E* curve for initially near linear *I-V* (nanowire 1) can be approximated with a linear fit (α is 1.0–1.1) for the whole explored range of E. Meanwhile, for initially non-linear *I-V* (nanowire 2), the power factor of the used approximation function, α changes as 1.1 below $E \sim 0.5 \cdot 10^5$ V/m, 2.4 at $(0.7–2.5) \cdot 10^5$ V/m, and 1.4 above $2.5 \cdot 10^5$ V/m (Fig. 3d). On one hand, decrease of α compared to initial (Fig. 3b) for both nanowires indicate rise of ohmic contribution in overall conduction mechanism. This becomes prominent at small E values below 10^5 V/m and is due to reduction of nanowire-electrode contact resistance by metallization. The ohmic conductivities extracted from the current densities of 10^3–10^5 A/m^2 corresponding to electric field of 10^4–10^5 V/m (Fig. 3d), can be higher by an order of magnitude than the ohmic conductivities before metallization. On the other hand, a decrease of α from 2.4 to 1.4 observed for nanowire 2 at high electric field can be related to approaching charge carrier velocity saturation regime. The order of current densities 10^6–10^7 A/m^2 at electric field of 10^6 V/m (Fig. 3b,d) remains similar before and after contact metallization, as expected for nanowire interconnects in the SCLC regime [28]. DEP aligned CuO nanowire interconnects with mechanical contacts were found to be able to withstand current densities reaching up to 10^8 A/m^2 and voltages in order of 30–50 V corresponding to electric fields above $6 \cdot 10^6$ V/m before electrical breakdown. Therefore, CuO nanowire interconnects with mechanical contacts are well suited for NEMS operating at relatively high electric fields, where SCLC dominates.

Nanowire DEP interconnects with mechanical contacts were compared with alternatively established interconnects made by dry mechanical transfer (DMT) of CuO nanowires on Au electrodes. In DMT, nanowires from Cu foil were transferred to a flat SiO_2 substrate with lithographically prepatterned Au electrodes, by pressing the surfaces of the two substrates together. From measurements on 16 DEP and 20 DMT

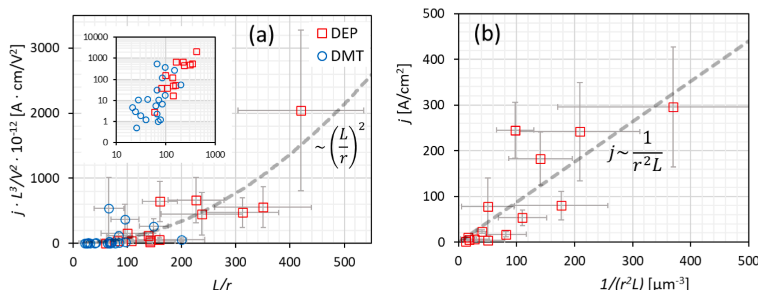

Fig. 4. (a) Relation between $j \cdot L^3/V^2$ vs. L/r for nanowire interconnects aligned by DEP (red squares) and by dry mechanical transfer (DMT, blue circles), dashed line is a guide for eyes – power function $(L/r)^2$; inset – Log-Log plot; (b) Current density j at 10 V vs. nanowire geometry factor $1/(r^2 \cdot L)$ for DEP nanowires with aspect ratios L/r from 60 to 420, dashed line is a linear fit of the data used for estimation of μ. Error bars represent total experimental uncertainties originating from j, L, V, r measurements for each datapoint (For interpretation of the references to color in this figure legend, the reader is referred to the web version of this article.).

single nanowires, most of their *I-V* show similar non-linear behavior following the power law at voltages near 5–10 V. The current densities of individual nanowires calculated at voltage of 10 V, where SCLC is expected to be dominating mechanism, vary from 10^3 to 10^7 A/m^2 and scale with the nanowire dimensions.

The nanowire interconnects aligned by DEP had effective lengths of 4–10 μm, radii of 23–109 nm and aspect ratios L/r of 60–420, close to nanowires aligned by DMT with effective lengths of 1.2–8 μm, radii of 35–134 nm and L/r of 20–150. For nanowires with high aspect ratios, current densities in SCLC regime correlate with material properties, geometry and applied voltage as [23,28,29]:

$$j = \varsigma_0 \left(\frac{L}{r}\right)^2 \varepsilon_0 \varepsilon_p \mu \frac{V^2}{L^3}, \qquad (2)$$

where ς_0 is a factor related to nanowire aspect ratio, and μ is the carrier mobility. The dependence between L/r and $j \cdot L^3$ calculated at 10 V is in agreement with a power law $j \cdot L^3 \sim (L/r)^2$ (Fig. 4a, dashed line) for both DEP and DMT nanowires in the examined range. Log-log plot (Fig. 4a, inset) demonstrates good overlap between DEP and DMT nanowire interconnects. Some scatter of the data on the plot can be explained with differences in aspect ratios which change ς_0, and deviations from pure SCLC regime for individual nanowires.

For long DEP aligned nanowire interconnects, current densities j at 10 V correlate with their geometrical factor $1/(r^2 \cdot L)$ (Fig. 4b). The average carrier mobility in order of 0.01 cm^2/(V · s) estimated from the slope of a linear fit of the graph (Fig. 4b, dashed line) is consistent with the range of values between 10^{-3} and 10 cm^2/(V · s) for CuO nanowires from literature [7,11,30].

4. Conclusions

In summary, we systematically investigated the amount and morphology of the nanowire interconnects formed by dielectrophoresis at frequencies between 500 Hz and 500 kHz. Percentage of single-nanowire interconnects increases near 100 kHz frequency, which is defined by dielectric properties of the nanowires and the liquid media. Using dielectrophoresis for nanowire alignment between metallic electrodes is an approach suitable for fabrication of single-nanowire devices.

Characterization of the nanowire-electrode electrical contact interfaces revealed both ohmic and space charge limited conduction mechanisms contributing to the overall conductivity. The contact properties for nanowires transferred from liquid by dielectrophoresis and nanowires aligned on electrodes by dry mechanical transfer are similar. Owing to space charge limited currents, the conductance of the nanowire interconnects increases at high voltages, compared to relatively low ohmic part below 10^5 V/m. These nanowires can conduct relatively high currents without the additional step of contact modification, which is advantageous for fabrication of devices with suspended nanowires, such as nanoelectromechanical systems.

CRediT authorship contribution statement

Matiss Martins Ramma: Investigation, Formal analysis, Methodology, Writing – original draft. **Juris Katkevics:** Conceptualization, Investigation. **Liga Jasulaneca:** Conceptualization, Investigation. **Gunta Kunakova:** Investigation. **Raitis Sondors:** Investigation, Visualization. **Raimonds Meija:** Conceptualization, Investigation. **Donats Erts:** Conceptualization, Methodology, Supervision, Writing – review & editing. **Jelena Kosmaca:** Conceptualization, Methodology, Investigation, Formal analysis, Supervision, Writing – original draft, Writing – review & editing.

Declaration of Competing Interest

The authors declare that they have no known competing financial interests or personal relationships that could have appeared to influence the work reported in this paper.

Acknowledgments

This work was supported by the European Regional Development Fund (project no. 1.1.1.1/16/A/256, "Creation of nanoelectromechanical switches"). The authors wish to thank Juris Prikulis, Edijs Kauranens and Daniels Jevdokimovs for their help throughout the course of this work. J.K. is grateful to Tom Yager for useful discussions.

References

[1] A.M.B. Gonçalves, L.C. Campos, A.S. Ferlauto, R.G. Lacerda, On the growth and electrical characterization of CuO nanowires by thermal oxidation, J. Appl. Phys. 106 (2009) 34303.
[2] Q. Zhang, K. Zhang, D. Xu, G. Yang, H. Huang, F. Nie, C. Liu, S. Yang, CuO nanostructures: synthesis, characterization, growth mechanisms, fundamental properties, and applications, Prog. Mater. Sci. 60 (2014) 208–337.
[3] S. Steinhauer, E. Brunet, T. Maier, G.C. Mutinati, A. Köck, O. Freudenberg, C. Gspan, W. Grogger, A. Neuhold, R. Resel, Gas sensing properties of novel CuO nanowire devices, Sens. Actuators B Chem. 187 (2013) 50–57.
[4] O. Lupan, V. Postica, V. Cretu, N. Wolff, V. Duppel, L. Kienle, R. Adelung, Single and networked CuO nanowires for highly sensitive p-type semiconductor gas sensor applications, Phys. Status Solidi (RRL) Rapid Res. Lett. 10 (2016) 260–266.

[5] E.P.S. Tan, Y. Zhu, T. Yu, L. Dai, C.H. Sow, V.B.C. Tan, C.T. Lim, Crystallinity and surface effects on Young's modulus of CuO nanowires, Appl. Phys. Lett. 90 (2007), 163112.

[6] R. Sondors, J. Kosmaca, G. Kunakova, L. Jasulaneca, R. Meija, M.M. Ramma, E. Kauranens, M. Antsov, D. Erts, Size distribution, mechanical and electrical properties of CuO nanowires grown by modified thermal oxidation methods, Nanomaterials 10 (2020) 1051.

[7] J. Wu, B. Yin, F. Wu, Y. Myung, P. Banerjee, Charge transport in single CuO nanowires, Appl. Phys. Lett. 105 (2014), 183506.

[8] Z. Lin, R. Zhan, L. Li, H. Liu, S. Jia, H. Chen, S. Tang, J. She, S. Deng, N. Xu, et al., Defect-concentration dependence of electrical transport mechanisms in CuO nanowires, RSC Adv. 8 (2018) 2188–2195.

[9] L. Jasulaneca, J. Kosmaca, R. Meija, J. Andzane, D. Erts, Review: electrostatically actuated nanobeam-based nanoelectromechanical switches-materials solutions and operational conditions, Beilstein J. Nanotechnol. 9 (2018) 271–300.

[10] L. Jasulaneca, A. Livshits, R. Meija, J. Kosmaca, R. Sondors, M. Ramma, D. Jevdokimovs, J. Prikulis, D. Erts, Fabrication and characterization of double- and single-clamped CuO nanowire based nanoelectromechanical switches, Nanomaterials 11 (2021) 117.

[11] D. Li, J. Hu, R. Wu, J.G. Lu, Conductometric chemical sensor based on individual CuO nanowires, Nanotechnology 21 (2010), 485502.

[12] Q. Li, S.-.M. Koo, M.D. Edelstein, J.S. Suehle, C.A. Richter, Silicon nanowire electromechanical switches for logic device application, Nanotechnology 18 (2007), 315202.

[13] E.M. Freer, O. Grachev, X. Duan, S. Martin, D.P. Stumbo, High-yield self-limiting single-nanowire assembly with dielectrophoresis, Nat. Nanotechnol. 5 (2010) 525.

[14] M. Collet, S. Salomon, N.Y. Klein, F. Seichepine, C. Vieu, L. Nicu, G. Larrieu, Large-scale assembly of single nanowires through capillary-assisted dielectrophoresis, Adv. Mater. 27 (2015) 1268–1273.

[15] S. Raychaudhuri, S.A. Dayeh, D. Wang, E.T. Yu, Precise semiconductor nanowire placement through dielectrophoresis, Nano Lett. 9 (2009) 2260–2266.

[16] M. Sam, N. Moghimian, R.B. Bhiladvala, Field-directed assembly of nanowires: identifying directors, disruptors and indices to maximize the device yield, Nanoscale 8 (2016) 889–900.

[17] B.C. Gierhart, D.G. Howitt, S.J. Chen, R.L. Smith, S.D. Collins, Frequency dependence of gold nanoparticle superassembly by dielectrophoresis, Langmuir 23 (2007) 12450–12456.

[18] T.H. Kim, S.Y. Lee, N.K. Cho, H.K. Seong, H.J. Choi, S.W. Jung, S.K. Lee, Dielectrophoretic alignment of gallium nitride nanowires (GaN NWs) for use in device applications, Nanotechnology 17 (2006) 3394.

[19] C. Huang, X. Tian, J. Liu, Z. Dong, Y. Wang, The assembly and fabrication of single CuO nanowire electronic device based on controllable DWS-DEP technology, IEEE Trans. Nanotechnol. 14 (2014) 101–107.

[20] H.T. Hsueh, T.J. Hsueh, S.J. Chang, F.Y. Hung, T.Y. Tsai, W.Y. Weng, C.L. Hsu, B. T. Dai, CuO nanowire-based humidity sensors prepared on glass substrate, Sens. Actuators B Chem. 156 (2011) 906–911.

[21] S.Y. Lee, T.H. Kim, D.I. Suh, J.E. Park, J.H. Kim, C.J. Youn, B.K. Ahn, S.K. Lee, An electrical characterization of a hetero-junction nanowire (NW) PN diode (n-GaN NW/p-Si) formed by dielectrophoresis alignment, Phys. E Low Dimens. Syst. Nanostruct. 36 (2007) 194–198.

[22] U.H. Choi, J. Kim, Precise placement of metallic nanowires on a substrate by localized electric fields and inter-nanowire electrostatic interaction, Nanomaterials 7 (2017) 335.

[23] A.A. Talin, F. Léonard, B.S. Swartzentruber, X. Wang, S.D. Hersee, Unusually strong space-charge-limited current in thin wires, Phys. Rev. Lett. 101 (2008) 76802.

[24] G. Kunakova, R. Viter, S. Abay, S. Biswas, J.D. Holmes, T. Bauch, F. Lombardi, D. Erts, Space charge limited current mechanism in Bi_2S_3 nanowires, J. Appl. Phys. 119 (2016), 114308.

[25] S. Alagha, A. Shik, H.E. Ruda, I. Saveliev, K.L. Kavanagh, S.P. Watkins, Space-charge-limited current in nanowires, J. Appl. Phys. 121 (2017), 174301.

[26] N.K.R. Palapati, E. Pomerantseva, A. Subramanian, Single nanowire manipulation within dielectrophoretic force fields in the sub-crossover frequency regime, Nanoscale 7 (2015) 3109–3116.

[27] Y. Liu, J.-.H. Chung, W.K. Liu, R.S. Ruoff, Dielectrophoretic assembly of nanowires, J. Phys. Chem. B 110 (2006) 14098–14106.

[28] F. Léonard, A.A. Talin, A. Katzenmeyer, B.S. Swartzentruber, S.T. Picraux, E. Toimil-Molares, J.G. Cederberg, X. Wang, S.D. Hersee, A. Rishinaramangalum, Electronic transport in nanowires: from injection-limited to space-charge-limited behavior, in: Proceedings of the Nanoepitaxy: Homo- and Heterogeneous Synthesis, Characterization, and Device Integration of Nanomaterials, 2009, p. 74060G.

[29] A.M. Katzenmeyer, F. Léonard, A.A. Talin, M.E. Toimil-Molares, J.G. Cederberg, J. Y. Huang, J.L. Lensch-Falk, Observation of space-charge-limited transport in InAs nanowires, IEEE Trans. Nanotechnol. 10 (2010) 92–95.

[30] L.B. Luo, X.H. Wang, C. Xie, Z.J. Li, R. Lu, X.B. Yang, J. Lu, One-dimensional CuO nanowire: synthesis, electrical, and optoelectronic devices application, Nanoscale Res. Lett. 9 (2014) 1–8.

Paper V

nanomaterials

MDPI

Article

High-Yield Growth and Tunable Morphology of Bi_2Se_3 Nanoribbons Synthesized on Thermally Dewetted Au

Raitis Sondors [1], Gunta Kunakova [1], Liga Jasulaneca [1], Jana Andzane [1], Edijs Kauranens [1], Mikhael Bechelany [2] and Donats Erts [1,3,*]

[1] Institute of Chemical Physics, University of Latvia, 19 Raina Blvd., LV-1586 Riga, Latvia; raitis.sondors@lu.lv (R.S.); gunta.kunakova@lu.lv (G.K.); liga.jasulaneca@lu.lv (L.J.); jana.andzane@lu.lv (J.A.); edijs.kauranens@lu.lv (E.K.)

[2] Institut Européen des Membranes, IEM-UMR 5635, ENSCM, CNRS, University of Montpellier, Place Eugène Bataillon, 34095 Montpellier, France; mikhael.bechelany@umontpellier.fr

[3] Faculty of Chemistry, University of Latvia, 19 Raina Blvd., LV-1586 Riga, Latvia

* Correspondence: donats.erts@lu.lv

Abstract: The yield and morphology (length, width, thickness) of stoichiometric Bi_2Se_3 nanoribbons grown by physical vapor deposition is studied as a function of the diameters and areal number density of the Au catalyst nanoparticles of mean diameters 8–150 nm formed by dewetting Au layers of thicknesses 1.5–16 nm. The highest yield of the Bi_2Se_3 nanoribbons is reached when synthesized on dewetted 3 nm thick Au layer (mean diameter of Au nanoparticles ~10 nm) and exceeds the nanoribbon yield obtained in catalyst-free synthesis by almost 50 times. The mean lengths and thicknesses of the Bi_2Se_3 nanoribbons are directly proportional to the mean diameters of Au catalyst nanoparticles. In contrast, the mean widths of the Bi_2Se_3 nanoribbons do not show a direct correlation with the Au nanoparticle size as they depend on the contribution ratio of two main growth mechanisms—catalyst-free and vapor–liquid–solid deposition. The Bi_2Se_3 nanoribbon growth mechanisms in relation to the Au catalyst nanoparticle size and areal number density are discussed. Determined charge transport characteristics confirm the high quality of the synthesized Bi_2Se_3 nanoribbons, which, together with the high yield and tunable morphology, makes these suitable for application in a variety of nanoscale devices.

Keywords: Bi_2Se_3; nanoribbon; synthesis; physical vapor deposition

Citation: Sondors, R.; Kunakova, G.; Jasulaneca, L.; Andzane, J.; Kauranens, E.; Bechelany, M.; Erts, D. High-Yield Growth and Tunable Morphology of Bi_2Se_3 Nanoribbons Synthesized on Thermally Dewetted Au. *Nanomaterials* **2021**, *11*, 2020. https://doi.org/10.3390/nano11082020

Academic Editor: Paolo Calvani

Received: 30 June 2021
Accepted: 5 August 2021
Published: 7 August 2021

Publisher's Note: MDPI stays neutral with regard to jurisdictional claims in published maps and institutional affiliations.

Copyright: © 2021 by the authors. Licensee MDPI, Basel, Switzerland. This article is an open access article distributed under the terms and conditions of the Creative Commons Attribution (CC BY) license (https://creativecommons.org/licenses/by/4.0/).

1. Introduction

Bismuth Selenide (Bi_2Se_3) is a layered narrow bandgap semiconductor, which has been widely studied and demonstrated potential for application in optical recording systems [1], photochemical devices [2], battery electrodes [3], and thermoelectric devices [4]. This material belongs to the recently discovered class of three-dimensional topological insulators (TI), exhibiting conducting states with nondegenerate spins protected by time-reversal symmetry [5]. The simple surface states make Bi_2Se_3 an ideal candidate to realize various unique physical phenomena, such as quantum anomalous Hall effect, superconductivity, topological magnetoelectric effect, enhancement of thermoelectric figure of merit [5–10], as well as the bulk bandgap of Bi_2Se_3 specifies great potential for possible high-temperature spintronic applications [11].

However, the unique properties of Bi_2Se_3 surface states are challenging to utilize practically, as the bulk carriers overwhelm the surface carriers. Bi_2Se_3 nanostructures, such as nanoplates, nanowires, and nanoribbons, have emerged as perfect candidates for exploiting properties of the topological surface states due to their high surface-to-volume ratio [12,13]. For example, complete suppression of bulk conduction has been demonstrated in Bi_2Se_3 nanoribbons thinner than 30 nm [13]. The surface-to-volume ratio has also been shown to play an important role in tuning thermoelectric properties [14].

Bi_2Se_3 nanoribbons can reach lengths of tens of micrometers and even millimeters [15], allowing one to easily make multiple electrical connections to probe topological transport properties, as well as can serve as field-effect transistor channels [16] and active elements in nanoelectromechanical devices [17,18]. Successful applications of Bi_2Se_3 nanostructures as nanowires and nanoribbons have been demonstrated in the areas of thermoelectrics [19–21], photodetection [22], topological insulator devices [23–25], and nanoelectromechanical devices [17,18].

Both applications of Bi_2Se_3 nanoribbons in nanoelectromechanical devices and fabrication of electron transport devices employing topological insulator properties of the material require certain morphology of the nanoribbons. Methods for obtaining Bi_2Se_3 nanostructures include sonochemical [26], solvothermal [27], metal–organic chemical vapor deposition [28], and both catalyst-free and catalyst-assisted physical vapor deposition [12,27]. Catalyst-free physical vapor deposition methods are especially attractive due to the high quality of the synthesized nanostructures and contamination-free process [29]; however, these methods result in the formation of diverse nanostructures as nanoplates, nanoribbons, and nanowires of random morphology formed during one synthesis run. For practical applications in devices, it is necessary to control the morphology during the synthesis and to increase the yield of the synthesized nanostructures with the required geometry.

A good candidate for control of the morphology of the Bi_2Se_3 nanoribbons is catalyst-assisted synthesis, which has been widely exploited for the production of highly crystalline nanoribbons that exhibit distinct topological properties [30]. In this method, either as-deposited or pre-annealed (dewetted) Au thin film or colloidal Au particles have been used as catalysts promoting vapor–liquid–solid (VLS) [30] or vapor–solid–solid (VSS) [31] growth of the Bi_2Se_3 nanostructures. In the classical vapor–liquid–solid (VLS) growth reported for the 20–30 nm Au nanoparticles, the source material in the vapor phase diffuses into a liquid-metal catalyst. The concentration of the source material is increased until the solubility limit is reached and precipitation of the solid nanostructure takes place. Depending on the size and temperature-dependent surface and body diffusion coefficients of adatoms, the nucleation and further growth of the nanostructures can occur on the top (the catalyst nanoparticle remains on the substrate, the nanostructure grows up) or bottom (the catalyst nanoparticle remains on the tip of the grown nanostructure) surface of the catalyst nanoparticle [32]. In the VSS growth mode, the vapor of the source material penetrates the catalyst particle remaining in the solid state; however, there are very limited reports on Au-catalyzed VSS growth of the Bi_2Se_3 nanostructures claiming the occurrence of this mode instead of VLS when the Au nanoparticle size is 300 nm and above [31]. While it has been reported that the presence of the Au catalyst influences the Bi_2Se_3 nanostructure morphology evolution at the initial growth stage, most of the studies of VLS Bi_2Se_3 growth employ only one particular size of the catalyst nanoparticles or thickness of the catalyst layer. To the best of knowledge, there are no reports on the systematic investigation of the dependence of morphology and yield of the Bi_2Se_3 nanoribbons on the size and areal number density of the Au catalyst nanoparticles.

In this work, the Bi_2Se_3 nanoribbon morphology and yield are studied in relation to the diameter and areal number density of Au nanoparticles formed during the pre-annealing of Au catalyst layers of different thicknesses. The contribution of two different growth mechanisms—catalyst-free and vapor–liquid–solid—to the outcome of the Bi_2Se_3 nanoribbon synthesis and mechanical transfer of the nanoribbons to other substrates resulting in the selective transfer of nanoribbons of certain geometry is discussed.

Charge transport properties of the Bi_2Se_3 nanoribbons grown on the Au catalyst layer promoting the highest yield indicate consistency with the previously reported nanoribbon magnetotransport characteristics.

2. Materials and Methods

Au films with thicknesses from 1.5 to 16 nm were deposited on microscope glass slides (25 × 75 mm^2) using thermal evaporation in a Sidrabe SAF EM metal deposition system. The films were annealed in an inert atmosphere by heating from room temperature to 585 °C for 45 min at a rate of 13 °C/min at a starting pressure of 2 Torr. The temperature was kept at 585 °C for 15 min, after which the substrate was allowed to cool naturally. Then, the size distribution and the areal number density of the formed Au nanoparticles were characterized using a scanning electron microscope (SEM, Hitachi FE-SEM S-4800, Tokyo, Japan). The obtained SEM images were analyzed with ImageJ software.

Bi_2Se_3 nanoribbons were grown on the as-produced dewetted Au substrates [29]. The source material (99.999% Bi_2Se_3 powder, Sigma-Aldrich, Burlington, MA, USA) was placed in the center of the quartz furnace tube where the temperature reaches a maximum of 585 °C during the deposition process. The substrates were placed downstream from the source material where the temperature reaches a maximum of 375–490 °C during the deposition process. The furnace was flushed with nitrogen for 3–5 min, then heated from room temperature at a rate of 13 °C/min for 45 min at a starting pressure of 2 Torr until the temperature in the center of the furnace reached 585 °C. The furnace was held at 585 °C for 15 min and cooled down to 535 °C at a cooling rate of 8 °C/min. When the temperature had dropped to 535 °C, a nitrogen gas flow at a constant pressure of 25 Torr was introduced into the furnace tube to induce the growth of nanoribbons. When the temperature had dropped to 475 °C, the synthesis was terminated by filling the tube with nitrogen until the pressure had reached 1 atm.

Number density and distribution of lengths and widths of the nanoribbons were determined by SEM by inspection of as-grown samples. The thicknesses of the nanoribbons were determined using an atomic force microscope (AFM, Asylum Research MFP-3D, Santa Barbara, CA, USA). For AFM characterization, the as-synthesized nanostructures were mechanically transferred to Si/SiO_2 chips by pressing the chip against the region of interest on the substrate.

The crystalline structure of the synthesized samples was studied using X-ray diffraction spectroscopy (powder diffractometer X'PERT MRD with Cu Kα radiation source, Malvern Panalytical Ltd., Malvern, UK), ref. card No. 96-901-1966 [33].

For determination of transport properties, nanoribbons grown on a dewetted Au layer of initial thickness 3 nm were transferred to Si/SiO_2 substrates, and electron beam lithography (Raith, eLine) followed by metal evaporation (5 nm Ti/80 nm Au, Sidrabe, Riga, Latvia) was used to fabricate electrical contacts. Magnetotransport measurements were performed with a Quantum Design DynaCool 9T physical property measurement system (San Diego, CA, USA). Resistance was recorded in a four-probe measurement setup, and the magnetic field was applied perpendicular to the nanoribbon top surface.

3. Results and Discussion

3.1. Yield and Morphology

Au nanoparticles with mean diameter from 10 nm to 148 nm and number density from 9 nps/μm^2 to 8000 nps/μm^2 were formed by dewetting Au layers with initial thickness from 1.5 nm to 16 nm, with thicker initial Au layers yielding larger Au nanoparticles (Figure 1a–c).

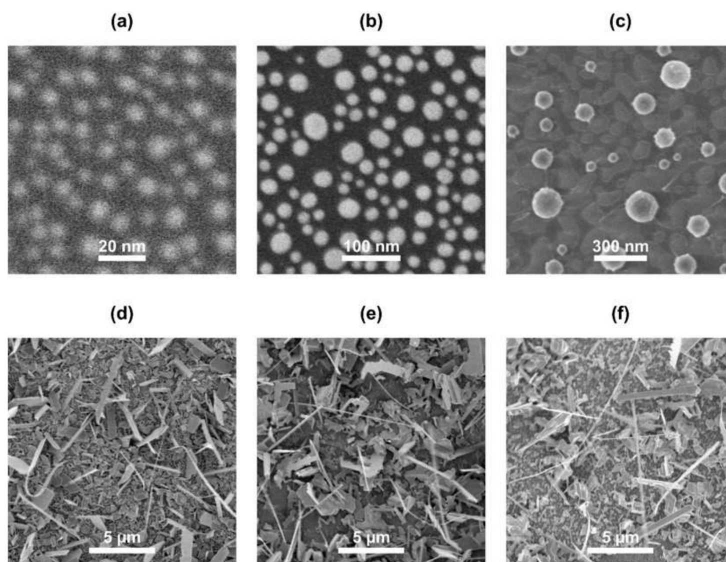

Figure 1. SEM images: (**a**–**c**) Thermally dewetted Au layers with various initial layer thicknesses: (**a**) 3 nm; (**b**) 9 nm; (**c**) 13 nm; (**d**–**f**) Bi_2Se_3 nanostructures synthesized on dewetted Au layers with various initial layer thicknesses: (**d**) 3 nm; (**e**) 9 nm; (**f**) 13 nm.

The effect of the initial Au layer thickness h on the mean dewetted Au nanoparticle diameter $\langle D \rangle$ was described, approximating $\langle D \rangle$ by a power function of h as $\langle D \rangle \sim h^Z$ [19] (Figure 2a). The blue line shows the equation fitted to the experimental data. Approximating the nanoparticles as perfect spheres and assuming conservation of volume, the resultant Au nanoparticle number density N can be estimated by dividing the initial Au volume per substrate area $\frac{V_L}{A_S}$ by the mean volume of the nanoparticle V_{NP}:

$$N = \frac{V_L}{A_S \cdot V_{NP}} = \frac{6h}{\pi \langle D \rangle^3}.$$

By comparing experimentally measured and calculated Au nanoparticle number density (Figure 2b), it can be seen that the theoretical model describes the experimental data reasonably well.

SEM images of the substrate with deposited Bi_2Se_3 showed that the surface of the substrate was covered with a layer of Bi_2Se_3 nanostructures (Figure 1d–f). Energy-dispersive X-ray spectroscopy measurements confirmed stoichiometric nanostructure growth in a region where the maximum temperature reached 443 ± 9 °C during Bi_2Se_3 deposition. In total, more than 70,000 measurements were made in this region to determine nanowire Bi_2Se_3 nanoribbon geometrical parameters.

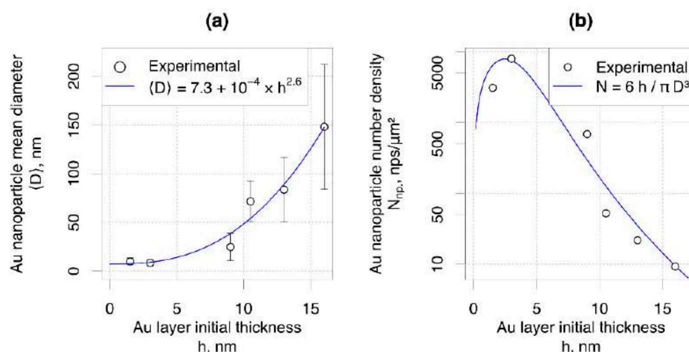

Figure 2. (**a**) Mean Au nanoparticle diameter, the blue line is a fitted power function; (**b**) Au nanoparticle number density (the blue line is the expected number density).

The areal number density of the Bi_2Se_3 nanoribbons vs. the initial Au layer thickness showed pronounced non-linear dependence with a maximum at 3 nm thin Au layer (Figure 3a); however, the number density of the nanoribbons per 1000 nanoparticles showed a linear increase with the increase of the nanoparticle diameter (Figure 3b), which may indicate increasing domination of the VLS growth mechanism over the catalyst-free growth, as discussed in detail in Section 3.2 of this article. The mean length of the synthesized Bi_2Se_3 nanoribbons showed almost no changes for the initial Au layer thicknesses below 5 nm and correspondingly for the Au nanoparticles with diameters below 50 nm; however, the increase of the initial thickness of the Au layer above 5 nm and consequently of the sizes of Au nanoparticle above 50 nm resulted in the pronounced increase of the mean lengths of the Bi_2Se_3 nanoribbons (Figure 3c,d). Bi_2Se_3 nanoribbon length dependence indicates that larger Au nanoparticles correspond to the increased growth rate of the nanoribbons, possibly because of an increased Au catalyst surface area, which enables a greater Bi_2Se_3 throughput. Positive dependences on the initial thickness of the Au layer and on the diameter of the Au nanoparticles were also observed for the mean thickness of the Bi_2Se_3 nanoribbons (Figure 3e,f). The nearly linear relationship between Bi_2Se_3 nanoribbon thickness and Au nanoparticle size can be explained by the effect of surface stresses at the VLS triple-phase junction during nanoribbon growth [34]—the angle between the Au nanoparticle and Bi_2Se_3 nanoribbon α is a function of surface tensions: $sin\alpha = \gamma_{VS}/\gamma_{VL} = T/D_{NP}$, where γ_{VS} is the vapor/solid surface tension, γ_{VL} is the vapor/liquid surface tension, T is nanoribbon thickness and D_{NP} is nanoparticle diameter. If the angle between the Au nanoparticle and Bi_2Se_3 nanoribbon surfaces is constant, then the nanoribbon thickness is expected to be directly proportional to nanoparticle diameter. In contrast, the mean width of the Bi_2Se_3 nanoribbons vs. Au layer thickness as well as vs. Au nanoparticle diameter showed pronounced non-linear dependence with a minimum at 3 nm thin Au film and Au nanoparticles with diameters ~10 nm (Figure 3g,h). Presumably, the widths of the nanoribbons may depend on the prevailing nucleation and growth mode and be governed either by the size of the Au nanoparticle or by the nanoplate seed, as is discussed in detail in the next section. It should also be noted that the widths of the nanoribbons were extracted from the SEM images of as-grown samples by measuring the visualized projections of the nanoribbons, which does not allow high-accuracy determination of actual nanoribbon width.

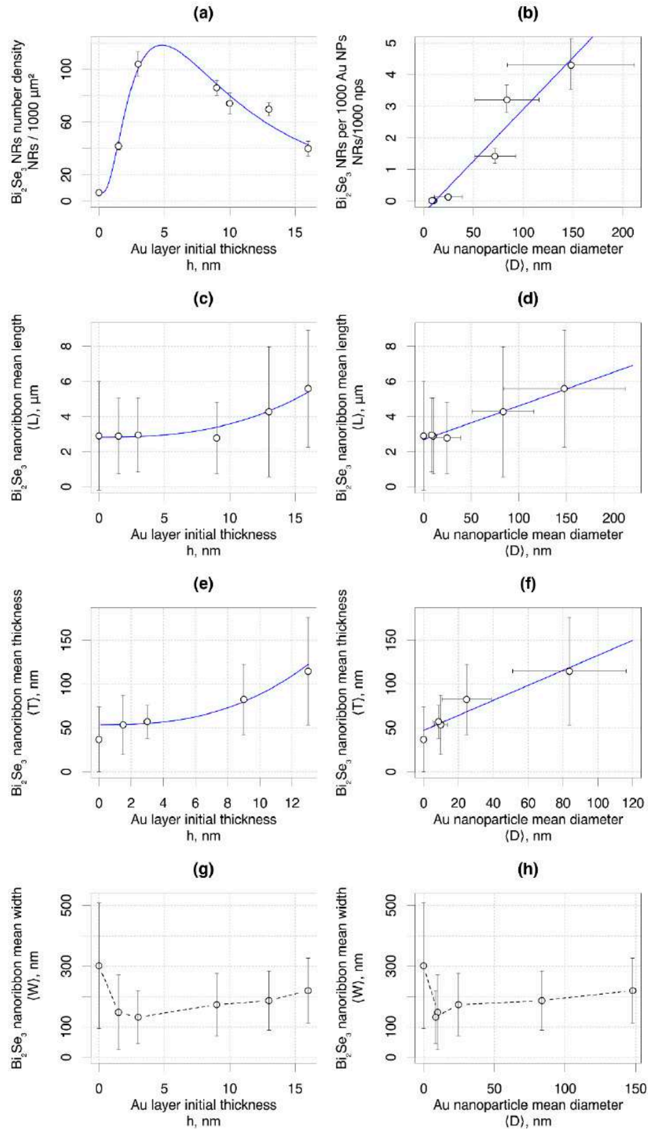

Figure 3. Various Bi_2Se_3 nanoribbon parameters as a function of initial Au layer thickness: (**a**,**c**,**e**,**g**) and Au nanoparticle mean diameter (**b**,**d**,**f**,**h**). The blue lines are guides to the eye.

3.2. Growth Mechanism

A significant part of the nanoribbons was found to be growing from the nanoplates seeds (Figure 4a), which is consistent with the growth mechanism observed in the similar two-step catalyst-free synthesis process [13,29] when the width of the nanoribbon is governed by the width of the nanoplate facet it starts from.

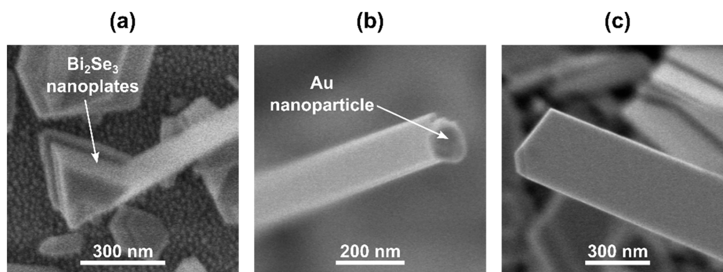

Figure 4. SEM images of synthesized Bi_2Se_3 nanostructures: (**a**) Nanoplates at the base of a nanoribbon; (**b**) nanoribbon with a Au nanoparticle at the tip; (**c**) nanoribbon with no Au nanoparticle droplet at the tip.

The XRD spectra of Bi_2Se_3 nanostructures synthesized on the dewetted layers of Au particles of mean diameters ~10 and ~85 nm, obtained from 3 nm and 13 nm thick Au layers, respectively, with the XRD spectra of Bi_2Se_3 nanostructures grown on a glass substrate by the catalyst-free method showed a decreased intensity of diffraction peaks corresponding to Bi_2Se_3 nanostructure growth with the c-axis perpendicular to the substrate surface (peaks at 9.26°, 18.58°, and 27.94° correspond to Bi_2Se_3 crystallographic planes (003), (006), and (009), all belonging to the (003n) group), accompanied by an increase of intensity for diffraction peaks related to other Bi_2Se_3 crystallographic planes (104), (015), (1010), and (110) (Figure 5). According to previous reports, the increase of intensity of these XRD peaks has a direct correlation with the number of the Bi_2Se_3 nanoplates tilted relative to the substrate surface under the angles of 35°, 54°, and >65°, respectively, which was confirmed by the AFM [35] and SEM [13] characterization.

These XRD peaks are the most intensive for the Bi_2Se_3 nanostructures grown on 3 nm (nanoparticle size ~10 nm) thick Au layer (Figure 5b), indicating the highest number of the tilted nanoplates in comparison to the other samples and explaining the highest yield of the Bi_2Se_3 nanoribbons per area unit (Figure 3a), as it was reported previously that the tilted nanoplates promote the nanoribbon growth [13]. Presumably, the large number of tilted nanoplates originates from their growth initiated by the VLS growth mechanism with prevailing Bi_2Se_3 nucleation mode on the top surface of the Au nanoparticles due to their small diameters [31,32]. Formed on the top of the catalyst nanoparticles, these nanoplates promote further catalyst-free growth of the nanoribbons. At the same time, ~20–30% of the Bi_2Se_3 nanoribbons grown on this sample had a Au nanoparticle on its tip, indicating a VLS growth mechanism with the nucleation on the bottom surface of the catalyst, which is expected for the Au catalyst nanoparticles of large diameters. In this case, the width of the nanoribbon is governed by the size of the Au nanoparticle. While typically, the VLS-grown anisotropic nanoribbons are wider than the diameters of the catalyst nanoparticles [36], the size of the nanoparticle limits the maximal widths of the nanoribbons. For example, the widths of the nanoribbons grown on 20 nm Au nanoparticles typically do not exceed 100 nm for the nanoparticles with a diameter ~20 nm [37]. Thus, the contribution of the relatively narrow VLS-grown nanoribbons results in an indicative decrease of their mean widths for the sample grown on 1.5 nm and 3 nm (nanoparticle size ~8–10 nm) thin Au layers in comparison with the nanoribbons grown by catalyst-free method (Figure 3g).

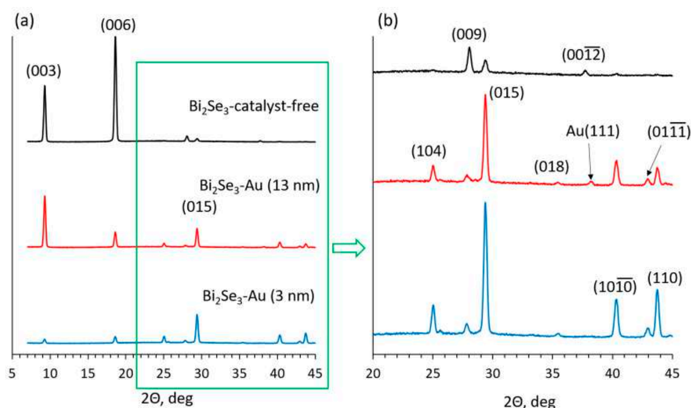

Figure 5. (**a**) XRD spectra of Bi_2Se_3 nanostructures grown on glass by the catalyst-free method (black curve), 13 nm thick dewetted Au layer (red curve), and 3 nm thick dewetted Au layer (blue curve); (**b**) closer look at the XRD diffraction peaks corresponding to the tilted Bi_2Se_3 nanostructures (ref. card No. 96-901-1966).

The sample grown on the 13 nm thin Au layer (mean Au nanoparticle diameter ~85 nm) had less intensive XRD peaks related to the tilted nanoplates (Figure 5b) in comparison with the sample synthesized on a 3 nm thin Au layer, which may explain the decrease of the areal number density of the nanoribbons grown on 13 nm thin Au layer (Figure 3a). At the same time, significantly higher in comparison with the samples synthesized on 3 nm Au layer proportion of the nanoribbons presented a Au nanoparticle on its tip (~60–70%) (Figure 4b). This indicates VLS [5] or even VSS [31] growth mechanism with Bi_2Se_3 nucleation and growth occurring on the bottom surface of the nanoparticle, which is expected for the Au catalyst nanoparticles with diameters above 20 nm at the growth temperature used in the experiments (~450 °C) [32]. Larger Au nanoparticle diameters result in larger widths of the grown nanoribbons due to the higher throughput of the source vapor. Additionally, the relatively large and rarely located Au nanoparticles formed by the dewetting of thicker than 5 nm (Figure 2) Au layers allow growth of the planar (with c-axis oriented perpendicularly to the substrate surface) Bi_2Se_3 nanoplates between the Au nanoparticles, which is proved by the presence of dominating (003) diffraction peak at 2Θ 9.26° in the XRD pattern of this sample (Figure 5). Some of the planar nanoplates become seeds for the catalyst-free growth of the Bi_2Se_3 nanoribbons, which are normally wider in comparison with the catalyst-grown (Figure 4c) [29]. The total contribution of the widths of the VLS-grown and catalyst-free grown nanoribbons to the statistics results in a slight increase of the mean widths of the nanoribbons with the increase of the thickness of the initial Au layer above 3 nm and diameters of the Au nanoparticles above 20 nm (Figure 3g,h).

The statistical results on the dependence of the mean length, thickness, and width of the Bi_2Se_3 nanoribbons clearly show that the required geometry of the nanoribbons can be obtained by choice of the initial thickness of the Au layer or by choice of diameter of catalyst nanoparticles; however, practical applications of the nanoribbons often require their transfer to other surfaces. Depending on the initial thickness of the Au layer and correspondingly, the diameters of the Au nanoparticles formed by dewetting of these layers, the nanoribbons of certain widths may be selectively transferred by a mechanical pressing process. In this process, only the nanoribbons having weak adhesion to the substrate/nanoplate seed and freestanding above the substrate surface are transferred. The mean width of the mechanically transferred Bi_2Se_3 nanoribbons vs. thickness of the initial Au layer showed a minimum for the catalyst-free synthesis and a maximum for the sample

synthesized on a 3 nm thin Au layer. The mean widths of the nanoribbons transferred from the samples grown on thicker Au layers showed a tendency for a slight decrease followed by a slight increase, but these deviations were within error limits (Figure 6a).

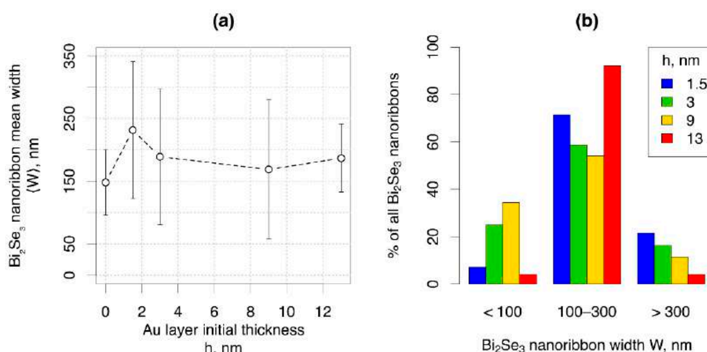

Figure 6. (**a**) Width distribution of Bi_2Se_3 nanoribbons mechanically transferred from the dewetted Au layers of various thicknesses; (**b**) width distribution histogram.

The width distribution histogram (Figure 6b) showed the differences in statistically prevailing nanoribbon widths in samples synthesized on Au layers of different thicknesses. The largest percentage (~25–35%) of the Bi_2Se_3 nanoribbons narrower than 100 nm was transferred from the samples synthesized on Au layers with thicknesses 3 nm and 9 nm. The percentage of Bi_2Se_3 nanoribbons wider than 300 nm was maximal (~20%) for the sample synthesized on a 1.5 nm thin Au layer and gradually decreased with the increase of the Au layer thickness. In turn, ~90% of the nanoribbons transferred from the sample grown on a 13 nm thin Au layer had widths between 100 and 300 nm. These findings are important for the applications employing blind transfer of the nanoribbons due to the high probability that the nanoribbons of the required geometry will be transferred to the desired locations.

3.3. Carrier Transport Properties

Due to their high yield, Bi_2Se_3 nanoribbons from the synthesis with an initial Au layer thickness of 3 nm were selected for electron transport property measurements. In total, four nanoribbons of different thicknesses (32–120 nm) were measured. A SEM image of one of the nanoribbon devices is shown in Figure 7a. Temperature dependence of the sheet resistance for all the measured nanoribbons is plotted in Figure 7b ($R_{xxSheet} = R_{xx}w/L$, where R_{xx} is the resistance measured with a four-probe configuration, L is the length and w is the width of a nanoribbon). Its nearly linear behavior indicates metallic conduction frequently observed in Bi_2Se_3 [38–40].

Magnetoresistance $R_{xx}(B)$ dependence at a temperature of 2 K shows oscillations at the magnetic field above ~4 T (Figure 7c, nanoribbon NW3, t = 120 nm). These are the Shubnikov–de Haas oscillations (SdHO). Residual resistance ΔR_{xx} obtained by removal of polynomial background is not strictly periodic in $1/B$ (Figure 7d), and Fourier transform gives three frequencies, all below 100 T (see in the inset of Figure 7c). The multiple-frequency SdHO (3 frequencies, all below 100 T) were also recorded for the three other nanoribbons of smaller thicknesses (32, 45, and 56 nm). The multi-frequency SdHO pattern has previously been reported for Bi_2Se_3 nanoribbons with thicknesses above ~30 nm [13,15,40,41]. Here, measured nanoribbons are of relatively large thicknesses, and the complex pattern of the SdHO originates from the coexistence of the 3D bulk carriers, the 2D topological surface states, and (or) trivial 2D states [13,40,41].

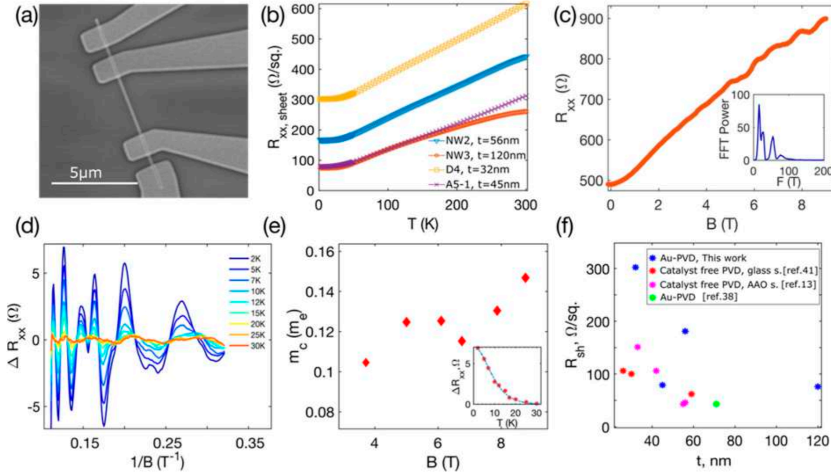

Figure 7. Magnetotransport in 3 nm Au-PVD Bi_2Se_3 nanoribbons: (**a**) SEM image of Bi_2Se_3 nanoribbon device used in transport measurements (nanoribbon A5-1); (**b**) sheet resistance $R_{xxSheet}$ ($= R_{xx}w/L$) as a function of temperature. (**c**) Magnetoresistance R_{xx} of the nanoribbon NW3 measured at 2 K. Inset: FFT spectra of Shubnikov–de Haas oscillations. (**d**) Shubnikov–de Haas oscillations with the subtracted background of the nanoribbon NW3, measured at temperatures 2–30 K. (**e**) Cyclotron mass versus magnetic field. Inset: oscillation amplitude as a function of temperature, dashed blue line is the LK fit yielding $m_c = 0.130m_e$ and the data correspond to the 2nd peak from the left in the $\Delta R_{xx}(1/\mathrm{B})$ plot. (**f**) Sheet resistance versus nanoribbon thickness for Bi_2Se_3 nanoribbons synthesized using different approaches: catalyst-free PVD on a glass substrate, data from [41], catalyst-free PVD on anodized alumina (AAO), data from [13], Au-PVD, data from [38].

The temperature dependence of the SdHO (Figure 7d) was measured to determine the cyclotron mass m_c. The values of m_c at a given magnetic field were estimated by fitting the oscillation amplitude ΔR_{xx} temperature dependence with the Lifshitz–Kosevich (LK) theory [42]. The ΔR_{xx}(T) dependence at B = 8 T with the corresponding LK fit is plotted in the inset of Figure 7e, and determined masses are shown in Figure 7e. The calculated m_c varies from ~0.105 to 0.147 m_e, where m_e is the electron mass. The previously reported value of 0.13 m_e determined by the ARPES of Bi_2Se_3 bulk single crystal [39] fits well within this range, indicating the high quality of the Bi_2Se_3 nanoribbons synthesized in this work.

Figure 7f summarizes determined $R_{xxSh.}$ for all four measured Bi_2Se_3 nanoribbons. These data are comparable to the sheet resistances of Bi_2Se_3 nanoribbons synthesized using the: (1) catalyst-free PVD on a glass substrate, (2) catalyst-free PVD on AAO substrate, and (3) Au-PVD approach. The nanoribbons grown using the 3 nm-Au-PVD approach have an $R_{xxSh.}$ approximately 2–3 times higher. This implies lower carrier density and indicates that the chemical potential in these nanoribbons could be tuned more efficiently by gating techniques, which is important in accessing the transport via the surface Dirac states.

4. Conclusions

Physical vapor deposition of Bi_2Se_3 nanoribbons on dewetted Au layers allows tuning Bi_2Se_3 nanoribbon morphology and yield through the initial Au layer thickness. The initial Au layer thickness impacts the size and number density of Au nanoparticles and, consequently, the yield of synthesized Bi_2Se_3 nanoribbons—the highest nanoribbon number density is achieved at an initial Au layer thickness of 3 nm. There are more tilted Bi_2Se_3 nanostructures synthesized on dewetted Au, compared to catalyst-free syntheses. A larger amount of tilted Bi_2Se_3 nanostructures corresponds to a larger nanoribbon number density.

Changes in nanoribbon geometry suggest that the dominating Bi_2Se_3 nanoribbon growth mechanism possibly depends on the diameter and number density of Au nanoparticles. For the initial Au layer thicknesses below 5 nm (average size of Au nanoparticles ~8–10 nm), the catalyst-free Bi_2Se_3 nanoribbon growth from the tilted relative to the substrate surface Bi_2Se_3 nanoplate seeds dominates. For the initial Au layers of thicknesses above 5 nm (average sizes of Au nanoparticles 20–150 nm), the vapor–liquid–solid mechanism with nucleation at the bottom surface of the Au catalyst nanoparticle becomes dominant.

Different frequencies extracted from observed Shubnikov–de Haas oscillations in the synthesized nanoribbons indicate the presence of 3D bulk carriers, as well as 2D topological surface states and (or) trivial 2D states. Determined values of the sheet resistance are about two times higher compared to the ones reported for catalyst-free synthesized nanoribbons, the potential for improving tunability of chemical potential via electrostatic gating and accessing the transport via topological surface states. This confirms that the use of thermally dewetted Au catalyst layers for the high-yield synthesis of Bi_2Se_3 nanoribbons with tuned morphology does not result in degradation of transport properties of the nanoribbons. The possibility of adjusting synthesis parameters in order to tune the yield and morphology of synthesized Bi_2Se_3 nanoribbons and good transport properties makes them great candidates for applications in nanoelectromechanical devices, where the geometry of the active element determines the operational parameters of the device. The mechanical transfer of the Bi_2Se_3 nanoribbons grown on Au layers of different initial thicknesses and, respectively, on Au nanoparticles of different diameters is found to be selective to the nanoribbon geometry. This allows transferring to the other substrates the nanoribbons of required geometry with an efficiency of up to 90%.

Author Contributions: Conceptualization, D.E.; formal analysis, J.A. and G.K.; investigation, R.S., L.J., J.A., E.K. and M.B.; writing—original draft preparation, R.S.; writing—review and editing, G.K., L.J., J.A., E.K. and D.E.; visualization R.S., G.K. and J.A.; supervision, D.E.; project administration, D.E. All authors have read and agreed to the published version of the manuscript.

Funding: This research was funded by the Latvian Council of Science (project "Topological insulator nanoelectromechanical current control devices for applications at cryogenic temperatures" (No. lzp-2019/1-0349)) and by the European Union's Horizon 2020 research and innovation program (grant agreement No. 766714/HiTIMe). L. J. acknowledges the support of the University of Latvia patron "Mikrotīkls". The patron's donations are administered by the University of Latvia Foundation. G.K. acknowledges the Latvian Council of Science (project "Highly tunable surface state transport in topological insulator nanoribbons" (No. lzp-2020/2-0343)).

Institutional Review Board Statement: Not applicable.

Informed Consent Statement: Not applicable.

Data Availability Statement: The data presented in this study are available on request from the corresponding author.

Conflicts of Interest: The authors declare no conflict of interest. The funders had no role in the design of the study; in the collection, analyses, or interpretation of data; in the writing of the manuscript, or in the decision to publish the results.

References

1. Watanabe, K.; Sato, N.; Miyaoka, S. New optical recording material for video disc system. *J. Appl. Phys.* **1983**, *54*, 1256–1260. [CrossRef]
2. Waters, J.; Crouch, D.; Raftery, J.; O'Brien, P. Deposition of bismuth chalcogenide thin films using novel single-source precursors by metal-organic chemical vapor deposition. *Chem. Mater.* **2004**, *16*, 3289–3298. [CrossRef]
3. Kumari, P.; Singh, R.; Awasthi, K.; Ichikawa, T.; Kumar, M.; Jain, A. Highly stable nanostructured Bi_2Se_3 anode material for all solid-state lithium-ion batteries. *J. Alloys Compd.* **2020**, *838*, 155403. [CrossRef]
4. Mishra, S.K.; Satpathy, S.; Jepsen, O. Electronic structure and thermoelectric properties of bismuth telluride and bismuth selenide. *J. Phys. Condens. Matter* **1997**, *9*, 461. [CrossRef]
5. Kong, D.; Randel, J.C.; Peng, H.; Cha, J.J.; Meister, S.; Lai, K.; Chen, Y.; Shen, Z.-X.; Manoharan, H.C.; Cui, Y. Topological insulator nanowires and nanoribbons. *Nano Lett.* **2010**, *10*, 329–333. [CrossRef]

6. Yu, R.; Zhang, W.; Zhang, H.-J.; Zhang, S.-C.; Dai, X.; Fang, Z. Quantized anomalous Hall effect in magnetic topological insulators. *Science* **2010**, *329*, 61–64. [CrossRef] [PubMed]
7. Kunakova, G.; Bauch, T.; Trabaldo, E.; Andzane, J.; Erts, D.; Lombardi, F. High transparency Bi_2Se_3 topological insulator nanoribbon Josephson junctions with low resistive noise properties. *Appl. Phys. Lett.* **2019**, *115*, 172601. [CrossRef]
8. Kunakova, G.; Surendran, A.P.; Montemurro, D.; Salvato, M.; Golubev, D.; Andzane, J.; Erts, D.; Bauch, T.; Lombardi, F. Topological insulator nanoribbon Josephson junctions: Evidence for size effects in transport properties. *J. Appl. Phys.* **2020**, *128*, 194304. [CrossRef]
9. Zhang, J.; Chang, C.-Z.; Tang, P.; Zhang, Z.; Feng, X.; Li, K.; Wang, L.; Chen, X.; Liu, C.; Duan, W. Topology-driven magnetic quantum phase transition in topological insulators. *Science* **2013**, *339*, 1582–1586. [CrossRef]
10. Sun, Y.; Cheng, H.; Gao, S.; Liu, Q.; Sun, Z.; Xiao, C.; Wu, C.; Wei, S.; Xie, Y. Atomically thick bismuth selenide freestanding single layers achieving enhanced thermoelectric energy harvesting. *J. Am. Chem. Soc.* **2012**, *134*, 20294–20297. [CrossRef]
11. Liu, Q.; Liu, C.-X.; Xu, C.; Qi, X.-L.; Zhang, S.-C. Magnetic impurities on the surface of a topological insulator. *Phys. Rev. Lett.* **2009**, *102*, 156603. [CrossRef]
12. Yan, Y.; Wang, L.-X.; Yu, D.-P.; Liao, Z.-M. Large magnetoresistance in high mobility topological insulator Bi_2Se_3. *Appl. Phys. Lett.* **2013**, *103*, 33106. [CrossRef]
13. Kunakova, G.; Meija, R.; Andzane, J.; Malinovskis, U.; Petersons, G.; Baitimirova, M.; Bechelany, M.; Bauch, T.; Lombardi, F.; Erts, D. Surface structure promoted high-yield growth and magnetotransport properties of Bi_2Se_3 nanoribbons. *Sci. Rep.* **2019**, *9*, 11328. [CrossRef]
14. Shin, H.S.; Hamdou, B.; Reith, H.; Osterhage, H.; Gooth, J.; Damm, C.; Rellinghaus, B.; Pippel, E.; Nielsch, K. The surface-to-volume ratio: A key parameter in the thermoelectric transport of topological insulator Bi_2Se_3 nanowires. *Nanoscale* **2016**, *8*, 13552–13557. [CrossRef]
15. Fang, L.; Jia, Y.; Miller, D.J.; Latimer, M.L.; Xiao, Z.L.; Welp, U.; Crabtree, G.W.; Kwok, W.-K. Catalyst-free growth of millimeter-long topological insulator Bi_2Se_3 nanoribbons and the observation of the π-Berry phase. *Nano Lett.* **2012**, *12*, 6164–6169. [CrossRef]
16. Zhu, H.; Richter, C.A.; Zhao, E.; Bonevich, J.E.; Kimes, W.A.; Jang, H.-J.; Yuan, H.; Li, H.; Arab, A.; Kirillov, O. Topological insulator Bi_2Se_3 nanowire high performance field-effect transistors. *Sci. Rep.* **2013**, *3*, 1757. [CrossRef]
17. Kosmaca, J.; Andzane, J.; Baitimirova, M.; Lombardi, F.; Erts, D. Role of nanoelectromechanical switching in the operation of nanostructured Bi_2Se_3 interlayers between conductive electrodes. *ACS Appl. Mater. Interfaces* **2016**, *8*, 12257–12262. [CrossRef] [PubMed]
18. Meija, R.; Livshits, A.I.; Kosmaca, J.; Jasulaneca, L.; Andzane, J.; Biswas, S.; Holmes, J.D.; Erts, D. Resonance assisted jump-in voltage reduction for electrostatically actuated nanobeam-based gateless NEM switches. *Nanotechnology* **2019**, *30*, 385203. [CrossRef]
19. Wei, P.C.; Chen, Y.Y. Thermoelectric Characteristics of A Single-Crystalline Topological Insulator Bi2Se3 Nanowire. *Nanomaterials* **2021**, *11*, 819.
20. Xiong, Y.; Zhou, G.; Lai, N.-C.; Wang, X.; Lu, Y.-C.; Prezhdo, O.V.; Xu, D. Chemically Switchable n-Type and p-Type Conduction in Bismuth Selenide Nanoribbons for Thermoelectric Energy Harvesting. *ACS Nano* **2021**, *15*, 2791–2799. [CrossRef]
21. Andzane, J.; Felsharuk, A.; Sarakovskis, A.; Malinovskis, U.; Kauranens, E.; Bechelany, M.; Niherysh, K.A.; Komissarov, I.V.; Erts, D. Thickness-dependent properties of ultrathin bismuth and antimony chalcogenide films formed by physical vapor deposition and their application in thermoelectric generators. *Mater. Today Energy* **2021**, *19*, 100587. [CrossRef]
22. Liu, J.L.; Chen, H.; Li, X.; Wang, H.; Zhang, Z.K.; Pan, W.W.; Yuan, G.; Yuan, C.L.; Ren, Y.L.; Lei, W. Ultra-fast and high flexibility near-infrared photodetectors based on Bi_2Se_3 nanobelts grown via catalyst-free van der Waals epitaxy. *J. Alloys Compd.* **2020**, *818*, 152819. [CrossRef]
23. Breunig, O.; Ando, Y. Fabrication of topological insulator devices. *arXiv* **2021**, arXiv:2101.12538.
24. Appelbaum, I.; Drew, H.D.; Fuhrer, M.S. Proposal for a topological plasmon spin rectifier. *Appl. Phys. Lett.* **2011**, *98*, 23103. [CrossRef]
25. Tian, J.; Hong, S.; Miotkowski, I.; Datta, S.; Chen, Y.P. Observation of current-induced, long-lived persistent spin polarization in a topological insulator: A rechargeable spin battery. *Sci. Adv.* **2017**, *3*, e1602531. [CrossRef] [PubMed]
26. Qiu, X.; Burda, C.; Fu, R.; Pu, L.; Chen, H.; Zhu, J. Heterostructured Bi_2Se_3 nanowires with periodic phase boundaries. *J. Am. Chem. Soc.* **2004**, *126*, 16276–16277. [CrossRef]
27. Hu, P.; Cao, Y.; Jia, D.; Wang, L. Selective synthesis of Bi_2Se_3 nanostructures by solvothermal reaction. *Mater. Lett.* **2010**, *64*, 493–496. [CrossRef]
28. Alegria, L.D.; Schroer, M.D.; Chatterjee, A.; Poirier, G.R.; Pretko, M.; Patel, S.K.; Petta, J.R. Structural and electrical characterization of Bi_2Se_3 nanostructures grown by metal–organic chemical vapor deposition. *Nano Lett.* **2012**, *12*, 4711–4714. [CrossRef] [PubMed]
29. Andzane, J.; Kunakova, G.; Charpentier, S.; Hrkac, V.; Kienle, L.; Baitimirova, M.; Bauch, T.; Lombardi, F.; Erts, D. Catalyst-free vapour–solid technique for deposition of Bi_2Te_3 and Bi_2Se_3 nanowires/nanobelts with topological insulator properties. *Nanoscale* **2015**, *7*, 15935–15944. [CrossRef] [PubMed]
30. Zhang, K.; Pan, H.; Wei, Z.; Zhang, M.; Song, F.; Wang, X.; Zhang, R. Synthesis and magnetotransport properties of Bi_2Se_3 nanowires. *Chin. Phys. B* **2017**, *26*, 96101. [CrossRef]
31. Zou, Y.; Chen, Z.-G.; Huang, Y.; Yang, L.; Drennan, J.; Zou, J. Anisotropic electrical properties from vapor–solid–solid grown Bi2Se3 nanoribbons and nanowires. *J. Phys. Chem. C* **2014**, *118*, 20620–20626. [CrossRef]

32. Li, X.L.; Wang, C.X.; Yang, G.W. Thermodynamic theory of growth of nanostructures. *Prog. Mater. Sci.* **2014**, *64*, 121–199. [CrossRef]
33. Nakajima, S. The crystal structure of Bi_2Te_3-xSex. *J. Phys. Chem. Solids* **1963**, *24*, 479–485. [CrossRef]
34. Song, M.; Zhang, Y.; Chun, J.; Hu, S.; Tang, M.; Li, D. Effects of catalyst droplets on wire growth and the resulting branched structures during VLS growth. *Nanoscale* **2020**, *12*, 7538–7543. [CrossRef]
35. Baitimirova, M.; Andzane, J.; Petersons, G.; Meija, R.; Poplausks, R.; Romanova, M.; Erts, D. Vapor–solid synthesis and enhanced thermoelectric properties of non-planar bismuth selenide nanoplates on graphene substrate. *J. Mater. Sci.* **2016**, *51*, 8224–8232. [CrossRef]
36. Peng, H.; Lai, K.; Kong, D.; Meister, S.; Chen, Y.; Qi, X.-L.; Zhang, S.-C.; Shen, Z.-X.; Cui, Y. Aharonov–Bohm interference in topological insulator nanoribbons. *Nat. Mater.* **2010**, *9*, 225–229. [CrossRef] [PubMed]
37. Münning, F.; Breunig, O.; Legg, H.F.; Roitsch, S.; Fan, D.; Rößler, M.; Rosch, A.; Ando, Y. Quantum confinement of the Dirac surface states in topological-insulator nanowires. *Nat. Commun.* **2021**, *12*, 1038. [CrossRef] [PubMed]
38. Hong, S.S.; Cha, J.J.; Kong, D.; Cui, Y. Ultra-low carrier concentration and surface-dominant transport in antimony-doped Bi_2Se_3 topological insulator nanoribbons. *Nat. Commun.* **2012**, *3*, 757. [CrossRef] [PubMed]
39. Analytis, J.G.; Chu, J.-H.; Chen, Y.; Corredor, F.; McDonald, R.D.; Shen, Z.X.; Fisher, I.R. Bulk Fermi surface coexistence with Dirac surface state in Bi_2Se_3: A comparison of photoemission and Shubnikov–de Haas measurements. *Phys. Rev. B* **2010**, *81*, 205407. [CrossRef]
40. Veyrat, L.; Iacovella, F.; Dufouleur, J.; Nowka, C.; Funke, H.; Yang, M.; Escoffier, W.; Goiran, M.; Eichler, B.; Schmidt, O.G. Band bending inversion in Bi_2Se_3 nanostructures. *Nano Lett.* **2015**, *15*, 7503–7507. [CrossRef]
41. Kunakova, G.; Galletti, L.; Charpentier, S.; Andzane, J.; Erts, D.; Léonard, F.; Spataru, C.D.; Bauch, T.; Lombardi, F. Bulk-free topological insulator Bi_2Se_3 nanoribbons with magnetotransport signatures of Dirac surface states. *Nanoscale* **2018**, *10*, 19595–19602. [CrossRef] [PubMed]
42. Shoenberg, D. *Magnetic Oscillations in Metals*; Cambridge University Press: Cambridge, UK, 2009; ISBN 1316583171.

Paper VI

nanomaterials

MDPI

Article

Fabrication and Characterization of Double- and Single-Clamped CuO Nanowire Based Nanoelectromechanical Switches

Liga Jasulaneca [1], Alexander I. Livshits [1], Raimonds Meija [1], Jelena Kosmaca [1], Raitis Sondors [1], Matiss M. Ramma [1], Daniels Jevdokimovs [1], Juris Prikulis [1] and Donats Erts [1,2,*]

[1] Institute of Chemical Physics, University of Latvia, 1 Jelgavas Street, LV-1004 Riga, Latvia; liga.jasulaneca@lu.lv (L.J.); aleksandrs.livsics@lu.lv (A.I.L.); raimonds.meija@lu.lv (R.M.); jelena.kosmaca@lu.lv (J.K.); raitis.sondors@lu.lv (R.S.); matiss_martins.ramma@lu.lv (M.M.R.); daniels.jevdokimovs@lu.lv (D.J.); juris.prikulis@lu.lv (J.P.)

[2] Faculty of Chemistry, University of Latvia, 1 Jelgavas Street, LV-1004 Riga, Latvia

* Correspondence: donats.erts@lu.lv; Tel.: +371-670-33-875

Abstract: Electrostatically actuated nanoelectromechanical (NEM) switches hold promise for operation with sharply defined ON/OFF states, high ON/OFF current ratio, low OFF state power consumption, and a compact design. The present challenge for the development of nanoelectromechanical system (NEMS) technology is fabrication of single nanowire based NEM switches. In this work, we demonstrate the first application of CuO nanowires as NEM switch active elements. We develop bottom-up and top-down approaches for NEM switch fabrication, such as CuO nanowire synthesis, lithography, etching, dielectrophoretic alignment of nanowires on electrodes, and nanomanipulations for building devices that are suitable for scalable production. Theoretical modelling finds the device geometry that is necessary for volatile switching. The modelling results are validated by constructing gateless double-clamped and single-clamped devices on-chip that show robust and repeatable switching. The proposed design and fabrication route enable the scalable integration of bottom-up synthesized nanowires in NEMS.

Keywords: nanoelectromechanical switch; NEMS; nanowires; bottom-up; CuO

Citation: Jasulaneca, L.; Livshits, A.I.; Meija, R.; Kosmaca, J.; Sondors, R.; Ramma, M.M.; Jevdokimovs, D.; Prikulis, J.; Erts, D. Fabrication and Characterization of Double- and Single-Clamped CuO Nanowire Based Nanoelectromechanical Switches. *Nanomaterials* **2021**, *11*, 117. https://doi.org/10.3390/nano11010117

Received: 30 November 2020
Accepted: 1 January 2021
Published: 6 January 2021

Publisher's Note: MDPI stays neutral with regard to jurisdictional claims in published maps and institutional affiliations.

Copyright: © 2021 by the authors. Licensee MDPI, Basel, Switzerland. This article is an open access article distributed under the terms and conditions of the Creative Commons Attribution (CC BY) license (https://creativecommons.org/licenses/by/4.0/).

1. Introduction

The nanoelectromechanical (NEM) switch stands out as an energy-efficient candidate for logic and memory applications, due to two most important characteristics of mechanical switching: well-defined ON and OFF states and zero OFF state current [1–3], thus making it the ideal switch. Because atomic diffusion does not significantly impact the performance of these devices, mechanical switches can withstand a higher temperature than their conventional electronic-only semiconductor counterparts [2,4]. Despite the promising characteristics, the scalable fabrication and reliability of NEM switches is still an ongoing effort from both the characterization and technological perspectives [1,2].

The operation and properties of NEM switches can be experimentally explored by two approaches: using nanomanipulations in situ inside transmission [5–9] or scanning [10–12] electron microscopes and as micro-/nanofabricated on-chip devices [13–18].

The ability of rapid adjustment of the NEM switch configuration is an advantage of the in situ electron microscopy approach while using nanomanipulations [10–12], which allows for exploring different working regimes without the repetitive nanofabrication of multiple devices. Novel methods for NEM switch operation have been previously demonstrated in situ, such as decreasing of the switch-ON and switch-OFF voltages by using oscillations at resonance frequencies [10,12]. In situ characterization inside TEM and SEM have also allowed for the determination of the mechanical properties of NEM switch active elements, such as Young's modulus [5,19–21], breaking strength [5], and resonant behavior [21,22].

The first on-chip devices were implemented while using carbon nanotube (CNT)-based nanorelays [13], followed by different metals [14,23], semiconductors [17,18], and, recently, also TiN ceramics [15] and Cu [16]. Most efforts in the fabrication of NEM switches have focused on the top-down approach, integrating the fabrication of the active element in a complex process flow [4,14,15,24]. However, this constrains the available materials and design architectures that are compatible with lithographic processing. The alternative use of bottom-up synthesized quasi-one-dimensional (1D) nanostructures (nanotubes, nanowires) [10,12,25] taps into an exciting field of various materials with different properties and versatile functionality for application in NEM switches.

Among the bottom-up synthesized 1D structures, CNTs are, by far, the most popular choice for NEM switches, due to their high Young's modulus [25] and high resonance frequencies [26]. However, CNT-based NEM switches suffer from ablation during contact and they require additional electrode coating (e.g., diamond-like-carbon) to enhance contact reliability [27]. Single-crystalline and defect-free semiconductor nanowires [28], such as Si [17], Ge [8,29], and GeSn [12], have also been explored as potential candidate materials and demonstrated reliable operation at voltages up to 40–50 V. This enables their applications for high-voltage and low-current devices. CuO is a narrow band gap semiconductor that can be thermally oxidized in order to produce nanowires. It has been recently shown that CuO nanowires exhibit mechanical and electrical properties that are suitable for NEM switch applications [30,31]. High yield, controllable morphology of the as-grown nanowires and the low cost and simplicity of the method motivate the investigation of CuO nanowire use in NEM switches.

One of the greatest challenges for NEM switch fabrication while using bottom-up methods is the precise positioning of the active elements relative to the metal electrodes. The assembly of bottom-up synthesized active elements for NEM switches can be realized by spin-coating of the nanowire suspension [32], using dry mechanical transfer [33], dielectrophoresis (DEP) [34–36], and mechanical manipulation [37,38]. Dry mechanical transfer by pressing the substrate with nanowires against the chip with electrodes is fast and cost-effective, but it cannot ensure the nanowire positioning in predefined locations. Mechanical manipulation allows for precise alignment, but it is very time consuming. The DEP technique that is used in the present study increases the device fabrication throughput significantly by careful tuning of process parameters. The suspended length of the nanowire, number of nanowires, and their alignment direction on the electrodes can be efficiently controlled by DEP parameters (frequency, voltage, time), hydrodynamic forces, distance between the electrodes, and their shape and size [34,35].

To the best of our knowledge, integration of bottom-up synthesized semiconductor nanowires in NEM switches on-chip and their operation has not yet been tested. Here, we develop a theoretical model for optimizing the device parameters for volatile NEM switch operation. The model is used to calculate the switch-ON voltages for different NEM switch dimensions. Based on the acquired theoretical results, the full fabrication process of single- and double-clamped NEM switch is performed: (1) a scalable cost effective synthesis of CuO nanowires [30] for use as the NEM switch active elements; (2) fabrication of micropatterned device electrodes; and (3) dielectrophoresis [33] to align the nanowires on the electrodes. The developed NEM switches are tested for volatile switching in order to validate the theoretical results for both double-clamped and single-clamped devices.

2. Materials and Methods

Copper oxide (CuO) nanowires were synthesized by thermal oxidation of a Cu foil (99.9% purity, 25 μm thickness; Goodfellow GmbH, Hamburg, Germany) in a tube furnace (GSL-1100X, MTI Corporation, Richmond, CA, USA) at 500 °C for 3.5 h in ambient air, as reported in [30,39]. Figure 1a shows the typical process flow for the fabrication of electrodes and alignment of the as-synthesized nanowires. For microelectrode fabrication, AZ 1505 photoresist (Microchemicals GmbH, Ulm, Germany) was spin coated on a silicon substrate with thermal silicon dioxide (Microchemicals GmbH, Ulm, Germany) and then patterned

using maskless optical lithography direct write system (Heidelberg μPG 101 Micro Pattern Generator, Heidelberg Instruments Mikrotechnik GmbH, Heidelberg, Germany) with a 375 nm laser source by the following procedure. Si substrates with 1000 nm thick thermal SiO_2 were cleaned, and then a pattern was defined in a first photoresist layer. After post-bake of the photoresist, the exposed SiO_2 was etched with a commercially available buffered oxide etch (BOE 7:1 with Surfactant; Microchemicals GmbH, Ulm, Germany) (Figure 1(a1)) in order to define the distance between the active element and the electrode. 10 nm Cr adhesion layer/70 nm Au layer (Kurt J. Lesker Company, Jefferson Hills, PA, USA) was thermally evaporated into the etched trenches (Figure 1(a2)) to obtain actuation electrodes. After lift-off, the second layer was aligned and patterned while using metal evaporation and lift-off (Figure 1(a3)) in order to define DEP electrodes. Nanowires were assembled on microelectrodes while using dielectrophoretic alignment (Figure 1(a4)) to yield final devices with nanowires that were suspended over a gold electrode (Figure 1(a5)).

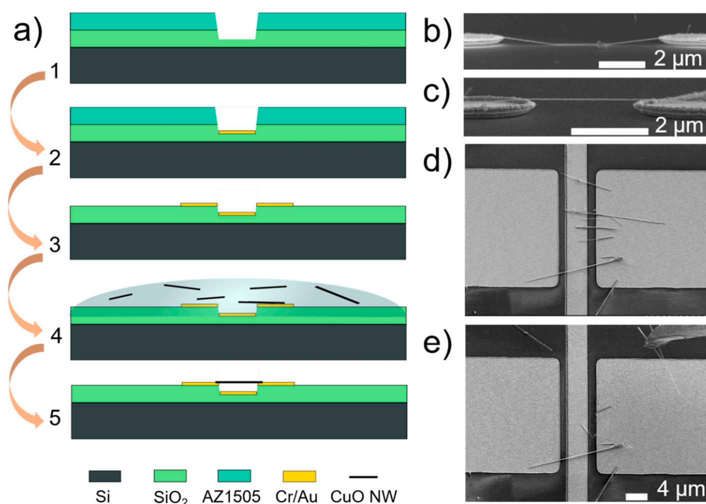

Figure 1. (**a**) Process flow for fabrication of microelectrodes involving etching of thermal SiO_2 (1), deposition of metal electrodes (2, 3) and dielectrophoretic assembly and supercritical drying (4) to yield the final suspended device (5). SEM images showing side view of a single nanowire aligned on 2 μm wide electrodes by (**b**) DEP without supercritical drying, (**c**) dielectrophoresis (DEP) followed by supercritical drying; (**d**) SEM image showing top-view of multiple nanowires aligned on 20 μm wide electrodes; and, (**e**) the removal of excess nanowires by nanomanipulations with etched gold tip (tip shown in upper right side of the image).

To remove the nanowires from the oxidized Cu foil, the sample was placed in isopropyl alcohol and then ultrasonicated for 3 s. For DEP alignment, the as-fabricated chips were immersed in a nanowire-isopropanol suspension, applying AC signal with frequency of 50 kHz [33]. A floating electrode DEP configuration [40,41] was employed, which consisted of an array of two opposing electrodes. One electrode was connected to a common line to which the AC signal was applied. The opposite DEP electrode was held at a floating potential. AC ground was connected to the back of the silicon substrate. Separate actuation electrodes were fabricated between pairs of DEP electrodes, so that the voltage bias could be individually applied to each single-nanowire device. This design allowed for decoupling

and analyzing single device characteristics from the DEP array without parallel interference from the other devices.

For the alignment of single nanowires in a double-clamped configuration, DEP was performed on 2 μm wide tapered electrodes (Figure 1b,c). In order to increase the yield of suspended nanowires, 20 μm wide electrodes for multiple nanowire DEP alignment in both single-clamped and double-clamped configurations were used (Figure 1d,e). Finally, to avoid nanowire's stiction by capillary forces to the substrate during drying (Figure 1b), supercritical CO_2 drying was carried out to produce suspended nanowires (Figure 1c).

Electrode structure and topography were inspected in a scanning electron microscope (Hitachi FE-SEM S-4800, Hitachi Ltd., Chiyoda, Tokyo, Japan) and atomic force microscope (AFM, MFP-3D, Asylum Research Inc., Santa Barbara, CA, USA) to find suitable devices. Nanowire manipulation (SmarAct 13D nanomanipulations system, SmarAct GmbH, Oldenburg, Germany) inside the SEM with etched sharp gold tips was used in order to remove other nanowires in cases where more than one nanowire was bridging the gap between the electrodes (Figure 1d,e).

The switches were electrically tested ex situ in a custom-built vacuum chamber and in SEM for visual inspection to monitor the structural stability of the switch.

Numerical calculations were carried out using FreeFem++ software (FreeFem++, version 3.5.8, http://www3.freefem.org/).

3. Results and Discussion

3.1. Fabricated CuO Nanowire-Based NEM Switch Configurations

The NEM switches that were fabricated in this work were tested in two different configurations—double-clamped and single-clamped. A single-nanowire double-clamped NEM switch device consists of a nanowire, lying flat on two gold electrodes that serve as both DEP electrodes for alignment and as the grounded switch source terminal (S) (Figure 2a–c). A single-nanowire single-clamped NEM switch has a similar configuration, but with the nanowire only fixed at one end (Figure 2a,e,f). A voltage was applied between the nanowire and lower gold drain electrode (D) to create electrostatic force F_E that pulls the nanowire towards D. When the switch-ON voltage V_{ON} was reached, a sharp current increase was detected in the circuit (Figure 2d,g). Switch-OFF voltage V_{OFF} was registered when the sum of F_E and adhesion force F_A in the contact became smaller than elastic tension force F_x in the nanowire and electric current fell to the current noise floor. Switch-OFF occurred at voltages that are lower than those for the switch-ON due to the presence of adhesion force F_A.

3.2. NEM Switch Model

We modelled the forces that lead to the switch-ON and switch-OFF events in order to find the optimal operational and design parameters for repeatable NEM switching in a double-clamped setup. The balance between the electrostatic, elastic, and adhesion forces during switching were analyzed by combining the analytic and numerical approaches. The V_{ON} was estimated for a range of nanowire diameters, corresponding to the diameter distribution acquired during synthesis. The characteristic range of nanowire diameters for CuO nanowires that were obtained by thermal oxidation in ambient air was approximately 50–200 nm [30] and the minimum distance between the side electrodes in the NEM switch was 6 μm (Figure 2b), which was chosen to ensure a reproducible photolithography process. The mechanical behavior of a double-clamped nanowire with suspended length L_0 in response to an external electrostatic force can be described while using the Euler–Bernoulli, Equation (1)

$$Y^{(4)}(\xi) - F_x(\xi)Y^{(2)}(\xi) - F_E(\xi) = 0,\ \xi = \frac{L}{L_0} \tag{1}$$

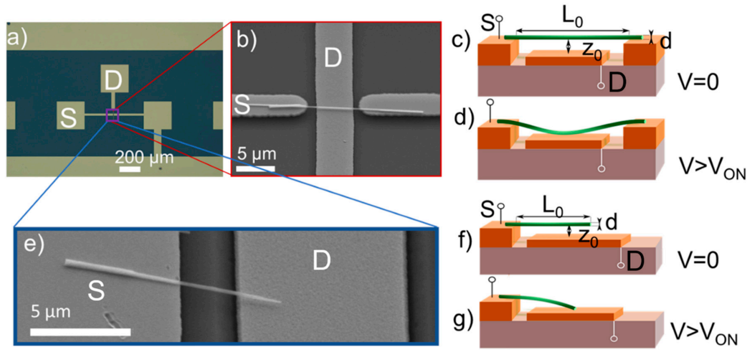

Figure 2. (**a**) Optical microscope image of a device connected to a micropatterned gold electrode line that joins it with other devices; (**b**) SEM image of a double-clamped single nanoelectromechanical (NEM) switch device in an array of 2 μm wide electrodes; (**c**) Schematics for a double-clamped nanowire switch in OFF and (**d**) ON state; (**e**) SEM image of a single-clamped nanowire in an electrically identical setup with wide (20 μm) DEP electrodes; (**f**) Schematics for a single-clamped nanowire switch in OFF and (**g**) ON state. Relevant design parameters shown in (**c**,**d**,**f**,**g**) are suspended nanowire length L_0, nanowire diameter d and distance between nanowire and electrode z_0.

In (1), Y stands for a perpendicular displacement, ξ-for the normalized coordinate along the nanowire, it coincides with the x axis, when the nanowire is not deformed (voltage is not applied), F_x is a tension force, and F_E is the linear density of the electrostatic force (Figure 3). The derivatives over the normalized coordinate are represented as upper indices in parentheses. Equation (1) can only be used in the case of small curvatures. The range of distances between the nanowire and the electrode D was chosen in order to ensure that the switch would operate in the small curvature regime. An extra-tension force is induced at the nanowire-electrode contacts due to large curvatures, as described in [42]. It should be mentioned that all of the physical quantities with the dimensionality of length are given in units of the nanowire length, except the nanowire's suspended length L_0 itself.

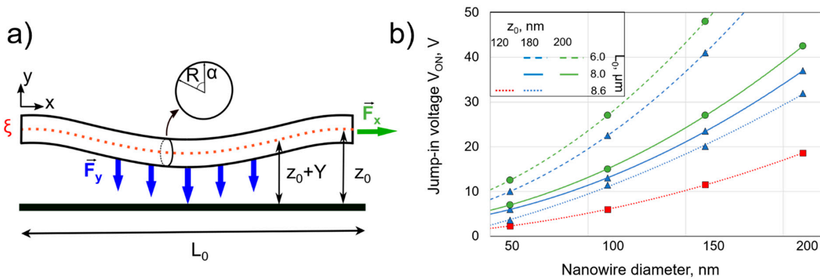

Figure 3. (**a**) Schematics of the relevant forces and parameters for the V_{ON} estimation for a double-clamped nanowire with suspended length L_0, diameter d (radius R) and initial distance to the electrode z_0. (**b**) Calculations of V_{ON} as a function of nanowire diameter for different distances between the nanowire and the electrode z and suspended lengths L_0 for a Young's modulus of 155 GPa, assuming a rigid clamping at the nanowire ends. The lines are drawn as guide to the eye. The suspended lengths are marked by line type (dashed line 6 μm, solid line 8 μm, dotted line 8.6 μm), distances are marked by colored shapes (red square corresponds to 120 nm, blue triangle to 180 nm, and green circle to 200 nm).

The linear density of the electrostatic force is given as an integral over the corresponding circular cross section perimeter (2) (Figure 3a).

$$F_E = \frac{4\varepsilon_0}{\pi E L_0 R^3} \int_0^{2\pi} \left(\frac{d\varphi}{dr}\right)^2 \cos\alpha d\alpha \tag{2}$$

In (2), E stands for the material Young's modulus, ε_0 for the permittivity of vacuum, R for the radius of the nanowire cross section, and φ for the electric potential on the surface. We consider the nanowire as an infinite conducting cylinder. The integration of electric potential over a cross-section perimeter of the nanowire is carried out in order to find the linear density of electrostatic force F_E. If the displacement in axial direction is forbidden, then the nanowire will experience tension force F_x. This allows for one to obtain an analytic formula for the electric potential, and, finally, using (2), for the required electrostatic force (3).

$$F_E = \frac{16}{EL_0R^4} \frac{V^2\varepsilon_0}{\sqrt{z^2 - R^2}Lnc^2},\ c = \frac{2z^2}{R^2}\left(1 - \sqrt{1 - \frac{R^2}{z^2}}\right) - 1 \tag{3}$$

In (3), z stands for the distance from the cylinder axis to the counter electrode, but V for the applied voltage. To use the obtained Formula (3) in Equation (1), it is necessary to adjust the distance to the counter electrode for each cross section according to the nanowire deflection.

$$z = z_0 + Y(\xi) \tag{4}$$

In (4), z_0 represents an initial distance from the nanowire axis to the counter electrode (Figure 3a).

The boundary conditions at the nanowire endpoints determine the tension force F_x in Equation (1). If at least one of the nanowire endpoints can slide in the axial direction, then the F_x is equal to zero. If they are fixed in the axial direction at both ends, then the nanowire will be under tension due to inevitable elongation when it is attracted to the counter electrode, and the tension force F_x can be written as:

$$F_x = \frac{4}{R^2}\left[1 - \int_0^1 \sqrt{1 - \left(Y^{(1)}(\xi)\right)^2}\, d\xi\right] \tag{5}$$

In all cases, we considered the nanowire axis direction to be fixed, because of the substantial length of nanowire lying on the electrode. This leads to the following boundary conditions for the perpendicular deflection of the nanowire:

$$Y(0) = Y(1) = Y^{(1)}(0) = Y^{(1)}(1) = 0 \tag{6}$$

In order to estimate the V_{ON}, the problem that is formulated by Equations (1) and (3)–(6) has been numerically solved for a set of increasing values of electric voltage. The threshold voltage, above which the solution could no longer be found (the deformed nanowire intersects the surface of the counter electrode) is reported as V_{ON}.

Figure 3b shows the calculated results for V_{ON} as a function of nanowire diameter for three different suspended lengths of the nanowires (6, 8, and 8.6 µm) and three different distances between the nanowire and the electrode (120, 180, and 200 nm). The L_0 and z_0 values were chosen according to the fabrication method. The calculated V_{ON} values ranged from 2 to 48 V for NEM switches while using nanowires with diameters in the range of 50–200 nm, which are typical for the used synthesis method. We use the model to find design parameters (L_0, and z_0) that allow for operating in the V_{ON} range below 50 V to prevent burn-out of the nanowire and minimizing the current induced changes in the contact [8,9,22].

For the switch-OFF to occur, the elastic force of the nanowire should exceed the adhesion force in the contact. For finding the adhesion force F_{adh}, we used the Maugis–Dugdale model adapted by Carpick et al. [43], which has been used for calculations of adhesion force in NEM switch nanowire–electrode contacts and it has shown good agreement with the experimental data [8–10].

The restoring elastic force F_{el} of the nanowire in contact was found when assuming that adhesion force in contact acts as a point force applied in the middle of the beam. The equation that describes such a case is

$$F_{el} = \frac{48EIz}{L_0^3} \tag{7}$$

where I is the second moment of area of the nanowire and L_0–suspended length of the nanowire.

We find that, for example, for a nanowire with a diameter of 150 nm, the optimal suspended nanowire's length is in the range of 6–8 µm and the initial distance between the nanowire and electrode z_0: 120–190 nm. If these conditions are satisfied, then the calculated elastic force (5.2–8.7 × 10^{-6} N) in the nanowire exceeds the adhesion force in the contact (4.1–7.9 × 10^{-6} N), thus allowing for a successful switch-OFF and repeated operation of the NEM switch.

3.3. Model Comparison with Experimental NEM Switch V_{ON} Data

Drawing on the modelling results, we chose distances between the nanowire and electrode to be 120 and 190 nm, suspended nanowire lengths from 6.2 to 9.2 µm to fabricate, and experimentally analyze CuO NEM switches. The resolution of the photolithography limited further downscaling of suspended lengths. The experimentally determined V_{ON} values fell within the pre-determined range for the calculated V_{ON} values: from 4.5 V for 50 nm thin nanowire up to 49 V for 210 nm thick nanowire for different suspended lengths from 6.2 to 9.2 µm (Figure 4a). Here, all of the fabricated NEM switches are taken into account, including those that only showed one or several operation cycles due to stiction failure. The next section, will consider a typical device that showed volatile operation through many cycles.

As the ends of the nanowire are held to the electrode substrate by adhesion force only, their sliding along the surface of the substrate must be considered. The experimentally determined values for V_{ON} were compared with calculated ones considering two different scenarios—with or without nanowire sliding at the contact (Figure 4a). For geometries that were considered in this work sliding during switch-ON can cause a decrease in V_{ON} up to 20 % (Figure 4a). The experimentally obtained V_{ON} values are higher in all cases. except for one (Figure 4a, device 6), which could indicate sliding in the contact in this single case. It also should be noted that the sliding could be overlooked if the Young's moduli of the individual nanowires are higher than the average value of 155 GPa [30] used in our calculations. The sliding-induced decrease of the V_{ON} in some cases can be observed during repeated cycling and its possible applications will be discussed later. In order to ensure a stable contact between the nanowire and the electrode, an additional fabrication step could be employed, either by lithography or electron beam induced deposition of a metal. However, this increases the complexity of the fabrication process.

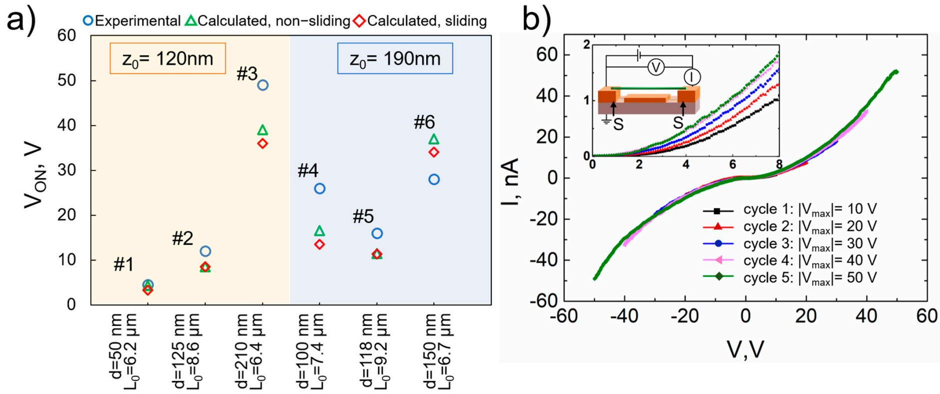

Figure 4. (**a**) Comparison of experimentally determined and calculated V_{ON} values for six samples (labeled 1 . . . 6) with different nanowire diameter d and suspended length L_0 values and two initial distances between the nanowire and the electrode z_0 (120 nm and 190 nm). V_{ON} was calculated for two different cases: with and without sliding of the nanowire ends. (**b**) I–V cycling characteristics of a single device (#6) with voltage applied between S contacts. I–V cycling starts—from maximum voltage absolute value $|V_{max}|$ of 10 V. The absolute value of maximum voltage is increased during every next cycle. Inset zooms in on the I–V plots for voltages up to 8 V, showing a reduction of contact resistance.

3.4. Characterization, Testing and Optimization of Fabricated NEM Switches

In the following section, we describe contact property engineering, operation, and stability of a typical volatile NEM switch device (#6).

3.4.1. Reduction of Nanowire-Electrode Contact Resistance by I–V Cycling

Nanowires that are aligned with DEP may have large contact resistances that can typically be improved by high temperature annealing or argon ion etching [44]. Here, we use an approach that was suggested by Meija et al. [22] employing I–V cycling to improve both contact electrical conductivity and its mechanical strength, which can reduce sliding in the contact. I–V cycling was carried out by applying voltage between the S-S electrodes that support the ends of the nanowire (Figure 4b inset). I–Vs were measured biasing from 0 V to 10 V and symmetrically from 0 V to −10 V with 0.1 V increment. For every next cycle, the absolute value of the maximum voltage $|V_{max}|$ was increased with a 10 V step until it reached 50 V (Figure 4b). SEM analysis showed no signs of nanowire degradation, which demonstrated the suitability of CuO active elements for high voltage applications. The symmetric and nonlinear shape of the I–V curves (Figure 4b) suggests that current conduction in these nanowires is a combination of ohmic and space-charge-limited currents, as reported previously [33,45]. The current flowing through the nanowire during I–V cycling induces Joule heating at nanowire-electrode contacts. The I–V characteristics of all NEM switches examined in this work showed an increase of CuO nanowire conductivity with cycling. Figure 4b shows the results for a single NEM switch. The conductivity of the system increased almost two times during 10 cycles. This may be attributed to both enhanced contact [22] and nanowire conductivity [46].

3.4.2. Initial Stages of NEM Switch Operation: V_{ON} Stabilization

The NEM switch operation was tested by applying the same voltage biasing scheme as during the reduction of contact resistance between the nanowire S and the lower electrode D (Figure 2). This approach is valuable for analyzing the stability of V_{ON} and V_{OFF} values.

Figure 5a shows the first five cycles of the NEM switch, when it is cycled between 0–30 V. In the first I–V (1), the switch-ON occurs at 28 V and switch-OFF at 1 V. In the second cycle, the V_{ON} decreases from 28 V to 15.5 V. During the next three cycles, it gradually decreases towards 12.5 V. As a result of the cycling, the value of V_{OFF} slightly increases from 1 V to 2.5–3.5 V. The initial decrease of V_{ON} may be attributed to the nanowire-upper electrode contact modification, which can result in the release of internal mechanical stresses, as well as sliding along the surface. This prevents the nanowire's return to its original position, and it remains in a slightly deformed shape. In every next voltage cycle, the nanowire slides again until a new stable equilibrium position is found for stable NEM switch operation. A similar step-wise decrease of initial V_{ON} value has been reported for the CNT bundle-based NEM switch, where the authors suggest a slipping of the CNT bundle on the support as the possible explanation [47]. This can be contrasted to the gradual voltage decrease observed in [27], which was interpreted as a removal of an outer layer of the nanowire material. The relatively constant ON current level suggests that mechanical effects are responsible for the observed changes in the NEM switch characteristics and there is not much dissipation of electrical power in the nanowire-electrode contact. After five cycles the V_{ON} value stabilized and a stable ON-OFF operation of NEM switch followed (Figure 5b), where the switch-ON occurred at 12.5 V and switch-OFF at 4.5–8 V. A decrease of the hysteresis loop may be beneficial for NEM switch operation, as it decreases energy dissipation. The switch-ON is much more abrupt than the switch-OFF, which can be explained by the relatively large contact area of the double-clamped nanowire that needs to detach from the electrode as the voltage is decreased. The differences in the V_{OFF} values between cycles can be explained by variations in contact area. Additionally, the sliding of the nanowire along the contacts can be deliberately employed in order to fine-tune the NEM switch V_{ON} to a desired value. When it is reached, the active element can be mechanically fixed while using an additional fabrication step (e.g., by lithography).

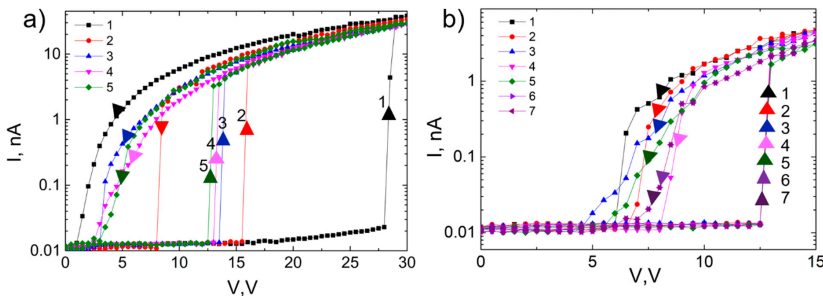

Figure 5. (**a**) Switch I–V cycling from 0 V to 30 V and back to 0 V shows stepwise decrease of V_{ON} for every next cycle (cycles from 1 to 5) until (**b**) reaching a stable NEM switch operation regime with constant V_{ON} at 12.5 V and V_{OFF} at 4.5–8 V (cycles 1 to 7: I–V cycling from 0 V to 15 V and back to 0 V). Upwards arrows mark transition to ON state, downwards arrows–transition to OFF state. For this device nanowire's diameter d = 150 nm, L_0 = 6.7 µm, and z_0 = 190 nm.

Figure 6a,b shows an example of a single-clamped NEM switch. The geometry of this switch was chosen according to the previous theoretical and experimental work conducted by our group [8,9,12]. V_{ON} for this device was 30 V and V_{OFF} 13–17 V. In contrast to the double-clamped case, the transition to ON/OFF states is sharp both for ON and OFF switching, which can be explained by the smaller contact area and faster detachment from the contact electrode. The calculated adhesion force [43] for this single-clamped nanowire (2×10^{-7} N) is an order of magnitude smaller than for a double-clamped case, which allows for a sharper transition between the ON and OFF states. The smaller adhesion force can

be explained by two orders of magnitude smaller effective contact area (78 nm^2 for a single-clamped and 7850 nm^2 for a double-clamped case).

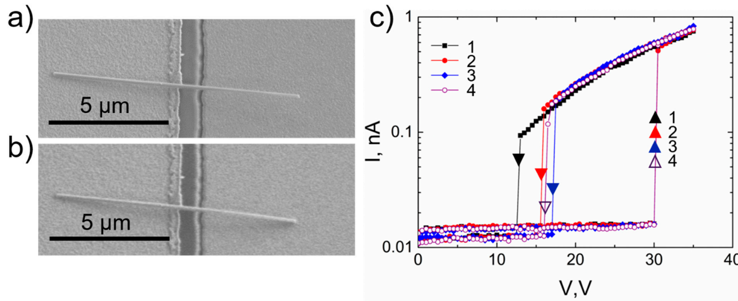

Figure 6. CuO nanowire-based NEM switch in a single-clamped configuration. SEM image of the NEM switch in (**a**) OFF state, (**b**) ON state; (**c**) Switch I–V cycling showing sharp transition to ON (at 30 V) and OFF (at 13–17 V) states, four switching cycles are shown. Upwards arrows mark transition to ON state, downwards arrows–transition to OFF state. Dimensions for this device: suspended length L_0 = 3 µm, diameter d = 80 nm, and the initial distance between nanowire and electrode z_0 = 190 nm.

3.4.3. Cycling of NEM Switch

Continued cycling of a double-clamped NEM switch was performed in order to demonstrate the stability of the NEM switch operational parameters. Voltage was applied in square pulses, alternating between 15 V (ON state), 0 V (OFF state), and 8 V (detachment test). The latter voltage value was chosen to be smaller than the switch-ON voltage, but larger than the non-conductive gap region observed in I–V characteristics of the nanowire (Figure 4b) in order to detect the nanowire detachment without visual inspection. The expected values for the current at each state were the following: signal in nA range for 15 V applied voltage and system noise for both 0 V and 8 V. Figure 7 shows a fragment of a typical ON/OFF I(t) cycling, where the switch remains for 15 s in each of the states.

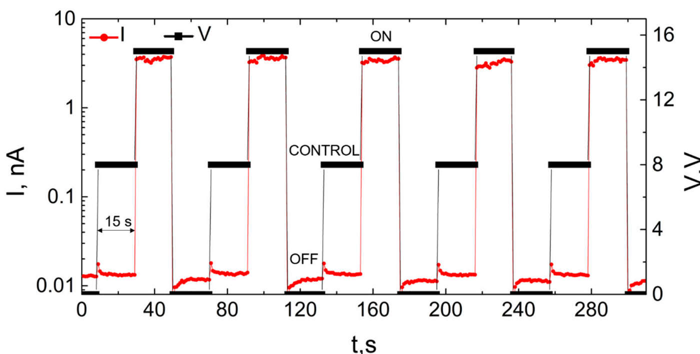

Figure 7. Variation of NEM switch current levels (red circles) at different applied voltages (black squares) of 0 V (OFF), 8 V (OFF, control), 15 V (ON) during repeatable switching. For 0 V and 8 V, the current stays at the noise level, whereas ON current reaches nA level, when applied voltage is 15 V.

4. Conclusions

In summary, we demonstrate the first fabrication and volatile operation of a NEM switch on-chip that employs bottom-up synthesized semiconductor nanowires as the active elements. It is shown that bottom-up synthesized CuO nanowires can serve as a robust and reliable material for the active element fabrication. By combining conventional lithography, dielectrophoresis, and nanomanipulations, as shown in this work, the fabrication yield can be increased, and device operation assessed more quickly.

We propose a theoretical model for estimating switch-ON voltage, adhesion, elastic force, and nanowires sliding dependence on nanowire's suspended length, diameter, and distance to the electrode in order to obtain parameters for successful volatile device operation. The model was validated by fabricating NEM switches with the predetermined geometry and testing their operation in gateless double-clamped setup. The calculated V_{ON} values were close to those obtained experimentally, and volatile operation was achieved. DEP alignment was successfully employed to also fabricate single-clamped NEM switches.

Both single- and double-clamped CuO nanowire-based switches exhibit abrupt switch-ON, requiring approximately 0.5 V to transit from OFF to ON state. Single-clamped devices show increased switching speeds from the ON to OFF state, which suggests that they can offer faster operation and better energy efficiency than double-clamped configuration switches. However, the demonstrated bottom-up fabrication approach using DEP is currently more suitable for scalable fabrication of double-clamped switches, due to the efficient control of suspended lengths of the nanowires by DEP parameters and electrode geometry. The scalable fabrication of single-clamped switches will require improved control over the suspended length of the nanowire. We also suggest that voltage cycling can be used as a step in NEM switch fabrication to stabilize V_{ON}. Further research will be devoted to improving the nanowire-electrode contact in order to improve NEM switch operational characteristics.

Author Contributions: The manuscript was written through contributions of all authors. L.J., J.K., R.M. and D.E. planned the experiments. R.S. synthesized CuO nanowires. A.I.L. and R.M. developed the theoretical model for determining NEM switch operational parameters. M.M.R. carried out dielectrophoretic alignment of CuO nanowires. L.J., R.M., J.K., R.S., M.M.R. performed experiments. D.J. and J.P. supported experimentation and data analysis. L.J. and R.M. wrote the manuscript. D.E., J.P., A.I.L. and D.E. reviewed the manuscript. All authors have read and agreed to the published version of the manuscript.

Funding: This research was funded by the European Regional Development Fund (project no. 1.1.1.1/16/A/256, "Creation of nanoelectromechanical switches").

Data Availability Statement: The data presented in this study are available on request from the corresponding author.

Acknowledgments: We would like to thank Tom Yager for careful reading and reviewing of the manuscript.

Conflicts of Interest: The authors declare no conflict of interest. The funders had no role in the design of the study; in the collection, analyses, or interpretation of data; in the writing of the manuscript, or in the decision to publish the results.

References

1. Jasulaneca, L.; Kosmaca, J.; Meija, R.; Andzane, J.; Erts, D. Review: Electrostatically actuated nanobeam-based nanoelectromechanical switches—Materials solutions and operational conditions. *Beilstein J. Nanotechnol.* **2018**, *9*, 271–300. [CrossRef]
2. Loh, O.Y.; Espinosa, H.D. Nanoelectromechanical contact switches. *Nat. Nanotechnol.* **2012**, *7*, 283–295. [CrossRef] [PubMed]
3. Peschot, A.; Qian, C.; Liu, T.-J.K. Nanoelectromechanical Switches for Low-Power Digital Computing. *Micromachines* **2015**, *6*, 1046–1065. [CrossRef]
4. Lee, T.-H.; Bhunia, S.; Mehregany, M. Electromechanical computing at 500 °C with silicon carbide. *Science* **2010**, *329*, 1316–1318. [CrossRef] [PubMed]
5. Zhu, Y.; Qin, Q.; Xu, F.; Fan, F.; Ding, Y.; Zhang, T.; Wiley, B.J.; Wang, Z.L. Size effects on elasticity, yielding, and fracture of silver nanowires: In situ experiments. *Phys. Rev. B* **2012**, *85*, 045443. [CrossRef]

6. Erts, D.; Lõhmus, A.; Lõhmus, R.; Olin, H. Instrumentation of STM and AFM combined with Transmission Electron Microscope. *Appl. Phys. A Mater. Sci. Process.* **2001**, *72*, S71–S74. [CrossRef]
7. Ziegler, K.J.; Lyons, D.M.; Holmes, J.D.; Erts, D.; Polyakov, B.; Olin, H.; Svensson, K.; Olsson, E. Bistable nanoelectromechanical devices. *Appl. Phys. Lett.* **2004**, *84*, 4074–4076. [CrossRef]
8. Andzane, J.; Petkov, N.; Livshits, A.I.; Boland, J.J.; Holmes, J.D.; Erts, D. Two-terminal nanoelectromechanical devices based on germanium nanowires. *Nano Lett.* **2009**, *9*, 1824–1829. [CrossRef]
9. Andzane, J.; Prikulis, J.; Dvorsek, D.; Mihailovic, D.; Erts, D. Two-terminal nanoelectromechanical bistable switches based on molybdenum-sulfur-iodine molecular wire bundles. *Nanotechnology* **2010**, *21*, 125706. [CrossRef]
10. Andzane, J.; Meija, R.; Livshits, A.I.; Prikulis, J.; Biswas, S.; Holmes, J.D.; Erts, D. An AC-assisted single-nanowire electromechanical switch. *J. Mater. Chem. C* **2013**, *1*, 7134. [CrossRef]
11. Ke, C.; Espinosa, H.D. In situ electron microscopy electromechanical characterization of a bistable NEMS device. *Small* **2006**, *2*, 1484–1489. [CrossRef] [PubMed]
12. Meija, R.; Livshits, A.I.; Kosmaca, J.; Jasulaneca, L.; Andzane, J.; Biswas, S.; Holmes, J.D.; Erts, D. Resonance assisted jump-in voltage reduction for electrostatically actuated nanobeam-based gateless NEM switches. *Nanotechnology* **2019**, *30*, 385203. [CrossRef]
13. Lee, S.W.; Lee, D.S.; Morjan, R.E.; Jhang, S.H.; Sveningsson, M.; Nerushev, O.A.; Park, Y.W.; Campbell, E.E.B. A three-terminal carbon nanorelay. *Nano Lett.* **2004**, *4*, 2027–2030. [CrossRef]
14. Czaplewski, D.A.; Patrizi, G.A.; Kraus, G.M.; Wendt, J.R.; Nordquist, C.D.; Wolfley, S.L.; Baker, M.S.; De Boer, M.P. A nanomechanical switch for integration with CMOS logic. *J. Micromech. Microeng.* **2009**, *19*, 85003. [CrossRef]
15. Muñoz-Gamarra, J.L.; Uranga, A.; Barniol, N. Nanomechanical switches based on metal-insulator-metal capacitors from a standard complementary-metal-oxide semiconductor technology. *Appl. Phys. Lett.* **2014**, *104*, 243105. [CrossRef]
16. Muñoz-Gamarra, J.L.; Uranga, A.; Barniol, N. CMOS-NEMS Copper Switches Monolithically Integrated Using a 65 nm CMOS Technology. *Micromachines* **2016**, *7*, 30. [CrossRef] [PubMed]
17. Arkan, E.F.; Sacchetto, D.; Yildiz, I.; Leblebici, Y.; Alaca, B.E. Monolithic integration of Si nanowires with metallic electrodes: NEMS resonator and switch applications. *J. Micromech. Microeng.* **2011**, *21*, 125018. [CrossRef]
18. Feng, X.L.; Matheny, M.H.; Zorman, C.A.; Mehregany, M.; Roukes, M.L. Low voltage nanoelectromechanical switches based on silicon carbide nanowires. *Nano Lett.* **2010**, *10*, 2891–2896. [CrossRef]
19. Jasulaneca, L.; Meija, R.; Livshits, A.I.; Prikulis, J.; Biswas, S.; Holmes, J.D.; Erts, D. Determination of Young's modulus of Sb_2S_3 nanowires by in situ resonance and bending methods. *Beilstein J. Nanotechnol.* **2016**, *7*, 278–283. [CrossRef]
20. Kosmaca, J.; Meija, R.; Antsov, M.; Kunakova, G.; Sondors, R.; Iatsunskyi, I.; Coy, E.; Doherty, J.; Biswas, S.; Holmes, J.D.; et al. Investigating the mechanical properties of GeSn nanowires. *Nanoscale* **2019**, *11*, 13612–13619. [CrossRef]
21. Kosmaca, J.; Jasulaneca, L.; Meija, R.; Andzane, J.; Romanova, M.; Kunakova, G.; Erts, D. Young's modulus and indirect morphological analysis of Bi_2Se_3 nanoribbons by resonance measurements. *Nanotechnology* **2017**, *28*, 325701. [CrossRef]
22. Meija, R.; Kosmaca, J.; Jasulaneca, L.; Petersons, K.; Biswas, S.; Holmes, J.D.; Erts, D. Electric current induced modification of germanium nanowire NEM switch contact. *Nanotechnology* **2015**, *26*, 195503. [CrossRef] [PubMed]
23. Lee, J.O.; Song, Y.H.; Kim, M.W.; Kang, M.H.; Oh, J.S.; Yang, H.H.; Yoon, J.B. A sub-1-volt nanoelectromechanical switching device. *Nat. Nanotechnol.* **2013**, *8*, 36–40. [CrossRef] [PubMed]
24. Qian, Y.; Soon, B.W.; Singh, P.; Campanella, H.; Lee, C. All metal nanoelectromechanical switch working at 300 °C for rugged electronics applications. *Nanoscale* **2014**, *6*, 5606–5611. [CrossRef] [PubMed]
25. Yu, M.-F.; Lourie, O.; Dyer, M.J.; Moloni, K.; Kelly, T.F.; Ruoff, R.S. Strength and breaking mechanism of multiwalled carbon nanotubes under tensile load. *Science* **2000**, *287*, 637–640. [CrossRef] [PubMed]
26. Kaul, A.B.; Wong, E.W.; Epp, L.; Hunt, B.D. Electromechanical carbon nanotube switches for high-frequency applications. *Nano Lett.* **2006**, *6*, 942–947. [CrossRef]
27. Loh, O.; Wei, X.; Sullivan, J.; Ocola, L.E.; Divan, R.; Espinosa, H.D. Carbon-Carbon Contacts for Robust Nanoelectromechanical Switches. *Adv. Mater.* **2012**, *24*, 2463–2468. [CrossRef]
28. Ngo, L.T.; Almécija, D.; Sader, J.E.; Daly, B.; Petkov, N.; Holmes, J.D.; Erts, D.; Boland, J.J. Ultimate-strength germanium nanowires. *Nano Lett.* **2006**, *6*, 2964–2968. [CrossRef]
29. Andzane, J.; Prikulis, J.; Meija, R.; Kosmaca, J.; Biswas, S.; Holmes, J.D.; Erts, D. Application of Ge Nanowire for Two-Input Bistable Nanoelectromechanical Switch. *Mater. Sci. Medzg.* **2013**, *19*, 254–257. [CrossRef]
30. Sondors, R.; Kosmaca, J.; Kunakova, G.; Jasulaneca, L.; Ramma, M.M.; Meija, R.; Kauranens, E.; Antsov, M.; Erts, D. Size distribution, mechanical and electrical properties of CuO nanowires grown by modified thermal oxidation methods. *Nanomaterials* **2020**, *10*, 1051. [CrossRef]
31. Tan, E.P.S.; Zhu, Y.; Yu, T.; Dai, L.; Sow, C.H.; Tan, V.B.C.; Lim, C.T. Crystallinity and surface effects on Young's modulus of CuO nanowires. *Appl. Phys. Lett.* **2007**, *90*, 163112. [CrossRef]
32. Cha, S.N.; Jang, J.E.; Choi, Y.; Amaratunga, G.A.J.; Kang, D.-J.; Hasko, D.G.; Jung, J.E.; Kim, J.M. Fabrication of a nanoelectromechanical switch using a suspended carbon nanotube. *Appl. Phys. Lett.* **2005**, *86*, 83105. [CrossRef]
33. Ramma, M.M.; Katkevics, J.; Jasulaneca, L.; Kunakova, G.; Sondors, R.; Meija, R.; Erts, D.; Kosmaca, J. Dielectrophoretically aligned CuO nanowire interconnects for NEMS sensors. *Surf. Interfaces* **2020**. submitted.

34. Collet, M.; Salomon, S.; Klein, N.Y.; Seichepine, F.; Vieu, C.; Nicu, L.; Larrieu, G. Large-scale assembly of single nanowires through capillary-assisted dielectrophoresis. *Adv. Mater.* **2015**, *27*, 1268–1273. [CrossRef] [PubMed]
35. Freer, E.M.; Grachev, O.; Duan, X.; Martin, S.; Stumbo, D.P. High-yield self-limiting single-nanowire assembly with dielectrophoresis. *Nat. Nanotechnol.* **2010**, *5*, 525–530. [CrossRef]
36. Subramanian, A.; Alt, A.R.; Dong, L.; Kratochvil, B.E.; Bolognesi, C.R.; Nelson, B.J. Electrostatic actuation and electromechanical switching behavior of one-dimensional nanostructures. *ACS Nano* **2009**, *3*, 2953–2964. [CrossRef]
37. Kosmaca, J.; Andzane, J.; Prikulis, J.; Biswas, S.; Holmes, J.D.; Erts, D. Application of a Nanoelectromechanical Mass Sensor for the Manipulation and Characterisation of Graphene and Graphite Flakes. *Sci. Adv. Mater.* **2014**, *3*, 552–557. [CrossRef]
38. Li, Q.; Koo, S.-M.; Edelstein, M.D.; Suehle, J.S.; Richter, C. A Silicon nanowire electromechanical switches for logic device application. *Nanotechnology* **2007**, *18*, 315202. [CrossRef]
39. Jiang, X.; Herricks, T.; Xia, Y. CuO Nanowires Can Be Synthesized by Heating Copper Substrates in Air. *Nano Lett.* **2002**, *2*, 1333–1338. [CrossRef]
40. Dong, L.; Chirayos, V.; Bush, J.; Jiao, J.; Dubin, V.M.; Chebian, R.V.; Ono, Y.; Conley, J.F.; Ulrich, B.D. Floating-potential dielectrophoresis-controlled fabrication of single-carbon-nanotube transistors and their electrical properties. *J. Phys. Chem. B* **2005**, *109*, 13148–13153. [CrossRef]
41. Palapati, N.K.R.; Pomerantseva, E.; Subramanian, A. Single nanowire manipulation within dielectrophoretic force fields in the sub-crossover frequency regime. *Nanoscale* **2015**, *7*, 3109–3116. [CrossRef] [PubMed]
42. Livshits, A.I.; Jasulaneca, L.; Kosmaca, J.; Meija, R.; Holmes, J.D.; Erts, D. Extra tension at electrode-nanowire adhesive contacts in nano-electromechanical devices. *Eur. J. Mech. A/Solids* **2017**, *66*, 412–422. [CrossRef]
43. Carpick, R.W.; Ogletree, D.F.; Salmeron, M. A general equation for fitting contact area and friction vs load measurements. *J. Colloid Interface Sci.* **1999**, *211*, 395–400. [CrossRef]
44. Kunakova, G.; Meija, R.; Bite, I.; Prikulis, J.; Kosmaca, J.; Varghese, J.; Holmes, J.D.; Erts, D. Sensing properties of assembled Bi_2S_3 nanowire arrays. *Phys. Scr.* **2015**, *90*, 094017. [CrossRef]
45. Wu, J.; Yin, B.; Wu, F.; Myung, Y.; Banerjee, P. Charge transport in single CuO nanowires. *Appl. Phys. Lett.* **2014**, *105*, 183506. [CrossRef]
46. Hummelgård, M.; Zhang, R.; Carlberg, T.; Vengust, D.; Dvorsek, D.; Mihailovic, D.; Olin, H. Nanowire transformation and annealing by Joule heating. *Nanotechnology* **2010**, *21*, 165704. [CrossRef] [PubMed]
47. Ryan, P.; Wu, Y.C.; Somu, S.; Adams, G.; McGruer, N. Single-walled carbon nanotube electromechanical switching behavior with shoulder slip. *J. Micromech. Microeng.* **2011**, *21*, 045028. [CrossRef]

Paper VII

nanomaterials

MDPI

Article

Size Distribution, Mechanical and Electrical Properties of CuO Nanowires Grown by Modified Thermal Oxidation Methods

Raitis Sondors [1], Jelena Kosmaca [1], Gunta Kunakova [1], Liga Jasulaneca [1], Matiss Martins Ramma [1], Raimonds Meija [1], Edijs Kauranens [1], Mikk Antsov [1] and Donats Erts [1,2,*]

[1] Institute of Chemical Physics, University of Latvia, 1 Jelgavas str., LV-1004 Riga, Latvia; raitis.sondors@lu.lv (R.S.); jelena.kosmaca@lu.lv (J.K.); gunta.kunakova@lu.lv (G.K.); liga.jasulaneca@lu.lv (L.J.); matiss_martins.ramma@lu.lv (M.M.R.); raimonds.meija@lu.lv (R.M.); edijs.kauranens@lu.lv (E.K.); antsof@gmail.com (M.A.)

[2] Department of Chemistry, University of Latvia, 1 Jelgavas str., LV-1004 Riga, Latvia

* Correspondence: Donats.Erts@lu.lv

Received: 27 April 2020; Accepted: 25 May 2020; Published: 29 May 2020

Abstract: Size distribution, Young's moduli and electrical resistivity are investigated for CuO nanowires synthesized by different thermal oxidation methods. Oxidation in dry and wet air were applied for synthesis both with and without an external electrical field. An increased yield of high aspect ratio nanowires with diameters below 100 nm is achieved by combining applied electric field and growth conditions with additional water vapour at the first stage of synthesis. Young's moduli determined from resonance and bending experiments show similar diameter dependencies and increase above 200 GPa for nanowires with diameters narrower than 50 nm. The nanowires synthesized by simple thermal oxidation possess electrical resistivities about one order of magnitude lower than the nanowires synthesized by electric field assisted approach in wet air. The high aspect ratio, mechanical strength and robust electrical properties suggest CuO nanowires as promising candidates for NEMS actuators.

Keywords: CuO; nanowire; synthesis; thermal oxidation; Young's modulus; electrical resistivity; NEMS

1. Introduction

Metallic, semiconducting and insulating Cu based nanomaterials have been demonstrated and are well recognized materials in the fields of electronic devices and catalysis. Metallic nanowires of Cu have mostly been used for applications in flexible and transparent electrode materials. Cu nanowires have been synthesized by several approaches, for example, the hydrothermal reduction process [1] and template-based electrodeposition [2], as well as the thermal reduction of copper(II) oxide CuO nanowires [3].

Semiconducting Cu-based nanowires, such as p-type CuO in particular, are commonly recognized as a catalyst material [4]. Nanowires of CuO have attracted broad interest in many applications including in sensors [5–7] and nanoelectronics (transistors [8,9], electric field emitters [10], memristors [11] and other), mainly due to their enhanced aspect ratio [12], achieved by using relatively simple and low cost synthesis. CuO nanowires also exhibit high stiffnesses [13], which make them promising candidates for high-frequency and speed nanoelectromechanical systems (NEMS) [14,15]. Nanoresonators [16] and switches [15,17] employ nanowires for both mechanical actuation and electrical signal transduction. To achieve improved performance of these devices, more extensive studies of mechanical and electrical

properties of the nanowires and the development of simple growth protocols to controllably achieve nanowires with required parameters are needed.

The growth of CuO nanowires can be realized through various routes; for example, hydrothermal [18], electrochemical [19], solid-state conversion [20] or thermal oxidation [12]. Thermal oxidation is considered as one of the simplest and cheapest methods for scalable synthesis of crystalline CuO nanowires [12]. In this process, the surface of Cu substrates becomes oxidized and forms a Cu_2O layer, which acts as a precursor for the formation of a CuO layer with nanowires. Previous studies revealed that synthesis parameters (temperature, time, air flow, etc.) can significantly affect both the yield and size distribution of the nanowires [21,22]. The synthesis typically utilizes a temperature range from 400 °C to 700 °C [12,23]. Nanowire synthesis in the presence of water vapour resulted in longer and thinner nanowires due to an increased oxidation rate of copper [24]. A similar effect was observed for nanowire synthesis in external electric field [25], where CuO nanowires grew longer [26] and had more uniform diameters [25]. However, a combination of both humidity and electric field during CuO nanowire synthesis by thermal oxidation has yet to be studied. Moreover, the crystalline structure of CuO nanowires, which is impacted by the synthesis method, may also influence their mechanical properties [13].

The mechanical and electrical characterization of nanowires is challenging, since it requires precise manipulation at the nanoscale. The Young's moduli must be carefully evaluated by measuring individual nanowires, because they can exhibit size-dependence arising from defects [13] and surface stress [27,28]. Previously reported Young's moduli for CuO nanowires synthesized by thermal oxidation were in the range of 70–300 GPa [13], and showed a significant increase for thin nanowires compared to bulk material [13]. The electrical transport mechanisms of similar nanowires contacted by metallic electrodes can be a combination of ohmic with resistivities of 10–40 Ωm [9,23], and space-charge-limited current (SCLC) [29,30], similar to other semiconductor nanowires [31,32]. Electrical properties of CuO nanowires were also observed to depend significantly on the defect concentrations [30].

In this work, we have investigated the electric field-assisted thermal oxidation of Cu foil to achieve a high yield growth of high aspect ratio CuO nanowires in conditions of wet air, and compared the properties of these nanowires with those synthesized by a simple thermal oxidation in dry air. Statistical analysis of the experimentally measured geometrical parameters of the nanowires grown by different methods and synthesis conditions (dry and wet air) was used to compose detailed distributions of the nanowire geometrical parameters. The Young's moduli were determined from mechanical resonance by in-situ electron microscopy [33,34] and bending tests by atomic force microscopy [33,35], which have proven suitability for assessing the properties of individual nanowires. Current-voltage characteristics were recorded for individual CuO nanowires of different lengths between the electrodes and the transfer length method was used to determine contact resistances and calculate the resistivities of the CuO nanowires. The determined characteristics of the nanowires were compared to properties of other nanomaterials, which have found application in NEMS.

2. Materials and Methods

Synthesis of the CuO nanowires on a Cu foil substrate (99.9% purity, 25 μm thickness) (Goodfellow GmbH, Hamburg, Germany) was performed in a GSL-1100X tube furnace (length 60 cm, diameter 46 mm) (MTI Corporation, Richmond, CA, USA). To prepare the substrates, the foil was cut in 16 × 25 mm pieces and rinsed in distilled water. The substrates were placed in the furnace tube and heated from room temperature up to 500 °C for 30 min at a constant heating rate of 16 °C/min. The temperature was maintained constant at 500 °C for 210 min, after which the furnace was turned off and left to cool down to room temperature. To increase air humidity during the initial stage of synthesis, a small vessel containing 7 μL of distilled water was placed inside the furnace tube near the substrate. This was done when the temperature had reached the critical temperature of water (374 °C) to avoid the formation of water droplets on the substrate. For generation of electric field, the Cu foil was

placed between two steel electrodes 1 cm apart, and a voltage of 200 V was applied by a Keithley 6487 Picoammeter/Voltage source (Tektronix (China) Co. Ltd, Shanghai, China) (Figure 1a).

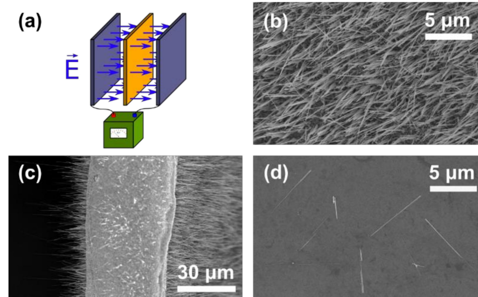

Figure 1. (**a**) Schematic representation of Cu foil between electrodes; SEM images: (**b**) CuO nanowires synthesized on a Cu foil (top view); (**c**) CuO nanowires synthesized on a Cu foil (side view); (**d**) transferred CuO nanowires on Si/SiO_2 substrate.

After synthesis, the oxidized foil was examined in a Hitachi S4800 scanning electron microscope (SEM, Hitachi Ltd., Chiyoda, Tokyo, Japan). The obtained images confirmed that nanowires had grown on both sides of the foil substrate (Figure 1b). The oxidized surface layer of foil containing synthesized nanowires was then mechanically removed and dispersed in isopropanol via ultrasonication for 3 s. The layer containing nanowires was removed from both the cathode and anode sides separately for the electric field assisted synthesis (Figure 1c).

The dispersed nanowires were then transferred to a Si/SiO_2 chip by placing a drop of the suspension on the substrate. After the isopropanol had evaporated the nanowires were examined in a SEM. The acquired images (Figure 1d) were analyzed with ImageJ software to determine nanowire lengths and diameters. SEM images with typical magnifications of ×1k and ×90k were used for the measurements of lengths and diameters, respectively. The measured length and diameter data were organized into separate datasets for each combination of synthesis parameters and used for extraction of the mean values and histograms.

Mechanical characterization of the nanowires was performed by 3-point bending tests on double-clamped nanowires by a Bruker Dimensions Edge atomic force microscope (AFM) (Bruker Corporation, Billerica, MA, USA) and mechanical resonance tests on single-clamped nanowires by in situ SEM [33,35]. For the bending tests, nanowires were transferred onto chemically etched trenches with heights of 0.5 µm and widths of 6 µm prepatterned on SiO_2 substrate surface by gently pressing the Cu foil against it. This resulted in randomly placed nanowires, and freely suspended nanowires with both ends supported were chosen for 3-point bending tests. Figure 2 shows a schematic of the AFM 3-point bending test and an SEM picture of a single nanowire on a trench. A number of force-displacement curves were measured, and Young's moduli were calculated by using finite element method (FEM) [35].

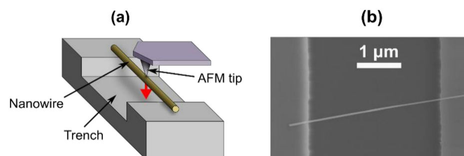

Figure 2. (**a**) Schematic of the AFM 3-point bending test; (**b**) SEM image of a typical CuO nanowire on a trench (top view).

For the resonance tests, nanowires in the isopropanol suspension were dielectrophoretically aligned [36,37] on the edges of pre-patterned Cr/Au electrodes with heights of 0.5 µm above the SiO_2 substrate surface. Aligned nanowires with one end supported on the electrode and the other end suspended were chosen for the resonance measurements. Nanowire vibrations were excited by AC/DC voltage applied between the nanowire and a metallic tip counter electrode (Figure 3a,b). The AC signal was generated by the AC sweep function generator Agilent N9310A (Agilent Technologies Inc., Santa Clara, CA, USA), the DC voltage was supplied by a Keithley 6487 voltage source, the signal was monitored by a TDS 1012 oscilloscope (Tektronix Inc., Beaverton, OR, USA). The resonance was detected visually from SEM images (Figure 3c,d). The Young's moduli were determined from nanowire resonance frequencies and geometry analytically using Euler–Bernoulli theory.

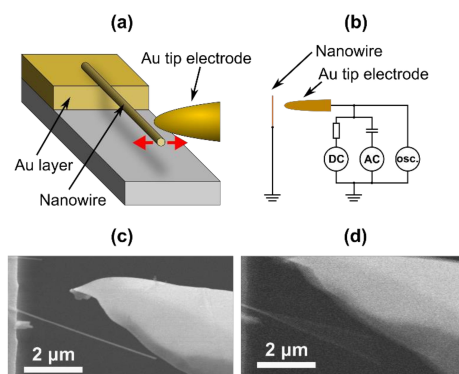

Figure 3. (**a**) Schematic of the in-situ SEM resonance test; (**b**) electric circuit during the resonance test; (**c**) CuO nanowire before resonance; (**d**) CuO nanowire during resonance.

To enable electrical transport measurements, CuO nanowires were mechanically transferred by gently pressing a peeled-off copper oxide layer on Si/SiO_2 substrates. Electron beam lithography was used to fabricate contacts to the individual nanowires. Sequential layers of Pd (3 nm) and Au (80 nm) were evaporated as the electrode material. Current–Voltage characteristics (IVC) were recorded at ambient conditions using a Keithley 4200SCS parameter analyser (Keithley Instruments, Inc., Cleveland, OH, USA).

3. Results and Discussion

3.1. Size Distribution of CuO Nanowires

The geometrical parameters of CuO nanowires (diameter and length) were determined using SEM images captured for nanowires transferred to Si/SiO_2 substrates. In total, more than eight thousand measurements of length and diameter were recorded and summarized in datasets. Statistical analysis was applied to evaluate the distributions of the nanowire dimensions in histograms and extract the mean values of diameters and lengths for each type of synthesis.

Figure 4a–f shows histograms of the diameters and lengths of nanowires synthesized by thermal oxidation with and without electric field and in wet or dry air. Diameters of the nanowires were found to be in a range from 20 to 320 nm for all the growth approaches and conditions used, with some of the thinnest nanowires reaching 5 nm in diameter (Figure 4a–c). However, these diameter distributions show a different percentage of nanowires with diameters below 100 nm for different growth approaches.

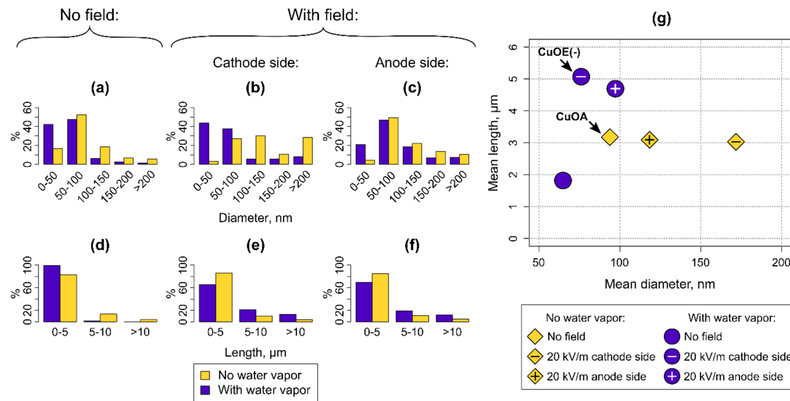

Figure 4. (**a**–**c**) Diameters and (**d**–**f**) lengths of CuO nanowires: (**a**) and (**d**) with no electric field; (**b**) and (**e**): with an applied 20 kV/m electric field on the cathode side of the substrate; (**c**) and (**f**) with an applied 20 kV/m electric field on the anode side of the substrate; (**g**) mean diameters and lengths of CuO nanowires synthesized by different methods. The nanowires selected for the mechanical and electrical characterization are denoted as CuOA—nanowires synthesized by thermal oxidation (dry air), CuOE(-)—nanowires synthesized in electric field (cathode side, wet air).

(1) Thermal oxidation without electric field. The synthesis in normal dry air conditions resulted in the relatively narrow, symmetrical distribution of nanowire diameters mainly being below 100 nm. Approximately 69% of the nanowires synthesized by this method were thin (<100 nm) (Figure 4a). Conditions of added water vapour resulted in notably increased ratio of the small diameter nanowires (50 nm and below) and increased the proportion of the thin nanowires up to 89% (Figure 4a). This phenomenon could be explained considering the fact that the water vapour initially increases the oxidation rate of copper [24], which is particularly important at the beginning of the growth. Under these conditions, grain size of CuO is expected to increase and eventually slow down the further oxidation of copper [38,39]. When the content of water vapour becomes reduced, further growth of the CuO nanowires takes place without the presence of the water vapour resulting in nanowires of narrower diameters.

(2) Thermal oxidation with electric field. The synthesis employing electric field yielded in broader distributions of nanowire diameters, compared to the results from conventional synthesis (Figure 4g). The nanowires can be obtained on both the cathode and anode sides of the substrate, and the nanowires from these sides were found to have different size distributions (Figure 4b,c). Obtained distributions of diameters of the nanowires from the substrate surface at the anode side were rather similar in both conditions of the synthesis (in dry and wet air, Figure 4c,g) and comparable to the ones synthesized without electric field (Figure 4a,g). Approximately half of the nanowires grown on the anode side of the substrate were with diameters of 50–100 nm (Figure 4c).

However, the distribution of the nanowire diameters obtained from the cathode side of the substrate is entirely different. Here the growth conditions more prominently affect the nanowire diameters, and wider distribution of dominating 100–150 nm, and >200 nm diameter nanowires were achieved for synthesis without water vapour (Figure 4b,g). As a result, the number of thin nanowires dropped from 69% down to 34%. Interestingly, nearly the opposite trend (narrower distribution with dominating thin <50 nm and 50–100 nm diameters of the nanowires) can be achieved if the water vapour is used (Figure 4b,g). The percentage of thin nanowires of 81% on the cathode side is close to

that in wet air thermal oxidation without electric field (89%), and suggests that humidity compensates the effect of electric field on nanowire diameter.

The lengths of the nanowires transferred from the synthesis substrate to surface of SiO_2 varied from 0.2 to 39 μm. The nanowires became shorter due to breakage during the ultrasonication process. Thinner nanowires are expected to break more than the thicker ones. This can explain why the nanowires with the smallest mean diameter have the shortest mean length (Figure 4g). Most of the transferred nanowires synthesized within all the approaches and conditions used were of lengths below 5 μm (Figure 4d–g). The number of nanowires with lengths >5 μm increased for the electric field assisted synthesis (Figure 4e–g), particularly within conditions without the water vapour.

The different diameter distribution on the cathode and anode sides could be due to the effect of the electric field on Cu+ ion diffusion direction and velocity. The growth mechanism is similar on both sides of the substrate placed between the cathode and anode electrodes [25,26,40]; therefore, the composition of the nanowires grown on both sides is expected to be similar. The electric field influences lengths and thicknesses of the nanowires, because it facilitates Cu and O ion diffusion along the growth direction of the nanowires parallel to the external electric field. The effect of electric field is more pronounced on the cathode side, since the direction of the external electric field matches the local electric field set up by the O ions at the solid/gas interface. This promotes the Cu ion diffusion and results in increased mass of the CuO nanowires, manifested through increased diameters (synthesis in dry air) or increased lengths (synthesis in wet air). Our results support previously observed changes in diameters and increased lengths and yields of the nanowires grown with electric field compared to the nanowires grown without electric field [25,26].

3.2. Mechanical Characterization

For the fabrication of NEM devices, longer nanowires with diameters below 100 nm are preferable, because they provide lower switch-on voltages and lower adhesion in the contact [41]. The best characteristics for application in NEMS are demonstrated for nanowires synthesized by simple oxidation of Cu in dry air (mean diameter appr. 90 nm and mean length 3 μm) and synthesized with the assistance of electric field on the cathode in a wet air atmosphere (mean diameter appr. 70 nm and mean length 5 μm) (Figure 4g). Nanowires from both batches were chosen for further mechanical and electrical characterization and in further text are denoted as CuOA (thermal oxidation in dry air) and CuOE(-) (electric field, oxidation on the cathode side, wet air).

The Young's moduli were found to be similar for the CuOA and CuOE(-) nanowires. Moreover, the Young's moduli determined from the AFM 3-point bending tests are in agreement with in-situ SEM resonance tests (Figure 5). The observed trend of the Young's moduli for the diameter range 20–160 nm can be described by an exponential trendline (Figure 5, dashed line). When increasing nanowire diameter, the exponential trendline approaches 95 GPa, which is close to the value of 82 GPa for bulk CuO [13]. The size-dependence becomes pronounced for nanowires with diameters below 50 nm. Such size-dependent behavior is in agreement with the previously reported experimental data on CuO nanowires synthesized by thermal oxidation in dry air [13]. The size-dependence of the nanowire Young's modulus can be attributed to the effects of tensile surface stresses [42], which depends on the loading mode (static bending/dynamic resonance) and boundary conditions of the nanowire [27,28]. This can explain a more pronounced size dependence in Young's moduli from bending than resonance. The highest Young's moduli determined for 20–30 nm diameter CuO nanowires can reach even up to ~500 GPa, which is comparable to the Young's moduli for NEMS active element materials, such as TiN and SiC [15].

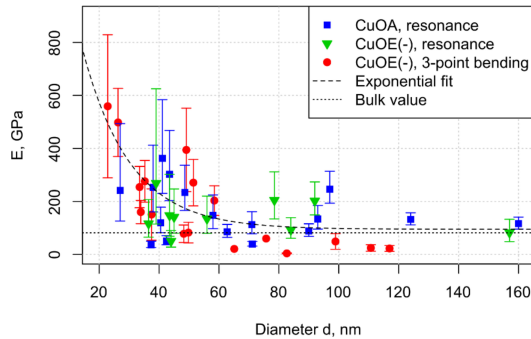

Figure 5. Experimental Young's moduli from resonance and bending tests obtained for 44 CuO nanowires vs. their mean diameters; CuOA—nanowires synthesized by thermal oxidation (dry air), CuOE(-)—nanowires synthesized in electric field (cathode side, wet air). The dashed line is a guide to the eye; the dotted line is the bulk Young's modulus determined in [13].

3.3. Electrical Characterization

A SEM image of one of the CuO nanowires with electrodes fabricated by e-beam lithography for four-point measurements is shown in Figure 6a. In total, seven nanowires—three of them grown by oxidation in dry air CuOA and the others via electric field assisted approach in the presence of added water—were incorporated into similar multiple-contact devices with the same distances between the electrodes. IVCs for the nanowire CuOA–D1 with diameter of 50 nm are plotted in Figure 6b. These IVCs were recorded in a two–electrode configuration, which also includes the contribution from contact resistance, and in the measurements a voltage range of ±2 V (Figure 7a) was used. The voltage range of ±1 V, where the IVCs were linear for all the measured nanowire lengths, was used to extract the resistance.

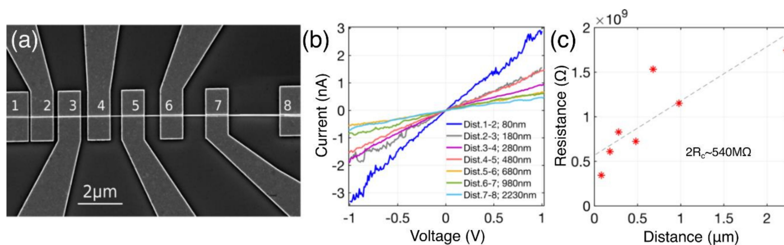

Figure 6. (**a**) SEM image of CuO nanowire with 8 electrodes of distances from 80–2380 nm; (**b**) current—voltage characteristics measured at room conditions and in 2-probe configuration; (**c**) resistance as a function of the nanowire length (different distance between the electrodes). Linear fit (dashed line) intercepts with the y axis at around 540 MΩ representing the contact resistance of the two electrodes 2Rc. SEM image and all the data shown here were recorded for CuO nanowire grown in dry air, without electrical field, nanowire CuOA–D1.

The resistance of the contacts to a single nanowire can be evaluated by the transfer length method where the total measured resistances are expected to scale with the nanowire lengths. Resistance as a function of the distance is shown in Figure 6c. The linear fit intercepts with the resistance axis at 540 MΩ, which represents resistance of the contacts $2R_c$. This extracted value of R_c is rather high

and more effort of CuO nanowire contact interface engineering is needed to achieve lower contact resistances. The extracted values of R_c were of the MΩ range for all the CuOA nanowires-540 MΩ (CuOA-D1); 330 MΩ (CuOA-E1) and 6.63 MΩ (CuOA-E2). The CuOE(-) nanowires showed far larger resistances especially for the long nanowire lengths (contact pairs 5–6, 6–7, 7–8, see SEM image, Figure 6a) making it impossible to obtain reasonable resistance–distance dependences. In the further calculations of resistivities for CuOE(-) nanowires, the largest determined contact resistance of 540 MΩ was accounted for.

IVCs recorded for nanowires of the same electrode separation (~180 nm, electrodes 2–3 in Figure 6a) and of diameters ranging from 36 to 50 nm are depicted in Figure 7a. In order to compare the two kinds of CuO nanowires, resistivities for all the measured nanowires were calculated as $\rho = (R - 2R_c)A/l$, where A and l are the cross-section area and the length of the nanowire, respectively.

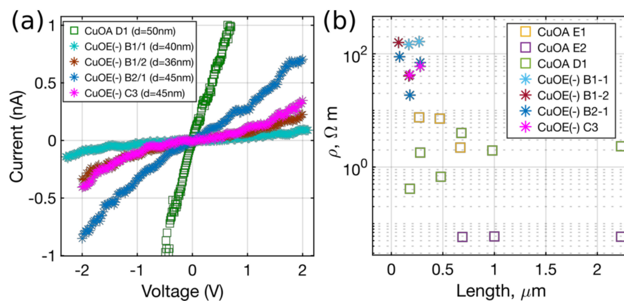

Figure 7. (**a**) IVCs of the CuO nanowires grown via two different approaches; (**b**) calculated resistivities ρ of CuO nanowires shown as a function of the measured nanowire length (distance).

Calculated resistivities for all the nanowires are plotted as a function of the distance (see Figure 7b). In the case of a uniform nanowire/contact resistance the resistivity should be the same for all the nanowire lengths in terms of a single nanowire. This case was entirely true for the CuOA–E1 nanowire of diameter 50 nm (violet squares, Figure 7b), but for the others the values of resistivity vary slightly for different nanowire lengths indicating nonuniform contact (nanowire) resistances. As one can see, the calculated resistivities of CuOA nanowires (0.05–7 Ωm) are lower compared to the ones extracted for CuOE(-) nanowires (20–160 Ωm). This could be explained assuming increased defect concentration [30] for the nanowires synthesized with the electric field assisted approach and in presence of water vapour. Despite the differences in resistivity for CuOA and CuOE(-) nanowires, in general, the resistivities of both types of nanowires are comparable to previously reported values of 10–40 Ωm for CuO nanowires synthesized by simple thermal oxidation method and measured in field effect transistor geometries [9,23]. These values match with characteristics of some materials applied in previously demonstrated NEM switch designs; for example, semiconductor Si and SiC [15]. The relatively high resistivities may be related to low mobility of charge carriers in CuO nanowires at room temperature [29]. The mobility can be increased by increasing the temperature. Due to a high melting point, CuO nanowires are able to withstand harsh environments, similarly to previously demonstrated high-temperature SiC switches [43]. Alternatively, such CuO nanowires are attractive for NEM switches and other devices with high operating voltages, where space-charge-limited currents are expected to dominate charge carrier transport in the nanowires [29,30,32].

4. Conclusions

In summary, CuO nanowires synthesized by a simple thermal oxidation and electric field assisted approach were investigated for different synthesis conditions (in dry and wet air). High

yields of large aspect ratio nanowires with diameters below 100 nm were achieved by increasing air humidity during the initial step of the electric field assisted synthesis. Nanowires synthesized by simple thermal oxidation in dry air and by electric field assisted approach in wet air exhibit similar mechanical properties. Nanowires with diameters less than 50 nm show higher Young's moduli of up to 200–500 GPa. The electrical resistivities are comparable with previously reported values for CuO nanowires, and show an increase for the nanowires synthesized by thermal oxidation with electric field in wet air. Relatively high electrical resistivities in combination with high mechanical stiffness and a high melting point can be favorable in NEM-switching devices operating in extreme conditions (harsh environments and high applied voltages).

Author Contributions: R.S., J.K., G.K. and D.E. designed the experiments; R.S. performed the synthesis and morphological characterization of the nanowires; R.S. and M.A. performed mechanical characterization; G.K. performed electrical characterization; R.S., J.K. and G.K. analyzed the data; L.J., M.M.R., R.M. and E.K. supported experimentation and data analysis; R.S. and G.K. wrote the paper; J.K., D.E., L.J. and R.M. reviewed the paper; D.E. and J.K. supervised the work. All authors have read and agreed to the published version of the manuscript.

Funding: This work was funded by the European Development Fund (project no. 1.1.1.1/16/A/256, "Creation of nanoelectromechanical switches").

Conflicts of Interest: The authors declare no conflict of interest.

References

1. Liu, Z.; Yang, Y.; Liang, J.; Hu, Z.; Li, S.; Peng, S.; Qian, Y. Synthesis of Copper Nanowires via a Complex-Surfactant-Assisted Hydrothermal Reduction Process. *J. Phys. Chem. B* **2003**, *107*, 12658–12661. [CrossRef]
2. Konishi, Y.; Motoyama, M.; Matsushima, H.; Fukunaka, Y.; Ishii, R.; Ito, Y. Electrodeposition of Cu nanowire arrays with a template. *J. Electroanal. Chem.* **2003**, *559*, 149–153. [CrossRef]
3. Han, J.-W.; Lohn, A.; Kobayashi, N.P.; Meyyappan, M. Evolutional Transformation of Copper Oxide Nanowires to Copper Nanowires by a Reduction Technique. *Mater. Express* **2011**, *1*, 176–180. [CrossRef]
4. Reitz, J.B.; Solomon, E.I. Propylene Oxidation on Copper Oxide Surfaces: Electronic and Geometric Contributions to Reactivity and Selectivity. *J. Am. Chem. Soc.* **1998**, *120*, 11467–11478. [CrossRef]
5. Hoa, N.D.; An, S.Y.; Dung, N.Q.; Van Quy, N.; Kima, D. Synthesis of p-type semiconducting cupric oxide thin films and their application to hydrogen detection. *Sens. Actuators B Chem.* **2010**, *146*, 239–244. [CrossRef]
6. Zappa, D.; Comini, E.; Zamani, R.R.; Arbiol, J.; Morante, J.R.; Sberveglieri, G. Preparation of copper oxide nanowire-based conductometric chemical sensors. *Sens. Actuators B Chem.* **2013**, *182*, 7–15. [CrossRef]
7. Luo, L.-B.; Wang, X.-H.; Xie, C.; Li, Z.; Lu, R.; Yang, X.-B.; Lu, J. One-dimensional CuO nanowire: Synthesis, electrical, and optoelectronic devices application. *Nanoscale Res. Lett.* **2014**, *9*, 637. [CrossRef]
8. Sung, S.-Y.; Kim, S.; Jo, K.-M.; Lee, J.-H.; Kim, J.-J.; Kim, S.-G.; Chai, K.-H.; Pearton, S.J.; Norton, D.P.; Heo, Y.-W. Fabrication of p-channel thin-film transistors using CuO active layers deposited at low temperature. *Appl. Phys. Lett.* **2010**, *97*, 222109. [CrossRef]
9. Li, D.; Hu, J.; Wu, R.; Lu, J.G. Conductometric chemical sensor based on individual CuO nanowires. *Nanotechnology* **2010**, *21*, 485502. [CrossRef]
10. Hsieh, C.-T.; Chen, J.-M.; Lin, H.-H.; Shih, H.-C. Field emission from various CuO nanostructures. *Appl. Phys. Lett.* **2003**, *83*, 3383–3385. [CrossRef]
11. Fan, Z.; Fan, X.; Li, A.; Dong, L. In situ forming, characterization, and transduction of nanowire memristors. *Nanoscale* **2013**, *5*, 12310–12315. [CrossRef]
12. Jiang, X.; Herricks, T.; Xia, Y. CuO Nanowires Can Be Synthesized by Heating Copper Substrates in Air. *Nano Lett.* **2002**, *2*, 1333–1338. [CrossRef]
13. Tan, E.P.S.; Zhu, Y.; Yu, T.; Dai, L.; Sow, C.-H.; Tan, V.; Lim, C.T. Crystallinity and surface effects on Young's modulus of CuO nanowires. *Appl. Phys. Lett.* **2007**, *90*, 163112. [CrossRef]
14. Loh, O.Y.; Espinosa, H.D. Nanoelectromechanical contact switches. *Nat. Nanotechnol.* **2012**, *7*, 283–295. [CrossRef] [PubMed]
15. Jasulaneca, L.; Kosmaca, J.; Meija, R.; Andzane, J.; Erts, D. Review: Electrostatically actuated nanobeam-based nanoelectromechanical switches—Materials solutions and operational conditions. *Beilstein J. Nanotechnol.* **2018**, *9*, 271–300. [CrossRef]

16. Husain, A.; Hone, J.; Postma, H.; Huang, X.M.H.; Drake, T.; Barbic, M.; Scherer, A.; Roukes, M.L. Nanowire-based very-high-frequency electromechanical resonator. *Appl. Phys. Lett.* **2003**, *83*, 1240–1242. [CrossRef]
17. Meija, R.; I Livshits, A.; Kosmaca, J.; Jasulaneca, L.; Andzane, J.; Biswas, S.; Holmes, J.D.; Erts, D. Resonance assisted jump-in voltage reduction for electrostatically actuated nanobeam-based gateless NEM switches. *Nanotechnology* **2019**, *30*, 385203. [CrossRef]
18. Xiao, H.-M.; Fu, S.-Y.; Zhu, L.-P.; Li, Y.-Q.; Yang, G. Controlled Synthesis and Characterization of CuO Nanostructures through a Facile Hydrothermal Route in the Presence of Sodium Citrate. *Eur. J. Inorg. Chem.* **2007**, *2007*, 1966–1971. [CrossRef]
19. Toboonsung, B.; Singjai, P. Formation of CuO nanorods and their bundles by an electrochemical dissolution and deposition process. *J. Alloy. Compd.* **2011**, *509*, 4132–4137. [CrossRef]
20. Liu, X.; Zhang, J.; Kang, Y.; Wu, S.; Wang, S. Brochantite tabular microspindles and their conversion to wormlike CuO structures for gas sensing. *CrystEngComm* **2012**, *14*, 620–625. [CrossRef]
21. Kumar, A.; Srivastava, A.K.; Tiwari, P.; Nandedkar, R.V. The effect of growth parameters on the aspect ratio and number density of CuO nanorods. *J. Physics: Condens. Matter* **2004**, *16*, 8531–8543. [CrossRef]
22. Liang, J.; Kishi, N.; Soga, T.; Jimbo, T. The Synthesis of Highly Aligned Cupric Oxide Nanowires by Heating Copper Foil. *J. Nanomater.* **2011**, *2011*, 1–8. [CrossRef]
23. Gonçalves, A.M.B.; Campos, L.C.; Ferlauto, A.; Lacerda, R.G. On the growth and electrical characterization of CuO nanowires by thermal oxidation. *J. Appl. Phys.* **2009**, *106*, 34303. [CrossRef]
24. Xu, C.; Woo, C.; Shi, S.-Q. The effects of oxidative environments on the synthesis of CuO nanowires on Cu substrates. *Superlattices Microstruct.* **2004**, *36*, 31–38. [CrossRef]
25. Li, X.; Zhang, J.; Yuan, Y.; Liao, L.; Pan, C. Effect of electric field on CuO nanoneedle growth during thermal oxidation and its growth mechanism. *J. Appl. Phys.* **2010**, *108*, 24308. [CrossRef]
26. Tang, C.; Liao, X.; Zhong, W.; Yu, H.; Liu, Z. Electric field assisted growth and field emission properties of thermally oxidized CuO nanowires. *RSC Adv.* **2017**, *7*, 6439–6446. [CrossRef]
27. He, J.; Lilley, C.M. Surface Effect on the Elastic Behavior of Static Bending Nanowires. *Nano Lett.* **2008**, *8*, 1798–1802. [CrossRef]
28. He, J.; Lilley, C.M. Surface stress effect on bending resonance of nanowires with different boundary conditions. *Appl. Phys. Lett.* **2008**, *93*, 263108. [CrossRef]
29. Wu, J.; Yin, B.; Wu, F.; Myung, Y.; Banerjee, P. Charge transport in single CuO nanowires. *Appl. Phys. Lett.* **2014**, *105*, 183506. [CrossRef]
30. Lin, Z.; Zhan, R.; Li, L.; Liu, H.; Jia, S.; Chen, H.; Tang, S.; She, J.; Deng, S.; Xu, N.; et al. Defect-concentration dependence of electrical transport mechanisms in CuO nanowires. *RSC Adv.* **2018**, *8*, 2188–2195. [CrossRef]
31. A Talin, A.; Leonard, F.; Katzenmeyer, A.M.; Swartzentruber, B.; Picraux, S.T.; E Toimil-Molares, M.; Cederberg, J.G.; Wang, X.; Hersee, S.D.; Rishinaramangalum, A. Transport characterization in nanowires using an electrical nanoprobe. *Semicond. Sci. Technol.* **2010**, *25*, 24015. [CrossRef]
32. Kunakova, G.; Viter, R.; Abay, S.; Biswas, S.; Holmes, J.D.; Bauch, T.; Lombardi, F.; Erts, D. Space charge limited current mechanism in Bi2S3 nanowires. *J. Appl. Phys.* **2016**, *119*, 114308. [CrossRef]
33. Jasulaneca, L.; Meija, R.; Livshits, A.I.; Prikulis, J.; Biswas, S.; Holmes, J.D.; Erts, D. Determination of Young's modulus of Sb2S3 nanowires by in situ resonance and bending methods. *Beilstein J. Nanotechnol.* **2016**, *7*, 278–283. [CrossRef] [PubMed]
34. Kosmaca, J.; Jasulaneca, L.; Meija, R.; Andzane, J.; Romanova, M.; Kunakova, G.; Erts, D. Young's modulus and indirect morphological analysis of Bi2Se3nanoribbons by resonance measurements. *Nanotechnology* **2017**, *28*, 325701. [CrossRef] [PubMed]
35. Kosmaca, J.; Meija, R.; Antsov, M.; Kunakova, G.; Sondors, R.; Iatsunskyi, I.; Coy, E.; Doherty, J.; Biswas, S.; Holmes, J.D.; et al. Investigating the mechanical properties of GeSn nanowires. *Nanoscale* **2019**, *11*, 13612–13619. [CrossRef] [PubMed]
36. Kunakova, G.; Meija, R.; Bite, I.; Prikulis, J.; Kosmaca, J.; Varghese, J.; Holmes, J.D.; Erts, D. Sensing properties of assembled Bi2S3nanowire arrays. *Phys. Scr.* **2015**, *90*, 94017. [CrossRef]
37. Ramma, M.M.; Katkevics, J.; Jasulaneca, L.; Kunakova, G.; Sondors, R.; Meija, R.; Erts, D.; Kosmaca, J. Dielectrophoretic alignment and electrical characterization of CuO nanowire-based systems. **2020**. Unpublished work.

38. Liang, J.B.; Li, X.Y.; Kishi, N.; Soga, T. Single Phase CuO Thin Films Prepared by Thermal Oxidation in Air with Water Vapor. *Adv. Mater. Res.* **2015**, *1109*, 544–548. [CrossRef]
39. Han, Z.; Lu, L.; Zhang, H.W.; Yang, Z.Q.; Wang, F.H.; Lu, K. Comparison of the Oxidation Behavior of Nanocrystalline and Coarse-Grain Copper. *Oxid. Met.* **2005**, *63*, 261–275. [CrossRef]
40. Farbod, M.; Ghaffari, N.M.; Kazeminezhad, I. Fabrication of single phase CuO nanowires and effect of electric field on their growth and investigation of their photocatalytic properties. *Ceram. Int.* **2014**, *40*, 517–521. [CrossRef]
41. Jasulaneca, L.; Livshits, A.; Meija, R.; Kosmaca, J.; Sondors, R.; Ramma, M.; Jevdokimovs, D.; Prikulis, J.; Erts, D. Fabrication and characterization of CuO nanowire based nanoelectromechanical switches. **2020**. Unpublished work.
42. Wang, G.; Li, X. Predicting Young's modulus of nanowires from first-principles calculations on their surface and bulk materials. *J. Appl. Phys.* **2008**, *104*, 113517. [CrossRef]
43. Lee, T.-H.; Bhunia, S.; Mehregany, M. Electromechanical Computing at 500°C with Silicon Carbide. *Science* **2010**, *329*, 1316–1318. [CrossRef] [PubMed]

© 2020 by the authors. Licensee MDPI, Basel, Switzerland. This article is an open access article distributed under the terms and conditions of the Creative Commons Attribution (CC BY) license (http://creativecommons.org/licenses/by/4.0/).

Paper VIII

IOP Publishing Nanotechnology

Nanotechnology **30** (2019) 385203 (6pp) https://doi.org/10.1088/1361-6528/ab2b11

Resonance assisted jump-in voltage reduction for electrostatically actuated nanobeam-based gateless NEM switches

R Meija[1], A I Livshits[1], J Kosmaca[1], L Jasulaneca[1], J Andzane[1], S Biswas[2], J D Holmes[2] and D Erts[1,3]

[1] Institute of Chemical Physics, University of Latvia, Latvia
[2] School of Chemistry, ERI and the Tyndall National Institute, University College Cork, Cork, Ireland
[3] Faculty of Chemistry, University of Latvia, Latvia

E-mail: raimonds.meija@lu.lv

Received 7 March 2019, revised 29 April 2019
Accepted for publication 19 June 2019
Published 8 July 2019

Abstract

Electrostatically actuated nanobeam-based electromechanical switches have shown promise for versatile novel applications, such as low power devices. However, their widespread use is restricted due to poor reliability resulting from high jump-in voltages. This article reports a new method for lowering the jump-in voltage by inducing mechanical oscillations in the active element during the switching ON process, reducing the jump-in voltage by more than three times. $Ge_{0.91}Sn_{0.09}$ alloy and Bi_2Se_3 nanowire-based nanoelectromechanical switches were constructed *in situ* to demonstrate the operation principles and advantages of the proposed method.

Supplementary material for this article is available online

Keywords: NEMS, nanowire, resonance, switch, Bi_2Se_3, GeSn

(Some figures may appear in colour only in the online journal)

Introduction

Nanoelectromechanical (NEM) systems have shown great promise in the automotive [1], space [2] and electronics [3] industries for applications such as high frequency resonators [4], mass sensing [5–7] and switches [8–12]. NEM systems represent the next technological advancement after micro-electromechanical systems in terms of switching speed, energy efficiency and integration density.

A NEM switch is a type of a NEM system, where mechanical and electrical properties of flexile nanostructures are exploited for switching between the ON and OFF positions. NEM switches have been proposed as low power [13] devices with small leakage currents and high on/off ratios [14–17]. Currently, the biggest challenge that delays the commercialization of NEM switches, especially proposed gateless switches with high jump-in voltages, is their insufficient durability [11, 12].

One of the main challenges for the durable operation of a gate-less NEM switch is controlling electric field induced effects. Uncontrolled, these effects may result in the permanent ON state (stiction) or burn-out of the flexile element of the switch. High electric fields, in the order of 10^8 V m^{-1}, between the contact electrodes may result in switch stiction due to the field-induced material transfer [18, 19]. For metal–metal nanocontacts, the material transfer induced stiction has been reported for the source–drain voltage exceeding 5 V [19]. Higher jump-in voltages can also result in electric field induced burn-out of the flexile element in two-terminal devices [8, 10, 20–22]. Low jump-in voltages for a particular switch architecture will therefore likely increase the durability of a switch.

Several approaches to lower the jump-in voltage for gate-less switches have been reported, with the most straightforward method being a reduction of the separation gap between the flexile element and the contact electrode [17, 23]. A drawback of this approach is a decrease of the restoring elastic force accompanying the separation gap reduction, often resulting in a permanent stiction of the flexile element in an ON state due to the adhesion in the contact with the electrode. Other more sophisticated ways to lower the jump-in

 © 2019 IOP Publishing Ltd Printed in the UK

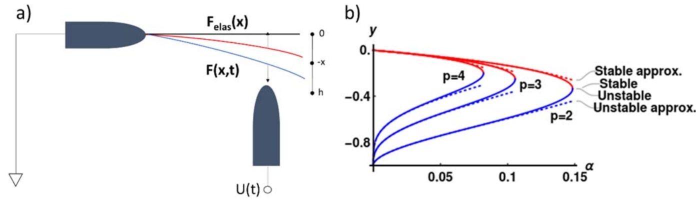

Figure 1. (a) Electrostatically actuated NEM switch. $U(t)$—voltage applied between the electrode and the flexile element, h—initial distance (gap) between the active element and the electrode, $-x$—the deflection of the active element. Black line—initial position of the nanowire, when $U(t) = 0$. When $U(t)$ is applied, red line is the stable deflection of the nanowire and blue line is the unstable deflection of the nanowire, which leads to jump in contact or return to the stable position. (b) Stable and unstable solutions of the equation (1). Numerical solution is given by the solid line, while approximation—by the dotted line. For each α there is a y value that represents the stable solution (red line) and the unstable solution (blue line) for the equation (4).

voltage have included using novel device architectures, e.g. pipe-clip design [15], and operating the switch in a dielectric liquid [24].

The flexile elements of NEM switches are either fabricated by top–down processes, using e-beam lithography techniques, or synthesized independently by a bottom-up technique and then arranged to the desired positions on the NEM device during its configuration. Using synthesized nanowires instead of lithography made nanobeams as flexile elements in the NEM switches offers increased control over their chemical composition and morphology. Other advantages include smooth contact surfaces, low defect densities and mechanical properties that approach the theoretical limits for strength [25].

We have previously shown that mechanical oscillations of a flexile element can be utilized to monitor switch dynamics and adjust contact adhesion between an electrode and the flexile element in a NEM switch [26, 27]. We have also reported a method for switching a nanowire flexile element in a NEM device from an ON to OFF state by inducing resonant mechanical oscillations [28], reducing the work of adhesion and consequently the switching voltage by up to 10 times for the gate-less NEM switches. Oscillations induced in the flexile element have also been used to monitor its mechanical strain [27] and the changes in NEM switch nanocontacts [29].

This article reports a novel approach to decrease the jump-in voltage (ON state) by inducing electrostatically induced mechanical oscillations in the flexile element of a NEM switch while it is in its OFF state. The method allows maintenance of a large initial separation gap between the flexile element and the contact electrode, leading to an elastic restoration force strong enough to overcome adhesion in the ON state contact. This approach also limits the jump-in current, thus preventing current-induced modifications in the contact during the ON state, which could result in a permanent stiction of the switch [17, 23, 29]. This method is presented for both cylindrical $Ge_{0.91}Sn_{0.09}$ (GeSn) and rectangular Bi_2Se_3 nanowires. We chose GeSn nanowires, because of their combination of high mechanical strength [30], lower resistivity [31] and absence of non-conductive germanium oxide outer shell [32] that is present in previously used Ge nanowires [8]. Bi_2Se_3 nanowires were chosen because of their lower resistivity and increased contact area due to their rectangular shape, thus making them more conductive [33, 34]. As Bi_2Se_3 is a thermoelectric material [35], they could be also used in novel applications, for example, to detect temperature difference across switch terminals.

Materials and methods

The experiments were carried out *in situ* SEM Hitachi S-4800. For the contact electrodes, electrochemically etched gold (GoodFellow 99.95%) tips were used. Sharp tips were used to achieve a smaller contact area and thus lower adhesion in the contact. A SmarAct 13D nanomanipulator was used to transfer nanowires from substrates used for their synthesis to gold tips, and for acquiring the desired switch geometry.

GeSn and Bi_2Se_3 nanowires (cylindrical and rectangular shapes) were used as switching elements. The GeSn nanowires were synthesized by a vapor–liquid–solid method [32] and the Bi_2Se_3 nanowires were synthesized by catalyst-free physical-vapor-deposition [33, 34].

For the electric measurements, Keithley 6430 and Keithley 6487 source-meters were used. An Agilent N9310A signal generator was used to induce the electrical oscillations between the nanowires and the gold electrodes. The methodology for the resonance frequency and Q-factor measurements was similar to that previously reported [12, 26].

Results and discussions

The schematics of an electrostatically actuated gate-less NEM switch in different OFF states can be seen in figure 1(a). The position of the flexile element (in our case nanowire) during the switch operation is determined by the resultant force arising from the superposition of an attractive electrical force $F(x, t)$ and a repulsive elastic force of the deflected from the equilibrium position nanowire $F_{elas}(x)$. The attractive force can be caused solely by an applied DC field between the electrodes, inducing deflection of the nanowire towards

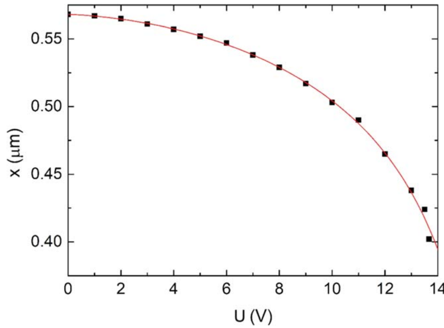

Figure 2. Deflection of a GeSn nanowire with $L_{\mathrm{GeSn}} = 14.8\ \mu$m, $R_{\mathrm{GeSn}} = 115$ nm, $f_0 = 623$ kHz, $Q = 550$ and $E = 106$ GPa as a function of static electric field applied between the NEM switch electrodes. Data points—experiment, red line—fitted theoretical calculations. After the last experimental point (13.7 V) the jump-in occurred at 13.8 V.

the opposite electrode or by the combination of AC and DC fields, inducing the deflection and mechanical oscillations of the nanowire at its resonance frequency simultaneously.

A theoretical model was developed to qualitatively describe the operation of this NEM switch. While not providing a quantitative description of the NEM switch operation, the model explains the main idea underlying the above configuration of the NEM switch, as well as illustrating the basic features of its operation.

Associating the coordinate x with the perpendicular deflection of the free end of the nanowire (figure 1(a)), the differential equation corresponding to the motion of the nanowire is given by the expression shown in equation (1):

$$\ddot{x}(t) + \frac{2\pi f_0}{Q}\dot{x}(t) + (2\pi f_0)^2 x(t) = F(x, t), \tag{1}$$

where f_0 stands for the oscillator's material dependent mechanical eigen frequency of a nanowire, Q for its quality factor and $F(x, t)$ for the external electrostatic force per mass unit. This force is proportional to the square of the electric field. The latter is proportional to the voltage applied between the switching element and the counter electrode. If both DC and AC voltages are applied the resulting force $F(x, t)$ can be written as shown in equation (2):

$$F(x, t) = g(x)\bigg(U_{dc}{}^2 + \frac{1}{2}U_{ac}{}^2 + 2U_{dc}U_{ac}\sin(2\pi ft) - \frac{1}{2}U_{ac}{}^2\cos(4\pi ft)\bigg), \tag{2}$$

where f is AC field frequency and U_{ac}, U_{dc} are AC and DC voltages—respectively.

The important feature of the force represented in equation (2) is that it depends not only on time directly, but also indirectly through the time-dependence on unknown function $g(x)$, as the coordinate x is also a function of time. An accurate enough model of the external force $F(x, t)$ can be obtained by solving the corresponding electrostatic problem (equation (2)) numerically. In this paper we are interested only in the first mode of oscillation, which has the highest amplitude for oscillations, which permits the nanowire to be considered just as a harmonic oscillator. A simple qualitative consideration can then be used, together with an analytic model function, for $g(x)$ as shown in equation (3):

$$g(x) = \frac{-K}{(x + h)^p}, K > 0, p > 2\,. \tag{3}$$

The proportionality constant K, the power parameter p, and the distance between the initial non-deformed nanowire and the counter electrode surface h are present in equation (3). h is expected to be positive and x to be negative, thus the attractive force grows when $x \to -h$. For simplicity a dimensionless coordinate $y = \frac{x}{h}$ will be used.

DC only

First, the static solution when only DC voltage was applied to the NEM switch [8–10, 22] was considered to estimate the free parameters for the setup used in our experiments. In such a case, equation (1) reduces to equation (4) as shown below:

$$y = \frac{-\alpha}{(y + 1)^p};\ \alpha = K\frac{U_{dc}{}^2}{(2\pi f_0)^2},\ \alpha_0 = \frac{K}{(2\pi f_0)^2}. \tag{4}$$

In figure 1(b), solutions to equation (4) in the interval $y\epsilon[0;1]$ are plotted. For the case of $p = 2$, by inspecting the roots of the corresponding cubic equation, if $\alpha < \frac{4}{27}$, two such solutions exist. The solution which corresponds to the smaller deflection (figures 1(a), (b) red line) represents a stable equilibrium. The solution which corresponds to the larger deflection (figures 1(a), (b) blue line) represents an unstable equilibrium from which a jump to contact can occur. The solution remains qualitatively unchanged if p is positive, which corresponds to all real experimental setups.

The approximate expression for the stable equilibrium (figures 1(a), (b)—dotted red line) can be found as a power expansion, shown in equation (5). To obtain this result one must represent the unknown function as a Taylor expansion around $\alpha = 0$. By taking derivatives of the equation (4) it is possible to get all of the necessary expansion coefficients, like $y(0) = 0$, $\frac{dy(0)}{d\alpha} = -1$, and so on

$$y_{stable} = -\alpha - p\alpha^2 - \frac{1}{2}(p + 3p^2)\alpha^3 - \frac{1}{3}(p + 6p^2 + 8p^3)\alpha^4 + \ldots \tag{5}$$

The approximate expression for the unstable equilibrium (figures 1(a), (b)—dashed blue line) can be written as detailed in equation (6). This result is achieved by rewriting the equation (4) as $y = -1 - \alpha^{1/p}/y^{1/p}$ and then expanding the unknown function in powers of $\alpha^{1/p}$ the same way as it was

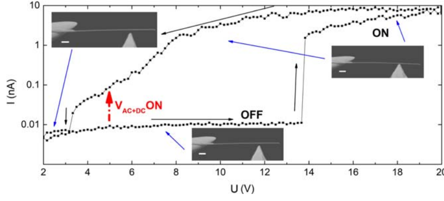

Figure 3. *I–V* characteristics of a DC-only driven NEM switch for a GeSn nanowire with $L_{\text{GeSn}} = 14.8\ \mu$m, $R_{\text{GeSn}} = 115$ nm, $f_0 = 623$ kHz, $Q = 550$ and $E = 106$ GPa. Black arrows show direction of the voltage sweep. Blue arrows show SEM images of the NEM switch in ON and OFF states during the sweep. Red arrow represents the jump-in voltage for the switch driven by a combined AC–DC field. White scale bars in SEM pictures represent 1 μm.

done for the stable solution (5)

$$y_{unstable} = -1 + \alpha^{\frac{1}{p}} + \frac{1}{p}\alpha^{\frac{2}{p}} + \frac{3+p}{2p^2}\alpha^{\frac{3}{p}} + \frac{8+6p+p^2}{3p^3}\alpha^{\frac{4}{p}} + \ldots \tag{6}$$

If the applied DC voltage increases, the parameter α which is proportional to the voltage squared (equation (4)) also increases, and the nanowire will deflect more. When α reaches its largest value (figure 1(b)—intersection between the blue and red lines), the jump-in voltage is reached, and the nanowire jumps into the contact with the electrode (figure 1(a)). The largest value of α depends on the chosen value of the parameter *p*. As can be seen from the figure 1(b), for $p = 3$ α is close to 0.105 and for $p = 4$ α is close to 0.081.

To test the above theoretical model and to find the exact values of parameters *p* and α for our setup, the deflection of a GeSn nanowire as a function of applied voltage between the electrodes (figure 2) was experimentally determined. The length of the GeSn nanowire was $L_{\text{GeSn}} = 14.8\ \mu$m, radius $R_{\text{GeSn}} = 115$ nm, $f_0 = 623$ kHz, $Q = 550$ and the Young modulus $E = 106$ GPa. The initial separation gap *h* between the nanowire and the gold tip was 0.57 μm. From the figure 2 it can be seen that the experimental points correspond well with the theoretical curve calculated for the parameters $\alpha_0 = \frac{K}{f_r^2} = (7.46 \pm 0.92) \times 10^{-4}$ and $p = 1.78 \pm 0.20$.

Figure 3 shows a DC-only driven gate-less NEM switch with a jump-in voltage of 13.8 V and jump-off voltage of 3.3 V. There is a hysteresis in the current when the voltage increases and decreases between 13.8 and 20 V, which is not desirable for a NEM switch. The increased current in the reverse part of the *I–V* curve indicates that the switch elements may have been changed [29]. Repeated *I–V* measurements for another GeSn nanowire-based device can be found in supplementary info (figure 1 of the supplementary information is available online at stacks.iop.org/NANO/30/385203/mmedia).

AC–DC combined

With all the experimental parameters for the theoretical model of a NEM switch acquired, the oscillations due to additionally applied AC voltage were considered.

To obtain the analytical expressions when both AC and DC voltages are applied between the NEM switch electrodes, the $g(y)$ function was approximated around its static solution y_0 as a linear function $g_{approx}(y)$, as shown in equation (7):

$$g_{approx}(y) = -K\left(\frac{1}{(y_0+1)^p} - \frac{p}{(y_0+1)^{p+1}}(y - y_0)\right)y_0 = y_{stable} \tag{7}$$

resulting in an equation of motion as shown in equation (8):

$$\ddot{y}(t) + \frac{2\pi f_0}{Q}\dot{y}(t) + (2\pi f_U)^2 y(t) = (2\pi f_U)^2 y_0 + g_{aprox}(y)\left(2U_{dc}U_{ac}\sin(2\pi ft) - \frac{1}{2}U_{ac}{}^2\cos(4\pi ft)\right)(2\pi f_U)^2 = (2\pi f_0)^2 - 2K\frac{\left(U_{dc}^2 + \frac{1}{2}U_{ac}^2\right)}{(y_0+1)^{p+1}}. \tag{8}$$

Equation (8) clearly demonstrates that the resonance frequency f_U of the oscillator decreases under the influence of the electric field. This means that when a combined AC+DC field is applied between the switch electrodes, the resonance frequency f_U of the nanowire will be lower than its eigenfrequency f_0. The solution to equation (8) can be obtained as an expansion in powers of U_{ac}. The linear term is presented in equation (9) below:

$$y = y_0 + y_1 U_{ac} + \ldots\ y_1 = \frac{-2KU_{dc}}{(y_0+1)^p}(S\sin(2\pi ft) + C\cos(2\pi ft))\ S$$
$$S = \frac{Q^2(f^2 - f_u^2)}{4\pi^2((f^2 - f_u^2)^2Q^2 + (ff_0)^2)}$$
$$C = \frac{Q(ff_0)}{4\pi^2((f^2 - f_u^2)^2Q^2 + (ff_0)^2)}. \tag{9}$$

The corresponding amplitude of the oscillations of the nanowire at any applied AC electric field frequency *f* is given by equation (10):

$$A = \frac{2KQU_{dc}U_{ac}}{4\pi^2(y_0+1)^p\sqrt{(Q^2(f^2 - f_u^2)^2 + (ff_0)^2)}}. \tag{10}$$

If this amplitude is larger than the difference between the unstable root, given in equation (6), and the stable root, given in the equation (5), then the jump-to-contact will occur. If the U_{ac} frequency *f* is equal to the field-modified resonance frequency f_u (equation (10)) then the condition for jump-to-

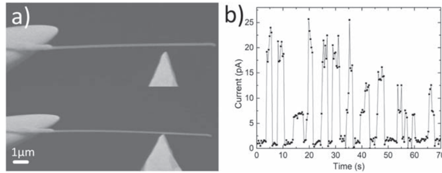

Figure 4. (a) SEM images of the switching element—GeSn nanowire; (b) $I(t)$ characteristics for combined AC+DC driven NEM switch. The different current values in ON states can be attributed to the different contact areas for each ON state.

contact can be represented by equation (11):

$$U_{acJumpT} \geqslant \frac{(4\pi^2)^2 (f_u f_0)^2 (y_{stable} + 1)^p (y_{stable} - y_{unstable})}{2KQU_{dc}}. \tag{11}$$

Equation (11) predicts that for our experimental setup with GeSn nanowire, where in a DC-only regime the jump-in voltage was 13.8 V, the combined AC+DC regime (with $U_{ACJumpT} = 0.15$ V at $f_U = 610.8$ kHz) will decrease the jump-in voltage down to $U_{dc} = 5$ V, which is almost a three times effective jump-in voltage reduction.

To prove the above assumption, an experiment with $U_{dc} = 5$ V and $f_U = 610.8$ kHz predicted by the theory was carried out with the same GeSn nanowire NEM device, but with a slightly larger $U_{AC} = 0.45$ V compared to the theoretical value of $U_{ACJumpT} = 0.15$ V (figure 4(a)). A higher AC voltage than the theoretically predicted was chosen to achieve a stable switching of the NEM device; operating at the theoretical limit or close to it was undesirable due to possible instability (for example, thermal drift) of the experimental system.

In comparison to DC only switching, the lower combined AC+DC jump in voltage is shown in figure 3 as a red arrow to emphasize the effect of the AC field on the jump in voltage. Such a reduction of the jump-in voltage may lead to a reduction of the current-induced effects and prolonged lifetime of the NEM switch [18].

The $I(t)$ characteristics of the subsequent switching for the same GeSn nanowire can be seen in figure 4(b). These characteristics indicate a clear ON–OFF behavior of the switch. The differences between the ON state current values most likely indicate some variations in the contact areas for each jump-in event. These differences may be due to the gold electrode which has a conic shape, and each time the cylindrical GeSn nanowire attaches in a slightly different position, thus changing the contact area. The demonstrated current switching can be used in biosensor applications where the signal is in picoampere range [36].

To show our AC+DC method's applicability for the nanowires with different geometries, similar experiments were carried out for rectangular Bi_2Se_3 nanowires [33, 34]. Due to their shape, resulting in a larger contact area and lower resistance [33, 34], a higher current through the circuit could be achieved at the same voltage as for the cylindrical GeSn nanowires.

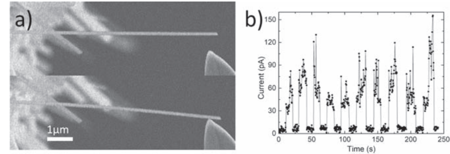

Figure 5. (a) SEM images of the NEM switch with Bi_2Se_3 flexile element in OFF and ON state; (b) $I(t)$ characteristics for this NEM switch.

However, Bi_2Se_3 nanowires are prone to burn-out at much lower jump-in voltages [21] in comparison to Ge [8, 22] and Si [9] nanowires, which makes them difficult to implement in electrostatically actuated NEM switches [21]. In our experimental setup, the Bi_2Se_3 nanowires switched ON–OFF in a combined AC+DC regime when $U_{dc} = 2.8$ V and $U_{ac} = 0.8$ V were applied between the switch electrodes (figures 5(a), (b)) respectively. After the AC+DC test was performed, it was not possible to test this nanowire in DC only regime in the same geometry, due to burning of the nanowire in jump-in when a $U_{dc} = 8.3$ V was applied. This fact confirms that the combined AC+DC driven operation is promising for the NEM switches with flexile elements made of materials that cannot withstand high jump-in voltages.

Conclusions

We have demonstrated both theoretically and experimentally a novel method that implements both AC voltage, at the resonance frequency of nanowires, and DC voltage to decrease the jump in voltage for electrostatically actuated nanobeam-based NEM switches. We have shown experimentally that for GeSn nanowires used as a NEM switching element that the jump-in voltage can be reduced almost 3 times when operating in the AC+DC instead of DC-only regime. For Bi_2Se_3 nanowires the AC+DC method provided a low enough jump-in voltage to construct an operating switch that did not fail due to burn-out. Using combined AC +DC operating regimes is a convenient method to increase the durability of a NEM switch, by decreasing the impact due to such phenomena as electrostatic discharge, Joule heating, Fowler–Nordheim tunneling etc.

Acknowledgments

This work was supported by ERDF project 'Creation of nanoelectromechanical switches' (Project No. 1.1.1.1/16/A/256) and Science Foundation Ireland (Project No.: 14/IA/2513).

ORCID iDs

R Meija https://orcid.org/0000-0003-2318-0297

References

[1] Pisano A P 2007 MEMS and nano technology for the handheld, portable electronic and the automotive markets *Transducers Eurosensors '07 - 4th Int. Conf. Solid-State Sensors, Actuators Microsystems* pp 1–3

[2] George T 2002 MEMS/NEMS development for space applications at NASA/JPL thomas *Proc. SPIE* vol 4755 ed J-C Chiao pp 556–67

[3] Kaul A B 2012 *Microelectronics to Nanoelectronics: Materials, Devices & Manufacturability* (Boca Raton, FL: CRC Press)

[4] Feng X L, He R, Yang P and Roukes M L 2007 Very high frequency silicon nanowire electromechanical resonators *Nano Lett.* **7** 1953–9

[5] Yang Y T, Callegari C, Feng X L, Ekinci K L and Roukes M L 2006 Zeptogram-scale nanomechanical mass sensing *Nano Lett.* **6** 583–6

[6] Hanay M S, Kelber S, Naik A K, Chi D, Hentz S, Bullard E C, Colinet E, Duraffourg L and Roukes M L 2012 Single-protein nanomechanical mass spectrometry in real time *Nat. Nanotechnol.* **7** 602–8

[7] Kosmaca J, Andzane J, Prikulis J, Biswas S, Holmes J D and Erts D 2014 Application of a nanoelectromechanical mass sensor for the manipulation and characterisation of graphene and graphite flakes *Sci. Adv. Mater.* **6** 1–6

[8] Andzane J, Petkov N, Livshits A I, Boland J J, Holmes J D and Erts D 2009 Two-terminal nanoelectromechanical devices based on germanium nanowires *Nano Lett.* **9** 1824–9

[9] Ziegler K J, Lyons D M, Holmes J D, Erts D, Polyakov B, Olin H, Svensson K and Olsson E 2004 Bistable nanoelectromechanical devices *Appl. Phys. Lett.* **84** 4074–6

[10] Andzane J, Prikulis J, Dvorsek D, Mihailovic D and Erts D 2010 Two-terminal nanoelectromechanical bistable switches based on molybdenum-sulfur-iodine molecular wire bundles *Nanotechnology* **21** 1–7

[11] Loh O Y and Espinosa H D 2012 Nanoelectromechanical contact switches *Nat. Nanotechnol.* **7** 283–95

[12] Jasulaneca L, Kosmaca J, Meija R, Andzane J and Erts D 2018 Review: electrostatically actuated nanobeam-based nanoelectromechanical switches—materials solutions and operational conditions *Beilstein J. Nanotechnol.* **9** 271–300

[13] Yousif M Y A, Lundgren P, Ghavanini F, Enoksson P and Bengtsson S 2008 CMOS considerations in nanoelectromechanical carbon nanotube-based switches *Nanotechnology* **19** 271–300

[14] Dadgour F H and Banerjee K 2009 Hybrid NEMS–CMOS integrated circuits: a novel strategy for energy-efficient designs *IET Comput. Digit. Tech.* **3** 593

[15] Lee J O, Song Y H, Kim M W, Kang M H, Oh J S, Yang H H and Yoon J B 2013 A sub-1-volt nanoelectromechanical switching device *Nat. Nanotechnol.* **8** 36–40

[16] Li P, Jing G, Zhang B, Sando S and Cui T 2014 Single-crystalline monolayer and multilayer graphene nano switches *Appl. Phys. Lett.* **104** 113110

[17] Sun J, Schmidt M E, Muruganathan M, Chong H M H and Mizuta H 2016 Large-scale nanoelectromechanical switches based on directly deposited nanocrystalline graphene on insulating substrates *Nanoscale* **8** 6659–65

[18] Doelling C M, Kyle Vanderlick T, Song J and Srolovitz D 2007 Nanospot welding and contact evolution during cycling of a model microswitch *J. Appl. Phys.* **101** 1–7

[19] Vincent M, Rowe S W, Poulain C, Mariolle D, Chiesi L, Houź F and Delamare J 2010 Field emission and material transfer in microswitches electrical contacts *Appl. Phys. Lett.* **97** 263503

[20] Loh O, Wei X, Ke C, Sullivan J and Espinosa H D 2011 Robust carbon-nanotube-based nano-electromechanical devices: understanding and eliminating prevalent failure modes using alternative electrode materials *Small* **7** 79–86

[21] Kosmaca J, Andzane J, Baitimirova M, Lombardi F and Erts D 2016 Role of nanoelectromechanical switching in the operation of nanostructured Bi_2Se_3 interlayers between conductive electrodes *ACS Appl. Mater. Interfaces* **8** 12257–62

[22] Andzane J, Prikulis J, Meija R, Kosmaca J, Biswas S, Holmes J D and Erts D 2013 Application of Ge nanowire for two-input bistable nanoelectromechanical switch *Medziagotyra* **19** 254–7

[23] Jang W W, Lee J M J O J M, Yoon J B, Kim M S, Lee J M J O J M, Kim S M, Cho K H, Kim D W, Park D and Lee W S 2008 Fabrication and characterization of a nanoelectromechanical switch with 15 nm thick suspension air gap *Appl. Phys. Lett.* **92** 103110

[24] Lee J O, Kim M W, Ko S D, Kang H O, Bae W H, Kang M H, Kim K N, Yoo D E and Yoon J B 2009 Three-terminal nanoelectromechanical switching device in insulating liquid media for low voltage operation and reliability improvement *Tech. Dig.—Int. Electron Devices Meet. IEDM* 227–30

[25] Ngo L T, Almécija D, Sader J E, Daly B, Petkov N, Holmes J D, Erts D and Boland J J 2006 Ultimate-strength germanium nanowires *Nano Lett.* **6** 2964–8

[26] Kosmaca J, Jasulaneca L, Meija R, Andzane J, Romanova M, Kunakova G and Erts D 2017 Young's modulus and indirect morphological analysis of Bi2Se3 nanoribbons by resonance measurements *Nanotechnology* **28** 325701

[27] Livshits A I, Jasulaneca L, Kosmaca J, Meija R, Holmes J D and Erts D 2017 Extra tension at electrode-nanowire adhesive contacts in nano-electromechanical devices *Eur. J. Mech.* A **66** 412–22

[28] Andzane J, Meija R, Livshits A I, Prikulis J, Biswas S, Holmes J D and Erts D 2013 An AC-assisted single-nanowire electromechanical switch *J. Mater. Chem.* C **1** 7134–8

[29] Meija R, Kosmaca J, Jasulaneca L, Petersons K, Biswas S, Holmes J D and Erts D 2015 Electric current induced modification of germanium nanowire NEM switch contact *Nanotechnology* **26** 195503

[30] Kosmaca J *et al* 2019 *Effect of tapering on mechanical and electrical properties of GeSn alloy nanowires submitted* Nanoscaleunpublished

[31] Sistani M, Seifner M S, Bartmann M G, Smoliner J, Lugstein A and Barth S 2018 Electrical characterization and examination of temperature-induced degradation of metastable Ge 0.81 Sn 0.19 nanowires *Nanoscale* **10** 19443–9

[32] Biswas S, Doherty J, Saladukha D, Ramasse Q, Majumdar D, Upmanyu M, Singha A, Ochalski T, Morris M A and Holmes J D 2016 Non-equilibrium induction of tin in germanium: Towards direct bandgap Ge 1-x Sn_x nanowires *Nat. Commun.* **7** 11405

[33] Andzane J, Kunakova G, Charpentier S, Hrkac V, Kienle L, Baitimirova M, Bauch T, Lombardi F and Erts D 2015 Catalyst-free vapour-solid technique for deposition of Bi_2Te_3 and Bi_2Se_3 nanowires/nanobelts with topological insulator properties *Nanoscale* **7** 15935–44

[34] Kunakova G, Galletti L, Charpentier S, Andzane J, Erts D, Léonard F, Spataru C D, Bauch T and Lombardi F 2018 Bulk-free topological insulator Bi_2Se_3 nanoribbons with magnetotransport signatures of dirac surface states *Nanoscale* **10** 19595–602

[35] Mishra S K, Satpathy S and Jespen O 1997 Electronic structure and thermoelectric properties of bismuth telluride and bismuth selenide *J. Phys.: Condens. Matter* **9** 461–70

[36] Vidal J C, Bonel L, Ezquerra A, Hernández S, Bertolín J R, Cubel C and Castillo J R 2013 Electrochemical affinity biosensors for detection of mycotoxins: a review *Biosens. Bioelectron.* **49** 146–58

Paper IX

BEILSTEIN JOURNAL OF NANOTECHNOLOGY

Review: Electrostatically actuated nanobeam-based nanoelectromechanical switches – materials solutions and operational conditions

Liga Jasulaneca[1], Jelena Kosmaca[1], Raimonds Meija[1], Jana Andzane[1] and Donats Erts[*1,2]

Review

Open Access

Address:
[1]Institute of Chemical Physics and [2]Department of Chemistry, University of Latvia, Raina Blvd. 19, Riga, LV-1586, Latvia

Email:
Donats Erts[*] - donats.erts@lu.lv

* Corresponding author

Keywords:
nanocontacts; nanoelectromechanical switches; nanowires; NEM; reliability

Beilstein J. Nanotechnol. **2018,** *9,* 271–300.
doi:10.3762/bjnano.9.29

Received: 20 February 2017
Accepted: 25 December 2017
Published: 25 January 2018

Associate Editor: J. Frommer

© 2018 Jasulaneca et al.; licensee Beilstein-Institut.
License and terms: see end of document.

Abstract
This review summarizes relevant research in the field of electrostatically actuated nanobeam-based nanoelectromechanical (NEM) switches. The main switch architectures and structural elements are briefly described and compared. Investigation methods that allow for exploring coupled electromechanical interactions as well as studies of mechanically or electrically induced effects are covered. An examination of the complex nanocontact behaviour during various stages of the switching cycle is provided. The choice of the switching element and the electrode is addressed from the materials perspective, detailing the benefits and drawbacks for each. An overview of experimentally demonstrated NEM switching devices is provided, and together with their operational parameters, the reliability issues and impact of the operating environment are discussed. Finally, the most common NEM switch failure modes and the physical mechanisms behind them are reviewed and solutions proposed.

Review
Introduction
Nanoelectromechanical (NEM) switches represent a class of nanoscale devices, integrating both electrical and mechanical functionality of nanostructures to process external stimuli applied to the device and controlling the electrical current. NEM switches have attracted attention as low-power [1] devices, demonstrating abrupt on/off switching characteristics and minimized sub-threshold swing, as well as reduced leakage currents leading to improved on/off ratios [2]. In the context of existing microelectromechanical (MEM) switches, downsizing to the nanoscale leads to lower power consumption, increased switching speed, integration density and higher precision. While the characteristic dimensions of MEM switch components are between 1 µm and 1 mm, for the NEM scale devices, it is below 100 nm. This means that NEM switches combine the advan-

tages of a smaller mass with a higher surface area to volume ratio. When the linear dimension scale decreases by three orders of magnitude, the area and volume decrease by six and nine orders of magnitude, respectively. Surface forces, proportional to area, become a thousand times larger than forces that are proportional to volume, making inertial forces negligible. At the nanoscale, van der Waals, capillary and electrostatic forces become the governing factors. It is important to note, that with the decrease of the size scale, breakdown of the predictions of continuum-based theories may occur. For instance, for cantilevered resonating nanostructures, continuum mechanics predictions fail when the cross-sectional area of the nanostructure is on the order of tens of lattice constants [3]. At this level, quantum effects, crystalline perfection, surface and interface interactions govern materials properties and behaviour [4]. Thus, NEM switches provide an exciting opportunity for gaining fundamental insight in such fields as surface science and electrical and mechanical processes in nanocontacts.

The NEM switch components can be produced from a wide range of nanostructures (e.g., thin films [5-7], nanobundles [8], nanowires [9-14], nanotubes [15,16]) fabricated from different materials (e.g., metals [17-19], semiconductors [9,10,20-23], carbon allotropes, including graphene [24-31] and carbon nanotubes [12,15,16,32-37]). With a proper choice of material and architecture, NEM switches can withstand relatively high radiation levels and extreme temperatures [19,25,38,39], highlighting their potential for applications in harsh environments.

Currently, the investigation of NEM switches is mostly focused on developing experimental approaches for device prototype fabrication and testing in laboratory environment and theoretical modelling based on continuum mechanics and molecular dynamics, allowing simulations to be performed on the processes occurring in NEM switching devices and the analysis of their working parameters [40-46]. A common approach for experimental investigation on NEM switches includes device fabrication and testing on chip. The fabrication can be based either on entirely top-down, or on a combination of top-down, bottom-up and nanomanipulation approaches. The top-down approach involves lithography, etching and coating technologies to fabricate device structures from bulk materials or thin films [7,19,23,39,47-50]. The combined approach of fabricating NEM switches requires subsequent transfer and alignment of synthesized nanostructures (nanowires, nanotubes, nanorods, graphene) with a good uniformity and desired properties. The microfabrication routine may be supplemented with some bottom-up approaches. Dielectrophoresis [33], controlled nanomaterial growth [34], and nanomanipulation [9] have been demonstrated as useful methods for small batch device fabrication with future prospects for scalable production of NEM switches on chip.

Another approach for fabrication and characterization of NEM device prototypes is in situ measurement technique, where the switch elements are positioned using nanomanipulators inside an electron microscope [8,10-15]. In situ studies of the dynamics of force interactions, conductance and adhesion in gold point contacts using combined transmission electron microscopy/scanning tunnelling microscopy (TEM-STM) [51,52] and atomic force microscopy/transmission electron microscopy (AFM-TEM) [53] showed suitability of these techniques for further NEM switch related research. A major advantage of in situ experiments is that the device geometry and operation can be visualized and adjusted in real time within one experimental session. This allows optimization of the geometry of a NEM device, avoiding the need for individual device fabrication of each control parameter. This approach is favourable for fundamental research on specific parts and simulation of processes in a NEM switch, where the assembly of the whole device is not required. Real-time visualization helps to evaluate the contact area [8,10,11,54], observe the electrical breakdown mechanism for a single nanostructure [55-58], and investigate the dynamic processes occurring in the switch nanocontact [54].

The durability of a NEM switch strongly depends on the evolution of the contact between the switching element and the contact electrode during NEM switch operation. The increase of adhesion in the contact or its conductivity reduction down to the noise level with repetitive switching degrades the device stability and often leads to device failure. The state of the art lifetime of NEM switches varies from one-off laboratory-scale measurements [59], demonstrating a few tens [10,11,26,47,49,60] of switching cycles, up to devices showing 10^4–10^8 [12,18,19,38,39,61] switching cycles. However, to achieve a technology readiness level suitable for commercial applications, NEM switches should endure up to 10^{15} cycles without failing [59,62,63]. Thus, the reliability of NEM switches is one of the most critical issues that slow down wider adoption of this technology. Further efforts are necessary to select the material combination and suitable architecture that meet the requirements for commercial applications.

Actuation of NEM switches includes a variety of methods, for example, electrostatic [7,12], thermal [64], piezoelectric [65], resonant [66] and free-floating [67] switching. Electrostatic actuation is one of the most widespread and actively studied actuation modes. It is a promising method for operating nanosized switches due to its simple process requirements. More advantages of the electrostatically actuated NEM contact switches are temperature-independent actuation characteristics

and reduction in power consumption with scaling. The device configurations where electrostatically actuated single- or double-clamped nanobeams are used as switching elements have great potential for architecture modification of the device and are widely used in development of NEM contact switch prototypes. The aim of this work is to review recent research carried out on electrostatically actuated nanobeam-based NEM contact switches, fabricated by different methods. The processes occurring in nanocontacts and the improvement of their reliability in terms of choice of materials for both electrodes and switching elements are covered in the light of the experimental findings in the field. Methods and approaches for investigating the behaviour of NEM switches as well as environmental considerations and failure modes are discussed. This review does not cover research into the use of other types of NEM switches based on, for example, free-floating [67] or resonant switching [66] principles, as well as thermal [64] or piezoelectric [65] actuation methods.

Main architectures and basic operational principles of electrostatically actuated nanobeam-based NEM switches

In general, electrostatically actuated nanobeam-based NEM switches can be divided into two main groups: two-terminal (2T) switches, employing only source and drain electrodes, and three-terminal (3T) and more terminal switches, employing an additional single or multiple gate electrodes in single-clamped and double-clamped configurations.

Two-terminal NEM switches

The full NEM switching cycle consists of establishment of a mechanical and electrical contact between a switching element and a contact electrode, which is followed by electrical-current-assisted processes in the on state, and a subsequent disengagement of both electrical and mechanical contacts while switching back to the off state. The switching cycle is based on balancing attractive (van der Waals (F_{vdW}) and electrostatic (F_{elec})) and repulsive elastic (F_{elas}) forces acting on a movable switching element in single (Figure 1a) or double-clamped (Figure 1c) position, and initially separated from the contact electrode by a distance z.

The operation principle of a NEM switch can be described from the viewpoint of potential energy $E = \int F\,dz$ of the switching element, where F is the force acting on the switching element and z is the separation distance between the switching element and the contact electrode. Its total potential energy can be expressed as follows:

$$E_T = E_{vdW} + E_{elas} + E_{elec}, \qquad (1)$$

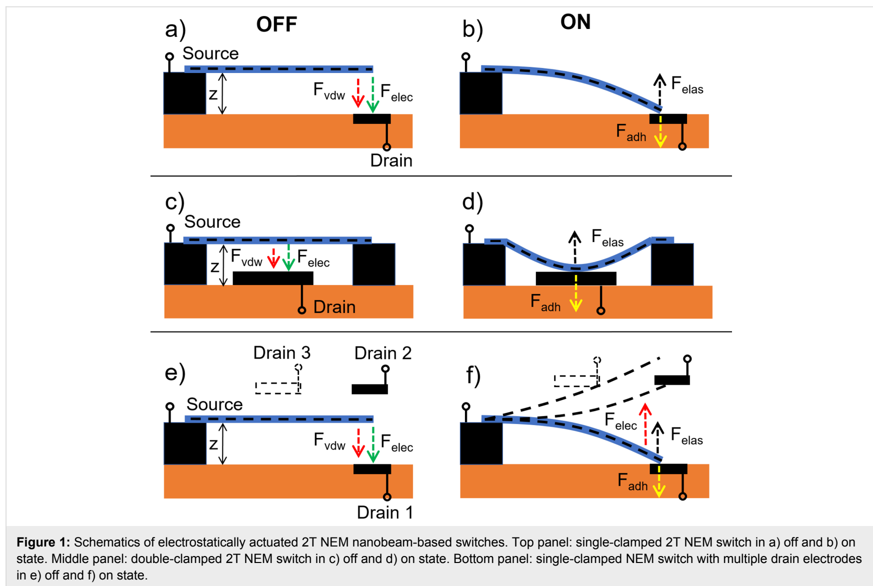

Figure 1: Schematics of electrostatically actuated 2T NEM nanobeam-based switches. Top panel: single-clamped 2T NEM switch in a) off and b) on state. Middle panel: double-clamped 2T NEM switch in c) off and d) on state. Bottom panel: single-clamped NEM switch with multiple drain electrodes in e) off and f) on state.

where E_{vdW} is the van der Waals (vdW) energy, E_{elas} is the elastic energy and E_{elec} is the electrostatic energy. An example of potential energy diagrams for the switching element–electrode interactions is shown in Figure 2a [13]. At low or no electrostatic field applied between the switching element and electrode there are two local minima located respectively at an initial switching element/electrode separation distance z_0, and at a few nanometres from the electrode surface z_{vdW}. The minimum located close to the electrode surface (at distance z_{vdW}) is related to attractive vdW forces. The minimum located at z_0 is related to the off state of the NEM switch, where the elastic energy of switching element that is freely suspended over the electrode is minimal (Figure 1a, c; Figure 2a solid line). For $z_0 >> z_{vdW}$, the $E_T(z)$ curve would be symmetric with respect to the minimum located at z_0. However, at close distances between the switching element and the electrode surface, the vdW interaction energy sufficiently reduces the total potential energy. Applying an increasingly larger electrostatic force diminishes the potential barrier until its complete elimination (Figure 2a dashed and dotted lines) and results in deflection of the switching element towards the contact electrode. For on and off states of a NEM switch to remain stable in the on state at room temperature, the potential barrier between energy minima must be much larger than $10k_BT$ (k_B is the Boltzmann constant and T is temperature) (Figure 2a, inset) [32].

When the gradient of total attractive force exceeds the spring constant of the switching element approaching the electrode surface, the switching element starts accelerating. This is followed by establishment of mechanical and electrical contact between them (jump-in), and consequently, initiation of a current flow in the circuit (Figure 1b,d; Figure 2b) [13,15,32,40,68].

The jump-in voltage depends on the geometry of the device and the stiffness of the switching element. Switching from the on to off state (jump-off) occurs when the spring constant of the switching element exceeds the gradient of the total attractive force F_{adh} at the contact between the switching element and the electrode, and can be seen in $I(V)$ curves as a sudden decrease of electrical current down to the noise level (Figure 2b).

Since operation of NEM switches is substantially determined by adhesion forces due to significant contribution of vdW forces [69], jump-off occurs at lower voltages in comparison to jump-in, and typical hysteresis loops in $I(V)$ curves of NEM switches are observed [8,10,15]. A hysteresis loop is illustrated in Figure 2b showing experimentally obtained results [15] in comparison with the results of calculations assuming that the switching element is a uniform linear elastic beam and a perfect conductor [41,42].

To expand the functionality of the 2T configuration switch, specially designed semi-paddle structures, allowing torsional movement of the switching element and consequently three different operation states can be used, as it was shown for a 2T TiN NEM switch [48] (Figure 3).

The off state is established when the switching element is separated from the contact electrode (Figure 3, state A), and two successive on states with different pull-in voltages (Figure 3, states B and C) can be established by making contact between the switching element and the electrode due to either torsional or flexural movement of the paddle anchors. Such architecture may serve for memory and logic applications.

A further variation of the 2T NEM switch is to use multiple drain electrodes. Recently, switching of a moving element

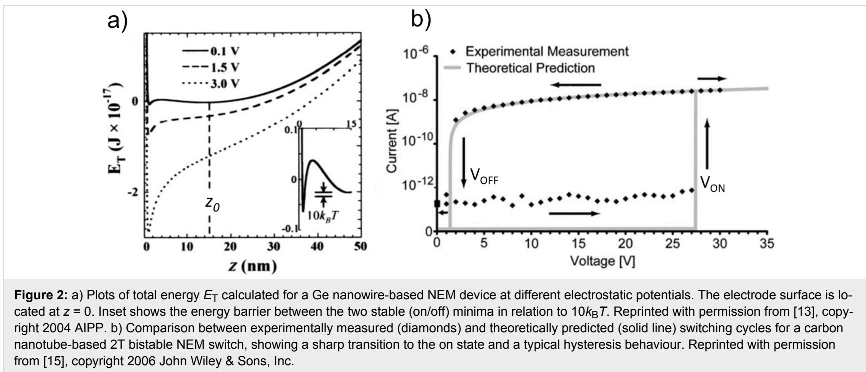

Figure 2: a) Plots of total energy E_T calculated for a Ge nanowire-based NEM device at different electrostatic potentials. The electrode surface is located at $z = 0$. Inset shows the energy barrier between the two stable (on/off) minima in relation to $10k_BT$. Reprinted with permission from [13], copyright 2004 AIPP. b) Comparison between experimentally measured (diamonds) and theoretically predicted (solid line) switching cycles for a carbon nanotube-based 2T bistable NEM switch, showing a sharp transition to the on state and a typical hysteresis behaviour. Reprinted with permission from [15], copyright 2006 John Wiley & Sons, Inc.

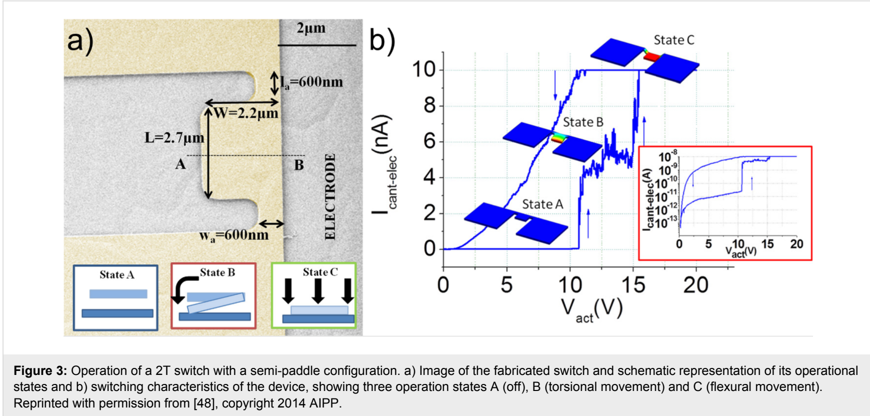

Figure 3: Operation of a 2T switch with a semi-paddle configuration. a) Image of the fabricated switch and schematic representation of its operational states and b) switching characteristics of the device, showing three operation states A (off), B (torsional movement) and C (flexural movement). Reprinted with permission from [48], copyright 2014 AIPP.

(Ge nanowire) between two drain electrodes located symmetrically (Figure 1e,f drains 1 and 2) [14] and asymmetrically (Figure 1e,f drains 1 and 3) [11] relative to the switching element in 2T configuration was demonstrated. While switching between symmetrically located drain electrodes may be applied for switching between two circuits (Figure 4), the location of the drain electrodes at different distances from the attached end of the switching element (Figure 1e,f drains 1 and 3) allows varying of resistance, and consequently, signal strength in the circuit by adjusting the length of the switching element connected to it.

Three-terminal NEM switches

In a 3T single-clamped configuration, an additional gate electrode is used to pull the switching element in contact with the drain (Figure 5).

In comparison with 2T switches, where minimal operating voltage in the on state is fundamentally limited by the V_{off} voltage (Figure 2b), the use of gate electrodes allows adjustment of the source–drain voltage independent from the V_{on} and V_{off} voltages. Switching to the off position may be realized by applying the same potential to the gate 1 and drain 1, resulting in repulsive electrostatic force (Figure 5b), or by applying attractive electrostatic force between the source and the gate 2 in single-clamped configuration (Figure 5a) and between the source and the gate in double-clamped configuration (Figure 5d). In comparison with 2T NEM switches, the possibility to apply an additional restoring force to the switching element in the 3T configuration reduces the requirements to elastic properties (stiffness) of the active element necessary for switching to the off position and allows reducing the jump-in voltage by diminishing the separation gap width. However, the

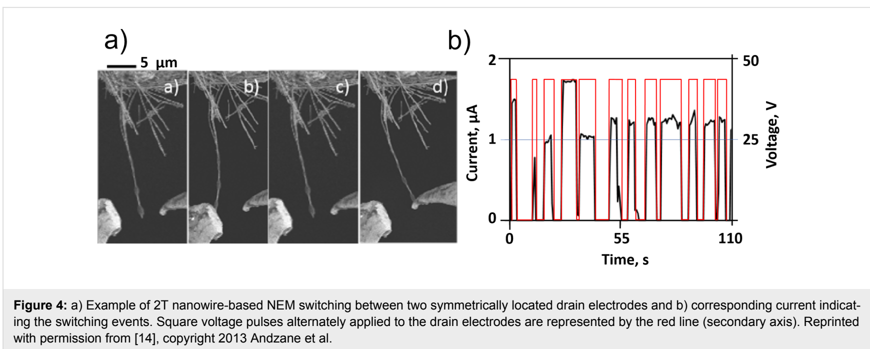

Figure 4: a) Example of 2T nanowire-based NEM switching between two symmetrically located drain electrodes and b) corresponding current indicating the switching events. Square voltage pulses alternately applied to the drain electrodes are represented by the red line (secondary axis). Reprinted with permission from [14], copyright 2013 Andzane et al.

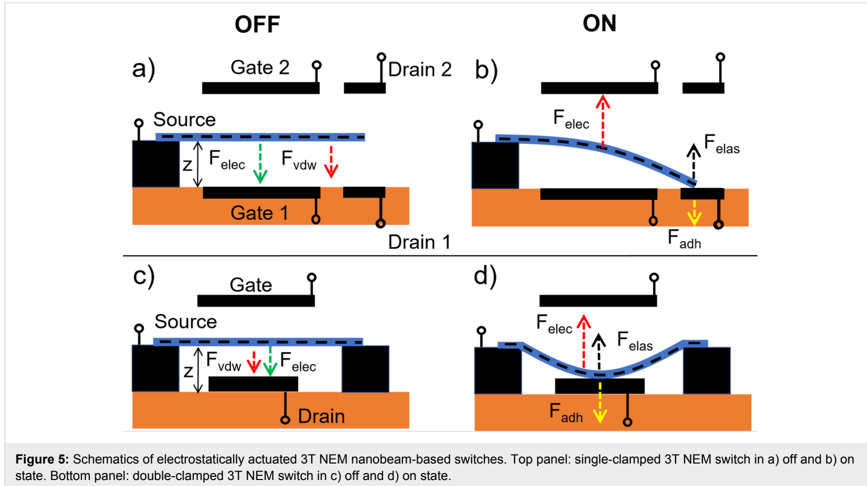

Figure 5: Schematics of electrostatically actuated 3T NEM nanobeam-based switches. Top panel: single-clamped 3T NEM switch in a) off and b) on state. Bottom panel: double-clamped 3T NEM switch in c) off and d) on state.

gap cannot be smaller than the critical distance at which vdW interactions become dominant. For nanostructures, the jump-in-contact of a switching element may occur from larger distances than theoretically predicted by the vdW interactions [53].

The strong nanoscale contact adhesion, comprising an unusually strong tangential component of adhesion force [70], often poses difficulties in returning the NEM switch to its off position. Inducing resonant oscillations in the NEM switching element in the on position was found to be an effective solution for its release from the contact. The resonant oscillation modes induced in the switching element by an external AC field (Figure 6a) [11] or mechanically (Figure 6b) [71] allowed to successfully overcome the adhesion potential in the contact and allowed for reduction of the operating voltage of the NEM switch [11] or a separation gap necessary for the release of the switching element from the contact [71] by nearly an order of magnitude.

Processes in NEM switch contacts

A reliable NEM switch contact is required to maintain stable characteristics over repetitive operation cycles. Assuming the switch is in an optimal operational environment, the contact properties are mostly defined by the contacting material properties and the real contact area. In non-vacuum environments the presence of contaminants can significantly impact these processes, as will be discussed later in this review. Despite the importance of understanding of the nanocontact evolution, only a few papers have been published with partial experimental analysis of the contact area and its influence on switching characteristics [8,10]. This section gives a brief overview of the main types of processes occurring in the nanocontacts during the operation of a NEM switch.

Mechanical contact

The size of the mechanical contact determines the adhesion force (F_{adh}) value which is responsible for keeping the contacting surfaces together. Fundamentally, the contact is formed by atoms interacting across the contact interface. At the nanoscale, many models of nanocontact behaviour are based on a single-asperity model, where contacting elements are represented by single asperities with curvature radii from tens of nanometres to micrometres and are assumed to be ideally smooth [72].

According to adhesion theories [73-76], the adhesion force can be evaluated as $F_{adh} \approx R \cdot \Delta\gamma$, where R is radius of contact area and $\Delta\gamma$ is energy of adhesion: $\Delta\gamma = \gamma_1 + \gamma_2 - \gamma_{12}$, where γ_1 and γ_2 are the surface energy of the contacting surfaces, and γ_{12} is the interfacial energy in the contact. $\gamma_{12} = 0$ if both surfaces are of the same material. Thus, the surface energy of the contacting materials is a critical factor in determining the strength of adhesion in the contact in line with the contact area.

It should be noted that a real contact may consist of a number of smaller asperities (multiasperity contact) so the true contact area is smaller than predicted by the single-asperity theory. However, simulations performed by Mo et al. [77] for multiasperity

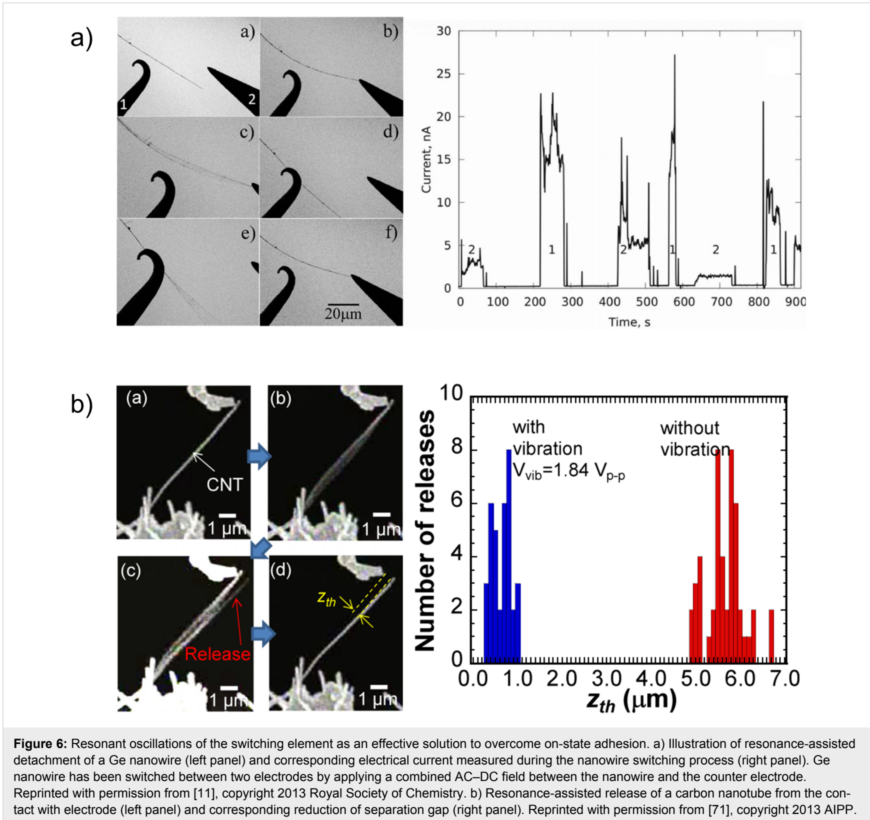

Figure 6: Resonant oscillations of the switching element as an effective solution to overcome on-state adhesion. a) Illustration of resonance-assisted detachment of a Ge nanowire (left panel) and corresponding electrical current measured during the nanowire switching process (right panel). Ge nanowire has been switched between two electrodes by applying a combined AC–DC field between the nanowire and the counter electrode. Reprinted with permission from [11], copyright 2013 Royal Society of Chemistry. b) Resonance-assisted release of a carbon nanotube from the contact with electrode (left panel) and corresponding reduction of separation gap (right panel). Reprinted with permission from [71], copyright 2013 AIPP.

contacts showed an excellent fit of this model with experimental data and the widely used Maugis–Dugdale single asperity adhesive theory model [78]. Despite the fact that such a good fit may be a result of the flexibility of the Maugis–Dugdale model, which masks its deficiencies [77], this model is a useful tool for the evaluation of adhesion in nanocontacts.

Estimations of nanocontact areas of 2T NEM switches with Ge and $Mo_6S_3I_6$ nanowires as switching elements and Au contact electrodes [8,10], performed using a convenient approximation for the Maugis–Dugdale theory of adhesion [74] proposed by Carpick, Ogletree and Salmeron [73], showed that the typical contact area between the switching element and the Au contact electrode is 30–50 and 400–700 times smaller than the cross-sectional area of Ge and $Mo_6S_3I_6$ switching elements, respectively [8,10] (Table 1). Thus, the contact area experiences higher current density than that inside the nanowire. This should be taken into account during analysis performed on NEM switch operation.

The nanocontact area and stiffness of the switching element determine the on–off hysteresis width of a NEM switch. With the same switching element, reduction of the contact area in 2T NEM switches results in a decrease of adhesion in the contact and consequent decrease of the hysteresis width, allowing reduction of the separation gap z for jump-in at lower voltages. Figure 7 illustrates the decrease of the hysteresis width for a $Mo_6S_3I_6$ nanowire bundle-based 2T NEM switch, when the $Mo_6S_3I_6$ –Au contact area was reduced from 100 nm^2 down to 45 nm^2 while maintaining the same V_{on} voltage.

Table 1: Parameters of nanocontact areas (nanowire radius r_{nw}, cross-sectional area of the nanowire S_{nw}, radius of electrode apex R_e, nanocontact area S_c) in Ge and $Mo_6S_3I_6$ nanowire-based 2T NEM contact switches.

Material	r_{nw} (nm)	S_{nw} (nm^2·10^3)	R_e (nm)	S_c, (nm^2)	S_{nw}/S_c
Ge [10]	30	2.8	100	78	36
	150	70.7	115	331	214
	75	17.7	420	321	55
	50	7.9	1300	259	30
	60	11.3	600	218	52
Ge [11]	50	7.9	–	965	8
$Mo_6S_3I_6$ [8]	100	31.4	–	100	314
	100	31.4	–	45	698

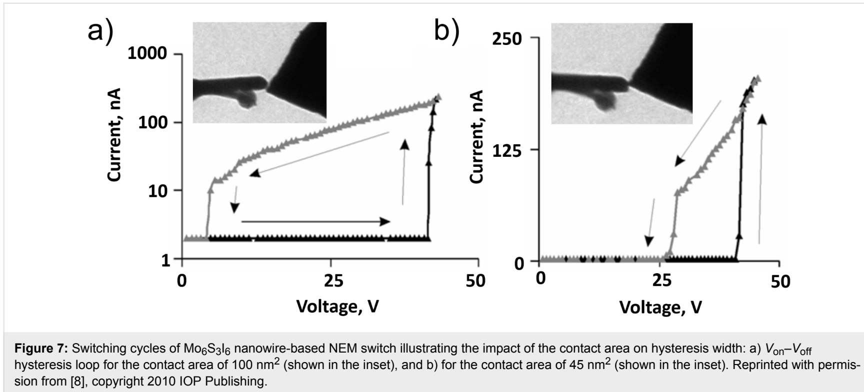

Figure 7: Switching cycles of $Mo_6S_3I_6$ nanowire-based NEM switch illustrating the impact of the contact area on hysteresis width: a) V_{on}–V_{off} hysteresis loop for the contact area of 100 nm^2 (shown in the inset), and b) for the contact area of 45 nm^2 (shown in the inset). Reprinted with permission from [8], copyright 2010 IOP Publishing.

However, such reduction of the contact area results in an increase of the electrical current density flowing through it, which may lead to modification of the properties of the contacting materials. Alternatively, modifying the stiffness of the switching element can shift the jump-in and jump-off voltages and thus change the on–off hysteretic loop.

Adhesion in the contact may be impacted by the surface wear occurring during repetitive on–off switching. An AFM-based study on the nanoscale wear of diamond-like carbon against and ultra-nanocrystalline diamond showed that the surface wear increases the size of the contact by gradually removing atoms at discrete sites and is a thermally activated stress-assisted process [79]. This experiment was carried out with an AFM in amplitude modulation mode complemented with molecular dynamics simulations. An exponential wear rate dependence on the peak force load was found, suggesting that lower contact forces are needed to reduce the wear rate. It should be noted that for soft materials, plastic deformation may have a bigger effect than wear.

The presence of chemically active elements at the contact interface may also significantly increase the adhesion in nanocontacts due to formation of chemical bonds (e.g., C–Au bonds [80], Au–S bonds [8,81]) between the contacting materials. Nearly an order of magnitude increase in adhesion force was reported in case of covalent Au–S bond formation for $Mo_6S_3I_6$ nanowire-based NEM 2T switches [8].

Electrical field and current induced processes in the contact

The electrical characteristics and performance of a NEM switch are determined by the electrical properties of the contact area between the NEM switching element and electrode. It should be noted that the true contact area does not need to be continuous, which becomes relevant when contact areas approach the size of the mean free path length of the electrons (e.g., for gold nanocontacts – 3.8 nm [82]). When the contact area becomes smaller than the mean free path of the electrons in the material, the electron transport enters ballistic conduction regime [83]. Nevertheless, typically, the metal–metal contact shows ohmic

characteristics, which are preferable for low-power NEM switches, but carry the risk of switch failure at higher operation voltages.

In NEM switches with metal–semiconductor contacts, the type of the contact is determined by the mutual arrangement of the Fermi level of the metal and the valence and conduction bands of the semiconductor. The contact has a Schottky barrier if the Fermi level of the metal falls in between the valence and conduction bands of the semiconductor. The type of the contact (ohmic or Schottky) between two semiconductors is determined by the Fermi energies of contacting materials.

The presence of a nonconductive oxide layer between the contacting materials (metal–metal, metal–semiconductor, and semiconductor–semiconductor) always results in the formation of a tunnel barrier in the contact.

In the presence of a potential barrier between the contacting NEM switch materials, the magnitude of the contact resistance depends on the width and height of the barrier. In general, the interfacial charge carrier transfer in the NEM contact can be based on two different mechanisms: thermionic emission [84,85], which is dominant at high temperatures, and quantum mechanical tunnelling of carriers across the barrier width – direct [85,86] and Fowler–Nordheim (FN) tunnelling [54,85,87,88]. The direct tunnelling occurs when the barrier is trapezoidal, and the FN tunnelling occurs when the barrier is triangular [10,89,90]. The shape of the initial potential barrier in the NEM switch contact depends on the size and topography of the contact area, as well as on the band structure of contacting materials [86], and can be modulated by an applied source–drain bias in the on state of a NEM switch. For example, the change in the transport mechanism from direct tunnelling at low drain bias to FN tunnelling at the higher drain bias was shown for a Pd–MoS_2 interface at low (123 K) temperatures [85].

Studies of intimate ZnO nanowire–Au contacts have also shown that the mechanism of nanoscale electrical transport through the potential barrier depends on the relation between contact area and diameter of the nanowire, allowing a controllable transition from Schottky to ohmic type of conduction for smaller contact area/nanowire diameter ratios (Figure 8a,b) [91]. This effect was explained by enhanced tunnelling at the contact edge as a result of the reduction of the depletion region (Figure 8c) [91]. This allows a good ohmic contact to be obtained at a semiconductor/metal interface by only changing the contact area/nanowire diameter ratio.

As soon as the electric current begins to flow in the NEM switch contact, it causes thermal heating in the switching element and may result in small structural modifications of the contacting surfaces, welding and even change of the chemical composition of the contacting materials. Electrical-current-induced thermal effects have been studied in various one-dimensional nanostructures such as Si [92], Ge [10,54], carbon nanotubes (CNTs) [93-95], GaN [96,97] and ZnTe [98].

The evolution of a nanocontact between a nanowire and a contact electrode may be observed and investigated using in situ methods. Recent report showed that in situ detection of the resonant frequency of the nanowire and monitoring of its shift mirrors the electrical-current-induced strengthening of the nanocontact between the Ge nanowire and the contact electrode [54] (Figure 9a). Applying a voltage between the electrodes 2 and 3 results in a current flow through the nanowire. After each voltage application, the AC field is applied between the elec-

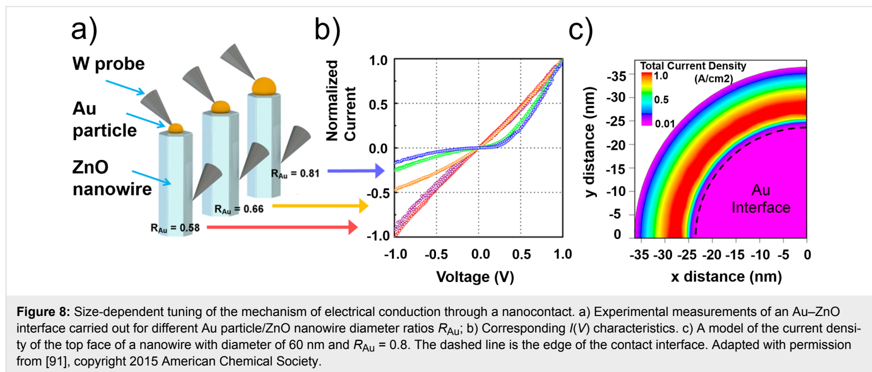

Figure 8: Size-dependent tuning of the mechanism of electrical conduction through a nanocontact. a) Experimental measurements of an Au–ZnO interface carried out for different Au particle/ZnO nanowire diameter ratios R_{Au}; b) Corresponding $I(V)$ characteristics. c) A model of the current density of the top face of a nanowire with diameter of 60 nm and R_{Au} = 0.8. The dashed line is the edge of the contact interface. Adapted with permission from [91], copyright 2015 American Chemical Society.

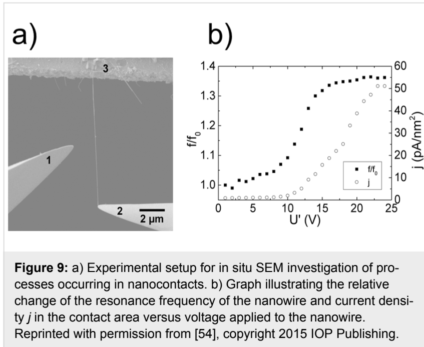

Figure 9: a) Experimental setup for in situ SEM investigation of processes occurring in nanocontacts. b) Graph illustrating the relative change of the resonance frequency of the nanowire and current density *j* in the contact area versus voltage applied to the nanowire. Reprinted with permission from [54], copyright 2015 IOP Publishing.

trode 1 and the nanowire (electrodes 2 and 3), and the resonant frequency is determined. Electric current flow through the contact causes immediate strengthening of the nanocontact, which gradually develops until the current density of 10^{-3}–10^{-2} nA/nm^2 (Figure 9b) is reached.

Self-heating behaviour in the switching element/electrode contact is determined by a combination of its electrical and thermal conductivity [10,96,99]. If there is a low current density in the contact (in the range of 1 pA/nm^2) and a good thermal contact, the temperature changes modestly ($\Delta T < 30$ K) and almost no Joule heating occurs [10]. However, even at current densities as low as 3 pA/nm^2, energy dissipation in the contact may result in a smoothening of the contacting surfaces because of local Joule heating and welding. The contact strengthening effect in Figure 9b was explained by smoothing and thinning of the native Ge oxide layer which results in an increase of contact area and adhesion force [54].

At higher current densities (1–10 nA/nm^2) a Joule heating induced rise of temperature (in the range of 1000 °C) may trigger a change of chemical composition of the material. For example, for $Mo_6S_3I_6$ bundles, a non-reversible transformation to Mo was reported, as a result of evaporation of S and I [100]. This effect may be used to anneal nanowires for enhancing electrical and field emission properties [100].

Current densities higher than 10 nA/nm^2 were reported to be applicable for Joule heating induced local welding of Ag (12 nA/nm^2) [101] and Pt (up to 14.5 nA/nm^2) [102,103] nanowires, as well as for welding of dissimilar materials.

To avoid high current densities, which is mostly a concern in 2T NEM switches operating at high voltages, a thin insulating layer between the contacting surfaces has been used [10,13,50]. Another solution for the limitation of the current density at the jump-in moment for NEM switches is the connection of series resistance of 25–500 MΩ in the circuit [8,10,13,17].

The electrical field between NEM switch elements may give rise to material transfer [104,105]. During switching to the on state, a reduction of the separation gap between the electrodes prior to their mechanical contact results in an increase of the electrostatic field between them, especially at their highest asperities [105], where the electrostatic field achieves high enough (≈10^8 V/m) values to induce FN electron emission from the electrode (cathode). This process causes a temperature increase of the other electrode (anode), resulting in thermal evaporation of the electrode material and its transfer to the opposite electrode. For metal electrodes, the material transfer issues are reported for the source–drain bias exceeding 5 V. When the contact electrodes are made of two different materials [106], material transfer results in an increase of adhesion in the contact and also makes the surfaces rougher, thus increasing resistance in the contact. For self-mated contacts, for example, in an all-molybdenum switch, material transfer was reported to be a possible cause for the observed contact resistance rise after approximately 10^4 switching cycles operating at 1 V drain voltage in a 3T configuration with 100 nm gap between the beam and the drain electrode [19].

Choice of material for the NEM switching element

The material properties (Young's modulus, free surface energy, electrical conductivity, melting temperature) govern device performance (switching speed, range of operational voltage and current, reliability and durability), as well as dictate suitable fabrication approaches. The following subsections provide a brief overview of materials and material combinations used in the fabrication of active elements of NEM contact switches.

A comparison of the physical properties of the materials, together with the reported fabrication approaches, advantages and challenges for each of the material classes, and their prospective applications, summarizes the overviewed materials for NEM switching elements in a concluding subsection.

Metals

Metal–metal contacts in NEM switches are particularly advantageous for radio frequency (RF) applications due to their low electrical resistance. Experimental studies of elastic properties of metals, supported by atomistic simulations, have revealed several different ways the size depends on elastic properties: (1) increase in the Young's modulus of metallic nanowires relative to the bulk value of the metal, as their diameters are reduced (e.g., Ag and Pd [107-109] nanowires); (2) decrease of

Young's modulus with decreasing size, for example, for Cr nanocantilevers [110]; (3) Young's modulus shows almost no dependence on the diameter of metal nanowires, for example, for Au [111]. The change of the Young's modulus can be explained by an increased influence of the surface atoms on the overall elastic behaviour of the nanostructure at sizes below a few nanometres [112,113], or by the noncrystalline structure of the studied samples [110]. Atomistic simulations for fcc noble metals [113] showed that either a decrease or increase of the Young's modulus for metallic crystalline nanowires can be achieved by variation of their size and operation temperature. The possibility to tune the Young's modulus by changing an element size combined with facile integration with existing complementary metal oxide semiconductor (CMOS) devices, make metals attractive candidates for the use in NEM switches. However, metal-based NEM components with nanometre-scale dimensions are difficult to fabricate due to their high intrinsic stress, large surface roughness and grain size, inherent porosity, and low strength. To date, there are rather few reports on metallic NEM switches [17,18,114,115].

Molybdenum is attractive as a NEM switch material due to its high melting temperature (2622 °C [116]) and Young's modulus (290-380 GPa) [117]. Recent reports on Mo-based NEM switches have proven the robustness of the material. An all-molybdenum 3T NEM switch was fabricated by a top-down approach by filling Mo into a SiO_2 mold, prepared by a one-mask photolithography process. This process was followed by etching of the SiO_2 sacrificial layer for the release of Mo switching structures [19,115]. Switches with 300 nm thick and 500–700 nm wide switching elements with lengths 28–40 µm showed jump-in voltages in the range of 12–24 V for separation gaps of 100–150 nm. Cycling tests performed with Mo-based switches showed 100% repeatable operation of the switch with aforementioned dimensions of the switching element [115], as well as stable operation up to 20,000 switching cycles in vacuum at 300 °C [19]. The low subthreshold swing of 2.5 mV/decade was kept until the very end of the cycling tests [19]. The reliability of Mo-based NEM switches was found to be size-dependent due to the influence of residual stress in the material on the shape of the switching element.

Copper has been used as a NEM switch structural material to increase the feasibility of fabrication benefitting from a commercial CMOS technology [17]. 2T switches have been fabricated using the back end of line (BEOL) Cu layers of a commercial 65 nm CMOS technology. As-fabricated NEM switches showed jump-in voltages as low as 5.5 V, a good on/off ratio (10^3), and high miniaturisation level, surpassing other [17,23,49,114] top-down NEM switch fabrication approaches.

Similarly to copper, the fabrication of a platinum cantilever NEM switching element involved an additional thermal annealing step at 300 °C to reduce the stress gradient in the beam. The usability of platinum for electron-beam lithography-based fabrication of NEM relay-only and CMOS–NEM hybrid circuits was demonstrated. Platinum cantilevers with thickness of ≈60–70 nm, length of ≈3.2–3.5 µm and gap of 100 nm, showed a jump-in voltage of 3.3 V in 3T configuration, and 5–6 V in the CMOS–NEM hybrid circuit [114].

Ruthenium also allows CMOS compatible fabrication in addition to such benefits as high stiffness (Young's modulus 447 GPa), hardness (5 GPa), and high melting point (2333 °C [116]). Ru-based NEM relays with small gap widths have shown an even smaller coupling area than that of Cu-based devices, with a pull-in voltage of 5 V [18], together with the best-achieved turn-on delay of 400 ns. When tested for durability, the Ru device withstood more than 2×10^6 switching cycles at 1 kHz frequency. However, when downscaling Ru NEM switches, residual stress must be accurately controlled to avoid the buckling of beams after etching of the sacrificial layer. Another concern is the edge roughness of the as-fabricated beams that leads to variation in jump-in voltages and contact resistances for a given design [18].

To our knowledge, metal alloys used as NEM switching elements have been reported in only one study using a TiW switching element and W as the contact electrode [49]. A jump-in voltage lower than 1 V and on/off current ratio higher than 10^5 were demonstrated for this 2T NEM switch, employing an innovative "pipe-clip" architecture. However, the device showed poor reliability with marked deterioration in performance after 10–20 switching cycles. This was attributed to physical degradation of contacts, as well as formation of Ti and W oxides during the device processing.

Carbon allotropes

Carbon nanotubes: Carbon nanotubes have diameters ranging from the subnanometre range to tens of nanometres and may exhibit length-to-diameter ratios of up to 132,000,000:1 [118], which is significantly larger than for any other material, and thus could offer improved sensitivity. They also possess extraordinary mechanical strength (Young's modulus up to 1 TPa [119,120]), high thermal (2–6 $kW \cdot m^{-1} \cdot K^{-1}$ [121]**)** and electrical (10^6–10^7 S/m) conductivity.

Several CNT-based relays and switches have been fabricated using the bottom-up arrangement of CNTs, including dielectrophoresis [33], controlled growth of CNTs [34,37], dispersion coating [12,35,36], nanomanipulation [15,32] techniques and electron beam lithography/metal sputtering for the fabrication

of electrical contacts. CNT-based NEM switches exhibit a high on/off current ratio (10^4–10^5) [59] and switching speed (≈1 ns) [37] in combination with a jump-in voltage that can be as low as a few volts [35,37]. Yet, most of these devices were unique laboratory scale demonstrations. To the best of our knowledge, the highest durability (10^6 on/off cycles, 10 ns response time) of a 2T CNT-based switch was demonstrated by Loh et al. for carbon–carbon contacts, using multiwall CNT as a switching element and diamond-like carbon (DLC) as a contact material [12]. However, the reported actuation voltages for these switches were relatively high at 20–40 V. The high current density that is caused by the high actuation voltage in CNTs during switching cycles can be lowered by the use of an insulating layer [15] or by the choice of the appropriate type of CNTs. For example, studies performed on properties and breaking parameters of different types of CNTs found that bamboo-like multiwall CNTs are the most suitable for applications in NEM contact switches due to much higher (≥25 V) burn-off failure voltages than for tube-like multiwall CNTs (4–5 V) [122].

Besides individual CNTs, films consisting of many CNTs have also been employed in the fabrication of NEM switches. Networks of CNTs are currently under ongoing research for use in 2T non-volatile memory devices, to date showing good reliability of $\approx 10^{12}$ non-volatile switching cycles with no observable wear or fatigue and read–write voltages below 5 V [123]. Here, the switching to the off state is achieved by applying a voltage pulse, presumably causing a phonon heating driven repulsion force [123].

However, practical challenges for the use of CNTs in NEM contact switches still remain, such as dependence of electrical properties of CNTs on mechanical strain [124,125], their electrical breakdown and mass loss caused by field evaporation [126].

Graphene: For fabricating NEM switches, monolayer [24-27] as well as few-layer [28-31] graphene materials are used. The mechanical properties are decisive for selecting the number of layers of the graphene structure [26]. Few-layer graphene is more favourable for reversible switching due to higher stiffness than single-layer graphene, but it requires larger jump-in voltages as a consequence. Graphene NEM switches are fabricated using dry or polymer-assisted transfer techniques of chemical vapour deposition (CVD)-synthesized or mechanically exfoliated graphene flakes to the desired position on the substrate, and photo- and electron-beam lithography and metal sputtering techniques for fabrication of the electrical contacts. A SiO_2 sacrificial layer may be used for the release of graphene switching elements.

When the bending occurs along the length, and the normal stress along the width is negligible, the narrow graphene strip behaves as a nanobeam [127]. Graphene switches reported to date are primarily 2T and operate by deflecting the double-clamped graphene beam suspended over the drain electrode. Another architecture of graphene-based devices includes circularly clamped graphene switching elements [25]. Such devices can operate in 2T or 3T configuration (Figure 10a) with sub-5 V actuation voltage and provide a “line” contact of graphene membrane during switching.

The typical number of on/off cycles performed by graphene-based devices varies from 4–30 [60] up to 5000 [26]. These switches have demonstrated jump-in voltages below 1–3 V, high on/off ratios ($\approx 10^5$) and switching speeds on the order of

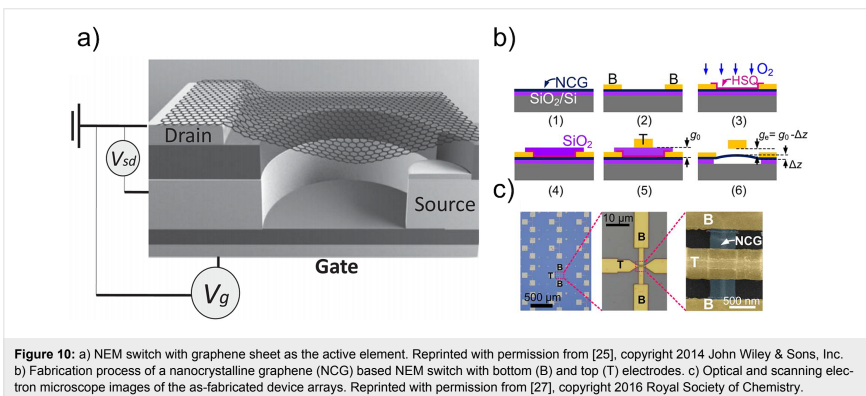

Figure 10: a) NEM switch with graphene sheet as the active element. Reprinted with permission from [25], copyright 2014 John Wiley & Sons, Inc. b) Fabrication process of a nanocrystalline graphene (NCG) based NEM switch with bottom (B) and top (T) electrodes. c) Optical and scanning electron microscope images of the as-fabricated device arrays. Reprinted with permission from [27], copyright 2016 Royal Society of Chemistry.

100 ns. The lack of reliability of graphene-based NEM contact switches is explained as follows: currently, large area graphene can be prepared by the CVD technique; synthesized by this method, graphene has a polycrystalline nature. Processes occurring at the grain boundaries of polycrystalline graphene as, for example, charge carrier scattering and mechanical stress, result in significant degradation of graphene properties and, consequently, poor performance of the CVD-graphene-based NEM switches. Also, the Young's modulus of CVD graphene is only about 40% of that of exfoliated pristine graphene (0.4 TPa vs 0.98 TPa [128]). CVD graphene NEM switching elements with comparable properties to mechanically exfoliated pristine graphene were fabricated from a single CVD grown graphene domain [26]. However, NEM switch fabrication using CVD synthesis of graphene is a complicated method, as it is followed by polymer-assisted graphene transfer to an insulator substrate and a microfabrication process to configure the NEM switch, posing challenges for large-scale production.

To facilitate the fabrication of graphene-based devices, direct growth of nanocrystalline graphene on insulating substrates using regular thin film process techniques (example of growth process is shown in Figure 10b) has been reported [27]. The nanocrystalline graphene on insulator had a very low thickness, good uniformity, and a Young's modulus comparable to mechanically exfoliated graphene [27]. Both single-crystalline and nanocrystalline graphene are promising for commercial integration in high-performance NEM switches regarding their physical properties. Similar to CNT [12], graphene NEM switches can find applications for data storage and logic [28]. Currently, scalable production methods of graphene requires temperatures of ≈800 °C [27] or higher, which are still too high for CMOS integration.

Semiconductors

Silicon and germanium: Both Si and Ge have a long history as semiconductor device materials. Comparable relatively high Young's moduli (Si, 130–188 GPa [129] and Ge, 103–150 GPa) [130,131] make these materials useful for applications in NEM devices. Due to the possibility of anisotropic etching, Si is widely used in top-down fabrication of NEM switches [20-22,50,132]. Top-down Si-based NEM devices of different designs (for example, U-shaped dual-beam structure with capacitive paddle (Figure 11a) [20], torsional [133]) are typically fabricated from single- or polycrystalline Si substrates using a SiO_2 layer as a sacrificial material to release free-standing elements [20-22,50,132,133]. 3T Si-based NEM switches can operate at jump-in voltages as low as 0.8 V [20].

Both Si and Ge nanowires are used in bottom-up fabricated NEM switches and in in situ testing of devices prototypes [9-11,13,14]. It was found that the presence of a native oxide layer on Si and Ge nanostructures implies some limitation on NEM switch operation at low voltages due to the high contact resistance expressed in low on/off ratio [9] and non-conductive gap below 2–4 V [10,13,54]. On the other hand, in 2T NEM switches, native oxide covered switching elements are able to operate without breakdown at voltages up to 40 V [10], required for repeatable on/off switching.

In terms of reliability, individual Ge nanowire-based 2T devices showed good durability with no signs of degradation during

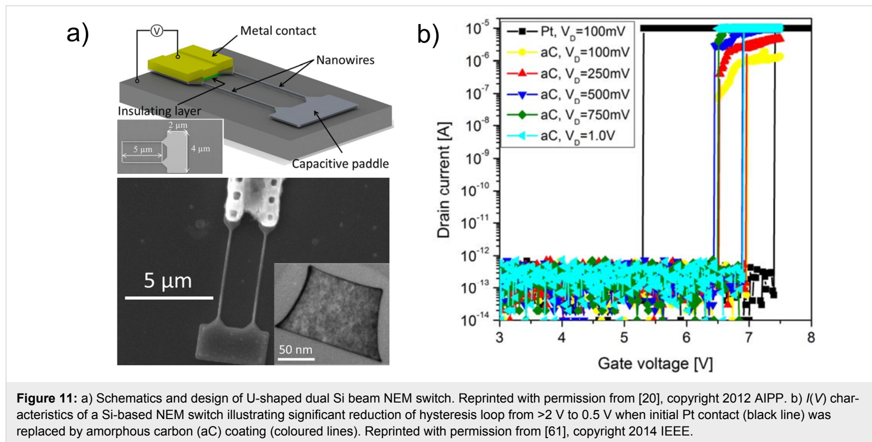

Figure 11: a) Schematics and design of U-shaped dual Si beam NEM switch. Reprinted with permission from [20], copyright 2012 AIPP. b) *I*(*V*) characteristics of a Si-based NEM switch illustrating significant reduction of hysteresis loop from >2 V to 0.5 V when initial Pt contact (black line) was replaced by amorphous carbon (aC) coating (coloured lines). Reprinted with permission from [61], copyright 2014 IEEE.

tens of switching cycles [10,11]. The operation at low on-state voltages is typically achieved by coating of Si or Ge NEM elements with some other conductive material like Au or Au alloys, Pt or amorphous carbon (aC) [9,61]. For example, coating Si NWs with metal (Au/Al) resulted in an improvement of the on/off current ratio by an order of magnitude [9], but coating of a Si-based NEM switch with amorphous carbon (aC) (Figure 11b) [61] allowed more than 10^8 switching cycles to be achieved. An alternative method of lowering the on-state voltage range is removing the native oxide layer from the nanowires' surface [10,13].

Molybdenum–sulfur–iodine: Excellent functional properties of nanowires based on transition metal chalcogenide-halides, combined with easy synthesis and intrinsic absence of impurities make them attractive NEM switch elements. The properties of these materials include high electrical conductivity [134], good thermal and mechanical stability and ability to withstand high (up to 50 V) operational voltages [8]. Molybdenum–sulfur–iodine ($Mo_6S_3I_6$) molecular wire bundles were investigated as NEM switching elements and as a contact material employing combined in situ TEM-nanomanipulation techniques aimed to determine how changes in the contact electrode material and geometry of 2T NEM switch influence the device characteristics [8]. The very low coefficient of friction of $Mo_6S_3I_6$ (0.03 [135]) could help to reduce surface wear originating from the tangential forces in the NEM contact when switching to the on state [70].

Silicon carbide: Silicon carbide (SiC), well-known for its resistance to corrosion, has been widely explored for harsh environment applications where traditional semiconductor materials fail. In addition, it has tribological characteristics superior to those of Si. SiC is a wide bandgap (2.4–3.3 eV) semiconductor with a bulk Young's modulus of 400–500 GPa [136] and high thermal conductivity on the order of 330 $W \cdot m^{-1} \cdot K^{-1}$ for bulk 3C–SiC [137], a larger than 1 MV cm^{-1} breakdown electric field as well as a high melting temperature. Regarding its elastic properties, despite the relatively large discrepancy in the results, the correlation between the diameter of SiC 1D nanostructures (down to 18 nm) and their Young's modulus was not found. The Young's moduli of 18–140 nm diameter SiC nanowires were determined to be in the range of 275–750 GPa [138,139], showing average value comparable with bulk values of 400–500 GPa [136]. Reported Q factors of electrically induced mechanical resonance of SiC nanowires varied from 3,500 to 160,000 [138].

SiC-based NEM switches fabricated by top-down approach have shown good durability. The approach involved electron beam lithography patterning and etching of the SiC layer deposited over the Si/SiO_2 substrate and following release of SiC nanostructures by removing the SiO_2 sacrificial layer. The as-fabricated 400–500 nm thick poly-SiC beam-based 3T switches showed stable operation during more than 10^6 cycles at both room temperature and as high as 500 °C [38,39]. Reducing the size of the switching element down to 25–50 nm resulted in the gradual structural deformation of the switching element [23]. SiC NEM switches with 25–50 nm thick switching elements exhibited unstable switching to the on state, lacking a distinct current rise (Figure 12a), presumably caused by the lower conductivity of SiC–SiC contacts in comparison to

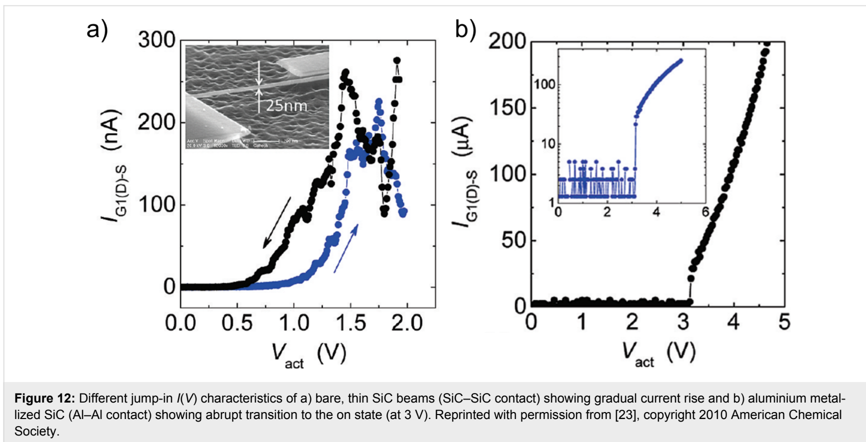

Figure 12: Different jump-in *I*(*V*) characteristics of a) bare, thin SiC beams (SiC–SiC contact) showing gradual current rise and b) aluminium metallized SiC (Al–Al contact) showing abrupt transition to the on state (at 3 V). Reprinted with permission from [23], copyright 2010 American Chemical Society.

metals. The metallization of SiC switches with aluminium resulted in a sharper on-state current rise (Figure 12b), but reduced durability of these NEM switches down to a few or in some cases singular switching events [23].

Ceramics

Titanium and tungsten nitride ceramics: Titanium nitride (TiN) has a low electrical resistivity that is comparable to some metals, high stiffness (Young's modulus of 427–590 GPa) and high hardness, high melting temperature (2930 °C), high corrosion resistance [140], and low surface energy [141] – all beneficial properties for NEM switch applications. TiN is also one of the materials used in almost all standard surface and bulk micromachining, thus available from routine CMOS production, and it can be integrated in existing devices. Meanwhile TiN exhibits strong residual stress within the thin film layers which has to be taken into account for NEM switch applications as it can cause unwanted out-of-plane deformations of switching elements [6,142]. Therefore, specific treatments for switching elements such as high-temperature annealing is necessary to release the residual stress [142]. Typical actuation voltages reported for TiN NEM switches were in the range of 5 V [48] to 14 V [47]. The 35 nm thick TiN beam-based NEM switch with a TiN/W contact electrode coated with a 8 nm thin SiO_2 layer and a 15 nm separation gap was operated in ambient air for more than 400 cycles with stable actuation voltages [47]. The jump-in voltage of TiN NEM switches can be lowered by using a harder material with higher melting temperature (for example, Al_2O_3) as the electrode coating [48]. Configuration of 2T TiN switches with three operation states (one off state and two on states with different jump-in voltages), presented in [48] can serve for memory and logic applications.

Amorphous tungsten nitride (WN_x) was proposed by Mayet et al. [5] as a prospective high-quality structural material for top-down fabrication of NEM switches. The amorphous WN_x thin film deposited using a tungsten target at room temperature has a Young's modulus as high as 300 GPa, which is comparable to the widely used WN_x protective coatings (300–390 GPa) [143]. 3T NEM switches were fabricated by a top-down approach using reactive ion sputtering over a SiO_2 sacrificial layer, employing electron beam lithography and etching methods. Experimental results on these NEM switches, where both the switching element and the contact electrode were fabricated from WN_x, indicated that this material is suitable for low-voltage switches. A NEM switch with design of relatively large dimensions (switching element size of 190 nm × 500 nm × 20 μm) [5] achieved a jump-in voltage of 0.8 V. High-contact resistance (10 MΩ) observed in the experiments indicated that these materials may be used in applications where current must be limited.

Comparison of NEM switching element materials

Although the above overviewed materials belong to different classes, their mechanical, electrical and thermal properties vary in a relatively narrow range (Figure 13). Typically, they can withstand high temperatures of at least 800 °C and are characterized by a Young's modulus of hundreds of GPa and have an electrical conductivity above 10^4 S/m. High Young's modulus values result in switching speed and a stiffness needed for the fast and volatile operation of a NEM switch. The electrical conductivity of the switching element is decisive for the desired application. For example, for RF applications, metallic conductivity is needed, while materials with relatively low conductivity are suitable for electrical current limitation applications. The ability of withstanding high temperatures is favourable for NEM switches operating in harsh environment. A demonstrative comparison of fabrication approaches, general advantages and challenges, together with some of the proposed applications of the materials for NEM switching elements is presented in Table 2.

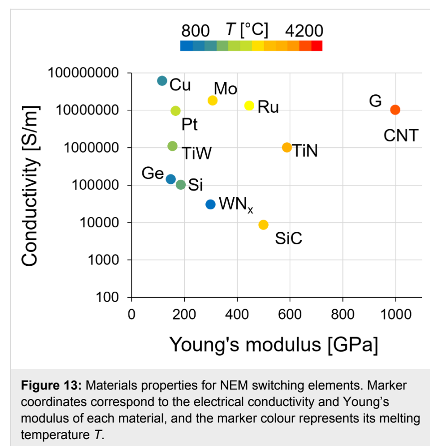

Figure 13: Materials properties for NEM switching elements. Marker coordinates correspond to the electrical conductivity and Young's modulus of each material, and the marker colour represents its melting temperature *T*.

Choice of electrical contact material

Despite numerous studies [51,52,82] on the properties of the electrical contacts at the nanoscale, there is a limited number of reports on the suitability of different materials combinations for NEM switch applications. At the same time, choosing the appropriate contact materials is one of the most important issues in scaling the NEM switch, as traditional contact materials (e.g., Pt, Au, Cu) struggle to show reliable and stable performance due to pronounced nanoscale adhesion, wear and dynamic evolution of the contact. The importance of choosing the appropriate materials is highlighted by NEM switch research, where

Table 2: Comparison of materials for NEM switching elements.

Materials		Device fabrication approaches (examples)	Advantages	Challenges	Possible applications
metals	Mo [19,115] Cu [17] Pt [114] Ru [18] TiW [49]	top-down (lithography, etching, thermal annealing, atomic layer deposition)	- high electrical conductivity	- surface oxidation (Mo, Cu, Ru, TiW) - scaling and grain boundary effects on mechanical properties - residual stress (Pt)	- RF applications
carbon allotropes	CNTs [12,15,32-37,59,123] graphene [24-31]	top-down (lithography, etching, metal sputtering) with bottom-up (dielectrophoresis, controlled growth, nanomanipulation)	- combination of high electrical conductivity and extraordinary mechanical strength - very high decomposition temperatures	- mechanical strain-dependent electrical properties (CNTs) - mass loss and electrical breakdown (CNTs) - grain boundary effects on mechanical and electrical properties (graphene)	- memory and logic applications
semiconductors	Si [20-22,50,132,133] Ge [9-11,13,14] $Mo_6S_3I_6$ [8] SiC [23,38,39]	top-down (lithography, etching) or bottom-up (nanomanipulation)	- operation at relatively high voltages up to 40–50 V (Si, Ge, $Mo_6S_3I_6$) - can withstand high temperatures (SiC)	- surface oxidation (Si, Ge) - mechanical and electrical properties may change with increasing temperature (Ge, Si)	- memory (Si) - logic and high-temperature applications (SiC)
ceramics	TiN [6,47,48,142] WN_x [5]	top-down (lithography, etching, sputtering, thermal anneal, atomic layer deposition)	- combination of high electrical conductivity and stiffness (TiN) -combination of high elasticity and hardness (WN_x)	residual stress (TiN)	- memory and logic applications (TiN) - electrical current limitation and low-voltage switches (WN_x)

classical switch architectures in combination with unconventional materials combinations, for example, SiC [7] and diamond-like carbon (DLC) [12] as electrical contact materials, have led to increased reliability. The following subsections summarize the advantages and drawbacks of some of the materials being used as electrical contacts in NEM switches.

Metals

The reliability of various metals as electrode materials has been examined both theoretically [144] and experimentally [63,145-152] using mechanical [145,146], electrical [145,146] or coupled electromechanical [63,147-152] testing experiments. The materials properties such as hardness, wear resistance, melting point, conductivity and oxidation characteristics should be considered for each particular application.

Theoretical studies have modelled the impact of NEM switch scaling on the properties of metal electrode materials, showing that a decrease in device dimensions will necessarily result in a large increase of contact resistance as well as the risk of stiction-induced failure [144]. It was found that no metal considered in this study (Ag, Al, Cu, Pt, Rh, Ru, Ti and W) can fulfil the requirements of an ideal contact simultaneously [144].

Au is a material with an exceptional conductivity and oxidation resistance. However, the reliability of pure Au–Au contacts is very low as Au is a soft material, which is likely to undergo material transfer and wear [144,153]. Alloying with another metal (for example, Ni) is a method to strengthen soft metals to increase wear resistance and reduce surface adhesion. Two-phase Au–Ni alloys (at 20% Ni) showed reduced wear rate and a small increase of contact resistance in comparison with pure Au electrodes in a MEM switch setup [150]. It was also shown that Au, alloyed with noble metals such as Pt, Rh and Ru, reduced the contamination build-up rate [147].

Other noble metals such as Ir and Pt are attractive due to their high Young’s modulus and oxidation resistance in ambient environment. Under $I(V)$ cycling with a Cr-coated AFM tip, both materials exhibited relatively low initial contact resistances in comparison with Ni and Cr [145]. Adhesion forces were measured to be more than four times higher for the Ir/Si

contact than for Pt/Si [145]. The electromechanical cycling of Pt/Pt contacts for 10^9 cycles in ambient air showed more than three orders of magnitude increase of contact resistance accompanied by only a moderate 12% increase of adhesion force and no signs of wear-related degradation [63]. TEM observations revealed an added layer of material on the switching element and molecular dynamics simulations in the same study showed that the presence of a tribopolymer layer between metal contacts would increase the contact resistance, but weaken the adhesive interactions, in comparison with a case with no tribopolymer.

The use of W as the contact material in NEM switches is advantageous due to the high hardness of the metal, high Young's modulus and high melting and boiling points. A W/Cr contact demonstrated the lowest adhesion force, compared to other metals (e.g., Pt and Ni) [145]. However, for a W contact material, relatively large changes in contact resistance [146] and degradation of the on state current during cycling [49] have been reported, which has been attributed to the impact of its native oxide [49,146].

Al and Cu electrode materials have demonstrated very low initial contact resistances during $I(V)$ cycling [145] due to the high conductivity of these electrode materials. However, both materials displayed either gradual (Al) or abrupt (Cu) increase of contact resistance after 10^4 $I(V)$ cycles [145].

Ti stands out with the combination of a hardness and Young's modulus relatively better than for other materials (e.g., Au, Al, Cu), showing reliable $I(V)$ cycling with low initial contact resistance [145]. However, the stable cycling performance is compromised by its larger resistivity in comparison with other metals.

Metals have been alloyed with semiconductors in search for novel NEM switch contact materials. Platinum silicide (Pt_xSi) thin films were proposed as the perspective contact material due to the combination of mechanical robustness and metal-like conductivity [63,154,155].

In summary, the highest reliability is achieved using a material with a combination of high Young's modulus, high hardness and high melting point, for example, Ti and W, while materials traditionally used for contacts (noble metals such as Au and Pt) are at risk of wear due to their low hardness and low Young's modulus [153].

Other materials

Electrically conductive stable oxides could also be considered as prospective NEM switch contact materials, as they have shown reliable performance for microscale contacts. For example, switches based on ruthenium oxide RuO_2–Au contacts [149,151,152] reached more than 10^{10} switching cycles without failure, surpassing such materials combinations as Pt–Au and Ir–Au [149]. As RuO_2 has lower surface reactivity than, for example, Pt, the RuO_2–Au contact material combination prevents cycling-induced tribopolymer accumulation [149]. However, the conductivity of RuO_2 is lower than that of Au [152].

Another perspective contact material is $Mo_6S_3I_6$, because of its low surface energy [134]. $Mo_6S_3I_6$ was tested in a NEM switch, where the switching element was $Mo_6S_3I_6$ nanowire bundles, and the contact electrode material was $Mo_6S_3I_6$ or Au. The performed tests showed reduction of adhesion per unit area by nine times for a $Mo_6S_3I_6$–$Mo_6S_3I_6$ contact in comparison with a $Mo_6S_3I_6$–Au contact [8].

Diamond-like carbon (DLC) and SiC have been suggested as electrode materials due to their mechanical robustness, demonstrating stable contact resistance over 10^6 switching cycles for CNT-based NEM switch [12] and over 10^7 cycles for SiC-based NEM switch [7]. The applications of these materials are, however, limited due to their high contact resistance.

Table 3 presents the advantages and drawbacks of the contact materials combinations discussed above, as well as their cycling behaviour, together with experimental setups used for testing.

Operating environment

Environmental conditions (e.g., pressure, temperature, humidity, presence of chemically active gases (among which the impact of oxygen is the most widespread and studied), contamination with carbonaceous compounds [63,156-158]) can impact both the switching element and contact materials, influencing NEM switch operational parameters such as switching speed, jump-in voltage, hysteresis width, contact resistance and adhesion. The environmental effects on the switching element may result in a delay of response or change in jump-in/jump-out voltage of the device. The most severe environmental impact is experienced in the contact region, where the dynamic relationship between contacting materials can introduce variability in electrical and mechanical NEM switch operational parameters over time.

Environmental damping of NEM switching element

In contrary to high-vacuum conditions, where the damping of the switching element is determined by intrinsic losses (e.g., imperfect clamping, structural defects in the switching element), in higher pressure (low vacuum, dry gas or liquid) environments it experiences additional external losses,

Table 3: Advantages and disadvantages of contact material/switching element combinations.

Contact material/ switching element	Advantages	Cycling performance	Drawbacks
Ir/Cr [145][a]; Ir/Pt [146][a]	- high hardness - high resistance to native oxide formation	good cycling characteristics for 10^5–10^9 [63,145] cycles; low initial contact	high adhesion force[a] in comparison with Cr, Ni, Ti, W, Pt [145]
Pt/Cr [145]; Pt/Pt [63][a], [144,146]	- lower adhesion force in comparison with Ir, Ti, Ni, Cr, Al, Cu [145] - harder than Au - high resistance to native oxide formation	resistance (in comparison with Ni and Cr) [145]	contact resistance increase over time [63,145] (more than 3 orders of magnitude after $2 \cdot 10^9$ switching cycles [63])
W/Cr [145]; W/TiW [49][b], [144]; W/Pt [146]	- lower adhesion force in comparison with Pt [145] - high hardness, high melting and boiling points (compared to, e.g., Pt)	good $I(V)$ cycling characteristics for 10^5 cycles [145]; larger changes in contact resistance (compared to, e.g., Ir, Ni, Pt) [146]; degradation of on state current [49]	formation of native oxide
Ti/Cr [144,145]	- combination of reliability, useful lifetime, hardness and Young's modulus relatively better than for other materials (e.g., Au, Al, Cu) - high corrosion resistance	good $I(V)$ cycling characteristics and stable contact resistance for 10^5 cycles [145]	higher resistivity in comparison with other metals
Ni/Cr [145]; Ni/Pt [146]	- good corrosion/oxidation resistance	poor $I(V)$ cycling performance [145]; less than 1% change in contact resistance over 10^5 cycles [146]	high initial contact resistance (3–5 orders of magnitude higher than W, Pt, Ti, Ir) [145]
Cr/Cr [145]	- high corrosion resistance and hardness	poor $I(V)$ cycling performance [145]	formation of native oxide
Al/Cr [144,145]	- low initial contact resistance	gradually became nonconductive after 10^4 $I(V)$ cycles [145]	high adhesion force, formation of native oxide
Cu/Cr [144,145]	- low initial contact resistance	abrupt large rise in contact resistance after 10^4 $I(V)$ cycles [145]	high adhesion force, formation of native oxide
Au/Au [147,148,150,153][c]	- no oxidation - very low initial electrical contact resistance	material transfer during cycling	high adhesion force, low hardness; rapid surface wear
Au–Ni alloy, 20 atom % Ni/Au [150]	- reduced wear rate in comparison with pure Au	larger number of switching cycles with stable contact resistance compared with pure Au	contact resistance higher than that of pure Au
$Mo_6S_3I_6$/Au $Mo_6S_3I_6$/$Mo_6S_3I_6$ [8][b]	- low surface energy [134]	larger number of switching cycles in comparison with Au electrode	S forms covalent bond with Au
DLC/CNT [12][b]	- low adhesion, mechanical robustness - high electrical resistivity, high corrosion resistance	stable contact resistance over 10^6 switching cycles	high contact resistance
SiC/SiC [7][b]	- stable performance over testing period of 7 days in ambient air - suitability for high temperature (500 °C) measurements	stable performance over 10^7 full switching cycles at room temperature	high contact resistance
RuO_2/Au [149,151,152][c]	- electrically conductive and stable oxide - extended lifetime (in comparison with Pt–Au and Ir–Au) due to catalytic behaviour	reached more than 10^9 switching cycles without failure [149]	lower conductivity that Au–Au contacts [152]
Pt_xSi [63,154,155]	- combination of mechanical robustness with metal-like conductivity - good oxidation resistance	no cycling tests performed	no cycling tests performed

[a]Metal-coated AFM tip/thin film-based nanoscale test platform. Si AFM tip was used in adhesion force measurements. [b]Representative NEM switching device. [c]Microscale test platform.

depending on the pressure and viscosity of the surrounding medium, which are mirrored by a decrease of quality factor of the switching element and may lead to reduction of the switching speed. Figure 14 illustrates the impact of air pressure on the quality factor for three different sized SiC nanocantilevers indicating the transition from molecular to viscous damping

[159], governed by collisions and viscosity of the medium, respectively.

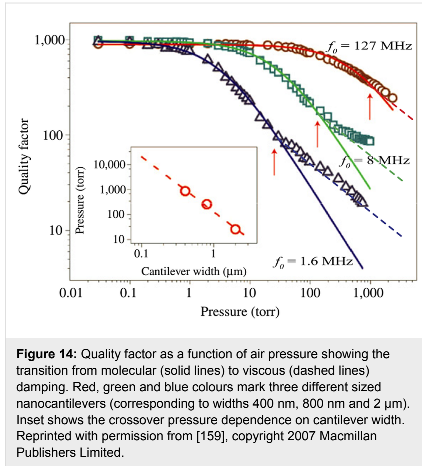

Figure 14: Quality factor as a function of air pressure showing the transition from molecular (solid lines) to viscous (dashed lines) damping. Red, green and blue colours mark three different sized nanocantilevers (corresponding to widths 400 nm, 800 nm and 2 μm). Inset shows the crossover pressure dependence on cantilever width. Reprinted with permission from [159], copyright 2007 Macmillan Publishers Limited.

Despite the negative impact on the quality factor of the switching element, operating a NEM switch in a water-free dielectric liquid with large dielectric constant has several significant advantages such as reduction of pull-in voltage, suppressed arcing, avoiding capillary forces and exposure of NEM switch components to oxygen, as well as reduction of van der Waals force in the contact [160]. Operation in insulating liquid media has been demonstrated for a few NEM/MEM switches. A top-down fabricated 3T NEM switch using a moving TiN cantilever and TiN electrode with a 40 nm gap operating in insulating transformer oil showed about 40% decrease in pull-in voltage due to the liquid's large dielectric constant [160]. The additional benefits were reduction in hysteresis width and improved cycling characteristics when compared to operation in air [160]. For a much larger microelectromechanical switch, a similar 31.8% reduction in pull-in voltage and a more than 94% decrease of the adhesion force have been reported when operating in mineral oil [161].

Operation in humid environments and ambient air

Capillary forces: If a NEM switch is fabricated using wet etching or is operating in humid environments, the capillary forces should be considered. It is increasingly important with down-scaling of a NEM switch, as the ratio of capillary to elastic restoring force of the switching element increases with reducing device dimensions (Figure 15) [144]. In humid environments, the capillary condensation from the surrounding vapour on the NEM switch nanocontacts impacts the adhesion behaviour during switching operation. During a NEM switch fabrication process, the capillary forces may arise from residuals left after lithographic processing using wet etching. The impact of wet fabrication steps can be minimized using super critical point drying [12,162,163]. To prevent the occurrence of capillary forces arising from the device fabrication process, it is recommended to use dry switching element release procedures (e.g., dry etching with HF [5-7], reactive ion etching [5,12,19]).

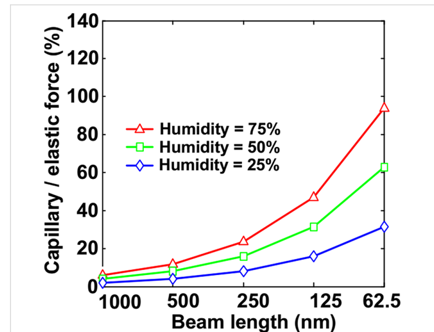

Figure 15: Scaling impact on the capillary/elastic force ratio. The impact of reducing the length of the switching element on the ratio of capillary to elastic force is shown for three different humidity levels. Reprinted with permission from [144], copyright 2011 IEEE.

Methods for minimising/elimination of capillary forces during operation include coating the switch elements with hydrophobic self-assembled monolayers (SAMs) [104,164] and immersing the NEM switch in an insulating liquid environment, which also significantly reduces vdW forces. However, coating with SAMs poses challenges in tailoring the electrical properties of the switch.

Oxidation: When designing a NEM switch for operation in ambient environment, the oxidation characteristics of materials must be considered. Regarding electrical contact materials, noble metals are highly resistant to oxidation and corrosion in ambient air at room temperature. However, for Pt-group metals (e.g., Pt, Ir, Ru) the formation of the surface oxide can be activated by the presence of water vapour at relatively low temperatures [165]. In contrast to noble metals, almost all base metals develop a thin oxide layer under ambient conditions. In this case, the chemical and mechanical properties of a native oxide determine the corrosion resistance of NEM switch contact materials. For example, Ni, Cr and Ti form protective layers, making them suitable as electrode coatings in a broad range of environments. The electrical conductivity of metal oxides of contact

materials spans a large range of values from metallic to insulating. For example, Ir can form an electrically conductive oxide under proper temperature conditions. Cr oxide is moderately conductive with resistivity in the range of 3×10^{-6} Ω·m [166]. Native oxide of Cu is semiconducting (with resistivity around 4.6×10^{4} Ω·m at room temperature), showing pronounced temperature dependence [167]. Ni oxidizes to form a crystalline, mechanically robust NiO film at room temperature with a resistivity of approximately 0.5 Ω·m [168]. Ti oxide has high bulk resistivity [169], but for thin films, it can significantly decrease due to the changes in material stoichiometry [170,171]. One of the metal oxides with the highest (5×10^{11} Ω·m [172]) is the brittle Al native oxide, growing rapidly under ambient conditions. Commonly used for NEM switching elements, semiconductors Si and Ge in ambient air develop few nanometre thick, insulating (1×10^{12} Ω·m (Si) [13,20] and 8×10^{8} Ω·m (Ge) [10,173]) oxide layers.

Typically, the oxidation of NEM switch component materials during fabrication or operation is accompanied by an increase of contact resistance and creation of a potential barrier in the contact [8,13,17,49], manifested in nonlinear $I(V)$ characteristics (Figure 16). Complete removal of the oxide layer leads to reduction of the potential barrier between the contacting surfaces, resulting in significant improvement of electrical contact and linear $I(V)$ characteristics, allowing operation at low voltages (Figure 16) [10].

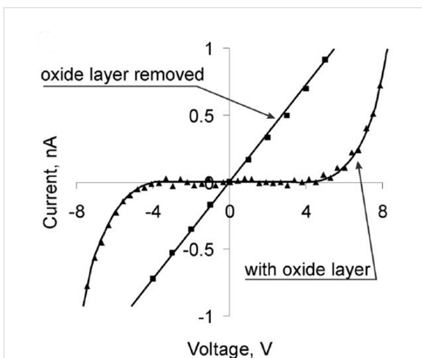

Figure 16: $I(V)$ characteristics of Ge nanowire with and without an oxide layer. Reprinted with permission from [10], copyright 2009 American Chemical Society.

Alternatively, repetitive cycling of a NEM switch may lead to modification (thinning) of the oxide layer in the nanocontact area, reported, for example, during $I(V)$ cycling of an oxide-covered Ge nanowire–Au nanocontact [54]. Current flow and heating caused by FN tunnelling through the oxide results in its smoothening and thinning in the nanocontact. This leads to a simultaneous increase of the nanocontact area and a decrease of the contact resistance [54].

The electrical charge stored in the poorly conductive oxide layer may enforce the electrostatic attractive force applied to the switching element. A decrease of jump-in voltage during cycling was attributed to the charge build-up effect, reported for NEM switches with Si [20] and Cu [17] switching elements. Also, it has been shown that an oxide layer can significantly alter the Young's modulus and consequently the stiffness of the switching element [174,175], affecting both jump-in and jump-off voltages of the switch.

Environmental contaminants: Ambient hydrocarbons and other organic compounds as traces of organic vapours may form an insulating high molecular weight carbonaceous deposit (tribopolymer) in the areas experiencing mechanical load [158], for instance, during the on switching events. The impact of tribopolymer on NEM switch operation has been experimentally investigated using controlled environmental setups, introducing known levels of organic contaminant gasses such as benzene [156,158]. The proposed explanation of the tribopolymer formation phenomena is adsorption of hydrocarbon molecules on a metal surface followed by chemical interaction between themselves and with the metal surface under mechanical load, becoming polymerized and dehydrogenated [157,158,176]. While a detailed understanding of the tribopolymer formation mechanism is lacking [157,168], it has been related to catalytic activity of contact metals. It has been shown that while Pt group metals are the most susceptible to formation of a tribopolymer layer, it deposits also on the surface of other metals such as Mo, Ta, Cr and Au [157]. The formation of tribopolymer on most metal layers results in significant reduction of adhesion between the contacting materials due to significantly (by approximately three orders of magnitude) decreased surface energy in comparison with pure metals [177]. Calculations have shown that every mechanical switching cycle creates about a monolayer of polymer [157].

The electrical current, flowing through the nanocontact during each switching cycle, has a twofold effect on formation and evolution of the tribopolymer layer. On the one hand, it causes dielectric breakdown of a layer grown during this cycle by permanently altering its structure to a conductive state [158]. On the other hand, similar to mechanical stress, the electrical current increases the rate of polymer growth by supplying additional energy to molecules adsorbed at the metal surface and helps to overcome the activation energy barrier for adsorbent

polymerization [156,158]. This process may result in an increase of the electrical resistance of the NEM switch contact by a few orders of magnitude over the contact lifetime of a few billion cycles [63].

Operation at extreme temperatures

One of the strengths of NEM switches are their proposed superiority for harsh environment applications such as extreme temperatures. The operational characteristics at 300 °C for a molybdenum NEM switch and 500 °C for SiC showed that the off-state leakage current is not influenced by temperature [7,19,38]. In comparison with room temperature, operation at higher temperatures has improved the stability of the contact resistance, suggesting that cleaning of the surfaces from moisture and contaminants is taking place [19,158]. Increased temperatures may also release residual stress in the switching element, thus reducing NEM switching hysteresis width (Figure 17) [6]. It is important to note that the temperature impact on Young's modulus and electrical resistivity of the switching element material needs to be considered when designing the NEM switch. For the majority of semiconductors, both the Young's modulus and the electrical resistivity significantly decrease with an increase of temperature (references for Si and Ge are given as an example [131,178,179]), while for metals, the high temperature related decrease of the Young's modulus is accompanied by an increase of electrical resistivity [180]. NEM switch operation has also been demonstrated at low temperatures, for example, for graphene NEM switches at 78 K and 10^{-6} Torr [25].

Clean environments

Due to the environmental effects described previously, clean environments such as high vacuum [19,152] or clean N_2 [149,181-183] are needed to reduce or eliminate oxidation and contamination, as well as to increase the switching speed. To achieve clean operation, sources of environmental contamination (sacrificial layers, organic solvents, exposure to air) must be eliminated during each stage of NEM switch fabrication and testing, including processing, transfer to and testing in the operating environment.

Encapsulation of NEM/MEM devices may be a solution to minimize environmental contamination- and oxidation-caused modification of nanocontacts. However, it increases the device size and the complexity of the fabrication process. Up to now, only a few reports on MEM switch encapsulation attempts can be found [184,185].

NEM switch failure modes and mechanisms

The following section provides a brief overview of specific nanobeam-based NEM switch related problems that cause a switch to malfunction. The most frequently observed failure modes, their mechanisms, as well as suggestions of possible solutions for preventing these failures are reviewed.

Mechanical tear

The estimations show that in NEM contact switches with 2T single-clamped architectures shown in Figure 1a,b, the speed of the free end of the switching element during the accelerated jump-in motion can be as high as 200 m/s [15]. Compressive stress of the switching element at the moment of contacting the drain electrode can reach 30 GPa. It is accompanied by deformation of the switching element, resulting in generation of a strong elastic compression wave propagating along it, and is superimposed on a bending stress in the switching element. This may lead to wear, tear and loss of the contacting material [24,29,186,187], especially over repetitive switching of CNTs used as switching elements [15]. The possible solution for this failure would be the reduction of the separation gap between the contact electrode and the switching element, but that would mean lower retraction forces and higher risk of device failure due to stiction. Another option is to use more durable materials such as semiconductor nanowires [8,10] for the switching elements.

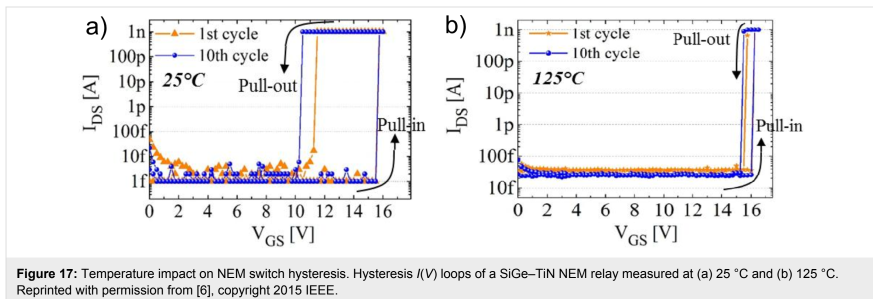

Figure 17: Temperature impact on NEM switch hysteresis. Hysteresis *I*(*V*) loops of a SiGe–TiN NEM relay measured at (a) 25 °C and (b) 125 °C. Reprinted with permission from [6], copyright 2015 IEEE.

Increase of switch resistance resulting in current drop down to the noise level in on state

The switch contact can become electrically insulating due to the oxidation of the switching material or build-up of a non-conductive tribopolymer layer under repetitively applied load in the contact [63,156,188]. Oxidation and tribopolymer formation issues were discussed previously. Both problems can be addressed by encapsulation of the switch in an inert atmosphere, preferably high vacuum, but it increases the device size and complexity of the fabrication process. Alternatively, the use of chemically inert materials or materials covered with electrically conductive oxides may be helpful in minimising these issues. If the dielectric layer has already formed, for example, during the fabrication process or mechanical cycling, it can be demolished by applying higher electrical fields, thus breaking it down [156]. However, this may result in the device failure.

Stiction

Permanent stiction occurs when adhesion in the contact between the switching element and the electrode exceeds the pull-out forces, leaving the switching element permanently attached to the contact electrode (on position). The most common ways to prevent stiction of the switching element already during the first switching cycle are: to decrease the contact area [8] (drawback – increased contact resistance and current density through the contact); to increase the initial separation gap between the switching element and the contact electrode [13] (drawback – increased jump-in voltage); to use materials with lower free surface energy [74-76].

During the on–off cycling of a NEM switch, there are several processes (discussed previously), which may eventually result in permanent stiction of the switch such as material transfer, dielectric charging, surface wear and the formation of chemical bonds at the contacting interface.

Material transfer: Material transfer caused by thermal evaporation of material from anode electrode (described in detail previously) may be avoided by reducing the source–drain voltage below a critical value [104,105,189]. However, this would increase the risk of stiction for 2T NEM switches due to lower restoring force of the switching element. Also, by increasing the switching speed, the field emission time would be shorter, thus minimising or avoiding the following thermal emission [105,189]. Considering the described material transfer mechanism, the materials with higher thermal conductivity and melting temperature are a preferable choice to resolve this problem.

Dielectric charging: Charging of the dielectric material (for example, thin native non-conductive oxide, tribopolymer) covering the contacting surfaces, may force the switch to jump to an on state at voltages lower than the jump-in voltage. For large charge build-up relative to the NEM switch separation gap, this effect may lead to permanent stiction of the device [190]. The charge accumulation issue may be partially resolved by using bipolar AC rather than DC voltage actuation [191]. However, it would require complex electronics [192,193] to drive the NEM switch in dielectric charging-free mode.

Surface wear: Surface wear, which develops during repeated on–off cycling of a NEM switch, can lead to an increase of the contact area to the point where stiction occurs. It can be minimised using materials with high hardness and good electrical conductivity, including innovative materials such as Pt_xSi [63]. Soft metals, traditionally used for electrodes, for example, Au, can be strengthened against wear by alloying with other metals [150], however, using of such alloys instead of pure Au may lead to increased current densities in contact. The physical properties of materials which are used in NEM switches were discussed in previous sections.

Chemical bonds: The formation of chemical bonds between the contact material and the switching element increases the adhesion forces in the contact. For instance, formation of covalent bonds between Au and S atoms significantly increasing adhesion in the contact, as was reported for a $Mo_6I_3S_6$-based NEM switch [8]. The process of chemical bond formation may be enhanced by a current-induced temperature increase in the contact area. Most graphene-based devices suffer from irreversible stiction after only a few switching cycles [24,25,27-31,60,80] due to the high current density and corresponding temperature increase in a graphene–gold switch contact. As a result, carbon–gold chemical bonds are established at the interface between the edge of a graphene nanoribbon switching element and a gold contact electrode and leads to permanent stiction of the switch [80].

Burn-out

The mechanism of electrical current induced burn-out of a NEM switching element is governed by a set of parameters, which include thermal and electrical conductivities of the switching element, electrode and nanocontact area.

One of the most common burn-out mechanisms is partial local melting of the electrode material at the contact point and partial ablation of the switching element at the contact. This burn-out mechanism is typical for jump-in events and can be explained by rapid local heating caused by electrostatic discharge at the jump-in-contact moment. In this process, charges accumulated in the off state give rise to a current peak through the contact area that is significantly larger than the steady-state on current

[16]. Due to high jump-in voltages, this is the main failure mode of bistable 2T NEM switches. As an example, the burn-out of a Ge nanowire occurred at a jump-in voltage of 13.5 V with current density of 3 nA/nm^2 in the contact (Figure 18a [10]).

Degradation of a switching element near the contact is also observed for NEM switches in the on state, even if materials with good thermal conductivity are used [10,14].

As the contact area is much smaller than the cross-sectional area of the switching element (see Table 1), the current density in the contact is high enough to cause migration of atoms in the material and lead to failure of the switching element due to large electromigration-induced mechanical stresses [96,99]. When the thermal conductivity of a switching element is relatively low, Joule heating at current densities >0.1 nA/nm^2 (for GaAs nanowires) and >10 nA/nm^2 (for $Mo_6S_3I_6$ nanowires) leads to a high temperature difference between the middle point and the ends and consequent thermal breakdown of the switching element into two halves [8,96] (Figure 18b,c). In $Mo_6S_3I_6$ nanowires, Joule heating also leads to chemical decomposition and transformation into Mo nanowires through thermal evaporation of S and I atoms. Breakdown of the transformed nanowires occurred at current densities of about 80 nA/nm^2 [100].

Native-oxide-coated nanowires may also experience meltdown of the core material at the moment of jump-in contact [10] or during the increase of current densities in on state [55], presumably, due to poor thermal contact between the nanowire and electrode. Figure 19a,b illustrates step-like degradation of a Bi_2Se_3 nanowire during the on state. One to several breakdown steps is typical for core/shell nanowires. The first current drop (Figure 19a, marked with 1) occurs when the nanowire core melts and is transformed to a shell-like structure filled with droplets (Figure 19b) [55]. In air ambient Bi_2Se_3 nanowires become covered with composite Bi and Se oxide shell [194]. As the melting temperature of Bi_2Se_3 (710 °C) is significantly higher than that of SeO_3 (118 °C) and SeO_2 (340 °C) and at the same time lower than that of Bi_2O_3 (817 °C), it is possible that after the core of the Bi_2Se_3 nanowire melts, a further voltage increase leads to conduction through the semiconducting Bi_2O_3 shell until the current drops (Figure 19a, marked with 2 and 3), indicating the successive burn-out of the oxide shell.

Germanium nanowire-based NEM switches demonstrated a similar burn-out mechanism for germanium nanowires covered with a native oxide layer [10]. An example of the core–shell burn-out of a native-oxide-covered Ge nanowire at a jump-in voltage of 37 V is shown in Figure 19c [10]. The core of the nanowire melted in the moment of contacting the electrode. As

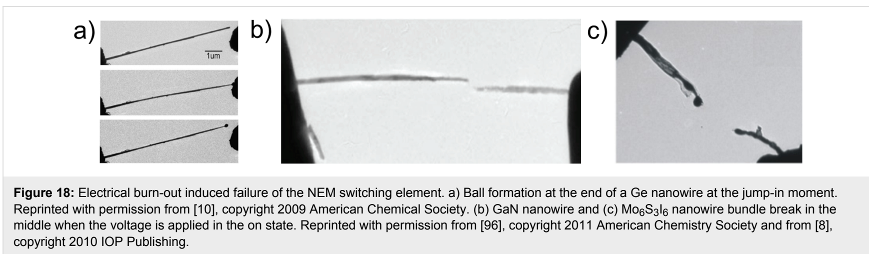

Figure 18: Electrical burn-out induced failure of the NEM switching element. a) Ball formation at the end of a Ge nanowire at the jump-in moment. Reprinted with permission from [10], copyright 2009 American Chemical Society. (b) GaN nanowire and (c) $Mo_6S_3I_6$ nanowire bundle break in the middle when the voltage is applied in the on state. Reprinted with permission from [96], copyright 2011 American Chemistry Society and from [8], copyright 2010 IOP Publishing.

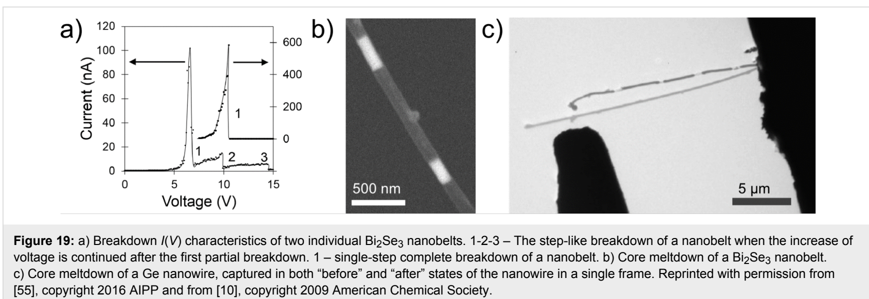

Figure 19: a) Breakdown *I*(*V*) characteristics of two individual Bi_2Se_3 nanobelts. 1-2-3 – The step-like breakdown of a nanobelt when the increase of voltage is continued after the first partial breakdown. 1 – single-step complete breakdown of a nanobelt. b) Core meltdown of a Bi_2Se_3 nanobelt. c) Core meltdown of a Ge nanowire, captured in both “before” and “after” states of the nanowire in a single frame. Reprinted with permission from [55], copyright 2016 AIPP and from [10], copyright 2009 American Chemical Society.

the core of Ge nanowire melted and divided in segments inside Ge oxide tube, the temperature of the nanowire was in the range between 938 and 1115 °C – the melting points of bulk Ge and GeO_2, respectively. Simulations performed for clarifying the burn-out process showed that when the nanowire in the active contact area is thermally isolated from the electrode, presumably due to the poor mechanical contact, its temperature increases rapidly, reaching the melting point of Ge in 100 ns [10].

Table 4 summarizes the main failure modes of NEM switches and their possible solutions, as well as the affected properties of the NEM switch, in case these solutions are employed.

Table 4: Main failure modes of NEM switches.

Failure mode	Reasons	Possible solutions	Affected properties of proposed solutions
mechanical tear [15,24,29,186,187]	high impact speed and following compression stress when active element jumps into the contact	lower switching speed (smaller jump-in voltages), more durable materials	lower jump-in voltages mean weaker retraction force and possible failure due to stiction
increase of switch resistance resulting in current drop in on state down to the noise level [63,156]	oxidation of the contact surfaces and contamination with hydrocarbons when operating in ambient environment	use of chemically inert materials or materials coated with electrically conductive oxides	presence of an oxide layer may lower contact conductivity
		application of higher voltage pulses for dielectric layer breakdown	risk of burn-out failure
		encapsulation	increases the device size and the complexity of the fabrication process
		operation in vacuum	may be insufficient to prevent adsorption of hydrocarbons if the vacuum is not high enough
stiction [24,25,27,31,60,80, 104,105,189,193]	adhesion between switching element and contact electrode exceeds restoring (elastic) force of the switching element	decrease of contact area	increase of contact resistance
		increase of initial gap thus increasing the retraction force	increase of jump-in voltage
		use of switching element with high Young's modulus, thus increasing the retraction force	increase of jump-in voltage
		use of materials with lower surface energy	increase of contact resistance
	material transfer	reduction of source–drain voltage below 5 V	increases risk of stiction in 2T NEM switches due to reduction of restoring force of switching element
		increase of switching speed	high mechanical impact forces
		use of materials with good thermal conductivity, high melting temperature, high work function and low roughness	–
	dielectric charging	use of bipolar AC rather than DC voltage actuation	the charging effect cannot be eliminated completely, more complex electronics required
burn-out [8,10,14,16,55,96, 99,100,194]	electrostatic discharge	decrease of jump-in voltage	increases risk of stiction
		use of dielectric layers to increase contact resistance and reduce charge dissipation rate	increase of power dissipation, delay, decrease of noise margin of the device
	Joule heating	use of insulating contact layer and materials with higher melting temperature	insulating layer increases charge buildup and enhances risk of unstable pull-in voltage
		addition of high resistance in series	decreases on/off state current ratio

Conclusion

This review highlighted the most significant advancements in nanobeam-based electrostatically actuated NEM switch technology that have taken place during the last decade. Progress has been made in various areas relevant for NEM switches, encompassing characterization of single nanostructures and nanocontacts, as well as engineering of different device designs to increase their reliability and longevity.

The field of NEM switch research continues to develop in various directions, exploring new material combinations, testing and fabrication methods, and operating environments. This review considered both the advantages and drawbacks of current nanobeam-based electrostatically actuated NEM switch research and development. For NEM switches to become useful for practical applications, further work should address the remaining challenges, particularly, improvement of reliability and durability of a NEM switch through prevention of its failure during operation. The development of in situ microscopy based methods for real-time monitoring of processes during the device operation are extremely important for designing NEM switches with improved reliability.

Selecting application-specific materials may help to find the best NEM switch design solution. The general materials requirements include high mechanical stiffness (high Young's modulus), high hardness, low density, low adhesion, low mechanical dissipation, chemical inertness, good electrical and thermal conductivity.

When choosing materials for NEM contact switch application, one should take into account not only the expected operational parameters of the projected NEM contact switch, but also its fabrication approach. Despite the recent improvements in nanofabrication, achieving a high manufacturing yield remains a challenge especially for devices based on materials not suitable for top-down fabrication.

When fabricating the device, the environment in which the device will operate must be taken into account, as the environment may have not only a negative, but also a positive effect on the NEM switch operation. For example, the fabrication of a NEM switch in an oxygen-rich environment may result in the formation of either stable electrically conductive oxides covering the nanostructures, or insulating oxides preventing burn-off of the switching element.

Acknowledgments

This work was supported by the Latvian Council of Science (project No. 549/2012) and the University of Latvia project No. AAP2016/B043 and No. ZD2010/AZ19.

References

1. Yousif, M. Y. A.; Lundgren, P.; Ghavanini, F.; Enoksson, P.; Bengtsson, S. *Nanotechnology* **2008,** *19,* 285204. doi:10.1088/0957-4484/19/28/285204
2. Dadgour, H. F.; Banerjee, K. *IET Comput. Digital Tech.* **2009,** *3,* 593–608. doi:10.1049/iet-cdt.2008.0148
3. Ekinci, K. L. *Small* **2005,** *1,* 786–797. doi:10.1002/smll.200500077
4. Fechnt, H.-J.; Werner, M., Eds. *The nano-micro interface: bridging the micro and nano worlds;* Wiley-VCH: Weinheim, Germany, 2004. doi:10.1002/3527604111
5. Mayet, A. M.; Hussain, A. M.; Hussain, M. M. *Nanotechnology* **2016,** *27,* 035202. doi:10.1088/0957-4484/27/3/035202
6. Ramezani, M.; Severi, S.; Moussa, A.; Osman, H.; Tilmans, H. A. C.; De Meyer, K. Contact reliability improvement of a poly-SiGe based nano-relay with titanium nitride coating. In *2015 Transducers - 18th International Conference on Solid-State Sensors, Actuators and Microsystems (TRANSDUCERS),* Anchorage, AK, U.S.A., June 21–25, 2015; 2015; pp 576–579. doi:10.1109/TRANSDUCERS.2015.7180989
7. He, T.; Yang, R.; Ranganathan, V.; Rajgopal, S.; Tupta, M. A.; Bhunia, S.; Mehregany, M.; Feng, P. X.-L. Silicon carbide (SiC) nanoelectromechanical switches and logic gates with long cycles and robust performance in ambient air and at high temperature. In *2013 IEEE International Electron Devices Meeting,* Washington, DC, U.S.A., Dec 9–11, 2013; 2013; pp 4–6. doi:10.1109/IEDM.2013.6724562
8. Andzane, J.; Prikulis, J.; Dvorsek, D.; Mihailovic, D.; Erts, D. *Nanotechnology* **2010,** *21,* 125706. doi:10.1088/0957-4484/21/12/125706
9. Li, Q.; Koo, S.-M.; Edelstein, M. D.; Suehle, J. S.; Richter, C. A. *Nanotechnology* **2007,** *18,* 315202. doi:10.1088/0957-4484/18/31/315202
10. Andzane, J.; Petkov, N.; Livshits, A. I.; Boland, J. J.; Holmes, J. D.; Erts, D. *Nano Lett.* **2009,** *9,* 1824–1829. doi:10.1021/nl8037807
11. Andzane, J.; Meija, R.; Livshits, A. I.; Prikulis, J.; Biswas, S.; Holmes, J. D.; Erts, D. *J. Mater. Chem. C* **2013,** *1,* 7134. doi:10.1039/c3tc31240b
12. Loh, O.; Wei, X.; Sullivan, J.; Ocola, L. E.; Divan, R.; Espinosa, H. D. *Adv. Mater.* **2012,** *24,* 2463–2468. doi:10.1002/adma.201104889
13. Ziegler, K. J.; Lyons, D. M.; Holmes, J. D.; Erts, D.; Polyakov, B.; Olin, H.; Svensson, K.; Olsson, E. *Appl. Phys. Lett.* **2004,** *84,* 4074–4076. doi:10.1063/1.1751622
14. Andzane, J.; Prikulis, J.; Meija, R.; Kosmaca, J.; Biswas, S.; Holmes, J. D.; Erts, D. *Mater. Sci. (MEDŽIAGOTYRA)* **2013,** *19,* 254–257. doi:10.5755/j01.ms.19.3.3086
15. Ke, C.; Espinosa, H. D. *Small* **2006,** *2,* 1484–1489. doi:10.1002/smll.200600271
16. Loh, O.; Wei, X.; Ke, C.; Sullivan, J.; Espinosa, H. D. *Small* **2011,** *7,* 79–86. doi:10.1002/smll.201001166
17. Muñoz-Gamarra, J. L.; Uranga, A.; Barniol, N. *Micromachines* **2016,** *7,* 30. doi:10.3390/mi7020030
18. Czaplewski, D. A.; Patrizi, G. A.; Kraus, G. M.; Wendt, J. R.; Nordquist, C. D.; Wolfley, S. L.; Baker, M. S.; de Boer, M. P. *J. Micromech. Microeng.* **2009,** *19,* 085003. doi:10.1088/0960-1317/19/8/085003
19. Qian, Y.; Soon, B. W.; Singh, P.; Campanella, H.; Lee, C. *Nanoscale* **2014,** *6,* 5606–5611. doi:10.1039/c3nr05255a
20. Qian, Y.; Lou, L.; Tsai, M. J.; Lee, C. *Appl. Phys. Lett.* **2012,** *100,* 113102. doi:10.1063/1.3693382

21. Soon, B. W.; Ng, E. J.; Qian, Y.; Singh, N.; Tsai, M. J.; Lee, C. *Appl. Phys. Lett.* **2013,** *103,* 53122. doi:10.1063/1.4817796
22. Yang, R.; He, T.; Tupta, M. A.; Marcoux, C.; Andreucci, P.; Duraffourg, L.; Feng, P. X.-L. *J. Micromech. Microeng.* **2015,** *25,* 95014. doi:10.1088/0960-1317/25/9/095014
23. Feng, X. L.; Matheny, M. H.; Zorman, C. A.; Mehregany, M.; Roukes, M. L. *Nano Lett.* **2010,** *10,* 2891–2896. doi:10.1021/nl1009734
24. Milaninia, K. M.; Baldo, M. A.; Reina, A.; Kong, J. *Appl. Phys. Lett.* **2009,** *95,* 183105. doi:10.1063/1.3259415
25. Liu, X.; Suk, J. W.; Boddeti, N. G.; Cantley, L.; Wang, L.; Gray, J. M.; Hall, H. J.; Bright, V. M.; Rogers, C. T.; Dunn, M. L.; Ruoff, R. S.; Bunch, J. S. *Adv. Mater.* **2014,** *26,* 1571–1576. doi:10.1002/adma.201304949
26. Li, P.; Jing, G.; Zhang, B.; Sando, S.; Cui, T. *Appl. Phys. Lett.* **2014,** *104,* 113110. doi:10.1063/1.4868869
27. Sun, J.; Schmidt, M. E.; Muruganathan, M.; Chong, H. M. H.; Mizuta, H. *Nanoscale* **2016,** *8,* 6659–6665. doi:10.1039/C6NR00253F
28. Wei, D.; Liu, Y.; Zhang, H.; Huang, L.; Wu, B.; Chen, J.; Yu, G. *J. Am. Chem. Soc.* **2009,** *131,* 11147–11154. doi:10.1021/ja903092k
29. Shi, Z.; Lu, H.; Zhang, L.; Yang, R.; Wang, Y.; Liu, D.; Guo, H.; Shi, D.; Gao, H.; Wang, E.; Zhang, G. *Nano Res.* **2012,** *5,* 82–87. doi:10.1007/s12274-011-0187-9
30. Kim, S. M.; Song, E. B.; Lee, S.; Seo, S.; Seo, D. H.; Hwang, Y.; Candler, R.; Wang, K. L. *Appl. Phys. Lett.* **2011,** *99,* 23103. doi:10.1063/1.3610571
31. Li, P.; You, Z.; Cui, T. *Appl. Phys. Lett.* **2012,** *101,* 93111. doi:10.1063/1.4738891
32. Rueckes, T.; Kim, K.; Joselevich, E.; Tseng, G. Y.; Cheung, C.-L.; Lieber, C. M. *Science* **2000,** *289,* 94–97. doi:10.1126/science.289.5476.94
33. Lee, S. W.; Lee, D. S.; Morjan, R. E.; Jhang, S. H.; Sveningsson, M.; Nerushev, O. A.; Park, Y. W.; Campbell, E. E. B. *Nano Lett.* **2004,** *4,* 2027–2030. doi:10.1021/nl049053v
34. Jang, J. E.; Cha, S. N.; Choi, Y.; Amaratunga, G. A. J.; Kang, D. J.; Hasko, D. G.; Jung, J. E.; Kim, J. M. *Appl. Phys. Lett.* **2005,** *87,* 163114. doi:10.1063/1.2077858
35. Cha, S. N.; Jang, J. E.; Choi, Y.; Amaratunga, G. A. J.; Kang, D.-J.; Hasko, D. G.; Jung, J. E.; Kim, J. M. *Appl. Phys. Lett.* **2005,** *86,* 83105. doi:10.1063/1.1868064
36. Deshpande, V. V.; Chiu, H.-Y.; Postma, H. W. C.; Miko, C.; Forro, L.; Bockrath, M. *Nano Lett.* **2006,** *6,* 1092–1095. doi:10.1021/nl052513f
37. Kaul, A. B.; Wong, E. W.; Epp, L.; Hunt, B. D. *Nano Lett.* **2006,** *6,* 942–947. doi:10.1021/nl052552r
38. Lee, T.-H.; Bhunia, S.; Mehregany, M. *Science* **2010,** *329,* 1316–1318. doi:10.1126/science.1192511
39. He, T.; Ranganathan, V.; Yang, R.; Rajgopal, S.; Bhunia, S.; Mehregany, M.; Feng, P. X.-L. Time-domain AC characterization of silicon carbide (SiC) nanoelectromechanical switches toward high-speed operations. In *2013 Transducers & Eurosensors XXVII: The 17th International Conference on Solid-State Sensors, Actuators and Microsystems (TRANSDUCERS & EUROSENSORS XXVII),* Barcelona, Spain, June 16–20, 2013; 2013; pp 669–672. doi:10.1109/transducers.2013.6626855
40. Dequesnes, M.; Rotkin, S. V.; Aluru, N. R. *Nanotechnology* **2002,** *13,* 120–131. doi:10.1088/0957-4484/13/1/325
41. Ke, C.; Espinosa, H. D. *J. Appl. Mech.* **2005,** *72,* 721–725. doi:10.1115/1.1985434
42. Ke, C.; Espinosa, H. D.; Pugno, N. *J. Appl. Mech.* **2005,** *72,* 726–731. doi:10.1115/1.1985435
43. Kinaret, J. M.; Nord, T.; Viefers, S. *Appl. Phys. Lett.* **2003,** *82,* 1287–1289. doi:10.1063/1.1557324
44. Dequesnes, M.; Tang, Z.; Aluru, N. R. *J. Eng. Mater. Technol.* **2004,** *126,* 230–237. doi:10.1115/1.1751180
45. Wagner, T. J. W.; Vella, D. *Nanotechnology* **2013,** *24,* 275501. doi:10.1088/0957-4484/24/27/275501
46. Niroui, F.; Wang, A. I.; Sletten, E. M.; Song, Y.; Kong, J.; Yablonovitch, E.; Swager, T. M.; Lang, J. H.; Bulović, V. *ACS Nano* **2015,** *9,* 7886–7894. doi:10.1021/acsnano.5b02476
47. Jang, W. W.; Lee, J. O.; Yoon, J.-B.; Kim, M.-S.; Lee, J.-M.; Kim, S.-M.; Cho, K.-H.; Kim, D.-W.; Park, D.; Lee, W.-S. *Appl. Phys. Lett.* **2008,** *92,* 103110. doi:10.1063/1.2892659
48. Muñoz-Gamarra, J. L.; Uranga, A.; Barniol, N. *Appl. Phys. Lett.* **2014,** *104,* 243105. doi:10.1063/1.4882918
49. Lee, J. O.; Song, Y.-H.; Kim, M.-W.; Kang, M.-H.; Oh, J.-S.; Yang, H.-H.; Yoon, J.-B. *Nat. Nanotechnol.* **2013,** *8,* 36–40. doi:10.1038/nnano.2012.208
50. Arkan, E. F.; Sacchetto, D.; Yildiz, I.; Leblebici, Y.; Alaca, B. E. *J. Micromech. Microeng.* **2011,** *21,* 125018. doi:10.1088/0960-1317/21/12/125018
51. Ohnishi, H.; Kondo, Y.; Takayanagi, K. *Nature* **1998,** *395,* 780–783. doi:10.1038/27399
52. Kizuka, T.; Ohmi, H.; Sumi, T.; Kumazawa, K.; Deguchi, S.; Naruse, M.; Fujisawa, S.; Sasaki, S.; Yabe, A.; Enomoto, Y. *Jpn. J. Appl. Phys.* **2001,** *40,* L170. doi:10.1143/JJAP.40.L170
53. Erts, D.; Lõhmus, A.; Lõhmus, R.; Olin, H.; Pokropivny, A. V.; Ryen, L.; Svensson, K. *Appl. Surf. Sci.* **2002,** *188,* 460–466. doi:10.1016/S0169-4332(01)00933-3
54. Meija, R.; Kosmaca, J.; Jasulaneca, L.; Petersons, K.; Biswas, S.; Holmes, J. D.; Erts, D. *Nanotechnology* **2015,** *26,* 195503. doi:10.1088/0957-4484/26/19/195503
55. Kosmaca, J.; Andzane, J.; Baitimirova, M.; Lombardi, F.; Erts, D. *ACS Appl. Mater. Interfaces* **2016,** *8,* 12257–12262. doi:10.1021/acsami.6b00406
56. Liu, X.; Zhu, J.; Jin, C.; Peng, L.-M.; Tang, D.; Cheng, H. *Nanotechnology* **2008,** *19,* 085711. doi:10.1088/0957-4484/19/8/085711
57. Huang, Y.-T.; Huang, C.-W.; Chen, J.-Y.; Ting, Y.-H.; Cheng, S.-L.; Liao, C.-N.; Wu, W.-W. *Nano Res.* **2016,** *9,* 1071–1078. doi:10.1007/s12274-016-0998-9
58. Peng, Y.; Cullis, T.; Inkson, B. *Appl. Phys. Lett.* **2008,** *93,* 183112. doi:10.1063/1.3005423
59. Loh, O. Y.; Espinosa, H. D. *Nat. Nanotechnol.* **2012,** *7,* 283–295. doi:10.1038/nnano.2012.40
60. Li, P.; Cui, T. *J. Micromech. Microeng.* **2015,** *25,* 075022. doi:10.1088/0960-1317/25/7/075022
61. Grogg, D.; Ayala, C. L.; Drechsler, U.; Sebastian, A.; Koelmans, W. W.; Bleiker, S. J.; Fernandez-Bolanos, M.; Hagleitner, C.; Despont, M.; Duerig, U. T. Amorphous carbon active contact layer for reliable nanoelectromechanical switches. In *2014 IEEE 27th International Conference on Micro Electro Mechanical Systems (MEMS),* San Francisco, CA, U.S.A., Jan 26–30, 2014; 2014; pp 143–146. doi:10.1109/memsys.2014.6765594
62. Peschot, A.; Qian, C.; Liu, T.-J. K. *Micromachines* **2015,** *6,* 1046–1065. doi:10.3390/mi6081046

63. Streller, F.; Wabiszewski, G. E.; Durham, D. B.; Yang, F.; Yang, J.; Qi, Y.; Srolovitz, D. J.; Rappe, A. M.; Carpick, R. W. Novel materials solutions and simulations for nanoelectromechanical switches. In *2015 IEEE 61st Holm Conference on Electrical Contacts (Holm),* San Diego, CA, U.S.A., Oct 11–14, 2015; 2015; pp 363–369. doi:10.1109/HOLM.2015.7355122
64. Maghsoudi, E.; Martin, M. J. Simulation of thermally actuated nano-electro-mechanical memory. In *2012 13th IEEE Intersociety Conference on Thermal and Thermomechanical Phenomena in Electronic Systems (ITherm),* San Diego, CA, U.S.A., May 30–June 1, 2012; 2012; pp 938–943. doi:10.1109/ITHERM.2012.6231526
65. Zaghloul, U.; Piazza, G. *IEEE Electron Device Lett.* **2014,** *35,* 669–671. doi:10.1109/LED.2014.2318049
66. Waggoner, P. S.; Craighead, H. G. *Lab Chip* **2007,** *7,* 1238–1255. doi:10.1039/b707401h
67. Fork, D. K.; Hantschel, T.; Van Schuylenbergh, K. F.; Lu, J. P. Electromechanical Switch. U.S. Patent 7453339, Nov 18, 2008.
68. Bulashevich, K. A.; Rotkin, S. V. *JETP Lett.* **2002,** *75,* 205–209. doi:10.1134/1.1475724
69. Mittal, K. L. *Contact angle, wettability and adhesion;* CRC Press, Inc.: Boca Raton, FL, U.S.A., 2008; Vol. 5.
70. Livshits, A. I.; Jasulaneca, L.; Kosmaca, J.; Meija, R.; Holmes, J. D.; Erts, D. *Eur. J. Mech. A* **2017,** *66,* 412–422. doi:10.1016/j.euromechsol.2017.08.009
71. Kagota, T.; Nagataki, A.; Takei, K.; Arie, T.; Akita, S. *Appl. Phys. Lett.* **2013,** *103,* 203504. doi:10.1063/1.4832059
72. Szlufarska, I.; Chandross, M.; Carpick, R. W. *J. Phys. D: Appl. Phys.* **2008,** *41,* 123001. doi:10.1088/0022-3727/41/12/123001
73. Carpick, R. W.; Ogletree, D. F.; Salmeron, M. *J. Colloid Interface Sci.* **1999,** *211,* 395–400. doi:10.1006/jcis.1998.6027
74. Maugis, D. *Contact, adhesion and rupture of elastic solids;* Springer Science & Business Media: New York, NY, U.S.A., 2013; Vol. 130.
75. Israelachvili, J. N. *Intermolecular and Surface Forces: With Applications to Colloidal and Biological Systems (Colloid Science);* Academic Press: Cambridge, MA, U.S.A., 1992.
76. Kim, S. H.; Dugger, M. T.; Mittal, K. L. *Adhesion aspects in MEMS/NEMS;* CRC Press: Boca Raton, FL, U.S.A., 2011.
77. Mo, Y.; Turner, K. T.; Szlufarska, I. *Nature* **2009,** *457,* 1116–1119. doi:10.1038/nature07748
78. Maugis, D. *J. Colloid Interface Sci.* **1992,** *150,* 243–269. doi:10.1016/0021-9797(92)90285-T
79. Vahdat, V.; Ryan, K. E.; Keating, P. L.; Jiang, Y.; Adiga, S. P.; Schall, J. D.; Turner, K. T.; Harrison, J. A.; Carpick, R. W. *ACS Nano* **2014,** *8,* 7027–7040. doi:10.1021/nn501896e
80. Sun, J.; Wang, W.; Muruganathan, M.; Mizuta, H. *Appl. Phys. Lett.* **2014,** *105,* 33103. doi:10.1063/1.4891055
81. Ploscaru, M. I.; Kokalj, S. J.; Uplaznik, M.; Vengust, D.; Turk, D.; Mrzel, A.; Mihailovic, D. *Nano Lett.* **2007,** *7,* 1445–1448. doi:10.1021/nl070051v
82. Erts, D.; Olin, H.; Ryen, L.; Olsson, E.; Thölén, A. *Phys. Rev. B* **2000,** *61,* 12725–12727. doi:10.1103/PhysRevB.61.12725
83. Sharvin, Y. V. *Sov. Phys. JETP* **1965,** *21,* 655.
84. Zhang, Z.; Yao, K.; Liu, Y.; Jin, C.; Liang, X.; Chen, Q.; Peng, L.-M. *Adv. Funct. Mater.* **2007,** *17,* 2478–2489. doi:10.1002/adfm.200600475
85. Ahmed, F.; Choi, M. S.; Liu, X.; Yoo, W. J. *Nanoscale* **2015,** *7,* 9222–9228. doi:10.1039/C5NR01044F
86. Léonard, F.; Talin, A. A. *Nat. Nanotechnol.* **2011,** *6,* 773–783. doi:10.1038/nnano.2011.196
87. Sasada, T.; Nakakita, Y.; Takenaka, M.; Takagi, S. *J. Appl. Phys.* **2009,** *106,* 073716. doi:10.1063/1.3234395
88. Ravindra, N. M.; Zhao, J. *Smart Mater. Struct.* **1992,** *1,* 197. doi:10.1088/0964-1726/1/3/002
89. Beebe, J. M.; Kim, B.; Gadzuk, J. W.; Frisbie, C. D.; Kushmerick, J. G. *Phys. Rev. Lett.* **2006,** *97,* 026801. doi:10.1103/PhysRevLett.97.026801
90. Sarker, B. K.; Khondaker, S. I. *ACS Nano* **2012,** *6,* 4993–4999. doi:10.1021/nn300544v
91. Lord, A. M.; Maffeis, T. G.; Kryvchenkova, O.; Cobley, R. J.; Kalna, K.; Kepaptsoglou, D. M.; Ramasse, Q. M.; Walton, A. S.; Ward, M. B.; Köble, J.; Wilks, S. P. *Nano Lett.* **2015,** *15,* 4248–4254. doi:10.1021/nl503743t
92. Menges, F.; Riel, H.; Stemmer, A.; Gotsmann, B. *Nano Lett.* **2012,** *12,* 596–601. doi:10.1021/nl203169t
93. Tsai, C.-L.; Liao, A.; Pop, E.; Shim, M. *Appl. Phys. Lett.* **2011,** *99,* 53120. doi:10.1063/1.3622769
94. Deshpande, V. V.; Hsieh, S.; Bushmaker, A. W.; Bockrath, M.; Cronin, S. B. *Phys. Rev. Lett.* **2009,** *102,* 105501. doi:10.1103/PhysRevLett.102.105501
95. Shi, L.; Zhou, J.; Kim, P.; Bachtold, A.; Majumdar, A.; McEuen, P. L. *J. Appl. Phys.* **2009,** *105,* 104306. doi:10.1063/1.3126708
96. Zhao, J.; Sun, H.; Dai, S.; Wang, Y.; Zhu, J. *Nano Lett.* **2011,** *11,* 4647–4651. doi:10.1021/nl202160c
97. Westover, T.; Jones, R.; Huang, J. Y.; Wang, G.; Lai, E.; Talin, A. A. *Nano Lett.* **2009,** *9,* 257–263. doi:10.1021/nl802840w
98. Davami, K.; Ghassemi, H. M.; Yassar, R. S.; Lee, J.-S.; Meyyappan, M. *ChemPhysChem* **2012,** *13,* 347–352. doi:10.1002/cphc.201100486
99. Yu, T.; Yan-Guo, W. *Chin. Phys. Lett.* **2013,** *30,* 17901. doi:10.1088/0256-307X/30/1/017901
100. Hummelgård, M.; Zhang, R.; Carlberg, T.; Vengust, D.; Dvorsek, D.; Mihailovic, D.; Olin, H. *Nanotechnology* **2010,** *21,* 165704. doi:10.1088/0957-4484/21/16/165704
101. Tohmyoh, H.; Fukui, S. *J. Nanopart. Res.* **2012,** *14,* 1116. doi:10.1007/s11051-012-1116-x
102. Tohmyoh, H.; Imaizumi, T.; Hayashi, H.; Saka, M. *Scr. Mater.* **2007,** *57,* 953–956. doi:10.1016/j.scriptamat.2007.07.018
103. Tohmyoh, H.; Fukui, S. *Phys. Rev. B* **2009,** *80,* 155403. doi:10.1103/PhysRevB.80.155403
104. Doelling, C. M.; Vanderlick, T. K.; Song, J.; Srolovitz, D. *J. Appl. Phys.* **2007,** *101,* 124303. doi:10.1063/1.2747229
105. Vincent, M.; Rowe, S. W.; Poulain, C.; Mariolle, D.; Chiesi, L.; Houzé, F.; Delamare, J. *Appl. Phys. Lett.* **2011,** *97,* 263503. doi:10.1063/1.3529474
106. Poulain, C.; Peschot, A.; Vincent, M.; Bonifaci, N. A Nano-Scale Investigation of Material Transfer Phenomena at Make in a MEMS Switch. In *2011 IEEE 57th Holm Conference on Electrical Contacts (Holm),* Minneapolis, MN, U.S.A., Sept 11–14, 2011; 2011; pp 1–7. doi:10.1109/HOLM.2011.6034801
107. Cuenot, S.; Frétigny, C.; Demoustier-Champagne, S.; Nysten, B. *Phys. Rev. B* **2004,** *69,* 165410. doi:10.1103/PhysRevB.69.165410
108. Wang, G.; Li, X. *J. Appl. Phys.* **2008,** *104,* 113517. doi:10.1063/1.3033634
109. Jing, G. Y.; Duan, H.; Sun, X. M.; Zhang, Z. S.; Xu, J.; Li, Y. D.; Wang, J. X.; Yu, D. P. *Phys. Rev. B* **2006,** *73,* 235409. doi:10.1103/PhysRevB.73.235409
110. Nilsson, S. G.; Borrise, X.; Montelius, L. *Appl. Phys. Lett.* **2004,** *85,* 3555. doi:10.1063/1.1807945

111. Wu, B.; Heidelberg, A.; Boland, J. J. *Nat. Mater.* **2005,** *4,* 525–529. doi:10.1038/nmat1403
112. Villain, P.; Beauchamp, P.; Badawi, K. F.; Goudeau, P.; Renault, P.-O. *Scr. Mater.* **2004,** *50,* 1247–1251. doi:10.1016/j.scriptamat.2004.01.033
113. Ao, Z. M.; Li, S.; Jiang, Q. *Appl. Phys. Lett.* **2008,** *93,* 081905. doi:10.1063/1.2976134
114. Chong, S.; Lee, B.; Parizi, K. B.; Provine, J.; Mitra, S.; Howe, R. T.; Wong, H.-S. P. Integration of nanoelectromechanical (NEM) relays with silicon CMOS with functional CMOS-NEM circuit. In *Electron Devices Meeting (IEDM), 2011 IEEE International,* Washington, DC, U.S.A., Dec 5–7, 2001; 2001; pp 30–35. doi:10.1109/IEDM.2011.6131645
115. Qian, Y.; Soon, B. W.; Lee, C. *J. Microelectromech. Syst.* **2015,** *24,* 1878–1886. doi:10.1109/JMEMS.2015.2449863
116. Haynes, W. M. *CRC handbook of chemistry and physics;* CRC Press, Inc.: Boca Raton, FL, U.S.A., 2014.
117. Dickinson, J. M.; Armstrong, P. E. *J. Appl. Phys.* **1967,** *38,* 602–606. doi:10.1063/1.1709381
118. Wang, X.; Li, Q.; Xie, J.; Jin, Z.; Wang, J.; Li, Y.; Jiang, K.; Fan, S. *Nano Lett.* **2009,** *9,* 3137–3141. doi:10.1021/nl901260b
119. Yu, M.-F.; Files, B. S.; Arepalli, S.; Ruoff, R. S. *Phys. Rev. Lett.* **2000,** *84,* 5552. doi:10.1103/PhysRevLett.84.5552
120. Yu, M.-F.; Lourie, O.; Dyer, M. J.; Moloni, K.; Kelly, T. F.; Ruoff, R. S. *Science* **2000,** *287,* 637–640. doi:10.1126/science.287.5453.637
121. Han, Z.; Fina, A. *Prog. Polym. Sci.* **2011,** *36,* 914–944. doi:10.1016/j.progpolymsci.2010.11.004
122. Selection of Application Specific Single and Multi Walled Carbon Nanotubes by In Situ Characterization of Conductive and Field Emission Properties. https://www.azonano.com/article.aspx?ArticleID=2038 (accessed Dec 19, 2017).
123. Ning, S.; Iwasaki, T. O.; Shimomura, K.; Johguchi, K.; Yanagizawa, E.; Rosendale, G.; Manning, M.; Viviani, D.; Rueckes, T.; Takeuchi, K. *IEEE Trans. Electron Devices* **2015,** *62,* 2837–2844. doi:10.1109/TED.2015.2450219
124. Tombler, T. W.; Zhou, C.; Alexseyev, L.; Kong, J.; Dai, H.; Liu, L.; Jayanthi, C. S.; Tang, M.; Wu, S.-Y. *Nature* **2000,** *405,* 769–772. doi:10.1038/35015519
125. Minot, E. D.; Yaish, Y.; Sazonova, V.; Park, J.-Y.; Brink, M.; McEuen, P. L. *Phys. Rev. Lett.* **2003,** *90,* 156401. doi:10.1103/PhysRevLett.90.156401
126. Umnov, A. G.; Mordkovich, V. Z. *Appl. Phys. A: Mater. Sci. Process.* **2001,** *73,* 301–304. doi:10.1007/s003390100906
127. Kaldor, S. K.; Noyan, I. C. *Appl. Phys. Lett.* **2002,** *80,* 2284–2286. doi:10.1063/1.1459762
128. Ruiz-Vargas, C. S.; Zhuang, H. L.; Huang, P. Y.; van der Zande, A. M.; Garg, S.; McEuen, P. L.; Muller, D. A.; Hennig, R. G.; Park, J. *Nano Lett.* **2011,** *11,* 2259–2263. doi:10.1021/nl200429f
129. Hopcroft, M. A.; Nix, W. D.; Kenny, T. W. *J. Microelectromech. Syst.* **2010,** *19,* 229–238. doi:10.1109/JMEMS.2009.2039697
130. Ngo, L. T.; Almécija, D.; Sader, J. E.; Daly, B.; Petkov, N.; Holmes, J. D.; Erts, D.; Boland, J. J. *Nano Lett.* **2006,** *6,* 2964–2968. doi:10.1021/nl0619397
131. Swarnakar, A. K.; van der Biest, O.; Vanhellemont, J. *Phys. Status Solidi* **2014,** *11,* 150–155. doi:10.1002/pssc.201300101
132. Han, J.-W.; Ahn, J.-H.; Kim, M.-W.; Lee, J. O.; Yoon, J.-B.; Choi, Y.-K. *Small* **2010,** *6,* 1197–1200. doi:10.1002/smll.201000170
133. Xiang, W.; Lee, C. *Appl. Phys. Lett.* **2010,** *96,* 193113. doi:10.1063/1.3428781
134. Kis, A.; Csanyi, G.; Vrbanic, D.; Mrzel, A.; Mihailovic, D.; Kulik, A.; Forró, L. *Small* **2007,** *3,* 1544–1548. doi:10.1002/smll.200700164
135. Vrbanić, D.; Remškar, M.; Jesih, A.; Mrzel, A.; Umek, P.; Ponikvar, M.; Jančar, B.; Meden, A.; Novosel, B.; Pejovnik, S.; Venturini, P.; Coleman, J. C.; Mihailović, D. *Nanotechnology* **2004,** *15,* 635. doi:10.1088/0957-4484/15/5/039
136. Maboudian, R.; Carraro, C.; Senesky, D. G.; Roper, C. S. *J. Vac. Sci. Technol., A* **2013,** *31,* 050805. doi:10.1116/1.4807902
137. Zekentes, K.; Rogdakis, K. *J. Phys. D: Appl. Phys.* **2011,** *44,* 133001. doi:10.1088/0022-3727/44/13/133001
138. Perisanu, S.; Gouttenoire, V.; Vincent, P.; Ayari, A.; Choueib, M.; Bechelany, M.; Cornu, D.; Purcell, S. T. *Phys. Rev. B* **2008,** *77,* 165434. doi:10.1103/PhysRevB.77.165434
139. Wong, E. W.; Sheehan, P. E.; Lieber, C. M. *Science* **1997,** *277,* 1971–1975. doi:10.1126/science.277.5334.1971
140. Birkholz, M.; Ehwald, K.-E.; Kulse, P.; Drews, J.; Fröhlich, M.; Haak, U.; Kaynak, M.; Matthus, E.; Schulz, K.; Wolansky, D. *Adv. Funct. Mater.* **2011,** *21,* 1652–1656. doi:10.1002/adfm.201002062
141. Pang, X.; Zhang, L.; Yang, H.; Gao, K.; Volinsky, A. A. *J. Mater. Eng. Perform.* **2015,** *24,* 1185–1191. doi:10.1007/s11665-015-1393-5
142. Seneviratne, D.; Nielson, G. N.; Takahashi, S.; Barbastathis, G.; Tuller, H. L. On the use of titanium nitride as structural material for nano-electro-mechanical systems (NEMS). In *5th IEEE Conference on Nanotechnology,* Nagoya, Japan, July 15, 2005; 2005; pp 138–141. doi:10.1109/NANO.2005.1500712
143. Polcar, T.; Parreira, N. M. G.; Cavaleiro, A. *Wear* **2007,** *262,* 655–665. doi:10.1016/j.wear.2006.07.010
144. Dadgour, H. F.; Hussain, M. M.; Cassell, A.; Singh, N.; Banerjee, K. Impact of scaling on the performance and reliability degradation of metal-contacts in NEMS devices. In *Reliability Physics Symposium (IRPS), 2011 IEEE International,* Monterey, CA, U.S.A., April 10–14, 2011; 2011; 3D.3.1–3D.3.10. doi:10.1109/IRPS.2011.5784489
145. Chowdhury, F. K.; Pourzand, H.; Tabib-Azar, M. Investigation of contact resistance evolution of Ir, Pt, W, Ni, Cr, Ti, Cu and Al over repeated hot-contact switching for NEMS switches. In *2013 IEEE 26th International Conference on Micro Electro Mechanical Systems (MEMS),* Taipei, Taiwan, Jan 20–24, 2013; 2013; pp 445–448. doi:10.1109/MEMSYS.2013.6474274
146. Tabib-Azar, M.; Hassan, N.; Pourzand, H.; Pai, P. Contact resistance, stiction force, and field-assisted growth and migration in MEMS and NEMS metals. In *IEEE. Sensors,* Valencia, Spain, Nov 2–5, 2014; 2014; pp 974–977. doi:10.1109/ICSENS.2014.6985165
147. Chen, L.; Lee, H.; Guo, Z. J.; McGruer, N. E.; Gilbert, K. W.; Mall, S.; Leedy, K. D.; Adams, G. G. *J. Appl. Phys.* **2007,** *102,* 74910. doi:10.1063/1.2785951
148. Yang, Z.; Lichtenwalner, D.; Morris, A.; Krim, J.; Kingon, A. I. *J. Micromech. Microeng.* **2010,** *20,* 105028. doi:10.1088/0960-1317/20/10/105028
149. Czaplewski, D. A.; Nordquist, C. D.; Patrizi, G. A.; Kraus, G. M.; Cowan, W. D. *J. Microelectromech. Syst.* **2013,** *22,* 655–661. doi:10.1109/JMEMS.2013.2239256
150. Yang, Z.; Lichtenwalner, D. J.; Morris, A. S.; Krim, J.; Kingon, A. I. *J. Microelectromech. Syst.* **2009,** *18,* 287–295. doi:10.1109/JMEMS.2008.2010850
151. Walker, M. J.; Berman, D.; Nordquist, C.; Krim, J. *Tribol. Lett.* **2011,** *44,* 305–314. doi:10.1007/s11249-011-9849-8

152. Walker, M.; Nordquist, C.; Czaplewski, D.; Patrizi, G.; McGruer, N.; Krim, J. *J. Appl. Phys.* **2010,** *107,* 84509. doi:10.1063/1.3353991
153. Patton, S. T.; Zabinski, J. S. *Tribol. Lett.* **2005,** *18,* 215–230. doi:10.1007/s11249-004-1778-3
154. Streller, F.; Wabiszewski, G. E.; Mangolini, F.; Feng, G.; Carpick, R. W. *Adv. Mater. Interfaces* **2014,** *1,* 1300120. doi:10.1002/admi.201300120
155. Bhaskaran, H.; Sebastian, A.; Despont, M. *IEEE Trans. Nanotechnol.* **2009,** *8,* 128–131. doi:10.1109/TNANO.2008.2005199
156. Brand, V.; Baker, M. S.; de Boer, M. P. *Tribol. Lett.* **2013,** *51,* 341–356. doi:10.1007/s11249-013-0166-2
157. Hermance, H. W.; Egan, T. F. *Bell Syst. Tech. J.* **1958,** *37,* 739–776. doi:10.1002/j.1538-7305.1958.tb03885.x
158. Brand, V.; Saleh, M. E.; de Boer, M. P. *Tribol. Int.* **2015,** *85,* 48–55. doi:10.1016/j.triboint.2015.01.001
159. Li, M.; Tang, H. X.; Roukes, M. L. *Nat. Nanotechnol.* **2007,** *2,* 114–120. doi:10.1038/nnano.2006.208
160. Lee, J.-O.; Kim, M.-W.; Ko, S.-D.; Kang, H.-O.; Bae, W.-H.; Kang, M.-H.; Kim, K.-N.; Yoo, D.-E.; Yoon, J.-B. 3-terminal nanoelectromechanical switching device in insulating liquid media for low voltage operation and reliability improvement. In *2009 IEEE International Electron Devices Meeting (IEDM),* Baltimore, MD, U.S.A., Dec 7–9, 2009; IEEE Publishing: Piscataway, NJ, U.S.A., 2009; pp 1–4. doi:10.1109/iedm.2009.5424380
161. Ko, S.-D.; Lee, J. O.; Yang, H.-H.; Kim, M.-W.; Song, Y.-H.; Yoon, J.-B. *Appl. Phys. Lett.* **2011,** *99,* 113516. doi:10.1063/1.3640228
162. Russick, E. M.; Adkins, C. L. J.; Dyck, C. W. Supercritical Carbon Dioxide Extraction of Solvent from Micromachined Structures. In *Supercritical Fluids;* Abraham, M. A.; Sunol, A. A., Eds.; American Chemical Society: Washington, DC, U.S.A., 1997; pp 255–269. doi:10.1021/bk-1997-0670.ch018
163. Jafri, I. H.; Busta, H.; Walsh, S. T. Critical point drying and cleaning for MEMS technology. In *Proceedings Volume 3880, MEMS Reliability for Critical and Space Applications,* Santa Clara, CA, U.S.A., Aug 18, 1999; 1999; pp 51–58. doi:10.1117/12.359371
164. Bhushan, B. *J. Vac. Sci. Technol., B: Nanotechnol. Microelectron.: Mater., Process ., Meas., Phenom.* **2003,** *21,* 2262. doi:10.1116/1.1627336
165. Luo, H.; Park, S.; Chan, H. Y. H.; Weaver, M. J. *J. Phys. Chem. B* **2000,** *104,* 8250–8258. doi:10.1021/jp001289+
166. Suzuki, K.; Tedrow, P. M. *Phys. Rev. B* **1998,** *58,* 11597–11602. doi:10.1103/PhysRevB.58.11597
167. Anderson, J. S.; Greenwood, N. N. *Proc. R. Soc. London, Ser. A* **1952,** *215,* 353–370. doi:10.1098/rspa.1952.0216
168. Slade, P. G. *Electrical contacts: principles and applications;* CRC Press, Inc.: Boca Raton, FL, U.S.A., 2013.
169. Breckenridge, R. G.; Hosler, W. R. *Phys. Rev.* **1953,** *91,* 793–802. doi:10.1103/PhysRev.91.793
170. Yildiz, A.; Lisesivdin, S. B.; Kasap, M.; Mardare, D. *J. Non-Cryst. Solids* **2008,** *354,* 4944–4947. doi:10.1016/j.jnoncrysol.2008.07.009
171. Boxley, C. J.; White, H. S.; Gardner, C. E.; Macpherson, J. V. *J. Phys. Chem. B* **2003,** *107,* 9677–9680. doi:10.1021/jp034874u
172. Sullivan, J. P.; Barbour, J. C.; Dunn, R. G.; Son, K. A.; Montes, L. P.; Missert, N.; Copeland, R. G. The Electrical Properties of Native and Deposited Thin Aluminum Oxide Layers on Aluminum: Hydration Effects. In *Proc. of the The Electrochemical Society Meeting,* Boston, MA, U.S.A., Nov 1–6, 1998; 1998; pp 111–117.
173. Ramana, C. V.; Troitskaia, I. B.; Gromilov, S. A.; Atuchin, V. V. *Ceram. Int.* **2012,** *38,* 5251–5255. doi:10.1016/j.ceramint.2012.03.035
174. Ma, J.; Liu, Y.; Hao, P.; Wang, J.; Zhang, Y. *Sci. Rep.* **2016,** *6,* 18994. doi:10.1038/srep18994
175. Ding, W.; Calabri, L.; Chen, X.; Kohlhaas, K. M.; Ruoff, R. S. *Compos. Sci. Technol.* **2006,** *66,* 1112–1124. doi:10.1016/j.compscitech.2005.11.030
176. Somorjai, G. A.; Li, Y. *Introduction to surface chemistry and catalysis;* John Wiley & Sons: New York, NY, U.S.A., 2010.
177. Zebda, A.; Sabbah, H.; Ababou-Girard, S.; Solal, F.; Godet, C. *Appl. Surf. Sci.* **2008,** *254,* 4980–4991. doi:10.1016/j.apsusc.2008.01.147
178. Vanhellemont, J.; Swarnakar, A. K.; van der Biest, O. *ECS Trans.* **2014,** *64,* 283–292. doi:10.1149/06411.0283ecst
179. Wolpert, D.; Ampadu, P. Temperature Effects in Semiconductors. *Managing temperature effects in nanoscale adaptive systems;* Springer: Berlin, Germany, 2012; pp 13–33. doi:10.1007/978-1-4614-0748-5_2
180. Desai, P. D.; Chu, T. K.; James, H. M.; Ho, C. Y. *J. Phys. Chem. Ref. Data* **1984,** *13,* 1069–1096. doi:10.1063/1.555723
181. Oh, C.; Streller, F.; Ashurst, W. R.; Carpick, R. W.; de Boer, M. P. *J. Micromech. Microeng.* **2016,** *26,* 115020. doi:10.1088/0960-1317/26/11/115020
182. Oh, C.; Streller, F.; Carpick, R. W.; de Boer, M. P. Effectiveness of oxygen plasma versus UHV bakeout in cleaning MEMS switch surfaces. In *2015 IEEE 61st Holm Conference on Electrical Contacts (Holm),* San Diego, CA, U.S.A., Oct 11–14, 2015; 2015; pp 358–362. doi:10.1109/HOLM.2015.7355121
183. de Boer, M. P.; Czaplewski, D. A.; Baker, M. S.; Wolfley, S. L.; Ohlhausen, J. A. *J. Micromech. Microeng.* **2012,** *22,* 105027. doi:10.1088/0960-1317/22/10/105027
184. Soon, B. W.; Qian, Y.; Ng, E. J.; Hong, V. A.; Yang, Y.; Ahn, C. H.; Kenny, T. W.; Lee, C. *J. Microelectromech. Syst.* **2015,** *24,* 1906–1915. doi:10.1109/JMEMS.2015.2451191
185. Majumder, S.; Lampen, J.; Morrison, R.; Maciel, J. A packaged, high-lifetime ohmic MEMS RF switch. In *2003 IEEE MTT-S International Microwave Symposium Digest,* Philadelphia, PA, U.S.A., June 8–13, 2003; IEEE Publishing: Piscataway, NJ, U.S.A., 2003; pp 1935–1938. doi:10.1109/MWSYM.2003.1210537
186. Younis, M. I.; Miles, R.; Jordy, D. *J. Micromech. Microeng.* **2006,** *16,* 2463–2474. doi:10.1088/0960-1317/16/11/030
187. Gladden, J. R.; Handzy, N. Z.; Belmonte, A.; Villermaux, E. *Phys. Rev. Lett.* **2005,** *94,* 035503. doi:10.1103/PhysRevLett.94.035503
188. Yang, F.; Carpick, R. W.; Srolovitz, D. J. *ACS Nano* **2017,** *11,* 490–500. doi:10.1021/acsnano.6b06473
189. Peschot, A.; Poulain, C.; Souchon, F.; Charvet, P.-L.; Bonifaci, N.; Lesaint, O. *Microelectron. Reliab.* **2012,** *52,* 2261–2266. doi:10.1016/j.microrel.2012.06.044
190. Czarnecki, P.; Rottenberg, X.; Soussan, P.; Ekkels, P.; Muller, P.; Nolmans, P.; De Raedt, W.; Tilmans, H. A. C.; Puers, R.; Marchand, L.; De Wolf, I. *Sens. Actuators, A* **2009,** *154,* 261–268. doi:10.1016/j.sna.2008.07.003
191. Shea, H. R.; Gasparyan, A.; Chan, H. B.; Arney, S.; Frahm, R. E.; López, D.; Jin, S.; McConnell, R. P. *IEEE Trans. Device Mater. Reliab.* **2004,** *4,* 198–207. doi:10.1109/TDMR.2004.826350

192. Peng, Z.; Yuan, X.; Hwang, J. C. M.; Forehand, D. I.; Goldsmith, C. L. *IEEE Trans. Microwave Theory Tech.* **2007,** *55,* 2911–2918. doi:10.1109/TMTT.2007.909475
193. Sounart, T. L.; Panchawagh, H. V.; Mahajan, R. L. *Appl. Phys. Lett.* **2010,** *96,* 203505. doi:10.1063/1.3389491
194. Kong, D.; Cha, J. J.; Lai, K.; Peng, H.; Analytis, J. G.; Meister, S.; Chen, Y.; Zhang, H.-J.; Fisher, I. R.; Shen, Z.-X.; Cui, Y. *ACS Nano* **2011,** *5,* 4698–4703. doi:10.1021/nn200556h

License and Terms

This is an Open Access article under the terms of the Creative Commons Attribution License (http://creativecommons.org/licenses/by/4.0), which permits unrestricted use, distribution, and reproduction in any medium, provided the original work is properly cited.

The license is subject to the *Beilstein Journal of Nanotechnology* terms and conditions: (https://www.beilstein-journals.org/bjnano)

The definitive version of this article is the electronic one which can be found at:
doi:10.3762/bjnano.9.29

Paper X

European Journal of Mechanics A/Solids 66 (2017) 412–422

Contents lists available at ScienceDirect

European Journal of Mechanics A/Solids

journal homepage: www.elsevier.com/locate/ejmsol

Extra tension at electrode-nanowire adhesive contacts in nano-electromechanical devices

Alexander I. Livshits [a], Liga Jasulaneca [a], Jelena Kosmaca [a, *], Raimonds Meija [a], Justin D. Holmes [c, d], Donats Erts [a, b]

[a] Institute of Chemical Physics, University of Latvia, Riga, 19 Raina Blvd., LV 1586, Latvia
[b] Department of Chemistry, University of Latvia, Riga, 1 Jelgavas Str., LV 1004, Latvia
[c] CRANN & AMBER, Trinity College Dublin, Dublin 2, Ireland
[d] Department of Chemistry and Tyndall National Institute, University College Cork, Cork, Ireland

A R T I C L E I N F O

Article history:
Received 23 January 2017
Received in revised form
10 August 2017
Accepted 14 August 2017
Available online 18 August 2017

Keywords:
Nano-electromechanical contact
Nano-electromechanical switch
Nanowire deflection

A B S T R A C T

We report a strong tangential component of the reaction force at electrode to nanowire adhesive contact which was previously established using electrostatic attraction. The reaction force tangential component absolute value was found to be comparable to or even bigger than the corresponding normal component. This effect is important for understanding of the mechanics of nano-electromechanical devices. Both the experiment and the corresponding theory are presented. Fitting of the obtained analytical solutions to experimental data was used to measure the reaction force acting at the contact for several nanowire-electrode configurations.

© 2017 Elsevier Masson SAS. All rights reserved.

1. Introduction

Nano-electromechanical systems (NEMS) utilize electrical and mechanical properties of nanomaterials for nanoscale devices. Their operation involves electromechanically driven motion of an active element, such as a nanowire or a nanotube. Current examples of NEMS include a range of nanorelays and switches (ON-OFF devices) (Loh and Espinosa, 2012; Hwang and Kang, 2005; Chen et al., 2008; Ke and Espinosa, 2006; Andzane et al., 2009, 2010; Ziegler et al., 2004; Lee et al., 2004; Viasnoff et al., 2006; Jang et al., 2008a, 2008b, 2005). These devices are an alternative to the complementary metal-oxide-semiconductor (CMOS) devices, for example, for memory applications (Loh and Espinosa, 2012; Jang et al., 2008a; Rueckes et al., 2000). Despite the benefits of the NEMS technology, which include further miniaturisation, significant reduction of power consumption and ability to operate in harsh environmental conditions, their reliability is still a critical issue (Loh and Espinosa, 2012). Failing due to adhesion, conductivity reduction due to surface wear and/or contamination, switching element burn-out due to electrical discharge and Joule heating are typical problems of NEMS. Solution of these problems requires a better understanding of the mechanics of NEMS and in particular of the conditions at the contacts.

Various systems, including carbon nanotubes, as well as metal and semiconductor nanowires, have been used as active components in NEM switches (Loh and Espinosa, 2012; Hwang and Kang, 2005; Chen et al., 2008; Ke and Espinosa, 2006; Andzane et al., 2009; Ziegler et al., 2004; Rueckes et al., 2000; Kim and Lieber, 1999; Kinaret et al., 2003). In the majority of cases such active elements can be considered as straight objects (thin rods), cylindrical or rectangular in cross-section. In these cases, usual linear beam bending theory can be used to describe their mechanical behaviour. In many cases, however, mechanical behaviour of the active element in a pre-bent configuration is the subject of interest.

A gateless two-source controlled nano-electromechanical switch based on individual, single-clamped Ge nanowire (Andzane et al., 2009, 2010, 2013) is an example of such a case. Initially the nanowire and the electrode are physically separated, representing an "off" state. Switching the device to an "on" state is achieved by applying an electrostatic potential between the single clamped active element (the source) and the electrode (the drain). If the applied voltage achieves a certain value, the jump-to-contact happens and after the voltage is switched off the device remains in the "on" state due to adhesion forces.

* Corresponding author.
E-mail address: jelena.kosmaca@lu.lv (J. Kosmaca).

http://dx.doi.org/10.1016/j.euromechsol.2017.08.009
0997-7538/© 2017 Elsevier Masson SAS. All rights reserved.

The scheme shown in Fig. 1 is equally applicable to nanorelays and two input switches. However, the shape and placement of electrodes may be different. In Fig. 1, the elastic beam, representing a nanowire, is fixed at a macroscopic electrode on the left. The beam is bent and kept in contact with another electrode on the right (Electrode 1 on Fig. 1) by the adhesion force. In case of nanorelays an additional electrode (Electrode 2 on Fig. 1) is needed to detach the active element from the contact. The detachment is achieved by applying an electric voltage pulse between the active element and the additional electrode. The latter cannot be reached by the nanowire. For the contrary, in case of nanoswitch the nanowire is supposed to establish contact with each of the electrodes in turn.

One of the reported difficulties (Andzane et al., 2013) in the implementation of this scheme is the high voltage between the Electrode 2 and the nanowire, required to pull the latter from the contact. A novelty idea demonstrated in (Andzane et al., 2013) for substantial reduction of the pull-off voltage without compromising the quality of the contact is to make use of mechanical resonance. Such a resonance can be generated by combination of DC/AC electrical fields. The pull-off voltages reported in (Andzane et al., 2013) are much lower compared to static-only NEMS switching devices. Though this result can be considered as a success, it also demonstrates that in other circumstances both unwanted mechanical and electrostatic interaction can compromise the stability of the contact. No attempts were made in (Andzane et al., 2013) to investigate the proposed mechanism theoretically. There were two reasons for that. First, it is necessary to describe the oscillations of the bent, while in contact, nanowire with full account of its curvature. Second, the conditions at the contact should be specially investigated because the magnitude and direction of the reaction force acting on the nanowire are unknown.

The knowledge of the reaction force at the contact has much more general applicability for NEMS development than the example which has been just described. Any atomic scale consideration of the processes at the contact requires a realistic macroscopic environment model to be imbedded in. The stress field around the contact is an important characteristic of such environment.

In this work, we first report an experiment. It shows that the reaction force, which an active element experiences at the contact, may contribute not only to its bending, but also to its axial tension. Second, a nonlinear equation of motion for the active element of a nanoswitch is derived. It takes full account of the curvature of the element and is exact in this sense. It also incorporates the roles of the pull-off force, of the reaction force and of the possible force moment at the contact. Third, a static solution of the problem is obtained and compared to the experimental shape of the nano element. The result of such a comparison allows us to estimate both normal and tangential components of the reaction force as well as the bending moment acting on the nanowire at the contact. Forth, small oscillations of the nanowire which is brought to contact with the electrode are considered. This leads us to an analytical formula for the nanowire resonant oscillation frequency as a function of deflection, reaction force and the force moment acting at the contact.

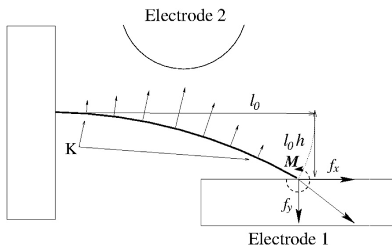

Fig. 1. Scheme of a gateless two input nanoswitch. l_0 – nanowire length, h – dimensionless vertical deflection, K – density of a distributed external force, usually of electrostatic nature, f_x and f_y - components of the reaction force at the contact, $\boldsymbol{M}$ – force moment at the contact.

2. Methods

2.1. Experimental

Monocrystalline Ge nanowires were grown using the supercritical fluid method (Holmes et al., 2003). The nanowires were suspended on a TEM grid surface pre-coated with a 5/20 nm thick Pt/Au layer (Gatan 682 PECS) and investigated in a scanning electron microscope (Hitachi S-4800 SEM) in order to select a suitable nanowire. The end of the selected nanowire was clamped at the edge of the grid with a platinum strip applying the focused e-beam technique (SEM-FIB TECNAI LYRA). The width of the strip exceeded the nanowire diameter which is sufficient to make the end of the nanowire fixed (Qin et al., 2012; Meija et al., 2015).

The switch elements were attached to positioners of a SmarAct 13D nanomanipulation system and staged inside the Hitachi S-4800 SEM equipped with Fisher electrical connectors in the walls of the specimen chamber, to control the stage and apply the voltage. Fine positioner's adjustment in range from several mm to a few nm allowed us to configure the measurement setup *in-situ* (Andzane et al., 2013; Meija et al., 2015, 2017; Kosmaca et al., 2017; Jasulaneca et al., 2016). A Pt/Au coated silicon chip was used as a plane counter electrode (Electrode 1 in Fig. 1). It was connected to Keithley-6430 DC voltage source. An electrochemically etched Au tip was grounded and used to ensure that the nanowire deflection occurs in plane. Continuous visualisation and imaging in SEM was used to control the setup configuration, determine nanowire size and shape during the experimental session. In particular, the length of the chosen nanowire was estimated as $l_0 = 138.7 \pm 0.1\ \mu m$ and the radius as $r = 99 \pm 2\ nm$. At the beginning of the experiment single clamped nanowire's resonant frequency was obtained by exciting the nanowire oscillations electrostatically. The nanowire's resonance was detected as a sharp increase of the nanowire oscillation amplitude at a certain AC frequency. This frequency was found to be equal to $7.31 \pm 0.01\ kHz$. This would give the estimation of the Young's modulus $E = 137 \pm 7\ GPa$ assuming that the nanowire's mass density is equal to the bulk value of Ge $\rho = 5323\ kg/m^3$and no surface layer, with mechanical properties different from the bulk, exists. In fact, some oxide layer was definitely present. All of the preparations and measurements mentioned above have been done for five similar nanowires. It has been found that for a single clamped nanowire two slightly different (not more than by 10%) resonant frequencies can be detected. They correspond to oscillations in perpendicular planes. This is a consequence of the imperfection of the nanowire's cylindrical symmetry. For the finally chosen sample we were unable to detect any difference between these frequencies.

Further measurements were performed in the following steps. 1) The plane electrode and the Au tip were moved towards the nanowire. 2) A DC voltage sweep starting from 0 V with a step width 0.1 V was applied between the plane electrode and the nanowire until the nanowire right end jumped into contact with the electrode surface. 3) The nanowire deflection was determined by comparing the SEM images before and after establishing the

contact (Fig. 2). The deflection was measured in thirteen to fifteen points evenly distributed along the whole nanowire length. On Fig. 2, H represents the deflection at the point of the nanowire right end. 5) The AC voltage of 2 V was applied between the Au tip and the rest of the system and the resonance frequency of the nanowire was determined. 6) The AC voltage of 1 V was applied between the Au tip and the rest of the system and the resonance frequency of the nanowire was determined once more. 7) The plane electrode was moved away from the nanowire until detachment happened.

These steps were repeated for a set of right end dimensionless deflection h (ratio of the deflection over the nanowire length l_0) absolute values increasing from 0.05 to 0.35. Then the procedure was repeated for a set of decreasing absolute values of h chosen in the same interval.

On Fig. 3 it is clearly seen that the measured resonance frequencies of the Ge nanowire are higher than the frequency of the "fixed-fixed" configuration and they are further growing with the value of the deflection h. In (Meija et al., 2015) slightly different experiment has been reported. A similar Ge nanowire was brought to contact with a counter electrode purely mechanically. The electrode was moved towards the nanowire until the contact has been established by adhesion forces. The electrostatic attraction was not employed in that experiment. The authors measured the resonance frequency and then applied some electric voltage pulse, which resulted in current flowing through the contact area. They repeated these measurements several times with increasing voltages applied. The main observation of that experiment was that the resonant frequency of the nanowire was growing each time after the voltage has been increased. The initial frequency was close to that of a "fixed-supported" rod and it approached the "fixed-fixed" value after several cycles. The conclusion of the authors was that the strength of the adhesion was increased as a result of electric current flow through the contact area.

In our experiment the nanowire has been brought to contact by electrostatic forces. Though the voltage was switched off after each jump-to-contact event, the electric current had enough time to modify the contact properties and some adhesion strengthening could be expected. It however cannot result in resonant frequencies being higher than that of the "fixed-fixed" configuration, unless the nanowire is experiencing an axial stretching or its linear density and/or Young's modulus are not constant. This subject is further discussed in our last section, after the corresponding theory is presented.

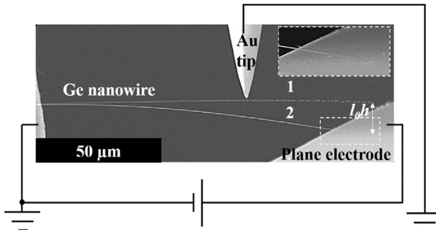

Fig. 2. Schematic of the experimental setup with over layered SEM images. The nanowire before (position 1) and after (position 2) establishing the contact with the plane electrode. The left end of the nanowire is fixed, whilst the right end, when the voltage is applied, consequently bends and jumps into contact with the plane electrode. The inset shows the nanowire's right end in contact with the electrode. Comparison of the nanowire shape in positions 1 and 2 is used for determination of the nanowire deflection along the whole nanowire length. l_0h represents the deflection at the point of the nanowire right end.

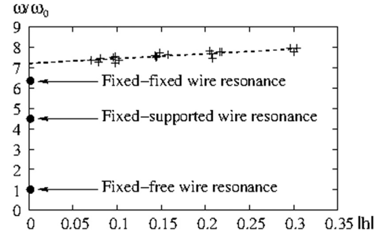

Fig. 3. Ratio of the resonant frequency − ω to that of the single-clamped nanowire − ω_0 as a function of deflection h. Black circles correspond to the "fixed-free", "fixed-supported" and "fixed-fixed" resonances of a straight thin rod without any axial stress. The dashed line represents the best fit of a linear function to the experimental data.

2.2. Theoretical basis

2.2.1. The equation of motion

The subject of our attention is the shape of a nanowire, while the latter is kept in contact with the electrode by adhesion forces. The nanowire may have a surface layer (oxide shell) with mechanical properties which differ from those of the core. This is why mass density ρ in all of the expressions below must be interpreted as an effective value. Flexural rigidity R for homogeneous rods is given by formula (1a). For the case of circular cross-section wire with core-shell model it is given by formula (1b) (Zhang et al., 2013). For the limiting case of very thin shell, (1b) reduces to a simple expression (1c) (Wang et al., 2013).

$$R = EI, \quad I = \frac{\pi D^4}{64} \tag{1a}$$

$$R = \frac{1}{64}\pi E^c D^4 + \pi E^s s\left(\frac{1}{8}D^3 + \frac{3}{8}D^2 s + \frac{1}{2}Ds^2 + \frac{1}{4}s^3\right), \tag{1b}$$

$$R = \frac{1}{64}\pi E^c D^4\left(1 + \frac{8sE^s}{E^c D}\right). \tag{1c}$$

E^c, E^s- stands for the Young's modulus of the core and shell correspondingly, D - is the core diameter, s − is the shell thickness. It must be said that the formula (1b) cannot be interpreted as (1a) with some kind of effective Young's modulus. This is because the effective value, which would be introduced this way, contradicts with the Young's modulus definition. If used, it would result in a wrong elongation of the rod under tension. To make our expressions general the flexural rigidity R will be used everywhere.

Beam bending (Timoshenko, 1953) is described in the spirit of the well-known Euler-Bernoulli theory, however, in its nonlinear generalized form. A short derivation of the main equation is presented below. We start with the equilibrium equation for a cylindrical beam and the expression for the bending moment (Landau and Livshitz, 2007):

$$\begin{aligned} &R\left[\frac{dr}{dl} \times \frac{d^3 r}{dl^3}\right] = \left[\tilde{F} \times \frac{dr}{dl}\right] \\ &\frac{d\tilde{F}}{dl} = -\tilde{K} \end{aligned} \tag{2a}$$

$$\tilde{M} = R\left[\frac{dr}{dl} \times \frac{d^2r}{dl^2}\right] \tag{2b}$$

The vector r is representing the coordinates of a point on a beam which is considered as a 1-D object, $\tilde{K}$– is a linear density of the external force $\tilde{F}$, l– is a coordinate along the beam. We assume that at the left end the beam is always parallel to x axis and that all of the deformation takes place in xy plane, so that the r has no z component.

Taking a derivative of the equation (2a), equation (3) can be written. The X and Y are the corresponding components of r. Starting from here all length related variables are expressed in units of the nanowire length $\xi = l/l_0$

$$\begin{gathered} X^{(1)}Y^{(4)} - X^{(4)}Y^{(1)} + X^{(2)}Y^{(3)} - X^{(3)}Y^{(2)} - \\ F_xY^{(2)} - F_yX^{(2)} + K_xY^{(1)} - K_yX^{(1)} = 0 \\ \begin{pmatrix} F_x \\ F_y \end{pmatrix} = \frac{l_0^2}{R}\begin{pmatrix} \tilde{F}_x \\ \tilde{F}_y \end{pmatrix}, \quad \begin{pmatrix} K_x \\ K_y \end{pmatrix} = \frac{l_0^3}{R}\begin{pmatrix} \tilde{K}_x \\ \tilde{K}_y \end{pmatrix} \end{gathered} \tag{3}$$

All derivatives are presented as upper indices in brackets and are taken with respect to the normalized coordinate ξ – along the beam.

Using an evident equality (4) all the derivatives of X can be expressed in terms of the derivatives of Y.

$$\left(X^{(1)}\right)^2 + \left(Y^{(1)}\right)^2 = 1 \tag{4}$$

This leads to (5).

$$\begin{gathered} \left(\frac{Y^{(2)}}{X^{(1)}}\right)^{(2)} - \frac{F_{tens}}{X^{(1)}}Y^{(2)} + K_xY^{(1)} - K_yX^{(1)} = 0 \\ F_{tens} = F_xX^{(1)} + F_yY^{(1)};\ X^{(1)} = \sqrt{1 - \left(Y^{(1)}\right)^2}; \quad X(l) = \int_0^l X^{(1)}dx \end{gathered} \tag{5}$$

Equation (5) in the case of small deflections can be written in a well recognizable linear form of (6).

$$Y^{(4)} - F_xY^{(2)} - K_y = 0 \tag{6}$$

Expressions for the transverse force are given in (7). The force acting on the beam has both concentrated and distributed components. The former is due to adhesion and short range repulsion. This force acts at the contact point and may contribute both to bending and axial tension. Two constants – (f_x, f_y) are used in (7) and below to characterize this force.

The distributed force density K, if present, may have contributions of different nature. An externally applied force, usually of electrostatic nature, is one of such contributions. It is strictly perpendicular to the nanowire axis and directed towards the Electrode 2. For a given shape of the beam this force density is described by a scalar function $g(\xi,t)$. If the nanowire is in motion the inertial and dissipative contributions to the force density should also be taken into account. In (7) they are represented by the corresponding time derivatives of the coordinates.

$$\begin{gathered} F_x = f_x + \int_\xi^1 K_x(u)du, \quad F_y = f_y + \int_\xi^1 K_y(u)du \\ K_x = -\mu Y^{(1)} - \ddot{X} - 2\lambda\dot{X} \\ K_y = \mu X^{(1)} - \ddot{Y} - 2\lambda\dot{Y} \\ \dot{X}(\xi,t) = -\int_0^\xi \frac{Y^{(1)}\dot{Y}^{(1)}}{X^{(1)}}du \\ \ddot{X}(\xi,t) = -\int_0^\xi \frac{Y^{(1)}\ddot{Y}^{(1)}}{X^{(1)}} + \frac{\left(\dot{Y}^{(1)}\right)^2}{\left(X^{(1)}\right)^3}du \\ T = l_0^2\sqrt{\frac{m}{R}}, \quad \mu = \frac{l_0^3 g(\xi,t)}{R}, \quad \lambda = \frac{l_0 c}{2\sqrt{Rm}} \end{gathered} \tag{7}$$

In (7) the nanowire linear mass density - $m = \pi D^2\rho/4$, the dissipative coefficient - c and the time unit – T have been introduced. The time derivatives are represented as dots over the corresponding function. Substitution of the first two expressions of (7) into the equilibrium equation (2a) leads to (8).

$$X^{(1)}Y^{(3)} - Y^{(1)}X^{(3)} = f_xY^{(1)} - f_yX^{(1)} + Y^{(1)}\int_\xi^1 K_x(u)du - X^{(1)}\int_\xi^1 K_y(u)du \tag{8}$$

At $\xi = 1$ the equation (8) can be reduced to (9).

$$f_y = -\left(\left[\frac{Y^{(3)}}{X^{(1)^2}} + \frac{Y^{(1)}Y^{(2)^2}}{X^{(1)^4}}\right] + f_x\frac{Y^{(1)}}{X^{(1)}}\right)_{\xi=1} \tag{9}$$

If the right end of the nanowire is free, the equation (9) reduces to usual “free end” boundary conditions (10).

$$Y^{(2)}(1) = Y^{(3)}(1) = 0 \tag{10}$$

If, however, it is in contact, the equation (9) allows us to eliminate the unknown f_y force component from the equation. Using (9) and (7) the equation of motion can be finally written in terms of y-displacement, its time and coordinate derivatives and integrals.

$$\begin{gathered} \left(\ddot{Y}+2\lambda\dot{Y}\right)X^{(1)} + Y^{(1)}\int_0^\xi \frac{Y^{(1)}\left(\ddot{Y}+2\lambda\dot{Y}\right)}{X^{(1)}} + \frac{\left(\dot{Y}^{(1)}\right)^2}{\left(X^{(1)}\right)^3}du + \\ \left(\frac{Y^{(2)}}{X^{(1)}}\right)^{(2)} - F_{tens}\frac{Y^{(2)}}{X^{(1)}} = \mu \\ F_{tens} = X^{(1)}\int_\xi^1 K_x du + Y^{(1)}\int_\xi^1 K_y du + \frac{f_x\left(X^{(1)}(1)X^{(1)} + Y^{(1)}(1)Y^{(1)}\right)}{X^{(1)}(1)} - \\ \left[\frac{Y^{(3)}}{X^{(1)2}} + \frac{Y^{(1)}Y^{(2)2}}{X^{(1)4}}\right]_{\xi=1} Y^{(1)} \end{gathered} \tag{11}$$

Unlike in the recent work (Wang and Wang, 2015), the equation (11) is exact with respect to curvature. It does not contain any truncated expansions. This is achieved because of the use of the

proper coordinate $\xi = l/l_0$ instead of the Cartesian x. Equation (11) does not describe the effect of axial elongation due to tension. This usually negligible effect can be accounted for when the solution of the problem has been obtained. Similar to (5) and (6), for small deflections equation (11) can be written in a well recognizable linear form:

$$\ddot{Y} + 2\lambda\dot{Y} + Y^{(4)} - f_x Y^{(2)} = \mu$$

2.2.2. Static solution

If the external field is constant in time and a static solution only is to be found, the equation (11) reduces to (12)

$$\left(\frac{Y^{(2)}}{X^{(1)}}\right)^{(2)} - F_{tens}\frac{Y^{(2)}}{X^{(1)}} = \mu(\xi)$$
$$F_{tens} = -X^{(1)}\int_{\xi}^{1}\mu Y^{(1)}du + Y^{(1)}\int_{\xi}^{1}\mu X^{(1)}du - \left[\frac{Y^{(3)}}{X^{(1)2}} + \frac{Y^{(1)}Y^{(2)2}}{X^{(1)4}}\right]_{\xi=1} Y^{(1)} + \frac{f_x\left(X^{(1)}(1)X^{(1)} + Y^{(1)}(1)Y^{(1)}\right)}{X^{(1)}(1)} \quad (12)$$

The distributed external force μ is usually of electrostatic nature. For a particular configuration, it should be obtained numerically as a solution of the corresponding 3-D electrostatic problem. A simple model of such a force is used in this work for general analysis. The force density is represented as an intensity multiplier times some normalized function. This function should be positive, have one extremum and approach zero on both ends of the nanowire. This is because the electrostatic force is directed normal to the surface and this normal changes direction at both ends of the nanowire. To make things simple this function is modelled by a polynomial expression and by Dirac Delta function (13).

$$\mu_n(\xi) = \mu_0\frac{(n!)^2}{(2n+1)!}(\xi(1-\xi))^n, \quad n = 1, \ 2, \ldots$$
$$\mu_\infty(\xi) = \mu_0\delta\left(\xi - 1/2\right) \quad (13)$$

At the left end the boundary conditions are trivial.

$$Y(0) = 0; \quad \left(Y^{(1)}\right)_{\xi=0} = 0 \quad (14)$$

The boundary conditions on the right end depend on the physical model under consideration. In this work, it is assumed that the y coordinate of the beam at contact is known.

If the switch contact takes place at the very end of the beam and the length of the contact along the beam is short enough, then the tangential vector of the beam does not need to be parallel to the electrode surface and so, unlike in (14), the first derivative is unknown. In this case the bending moment at contact point should be used instead. Using expressions (2b) and (4) the boundary conditions can be written as (15), where h is the distance (dimensionless value) between the x axis and the surface of the electrode.

$$Y(1) = h$$
$$\left(\frac{Y^{(2)}}{X^{(1)}}\right)_{\xi=1} = \frac{l_0\tilde{M}_z}{R} = M \quad (15)$$

The second expression in (15) becomes linear only if the bending moment is neglected. This however is usually not possible for nano-electromechanical devices due to physical reasons. The repulsive component of the reaction force, because of its short range, can be treated as one applied at a well-defined position – at the point of contact. The attractive component however has longer range. Its "centre of mass" may be close to the point of contact, but does not coincide with it. Thus, in general the pair of forces leads to appearance of some bending moment.

Equation (12), together with the boundary conditions (14) and (15), determine the shape of the bent nanowire brought to contact with an electrode. This shape is dependent on four parameters: f_x– the tangential component of the reaction force at contact, M – the bending moment, h– the deflection and μ_0 – the intensity of the external distributed force.

Solution of the problem can be obtained as an expansion (16).

$$Y(\xi) = \sum_{i,j,k=0,\ i+j+k>0}^{i,j,k=\infty} \mu_0^i h^j M^k y_{ijk}(\xi) \quad (16)$$

It appeared however that the complexity of the solution so rapidly grows with indices that it becomes impossible to use more than the three leading terms. Even these terms are complicated enough to make direct calculations problematic due to numerical loss of precision. At the same time, it is easy to show that in the case of $f_x = 0$ the solution reduces to a set of polynomials.

Taking into account the fact that the tangential component of the reaction force at contact is supposed to be small and in any case, is limited by the static friction, it is also treated as an expansion parameter. In this way, all of the solution components become polynomials, which can be obtained with the help of any computer algebra system.

$$Y(\xi) = \sum_{i,j,k,l=0,\ i+j+k+l>0}^{i,j,k,l=\infty} \mu_0^i h^j M^k f_x^l y_{ijkl}(\xi) \quad (17)$$

Several analytically obtained members of the expansion (17) can be found in the Appendix.

As it can be seen in Fig. 4, the expansion in h up to the order of five has been practically converged even for the unrealistically big deflection of $h = 0.65$. The graphs which are shown in Fig. 4 correspond to the situation when neither forces parallel to the electrode surface nor distributed electrostatic force are applied. Fig. 5 demonstrates the effect of a force parallel to the electrode surface. The same deflection value of $h = 0.65$ have been chosen. The solutions shown are of the fifth order in deflection and they correspond to three values of the force $f_x = [3, 0, -3]$.

In Fig. 6 the effect of the bending moment M and the tangential force are shown. It is important that when the bending moment is

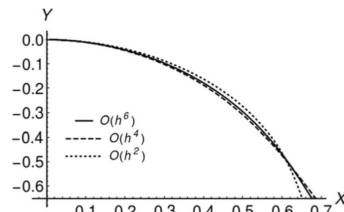

Fig. 4. Static deflection solutions up to the first –"O(h^2)", third –"O(h^4)"and fifth –"O(h^6)" order in deflection h. $h = 0.65$, $f_x = 0$.

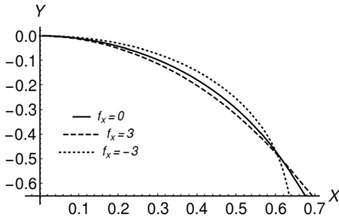

Fig. 5. The influence of the static friction force on the nanowire shape. The example solutions are of the fifth order of both deflection and force. Deflection *h = 0.65*.

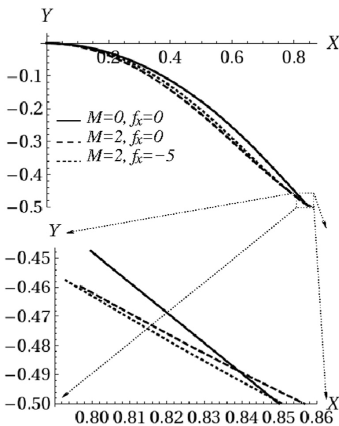

Fig. 6. The influence of bending moment and of tangential reaction force on the nanowire shape. Example solutions of the third order of deflection are shown. Deflection $h = -0.5$. Solid line: $M = 0, f_x = 0$. Dashed line: $M = 2, f_x = 0$. Dotted line: $M = 2, f_x = -5$. Inset – contact point vicinity.

applied, the contact point on the electrode changes position. To keep in our simulations, the contact position the same it is necessary to use some tangential reaction force as well.

Substitution of solution into the expressions (12) results in tension force formula. The result is rather lengthy and is not presented here but can be easily reproduced. An important consequence of it is that unlike in the case of a musical instrument string, the tension is not constant along the nanowire length. The averaged along the whole length tension force is given by expressions (18) where only linear and quadratic terms are shown for several model external distributed force functions.

$$\langle F_{tens}\rangle = f_x + 3\ h^2 - \frac{3}{2}hM + \begin{cases} -\frac{3}{5}h\mu_0 - M\frac{\mu_0}{40} + \frac{2}{315}\mu_0^2 & n=1 \\ -\frac{33}{56}h\mu_0 - M\frac{\mu_0}{56} + \frac{1795}{288288}\mu_0^2 & \text{if} \quad n=2 \\ -\frac{51}{88}h\mu_0 - M\frac{\mu_0}{88} + \frac{26621}{4434144}\mu_0^2 & n=4 \end{cases} \tag{18}$$

The formulas (18) demonstrate that the resonance frequency of a nanowire oscillations, while in contact, must depend on the deflection h, the bending moment M, the external force intensity μ_0 and the tangential reaction f_x.

2.2.3. Small oscillations

In this section the equilibrium static solution S is supposed to be known. The aim now is to obtain small oscillations around it induced by a harmonic in time external distributed force.

$$\mu(\xi,t) = \mu_{static}(\xi) + \mu_{dynamic}(\xi)\exp(-i\omega t) = (\mu_0 + \nu_0 \exp(-i\omega t))\frac{\mu(\xi)}{\langle\mu(\xi)\rangle} \tag{19}$$

The consequence of the electrostatic nature of the force is that the spatial distribution of the dynamic force is proportional to that of the static part. The intensity factors however must be taken as independent parameters because they depend on the choice of the AC and DC voltages applied.

The first dynamic correction to the static solution has been obtained in a form of truncated expansion in orders of amplitude of the time dependent part of the force.

$$Y(\xi,t) = S(\xi) + \nu_0 D(\xi,t) \tag{20}$$

$$\begin{aligned} &D(\xi,t) = \psi(\xi)\cos(\omega t) \\ &\psi(\xi) = N(\sin(\chi\xi) - \sinh(\chi\xi)) - \cos(\chi\xi) + \cosh(\chi\xi) \\ &N = \frac{\cos(\chi) - \cosh(\chi)}{\sin(\chi) - \sinh(\chi)} \end{aligned} \tag{21}$$

The result of the transformations mentioned above has a familiar general form of (22). It determines the value of the resonant frequency as a function of all of the parameters. Because the static solution is represented as a power expansion in its parameters, all of the coefficients in (22), for a given value of χ, have this structure.

$$A(\mu_0,h,M,f_x,\chi) + iB(\mu_0,h,M,f_x,\chi)\lambda\omega + C(\mu_0,h,M,f_x,\chi)\omega^2 = 0 \tag{22}$$

It must be said that in present work the dissipative coefficient λ is supposed to be negligible. That is because our estimation of the quality factor of our resonator is equal to at least several hundreds. So, the corresponding term in (22) is ignored.

The boundary conditions for the dynamic correction at $\xi = 0$ are trivial.

$$D(0,t) = D^{(1)}(\xi,t)\Big|_{\xi=0} = 0 \tag{23}$$

At $\xi = 1$ however, two limiting cases are considered in this work. First, the conditions (24) will be considered. These conditions mean that both the bending moment and the deflection in this point are static. This case is denoted below as Case-1.

$$D(1,t) = D^{(2)}(\xi,t)\Big|_{\xi=1} = 0 \tag{24}$$

For this case the parameter χ is the smallest positive solution of the equation (25).

$$\begin{aligned} &\cos(\chi)\sinh(\chi) - \sin(\chi)\cosh(\chi) = 0 \\ &\chi \approx 3.926602312047918778 \end{aligned} \tag{25}$$

Another right end boundary condition, considered here, means that the tangential direction of the nanowire is fixed at the static

solution. The assumption behind this is that the nanowire is strongly bound to the electrode at the contact. This case is denoted below as Case-2.

$$D(1,t) = D^{(1)}(\xi,t)\Big|_{\xi=1} = 0 \tag{26}$$

For this case χ must satisfy (27).

$$\begin{aligned} &\cos(\chi)\cosh(\chi) = 1 \\ &\chi \approx 4.730040744862704026 \end{aligned} \tag{27}$$

In both cases the resonant frequency squared is obtained as a ratio of polynomials.

$$\omega^2 = \frac{\sum_{i,j,k,l} \alpha_{i,j,k,l} \mu_0^i h^j M^k f_x^l}{\sum_{i,j,k,l} \beta_{i,j,k,l} \mu_0^i h^j M^k f_x^l} \tag{28}$$

The most important terms of both the numerator and the denominator expansions for the resonant frequency square are given in the following tables. Universal coefficients – the ones that do not depend on the choice of the $\mu(\xi)$ function, are collected in Table 1. The coefficients which are $\mu(\xi)$- dependent are presented for two limiting cases. For the cases of constant force density and concentrated force applied at a half-length they are given in Table 2 and Table 3 correspondingly.

3. Results

The interpretation of the collected experimental data for the static nanowire shapes required two stages. Because all of the solutions obtained represent the nanowire shape in parametric form, the parameter values (the length along the nanowire from its left end to the data point) for all data points must be obtained first of all. For this to be done the experimental nanowire shape was approximated by a polynomial of the seventh order *P(x)*. According to boundary conditions (14) such a polynomial's youngest member is quadratic. The remaining six coefficients were routinely found using *Mathematica* (Wolfram Research I, 2015) built in fitting procedure. Then, for each data point "*i*" the corresponding arc lengths has been obtained by integration.

$$\xi_i = \int_0^{x_i} \sqrt{1 + \left(\frac{dP(x)}{dx}\right)^2}\, dx \tag{29}$$

The solutions in the form of expansion (17) (first three members – of the first, third and fifth power in *h*and *M* and up to the fifths power in f_x) were used to approximate the obtained data sets (ξ_i, X_i, Y_i) with f_x and *M* as fitting parameters.

It was found that the experimental shape of the nanowire in contact can be reproduced by our analytical formulas only if some static friction force and some bending moment are applied at the contact. A typical example of the nanowire shape for deflection

Table 3
Resonant frequency square expansion members that are pull-off force dependent. Concentrated force applied at the $\xi = 1/2$ point.

ijkl	Case-1, α	Case-1, β	Case-2, α	Case-2, β
1000	0	0	0	0
1001	0	0	0	0
1002	0	0	0	0
1010	0.19644	0.000894776	−1.05732	0.000869091
1011	0.00156322	−0.00010094	0.113737	−0.0000960341
1100	−15.4466	0.00508259	−23.2536	−0.00309118
1101	−0.0356086	−0.000338252	1.05603	0.0000720121
2000	0.0966375	−0.000143836	0.132992	−0.000135408
2001	−0.00760279	0.0000135444	−0.0134202	0.0000127182

Table 1
Resonant frequency square expansion in *h*, *M* and f_x.

ijkl	Case-1, α	Case-1, β	Case-2, α	Case-2, β
0000	237.7210675	1	500.5639017	1
0001	11.51253004	0	12.30261862	0
0002	0	0	0	0
0010	0	0	0	0
0011	0	0	0	0
0020	272.2614859	−0.7220805270	584.8793026	−0.6218821707
0021	15.63575828	0.00428699475	0.09829446954	−0.001699025252
0100	0	0	0	0
0101	0	0	0	0
0110	−23.35824244	0.01569550281	47.92548197	0.04296501810
0111	1.216236798	0.00058214088	−4.402219269	−0.00106893613
0200	−6.528136623	−0.00203628349	2.709083522	−0.00195673476
0201	0.1741478139	0.000211419635	−0.2551818022	0.000202381769

Table 2
Resonant frequency square expansion members that are pull-off force dependent. Constant force-density case.

ijkl	Case-1, α	Case-1, β	Case-2, α	Case-2, β
1000	0	0	0	0
1001	0	0	0	0
1002	0	0	0	0
1010	−0.04018499464	0.0005325893955	−0.6676393260	0.0005029334646
1011	0.00841821066	−0.0000593130197	0.0000557155536	−0.008418210660
1100	−10.46078518	0.002083298739	−15.83077561	−0.002519552147
1101	−0.00695807957	−0.0001763587784	0.6272096067	0.0000671334406
2000	0.05709435166	−0.000044226255	0.0484289140	−0.0000401832005
2001	−0.00374210558	$4.484255673 \cdot 10^{-6}$	−0.004934568696	$4.123844225 \cdot 10^{-6}$

$h = 0.21$ is shown in Fig. 7.

The reaction force components as functions of deflection h, measured by curve fitting, are shown in Fig. 8 and Fig. 9.

The parallel to the electrode surface force component, i.e. static friction (Fig. 8), seems to be random. The value of this component may be positive or negative. It was a surprise for the authors to find that the absolute value of this force may be comparable or even bigger than that for the normal component. It is easy to see from the expression (9), that the normal reaction component which is required to keep the nanowire in contact with the electrode, is linearly dependent on the static friction. The bigger (positive) the f_x, the bigger (negative) the required f_y. On the other hand, because the f_x component may be negative, the corresponding f_y may be close to zero, or even positive. That means that in such a case the bent nanowire experiences axial contraction and applies pressure to the electrode.

The reaction force moment fitted values are shown in Fig. 10. They are always positive. This is in agreement with the fact that the attractive forces are of long range compared to the repulsive ones and because of that their "centre of mass" is not at the very end of the nanowire.

As it was mentioned in the experiment section above, the nanowire deflection measurements were done by comparing the corresponding overlaid images. The accuracy of such measurement is limited. This can influence the accuracy of the optimal values of the parameters f_x and M obtained by fitting procedure. It is generally important to have an independent from the measurement confirmation of the reliability of results. The values of the fitted parameters, the expression (29) and the coefficients from Table 1 have been used to obtain the resonant frequencies of the nanowire for the whole set of deflections. The results are shown in

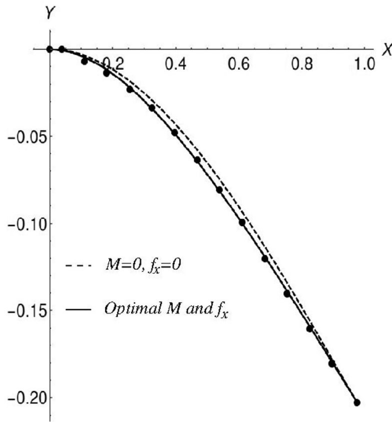

Fig. 7. Typical example of the nanowire shape while in contact. Circles - experimental points, dashed line – solution for $f_x = 0$and $M = 0$, solid line – fitted solution with the optimal f_x and $\boldsymbol{M}$ values for deflection $h = 0.21$.

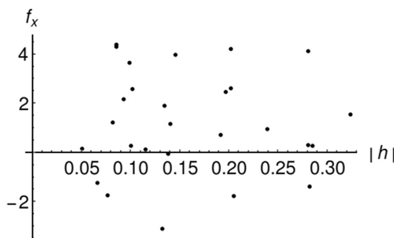

Fig. 8. Reaction force $\boldsymbol{x}$ component for a set of deflections (h).

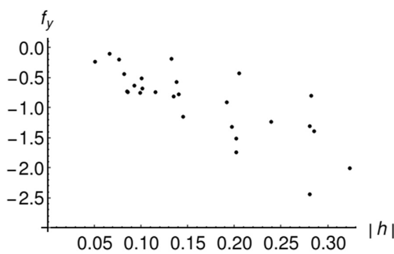

Fig. 9. Reaction force $\boldsymbol{y}$ component for a set of deflections (h).

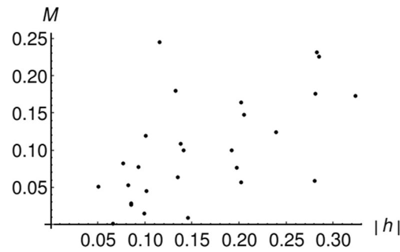

Fig. 10. Reaction moment at the contact.

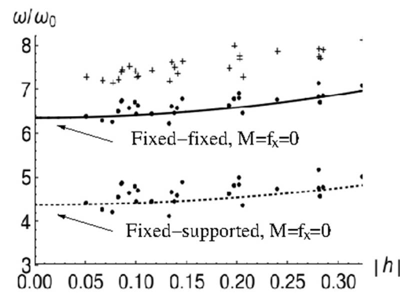

Fig. 11. The resonant frequencies. Experimental – the upper group, predicted with fixed-fixed boundary condition – the middle group, predicted with fixed-supported boundary condition – the lower group. The solid line – prediction for fixed-fixed boundary condition in while the dotted line – prediction for fixed-supported boundary condition the case of $f_x = M = 0$.

Fig. 11.

The upper group of points in Fig. 11 represent our experimental results. The middle group is our prediction for the case of fixed-fixed boundary condition based on the obtained values of the reaction force f_x and moment M. Prediction for this boundary condition with $f_x = M = 0$ is shown as a solid line. The lower group of points and a dotted line represent the case of fixed-supported boundary condition. It is easy to see that our predicted values are representing the general tendency of frequency growth with deflection. The distribution of values due to variation of reaction force is also reproduced well. It however still should be explained why the experimental frequencies are about *15%* higher than the predicted ones.

4. Discussion

Better understanding of the mechanics and in particular contact mechanics of nano-system elements is vitally important for the NEMS development. Description of contact formation and termination is one of the challenging problems in this area. This problem can be approached on different levels and scales. A macroscopic approach of geometrically nonlinear beam bending theory has been used in this work. This is justified for long (with length to diameter ratio of more than a hundred) nanowires. One must be careful however in choosing the right elastic parameters for the material. This is because, at the nanoscale, surface effects become important and the bulk values may be inaccurate (Chen et al., 2006). Current formulation is expected to yield accurate results for nanowires having diameters in range of tens nanometers, where these effects have only minor impact on the material elastic properties. For sizes below ten nanometers, the continuum approach would be outperformed by atomistic simulations (Miller and Shenoy, 2000; Villain et al., 2004).

5. Conclusions

Our main theoretical result is the equation (11). This equation is exact in terms of big curvature. The equation contains a parameter, the tangential to the electrode surface reaction force component. Hence, fitting of the solutions to experimental data can be used to measure the reaction force acting at the contact. Our results demonstrate that the tangential force component can be comparable or even bigger than the corresponding normal component. This result is unexpected for the authors and may be important for better understanding of the processes in nano-contacts.

It is clearly beyond the scope of this paper to investigate the origin of the discovered tangential forces. The hypothetical explanation however can be proposed. We believe that when the nanowire's free end hits the electrode surface (when jump to contact takes place) the shape of the nanowire is influenced by the electrostatic attraction forces as well as by the dynamics of the jump. Later, when the electric contact is established and the voltage is switched off, the force distribution along the nanowire changes. The point of contact however in the case of strong adhesion is fixed. As a result, the nanowire may be finally caught by adhesion forces in a slightly stretched/compressed condition. This may change the resonance frequency of the nanowire in contact and affect the following process of the off switching.

Finally, it should be mentioned that we made our best to choose the best nanowire sample. We examined single-clamped nanowire resonant frequencies for different oscillation directions. We inspected our nanowire images to find any sign of variation of diameter along the wire. Despite our efforts, the resonant frequency of the nanowire in contact appeared to be too high relative to its single-clamped frequency. We believe that this is an evidence of non-constant mass and/or elastic property distribution along the length of our sample.

Acknowledgements

This work has been done within the project Nr. 549/2012 of the Latvian Council of Science.

Appendix

Several nonzero members of the expansion (17).

Expansion members that do not depend on the force model.

Indices i,j,k,l	$y_{i,j,k,l}(\xi)$
0,0,1,0	$\frac{1}{4}(-\xi^2+\xi^3)$
0,0,1,1	$\frac{1}{240}(3\xi^2-\xi^3-5\xi^4+3\xi^5)$
0,0,1,2	$\frac{1}{100800}(-66\xi^2+22\xi^3+105\xi^4-21\xi^5-70\xi^6+30\xi^7)$
0,0,1,3	$\frac{1}{100800}(201\xi^2-67\xi^3-330\xi^4+66\xi^5+210\xi^6-30\xi^7+75\xi^8+25\xi^9)$
0,0,3,0	$\frac{1}{13440}(-9\xi^2+17\xi^3+70\xi^4-294\xi^5+378\xi^6-162\xi^7)$
0,0,3,1	$\frac{1}{1612800}(111\xi^2-221\xi^3-1350\xi^4+4218\xi^5-700\xi^6-9348\xi^7+10935\xi^8-3645\xi^9)$
0,1,0,0	$\frac{1}{2}(3\xi^2-\xi^3)$
0,1,0,1	$\frac{1}{40}(4\xi^2-8\xi^3+5\xi^4-\xi^5)$
0,1,0,2	$\frac{1}{8400}(-24\xi^2+8\xi^3+70\xi^4-84\xi^5+35\xi^6-5\xi^7)$
0,1,0,3	$\frac{1}{3024000}(384\xi^2-128\xi^3-720\xi^4+144\xi^5+840\xi^6-720\xi^7+225\xi^8-25\xi^9)$
0,1,2,0	$\frac{1}{1120}(-13\xi^2+9\xi^3-105\xi^4+343\xi^5-315\xi^6+81\xi^7)$
0,1,2,1	$\frac{1}{268800}(546\xi^2-558\xi^3+580\xi^4+3636\xi^5+20832\xi^6+31208\xi^7-18225\xi^8+3645\xi^9)$
0,2,1,0	$\frac{1}{1120}(-51\xi^2+171\xi^3+630\xi^4-1470\xi^5+882\xi^6-162\xi^7)$
0,2,1,1	$\frac{1}{44800}(515\xi^2-513\xi^3+1930\xi^4-13574\xi^5+26628\xi^6-22276\xi^7+8505\xi^8-1215\xi^9)$
0,3,0,0	$\frac{1}{280}(180\xi^2-144\xi^3-315\xi^4+441\xi^5-189\xi^6+27\xi^7)$
0,3,0,1	$\frac{1}{22400}(1344\xi^2-3072\xi^3-3840\xi^4+18240\xi^5-22344\xi^6+12912\xi^7-3645\xi^8+405\xi^9)$

Expansion members for the case of constant force density, n = 0.

Indices i,j,k,l	$y_{i,j,k,l}(\xi)$
1,0,0,0	$\frac{1}{48}(3\xi^2 - 5\xi^3 + 2\xi^4)$
1,0,0,1	$\frac{1}{2880}(-6\xi^2 + 2\xi^3 + 15\xi^4 - 15\xi^5 + 4\xi^6)$
1,0,0,2	$\frac{1}{403200}(39\xi^2 - 13\xi^3 - 70\xi^4 + 14\xi^5 + 70\xi^6 - 50\xi^7 + 10\xi^8)$
1,0,0,3	$\frac{1}{72576000}(-342\xi^2 + 114\xi^3 + 585\xi^4 - 117\xi^5 - 420\xi^6 + 60\xi^7 + 225\xi^8 - 125\xi^9 + 20\xi^{10})$
1,0,2,0	$\frac{1}{322560}(-159\xi^2 + 53\xi^3 - 1260\xi^4 + 6468\xi^5 - 11060\xi^6 + 8172\xi^7 - 2214\xi^8)$
1,0,2,1	$\frac{1}{6451200}(506\xi^2 - 110\xi^3 + 3095\xi^4 - 13275\xi^5 + 7336\xi^6 + 29536\xi^7 - 53149\xi^8 + 33585\xi^9 - 7524\xi^{10})$
1,1,1,0	$\frac{1}{26880}(-237\xi^2 + 107\xi^3 + 1820\xi^4 - 5628\xi^5 + 7028\xi^6 - 3828\xi^7 + 738\xi^8)$
1,1,1,1	$\frac{1}{1612800}(1530\xi^2 - 310\xi^3 - 4125\xi^4 - 14043\xi^5 + 8285\xi^6 - 147012\xi^7 + 122529\xi^8 - 48945\xi^9 + 7524\xi^{10})$
1,2,0,0	$\frac{1}{8960}(-683\xi^2 + 1329\xi^3 - 2380\xi^4 + 4340\xi^5 - 4004\xi^6 + 1644\xi^7 - 246\xi^8)$
1,2,0,1	$\frac{1}{537600}(1794\xi^2 - 222\xi^3 - 15455\xi^4 + 62283\xi^5 - 123200\xi^6 + 129496\xi^7 - 72623\xi^8 + 21435\xi^9 - 2508\xi^{10})$
2,0,1,0	$\frac{1}{967680}(159\xi^2 - 98\xi^3 + 945\xi^4 - 5733\xi^5 + 1224\xi^6 - 12699\xi^7 + 6483\xi^8 - 1300\xi^9)$
2,0,1,1	$\frac{1}{2554675200}(-63873\xi^2 + 30619\xi^3 - 256080\xi^4 + 1325940\xi^5 - 1130052\xi^6 - 2998908\xi^7 + 7583103\xi^8 - 7004965\xi^9 + 3022536\xi^{10} - 508320\xi^{11})$
2,1,0,0	$\frac{1}{967680}(1761\xi^2 - 875\xi^3 - 10710\xi^4 + 34146\xi^5 - 52122\xi^6 + 41958\xi^7 - 16785\xi^8 + 2600\xi^9)$
2,1,0,1	$\frac{1}{425779200}(-79216\xi^2 + 30688\xi^3 + 138490\xi^4 + 664510\xi^5 - 368670\xi^6 + 7376160\xi^7 - 7747311\xi^8 + 4501255\xi^9 - 1367256\xi^{10} + 169440\xi^{11})$
3,0,0,0	$\frac{1}{46448640}(-603\xi^2 + 417\xi^3 - 3780\xi^4 + 26460\xi^5 - 67788\xi^6 + 90180\xi^7 - 66726\xi^8 + 26000\xi^9 - 4160\xi^{10})$
3,0,0,1	$\frac{1}{30656102400}(57498\xi^2 - 31574\xi^3 + 216315\xi^4 - 1266903\xi^5 + 1319472\xi^6 + 3262248\xi^7 - 10434303\xi^8 + 12500675\xi^9 - 7826148\xi^{10} + 2541600\xi^{11} - 338880\xi^{12})$

Expansion members for the case of parabolic force density, n = 1.

Indices i,j,k,l	$y_{i,j,k,l}(\xi)$
1,0,0,0	$\frac{1}{120}(9\xi^2 - 13\xi^3 + 6\xi^5 - 2\xi^6)$
1,0,0,1	$\frac{1}{33600}(-87\xi^2 + 29\xi^3 + 210\xi^4 - 182\xi^5 + 40\xi^7 - 10\xi^8)$
1,0,0,2	$\frac{1}{6048000}(726\xi^2 - 242\xi^3 - 1305\xi^4 + 261\xi^5 + 1260\xi^6 - 780\xi^7 + 100\xi^9 - 20\xi^{10})$
1,0,0,3	$\frac{1}{13970880000}(-81561\xi^2 + 27187\xi^3 + 139755\xi^4 - 27951\xi^5 - 100485\xi^6 + 14355\xi^7 + 51975\xi^8 - 25025\xi^9 + 2100\xi^{11} - 350\xi^{12})$
1,0,2,0	$\frac{1}{268800}(-81\xi^2 + 33\xi^3 - 1400\xi^4 + 6160\xi^5 - 8820\xi^6 + 2932\xi^7 + 3950\xi^8 - 3620\xi^9 + 846\xi^{10})$
1,0,2,1	$\frac{1}{3725568000}(191133\xi^2 - 28599\xi^3 + 2431275\xi^4 - 8804565\xi^5 + 2377914\xi^6 + 24052314\xi^7 - 33322905\xi^8 + 7946015\xi^9 + 12560548\xi^{10} - 9269820\xi^{11} + 1866690\xi^{12})$
1,1,1,0	$\frac{1}{33600}(-198\xi^2 - 47\xi^3 + 2730\xi^4 - 7812\xi^5 + 7686\xi^6 - 186\xi^7 - 4170\xi^8 + 2420\xi^9 - 423\xi^{10})$
1,1,1,1	$\frac{1}{310464000}(196080\xi^2 + 43056\xi^3 - 764610\xi^4 - 3288516\xi^5 + 17660874\xi^6 - 27078018\xi^7 + 12964875\xi^8 + +7246855\xi^9 - 10735186\xi^{10} + 4376820\xi^{11} - 622230\xi^{12})$
1,2,0,0	$\frac{1}{22400}(-1725\xi^2 + 3337\xi^3 - 6720\xi^4 + 11760\xi^5 - 7308\xi^6 - 2436\xi^7 + 4830\xi^8 - 2020\xi^9 + 282\xi^{10})$
1,2,0,1	$\frac{1}{103488000}(287097\xi^2 + 50909\xi^3 - 3322935\xi^4 + 13334013\xi^5 - 23867382\xi^6 + 17999586\xi^7 + 241395\xi^8 - 9606905\xi^9 + 6564712\xi^{10} - 1887900\xi^{11} + 207410\xi^{12})$
2,0,1,0	$\frac{1}{576576000}(82713\xi^2 - 68703\xi^3 + 930930\xi^4 - 4510506\xi^5 + 7261254\xi^6 - 2250534\xi^7 - 6091800\xi^8 + 6380660\xi^9 - 586014\xi^{10} - 2102100\xi^{11} + 1139320\xi^{12} - 185220\xi^{13})$

(continued on next page)

(*continued*)

Indices i,j,k,l	$y_{i,j,k,l}(\xi)$
2,0,1,1	$\frac{1}{484323840000}(-11115675\xi^2+6478559\xi^3-83699490\xi^4+337930950\xi^5-121705584\xi^6-1098861192\xi^7+1766739975\xi^8-$ $-389108005\xi^9-1212340558\xi^{10}+1026785760\xi^{11}-$ $-63843780\xi^{12}-263069520\xi^{13}+123680400\xi^{14}-17871840\xi^{15})$
2,1,0,0	$\frac{1}{96096000}(191505\xi^2-53461\xi^3-1471470\xi^4+4210206\xi^5-4450446\xi^6-$ $-462462\xi^7+4611750\xi^8-$ $-2882880\xi^9-462462\xi^{10}+1173900\xi^{11}-465920\xi^{12}+61740\xi^{13})$
2,1,0,1	$\frac{1}{80720640000}(-15900057\xi^2+3969801\xi^3+32023950\xi^4+168541254\xi^5-$ $-462462\xi^7+4611750\xi^8-831670125\xi^9+1031573686\xi^{10}-$ $-275129400\xi^{11}-216301540\xi^{12}+187211640\xi^{13}-55038000\xi^{14}+5957280\xi^{15})$
3,0,0,0	$\frac{1}{11531520000}(-185145\xi^2+156633\xi^3+1801800\xi^4+9993984\xi^5-$ $-18270252\xi^6+6333756\xi^7+21282690\xi^8-26137540\xi^9+894894\xi^{10}+$ $+16325400\xi^{11}-9529520\xi^{12}-1040760\xi^{13}+2934000\xi^{14}-1092960\xi^{15}+136620\xi^{16})$
3,0,0,1	$\frac{1}{82335052800000}(191571816\xi^2-124610818\xi^3+1208486055\xi^4-5427674133\xi^5+$ $+2251042794\xi^6+21120717618\xi^7-38227608705\xi^8+8984040065\xi^9+$ $+36296478218\xi^{10}-35275312800\xi^{11}-32316830\xi^{12}+16830129540\xi^{13}-$ $-8641542000\xi^{14}-312789120\xi^{15}+1654159500\xi^{16}-556617600\xi^{17}+61846400\xi^{18})$

References

Andzane, J., Petkov, N., Livshits, A.I., et al., 2009. Two-terminal nanoelectromechanical devices based on germanium nanowires. Nano Lett. 9, 1824–1829.

Andzane, J., Prikulis, J., Dvorsek, D., et al., 2010. Two-terminal nanoelectromechanical bistable switches based on molybdenum–sulfur–iodine molecular wire bundles. Nanotechnology 21, 125706.

Andzane, J., Meija, R., Livshits, A.I., et al., 2013. An AC-assisted single-nanowire electromechanical switch. J. Mater Chem. C 1, 7134–7138. http://dx.doi.org/10.1039/C3TC31240B.

Chen, C.Q., Shi, Y., Zhang, Y.S., et al., 2006. Size dependence of Young's modulus in ZnO nanowires. Phys. Rev. Lett. 96, 75505.

Chen, Z., Tong, L., Wu, Z., Liu, Z., 2008. Fabrication of electromechanical switch using interconnected single-walled carbon nanotubes. Appl. Phys. Lett. 92, 103116.

Holmes, J.D., Lyons, D.M., Ziegler, K.J., 2003. Supercritical fluid synthesis of metal and semiconductor nanomaterials. Chem. Eur. J. 9, 2144–2150.

Hwang, H.J., Kang, J.W., 2005. Carbon-nanotube-based nanoelectromechanical switch. Phys. E Low-dimen. Syst. Nanostruct. 27, 163–175.

Jang, J.E., Cha, S.N., Choi, Y., et al., 2005. Nanoelectromechanical switches with vertically aligned carbon nanotubes. Appl. Phys. Lett. 87, 163114.

Jang, J.E., Cha, S.N., Choi, Y.J., et al., 2008. Nanoscale memory cell based on a nanoelectromechanical switched capacitor. Nat. Nanotechnol. 3, 26–30.

Jang, W.W., Lee, J.O., Yoon, J.-B., et al., 2008. Fabrication and characterization of a nanoelectromechanical switch with 15-nm-thick suspension air gap. Appl. Phys. Lett. 92, 103110.

Jasulaneca, L., Meija, R., Livshits, A.I., et al., 2016. Determination of Young's modulus of Sb2S3 nanowires by in situ resonance and bending methods. Beilstein J. Nanotechnol. 7, 278–283.

Ke, C., Espinosa, H.D., 2006. In situ electron microscopy electromechanical characterization of a bistable NEMS device. Small 2, 1484–1489.

Kim, P., Lieber, C.M., 1999. Nanotube nanotweezers. Science 286, 2148–2150.

Kinaret, J.M., Nord, T., Viefers, S., 2003. A carbon-nanotube-based nanorelay. Appl. Phys. Lett. 82, 1287–1289.

Kosmaca, J., Jasulaneca, L., Meija, R., et al., 2017. Young's modulus and indirect morphological analysis of Bi2Se3 nanoribbons by resonance measurements. Nanotechnology 28, 325701.

Landau, L.D., Livshitz, E.M., 2007. Teoriya Uprugosti. Fizmatlit, Moscow.

Lee, S.W., Lee, D.S., Morjan, R.E., et al., 2004. A three-terminal carbon nanorelay. Nano Lett. 4, 2027–2030.

Loh, O.Y., Espinosa, H.D., 2012. Nanoelectromechanical contact switches. Nat. Nanotechnol. 7, 283–295.

Meija, R., Kosmaca, J., Jasulaneca, L., et al., 2015. Electric current induced modification of germanium nanowire NEM switch contact. Nanotechnology 26, 195503.

Meija, R., Signetti, S., Schuchardt, A., et al., 2017. Nanomechanics of individual aerographite tetrapods. Nat. Commun. 8, 14982.

Miller, R.E., Shenoy, V.B., 2000. Size-dependent elastic properties of nanosized structural elements. Nanotechnology 11, 139.

Qin, Q., Xu, F., Cao, Y., et al., 2012. Measuring true Young's Modulus of a cantilevered nanowire: effect of clamping on resonance frequency. Small 8, 2571–2576.

Rueckes, T., Kim, K., Joselevich, E., et al., 2000. Carbon nanotube-based nonvolatile random access memory for molecular computing. Science 289, 94–97.

Timoshenko, S., 1953. History of Strength of Materials: with a Brief Account of the History of Theory of Elasticity and Theory of Structures. McGraw-Hill, New York.

Viasnoff, V., Meller, A., Isambert, H., 2006. DNA nanomechanical switches under folding kinetics control. Nano Lett. 6, 101–104.

Villain, P., Beauchamp, P., Badawi, K.F., et al., 2004. Atomistic calculation of size effects on elastic coefficients in nanometre-sized tungsten layers and wires. Scr. Mater. 50, 1247–1251.

Wang, K.F., Wang, B.L., 2015. A general model for nano-cantilever switches with consideration of surface effects and nonlinear curvature. Phys. E Low-dimen. Syst. Nanostruct. 66, 197–208.

Wang, Y., Song, J., Xiao, J., 2013. Surface effects on in-plane buckling of nanowires on elastomeric substrates. J. Phys. D Appl. Phys. 46, 125309.

Wolfram Research I, 2015. Mathematica. Version 10. Wolfram Research, Inc., Champaign, Illinois.

Zhang, Y., Zhuo, L.J., Zhao, H.S., 2013. Determining the effects of surface elasticity and surface stress by measuring the shifts of resonant frequencies. In: Proc. R. Soc. London A Math. Phys. Eng. Sci, p. 20130449.

Ziegler, K.J., Lyons, D.M., Holmes, J.D., et al., 2004. Bistable nanoelectromechanical devices. Appl. Phys. Lett. 84, 4074–4076.

Paper XI

IOP Publishing

Nanotechnology

Nanotechnology **28** (2017) 325701 (6pp)

https://doi.org/10.1088/1361-6528/aa79cd

Young's modulus and indirect morphological analysis of Bi_2Se_3 nanoribbons by resonance measurements

J Kosmaca[1], L Jasulaneca[1], R Meija[1], J Andzane[1], M Romanova[1], G Kunakova[1] and D Erts[1,2]

[1] Institute of Chemical Physics, University of Latvia, 19 Raina blvd., Riga, LV-1586, Latvia
[2] Department of Chemistry, University of Latvia, 19 Raina blvd., Riga, LV-1586, Latvia

E-mail: donats.erts@lu.lv

Received 10 March 2017, revised 22 May 2017
Accepted for publication 15 June 2017
Published 18 July 2017

Abstract

An electrostatically induced resonance behaviour of individual topological insulator Bi_2Se_3 nanoribbons grown by a catalyst free vapour–solid synthesis was studied *in situ* by scanning electron microscopy. It was demonstrated that the relation between the resonant frequencies of vibrations in orthogonal planes can be applied to distinguish the nanoribbons with rectangular cross-sections from the nanoribbons having step-like morphology (terraces). The average Young's modulus of the Bi_2Se_3 nanoribbons with rectangular cross-sections was found to be 44 ± 4 GPa.

Supplementary material for this article is available online

Keywords: bismuth selenide nanoribbon, resonance, *in situ*, terraces, Young's modulus, topological insulator

(Some figures may appear in colour only in the online journal)

1. Introduction

Bismuth selenide (Bi_2Se_3) is a narrow-gap semiconductor commonly considered for applications as a thermoelectric material [1–3]. More recently, Bi_2Se_3 has been recognized as a 3D bulk topological insulator possessing protected conducting states on the surface and insulating bulk states in the interior [4, 5]. This behavior can be exploited in many fields, for example, in spintronics [6] and magnetoelectric applications [7]. Significantly, the topological behaviour of Bi_2Se_3 can be tuned by a mechanical strain [8]. This has led to investigation of the mechanical properties of the material, both theoretically [9, 10] and experimentally for a bulk crystal [11, 12] and nanostructured 2D nanosheets [13].

Bi_2Se_3 nanoribbons are 1D nanostructures attractive for both increasing device thermoelectric efficiency and for exploring topological characteristics [3–5], moreover, thanks to their shape and elasticity, these nanoribbons are promising for applications in nanoelectromechanical systems (NEMS) and sensors as active elements [14]. For NEMS switches, high mechanical stiffness yields a fast and robust switching behaviour [15]. For Bi_2Se_3, previous reports have shown differences in the Young's modulus for 2D nanosheets and the bulk material [13]. However, to the best of our knowledge the mechanical properties of 1D Bi_2Se_3 nanoribbons have yet to be studied.

Mechanical resonance measurements are an efficient technique for characterization of the mechanical properties of 1D nanostructures, and have been previously applied for nanotubes [16], nanowires [17, 18], and nanobelts [19]. In this method, the relation between the resonant frequency and the material properties, geometry and boundary conditions is used to describe the vibrational behaviour and determine the Young's modulus of the nanostructures. Typically, the resonance measurements are performed by *in situ* electron microscopy [16, 17, 19], which enables size and shape characterization along with the real-time mechanical response observation of the nanostructure.

Recent reports have shown that Bi_2Se_3 nanoribbons in some cases exhibit step-like morphology, i.e. terraces located

 © 2017 IOP Publishing Ltd Printed in the UK

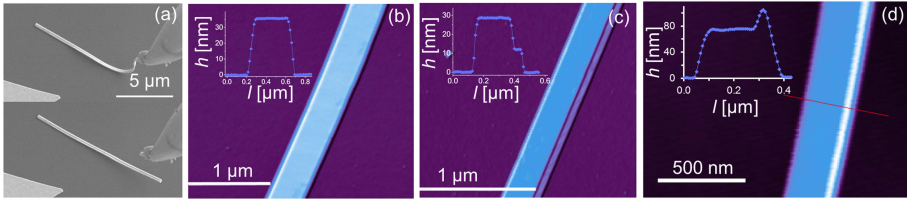

Figure 1. (a) Transfer of nanoribbon from Au tip to substrate: nanoribbon is lying on the substrate while still clamped to Au tip in the top panel and fully detached from the tip in the bottom panel; AFM images and corresponding thickness profiles for a nanoribbon with a rectangular cross-section (b) and nanoribbons with terraces (c), (d).

near the edges of their facets [5, 20]. Direct resolution of these terraces by scanning electron microscopy (SEM) is challenging. Alternatively, the terraces can be measured by atomic force microscopy (AFM), which requires nanoribbon transfer to a flat surface and thus is inconvenient for characterization of vertically aligned nanoribbons.

In this work, the influence of terraces on the resonance of Bi_2Se_3 nanoribbons is explored. A novel method is proposed for indirect cross-section profile characterization. It is based on resonance measurements that can be performed by *in situ* SEM. The experimental Young's modulus of Bi_2Se_3 nanoribbons is determined and compared to that of bulk crystal.

2. Methods

Bismuth selenide nanoribbons were synthesized on a glass substrate with a two-stage catalyst free vapor-solid synthesis technique reported previously by Andzane *et al* [5].

The size and shape of individual Bi_2Se_3 nanoribbons were studied *in situ* by SEM (Hitachi S-4800 equipped with a Smaract 13D nanomanipulation system) and AFM (Asylum Research MFP-3D using Olympus AC160TS AFM tips, and Bruker Dimension ICON SPM using NSG10 and NSC15 AFM tips).

For the characterization *in situ* by SEM, electrochemically etched gold tips were used to select and detach individual nanoribbons from the glass substrate. Next, these nanoribbons were clamped near the tip apexes with platinum strips deposited by the e-beam deposition technique [21] in SEM (Tescan Lyra). The clamp size exceeded the width of the nanoribbon to ensure that the clamped end of the nanoribbon was fixed [22]. To determine the dimensions of the clamped nanoribbons, they were rotated in the SEM chamber with a micromotor (Faulhaber ADM0620) and examined from different viewing angles. The lengths of the clamped nanoribbons were measured as the distances from the edge of the clamping strip to the free end of the nanoribbon. Special attention was paid to check uniformity of width and thickness along the length of the nanoribbons in order to avoid cross-section shape perturbations, that may affect nanostructure resonant frequency [23, 24].

AFM measurements of the morphology were performed for individual nanoribbons. The nanoribbons were mechanically transferred to a flat Si/SiO_2 substrate directly from the glass substrate, as well as from the Au tips (figure 1(a)). The transfer procedure for the clamped nanoribbons is practically challenging, as the nanoribbon must be detached from the Au tip without damaging its structure and placed flat on the substrate.

Vibrational analysis of individual free-standing Bi_2Se_3 nanoribbons clamped to Au tips was performed *in situ* inside the SEM. To determine the resonant frequencies of the nanoribbons, their mechanical vibrations were excited electrostatically. The electrical AC signal was powered by an Agilent N9310A RF Signal Generator and a Hung Chang 8205A Sweep Function Generator. The DC signal was powered by Keithley 6430 and 6487 Voltage Sources. The combined AC+DC signal was monitored with a Textronix TDS-1012 oscilloscope. The resonant frequencies of the nanoribbons were detected by observation of their vibrational amplitude, direction and shape dependence on the excitation signal [16, 17, 25].

3. Results and discussion

As-synthesized nanoribbons had single-crystalline structure with growth in [110] direction resulting in their rectangular cross-sections [5, 26]. From SEM measurements, these nanoribbons were found to have lengths 5–50 μm, widths 70–500 nm and thicknesses 30–100 nm. Thickness profiles obtained for 79 nanoribbons by AFM indicated that 57 have smooth upper facets (figure 1(b)) and 22 of them have terrace-like features (figures 1(c), (d)). Since the AFM analysis explores only the upper of the two surfaces, we assume the proportion of the terraced facets can be doubled, estimated as 56%. The widths of the terraces were in range of 30–200 nm and thicknesses up to 34 nm.

The vibrational analysis performed *in situ* inside the SEM for relatively long (8–32 μm), straight nanoribbons, showed that their resonant vibrations occur in two orthogonal planes (figures 2(a), (b)) at the different frequencies f_1 and f_2, as expected for rectangular cross-section beams. A SEM image of a typical nanoribbon clamped to Au tip and its resonance in two directions is illustrated in figure 2(b). Its resonant frequencies $f_1 = 53.3$ kHz and $f_2 = 106$ kHz, and the quality factor $Q \approx 500$ were determined from Lorentzian fits of the vibration amplitude-frequency diagrams (figure 2(b)).

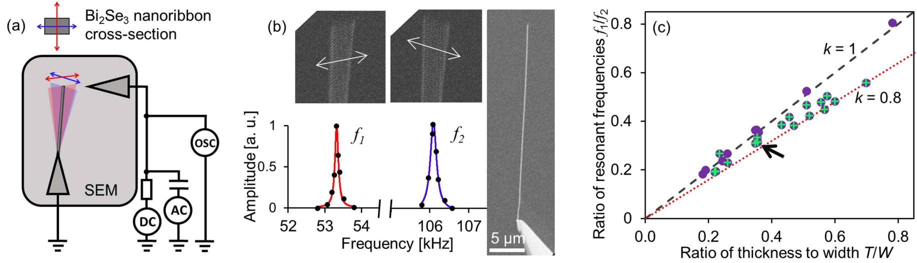

Figure 2. (a) Setup for the excitation and observation of the mechanical vibrations of the nanoribbon. The indicative arrows distinguish directions for the resonant vibrations of the nanoribbon in two orthogonal planes; (b) SEM image of Bi_2Se_3 nanoribbon with length $L = 28\ \mu$m, thickness $T = 108$ nm and width $W = 188$ nm (#19 in table S1 in the supplementary) clamped to an Au tip, its resonant vibrations in two directions (indicative arrows are added for clarity) and corresponding vibration amplitude-frequency diagrams for the resonance at f_1 and f_2; (c) ratio of the resonant frequencies versus ratio of thickness to width for the Bi_2Se_3 nanoribbons. The lines with the slope coefficients $k = 1$ (dashed black line) and $k = 0.8$ (dotted red line) are added for clarity. The experimental data points are marked with circles; crossed circles represent measurements with $\Delta k > 5\%$. Experimental point for nanoribbon investigated by *in situ* SEM and following AFM analysis is marked by an arrow.

The measured dimensions and the resonant frequencies obtained in the resonance experiments for 27 nanoribbons are summarized in table S1 available online at stacks.iop.org/NANO/28/325701/mmedia in the supplementary.

The relation between the nanoribbon dimensions and its resonant frequencies can be described by using the Euler–Bernoulli analysis formulae [27]

$$f_1 = \frac{\beta^2}{2\pi L^2}\sqrt{\frac{EI_1}{\rho A}} \text{ and } f_2 = \frac{\beta^2}{2\pi L^2}\sqrt{\frac{EI_2}{\rho A}}, \tag{1}$$

where E is the Young's modulus, ρ is the mass density, L is nanoribbon length, A is the cross-section area, I is the moment of inertia of the area about the principal axis, and $\beta = 1.875$ is the characteristic constant for the first fundamental mode of a single-clamped beam [27]. For the nanoribbons of the measured dimensions, the nanoscale size and surface effects can be assumed to have only a minor influence on their resonant frequencies [28, 29].

The corresponding area moments of inertia I_1 and I_2 for a rectangular cross-section with thickness T and width W are

$$I_1 = \frac{T^3W}{12} \text{ and } I_2 = \frac{TW^3}{12}. \tag{2}$$

We assume that the Young's modulus and the boundary conditions remain the same for the vibrations in two planes, which allows extracting direct correlation between the resonant frequencies and the area moments of inertia. From (1) and (2) follows, that the ratio of the resonant frequencies for vibrations in orthogonal planes f_1/f_2 is proportional to the ratio of thickness and width of a nanoribbon

$$\frac{f_1}{f_2} = \sqrt{\frac{I_1}{I_2}} = \frac{T}{W}. \tag{3}$$

A large part of the nanoribbons characterized by *in situ* SEM exhibit f_1/f_2 that match their T/W, aligning on a straight line with a slope coefficient $k = 1$ (figure 2(c), black dashed line), as expected for nanoribbons with rectangular cross-section. At the same time, for a significant proportion of the characterized nanoribbons, the frequency f_1/f_2 and thickness to width ratios T/W are not equal (table S1 in the supplementary). They are better characterized by $k < 1$, where

$$k = \frac{(f_1/f_2)}{(T/W)}, \tag{3a}$$

and the difference from $k = 1$, Δk, for individual nanoribbons can reach up to 21%. These differences may be related to the presence of terraces for the corresponding nanoribbons which thus would need their area moments of inertia to be expressed other than (2), consequently their ratios of resonance frequencies are expected to differ from *T/W*.

Calculation of the centroids and area moments of inertia performed analytically [30] showed that the presence of a cut-out (terrace) in the cross-section shifts the position of the centroid C, which is center of mass for the area A, and changes the directions of the principal axes (figure 3(a)). Area moments of inertia I_1 and I_2, describing vibrational behaviour of nanoribbons with terraces, are more complex compared to those given by (2) for the beam with rectangular cross-section, and can be expressed as follows:

$$I_1 = \frac{1}{2}(I_1' + I_2') - \sqrt{\frac{1}{4}(I_1' - I_2')^2 + (I_{12}')^2}, \tag{4}$$

$$I_2 = \frac{1}{2}(I_1' + I_2') + \sqrt{\frac{1}{4}(I_1' - I_2')^2 + (I_{12}')^2},$$

where I_1' and I_2' are the area moments of inertia and I_{12}' is the product of inertia of the area about the centroid axis $x_c y_c$ (figure 3(a)). The full derivations for I_1', I_2' and I_{12}' can be simplified, with the substitutions $t/T = \hat{t}$ and $w/W = \hat{w}$, denoting the relative thickness and relative width of a terrace, and expressed as

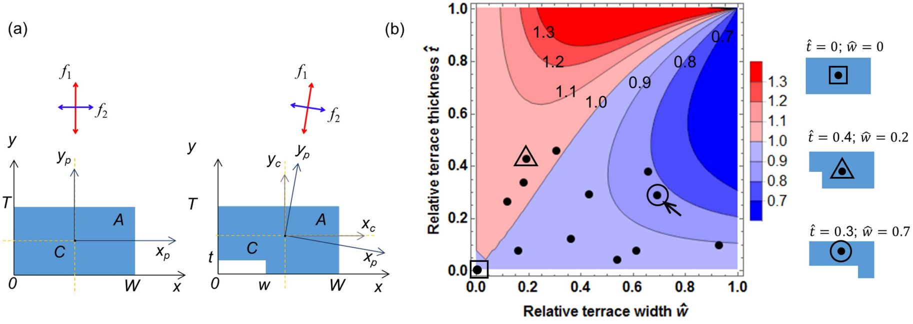

Figure 3. (a) Beam cross-sections and directions of the resonant vibrations. The resonant vibrations at f_1 and f_2 occur in direction of the principal axes $x_p y_p$, which begin at the centroid *C*. For a rectangular cross-section beam with width *W*, thickness *T*, and cross-sectional area $A = TW$, the principal axes $x_p y_p$ are aligned parallel to the reference axis *xy*. For terrace-affected beam with total cross-sectional area $A = TW - tw$, where *w* and *t* denote the width and thickness of the terrace respectively, the centroid *C* is shifted, and the principal axes $x_p y_p$ are rotated about the reference axes *xy*; (b) dependence of coefficient *k* on relative terrace dimensions $\hat{t}$ and $\hat{w}$. Isolines and colours correspond to different *k* values from 0.7 to 1.3. The coordinates denoting $\hat{t}$ and $\hat{w}$ for the terraces measured with AFM are marked with black dots. The nanoribbon cross-sections are represented schematically for the selected coordinates (square, triangle, circle). Experimental point for nanoribbon investigated by *in situ* SEM and following AFM analysis is marked by an arrow.

$$I_1' = \frac{T^3W}{12} \cdot \frac{1 - 4\hat{t}\hat{w} + 6\hat{t}^2\hat{w} - 4\hat{t}^3\hat{w} + \hat{t}^4\hat{w}^2}{1 - \hat{t}\hat{w}},$$
$$I_2' = \frac{TW^3}{12} \cdot \frac{1 - 4\hat{t}\hat{w} + 6\hat{t}\hat{w}^2 - 4\hat{t}\hat{w}^3 + \hat{t}^2\hat{w}^4}{1 - \hat{t}\hat{w}}, \qquad (5)$$
$$I_{12}' = -\frac{T^2W^2}{4} \cdot \frac{\hat{t}\hat{w}(1 - \hat{t})(1 - \hat{w})}{1 - \hat{t}\hat{w}}.$$

The ratio of the two resonant frequencies f_1/f_2 for a nanoribbon with a terrace is equal to the ratio of the area moments of inertia $\sqrt{I_1/I_2}$, given by (4) and (5). Therefore, the coefficient *k* from (3) can be expressed as

$$k = \frac{\sqrt{I_1/I_2}}{(T/W)}. \qquad (3b)$$

A plot in figure 3(b) illustrates how the value of the coefficient *k* given by (3*b*) changes with respect to the relative terrace dimensions $\hat{t}$ and $\hat{w}$. Black dots on the *k* plot represent relative dimensions of terraces for typical nanoribbons, measured by the AFM. In most of the cases these terraces would result in *k* values smaller than one (figure 3(b)). This is similar to *in situ* SEM data shown in figure 2(c), where downshifted ratios of the resonant frequencies f_1/f_2 result in values of $k < 1$.

Conformity of AFM data with the *in situ* SEM resonance data was investigated for the example of a terraced nanoribbon, that showed a uniform cross-section profile along the full length (figures 1(a), (d)) with the dimensions $T = 103$ nm, $W = 290$ nm, $t = 30$ nm, $w = 200$ nm (figure 1(d)) and the resonant frequencies $f_1 = 267$ kHz, $f_2 = 846$ kHz (#17 in table S1 in the supplementary). The coefficient *k* value for the nanoribbon, calculated with (3*a*) from the resonant frequencies (figure 2(c), arrowed circle) and also with (3*b*) from the thickness profile (figure 3(b), arrowed dot), was convincingly smaller than one. In the case that there are terraces on both the top and the bottom facets of the nanoribbon, the coefficient *k* values are calculated to remain smaller than one, not exceeding a variation within ±15%, depending on the geometry of the second terrace. The similar results obtained from SEM and AFM data suggest that the terraced nanoribbons can be revealed from their ratio of the resonant frequencies measured *in situ* SEM. Thereafter, the measurement data in figure 2(c) indicate which of the *in situ* characterized nanoribbons have terraces, and can be grouped for more accurate determination of nanoribbons Young's modulus by the resonance method.

The Young's modulus of nanoribbons *E* can be extracted from the sound velocity in a material, given by $\sqrt{E/\rho}$ in (1) [18, 31]. Its average value can be determined graphically from a slope of a linear fit for the resonant frequencies plotted versus beam dimensions, which for the rectangular cross-section nanoribbons are related as:

$$F_1 = T \cdot \sqrt{\frac{E}{\rho}} \text{ and } F_2 = W \cdot \sqrt{\frac{E}{\rho}}, \qquad (6)$$

where $F_1 = \frac{4\sqrt{3}\pi f_1 L^2}{\beta^2}$ and $F_2 = \frac{4\sqrt{3}\pi f_2 L^2}{\beta^2}$.

Nanoribbons with $\Delta k \leqslant 5\%$ (figure 2(c), filled circles) were selected for the determination of Young's modulus as suitable for the rectangular model, within the measurement precision of the *in situ* experiments. From the graphical representation of (6), where F_1 and F_2 are plotted versus thickness *T* and width *W*, respectively, it can be seen that the experimental data are well described by the linear fit $y = gx$ (figure 4), meaning the Young's modulus of the nanoribbons is not dependent on their cross-sectional dimensions. The average Young's modulus of 44 ± 4 GPa was extracted from the slope coefficient $g = (2.4 \pm 0.1) \times 10^3$ of the fitted linear function (figure 4, black dashed line), for a mass density of 7680 kg m^{-3} for bulk Bi_2Se_3 crystal [32, 33]. This obtained

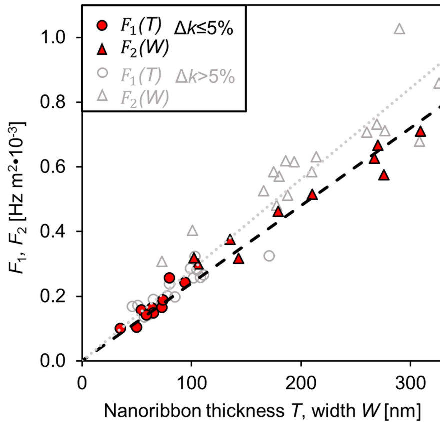

Figure 4. F_1 and F_2 versus the nanoribbon thickness T (filled circles) and width W (filled triangles), with a linear fit function $y = gx$ (black dashed line) for the nanoribbons with $\Delta k \leqslant 5\%$. The hollow grey markers for the nanoribbons with $\Delta k > 5\%$ are overlaid for comparison.

value for the Young's modulus of Bi_2Se_3 nanoribbons is significantly higher than the experimental values of 18–25 GPa for 2D nanosheets [13]. However, it is in close agreement with the experimental value of 47 ± 9 GPa for the Bi_2Se_3 bulk crystal [12], and with the values of 41–48 GPa that can be calculated from the previously reported Bi_2Se_3 average sound velocity (2.3–2.5) × 10^3 m s^{-1} [10, 32]. For nanoribbons of the measured dimensions, the agreement with the bulk values is not surprising, and confirms that they are of good quality, since previous studies indicated that for crystalline nanostructures pronounced scaling effects may be expected below sizes of ~30 nm [34, 35]. In general, the resonance method can be considered valid when the nanoribbons have uniform cross-sections and isotropic elasticity with negligible size-dependence [36, 37].

The average Young's modulus was estimated assuming the rectangular model in the cases where precise cross-sectional profile was not known for the nanoribbons with $\Delta k > 5\%$. In the graphical representation of the relation (6) for the nanoribbons with $\Delta k > 5\%$ (figure 4, hollow markers), however, the experimental points are more scattered than for the nanoribbons with $\Delta k \leqslant 5\%$, presumably due to their non-rectangular morphology. An overlap with the data of the $\Delta k \leqslant 5\%$ can be due to a lesser impact of terraces on $F_1(T)$ than on $F_2(W)$. The Young's modulus of these nanoribbons, calculated from the extracted linear fit coefficient $g = (2.8 \pm 0.1) \times 10^3$ (figure 4, grey dotted line) turned out to be higher than for the nanoribbons with $\Delta k \leqslant 5\%$ by more than 30%. The increase of experimentally determined Young's modulus for nanoribbons with terraces could be explained by the higher surface-to-volume ratio [38].

4. Conclusions

The mechanical resonance behaviour of individual Bi_2Se_3 nanoribbons was studied by *in situ* SEM and interpreted using an analytical model for vibrations of thin beams. The experimentally determined Young's modulus of 44 ± 4 GPa for the rectangular cross-section nanoribbons was close to the value previously reported for bulk crystal and did not exhibit dependence on the cross-sectional dimensions. It was estimated to be higher for the terraced nanoribbons, which may indicate that the Young's modulus of Bi_2Se_3 nanoribbons is morphology-dependent. The relatively high Young's modulus makes Bi_2Se_3 nanoribbons suitable candidates for applications in NEMS.

It was demonstrated that shifts of the resonant frequencies ratios can be used to distinguish the nanoribbons with terraces from the nanoribbons with rectangular cross-section during *in situ* SEM experiments, when direct determination of nanoribbons' morphology is difficult due to the limitations of the experimental setup. The proposed resonance based method enables morphological characterization of free-standing nanostructures. In contrast to traditional methods it does not require their transfer to a substrate, which simplifies the processing of nanostructure based devices. Such an approach can be useful for quality control during precise engineering of NEMS, for example, configuring resonance controlled NEMS switches [15], as well as the investigation of nanocontacts using resonance methods [21].

Acknowledgments

This work was supported by Latvian Council of Science project No. 549/2012, University of Latvia project No. AAP2016/B043, and No. ZD2010/AZ19. The authors are thankful to M Baitimirova and G Petersons for synthesizing Bi_2Se_3 nanoribbon samples, and to A I Livshits for useful discussions about the theory of the beam vibrations. J K is grateful to T Yager for careful reading of the manuscript.

References

[1] Sun Y, Cheng H, Gao S, Liu Q, Sun Z, Xiao C, Wu C, Wei S and Xie Y 2012 Atomically thick bismuth selenide freestanding single layers achieving enhanced thermoelectric energy harvesting *J. Am. Chem. Soc.* **134** 20294–7

[2] Kadel K, Kumari L, Li W Z, Huang J Y and Provencio P P 2010 Synthesis and thermoelectric properties of Bi_2Se_3 nanostructures *Nanoscale Res. Lett.* **6** 57

[3] Tang H, Wang X, Xiong Y, Zhao Y, Zhang Y, Zhang Y, Yang J and Xu D 2015 Thermoelectric characterization of individual bismuth selenide topological insulator nanoribbons *Nanoscale* **7** 6683–90

[4] Xia Y *et al* 2009 Observation of a large-gap topological-insulator class with a single Dirac cone on the surface *Nat. Phys.* **5** 398–402

[5] Andzane J, Kunakova G, Charpentier S, Hrkac V, Kienle L, Baitimirova M, Bauch T, Lombardi F and Erts D 2015 Catalyst-free vapour–solid technique for deposition of

Bi_2Te_3 and Bi_2Se_3 nanowires/nanobelts with topological insulator properties *Nanoscale* **7** 15935–44
[6] Pesin D and MacDonald A H 2012 Spintronics and pseudospintronics in graphene and topological insulators *Nat. Mater.* **11** 409–16
[7] LaForge A D, Frenzel A, Pursley B C, Lin T, Liu X, Shi J and Basov D N 2010 Optical characterization of Bi_2Se_3 in a magnetic field: infrared evidence for magnetoelectric coupling in a topological insulator material *Phys. Rev.* B **81** 125120
[8] Young S M, Chowdhury S, Walter E J, Mele E J, Kane C L and Rappe A M 2011 Theoretical investigation of the evolution of the topological phase of Bi_2Se_3 under mechanical strain *Phys. Rev.* B **84** 85106
[9] Gao X, Zhou M, Cheng Y and Ji G 2016 First-principles study of structural, elastic, electronic and thermodynamic properties of topological insulator Bi_2Se_3 under pressure *Phil. Mag.* **96** 208–22
[10] Koc H, Ozisik H, Deligöz E, Mamedov A M and Ozbay E 2014 Mechanical, electronic, and optical properties of Bi_2S_3 and Bi_2Se_3 compounds: first principle investigations *J. Mol. Model.* **20** 1–12
[11] Vilaplana R *et al* 2011 Structural and vibrational study of Bi_2Se_3 under high pressure *Phys. Rev.* B **84** 184110
[12] Cavallin A, Sevriuk V, Fischer K N, Manna S, Ouazi S, Ellguth M, Tusche C, Meyerheim H L, Sander D and Kirschner J 2016 Preparation and characterization of Bi_2Se_3 (0001) and of epitaxial FeSe nanocrystals on Bi_2Se_3 (0001) *Surf. Sci.* **646** 72–82
[13] Yan H, Vajner C, Kuhlman M, Guo L, Li L, Araujo P T and Wang H-T 2016 Elastic behavior of Bi_2Se_3 2D nanosheets grown by van der Waals epitaxy *Appl. Phys. Lett.* **109** 32103
[14] Kosmaca J, Andzane J, Baitimirova M, Lombardi F and Erts D 2016 Role of nanoelectromechanical switching in the operation of nanostructured Bi_2Se_3 interlayers between conductive electrodes *ACS Appl. Mater. Interfaces* **8** 12257–62
[15] Andzane J, Meija R, Livshits A I, Prikulis J, Biswas S, Holmes J D and Erts D 2013 An AC-assisted single-nanowire electromechanical switch *J. Mater. Chem.* C **1** 7134–8
[16] Poncharal P, Wang Z L, Ugarte D and De Heer W A 1999 Electrostatic deflections and electromechanical resonances of carbon nanotubes *Science* **283** 1513–6
[17] Jasulaneca L, Meija R, Livshits A I, Prikulis J, Biswas S, Holmes J D and Erts D 2016 Determination of Young's modulus of Sb_2S_3 nanowires by *in situ* resonance and bending methods *Beilstein J. Nanotechnol.* **7** 278–83
[18] Belov M, Quitoriano N J, Sharma S, Hiebert W K, Kamins T I and Evoy S 2008 Mechanical resonance of clamped silicon nanowires measured by optical interferometry *J. Appl. Phys.* **103** 74304
[19] Bai X D, Gao P X, Wang Z L and Wang E G 2003 Dual-mode mechanical resonance of individual ZnO nanobelts *Appl. Phys. Lett.* **82** 4806
[20] Fang L, Jia Y, Miller D J, Latimer M L, Xiao Z L, Welp U, Crabtree G W and Kwok W-K 2012 Catalyst-free growth of millimeter-long topological insulator Bi_2Se_3 nanoribbons and the observation of the π-Berry phase *Nano Lett.* **12** 6164–9
[21] Meija R, Kosmaca J, Jasulaneca L, Petersons K, Biswas S, Holmes J D and Erts D 2015 Electric current induced modification of germanium nanowire NEM switch contact *Nanotechnology* **26** 195503
[22] Qin Q, Xu F, Cao Y, Ro P I and Zhu Y 2012 Measuring true Young's modulus of a cantilevered nanowire: effect of clamping on resonance frequency *Small* **8** 2571–6
[23] Guillon S, Saya D, Mazenq L, Perisanu S, Vincent P, Lazarus A, Thomas O and Nicu L 2011 Effect of non-ideal clamping shape on the resonance frequencies of silicon nanocantilevers *Nanotechnology* **22** 245501
[24] Gil-Santos E, Ramos D, Mart'/inez J, Fernández-Regúlez M, Garc'/ia R, San Paulo Á, Calleja M and Tamayo J 2010 Nanomechanical mass sensing and stiffness spectrometry based on two-dimensional vibrations of resonant nanowires *Nat. Nanotechnol.* **5** 641–5
[25] Kosmaca J, Andzane J, Prikulis J, Biswas S, Holmes J D and Erts D 2015 Application of a nanoelectromechanical mass sensor for the manipulation and characterisation of graphene and graphite flakes *Sci. Adv. Mater.* **7** 552–7
[26] Kong D, Randel J C, Peng H, Cha J J, Meister S, Lai K, Chen Y, Shen Z-X, Manoharan H C and Cui Y 2009 Topological insulator nanowires and nanoribbons *Nano Lett.* **10** 329–33
[27] Meirovitch L 1986 *Elements of Vibration Analysis* (New York: McGraw-Hill)
[28] Hosseini-Hashemi S, Fakher M and Nazemnezhad R 2013 Surface effects on free vibration analysis of nanobeams using nonlocal elasticity: a comparison between Euler–Bernoulli and Timoshenko *J. Solid Mech.* **5** 290–304
[29] Ilic B, Krylov S and Craighead H G 2010 Young's modulus and density measurements of thin atomic layer deposited films using resonant nanomechanics *J. Appl. Phys.* **108** 44317
[30] Marghitu D B and Dupac M 2012 Centroids and moments of inertia *Advanced Dynamics* (New York: Springer) pp 73–141
[31] Yang Y T, Ekinci K L, Huang X M H, Schiavone L M, Roukes M L, Zorman C A and Mehregany M 2001 Monocrystalline silicon carbide nanoelectromechanical systems *Appl. Phys. Lett.* **78** 162
[32] Madelung O 2004 *Semiconductors: Data Handbook* (Berlin: Springer)
[33] Giraud S, Kundu A and Egger R 2012 Electron-phonon scattering in topological insulator thin films *Phys. Rev.* B **85** 35441
[34] Miller R E and Shenoy V B 2000 Size-dependent elastic properties of nanosized structural elements *Nanotechnology* **11** 139
[35] Villain P, Beauchamp P, Badawi K F, Goudeau P and Renault P-O 2004 Atomistic calculation of size effects on elastic coefficients in nanometre-sized tungsten layers and wires *Scr. Mater.* **50** 1247–51
[36] Li X, Ono T, Wang Y and Esashi M 2003 Ultrathin single-crystalline-silicon cantilever resonators: fabrication technology and significant specimen size effect on Young's modulus *Appl. Phys. Lett.* **83** 3081–3
[37] Nilsson S G, Borrise X and Montelius L 2004 Size effect on Young's modulus of thin chromium cantilevers *Appl. Phys. Lett.* **85** 3555
[38] Cuenot S, Frétigny C, Demoustier-Champagne S and Nysten B 2004 Surface tension effect on the mechanical properties of nanomaterials measured by atomic force microscopy *Phys. Rev.* B **69** 165410